New fortuitous materials for luminescence dosimetry following radiological emergencies

LILY BOSSIN

New fortuitous materials for luminescence dosimetry following radiological emergencies

Lily Bossin

A Thesis presented for the degree of

Doctor of Philosophy

Department of Physics
Department of Archaeology
University of Durham
England

December 2018

New fortuitous materials for luminescence dosimetry following radiological emergencies

Lily Bossin

Submitted for the degree of Doctor of Philosophy

December 2018

Abstract

The effective management of radiological emergencies where members of the public not carrying conventional dosimeter have been exposed to doses of ionising radiation requires individual dose estimates to support medical triage. Biological and physical methods have been developed to address this issue. New materials and techniques have been sought to reinforce preparedness for such emergencies. Alternative materials, such as clothing, shoes, paper, plastic items, nail polish or banknotes were investigated using thermoluminescence (TL) and optically stimulated luminescence (OSL). Most of the materials and fabric tested exhibited either no detectable response to dose using luminescence technique, or a weak response yielding detection limits above 2 Gy, with the exceptions of a blue polyester fabric responding to infra-red stimulated luminescence (IRSL) and some types of polymer - based fabric that were found to have luminescence favourable characteristics for short - term dosimetry and particularly those containing mineral fillers. The most promising were fabrics containing calcium carbonate fillers, where the TL response to β radiations was measured with a detection limit as low as 4 mGy, and a relatively low native signal in the region of interest ($\leq$ 200 °C). The fading was found to be slower for samples stored at -15 °C compared with samples stored at ambient temperature. A blind test was carried out and confirmed the potential of bags containing calcium carbonate fillers to provide reliable dose estimate for radiological triage. Furthermore, the TL signal of calcium carbonate fillers contained in the fabric of bags offers several advantages for accident dosimetry compared with other methods, such as a rapid dose assessment, the low cost value of the material and availability, and the possibility to map radiological doses is the fabric covers sufficient surface.

Contents

Declaration

The work in this thesis is based on research carried out at the Department of Physics and the Department of Archaeology, Durham University, England. No part of this thesis has been submitted elsewhere for any other degree or qualification and it is all my own work unless referenced to the contrary in the text.

Acknowledgements

I am deeply grateful to my five PhD supervisors Ian Bailiff, Ian Terry, Rick Tanner, Jon Eakins and Liz Ainsbury for giving me the opportunity to pursue a PhD, for their incredible friendly support, guidance, encouragement and patience during my PhD. Their critical inputs have helped me constantly during my PhD, both in producing results and writing up this thesis. I could not have hoped for better support and would like to thank them for their incredible implication in this project. I would also like to thank Public Health England, who supported and funded this project, for their financial support and access to their facilities in Chilton.

I would like to express my gratitude to the Medical Research Council and Mark Hill for providing access to their gamma irradiation facility on Harwell campus. I would like to thank Steve Barnard for helping out with the blind test irradiation at the MRC facility and Jayne Moquet and the cytogenetic group of Public Health England for carrying out the dicentric chromosome assay presented in the blind test. I am also indebted to Fero Ibrahimi and Effie Kouroukla of the Radiation Metrology group of Public Health England for irradiating samples and Luke Hager for sorting out the TLDs used in the blind test.

I am very thankful to Budhika Mendis and Leon Bowen of the Durham G. J. Microscopy Facility who taught me to use the scanning electron microscope and for their technical assistance and advices. I would also like to express my gratitude to Virgilio Correcher (CIEMAT) for carrying additional CL measurements in the environmental SEM. I would also to thank Kamal Bradeshany for teaching me how to use various bits of instrumentation around the archaeology department and Andy Beeby for letting me use his photoluminescence setup in the chemistry department of Durham University.

I am very grateful to the members of the Physics and Archaeology departments of Durham University for welcoming me at the start of my PhD and supporting me during this long process, and especially to my luminescence colleague Lisa Snape for her kind help and support and guiding me around the luminescence laboratory.

I would not have been able to go through this PhD without the support of my family, if it were not for their unimaginable support and understanding. To my parents, Isabelle Deplaix and Thierry Bossin for teaching me the power of education, for their unconditional love and endless encouragements, to my grandparents James and Louisette Deplaix (who provided the "blue polyester" shirt F# 3, see Chapter 8), Maurice and Janine Bossin for their unlimited care and support and to my aunt Maryline Deplaix for supporting me during my Master and keeping my feet on the ground.

I am also deeply grateful to all my friends : to Coline for her advices, support and friendship since our high school years, and for visiting me wherever I went. To Xiao, Ben and Joschka for 3 years of support during our PhDs (and enlightening pub trips). To Anthony, Aurelie, Judi and Ludivine for their support and dedication - I will not forget that you went all the way to the North-East of England just to visit me. And to all the people I met during my postgrads.

And finally to the French Republic for providing me 20 years of free education - from nursery school to Master's.

Nomenclature

α	Absorption coefficient
β	Heating rate ($^{\circ}$C.s^{-1} or K.s^{-1})
$\hat{H}$	Hamiltonian
$\hat{p}$	Momentum operator
Φ	Optical cross section
ψ	Wave function
τ	Lifetime (s)
A_m	Recombination probability of electrons (cm^{3}s^{-1})
A_n	Retrapping probability (cm^{3}s^{-1})
A_{me}	Transition probability coefficient for the recombination of an electron into the excited state to the recombination centre (cm^{3}s^{-1})
B	Trapping probability of holes in centres (cm^{3}s^{-1})
D_T	Mean organ absorbed dose
E	Activation energy (eV)
E	Effective dose
$H'(d,\Omega)$	Directional dose equivalent for angle Ω
$H^*(d)$	Ambient dose equivalent

$H_p(d,\Omega)$ Personal dose equivalent at tissue depth d for angle Ω

H_T Organ equivalent dose

K Kerma

k Boltzmann constant, $k = 8.6173303(50) \times 10^5$ eV.K^{-1}

L_C Critical level

L_D Detection limit

M Concentration of recombination centres (cm^{-3})

m Concentration of holes in recombination centres (cm^{-3})

m_v Concentration of free holes in the Valence band (cm^{-3})

N Concentration of trapping states (cm^{-3})

n Concentration of filled electrons trap (cm^{-3})

n_c Concentration of free electrons in the conduction band (cm^{-3})

n_e Concentration of electrons in excited localised states (cm^{-3})

n_g Concentration of electrons in ground states (cm^{-3})

p Probability per unit time for thermal excitation

s Frequency factor (s^{-1})

T Temperature (°C or K)

w_R Radiation weighting factor

w_T Tissue weighting factor

X Rate of production of electron-hole pairs by the excitation irradiation per unit volume per second (cm^{-3}s^{-1})

AP Anterior-posterior

ARS Acute Radiation Syndrome

CB Conduction Band

CL Cathodoluminescence

CW-OSL Continuous-wave optically stimulated luminescence

DCA Dicentric Chromosome assay

EPD Electronic Personal Dosimeters

EPR Electron Paramagnetic Resonance

ESEM Environmental Scanning Electron Microscope

EURADOS European Radiation Dosimetry Group

GUM Guide to the Expression of Uncertainty in Measurement

Gy Gray

IAEA International Atomic Energy Authority

ICRP International Commission on Radiological Protection

ICRU International Commission on Radiation Units

IRSL Infra-red stimulated luminescence

ISO Isotropic

LED Light-emitting Diode

LLAT Left-lateral

LM-OSL Linear modulated optically stimulated luminescence

MCNP Monte Carlo N Particle transport code

N_2 Nitrogen

NRC Nuclear Regulatory Commission

OSL Optically stimulated luminescence

PA Posterior-anterior

PL Photoluminescence

PMMA Poly(methyl methacrylate)

PMT Photomultiplier tube

PSTL Photo-stimulated Thermoluminescence

PTTL Phototransfer Thermoluminescence

PU Polyurethane

RBE Relative biological effectiveness

RDS Radiological Dispersal Device

ReneB Running the European Network of Biological and retrospective Physical dosimetry

RLAT Right-lateral

RT Room temperature

SEM Scanning Electron Mocroscope

Sv Sievert

TA-OSL Thermally-assisted optically stimulated luminescence

TGA Thermogravimetric Analysis

TL Thermoluminescence

TLD Thermoluminescence Dosimeter

UV Ultra-violet

VB Valence Band

XRD X-ray Diffraction

XRF X-ray Fluorescence

List of Figures

List of Tables

List of publications

Some of the work presented in this thesis has been the object of publications :

Bossin, L., Bailiff, I. K., and Terry, I. (2017). Luminescence characteristics of some common polyester fabrics: Application to emergency dosimetry. *Radiation Measurements*, 106, 436-442. (Chapter 8)

Bossin, L., Bailiff, I. K., and Terry, I. (2018). Phototransferred TL properties of alumina substrates. *Radiation Measurements*, accepted for publications. (Chapter 11)

Chapter 1

Introduction

1.1 Context

In the immediate aftermath of a large scale radiological accident, emergency workers would have to respond within 12 hours to an influx of patients suffering from traumatic injuries (including injuries from building collapse, broken glass or car accidents), burns, radiation injuries and psychological trauma, depending on the exact nature of the event (Hick et al., 2011). In addition to the rush of casualties, societies hit by such events may have to deal in the long term with contamination of radiological material, psychological trauma, environmental impact and economical consequences due to the destruction or contamination of infrastructure (Ferguson, 2009). Thus, preparedness for such events is necessary to improve a society's resilience (Coleman et al., 2015) and the response to radiological catastrophes and accidents requires specific and tailored preparedness (Hick et al. 2011; Knebel et al. 2011, see Chapter 2 for more details).

Although the controlled use of ionising radiation has many applications beneficial to the society (e.g., energy produced by nuclear power plants, medical imaging, cancer treatment, food sterilisation,...), the health and environmental effects induced by an uncontrolled use of ionising radiation and exposure to high levels of radiation can have severe consequences on the health of individuals (Fig. 1.1), including increase risk of cancer, nausea, low blood count and acute radiation syndrome that can lead to death (Domenech, 2016). Uncontrolled exposure to ionising radiation can occur in various scenarios, e.g., power plant meltdown, detonation of a nuclear device, lost or stolen radioactive material, some of which have already occurred in the past (e.g., Chernobyl, Hiroshima,

Goiania).

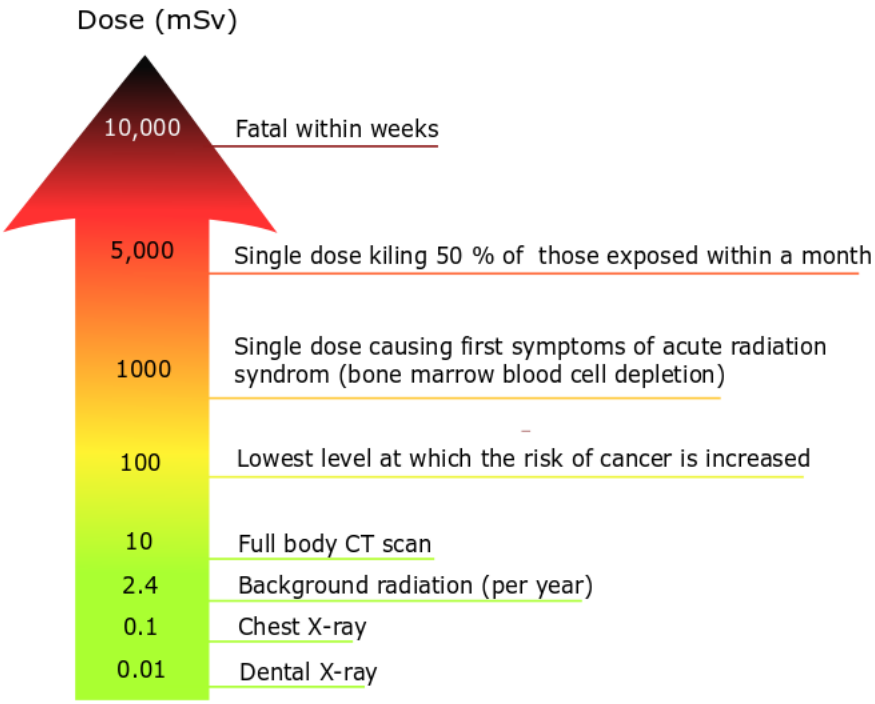

Fig. 1.1. Effect of levels of radiation dose on the human body. Data taken from https://cna.ca/issues-policy/radiation/quantifying-radiation and ICRP (2012).

Radiological incidents differ in severity; the scale developed by the International Atomic Energy Agency (IAEA) indicates that the least severe incidents (level 1) do not result in casualties, although it may result in the over-exposure of a member of the public above the statutory limits (e.g., Penly reactor, France, 2012; Tricastin Nuclear Power Plant, France, 2008). Major accidents (level 7), however, result in widespread contamination by radiological material of both people and the environment. Two level 7 accidents have occurred in recorded history (Chernobyl, 1986 and Fukushima, 2011) that both caused the death of civilians and long term contamination of the environment. A major accident can potentially expose many members of the public, who may require medical attention. Thus, the medical responders may have to deal with a large influx of patients but with scarce medical resources (Coleman et al., 2009). In preparing for an event which results in large numbers of casualties, a system of triage has been developed to target the patients that require the most urgent medical care and to preserve the scarce medical resources. The management of the triage of large scale nuclear accidents differs from other disasters partly by the nature

of the radiation injuries : unless acute exposure occurred, a physical examination of the individuals in the hours following the event may not provide a satisfactory means of triage. In radiological emergencies, the triage is performed according to the level of absorbed dose (Coleman et al., 2011) where typically, the patients with a dose above 2 Gy would require immediate medical attention, whereas patients with a dose below 2 Gy may received delayed medical care.

An estimate of the level of dose to individuals in the aftermath of a radiological accident is thus necessary to either 1) support medical treatment, where the symptoms of radiation exposure are not immediately obvious and 2) to provide a means of triage in large scale accidents.

1.2 Problem and significance

Biological and physical methods of dosimetry have been developed for dose assessment in radiological emergency situations. Biological methods include (though not exhaustively) dicentric chromosome assay, gene expression, γ-H2AX protein biomarker or fluorescence in situ hybridisation (FISH) assays (Ainsbury et al., 2010). Some of these techniques (e.g., dicentric chromosome assay) are well validated and perform well in blind tests and inter-comparison exercises (Wilkins et al., 2008). However, biological methods tend to be quite lengthy between reception of the sample and the dose estimate (50 h for the dicentric chromosome assay). Physical dosimetry mainly comprises electron paramagnetic resonance (EPR) and luminescence techniques (optically stimulated luminescence and thermoluminescence).

Physical dosimetry can either employ biological material (i.e., EPR using tooth enamel) or material found in the environment or in the possession of individuals. The EPR signal of tooth enamel offers accurate estimates of dose, although it is an invasive procedure that requires the extraction of teeth from the patients (Fattibene and Callens, 2010). Other materials investigated using EPR include sugar (Nakajima and Otsuki, 1990), cotton (Barthe et al., 1989; Trompier et al., 2010), plastic items (cards, buttons, phone cases; Sholom and Chumak 2010; Trompier et al. 2010), fingernails (Reyes et al., 2009) or glass (Trompier et al., 2011; Fattibene et al., 2014). However, the use of these materials in an emergency situation is either limited by the unavailability of the materials, an instability of the signal, a non linear response to dose, or a weak response to dose.

Optically stimulated luminescence and thermoluminescence are widely accepted methods for occupational dosimetry in radiation facilities (Bøtter-Jensen et al., 2003), due to their sensitivity

and ease of processing dosimeters. The quartz contained in bricks and ceramics was the first material to be used to retrospectively assess gamma dose following radiological accidents (Hutt et al., 1993; Haskell et al., 1994; Bailiff, 1995; Bailiff et al., 2004b), and although the sensitivity of the luminescence signal of quartz and its stability provide reliable dose assessment, brick and cement samples do not provide the dose received by individuals but they are used to obtain a spatial average of dose to structures. To provide an individual specific dose assessment, materials that are likely to be carried by members of the public were examined for their luminescence response to ionising radiation. Amongst the materials investigated, alumina substrate resistors such as those found on the circuit boards of mobile phones showed favourable characteristic for short term dose assessment (Inrig et al., 2008a; Bassinet et al., 2014; Beerten and Vanhavere, 2010; Ekendahl and Judas, 2011; Kouroukla, 2015). Despite their favourable characteristics (ubiquity amongst members of the public, linear response to ionising radiation dose, capability to detect levels of dose well below the threshold required for triage, dose recovery capability), several issues remain. Firstly, the luminescence signal is unstable at room temperature (Inrig et al., 2010a); secondly, the difficulty to obtain mobile phones in an emergency situation, both because members of the public may be reluctant to give up their phones in an emergency situation and because security services may seize the phones for the information stored in them; thirdly, technological advances lead to increasingly smaller resistors being used in mobile phones, which makes it harder to extract the resistors from the circuit board and to remove enough material to yield sufficient signal.

Although these techniques have known considerable developments, concerns still exist as to the feasibility of using them in a large scale emergency scenario. Furthermore, availability of a number of techniques and materials is needed to strengthen the emergency response in place in such a situation.

1.3 Response

To address above concerns, new surrogate materials for use with luminescence techniques for dosimetry are actively being sought. Ideally the new dosimeters investigated should be commonly found amongst members of the public, carried near the individual, have a signal sufficiently strong to enable the detection of dose at the threshold required for triage, have a signal sufficiently stable over time and be available in the aftermath of a radiological event. Besides, the processing of the samples

should be straightforward and quick to allow a large number of samples to be assessed in a short time. The objective of this thesis is thus to identify new materials that can best match this need. Some personal objects have already been examined for their luminescence response by Sholom and McKeever (2014), and this thesis will aim to take such work further. A screening of commonplace materials was carried out to characterise their luminescence response to ionising radiation, and to target the most suitable materials.

1.4 Research questions and design of the thesis

This thesis aims to address the issues highlighted above, and to respond to the following questions :

1. Which materials are suitable for luminescence emergency dosimetry and which ones are not?
2. What are the luminescence characteristics of the new materials investigated? What is the physical origin of the luminescence emission?
3. How accurate are the dose estimates obtained using the new surrogate dosimeter materials?
4. What are the advantages / disadvantages of the new surrogate dosimeters materials?

Following this introduction (**Chapter 1**), the first part of the thesis will set up the theoretical framework. The context in which emergency dosimetry might be needed, and how this is integrated in a radiological emergency response plan is discussed in **Chapter 2**. **Chapter 3** will define the concepts used in dosimetry, and review which techniques and materials are now available for dosimetry in radiological emergency situations. A focus will be made on luminescence techniques (optically stimulated luminescence and thermoluminescence), as being the main techniques of interest in this study, for which a theoretical description is given in **Chapter 4**. **Chapter 5** will show how a radiation induced luminescence signal can be used to determine the absorbed dose in a sample.

The second part of the thesis will present the experimental results obtained. The instrumentation used is described in **Chapter 6**. **Chapter 7** contains a survey of all materials that were investigated during the course of the research work, with the focus being on fabrics. Three types of fabrics exhibited a particularly favourable response to dose, that prompted further testing for

their luminescence characteristics : a blue polyester fabric (**Chapter 8**), a class of fire retardant upholstery fabric (**Chapter 9**) and the fabrics of bags (**Chapter 10**), whose thermoluminescence response to dose is attributed to the presence of carbonate mineral fillers. In addition, the issue of the fading of alumina substrate resistors is addressed in **Chapter 11**, with an attempt to reduce the rate of fading by using photo-transfer TL. A blind test replicating a radiological exposure comprising a phantom carrying bags was carried out to test the potential of bag fabrics as dosimeters in a real-case scenario (**Chapter 12**). The conclusion of this thesis (**Chapter 13**) summarises the work carried out, and outlines the potential for future work using mineral fillers as dosimeters.

Chapter 2

Radiological accidents, emergency preparedness and response

Since their discovery in the late 19th century, ionising radiation has found tremendous use within society. From X-rays used in medical imaging, to alpha sources used in smoke detectors, or beta radiation used in industry to monitor wall thickness to gamma rays used in cancer treatment or sterilisation, and finally the development of nuclear power plants, ionising radiation appears to have become prevalent in the modern world. Despite all their benefits, ionising radiation can cause harmful health effects if not handled properly.

Whereas societies have always been required to cope with the notion of risk (volcanic eruptions, hurricanes, flood), the recent appearance of the "radiological risk", a man-made risk, differs from natural environmental disasters in many ways, and needs to be addressed specifically. The health hazards induced by exposure to ionising radiation necessitate prompt and specific treatment to preserve life, for which preparedness and quick response are essential factors.

To prevent nuclear hazards, the International Atomic Energy Authority (IAEA) defines nuclear security and nuclear safety conditions to be achieved at all times. A state of nuclear security is defined as "*the prevention and detection of, and response to, theft, sabotage, unauthorized access, illegal transfer or other malicious acts involving nuclear material, other radioactive substances or their associated facilities*", whereas nuclear safety is "*the achievement of proper operating conditions, prevention of accidents and mitigation of accident consequences, resulting in protection of workers, the public and the environment from undue radiation hazards*".

There is a wide range of scenarios in which the security and safety might fail and lead to catastrophes harming members of the public. Politicians and scientists have worked together over the past decades to assess the level of risk associated with each type of these radiation accidents and incidents, and to plan subsequent preparedness and response.

This chapter will firstly examine the health hazards associated with prolonged or high exposure to ionising radiation that can occur if radiation protection measures fail, in order to emphasise the potential medical consequences on populations due to a nuclear event. The nuclear events by which members of the public could be exposed to radiation will be then reviewed, before discussing some elements of the emergency preparedness and response specific to nuclear accidents.

2.1 Effects of ionising radiation on the human body

Two types of exposures from radioactive sources can occur : internal contamination, where the subject ingested a radioactive substance, and external exposure, where the subject was exposed to radioactive sources outside of their body, but ionising radiation is still interacting with the individual's cells. In many scenarios, both types could occur simultaneously, e.g. a person surrounded by and breathing in a cloud of radionuclides. For the same level of dose, cases of internal contamination tend to have more severe consequences than external exposures, as exposure happens the entire time during which the nuclides are inside of the body. Moreover, there are no barriers such as skin between the radiation source and the cells, and some target organs may absorb the radioactive material.

Ionising radiation can cause severe damage to biological systems by damaging cells. The effect can be either direct, by causing damage to the cells' DNA, or indirect, by ionising water molecules (Domenech 2016; Reisz et al. 2014). Ionised water molecules produce free radicals (e.g. hydroxyl radicals OH^{-}, or hydrogen radicals H^{+}) that can combine to form toxic species, such as H_2O_2, which damage other cells. Ionising radiation breaks the DNA double strands, and once damaged, DNA can repair itself, by replicating the other strand of its helix. However, if the damage is severe, the repair process can lead to mutation or death of the cell (ICRP, 2012), and damaged cells on a large scale can induce a series of health hazards to living organisms. The death of cells leads to deterministic effects, and mutations to stochastic effects. Deterministic and stochastic effects will

be explained in more detail in Sections 2.1.1 and 2.1.2.

Our knowledge of the effects of ionising radiation on the human body is mainly drawn from two types of study : a) people who suffered from exposure to ionising radiation (A-bomb survivors, radiotherapy patients, nuclear incident or accident survivors), and b) laboratory animal studies. On the basis of these studies, radiation effects are classified into two categories of effects, deterministic effects, due to the killing of cells at high dose, and stochastic effects, due to the mutation of somatic cells (ICRP, 2007). The severity of deterministic effects increase with the dose, and there is a threshold below which they are not expected to occur. Stochastic effects, on the other hand, only have the potential to arise, the likelihood increasing with dose without a threshold in dose.

The quantity used in radiation protection is the equivalent dose, H, expressed in Sieverts (Sv; Sv=J.kg^{-1}). This quantity is derived from the physical quantity the absorbed dose (Gy), but takes into account the relative biological effectiveness (RBE, see Chapter 3) of the type of incident radiation (ICRP, 2007). Whilst the equivalent dose (Sv) represents a biological effect, the absorbed dose (Gy) represents one joule of radiation energy deposited per kilogram of matter. Hence one Sievert is the dose of ionising radiation equivalent in biological effectiveness to one Gray of gamma radiation. Chapter 3 will look more closely at the definition and physical origins of these units.

2.1.1 Deterministic effects

Deterministic effects are also referred to as “harmful tissue reactions”, and vary from one type of tissue to another, depending on the cellular composition, proliferation rate, and response to radiation. Deterministic effects include, amongst others, skin burns, cataracts (although still debated), haematological deficiencies, reduced fertility, or brain damage in utero (ICRP, 2012).

These symptoms only appear at relatively high doses administered at an acute dose rate, and their appearance is characterised by a threshold dose, below which those effects are not expected to be observed. The threshold dose depends on the effect, but the minimum threshold for any deterministic effect is $\sim$ 1 Sv (ICRP, 2007). In addition, severity of the effect increases with increasing dose above threshold.

Exposure of the whole body to a very high dose of penetrating radiation within a very short

time can lead to acute radiation syndrome. The acute radiation syndrome is characterised by three stages : the prodomal reaction, the latent stage, and the main stage (Finch, 1987). The prodomal stage lasts a few hours to a few days and consists of clinical symptoms such as nausea, vomiting, weakness, diarrhoea, reduced state of consciousness, and radiological burns, depending on the dose and time following irradiation. The latent stage follows, where the patient feels better (days to weeks), and during the main stage, the symptoms include, for doses $\leq 6-8$ Gy, bleeding, infections, severe gastrointestinal disturbance, cerebral and neurovascular troubles due to damage to the central nervous system, and haematopoietic effects related to damage of the bone marrow (Finch 1987, Hempelmann et al. 1952, Walker et al. 1989) that can lead to the death of the patient. Hence, doses need to be accurately estimated to support medical intervention, and the estimation of the body dose within hours is of critical importance to support prompt medical treatment. Although a whole body dose is more likely to cause severe effects, partial body exposures can also be important and lead to serious health risks, depending on the region of the body exposed to ionising radiation. However, in the events considered in this thesis they are assumed less likely to occur in "mass casualty" scenarios.

2.1.2 Stochastic effects

Stochastic effects appear in terms of increased cancer risks and genetic effects (Walker et al., 1989) and can appear at relatively low doses (100 mSv) as they are more closely related to repeated exposures of low dose.

Stochastic effects have no threshold, so a linear response from a 0 Gy dose is assumed. However, epidemiologically, it is very hard to get any evidence with sufficiently low uncertainty to fill in the gap $<$ 100 mGy. Above 100 mSv there is a proportional increment in the risk of developing cancers (ICRP, 2007), which is known as the "linear no threshold" model (or "LNT"), and assumes that the risk of cancer is related to cumulative dose, regardless of dose rate. Repeated small exposures are thought to have the same effect on health as one shorter, larger, exposure.

So far, no genetically transmitted effects of radiation have been observed in humans, but there is evidence of inherited effects in animals. However, if for protection purposes a small probability is assumed, as the risk of cancer being higher than the genetic risks, a system covering cancer risks would also prevent genetic effects (ICRP, 2007).

Fig. 2.1 summarises the different types of health hazards due to the exposure to ionising radiation (ICRP, 2012).

Table 2.1: Effect of levels of radiation dose on the human body (ICRP, 2012). The tolerance dose is defined at the maximum dose that can be absorbed without the effect being observed.

Organ	**Effect**	**Tolerance dose (Gy)**
Total bone marrow	Blood cell depletion	1-2
Ovary	Permanent sterilisation	2-6
Testis	Permanent sterilisation	3-4
Eye	Cataracts	0.5
Kidney	Nephrosclerosis	~ 25
Liver	Loss of function, ascites	~ 35
Lung	Pneumonitis	~ 40
Heart	Pericarditis	~ 40
Lymph nodes	Hypoplasia, firbosis	35-45
Thyroid	Hypoplasia	≥ 45
Other organs	Hypoplasia, firbosis	≥ 45

The dosimetric quantities needed differs when acute irradiation occurs; some organs are more at risk than others (brain, intestines, bone marrow) and optimal medical treatment requires knowledge of the dose to specific organs. If the irradiation was very localised, the dose at different locations would be needed (point of the irradiation, and gradient of doses around) as, in acute cases, amputation would be necessary to prevent necrosis. On the other hand, when stochastic effects are expected, the whole-body dose is sufficient. The quantities routinely used in radiation protection will be defined in Chapter 3. The ideal whole-body dosimeter for deterministic effects would therefore provide full dose map of the body in order to target the treatment (Eakins and Ainsbury, 2018a).

2.2 Types of radiological risks

The International Atomic Energy Authority (IAEA) distinguishes seven levels of severity of radiological events (Fig. 2.1), from "anomaly" to "major accident" (IAEA, 2008). Events of level 1 to 3 are considered as "incidents", whilst levels 4 to 7 are treated as "accidents". Three areas of impact are considered in order to rate an event : 1) consequences for the people (dose received) and the environment (amount of radiological material), 2) extent of damages on the security system preventing the spread of radiological material, and 3) the "safety in depth" evaluating the failure of the safety measures preventing the occurrence of an accident.

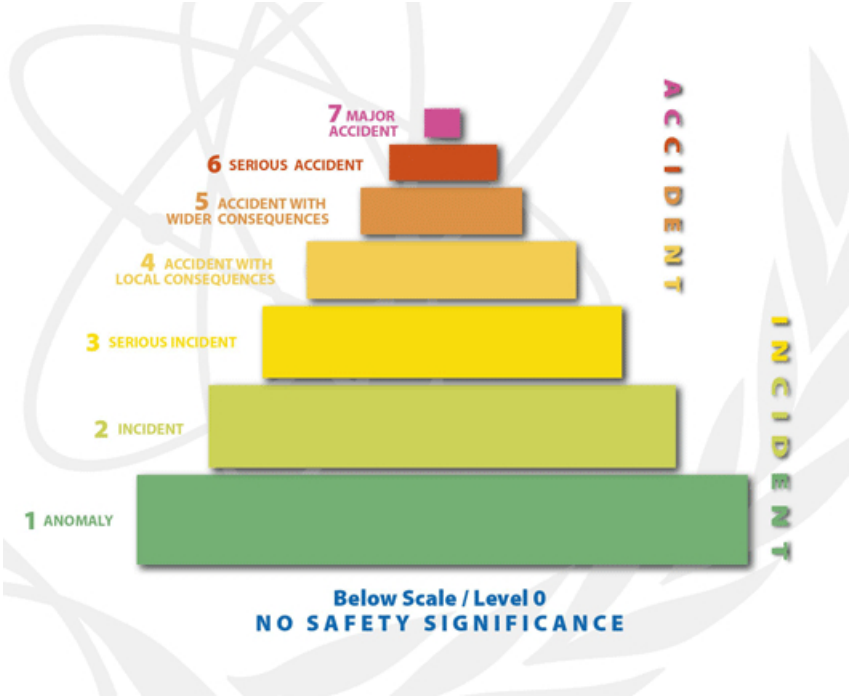

Fig. 2.1. International Nuclear and Radiological Event Scale (INES) tool developed by the IAEA. Reproduced from the IAEA https://www.iaea.org/topics/emergency-preparedness-and-response-epr/international-nuclear-radiological-event-scale-ines.

The impact on people and environment of each level are summarised in Table 2.2, along with significant examples for each level. The assessment of the consequences on the people thus involves an evaluation of the dose they have been exposed to. As will be discussed later, emergency dosimetry evaluate consequences on the people by assessing the radiation doses received by members of the

general public not carrying conventional dosimeters. The latter would therefore correspond to high level events; typically from level 5 and higher. Although these levels of events are rarer, they also have the most severe consequences, and need appropriate planned countermeasures (levels 6 and 7), amongst which emergency and retrospective dosimetry plays a central role.

The current dosimetry system for accidents harming members of the public include methods such as clinical symptoms, physical dose reconstruction, cytogenetic biodosimetry tests, modelling based on Monte Carlo simulations, physical dosimetry using building materials and teeth enamel, and in-situ dosimetry using physical methods (Ishii et al., 1990; IAEA, 1998a,b, 2009, 2004, 2002, 2014).

Table 2.2: Description of International Nuclear and Radiological Event Scale (INES)levels with associated examples for each level. Adapted from IAEA (2008).

Level	**Severity**	**Impact on environment and people**	**Example of events**
1	Anomaly		*Tricastin, 2008* - Leak of water containing enriched uranium into the environment.
2	Incident	Exposure of a member of the public in excess of 10 mSv; exposure of a worker in excess of the statutory annual limits.	*Asco, 2008* - Radioactive contamination caused by a leak in a nuclear powerplant.
3	Serious incident	Exposure in excess of ten times the statutory annual limit for workers; non-lethal deterministic health effect (e.g., burns) from radiation.	*Sellafield, 2005* - Leak of radioactive material, contained within the facility.

4	Accident with local consequences	Minor release of radioactive material unlikely to result in implementation of planned countermeasures other than local food controls; at least one death from radiation.	*Tokaimura, 1999* - Criticality accident at a reprocessing facility.
5	Accident with wider consequences	Limited release of radioactive material likely to require implementation of some planned countermeasures; several deaths from radiation.	*Three Miles Island, 1979* - Partial meltdown of a reactor core, release of radioactive gas in the environment; *Goiania, 1987* - Theft of a radioactive source.
6	Serious accident	Significant release of radioactive material likely to require implementation of planned countermeasures.	*Kyshtym, 1957* - Explosion of a high activity waste tank, significant release of material.
7	Major accident	Major release of radioactive material with widespread health and environmental effects requiring implementation of planned and extended countermeasures.	*Chernobyl, 1986* - Explosions of nuclear powerplant, significant release of radioactive material in the environment; *Fukushima, 2011*- Major damages caused by a tsunami to a nuclear powerplant, leak of radioactive material.

The causes of radiological incidents and accidents are extensively varied, but can be separated between accidental release of radiological material and events deliberately caused. The next section will summarise the different types of radiological accidents that can occur.

2.2.1 Radiological accidents and incidents

Nuclear power plant accidents

In 1975, the United States Nuclear Regulatory Commission (NRC) evaluated the chance of a nuclear reactor accident at 1 in 5,000,000,000 per year for a park of 100 reactors (United States Nuclear Regulatory Commission, 1975). However, a risk of zero cannot be assumed, and Sovacool (2010) listed 99 nuclear plant accidents between 1952 and 2009.

Nine classes of incidents and accidents that can occur in a nuclear reactor have been listed by the NRC (Lamarsh and Baratta, 2013, p. 682), from the class 1 trivial incidents, to the class 9 (which differs from the IAEA scale) "very serious" accidents, but considered so unlikely that they are omitted in risk analysis. The most critical accident that can happen in a nuclear reactor, causing the spread of radiological contamination, is a nuclear meltdown (i.e., melting of the reactor's core, often due to a lack of coolant; Lamarsh and Baratta 2013, p. 682).

Three large scale nuclear meltdowns have occurred in civilian power plants : Three Mile Island (1979), Chernobyl (1986) and Fukushima (2011), the last two of them (Chernobyl and Fukushima) were rated at 7 on the IAEA scale, and led to large scale exposure of members of the public. In the case of the Chernobyl accident, a lack of coolant triggered the meltdown (Lamarsh and Baratta 2013, p. 690; Kortov and Ustyantsev 2013), and led to the dissemination of radioactive nuclides to the nearest town of Pripyat and its countryside. Workers of the facilities, but also inhabitants of the surroundings, were exposed to potentially high levels of radiation, up to 200 mGy/h on the soil of Pripyat 10 days after the accident (Kortov and Ustyantsev, 2013).

The accident of Fukushima was caused by the earthquake and the tsunami that hit Japan on the 11^{th} of March 2011 (Yotaro et al. 2014, p. 27; Kortov and Ustyantsev 2013; Baba 2013; Tominaga et al. 2014). These natural catastrophes led to the explosion of the reactor, large amounts of radioactive materials were released into the environment, and consequently, vast portions of territories had to be evacuated (estimated at 83,000 individuals; Kortov and Ustyantsev 2013).

Transport accidents and loss of radiological material

Another type of unintentional radiological accident likely to harm members of the general public is the loss of radioactive material. Safety standards exist for the transfer and decommissioning of nuclear sources (IAEA, 2002), as unsafe transport of radioactive material can lead to the exposure

of nearby passengers (in case of an exposed source, or a source with a faulty shielding), or even the complete loss of the source. The IAEA identified between 100 and 140 incidents over the last 10 years related the discovery of uncontrolled radioactive sources, unauthorised shipment or disposal (IAEA, 2017). This figure only includes incidents not connected to malicious use. In addition, between 20 to 50 incidents per year over the same period of 10 years were reported, but whether the intent was malicious or not was not determined.

A few accidents harming populations resulted from the loss or faulty transport of radioactive materials. In 2002, an unshielded source of ^{192}Ir was transported on board of a passenger bus departing from Cochachamba, Bolivia (IAEA, 2004). However, the source irradiated passengers throughout the eight hour journey, with a maximum calculated absorbed dose of 2.77 Gy. The investigation found that workers did not carry out a number of security checks, notably omitting to check whether the source had retracted into its shielded position.

"Orphan source" is a term use to designate a source no longer under regulatory control, either for being abandoned, stolen or misplaced (Ortiz et al., 1999). Orphan sources are not expected to cause large scale incidents, but can nonetheless harm members of the general public. They can easily be mistaken for scrap metal by unaware workers or members of the public. In 1983, Mexican foundries used steel from a scrap yard, unaware that a capsule of ^{60}Co had contaminated the scrap (Lister, 1985). The contaminated steel was later used as table bases, and sold to members of the public, although no fatalities amongst them were reported. A more tragic event occurred in Goiania, Brazil, when two scavengers stole a ^{137}Cs radiotherapy source from an abandoned hospital (Roberts, 1987), sold it dismantled to a scrap dealer. The caesium then passed from hand to hand in the city, contaminating many people. As a result, four fatalities were recorded, and 249 people were found to have received significant doses. The incident of Tammiku is another example, where three men stole a metal container with a ^{137}Cs source enclosed from a waste repository, and brought it back to their to their home subsequently irradiating inhabitants of the household (IAEA, 1998b). A larger scale incident occurred in Taiwan, where concrete contaminated with^{60}Co was found in the structure of 1700 apartments (Chen et al., 2007).

Unintentional radiological accidents potentially harmful on a large scale to populations can be divided into two categories, either being caused by a nuclear reactor accident, or by uncontrolled

sources. The hazards related to these types of accident are, however, put on the same level as intentional threats.

2.2.2 Intentional radiological incidents

Waselenko et al. (2004) distinguished five types of intentional radiological threats : 1) an attack on a nuclear power plant, 2) a malevolent act using simple radiological devices, 3) use of a radiological dispersal device, 4) detonation of an improvised nuclear device, and 5) detonation of a sophisticated nuclear weapon. In addition to these, Valentin (2005) also listed the contamination of food and water supplies, and the contamination of a specific site or building by radioactive material.

All of these scenarios have the potential to deliver high levels of dose to members of the public. In addition to health hazards to the population, a radiological attack could lead to large scale movements of panicked population groups, and cause psychological effects on the public due to the fear of radiation. Furthermore, economical consequences could also ensue, through radiological contamination of properties, and if a mass evacuation of people was needed (Ferguson, 2009).

Attack on nuclear facilities

Although an attack or intrusion inside a nuclear reactor is considered to have low probability (Flynn and Goans, 2006), there had been no less than 80 identified incidents implicating infiltration of individuals inside of nuclear installations during the past 60 years (Ackerman and Halverson, 2016). An attack on a nuclear facility (power plants, research facilities, fuel reprocessing plants, or radioactive waste units) could be lead by two motivations : 1) either the theft of radiological material aiming to build a nuclear device, or, 2) in the case of a power plant, to sabotage the reactors itself, causing the dispersal of radiological material, or worse, a meltdown (Ackerman and Halverson, 2016; Helfand et al., 2002; González, 2005). In this last case, the consequences would be similar to the reactor accidents described above, such as Chernobyl and Fukushima (i.e., contamination of the public, possibly on a large scale).

Simple radiological device

A simple radiological device attack would consist of placing a radioactive source in a populated area, without dispersing by detonation (e.g., by chemicals). Examples of scenarios were given by

Valentin (2005), and included concealing a radioactive source in clothing, luggage, transportation, home, or workplace. The hidden source could remain for prolonged periods of time before being discovered, and unknowingly harm members of the public. Severe exposures are not expected from this scenario (Flynn and Goans, 2006), but the threat mostly relies on the psychosis and political crisis it would cause. In addition, this scenario is by far the simplest, hence the easiest to realise.

Radiological dispersal device

A radiological dispersal device is more often referred as a "dirty bomb", and designates a conventional detonating device, which, upon detonation would disperse radiological material (Flynn and Goans 2006; Harper et al. 2007). This type of device is relatively simple in design, and would not necessitate neither extensive engineering skills to be manufactured, nor very large sources to cause harm (Harper et al., 2007), and is consequently considered as the scenario most likely to occur (Barnett et al., 2006). The concerns over this threat were further prompted by the high prevalence of radiological material worldwide (González, 2005), and the existence of illicit trafficking of nuclear material (Shelley, 2006). Furthermore, the types of sources would be typically those used for medical diagnosis/therapies (i.e. ^{60}Co, ^{137}Cs, ^{192}Ir, ^{241}Am; Barnett et al. 2006). In this context, Eakins and Kouroukla (2015) computationally modelled a relevant radiological incident where they approximated an uniform soil contamination within a 2 m radius discs of radioactive nuclides, and a cloud of nuclides, caused by aerosol debris (isotropic irradiation) by a source isotropically emitting photons towards the phantom from a 1.2 m sphere centred at the phantom midpoint. They also calculated the concentration of different isotopes that would be required to achieve a 1 Gy.h^{-1} dose rate for floor contamination and isotropic irradiation.

However, the impact of a radiological dispersal device is mitigated (Sabol and Sestak 2017 Barnett et al. 2006) by the spread of radiological material that reduces its initial concentration, and the blast alerts people to an immediate danger, leading to evacuation of the area.

Nuclear device

The first intended use of a nuclear device to harm population was set in place in August 1945, when the US army dropped an atomic bomb on each of the cities of Hiroshima and Nagasaki, Japan. Of

the 320,081 inhabitants of Hiroshima, 122,358 died from the nuclear blast (González, 2005). Even now, the detonation of a nuclear device is considered as a possible scenario, and even though the probability is recognised to be low, the consequences would be devastating (Valentin, 2005). As for preparedness, this scenario can be considered as the worst-case scenario. The first scenario of the National Planning Scenario document, for example, is the detonation 10-Kiloton improvised nuclear device (Howe, 2004).

The dosimetry system proposed in 1965 following the attack of Hiroshima and Nagasaki included biological methods, electron paramagnetic resonance (Nakamura et al., 1998) and thermoluminescence techniques using building materials (Haskell et al., 1984; Bailiff, 1997).

2.3 Emergency preparedness and response to radiological risks

The limitations of radiological accidents and incidents, such as described above, or the limitation of their consequences are enhanced by both hazard mitigation, emergency preparedness, and recovery preparedness (National Research Council, 2006). Emergency and retrospective dosimetry are subsequent parts of the preparedness and recovery plans.

2.3.1 Preparedness for radiological emergencies

The European research project of Shamisen (Oughton et al., 2017) aimed to draw lessons from the power plant accidents of Fukushima and Chernobyl, and to draft recommendation for preparedness and response to a large scale accident or future accidents. The report states that an effective preparedness for a radiological accident is based, amongst others, on continuous planning, training of the first responders, evaluation and emergency exercises. More precisely, this encompasses, for example, planning the evacuation of the population, establishing communication protocols, preparing epidemiological studies, and setting up a framework of dosimetry, i.e., actions to be taken to assess the doses received by workers and the public.

These general considerations require adaptation for each scenario, and even each scenario has to be adapted for the environment in which it would occur. Contamination and casualties would vary depending on the location, time of the day, weather, type of accident (Coleman et al., 2009). For example, the preparedness would be different between an accident happening in a large metropolitan

area and a zone with a low population density. Here research plays an important role, as each type of accident can be either modelled with particle transport codes, or tested under safe controlled conditions before the actual occurrence of the catastrophe (Harper et al., 2007). The physical aftermath of an accident is therefore predicted in advance (Knebel et al., 2011). For example, the fallout pattern is estimated for a certain type of accident, determining a zone where radiation injuries can occur (Buddemeier and Dillion, 2010); meteorological modelling is carried out to predict the distribution of radioactive fallout in an urban area as a function of the weather forecast (Baklanov et al., 2006); building type and construction material play a role in the dose reduction factor (Knebel et al., 2011) and help the assessment of the benefits of sheltering versus evacuating in terms of exposures (Buddemeier and Dillion, 2010). Harper et al. (2007) reported the results of extensive aerosolisation tests aiming to simulate radiological dispersal devices' explosions, and to answer the question of whether evacuation or sheltering was preferable.

The questions that these research addressed are : 1) How many people would be affected by the event? 2) How dangerous would be the event for the affected people within a specific area? and therefore, 3) What strategies to adopt (Buddemeier and Dillion, 2010)? By addressing these scenarios issues before the accident decision makers may issue recommendations quickly after the accident, for example in terms of evacuation or medical resources required.

The studies described above mostly focus on the prompt response. Planning and research do not stop on the preparedness of the immediate aftermath, but also investigate what actions would need to be taken immediately following the event. In their priority list of research areas for developing radiological threat countermeasures, Pellmar and Rockwell (2005) assigned the highest priority to research on radiation treatment, to minimise the effects of exposure, and also to physical and biological dosimetry to obtain accurate measures of exposure for use in planning treatment.

The medical preparedness is crucial, as emergency medical services providers (i.e., paramedics and fire first responders) are likely to be amongst the first called on the site of an accident. On a small scale accident, people could be sent off to the nearest hospital for a first assessment, primarily, of their physical condition. However, in a larger scale event, the number of casualties could reach hundreds of thousands (Coleman et al., 2009). An assessment of the available resources for such a number of casualties is necessary, as this might exceed the available resources, in terms of hospital beds, staff, blood products and skin grafts (DiCarlo et al., 2011). In this scope, the medical studies

have emphasised the importance of having trained agents, able to recognise symptoms of radiation, and possibly to carry out a triage of the population according to the severity of the radiation dose they received (Hick et al., 2011). Whilst emergency medical services would be the first on site to respond and should be specially trained in identifying the threat (Kollek et al., 2009), all healthcare workers should also be prepared to face such an event. The main challenge faced in medical and hospital preparedness is the low occurrence of these events, hence healthcare workers would have little experience in dealing with and recognising radiological injuries and sickness (Jasper et al., 2005). Thus an additional objective system of triage is necessary. In its 2018 recommendations to the management of radiological accidents, to the National Health Services, Public Health England gave a comprehensive table of triage categories of the members of the public based on clinical symptoms (Public Health England, 2018), and stated that, considering the possibility of radioactive contamination, treatment should be administered as soon as possible to the patient prioritised by the triage. Triage and treatment of the patients would occur prior to any decontamination activities, although all patients should be assumed to be contaminated on a first instance. Furthermore, arrangements for appropriate triage to ensure medical treatment is listed as one of the requirements to governmental agencies for the response and preparedness of radiological events, as developed by the IAEA (International Atomic Energy Agency, 2015).

The scope and challenges of biological and physical emergency or retrospective dosimetry will be further explored in Chapter 3, but in brief, retrospective and emergency dosimetry aim to assess the dose received by individuals not carrying conventional dosimeters (i.e. the general public) following a radiological incident or accident. Biological and physical methods have been developed (Ainsbury et al., 2010), and are still under development. The specific preparedness regarding biological and physical dosimetry encompasses all of the general guidelines described above: research is carried out to identify most suitable materials / procedures; inter-comparisons and field tests are used to test the efficiency and reliability of the techniques; and the accepted research is implemented into a framework. The European network "Realizing the European Network of Biological Dosimetry" (ReneB) launched in 2012 (Kulka et al., 2017), for example, was built to respond to the needs of dosimetry preparedness. Its main aim is to set up an operational and certified basis for biological and physical dosimetry; to provide education and training in the goal of quality assurance; and finally to further develop new techniques and include them in the network (Kulka et al., 2017; Trompier

et al., 2017). Accident simulation exercises and intercomparisons proved the resilience of the network to quickly respond to an accident, using both biological and physical methods (Brzozowska et al., 2017). The capability of the ReneB (Running the European Network of Biological and retrospective Physical dosimetry) network varies according to the method employed; it is estimated that the network could process 3845 samples per week using γ-H2AX assays, 2049 using dicentric assays, 1200 using luminescence techniques, and 850 using electron paramagnetic resonance (EPR) (Monteiro Gil et al., 2017).

In parallel, the EURADOS (European Radiation Dosimetry Group) network carries similar preparedness activities, although being more focused on research and development (Bassinet et al., 2014). Once approved, the techniques developed are integrated in the ReneB network (Ainsbury et al., 2017).

All of the results of this research and studies help to implement a framework of action to be taken in the case of an accident. Coleman et al. (2009) pointed out that an effective governmental response, which includes emergency dosimetry, is shaped by "*basic research, interagency meetings, multiagency partnerships, and a variety of exercises*".

As pointed by Coleman et al. (2015) what is needed throughout all of the process of preparedness is an answer to the question : what do we do?

2.3.2 Response to radiological accidents : during and after the accident

The prompt response to a radiological event focuses on gathering minimum information about the event (location, basic description, initial dose assessment); provide timely and reliable communication to the public and affected population, provide sheltering advice and support, assess whether the population should be evacuated (balance exposure risk versus other risks) and collect minimum information on the population to facilitate follow up measures (Oughton et al., 2017).

The system of response that has been developed may vary from one country to another, but Fig. 2.2 shows a relatively general system of response. In this scheme, emergency dosimetry appears as the tenth step, which would be required relatively early after the event ($\sim$ 24 hours). Furthermore,

the last step in Fig. 2.2 is the long-term follow-up and epidemiological studies, which needs to be coupled with retrospective dosimetry.

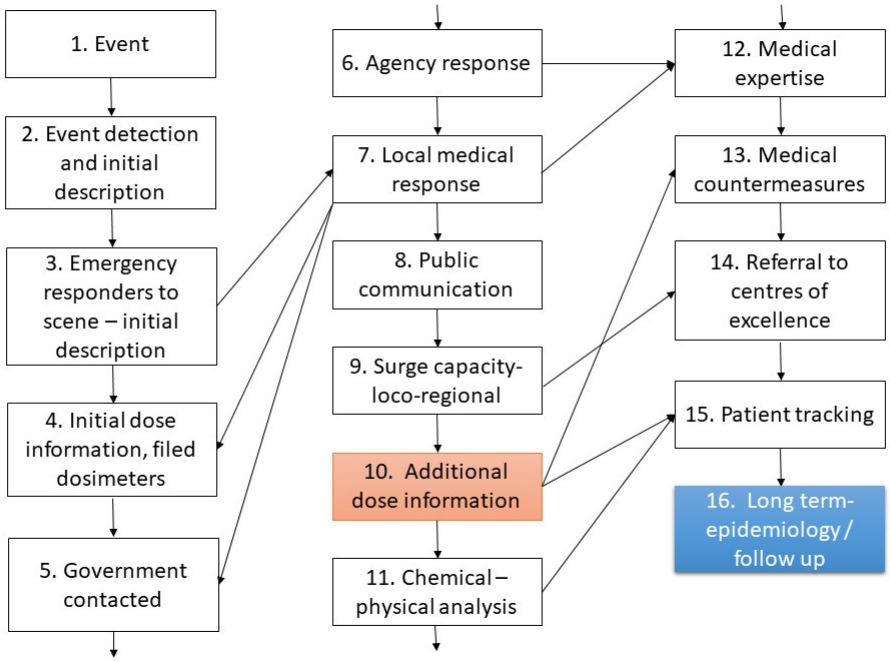

Fig. 2.2. Flow diagram of the chain of medical response. Each box represents a step in the response plan, and the arrows the relationships between each one of them. The red box indicates where emergency dosimetry would be needed and the blue box where retrospective dosimetry would intervene (epidemiological studies). Redrawn from Coleman et al. (2009).

The medical response depends on the type of the event and the numbers of casualties. For a large-scale event, the cohort of radiation casualties would combine various level of severity; people hit by the initial blast, sometimes with traumatic injuries would be severely injured and treated along with people injured by the fallout. The first victims are expected to reach the hospital emergency services within 12 hours (Hick et al., 2011). For accidents reaching hundreds of thousands of casualties (Coleman et al., 2009), there will be an obvious need for triage, as hospitals cannot handle such large numbers of patients.

The management of mass casualties following large scale catastrophic events is a recurring issue for all types of events. A triage is applied according the level of care required to optimise the use

of limited medical resources. Triages aim to be specific to the type of accidents they respond to (Bostick et al., 2008), and tailored to the availability of resources. Several levels of triage are used in large scale accidents. Bostick et al. (2008) distinguished four levels of triage in case of radiological accidents. First order triage is applied at a community level, and in the case of radiological accidents would consist of citizens assessing themselves whether they need assistance, mostly depending on their location at the time of the accident. Second order triage is referred as the "pre-hospital" triage and aims to identify patients that require hospital assessment (third level triage) and/or treatment, and this is the stage at which emergency dosimetry could be applied. The time frame in which the results of emergency dosimetry measurements could be obtained would be in the intermediate (24-96 hours) to the later ($\geq$ 96 hours) phase. In this case, members of the public with no other severe physical symptoms would be told to go home to wait for the results of the physical or biological dosimetry dose assessment, hence considerably diminishing the burden placed upon hospitals.

For radiation accidents, the criteria of triage are based on the estimate of the dose received by each individual. Four categories are usually distinguished (Coleman et al., 2011): 1) below 0.5 Gy no symptoms due to radiation exposure are expected, patients do not need medical care and can go home; 2) 0.5 - 2 Gy patients require medical care, but it can be delayed until after the initial 4 days stage; 3) 2 - 6 Gy, patients need immediate care; 4) above 6 Gy patients are administered palliative care. However, for emergency dosimetry, the levels of triage were simplified in only two categories (below and above 2 Gy) in the first instance triage (Bailiff et al., 2016). The critical threshold dose of 2 Gy also derives from the data of the Chernobyl cohort, for whom no deaths were observed below 2 Gy (Guskova et al., 1988). Sullivan et al. (2013) produced a chart representing the ideal triage model in case of an improvised nuclear device detonation. This model includes two stages of triage. In the initial screening, the "Point of Care Device" relies on a 2 Gy threshold. Individuals below this threshold are evacuated, and those above are sent to High Throughput Dosimetry Systems, where the dose assessment is performed. Fig. 2.3 shows how the Point of Care device and the High Throughput Dosimetry system would be implemented within the general triage system.

The clinical symptoms of radiation exposure have been described above, and a medical triage can be performed on their basis. However, the need for an alternative method of triage is enforced by the nature of radiation injuries, invisible with a simple physical examination for the first 12 hours. This means that even people with no physical signs of injuries would need to be examined for radiation exposure (Coleman et al., 2011). Moreover, some medical symptoms of radiation ex-

posure such as nausea and neurological symptoms can also be induced by stress and mental trauma (Hick et al., 2011), which may lead to hospital admissions for the "worried well". Symptoms of stress can be mistaken for radiation injuries; which can contribute to the spread of panic. The need for an emergency/retrospective dosimetry system also becomes evident to counter this situation, by providing a reliable dose estimate.

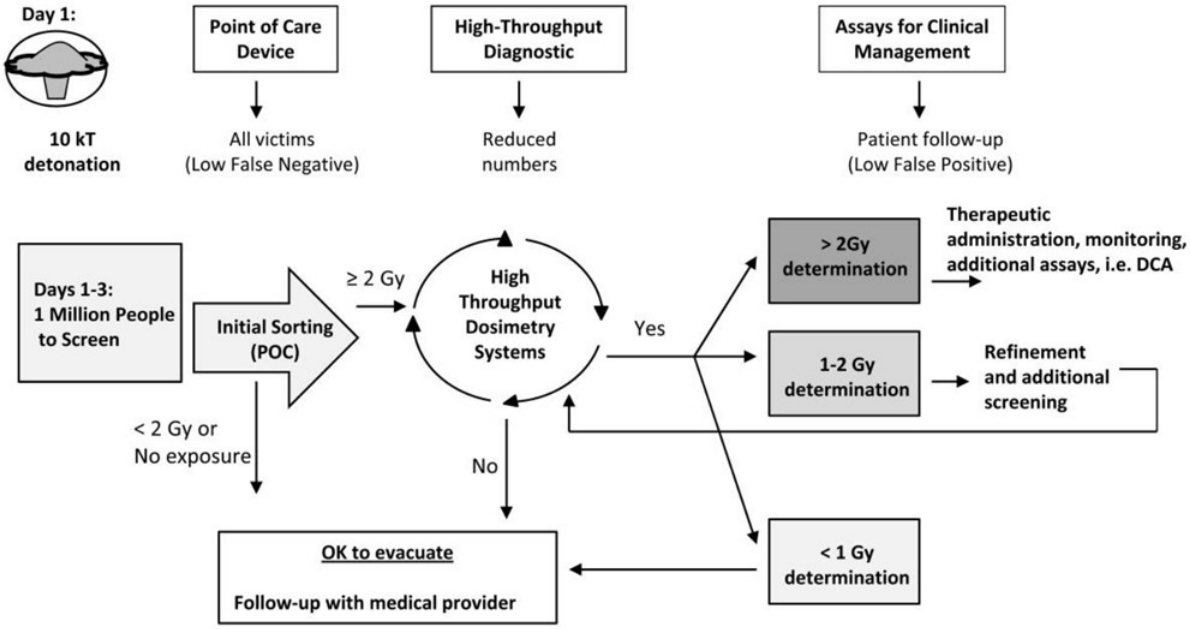

Fig. 2.3. Medical triage model after an improvised nuclear device, using two stages of triage, 1) the Point of Care and 2) the High-Throughput diagnostic. Reprinted from Sullivan et al. (2013).

Finally, the last phase of the accident ($\geq$ 96 hours) is considered as the recovery phase, and can last for years. During this stage, the follow-up assessment of the population continues, in addition to launching epidemiological studies, if they are thought to be informative (Coleman et al., 2009). Here again, physical and biological methods would be needed to assess the doses, sometimes years after the accidents, and relate them to health studies. This was already applied to the accident

of Chernobyl (Bailiff, 1995), and to A-bomb survivors of Hiroshima and Nagasaki (Haskell et al., 1984; Santoro et al., 2002).

2.4 Summary

This chapter highlighted how unwanted exposure to high levels of ionising radiation can have severe consequences on the health, which requires medical treatment (Section 2.1). Many scenarios exist in which unwanted exposure of members of the public to ionising radiation could occur (Section 2.2). The preparedness to these scenarios highlighted some areas of concern (Section 2.3) : 1) the immediate response following a nuclear accident or incident requires a knowledge of the dose in the contaminated area and surroundings, for which dosimetry is needed, and employing different dosimetry techniques would enforce the preparedness scheme. 2) Medical treatment of the exposed individuals requires the knowledge of the dose absorbed by those individuals, hence how to perform dosimetry for members of the public not carrying conventional dosimeters? 3) In some of the worst case scenarios, the number of individuals having potentially been exposed would exceed by far the local hospitals' capacity. To remedy this situation, a pre-hospital triage would be needed. Where biological symptoms can be ambiguous, performing personal dosimetry is a necessity. 4) Post-accident epidemiological studies may be carried out, such as to improve knowledge of the effects of ionising radiation on health. Epidemiological data are only valid if coupled with an estimate of the individual dose.

The points above stressed the need for a dosimetry system suitable for use in radiological emergencies. In this scope, biological and physical methods have been developed to offer a retrospective dose assessment of members of the public in case of radiological accidents, and these methods will be reviewed in the next chapter. The work presented in this thesis therefore aims to offer further development to this emergency dosimetry system, notably by investigating new materials to be used as surrogate dosimeters in a radiological emergency.

Chapter 3

Emergency and retrospective dosimetry of ionising radiation

3.1 Introduction

Dosimetry, in general, aims to measure the dose absorbed in a material. Measurements and methods to assess the "amount" of ionising radiation dose received by workers in radiation facilities are now well developed, but the scenarios described in Chapter 2 required the development of new techniques for the assessment of radiation dose in public environments where conventional dosimetry techniques are not routinely available. Radiation doses received by members of the public not carrying conventional dosimeters can be assessed indirectly using emergency and retrospective dosimetry methods. Preparedness and response to radiological events have emphasised the need for such techniques in the aftermath of large scale events and many techniques have been developed, with varying degrees of readiness, in terms of development, validation and standardisation.

In this chapter, the quantities of interest in ionising radiation dosimetry will be reviewed (i.e., what is being measured and what quantities are needed for emergency dosimetry), before examining in more detail the techniques developed for the retrospective assessment of radiation dose and the uncertainties and detection limits associated with these techniques.

3.2 Quantities for ionising radiation dosimetry

Radiation monitoring historically aims to assist in the protection of both the environment and human health, which requires quantitative measurements of ionising radiation at certain points in space. To evaluate this, the International Commission on Radiological Units (ICRU) developed in its 1956 recommendations (cited in ICRP 2007) physical dose quantities, and incorporated the notion of relative biological effectiveness (RBE) to support the assessment of radiological risk on health. The ICRP (International Commission on Radiological Protection) later developed "protection quantities" for the purpose of assessing radiological risk. Protection quantities aim to assess the absorbed or equivalent dose in an organ or in bodily tissue and to assess the effective dose, with both being used to control the risks to the human body by defining dose limits. In practice, the protection quantities are not measurable, but they are estimated using the operational quantities, which are in turn themselves measured using radiation monitors. Operational quantities (i.e., ambient dose equivalent, personal dose equivalent, later defined in Section 3.2.3) are measured at a certain point in space and are routinely used in radiation facilities to ensure that dose limits are not approached and that the safety of operating conditions for workers and members of the public is maintained. Table 3.1 summarises the protection and operational quantities, and Sections 3.2.2 and 3.2.3 will later explain in more detail the physical origins and implications of these quantities.

Table 3.1: Protection and operational quantities. The "protection" and "operational" quantities will later be explained in Sections 3.2.2 and 3.2.3 respectively.

Protection quantities	**Operational quantities**
Mean absorbed dose, D_T	Ambient dose equivalent $H^*(d)$
Organ absorbed dose, D_T	Directional dose equivalent $H'(d,\Omega)$
Organ equivalent dose, H_T	Personal dose equivalent $H_p(d,\Omega)$
Effective dose, E	

Both operational and protection quantities are derived from radiometric (e.g., flux and fluence, see Section 3.2.1) and physical dosimetric quantities (e.g., kerma and absorbed dose). Fig. 3.1 shows how these parameters are related one to another. In an effort to harmonise and standardise the quantities and units used in radiation protection, the International Commission on Radiological

Units (ICRU) and the International Commission on Radiological Protection (ICRP) have published several reports defining physical, operational and protection quantities used in ionising radiation dosimetry (ICRP, 2007, 1996, 1991; ICRU, 2011). However, for emergency dosimetry, the quantity of primary interest is the absorbed doses to materials (physical quantity) or tissues.

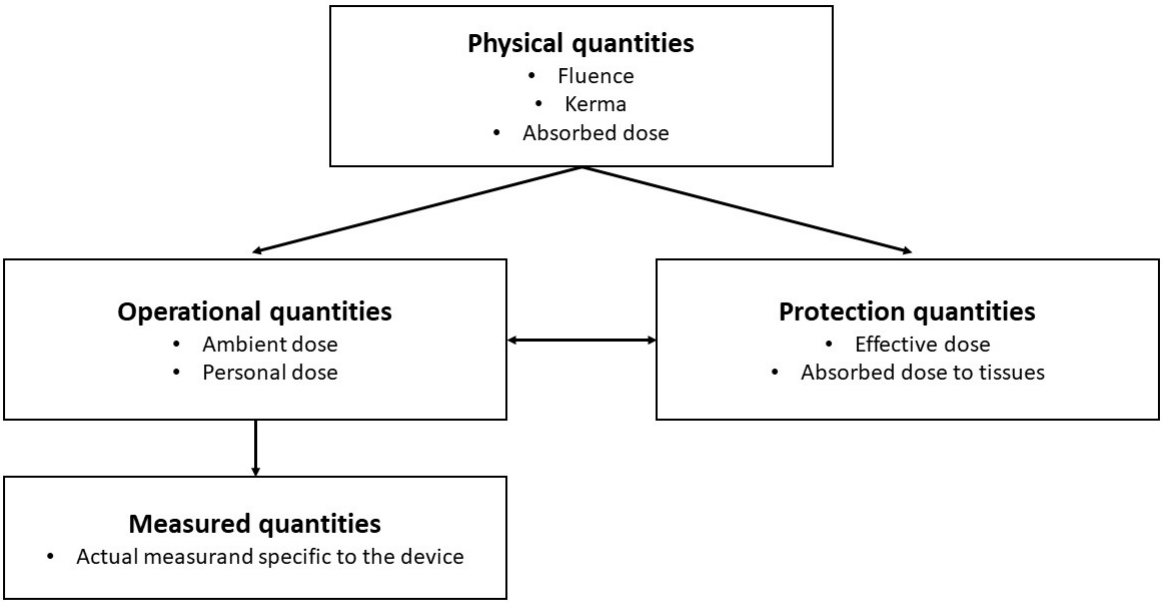

Fig. 3.1. Relationships between quantities for ionising radiation dosimetry. The meaning of physical quantities is explained in section 3.2.1, operational quantities are reviewed in Section 3.2.3 and for the meaning of protection quantities, see 3.2.2. The arrows indicate the derived quantities. Redrawn from ICRP (1996).

The scenarios of radiological accidents explored so far for emergency and retrospective dosimetry (see Chapter 2) mainly target high energy photons as particles of interest, as the sources most likely to be implicated in radiation accidents are photon sources, due to their prevalence (e.g., ^{60}Co, ^{137}Cs).

3.2.1 Physical mechanisms and physical quantities

In order to understand the physical quantities, and how they are derived from physical phenomenon, it is necessary to understand how photons and electrons interact with matter. Chapter 2 dealt with the effects of ionising radiation on the human body, and this section will review how energy is transferred to matter and how this ultimately damages human cells. Photons can interact with matter and be absorbed mainly in three different ways in the typical range of interest (10 keV to 10 MeV), depending on the energy of the photon and the composition of the material.

Firstly, high energy photons ($\geq$ 1.022 MeV) may induce pair production, characterised by the production of an electron and a positron as a consequence of the nucleus interacting with a photon. Secondly, photons of energy between approximatively 100 keV to 10 MeV may cause Compton scattering, a process where photons are inelastically scattered by electrons in the material resulting in a range of photon energies lower than those of the incident energy value, as well as scattered secondary electrons being released. Compton scattering can also occur beyond this range but is less important. Finally, low energy photons (generally $\leq$ 100 keV) interact with matter through the photoelectric effect. During this process, if the incident photon is of appropriate energy, an electron of the tightly bound shell of the atom can be ejected. The resulting particle is called a photo-electron. The relative importance of those three interactions, and their dependence on photon energy and material composition are plotted in Fig. 3.2. This graph shows how both the nature of the material (atomic number, Z, of the absorber) and the energy of the incident radiation influences the response. These physical mechanisms result in the ionisation and damage of cells, and in the production of particles whose rate of production can be characterised using physical quantities.

Physical quantities are the measurable properties of a system or phenomenon. The ICRU report 51 (ICRU, 1993) listed four attributes of physical quantities, such as they should be general, unequivocal, necessary and accessible via measurement and calculation. In practice, this means that physical quantities should be widely applicable, unique, and that the name should be explicit as to the nature of the quantity.

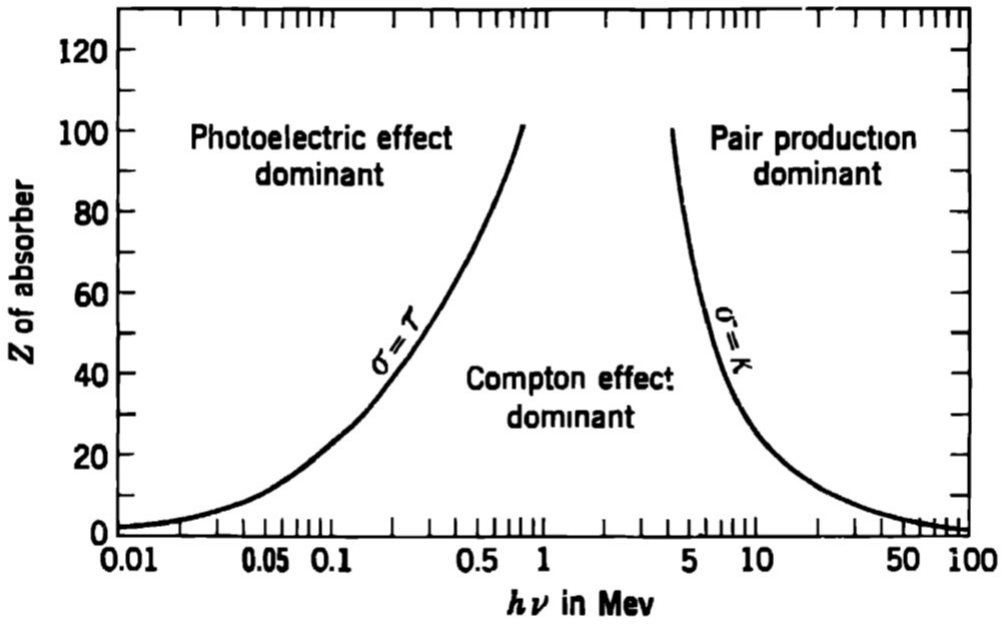

Fig. 3.2. Dominant interactions for a given atomic number, Z, and photon energy. The lines show the values of atomic number and energy for which the effects are equal. σ, τ and κ stand for the linear absorption coefficients for the Compton effect, the photoelectric effect and for the pair production respectively. Reprinted from Evans (1955, p. 712).

Particle and energy fluence

The most important physical quantity for dosimetry is the fluence, defined at a point of interest. Two classes of fluence can be defined : particle fluence and the fluence of the energy transported by particles.

The particle fluence (m^{-2}) designates the number of particles, N, entering a sphere through an element of area dα, such as :

$$\Phi = \frac{dN}{d\alpha}, \tag{3.1}$$

where dN is the differential of the number of particles crossing an infinitesimal sphere through an area $d\alpha$ around the point of interest (Fig. 3.3). Similarly, the energy fluence is given as :

$$\Psi = \frac{dR}{d\alpha}, \tag{3.2}$$

where dR is the differential of the radiant energy R (i.e., the kinetic energy of particles that are emitted, transferred or received) entering the element of area $d\alpha$.

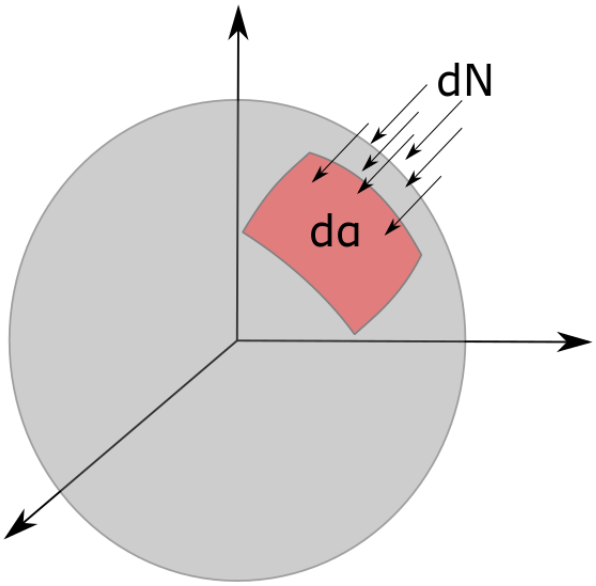

Fig. 3.3. Schematic representation of particle fluence; the red region indicates the element of area, $d\alpha$, and the arrows represent the number of particles, dN, crossing $d\alpha$.

Kerma

Energy is transferred from uncharged particles such as photons to matter by liberating and slowing down secondary charged particles of the matter being hit by the ionising radiation.

The quantity derived from the energy liberated is the kerma, the kinetic energy released per unit mass, K, which represents the ratio of the sums of the initial kinetic energies of all the charged particles liberated by uncharged radiation, dE_{tr}, to the mass in which the energy is deposited, dm, and is given by :

$$K = \frac{dE_{tr}}{dm} \tag{3.3}$$

Its unit is J.kg^{-1}, or Gray (where 1 J.kg^{-1}=1 Gy). The kerma is itself divided in two parts: the collision kerma, K_{coll} and the radiative kerma, K_{rad} (Attix, 1986). The collision kerma is calculated by only taking into consideration the part of the kinetic energy of the secondary particles lost by collision in the mass. On the other hand, the radiative kerma originates from the production of photons caused by the deceleration of secondary electrons.

The kerma and the fluence are related by the relationship:

$$K = \Phi E \frac{\mu_{tr}}{\rho}, \tag{3.4}$$

where Φ is the fluence of the uncharged particles of energy E, and $\frac{\mu_{tr}}{\rho}$ is the mass-energy transfer coefficient for those particles (ICRU, 2011).

Absorbed dose

The absorbed dose is the fundamental unit of radiation dosimetry. The definition of the absorbed dose relies on the energy imparted to matter. The imparted energy is itself defined as :

$$\epsilon = \sum T_{in} - \sum T_{out} + \sum Q, \tag{3.5}$$

where $\sum T_{in}$ is the sum of all the kinetic energies of the particles which have entered the volume; $\sum T_{out}$ is the sum of the kinetic energies of particles that have left the volume; and $\sum Q$ is the sum of all the changes that occurred in the rest mass energy of the volume (Carlsson, 1979).

The absorbed dose (units : Gy) is defined as the differential of the mean energy $d\bar{\epsilon}$ imparted to matter by ionising radiation within a mass dm, such as :

$$D = \frac{d\bar{\epsilon}}{dm} \tag{3.6}$$

The absorbed dose, D, is therefore related to the energy that remains in the mass after the event. There are some significant differences between the kerma and the absorbed dose; the absorbed dose is used to quantify the effects of radiation whilst the kerma characterises a radiation field. All of the energies deposited in the volume are considered in the calculation of the absorbed dose, whereas only the energies transferred due to the interactions of uncharged particles are taken into account in the kerma calculation. Finally, for the absorbed dose, the volume of interest is the volume in which the kinetic energy of the charged particle is spent, and all the charged particles entering this

volume of interest contribute to D. On the other hand, for the kerma, the volume of interest is the volume in which the energy is transferred from uncharged particles to charged particles, and the charged particles entering the volume do not contribute to K. Thus, the energy imparted to the mass (kerma) is not necessarily the same as the energy absorbed in the mass (absorbed dose). However, a simple relationship can be obtained between absorbed dose and kerma if the system satisfies the charged particle equilibrium condition (CPE).

The charged particle equilibrium exists if and only if the number of charged particles of a certain type, energy and direction entering a certain volume V is equal to the number of identical charges leaving it, in terms of expectation values (Attix, 1986; Bos, 2011). However, charged particle equilibrium occurs in a homogeneous medium, at a point where the boundary of the material is further than the maximum range of the secondary particles. Consequently, even for an uniform irradiation, the absorbed dose would not be homogeneous within the medium. If particles travel from a material M_1 to a material M_2, where M_1 is vacuum and M_2 is a material with attenuation, this results in a zero dose at the border between the materials, the dose will then increase with depth (build-up region), before reaching a constant value equal to the collision kerma K_{coll} once charge particle equilibrium is reached (Fig. 3.4a), assuming that the attenuation of the primary photon beam may be neglected. In this case, one can write :

$$D \overset{CPE}{=} K_{coll}, \tag{3.7}$$

where CPE denotes the point at which charge particle equilibirum is reached, and where D is the absorbed dose, and K_{coll} the collision kerma.

The parameter β quantifies the ratio of dose versus collision kerma, such as $\beta = D/K_{coll}$. During the build-up stage, $\beta < 1$, and for charge particle equilibrium, $\beta = 1$. However, if there is attenuation across the medium, the charged particle equilibrium is said to be transient (transient charged particle equilibrium, TCPE), and $\beta > 1$. In this case (Fig. 3.4b), the collision kerma decreases beyond the build-up region, and Eq. (3.7) becomes ;

$$D \overset{TCPE}{=} \beta K_{coll}. \tag{3.8}$$

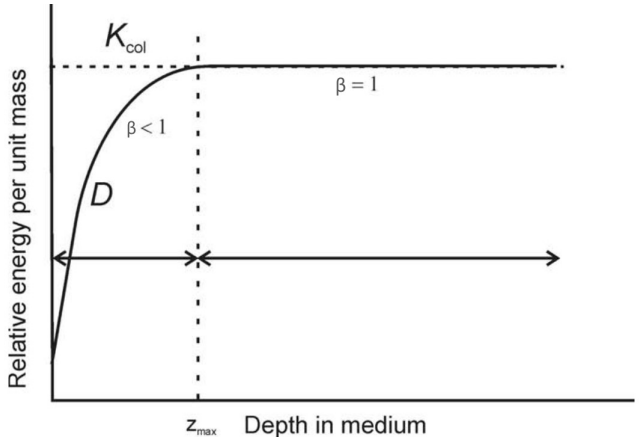

(a)

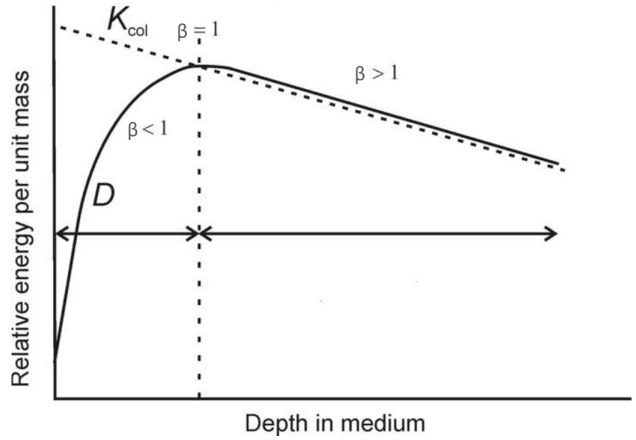

(b)

Fig. 3.4. Collision kerma as a function of depth for a) the build-up stage ($\beta < 1$) and b) for charge particle equilibrium ($\beta = 1$). $\beta > 1$ indicates the effect of attenuation. Redrawn from Podgorsak et al. (2005, p. 59).

3.2.2 Protection quantities

Mean absorbed dose in tissue and organ equivalent dose

The mean absorbed dose in an organ $D_{T,R}$ (Gy) is defined as :

$$D_{T,R} = \frac{1}{m_T} \int D dm, \tag{3.9}$$

where m_T is the mean mass of the tissue, D is the absorbed dose in a mass element dm, T the type of organ, and R the type of radiation. Consequently, the organ equivalent dose, H_T, was defined by the product of the organ absorbed dose $D_{T,R}$ with the radiation weighting factor, w_R, summed over all the types of radiation of the exposure, expressed as :

$$H_T = \sum_R w_R D_{T,R} \tag{3.10}$$

The unit of the organ equivalent dose is the Sievert (Sv) and differs from the Gray as it takes into account the radiation weighting factor. The values of radiation weighting factors w_R for other particles (ICRP, 2007) are listed in Table 3.2.

Table 3.2: Radiation weighting factors (ICRP, 2007).

Radiation type	Radiation weighting factor w_R
Photons	1
Electrons and muons	1
Protons and charged pions	2
Alpha particles, fission fragments, heavy ions	20
Neutrons	Continuous function of neutron energy

Effective dose

The effective dose was introduced to evaluate the radiological impact on the body, and accounts for the different radiation sensitivities of organs or tissues. Some organs, such as the brain, stomach

and bone marrow, in particular, are more sensitive. The value of the effective dose is defined for the whole body, and is calculated as the weighted sum of the absorbed dose to all organs of the body, expressed as:

$$E = \sum_T w_T H_T = \sum_T w_T \sum_R w_R D_{T,R}, \tag{3.11}$$

where w_T and w_R are the tissue and radiation weighting factors respectively; H_T is the equivalent dose absorbed by tissue T and $D_{T,R}$ is the mean absorbed dose in tissue T by radiation type R. The values of tissues weighting factors can be found in ICRP (2007).

Phantoms

Assessing the effective dose requires the use of computational phantoms. Computational phantoms are mathematical models configured to replicate the human body and to calculate the energy deposition in specific organs resulting from external or internal exposure to ionising radiation. The mathematical anthropomorphic phantom is divided into voxels (volume pixel), small cubic elements filled with tissue material specific to each organ. Particle transport codes incorporating the phantom model are used to relate the dose to a point to the dose in each voxel cell, that can later be added together to obtain the dose to an organ and the effective dose. Standardised phantoms are described in the ICRP publication 110 (ICRP, 2009), and Fig. 3.5 shows an example of the male ICRP phantom.

3.2.3 Operational quantities

Operational quantities are only defined at points in space. They are directly measurable using adequate radiation monitors calibrated in terms of measurable quantities, providing this can be achieved (i.e., capable of making the measurement at a point) and take into account the type of tissue (defined here as an ensemble of similar cells in the human body, such as organs). Operational quantities are defined in terms of doses to ICRU 4-element tissue and are given in Sievert (Sv, with 1 Sv = 1 J.kg^{-1}).

The main operational quantity is the dose equivalent. The dose equivalent H is obtained by multiplying the absorbed dose by a quality factor Q, expressed as :

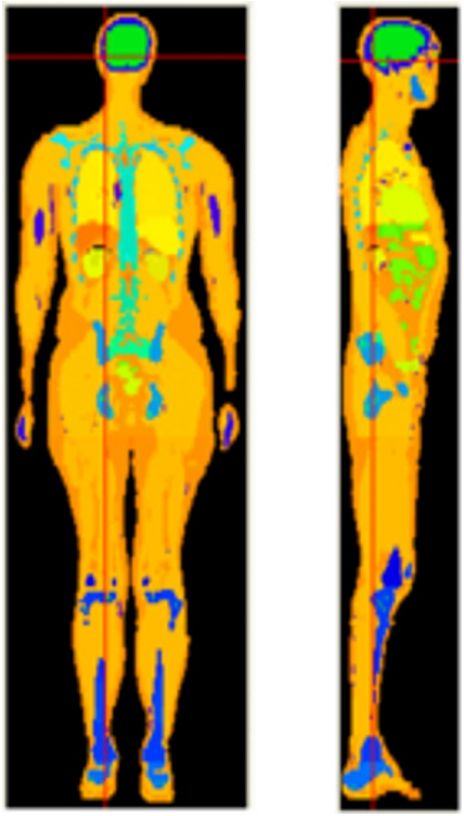

Fig. 3.5. Frontal and sagittal slices of the ICRP adult male reference computational phantom. The colours indicate the type of tissue. Reprinted from Hadid et al. (2010).

$$H = Q \times D \tag{3.12}$$

The Q factor was introduced to consider biological effectiveness (RBE) depending on the quality of the radiation; some type of radiation are more harmful than others, which is taken into account in this factor (ICRP, 2003). For photon and electrons, it is equal to 1. The quality factor Q is, however, different from the radiation weighting factor as it is a function of linear energy transfer L (LET). The linear energy transfer L ($\mathrm{J.m^{-1}}$ or $\mathrm{eV.m^{-1}}$), also known as the linear collision stopping power, is defined as the quotient :

$$L = \frac{dE}{dl}, \tag{3.13}$$

where dE is the mean energy lost by a particle, due to collisions with electrons in a distance dl (ICRU, 1993). The quality factor Q is obtained by integrating $Q(L)$ over L, and normalising by

the absorbed dose D.

Personal dose equivalent

To provide a conservative and more easily measurable surrogate for effective dose, the personal dose equivalent quantity was introduced. The personal dose equivalent $H_p(d)$ is the dose equivalent at a certain depth d in soft tissue. The most common depth considered is 10 mm ($H_p(10)$), as this is a minimal depth of most organs and can be shown to be conservative of E in most exposure situations. The $H_p(10)$ is often measured on a phantom, as backscatter is an important component of the field, and is also used to estimate the effective dose.

Other personal dose equivalent quantities include $H_p(3)$, used to determine the eye lens dose, and $H_p(0.07)$, used to assess local skin dose.

Ambient dose equivalent

The ambient dose $H^*(10)$ corresponds to the dose equivalent deposited at a depth of 10 mm along the radius vector opposing the direction of an expanded and aligned radiation field in a sphere of 30 cm of material composed of tissue equivalent material (also known as the ICRU sphere, ICRU 1980). Fig. 3.6 illustrates the situation of an ICRU sphere in a radiation field, and indicates the area whose dose gives the ambient dose equivalent for the point of interest O. It is used to assess the upper limit of a personal dose equivalent at 10 mm depth ($H_p(10,\theta)$, with $H_p^*(10) = H_p(10,0)$) that a person standing in the radiation field could receive. The measurement of $H^*(10)$ is always made free in air (detector not attached to any phantom), and is used for area monitoring rather than individual monitoring.

3.2.4 Quantities for emergency dosimetry

Chapter 2 discussed the necessity of a triage in case of large scale radiological events based on dose, but it has not been clarified yet which dose is to be used for triage. The primary dose calculated in physical dosimetry is the absorbed dose to the object (i.e., dose to quartz, resistors, teeth,...), whereas the dose of interest is the dose to the individual. Furthermore, in a scenario where the radiation field is not isotropic, a physical dosimeter may thus underestimate or overestimate the dose to the individual. Conversion from the absorbed dose to the dosimeter to another quantity

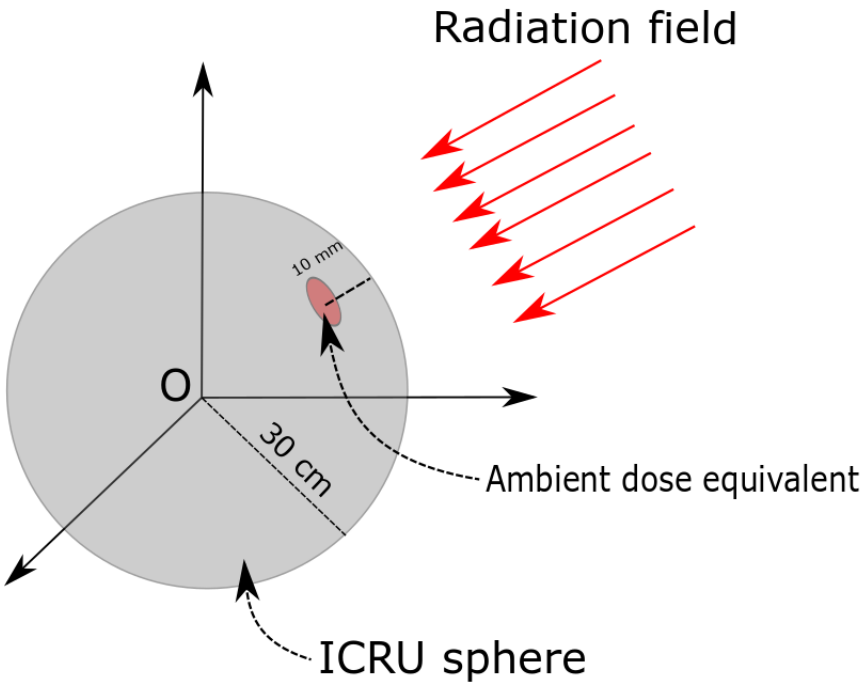

Fig. 3.6. Schematic representation of the ICRU sphere exposed to a radiation field. The ICRU sphere is composed of tissue equivalent material, and has a radius of 30 cm. The red area indicates where the ambient dose equivalent is calculated for the point of interest, O.

might be therefore needed.

The quantities traditionally used in conventional dosimetry may not operate well for emergency dosimetry. The first approach to evaluate the dose used for patient triage in emergency dosimetry would be to use a whole-body dose. The dose absorbed to the body (if the body is considered as a homogeneous mass) would not provide satisfactory evaluation of the biological risk for low penetrating non-uniform fields (Eakins and Ainsbury, 2018a). The personal dose equivalent may not operate well for emergency dosimetry in scenarios where the radiation field is not well characterised. The protection quantities, such as the effective body dose are used for radiation protection, and are supposedly the quantities that would be used for the triage of a population group in the aftermath of a mass casualty radiological event. However, the ICRP recommends that the effective dose is used

for high dose exposure, and that no medical treatment should rely on the effective dose assessment (ICRP, 2007). Moreover, both protection and operational quantities (given in Sv) are designed to account for long term stochastic risks, and not for short term, tissue reactions, for which a quantity given in Gy might more appropriate. This is quite obviously problematic for emergency dosimetry, and to address this issue, Eakins and Ainsbury (2018b) recommended that the dose determined in emergency dosimetry for triage is the dose to a few target critical organs, which would be determined by translating the dose to the dosimeter to the organ dose using computational methods. However, this might also lead to an increase in errors, if the geometry of exposure is not precisely known, and would considerably increase the time needed for dose assessment. Thus, for large scale accident, the absorbed dose to the material might be more reliable.

3.3 Retrospective and emergency dosimetry methods

The quantities described above were created for radiation protection purposes, and are used routinely in radiation facilities to protect the people and the environment. In this scope, various types of radiation meters, such as ionisation chambers, electronic personal dosimeters (EPD), Thermoluminescence dosimeters (TLD), or scintillation counters (Shani, 2000) have been developed and are commonly used by workers involved in the use of ionising radiation (e.g., industries, medical units, nuclear power plants, research facilities). The dosimetry in radiation protection schemes is carefully planned, and the instrumentation and materials used are designed for this purpose. For example, passive dosimetry can be performed using TLDs. The most commonly used material for TLDs is lithium fluoride, whose properties are highly desirable for personal dosimetry (flat energy response, linear dose response, tissue equivalence, high sensitivity and negligible fading). The properties desired for a dosimeter will be the subject of Section 5.2 in Chapter 5.

The routine measurements of doses ensure that dose limits are respected at all time to prevent radiation accidents. However, Chapter 2 highlighted scenarios in which radiation protection measures may fail and result in incidents of various scales. Chapter 2 also emphasised the reasons why dose assessments during and after a large scale radiological accident would be a primary necessity, but most of the techniques developed for conventional dosimetry would not be available or suitable. Hence, performing "unplanned" dosimetry in the aftermath of radiological accidents is a challenging task, and some of the methods that have been developed to retrospectively assess radiation doses

amongst members of the public following a radiological emergency will be explored in this section.

Chapter 2 also showed that the need for dosimetry in the follow-up of a radiation accident was twofold : to perform triage of the affected population groups and to follow-up epidemiological studies. Dosimetry shortly after the accident would aim to implement a rapid assessment procedure, only sending to an hospital the individuals whose absorbed body dose was measured to be above an agreed threshold, such as 2 Gy. This is referred to as emergency dosimetry, as the actions would be needed in the immediate aftermath of the accident, from hours to weeks after the exposure. Retrospective dosimetry, on the other hand, designates the dosimetry methods applied years to decades after the event, and has the potential to be coupled to epidemiological studies (Bailiff et al., 2016). McKeever and Sholom (2016) listed the desired properties that the dosimetry system developed to perform the triage of a population should meet :

1. To have a minimal measurable dose (defined later) of 0.5 Gy, to enable a triage threshold of 2 Gy

2. To be induced by ionising radiation only, not to induce false positives

3. To be sufficiently stable over few days to weeks following onset exposure

4. To be simple and quick, automation being an advantage

In addition to these, it could be added that, for emergency dosimetry the surrogate material dosimeter should be, for physical dosimetry : 1) ubiquitous amongst the population and 2) found next the person's body. The difficulty in finding new materials resides in the number of requirements that these materials must meet; be ubiquitous, found near of body of each individual, have sufficient sensitivity, and a rate of fading enabling the readout of the signal from days to weeks after the accident.

This section will review the two main types of emergency/retrospective dosimetry methods that have been developed : dosimetry performed 1) by using the biological markers induced by radiation (biological dosimetry), and 2) by using the radiation induced physical properties of materials found in the environment (physical dosimetry).

3.3.1 Biological dosimetry

Biological dosimetry methods such as cytogenetic assays are gold standards and routinely used for dose assessment. Although biological dosimetry methods are introduced here, this thesis will focus on physical dosimetry.

Biological methods use the radiation sensitivity of some bio-markers of the human body. They provide a whole-body dose, as, for example, blood circulates throughout the body. Several biological techniques have been developed, some being very well accepted, others being still under development (International Atomic Energy Agency, 2011; Kulka et al., 2012; Blakely et al., 2009).

Cytogenetic techniques

Cytogenetic techniques observe chromosome damage due to ionising radiation. Radiation damages to the chromosome were already discussed as a potential health effect leading to more serious conditions in Chapter 2, Section 1. For emergency dosimetry, the chromosomes studied are the ones contained in peripheral blood lymphocytes (Ainsbury et al., 2010). Cytogenetic techniques are the most developed in biological dosimetry (Simon et al., 2010), the most employed one being the dicentric chromosome assay.

Dicentric chromosome is a type of chromosome aberration, where the chromosome forms two centromers, due to misrepair of the DNA strands after being directly broken by radiation (International Atomic Energy Agency, 2011). They are almost exclusively induced by radiation, and their frequency follows a quadratic response to absorbed dose. Doses as low as 0.1 Gy can be estimated using this technique, and the signal can be used months after the exposure (Ainsbury et al., 2010). However, despite its many advantages, this technique is quite slow, with an estimate of 55 hours from sample receipt to dose estimate.

Other cytogenetic techniques include the premature chromosome condensation (Pantelias and Maillie, 1984), the micronucleus assay (Huber et al., 1983), and the fluorescence in situ hybridisation (FISH) assays (Finnon et al., 1995).

Genetic techniques

Genetic techniques relate to the gene expression; the process in which the gene is used to synthesise products such as proteins or ribonucleic acid (RNA). The main genetic technique used for emergency

dosimetry is the gene expression assay (Manning et al., 2017). The expression of a gene is modulated as function of the exposure of the individual to ionising radiation, and profiles have been drawn for radiation workers and radiotherapy patients. However, this technique was proven to be unstable over time (Ainsbury et al., 2010).

Haematological techniques

Haematological techniques rely on the blood cells counts after the accident. Changes are observed for doses $\geq$ 5 Gy, but the susceptibility to dose varies from person to person and a reference background for each individual is needed (typically taken as soon as possible after the irradiation), which can lead to high uncertainties (Ainsbury et al., 2010).

Protein biomarkers

Protein biomarker techniques for dose evaluation relies on proteins and enzymatic modifications. The most promising one identified as a radiation marker is the γ-H2AX protein (Moquet et al., 2017). When the DNA double strands break, which leads to the formation of the γ-H2AX at the point where the DNA strand broke. γ-H2AX can be counted using immunostaining techniques (Moroni et al., 2013). However, this protein is not stable over time, and the foci decay within several days.

3.3.2 Physical dosimetry

Physical methods include electron paramagnetic resonance (EPR), and luminescence techniques, employing measurements of thermoluminescence, TL, and optically stimulated luminescence, OSL (Bailiff et al., 2016; Ainsbury et al., 2010). They can measure the absorbed dose in materials such as quartz contained in bricks, salt, alumina substrate surface mount resistors or teeth enamel, to name a few.

Thermoluminescence (TL) and optically stimulated luminescence (OSL) of commonplace materials

Thermoluminescence (TL) and optically stimulated luminescence (OSL) techniques rely on a similar physical principle. Ionising radiation imparts energy to an electron in the valence band to be

transferred to metastables states or traps between the valence band and the conduction band of a semi-conductor or insulator, creating electron-hole pairs within the solid. The number of pairs thus created is proportional to the absorbed dose. Upon readout, additional energy is brought to the system by either heating (TL) or exposure to light (OSL), which prompts the electrons to be excited from the traps and to travel via the conduction band recombining with vacant holes, and leads to the emission of photons. The mechanisms that govern the emission of TL and OSL will be discussed in depth in Chapter 4.

TL and OSL techniques have been used for sometime in radiation dosimetry because of their sensitivity and ease of use. Many materials have been developed for personal dosimetry, such as lithium fluoride, calcium fluoride, aluminium oxide, beryllium oxide or calcium sulphate and are now routinely used in radiation facilities (McKeever et al., 1995). Luminescence dosimetry presents many advantages which would make of it a valuable emergency dosimetry tool, such as rapid dose assessment, low cost and high sensitivity to dose. Furthermore, natural minerals, such as quartz or feldspars also exhibit a TL/OSL response following exposure to ionising radiation, which prompted their use for archaeological dating (Aitken, 1985). Many other materials found in the environment may also show radiation sensitivity detectable using luminescence techniques, thus, luminescence techniques were rapidly adopted as an alternative candidate technique to biodosimetry for emergency and retrospective dosimetry.

Building materials Luminescence techniques were perhaps amongst the first to be used for dose assessment long after the exposure in case of radiological accidents. Pioneering work started in the 1960s, with work aiming to assess the dose to tiles of houses of the regions of Hiroshima and Nagasaki remaining after the explosion of the A bomb in August 1945 using TL techniques (Higashimura et al., 1963; Hashizume et al., 1967). Tiles, and more generally ceramic building materials such as bricks (Meckbach et al., 1996) contain the most favoured material for TL and OSL retrospective dosimetry, namely quartz grains. Natural quartz has been widely used as a dosimeter in archaeological dating, as its sensitivity and the stability of its signal makes it a reliable dosimeter.

TL measurements conducted with tiles from Hiroshima issued from various locations (Nagatomo et al., 1992; Ichikawa et al., 1987; Nagatomo et al., 1995), found good agreement with radiation transport simulation (Roesch, 1987). Following the first studies carried on tiles from Hiroshima and

Nagasaki, much work followed; other studies using luminescence measurements for dose assessment have been carried in Chernobyl settlements (Bailiff et al., 2004a, 2005; Sato et al., 2002), Semipalatinsk nuclear test site (Bailiff et al., 2004b; Sato et al., 2006; Göksu et al., 2006), or the Techa river site (Göksu et al., 2002; Bougrov et al., 1998).

Besides bricks, other building materials that may be used for dose reconstruction include cement (Göksu et al., 2003) or bricks containing calcium silicate (Bailiff and Mikhailik, 2004).

One should note that TL and OSL dose estimation using building materials is used for retrospective dosimetry, years to decades after the accident. It does not provide the dose received by individuals and is mainly used in the frame of long term epidemiological studies to validate other techniques including computational modelling and biodosimetry techniques. The dose assessed in retrospective dosimetry is the absorbed dose to environment materials, and here, for example to ceramic building materials. As emphasised in the previous chapter, dosimetry would not only be needed for epidemiological studies, but also for triage, in the immediate aftermath of the catastrophe (i.e., for emergency dosimetry). For this reason, new materials were sought for emergency dosimetry.

Alumina substrate resistors Alumina substrate are used in the manufacture of surface mounts resistors, commonly used in circuitry. Nowadays, most electronic devices are likely to contain a circuit including surface mounts resistors - or chips. Fig. 3.7 shows an example of the circuit of a mobile phone containing surface mount resistors.

The use of alumina substrate resistors to act as surrogate dosimeters was first suggested by Inrig et al. (2008b), and since then, the potential of this material for emergency dosimetry has been examined, using both TL and OSL techniques (Ekendahl and Judas, 2012; Beerten et al., 2009; Bassinet et al., 2014; Lee et al., 2017; Woda et al., 2010; Kouroukla et al., 2014). Their good characteristics in terms of dose response (linear in the range 10 mGy - 100 Gy), and mostly their presence in mobile phones used by the general public, make them the most promising material for use in emergency dosimetry. The luminescence signal of an alumina substrate was observed to exhibit anomalous fading (Inrig et al., 2010b; Ademola and Woda, 2017; Kouroukla, 2015), although in Chapter 11 we will discuss how this fading can be significantly reduced using phototransferred TL measurement techniques. Although not yet applied to real scenarios, inter-laboratory comparisons

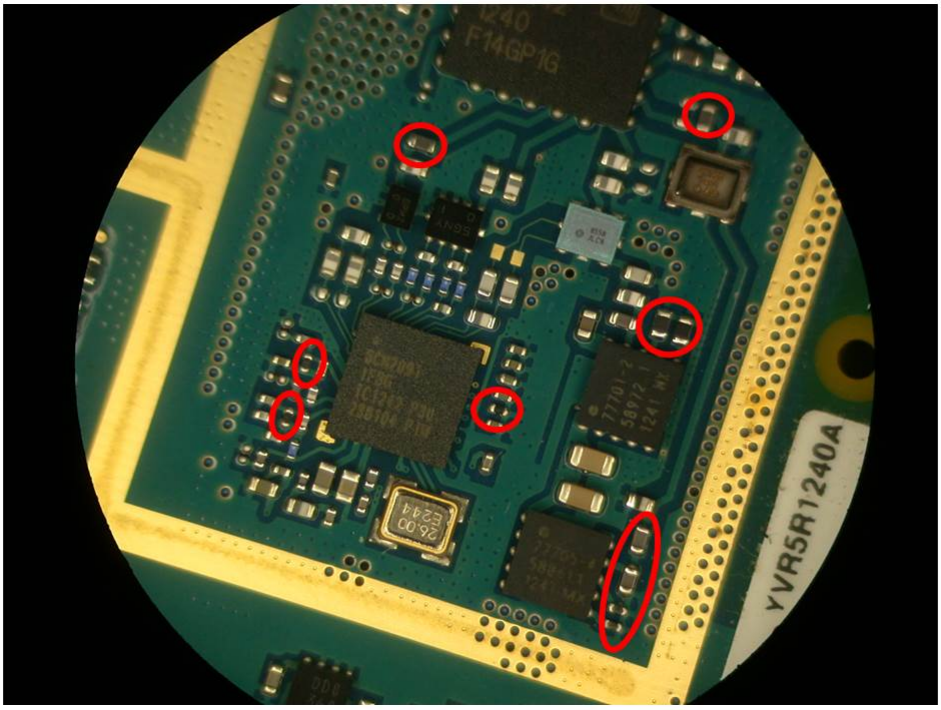

Fig. 3.7. Electronic circuit of a mobile phone including alumina substrate surface mount resistors. The resistors are circled in red.

using the OSL signal of resistors extracted from the circuit board of mobile phones have already taken place (Bassinet et al., 2014), that confirmed the potential of this technique. However, technical developments are still needed to address the issue of the decreasing resistors size trend. Concerns were also expressed regarding the likely difficulty to obtain mobile phones in an emergency situation, where they are likely to be handled by security forces. This issue also prompted the development of techniques using alternative materials.

Glass display TL measurements on mobile phone glass displays also gave promising results for dose assessment. Although the presence of a native signal was detected, the region 150-250 °C of the glow curve typically exhibit a TL response emitting in the blue (Discher and Woda, 2014), with a dose response linear for absorbed doses 10 mGy - 20 Gy, and the fading was observed to be correctable using an universal fading correction (Discher and Woda, 2013). Furthermore, the energy response of the TL signal was generally observed to be relatively flat for energies above 200 keV (Discher et al., 2014).

Commonplace materials The dosimetric properties of many more materials have been investigated using OSL and TL (Table 3.3). The work done on commonplace materials (such as clothing, banknotes, coins,...) showed a great variability in the sensitivity of the signal that was sometimes attributed to dust or other kinds of impurities (Sholom and McKeever, 2014). On the other hand, salt, for example showed great sensitivity (with a detection limit of ca 4 mGy, Christiansson et al. 2014), but is not likely to be found in the possession of individual on the scene of the accident, although a sachet could be carried by individuals, providing affordable dosimeters.

The search for commonplace materials with suitable dosimetric properties with luminescence techniques continues, with the goal of having the largest possible catalogue of materials susceptible to act as surrogate dosimeters.

Table 3.3: Materials reported in the literature for their use as surrogate dosimeters using luminescence techniques. The detection limit is defined in Section 3.4 of this chapter. A material is considered as stable here if the loss of the signal is ≤ 5 % after 1 month.

Materials	Detection limit (mGy)	Stable	References
Quartz contained in bricks, ceramics	~ 100	Yes	Bailiff (1995)
Dental repair materials	5	No	Bailiff et al. (2002); Ekendahl et al. (2013)
Calcium silicate bricks	20	Yes	Bailiff and Mikhailik (2004)
Cement	100	Yes	Göksu et al. (2003)
Gypsum wall boards	500	No	Thompson et al. (2010)
Medicines tablets (Crocin, Paracad, Ultramol, Calcium with Vitamin D3)	120-275	Yes	Menon et al. (2017)
Table vitamins (B1, B2, B12, Complete Multivitamins Adults 50+ and Men 50+, Multivitamins Men 50+ and Women 50+, L-lysine, calcium 500+D)	500	No	Sholom and McKeever (2016b)

Alumina substrate resistors	∼ mGy	No	Inrig et al. (2008b); Ekendahl and Judas (2012); Beerten et al. (2009); Bassinet et al. (2014); Woda et al. (2010); Kouroukla et al. (2014)
Mobile phone screen display	300-400	No	Bassinet et al. (2010); Discher and Woda (2013); Mrozik et al. (2014b)
Integrated circuits	170-260	No	Sholom and McKeever (2016a)
SIM cards	7	No	Pascu et al. (2013)
Chip cards	3-200	No	Woda et al. (2012)
Clothing (cotton, silk, linen, hemp, nylon, rayon, lycra, fleece)	45-1200	No	Sholom and McKeever (2014)
Shoe sole	50-550	No	Sholom and McKeever (2014)
Plastic buttons	3-150	No	Sholom et al. (2011b)
Paper banknotes	20-2000	No	Mrozik et al. (2017); Sholom and McKeever (2014)
Coins	30-5000	No	Sholom and McKeever (2014)
Bank cards	8-1500	No	Sholom and McKeever (2014)
Business cards	4-1000	No	Sholom et al. (2011b)
Fingernails	100-5000	No	Sholom et al. (2011b)
Tooth enamel	27-5000	No	Sholom et al. (2011a); DeWitt et al. (2010)
Dust	500	Yes	Bortolin et al. (2011)
Salt	0.2-1	Yes	Bernhardsson et al. (2009); Christiansson et al. (2014)
Watch glass	0.5	No	Ayda et al. (2016)
Glass bottles	2000 - ca 105	No	Sahiner (2017)
Colour pencils	750-1000	No	Meriç et al. (2015)
Desiccants	8-450	No	Geber-Bergstrand et al. (2015)
Washing powder	5-100	No	J. Thomsen et al. (2002)
Insect wings	480-2400	No	Kazakis et al. (2016)

Electron paramagnetic resonance (EPR)

Similarly to TL and OSL, EPR uses electron-hole pairs produced in the solid by exposure to ionising radiation. Using EPR, the detection of the radiation-induced signal requires the application of a magnetic field to the trapped unpaired electrons' (or radicals') spin. Exposed to a magnetic field, the radicals split into energy states according to the spin orientation relative to the field; i.e., whether the spin is anti-parallel to the field (higher energy state) or parallel (lower energy state). The magnetic field removes the degeneracy of the possible spin states (s=$\pm$1/2) of the electron with the s=-1/2 state having the lowest energy. In a typical EPR measurement magnetic fields of $\leq$ 1 T are applied to the sample which results in an energy (Zeeman) splitting of the two electron spin states that corresponds to photons with microwave frequencies. EPR spectrometers usually operate with a fixed microwave frequency and the magnetic field increased in strength while the microwave absorption within the cavity is recorded. When the magnitude of the strength of the magnetic field reaches the value for which energy separation of the two spin states is equal to the microwave photon energy, the system is in resonance and photons are absorbed. The value of the absorption is related to the amount of unpaired electrons in the samples, hence linked to the absorbed dose. Furthermore, EPR provides an indication on the nature of the paramagnetic centres or traps, which can be of interest in characterising the materials for TL/OSL.

The use of EPR for emergency and retrospective dosimetry has mostly focused on biological materials, such as bone and tooth enamel. However, teeth and bones are not likely to be employed for the triage system of situations described in Chapter 2, as it would require medical procedures to extract them (even if in vivo systems are still under development). Although not practicable for emergency dosimetry, EPR dosimetry using tooth enamel is an efficient dosimeter for retrospective dosimetry. Once extracted, teeth need to be sterilised before the enamel is separated from the dentin. The extracted enamel is then ground and purified for the EPR measurements (Fattibene and Callens, 2010). Cevc et al. (1972) associated the EPR signal originating from exposure to ionising radiation to the $CaCO_3^{-3}$ anion radical in teeth enamel, but later work attributed this signal to the CO_2^- radical (Zdravkova et al., 2005), although it is accepted that several radicals derived from carbonate, such as CO_3^{3-}, CO_3^-, or CO^- contribute to the signal (Fattibene and Callens, 2010). This radical is easily seen in the EPR spectrum with features growing with dose at g=2.002 and g=1.998 (where g is a constant of proportionality linking the strength to the state

energy difference) of the magnetic field (Ivannikov et al., 1997), and one of its important feature also identified by Cevc et al. (1972) is the stability of this radiation damage. Two signals arise from the EPR spectrum of teeth enamel; the background signal (non radiation induced) and the radiation induced signal. The two components can be identified and separated (Sholom et al., 1998; Sato et al., 2007; Lanjanian et al., 2008). The radiation induced signal shows a linear growth with dose, with a detection limit of ca 50-100 mGy (Romanyukha and Regulla, 1996; Bailiff et al., 2016). Studies have since confirmed the applicability of this technique in dose assessment of individuals and real case scenarios. EPR measurements of tooth enamel of Chernobyl liquidators enabled dose assessment of 770 individuals, for whom epidemiological studies were carried out (Chumak et al., 1999). The teeth of the general population of Chernobyl were also examined (Skvortsov et al., 2000; Gualtieri et al., 2001; Chumak et al., 1998), and the dose resulting from the EPR measurements correlated with the level of ^{137}Cs contamination on the ground. The dose to tooth enamel of 69 Hiroshima A bomb survivors was assessed by EPR spectroscopy by Nakamura et al. (1998), and good agreement was found with the cytogenetic data of the same group of individuals. The nuclear test site of Semipalatinsk (Ivannikov et al., 2006; Romanyukha et al., 2006, 2002), Mayak nuclear workers (Wieser et al., 2000; Romanyukha et al., 1994), the inhabitants of the Techa river (Romanyukha et al., 2001), contaminated by radioactive release, and the population of Goiana, exposed to a lost radioactive source (Rossi et al., 2000) have also been the subject of EPR studies.

However, the invasive nature of EPR spectroscopy on teeth is its main drawback; in many scenarios it could be difficult to obtain teeth from the public, either because subjects would be reluctant to have a tooth extracted, or because the extraction itself requires time. To address this issue, the possibility of in vivo measurements is still under investigation (Ikeya and Ishii, 1989; Yamanaka et al., 1993; Zdravkova et al., 2003; Schreiber et al., 2016). Another alternative relies on the use of biopsies, where only a small amount of the tooth is extracted (between 10 to 70 mg), which later can be reconstructed with resins.

Bone also shows EPR characteristics similar to tooth enamel, as some of the radicals in bone and tooth enamel are similar (Callens et al., 1998), making it suitable as a dosimeter (Brady et al., 1968). However, the main issue remains the extraction of bones, that, although available in some cases (Trompier et al., 2007b; Krefft et al., 2014) are very unlikely to be obtained in large scale scenarios.

Other materials investigated using EPR include plastics, paper, buttons, human hair (Nakajima, 1982), natural rocks (Ikeya and Ishii, 1989), clothing (Barthe et al., 1989; Kamenopoulou et al., 1986), sugar (Trivedi and Greenstock, 1993; Fattibene et al., 1996), glass (Engin et al., 2006; Wu et al., 1995), fingernails (Trompier et al., 2007a), or even shells (Nakajima et al., 1993). The applicability of these materials is very variable; the detection limit is between 0.1 Gy for tooth enamel to 10 Gy for cottons. Furthermore, materials such as plastics exhibit relatively strong fading.

3.3.3 Computational dosimetry

Radiation transport codes using Monte Carlo techniques can also be used in dosimetry. Historically, Monte Carlo techniques use repeated random sampling of the variables within the probability distribution and produce a probability distribution for the outcome by simulating the physical processes for random points of the variables' distribution. Monte Carlo radiation transport codes simulate the transport of particles in a specified geometry, and the absorbed dose can be calculated for each point of the geometry. A map of the radiation field can therefore be constructed, from which the absorbed dose can be assessed (Ainsbury et al., 2010). One of the most widely used codes is the Monte Carlo N Particle code (MCNP), developed by the Los Alamos National Laboratory. MCNP is a general-purpose Monte-Carlo N Particle code that can be used for neutron, photon, electron, coupled neutron/photon/electron, or over 1000 other ions and particle species transport (X-5 Monte Carlo Team, 2003). The range of application of MCNP is quite wide, including dosimetry, radiation protection, detector design, radiography, medical physics, and nuclear reactor design (Goorley et al., 2012).

Historically, the first use of Monte Carlo transport codes applied to retrospective dosimetry provided a mapping of the absorbed dose in the environment. Particle transport code calculations were integrated to the Hiroshima and Nagasaki dosimetry system (Santoro et al., 2002); to the Techa river site (Taranenko et al., 2003); to the Chernobyl accident (Göksu et al., 1996), and to the 2001 Georgia accident (Clairand et al., 2006). In some of these cases, Monte Carlo simulations were coupled to luminescence or EPR measurements.

Another use of radiation transport codes for emergency dosimetry consists of relating the dose to the materials measured using physical dosimetry techniques (e.g., resistors, glass displays and

teeth enamel) to organ dose or individual body dose. This technique provides a means of offering efficient and targeted treatment to the exposed individuals. Ongoing work, started by Eakins and Kouroukla (2015), aimed to related the absorbed dose in the resistors of mobile phones to the organ dose of an individual, using MCNP6 and voxelised phantoms, depending on the position at which the mobile phone would have been located relative to the body and the source of ionising radiation during the accident. A later chapter of this thesis will continue with work using a similar approach to relate the dose of new materials investigated to the organ/body dose.

3.3.4 Comparison of physical dosimetry and biological dosimetry

Both physical and biological dosimetry present advantages and drawbacks to perform triage of the population following radiological emergencies. So far, no ideal system gathering the desired properties listed at the beginning of this section seems to be emerging.

Biological dosimetry estimates absorbed dose using biological markers, as described in Section 3.3.1. The dose determined is the whole body dose of the individual, and as being based on biological material, can be performed on each individual. Some of its techniques, such as dicentric chromosome assay are now well established, tested and proven to perform well in inter-laboratory comparisons (Wilkins et al., 2008). When calibrating a biological marker, standard universal calibration curves are used and as they are not sample specific, an issue might arise with inter individual variations. EPR with tooth enamel yield similar issues, although the doses evaluated for Chernobyl clean-up workers using dicentric chromosome assay and EPR of teeth enamel strongly correlate, indicating the robustness of those two techniques (Khvostunov et al., 2014). Biological methods are relatively time-consuming, with a time estimate for the effects to develop (between the sample receipt and the dose estimate) of 55 hours for dicentric chromosome assay, 120 hours for the FISH assay, up to 36 hours for gene expression, but only 3 hours for γ-H2AX (Ainsbury et al., 2010). Automation for these techniques is, however, already in use, or under development (Romm et al., 2013).

On the other hand, physical dosimetry can provide an estimate of external dose using detectors close to the body. The use of transport simulation code can provide organ specific dose or the whole body dose using the external dose estimate. Furthermore, the difficulty of physical dosimetry resides in finding materials that are ubiquitous amongst a population. The dose assessment with OSL and TL is, however, much faster than dicentric chromosome assay, and can be done between a

few tens of minutes to a day, depending on the sample and protocol. Calibration can be performed on a specific sample, at several levels of dose. If biological methods, such as dicentric chromosome assay are now well developed, emergency dosimetry with TL and OSL methods is more recent, and still under development.

McKeever and Sholom (2016) compared data from inter-comparisons for both physical and biological dosimetry, and found that all techniques follow a similar trend of having narrower distribution of the results when the dose increases, that for every method employed, an individual laboratory can substantially be in error when estimating the dose, and that in terms of error the dicentric chromosome assay appears to be the most favourable technique so far. It is, however, expected than in the case of a large scale accident, biodosimetry and physical dosimetry methods would be effective when combined. Ideally, a robust dosimetry system would use several techniques of dose estimation, and integrate a comparison of the results.

3.4 Statistical approaches to dose estimation in retrospective and emergency dosimetry

3.4.1 Uncertainties in retrospective and emergency dosimetry

The assessment of uncertainties in emergency dosimetry is of fundamental importance as it aims to give an indication to the medical team performing a triage of the population of the extent to which the dose assessment is reliable (i.e. the confidence interval). The risk of putting an individual in the wrong category during the triage phase could lead to serious consequences, e.g., sending back home a patient that would require urgent care, or (albeit less seriously), wasting limited medical resources on people who do not need them. In an effort to address this issue, work has been performed to integrate uncertainty analysis techniques to the dosimetry system (Ainsbury et al., 2018).

The *Guide to the Expression of Uncertainty in Measurement* (or GUM, Bureau International des Poids et Mesures et al. 1995) provide an indication on how uncertainty analysis should be approached, and is still used for uncertainty analysis in emergency dosimetry. It lists parameters that could be the source of uncertainty in measurements, many of which apply to emergency dosimetry using OSL and TL.

For example, a luminescence reader is able to detect a finite range of light intensities, above which the photo-multiplier response may saturate, and below which the photon counts will be too low to be detected above background. The calibration of the dose rate of the radiation source integrated in the reader may also be a source of uncertainties. Often a series of assumptions are used for calculating the accident dose (e.g., universal fading rates for components made of the same material), that could lead to increased errors in the dose assessment. Repeatability of the measurements is also a known issue, as it is rare that two measurements would yield the same value of photon counts, and this is assessed by carrying out reproducibility tests. Moreover, if the scenario of radiation exposure is unknown or only partially known (i.e., absence of knowledge about the geometry, the type of ionising radiation), relating the measured dose to the effective body dose would also be an important source of uncertainty.

Two types of categories are considered in uncertainty analysis, namely type A and type B errors (Bureau International des Poids et Mesures et al., 1995). They differ by the way of evaluating measurement uncertainties; whilst they are both built upon probability distributions, type A errors are estimated from a probability density function derived from an observed frequency distribution, and type B errors are calculated assuming a probability density function describing the degree of belief that an event will occur (Bureau International des Poids et Mesures et al., 1995, p. 7).

The GUM method (Guide to the Expression of Uncertainty in Measurement Bureau International des Poids et Mesures et al. 1995) was developed to assess uncertainties by assuming a normal probability distribution. The error associated to each variable is propagated in calculations using first-order Taylor series approximations.

If the GUM method is currently the standard method used for error approximation in emergency dosimetry, other methods, such as Monte-Carlo or Bayesian statistics provide a more accurate estimate of uncertainties, and are increasingly implemented to dose assessments. Uncertainty analysis using Monte-Carlo methods enables sampling of non-normal distributions and cross-correlations between measurement variables, by using random sampling methods. Bayesian techniques may also be integrated to uncertainty analysis, and are particularly useful as they enable the use of prior knowledge. They assume that the parameters and variables are probabilistic and assign a prior distribution to each. Coupled with the experimental data, this results in a probability density function (PDF) describing the likelihood of the results (Ainsbury et al., 2018). Bayesian techniques are

mostly implemented in biological dosimetry, whilst so far, physical dosimetry has mostly made use of GUM and Monte-Carlo techniques.

In the case of TL and OSL, in the simplest approach (i.e., no fading, linear dose response curve passing through the origin), the dose absorbed during the radiological accident, the accident dose D_{acc}, is determined by dividing the accident signal, L_{acc} by the signal L_{cal} recorded for a known calibration dose, D_{cal}, such as :

$$D_{acc} = \frac{L_{acc} \times D_{cal}}{L_{cal}}. \tag{3.14}$$

The TL/OSL signals have an associated uncertainty, in terms of photon counts, often taken as a Poisson error. However, most of the materials used for emergency dosimetry exhibit fading. The fading is characterised by a known function f, which itself comes with associated uncertainties. The accident dose is then determined as :

$$D_{acc} = f\frac{L_{acc} \times D_{cal}}{L_{cal}}. \tag{3.15}$$

Applying the GUM method, this gives the uncertainty as

$$\delta D_{acc} = D_{acc}\sqrt{\left(\frac{\delta f}{f}\right)^2 + \left(\frac{\delta L_{acc}}{L_{acc}}\right)^2 + \left(\frac{\delta L_{cal}}{L_{cal}}\right)^2 + \left(\frac{\delta D_{cal}}{D_{cal}}\right)^2} \tag{3.16}$$

However, the case considered here assumed a linear dose response, which is not always the case. Some materials, for example, may exhibit a quadratic dose response and, in this case, more than one calibration point would be needed. Correction for sensitisation, the increase of the signal over the cycle of measurement for a similar administered dose may also be required in some cases. These corrections would once again come with associated uncertainties that would have to be embedded in the final uncertainty estimate.

Monte-Carlo simulations can here be used for uncertainty propagation as well as in the GUM method. A supplement was added to the GUM manual, providing guidance for the use of Monte-Carlo simulations for uncertainty analysis (Bureau International des Poids et Mesures et al., 2008). Rather than applying a deterministic formula, the Monte-Carlo simulation performs a series of random sampling of values taking into account the distribution of each of the parameters, producing a distribution of the outcomes. Monte-Carlo procedures for uncertainty estimates are now straightforward to implement and this thesis, the errors have been propagated using a Monte-Carlo procedure

implemented in the software R.

The robustness of a method is tested through inter-laboratory blind comparisons. In addition to the assessment of uncertainty of a measurement, tests are carried out to assess whether independent laboratories are able to reconstruct the absorbed dose for samples irradiated with an unknown gamma dose. Participating laboratories are required to follow similar protocols and methods of analysis on identical materials, and the comparison of the results provides a good indicator of whether the method is reliable and applicable to real case scenarios. A "good intercomparison" would have all the participating laboratories assessing correctly the absorbed dose, or at least sending the sample to the right triage category (high dose, low dose, no dose). Discrepancies in results may also indicate sources of uncertainty that have not been thought of before, for example, uncertainties arising from unknown storage conditions during transportation. Inter-laboratory comparisons may also help assessing the performance of a laboratory (Oestreicher et al., 2017). In this scope, several inter-laboratory comparisons were run in both biological and physical emergency dosimetry. OSL and TL intercomparisons have been prepared with alumina substrates (Bassinet et al., 2014). In their critique of biological dosimetry versus physical dosimetry, McKeever and Sholom (2016) recommended more inter-comparison exercises to be carried out for both methods to obtain a more realistic estimate of the uncertainties.

3.4.2 Detection limit and decision threshold

The detection limit is a key criteria of a dosimeter as it is the parameter defining whether the sensitivity is sufficient to register low levels of dose. As explained above, in emergency dosimetry, the threshold dose for triage is of 2 Gy, for which a dosimetry method with a detection limit of 0.5 Gy is desirable. Two concepts will be clarified here : the decision threshold (minimum dose that can be detected, above which it can be said that exposure to ionising radiation occurred) and the detection limit, or minimal measurable dose (the minimum dose that can be determined, above which a dose value can be determined), as proposed by Currie (1968).

The detection limit derives from the decision threshold (Currie, 1968), defined as the limit above which the result of the measurement and analysis indicates detection (i.e., a positive measurand). The International Organization for Standardization (ISO) established a standard for the determi-

nation of the characteristic limits (decision threshold, detection limit and limits of the confidence interval) for measurements of ionising radiation (ISO 11929, 2010), where it stipulated that if and only if the measurement value is above the decision threshold, it can be concluded that the physical effect is present, but it cannot be concluded that the effect is absent if the measurement value is below the decision threshold. A critical "decision" in emergency dosimetry is whether the patient was exposed to a significant level of dose that requires immediate treatment, and the decision threshold set is 2 Gy (Coleman et al., 2011). However, for a dosimeter, the decision threshold (i.e. whereas the dosimeter has received a dose) can be lower. Two types of errors can arise when trying to determine whether, for example, a person has been exposed to a significant. The first type would be to decide that the individual has been significantly exposed when they had not (type α error, of the first kind, related to the decision threshold D_T), the second type being to fail to determine that the patient had been exposed (type β error, of the second kind, related to the decision limit D_L). Analysing data from both biodosimetry and physical dosimetry inter-laboratory comparisons, McKeever and Sholom (2016) reported 35% of false negatives for a 2.2 Gy dose with the dosimetry methods used.

The standard deviation of the net signal of an irradiated sample ($\sigma_S = (\sigma^2_{S+B} + \sigma^2_B)^{1/2}$, where σ_B is the standard deviation of the background) when the mean is equal to zero, and the maximum acceptable value for α, determine the decision threshold, or critical level, L_C.

The critical level is defined at the level at which decisions can be made. The detection limit, on the other hand, is the limit above which an analytical procedure may be relied upon to determine the true value of the measurand following the measurement procedure (Currie, 1968); it is the smallest value of the measurand that can be detected using the measurement procedure. Mathematically, Currie (1968) defined the critical level L_C and the detection limit D_T as :

$$L_C = k_\alpha \sigma_0, \tag{3.17}$$

$$L_D = L_C + k_\beta \sigma_D, \tag{3.18}$$

where k_α and k_β are the abscissa of the standardised normal distribution corresponding to probability levels $1 - \alpha$ and $1 - \beta$, with α and β referring to errors of the first and second kinds, as explained above; and where σ_0 is the standard deviation of the net signal when the mean of the

net signal is equal to zero, and σ_D the standard deviation of the signal when its true value is equal to L_D. A schematic representation of the critical level and detection limit is shown in Fig. 3.8.

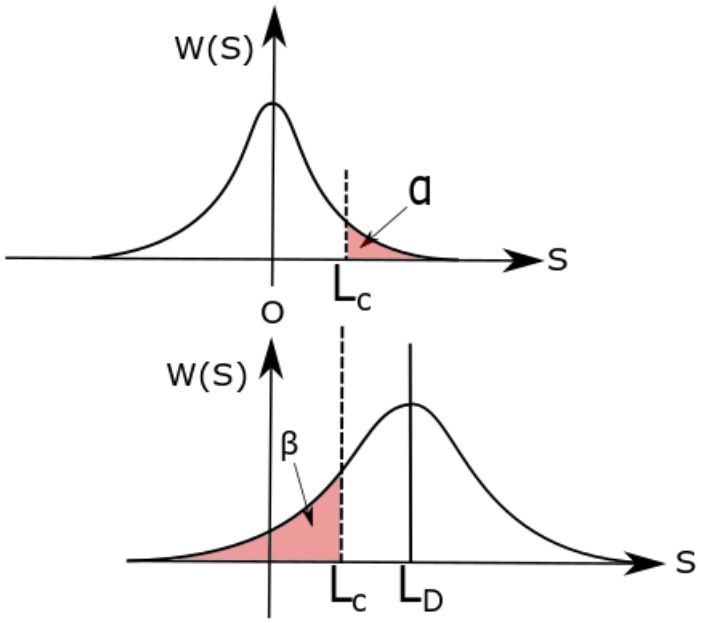

Fig. 3.8. Probability distributions ($W(S)$) for a limiting mean value equal to 0 (upper graph) and L_D (lower graph). α and β refers to errors of the first and second kinds, and are indicated in the red areas. Redrawn from Currie (1968).

Following this definition, if $\alpha = \beta$ (the risk of false positive equal the risk of false negative), $k_\alpha = k_\beta$ and Eq. (3.18) becomes :

$$L_D = 2L_C = 2k\sigma. \tag{3.19}$$

Furthermore, if the standard deviation of the signal, σ, is taken to be independent of the background :

$$\sigma_S = (\sigma_{S+B}^2 + \sigma_B^2)^{1/2} = \sqrt{2}\sigma_B. \tag{3.20}$$

Currie (1968) derived a working expression for the decision threshold and the detection limit, accommodating a 5% error in false positive or negatives. This would give expressions of L_D and

L_C such as :

1. Decision threshold : $L_C = 2.33\sigma_B$
2. Detection limit : $L_D = 4.65\sigma_B$

In the literature of emergency dosimetry, the term "detection limit" is rarely used, and the term "minimal measurable dose" much more widely used. The minimal measurable dose is defined as the background plus two (or three) standards deviations from the signal of an unexposed dosimeter (Yukihara and McKeever, 2011). In this thesis, the term "detection limit" is preferred, and is calculated as the dose for which the signal is equal to the background plus three times the standard deviation of the background.

3.5 Summary

This chapter has defined quantities that are measured in radiation dosimetry relevant to this study, and emphasised that although physical quantities are directly accessible via measurement (i.e., particle fluence, kerma, absorbed dose) the quantities of interest in radiation protection, the protection quantities (effective dose, mean absorbed dose of an organ or tissue) are derived from the physical quantities via calculation. A latter section addressed the challenge of assessing these quantities in radiological emergency contexts, and thus explored the techniques developed for emergency dosimetry. Of these techniques, those of interest in this thesis - luminescence techniques - have been applied to radiological accidents such as Hiroshima, Chernobyl or Semipalatinsk via the dose assessment of quartz contained in bricks. However, new materials are continuously sought to optimise and broaden the emergency dosimetry system using the luminescence system. A short review of the materials investigated under luminescence techniques was provided, and although some appear to be promising (e.g., alumina substrate resistors), it is still desirable to seek new materials that would fulfil or approach the criteria of "ideal" dosimeters to strengthen the potential of luminescence techniques for emergency dosimetry. Finally, the last section of this chapter addressed the questions of uncertainty assessment and detection limits in emergency dosimetry, that are a crucial point in determining whether the dose estimate provided using emergency dosimetry techniques are reliable.

The next chapter will review the mechanisms that govern thermoluminescence and optically stimulated luminescence, and particularly, what physical mechanisms give rise to luminescence

emission proportional to the absorbed dose.

Chapter 4

Theory of thermoluminescence and optically stimulated luminescence

4.1 Introduction

Chapters 2 and 3 have examined how luminescence techniques can be employed for absorbed dose assessment in radiological emergency situations. It has been argued that dosimetry is needed for the management of large-scale radiological accidents harming members of the general public (Chapter 2) and that luminescence techniques can be employed for dose assessment using surrogate dosimeters found in the environment (Chapter 3). This chapter will aim to explain what is meant by "luminescence techniques". In earlier chapters, two types of luminescence have been mentioned : thermoluminescence (TL) and optically stimulated luminescence (OSL); the differences and similarities between these two techniques will be also explained in this chapter.

A luminescence dosimeter can briefly be described as a material that has the property to store charge, resulting from exposure to ionising radiation, at defect sites and to later release it, resulting in the emission of visible /UV photons. The primary questions addressed in this chapter are : 1) Where does the luminescence emission of luminescence dosimeters originate? 2) What mechanisms govern the emission of luminescence? 3) What models can be used to describe the luminescence emission in some solids? ; 4) What information can be derived from the TL/OSL and how is this achieved?

4.2 The origins of luminescence emission in solids

4.2.1 Band-gap model and energy levels

Energy levels in crystals

A perfect crystal, i.e., a solid constituted of atoms or ions arranged in a periodic lattice, is firstly considered here. The atoms of such a crystal give rise to a periodic electrostatic potential that gives rise to permitted electronic states in defined energy bands. However, the description of energy bands in crystals will begin by considering the free electron model where electrons in the solid experience constant potential in all space.

Free electron model For the sake of simplification, the motion of a free electron in space will be considered, which can be described by Schroedinger's equation (Kittel and Holcomb, 1967):

$$\hat{H}\psi = E\psi, \tag{4.1}$$

where $\hat{H}$ is the Hamiltonian of the system, defined in the case of a free electron by

$$\hat{H} = \frac{\hat{p}^2}{2m_e}, \tag{4.2}$$

with $\hat{p} = -i\hbar\nabla$ the momentum operator, and m_e the mass of the particle. ψ represents here the wave function and E the eigenvalues of the Hamiltonian, that physically, correspond to the energy values of the particle.

By solving Schroedinger's equation, the eigenvalues of the Hamiltonian are given such as:

$$E = \frac{\hbar^2 k^2}{2m_e}, \tag{4.3}$$

where $\vec{k}$ is a wave vector of the electron which is quantized and is inversely proportional to the size of the potential well; hence each value of $\vec{k}$ corresponds to a given value of the energy, E.

In practice the spacing between each energy level is very small compared with the typical energies, effectively creating a continuum of states within the solid.

The free electron model provides some insight into the electronic properties of metals, but it cannot explain why some energy values of electronic states are forbidden, which occurs in insulators

(e.g., 8-10 eV gap) and semiconductors (few eV gap) as a result of the "forbidden gap", or band gap.

Periodic potential, the nearly free electron approximation and the origin of the band gap The ionic cores in perfect crystals such as described above (i.e. without any impurities or imperfections) can be modelled as a periodic potential V depending on their position $\vec{r}$ in the lattice such as $V(\vec{r}) = V(\vec{r} + \vec{R})(\neq 0)$ where $\vec{R}$ is the translation vector of the lattice. Hence the Hamiltonian of the conduction electrons becomes :

$$\hat{H} = \frac{\hat{p}^2}{2m_e} + V(\vec{r}) \tag{4.4}$$

Assuming that the potential is periodic within the crystal, the wave function can be written as a Bloch function such as :

$$\psi(\vec{r}) = \sum_{\vec{k}} u_{\vec{k}}(\vec{r}) \exp(i\vec{k} \cdot \vec{r}), \tag{4.5}$$

where $u_{\vec{k}}(\vec{r})$ is a periodic function with the same periodicity as the lattice, and $u_{\vec{k}}(\vec{r}) = u_{\vec{k}}(\vec{r} + \vec{R})$. The general solution for the Schroedinger equation in a periodic potential is therefore related to the superposition of plane waves. As a consequence, all the independent values of $\vec{k}$ lie within a periodically reproducible zone called a "Brillouin zone", whose edge (the concept of Brillouin zone edge is further explained below with Eq. 4.7) depends on the limit condition of the potential imposed by the solid (often either periodical or null potential at the zone edge).
Using the expression of the Hamiltonian (4.4) and the Bloch wave function (4.5), the central equation (4.6) is obtained :

$$\left(\frac{\hbar^2 k^2}{2m_e} - E\right) u_{\vec{k}} + \sum_{\vec{G}} V_{\vec{G}} u_{\vec{k}-\vec{G}} = 0 \tag{4.6}$$

Where $\vec{G}$ are reciprocal lattice vectors, each one existing in a reciprocal space and representing a set of crystal planes. This new equation for the energy distribution leads to a dual solution for the energy whenever $\vec{k}$ lies on a Brillouin zone edge such as:

$$E_{\pm} = V_0 + \frac{E_k^0 + E_{k-G}^0}{2} \pm \sqrt{\left(\frac{E_k^0 - E_{k-G}^0}{2}\right)^2 + |V_G|^2}, \tag{4.7}$$

where V_0 is the value of the potential, and $E_k^0 = \frac{\hbar^2 k^2}{2m_e}$ for a nearly free electron.

Energy levels : the band gap model

For plane waves with a wavelength twice that of the separation between the planes, there is a back reflection of the electron, interference and standing waves are set up with antinodes either at the the position of the atomic cores or between atoms. Those with electron density concentrated at atomic cores have a lower energy than that of the corresponding plane wave, while those with high electron density between the atomic cores have a higher energy than that of the plane wave. The energies of these two stationary states determine the edges of the forbidden energy.

This difference in energy at the Brillouin zone edge causes the permitted energy levels to split into two levels, the Conduction band (excited state) and the Valence band (ground state) with a gap between the two bands (Fig. 4.1)

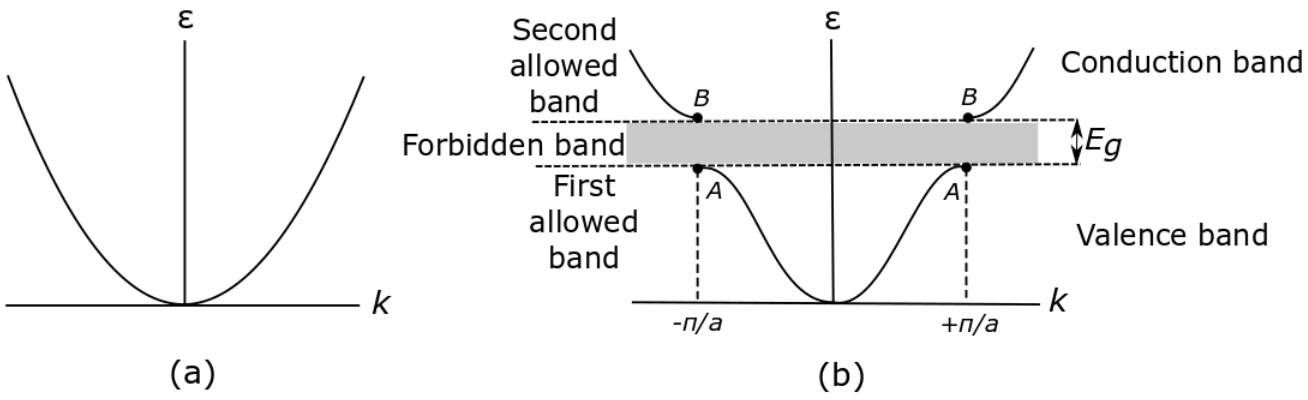

Fig. 4.1. (a) Plot of energy, ϵ, versus wavevector k for a free electron. (b) Plot of energy, ϵ, versus wavevector for an electron in a monoatomic lattice of lattice constant a. A is the value of energy E_- at the Brillouin zone edge, B the value of energy E_+ at the Brillouin zone edge and E_g the width of the enery band gap. Redrawn from Kittel and Holcomb (1967), Chapter 7, page 164.

The width of the energy gap at room temperature determines whether the solid is an insulator (one band empty or completely filled, ~ 8 eV gap and larger), a metal (one or more bands partially filled) or a semiconductor (up to a few eV gap; Kittel and Holcomb 1967). The case of semiconductors and insulators is of interest in this thesis as it allows electron transitions from the valence

band to the conduction band if sufficient energy is given to the system. At room temperature T the thermal energy of the system, given by $E = k_B T$, is about 0.026 eV, where k_B is the Boltzmann constant, which is not sufficient enough to cause the electrons to move from one band to another.

4.2.2 Configuration coordinate and Jablonski diagrams : luminescence emission in solids and selection rules

The configuration coordinate diagram was developed to clarify particle transitions between two energy states in a solid, in particular leading to the emission of visible/UV photons. In such a diagram (e.g., Fig. 4.2), each energy state is represented as a parabola of the energy E versus the vibrational distance R. The parabola shape results from the harmonic oscillation of the localised charge in its energy state. The particle is hence subject to a force F such as:

$$F = -C(R - R_0), \tag{4.8}$$

where C is a constant. Therefore the corresponding energy dependence on the distance R is:

$$E = \frac{1}{2}C(R - R_0)^2 \tag{4.9}$$

The energy eigen value of an harmonic oscillator is given by the form :

$$E_n = (n + \frac{1}{2})h\nu, \tag{4.10}$$

where $n = 0, 1, 2, ...$ represents the frequency and ν is the oscillation frequency. The energy eigen values are therefore distributed in discrete energy levels, some of them being represented as horizontal lines on the parabola of Fig. 4.2.

Absorption of excitation energy

During an optical absorption (Fig. 4.2), energy is delivered to the system by exposure to light, and the electron is given energy to transfer from the lowest level $n = 0$ of the ground state to the edge of the parabola of an excited state, as symbolised with the vertical arrow on Fig. 4.2. This optical absorption is characterised by its width, which depends on the distance $R'_0 - R_0$ that lies between the two parabola; if $\Delta R = 0$, the two parabola are superimposed and the absorption band becomes a narrow line. To consider the total absorption band, a sum is made over all of the vibrational

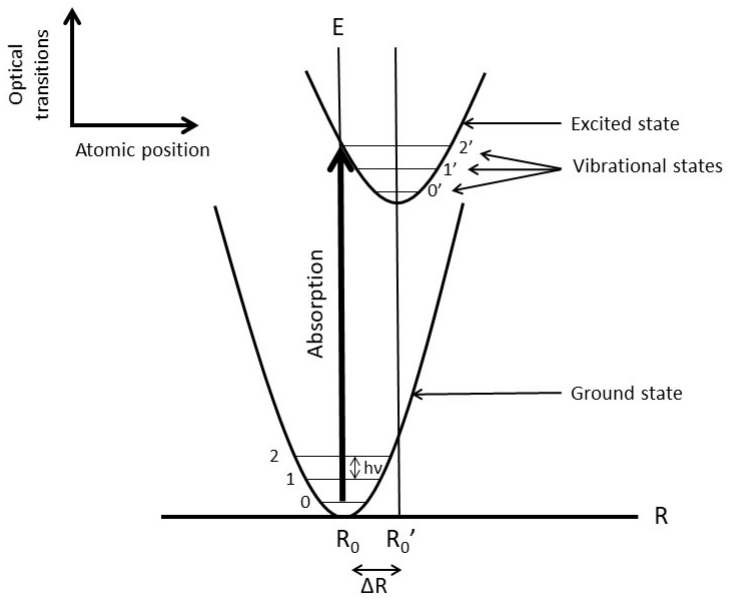

Fig. 4.2. Configuration coordinate diagram for the absorption of excitation energy, represented by the vertical arrow. The ground state at an equilibrium distance R_0, and the excited state at a distance R_0' are are illustrated as parabolas. The ground and excited vibrational states are also shown, respectively [0,1,2] and [0',1',2']. Redrawn from Blasse and Grabmaier (2012, p. 13).

levels of the excited state n'; hence if $\Delta R = 0$, the particle is only absorbed to the vibrational level $n' = 0$.

Emission of energy : radiative return to the ground state

Following the absorption stage, the particle is placed in a high vibrational state of the excited state; the relaxation is therefore the atomic process by which the system returns to the lowest vibrational state, as can be seen on Fig. 4.3. It is important to note that there is no radiative emission occurring during the return to the lowest vibrational state. The return to the ground state from the lowest vibrational level of the excited state can occur in several ways : via a radiative return (emission of radiation), via a non-radiative return, or via transfer of the excitation energy from one ion to another (Blasse and Grabmaier, 2012, p. 33). The first two cases are more important here and will be discussed further below.

When the system readjusts its position to the lowest vibrational stage of the excited state during the relaxation, there is an excess of energy. hlThe particle can either spontaneously return to the ground state if the levels are at a distance ΔR close enough, or remain in the excited state until additional energy (thermal or optical) is brought to the system to return to the ground state. Upon returning to the ground state, the centre reaches a high vibrational level, from which another relaxation occurs to bring the centre back to the lowest level. Therefore, as two relaxations take place during the emission, the energy of the emission will be lower than the energy of absorption. The shift between the two is called the Stokes shift and is directly dependent on the parabola offset ΔR.

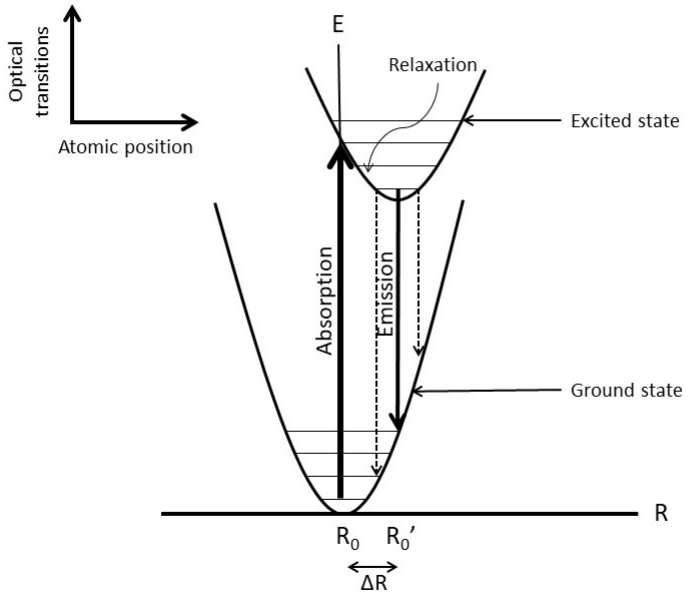

Fig. 4.3. Configurate diagram displaying the absorption, relaxation and emission from a centre. Redrawn from Blasse and Grabmaier (2012, p. 34).

Non-radiative return to the ground state

A non-radiative return is a return to the ground state without the emission of radiation. For a luminescent material, this process is therefore undesirable, and a phosphor would be judged as

efficient only if the probability of radiative return is higher than the probability of a non-radiative return. To quantify the probability of having a radiative process instead of a non-radiative one, the quantum efficiency factor was defined as the ratio of the number of emitted quanta by the number of absorbed quanta. In the case of photoluminescence, the quantum efficiency is defined as (Blasse and Grabmaier, 2012, p. 84):

$$q = \frac{\text{Number of emitted quanta}}{\text{Number of absorbed quanta}}, \tag{4.11}$$

whereas the radiant efficiency is:

$$\eta = \frac{\text{Emitted luminescent power}}{\text{Power absorbed by the material from the exciting radiation}}, \tag{4.12}$$

and the luminous efficiency is :

$$L = \frac{\text{Luminous flux emitted by the material}}{\text{Absorbed power}}, (\text{Unit : lumen/W}). \tag{4.13}$$

Non-radiative returns can be caused by different factors. At high temperature, the centre may cross the two parabola and return to the ground state via a non-radiative route and the excitation energy is diffused as phonons; if the two parabola are parallel and the energy difference is such as $\Delta E \leq 5$ times the higher vibrational frequency of the surroundings, high energy vibrations can be excited, making radiative transitions unlikely (multi-phonon emission); finally both previous processes can occur simultaneously in a three parabola configuration.

Optical transition rules

The transition rate of an optical transition is strictly governed by rules about the quantum numbers of the initial and final states. If the quantum numbers do not follow those rules, the transition rate will be zero (forbidden transitions). Selection rules mathematically arise from the description of the dipole potential of the harmonic system with spherical harmonics. The potential of a "2^l" pole (if $l = 1$, it is then referred as a "dipole") can be written as (Curie, 1963, p. 14):

$$V_l = \frac{1}{R^{l+1}} \Sigma_{m=-l}^{m=l} a_l^m Y_l^m(\theta, \phi), \tag{4.14}$$

where the Y_l^ms are derived from the expression of the Legendre Polynomial of degree l, R is the distance and the coefficients a_l^m are given by :

$$a_l^m = \frac{4\pi}{2l+1} Q_l^m, \tag{4.15}$$

with $Q_l^m = \delta Y_l^m(\theta', \phi')\rho dv$, the multipole electric moment, of order l, and where $m = -l, -l+1, ...l-1, l$.

This expression is therefore indeed dependent on the quantum numbers number l and m, defining the quantum states of the system;

- $l = 0, 1, 2, ...n-1$ is the angular momentum quantum number with $n = 1, 2, ...\infty$ the principal quantum number describing the energy level,
- $-l \leq m \leq l$ is the correlated magnetic moment quantum number,
- and $s = \pm\frac{1}{2}$ the spin moment quantum number

The total angular momentum for a single particle is a function of the quantum numbers l and s, such as:

$$j = l + s \tag{4.16}$$

For each transition between two quantum states, the variations between the associated quantum numbers must fulfil the following rules for the transition to occur (Fox, 2002, p. 348):

$$\begin{aligned} \Delta l &= \pm 1 \\ \Delta m &= 0, \pm 1 \\ \Delta s &= 0 \end{aligned} \tag{4.17}$$

The transition rules also yield a physical meaning, as follows :

- $\Delta l = \pm 1$ derives from the parity of the wave function $(-1)^l$,
- $\Delta m = 0, \pm 1$ derives from the polarization of light carrying an angular angular momentum, and the need to conserve the above-mentioned angular momentum throughout the transition,
- $\Delta s = 0$, as photons do not interact with the electron spin in this case.

4.2.3 Phosphorescence, fluorescence and stimulated luminescence

Section 4.2.2 briefly described the condition under which a transition is said to be allowed; i.e. under which the electric-dipole transition rate will be different from zero and a photon can be emitted. As such, an allowed transition has a high transition rate, the radiative lifetime is short (1-10 ns), and the process is said to be "prompt". A radiative transition occurring within nanoseconds is called "fluorescence"; if the transition is delayed for a substantial time ($\geq$ 10 ns), it is then referred as "phosphorescence". Fig. 4.4 summarises the different types of luminescence emission in solids as a function of the delay between excitation and emission. The line of 10^{-8} s drawn between fluorescence and phosphorescence here is debatable, and should not be considered as a clear cut. Phosphorescence can be divided between short period ($\leq 10^{-4}$ s) and long period ($\geq 10^{-4}$ s) emission, the latter, if prolonged over periods of minutes and longer, is then referred as "thermoluminescence" or "optically stimulated luminescence". This type of emission is different in the sense that the emission has to be triggered by additional energy brought to the system, thermally or optically. It is that last phenomena, by its subsequent persistence of particular interest, that constitutes the main topic of investigation in this thesis.

Short- and long-term luminescence are also differentiated by the physical processes involved; fluorescence is a direct process in which the absorption and emission occur solely between a ground state and one excited state, explaining its rapid nature. Phosphorescence, however necessitates an extra transitional state (or meta-stable state) via an inter-system crossing, from which the phosphorescence transition back to the ground state are spin-forbidden are therefore occur on a slow time scale. A Jablonski diagram, illustrating the different luminescence transitions within a molecule (typically anthracene) is shown in Fig. 4.5.

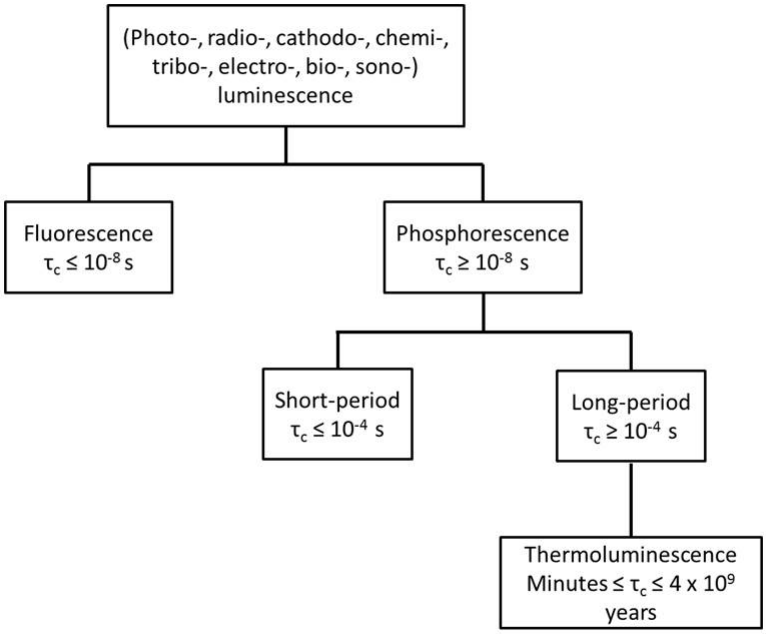

Fig. 4.4. Tree of luminescence phenomena as function of the delay between excitation and emission τ_c. The prefixes indicate the mode of excitation. Redrawn from McKeever (1988, p. 3)

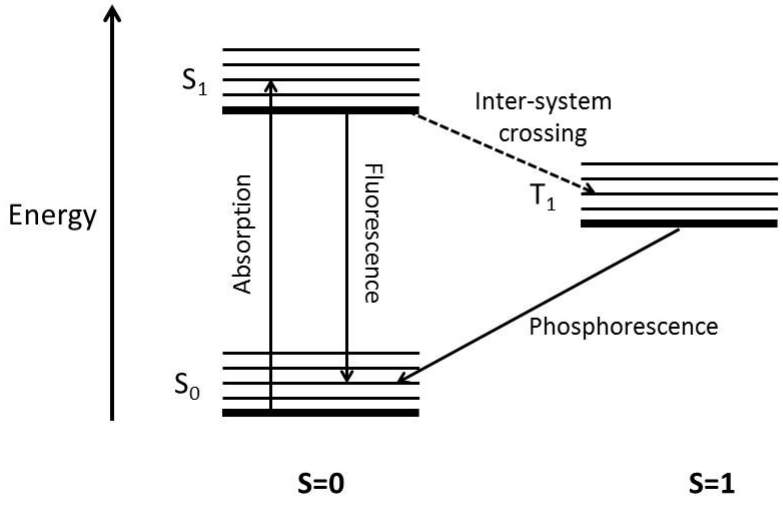

Fig. 4.5. Jablonski diagram of absorption, fluorescence and phosphorescence emissions. Redrawn from Fox (2002, p. 228)

As discussed above, stimulated luminescence, is considered as a sub-case of phosphorescence (Fig. 4.4), because of the similarity of the mechanism. In stimulated luminescence, the electrons are also excited from the valence band to the conduction band, from which they become trapped in metastable states, discrete energy levels created by the defects in the crystals (i.e., impurities, dislocations, lattice defects or other perturbations). Whilst impurity atoms and larger complexes can function as luminescence centres, smaller and minor perturbations provide electron trapping levels right below the conduction band, and above Fermi level. Electrons remain in those traps until additional energy is brought to the system, by either heating it (thermoluminescence) or exposing it to light (optically stimulated luminescence). If the system gains sufficient energy, the electrons can physically move within the conduction band and reach a recombination centre that contains a bound hole, from which they will emit light. Recombination can either occur in the valence band, or in a intermediate state. The differences in transitions associated with fluorescence, and phosphorescence/stimulated luminescence are further explained in Fig. 4.6.

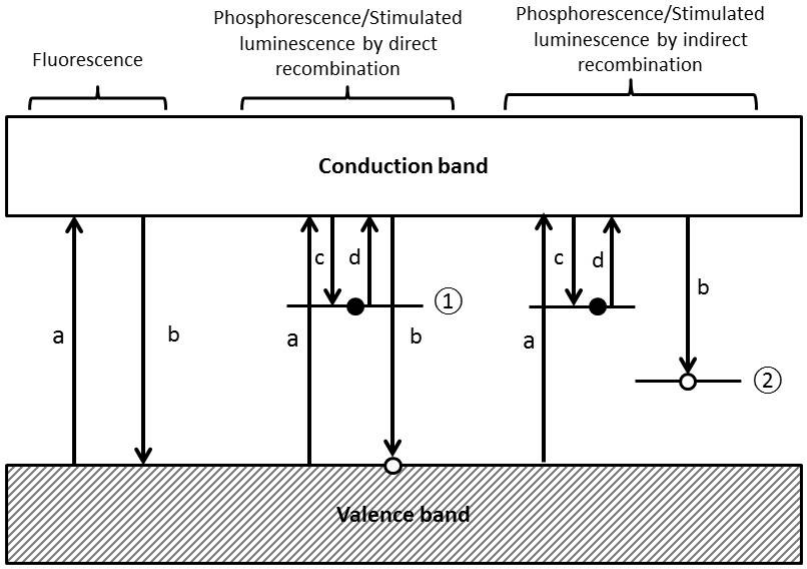

Fig. 4.6. Band gap diagram of the allowed transitions in semi-conductors or insulators leading to fluorescence, and phosphorescence/stimulated luminescence emission. 1) Electron trap, 2) Recombination centre, a) Ionisation, b) Recombination, c) Electron trapping, and d) Electron release.

4.3 Basic concepts of thermoluminescence and optically stimulated luminescence

Thermoluminescence (TL) and optically stimulated luminescence (OSL) both rely on the storage of electrons in defects within the crystalline or polycrystalline structure and release of the charge into the conduction band by heat (TL) or light (OSL). After being released, the electrons are delocalised and can travel in the conduction band to the recombination centres (Fig. 4.6), where they emit visible/UV photons, detectable in the laboratory using a photomultiplier tube (PMT).

4.3.1 Basic concept of thermoluminescence

During a thermoluminescence (TL) measurement, the temperature ramps up at a defined rate (heating rate, β in $^{\circ}C.s^{-1}$) to a maximum temperature. The emitted photons are detected by the photomultiplier, integrated over a temperature interval during the measurement, and plotted against the temperature. The resulting graph is called a TL glow curve, and offers a visual representation of the traps being progressively depleted when the temperature increases - an example of TL glow curve comprising at least 4 peaks is given in Fig. 4.7.

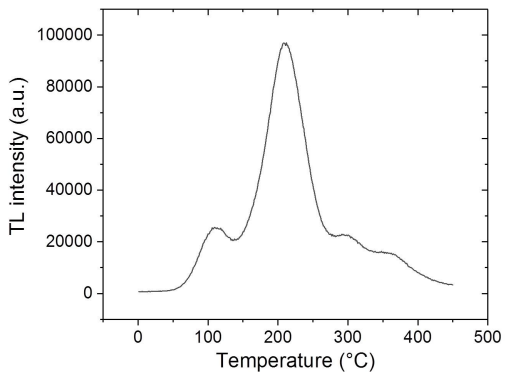

Fig. 4.7. Example of a TL glow curve from an alumina substrate following a 10 Gy β dose. Detection window : U-340 filter, heating rate : 5 $^{\circ}C.s^{-1}$.

In 1945, Randall and Wilkins (1945) stated that the rate of thermal excitation of electrons from the trap to the conduction band (transition (d), Fig. 4.6) is given by the equation :

$$-\frac{dn}{dt} = np = ns\exp\left(\frac{-E}{kT}\right), \tag{4.18}$$

where n (cm^{-3}) is the concentration of filled electron traps, p the probability per unit time for thermal excitation, s (s^{-1}) the frequency factor, describing the probability of an attempt to escape of the electrons from the trap, E (eV) the activation energy, k_B ($\mathrm{eV.K}^{-1}$) the Boltzmann constant, and T (K) the temperature. During thermal stimulation, the trap loses charge, indicated by the negative sign of the equation. Upon the absence of re-trapping into the level, the luminescence intensity is proportional to the rate of decay (Chen and McKeever, 1997, p. 19), and therefore :

$$I(t) = -\eta\frac{dn}{dt} = \eta np = \alpha n, \tag{4.19}$$

where I is the luminescence intensity, η a constant, and $\alpha = \eta p$.

4.3.2 Basic concept of optically stimulated luminescence

Optically stimulated luminescence (OSL) uses optical stimulation instead of heat to release trapped charges, and thus for optical stimulation, the probability for stimulation p becomes (Bøtter-Jensen et al., 2003, p. 18):

$$p(E_0) = \Phi\sigma(E_0), \tag{4.20}$$

where Φ is the optical simulation intensity, $\sigma(E)$ the photo-ionisation cross section, and E_0 the threshold of stimulation energy required to release a charge. The light is absorbed in the material following the Beer-Lambert law :

$$I(\lambda, x) = I_0(\lambda)\exp\left(-\alpha(\lambda)x\right), \tag{4.21}$$

where $\alpha(\lambda)$ is the absorption coefficient, depending on the material, λ the wavelength and $I(\lambda, x)$ is the light intensity as a function of x, the depth.

Similarly to TL, the emitted luminescence intensity during the stimulation of previously irradiated material will therefore be :

$$I(t) = -\eta\frac{dn}{dt} = \eta n\Phi\sigma(E_0) = \eta np \tag{4.22}$$

Therefore, the main difference between TL and OSL lies in the expression of the stimulation probability p. For thermal stimulation (TL), the probability of electrons escaping from the traps p follows an Arrhenius law, such as :

$$p(T) = s \exp\left(-\frac{E}{kT}\right), \tag{4.23}$$

and under optical simulation (OSL) :

$$p(t) = Ct, \tag{4.24}$$

where C is a decay constant.

Another interesting process, the photoluminescence (PL), is characterised by the light emitted by a sample when light of a certain wavelength is absorbed.

In the case of OSL, an optical filter is placed between the detection unit (photomultiplier) and the sample, in order to discriminate the light emitted by the sample to the stimulation light shone onto the sample. Typically, two wavelengths are used : either blue LEDs (470 nm) or infra-red diodes (850 nm) where the latter is referred as infra-red stimulated luminescence (IRSL).

Continuous wave OSL (CW-OSL)

When the temperature T, the wavelength λ and the optical stimulation intensity Φ are fixed, the mode of stimulation is commonly referred as "continuous wave OSL" (or CW-OSL). The output is a curve decaying over the time of illumination, as the charges are progressively being depleted from the traps. An example of CW-OSL decay curve, with a schematic representation of the stimulation mode is given in Fig. 4.8.

Linear-modulated OSL (LM-OSL)

Alternatively, the intensity of the illumination may vary over time at a fixed wavelength, for what is called Linear Modulated OSL (LM-OSL). If the intensity varies linearly with time :

$$\Phi(t) = \Phi_0 + \beta_\Phi t, \tag{4.25}$$

where $\beta_\Phi = d\Phi/dt$. LM-OSL was introduced by Bulur (1996) to separate overlapping OSL signals corresponding to different traps. At low intensity, the shallower traps, easier to bleach

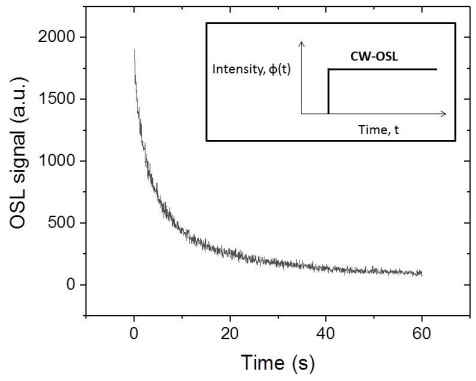

Fig. 4.8. Example of a CW-OSL decay curve of alumina substrate following a 10 Gy β irradiation. A schematic representation of the CW-OSL mode of stimulation is presented in the top right corner. Detection window : U-340 filter, sample temperature : 50 °C.

(i.e. loss of trapped charges induced by exposure to light), are depleted, and while the intensity increases, "hard-to-bleach" deeper traps are depleted. This allows the observation of a peak shaped signal instead of a decay curve, and enhances the precision of trap depth parameters obtained by deconvolution. In the example of the LM-OSL decay curve given in Fig. 4.9, a single narrow peak, with a fast increase is observed.

A third mode of excitation consists in stimulating with pulses of light of different duration t and intensity Φ, whilst keeping the ratio Φt constant (McKeever et al., 1996). The main advantage of this technique is to observe the amount of trapped charges relaxing during the pulse of light, and after the end of the illumination.

4.4 Mathematical description of TL and OSL

A very simplified band diagram model of the transition occurring in a phosphor was shown in Fig. 4.6. A mathematical explanation of this model will be examined here, and more complex and realistic kinetic models, incorporating the motion of charges, will also be explored.

The nomenclature used in this section is summarised in Table 4.1, and those symbols are placed on a schematic representation of a model including one trap and one recombination centre in Fig. 4.10.

Table 4.1: Kinetics model nomenclature

Symbol	Unit	Meaning
n	cm^{-3}	Concentration of electrons in traps
m	cm^{-3}	Concentration of holes in recombination centres
n_e	cm^{-3}	Concentration of electrons in excited localised states
n_g	cm^{-3}	Concentration of electrons in ground states
N	cm^{-3}	Concentration of trapping states
M	cm^{-3}	Concentration of recombination centres
E	eV	Activation energy
s	s^{-1}	Frequency factor
p	s^{-1}	Stimulation probability of electrons escaping from the trap
n_c	cm^{-3}	Concentration of free electrons in the conduction band
m_v	cm^{-3}	Concentration of free holes in the valence band
A_n	$\mathrm{cm}^3.\mathrm{s}^{-1}$	Retrapping probability
A_m	$\mathrm{cm}^3.\mathrm{s}^{-1}$	Recombination probability of electrons
A_{me}	$\mathrm{cm}^3.\mathrm{s}^{-1}$	Transition probability coefficient for an electron occupying the excited state of the recombination centre
B	$\mathrm{cm}^3.\mathrm{s}^{-1}$	Trapping probability of holes
X	$\mathrm{cm}^{-3}.\mathrm{s}^{-1}$	Rate of production of electron-hole pairs by the excitation irradiation per unit volume per second
τ_c	s	Critical lifetime of tunnelling
ρ'		Dimensionless number density of acceptors

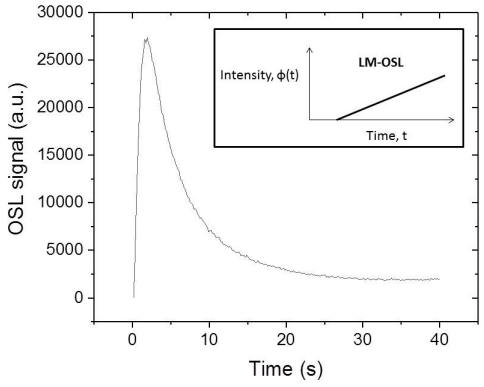

Fig. 4.9. Example of a LM-OSL curve of a polyester fabric following a 10 Gy β dose. A schematic representation of the LM-OSL mode of stimulation is presented in the top right corner. Detection window : U-340 filter, sample temperature : 50 °C.

4.4.1 One-Trap - One Recombination centre : the OTOR model

The simplest model accounting for the emission of TL and OSL is shown in Fig. 4.10; with one trap and one recombination centre (OTOR), the electrons are being captured during the excitation process by the trapping centre, and free bound holes are created in the recombination centres. Following heating or illumination, electrons are released from the trapping state to the conduction band, where they travel freely until reaching the recombination centre and emit photons after recombining with the bound holes.

The first part of the process, the excitation stage where the sample is exposed to ionising radiation, and thus the traps are filled with charges, is mathematically described by the following set of equations (Chen and Pagonis, 2011, p. 40), where one equation represents one trap in conventional models:

$$\frac{dn}{dt} = A_n(N-n)n_c - sn\left(-\frac{E}{kT}\right), \tag{4.26}$$

$$\frac{dm}{dt} = B(M-m)m_v - A_m m n_c, \tag{4.27}$$

$$\frac{dn_c}{dt} = X - A_n(N-n)n_c - A_m m n_c, \tag{4.28}$$

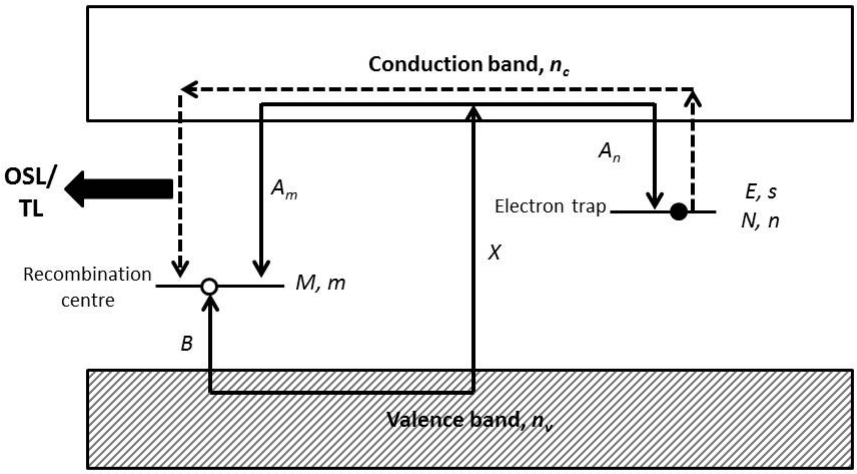

Fig. 4.10. Schematic diagram of a luminescence kinetic model involving one trap and one recombination centre. Redrawn from Chen and Pagonis (2011, p. 40).

$$\frac{dm_v}{dt} = \frac{dn}{dt} + \frac{dn_c}{dt} - \frac{dm}{dt}. \tag{4.29}$$

At the end of the excitation stage, a certain amount of electrons are transferred to the trapping states, and holes to the recombination centres. One can also approximate Eq. 4.26 by considering that, at room temperature, the second term of this equation is negligible. The equations describing the stimulation stage are given by :

$$\frac{dn}{dt} = A_n(N-n)n_c - pn, \tag{4.30}$$

$$I = -\frac{dm}{dt} = A_m m n_c - B(M-m)n_v, \tag{4.31}$$

$$\frac{dm}{dt} = \frac{dn}{dt} + \frac{dn_c}{dt}, \tag{4.32}$$

where p is the stimulation rate, differing from TL ($p(T) = s\exp(-E/kT)$; for a linear heating rate) to OSL ($p(t) = C$, a constant for CW-OSL), and I is the luminescence intensity emitted. In Eq. 4.30-4.32, the number of holes must be equal to the number of electrons in traps plus the number of electrons in the conduction band to obtain charge neutrality, i.e.:

$$m = n + n_c. \tag{4.33}$$

Another important assumption of this model is that the number of electrons in the conduction band is quasi-stationary, such that :

$$\left|\frac{dn_c}{dt}\right| << \left|\frac{dn}{dt}\right|, \left|\frac{dm}{dt}\right|. \tag{4.34}$$

In other words, the concentration of charges in the conduction band is less than the concentration of trapped charge Chen and McKeever (1997, p. 27). Therefore, the concentration of trapped charge is approximatively equal to the concentration of holes, $n(t) \simeq m(t)$.

These equation can be analytically solved following the quasi-equilibrium approximation (Eq. 4.34), giving the emitted luminescence intensity as a function of the stimulation temperature/duration. Following those assumptions, Halperin and Braner (1960) stated that, for carriers travelling through the conduction band, the luminescence intensity is:

$$I = -\frac{dm}{dt} = p(t)\frac{nmA_m}{A_m m + A_n(N-n)}. \tag{4.35}$$

This equation still comprises unknown variables, n and m, and cannot yet be solved analytically; we will see in the next section how further assumptions can be made, leading to expressions applicable to the fitting of experimental data.

4.4.2 First, second and general order kinetics

First order kinetics

In 1945 Randall and Wilkins (1945) made the assumption of negligible re-trapping; if a delocalised electron is freed from its trap, it will travel straight to the luminescence centre without falling back to another trap. This leads to considerable simplification of Eq. 4.35, as the recombination probability coefficient, A_m, becomes much larger than the re-trapping probability coefficient, A_n, i.e. $A_m m >> A_n(N-n)$. Therefore :

$$I = -\frac{dn}{dt} = np. \tag{4.36}$$

As discussed above the decay of luminescence at a fixed temperature was described by Eq. 4.18. In this equation the luminescence intensity is proportional to the number of charges in trapping centres.

By integrating Eq. 4.18 from $t = 0$ to t, Randall and Wilkins (1945) developed an expression for the TL glow curve of phosphors containing traps of one depth:

$$I_{TL} = n_0 s \exp\left\{-\frac{E}{kT}\right\} \exp\left\{-\left(\frac{s}{\beta}\right)\int_{T_0}^{T} \exp\left\{-\frac{E_t}{k\theta}\right\} d\theta\right\}, \tag{4.37}$$

where n_0 is the initial value of n at $t = 0$, β the heating rate, assumed constant in this equation. Later, Kitis et al. (1998), by using a development of the integral into a series, developed analytical expressions for a first order TL peak, and obtained the expression used for glow curve deconvolution :

$$I(T) = I_m \exp\left[1 + \frac{E}{kT}\frac{(T - T_m)}{T_m} - \frac{T^2}{T_M^2} \times \exp\left(\frac{E}{kT}\frac{(T - T_m)}{T_m}\right)(1 - \Delta) - \Delta_m\right], \tag{4.38}$$

where T (K) is the temperature, I_m (a.u.) the maximum intensity of the peak, T_m (K) the peak position (temperature) at maximum, $\Delta = 2kT/E$, and $\Delta_m = 2kT_m/E$.

For OSL, a similar expression can be developed for first order kinetics, such as :

$$I(t) = I_0 \exp(-\alpha t), \tag{4.39}$$

where I_0 is the intensity at $t = 0$ and α a constant characteristic of the decay of luminescence during stimulation. However, we have so far neglected the re-trapping of the charges, which might occur in more realistic model.

Second order kinetics

In 1948, Garlick and Gibson (1948) considered the alternative case where re-trapping is significant (second order kinetics). In Fig. 4.10, the re-trapping is indicated by an arrow drawn to the right of coefficient A_n, which, according to Garlick and Gibson (1948) depends at all times on the relative numbers of empty electron traps and recombination centres, and on their respective cross sections.

Second order kinetics is therefore assumed in the case of $A_m m << A_n(N-n)$, and where $m = n$ (case of the OTOR model), leading to the following equation for the luminescence intensity :

$$I = -\frac{dn}{dt} = n^2 p. \tag{4.40}$$

Similarly to first order kinetics, the analytical expression developed by Kitis et al. (1998) gave, in the case where re-trapping predominates, an expression for a single TL peak of :

$$I(T) = 4I_m \exp\left(\frac{E}{kT}\frac{(T-T_m)}{T_m}\right) \times \left[\frac{T^2}{T_m^2}(1-\Delta)\exp\left(\frac{E}{kT}\frac{(T-T_m)}{T_m}\right) + 1 + \Delta_m\right]^{-2}, \tag{4.41}$$

where symbols and notation have the same meaning as in Eq. 4.38 above.

For OSL :

$$I(t) = \frac{n_0 \alpha I_0}{1 + \alpha I_0 t^2} \tag{4.42}$$

General-order kinetics

Two extreme cases of Eq. 4.35 were considered in the above; the complete absence of re-trapping (first order kinetics) and a system were re-trapping is predominant (second order kinetics). However, in their study of different types of salt , May and Partridge (1964) came to the conclusion that intermediate cases should be considered, and that assuming the order of kinetics prior to the kinetics analysis could lead to errors. Consequently, they developed a "general-order" kinetics (GOK), such as :

$$I = -\frac{dn}{dt} = n^b p, \tag{4.43}$$

where b is the order of kinetics, that remains to be determined on a case-by-case basis. Furthermore, b may be other than and 1 and 2. A physical explanation of general order was attempted by Christodoulides (1990), suggesting that a general order TL peak results from a continuum of traps with identical activation energies, but different values of frequency factors. The analytical expression of a general order TL by is given by (Kitis et al., 1998) :

$$I(T) = I_m b^{\frac{b}{b-1}} \exp\left(\frac{E}{kT}\frac{T-T_m}{T_m}\right) \times \left[(b-1)(1-\Delta)\frac{T^2}{T_m^2}\exp\left(\frac{E}{kT}\frac{T-T_m}{T_m}\right) + Z_m\right]^{-\frac{b}{b-1}}, \tag{4.44}$$

with $Z_m = 1 + (b-1)\Delta_m$.

And the expression for OSL is given by :

$$I(t) = n_0 \alpha I_0 \left[(b-1)\alpha I_0 t + 1\right]^{-\frac{b}{b-1}} \tag{4.45}$$

4.4.3 Competition between traps and recombination centres

Although the model of one trap - one recombination centre (OTOR) presented above is sufficient to explain some features of the TL glow curves (peak shape, position, influence of the heating rate, trap depth), it fails to explain phenomena such as supralinearity. Furthermore, the OTOR model describes a single non-interacting type of trap, which is not likely to occur in physical experiments. To address this issue, the interactive multi traps system (IMTS) was developed (Sunta et al., 1994). In this model, multiple traps of different depth interact with each other.

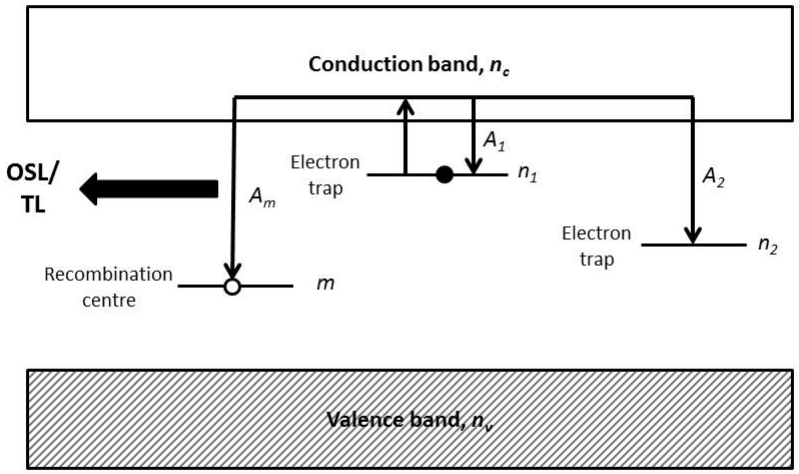

Fig. 4.11. Schematic diagram of an energy level diagram with two electron traps of different depths and a recombination centre, representing the excitation stage of the interactive traps models.

On the schematic representation given in Fig. 4.11, electron trap (1) is emptied upon stimulation (TL or OSL), and the electron traps (2) remains intact. Re-trapping can occur both in trap 1 and

trap 2, meaning that trap 2 can capture charge originating from trap 1, in which case the traps are said to be "interactive". The charge neutrality condition in this case is thus (Chen and McKeever, 1997, p. 35):

$$m = n_1 + n_2, \tag{4.46}$$

and the new equation to be added to the OTOR model :

$$\frac{dn_2}{dt} = (N_2 - n_2)v\sigma_h, \tag{4.47}$$

where N_2 is the number of deep traps, σ_2 the capture cross section of the deep traps, and v, the carriers' velocity. Here, the traps are considered to be thermally disconnected from one another. Consequently, the equation for the concentration of electrons in the conduction band becomes :

$$\frac{dn_c}{dt} = \frac{dm}{dt} - \frac{dn_1}{dt} - \frac{dn_2}{dt}. \tag{4.48}$$

However, the assumption of thermally disconnected traps is, again, simplistic; in semi-crystalline materials, vitreous materials, or materials with a high concentration of defects, the population of traps can be expected to be spread within a wide range of activation energies, leading to a continuous or quasi-continuous distribution of activation energies rather than a discrete distribution (Chen and McKeever, 1997, p. 41). In this case, the traps are likely to be highly interactive between each other. The TL peaks arising from this type of configuration overlap, often resulting in the appearance of a single peak of extended width.

4.4.4 Localised transitions

In the models discussed above, transitions between metastable states were occurring via the conduction band; however, as early as 1960, Halperin and Braner (1960) explored the possibility of localised transitions. In this model, the existence of localised states, energy states located between the energy of the electron traps and the conduction band edge through which charge can travel before reaching recombination centres (Fig. 4.12) provides an alternative recombination route. If we denote n_e (cm^{-3}) as the concentration of electrons in these localised states, the charge equilibrium of Fig. 4.12 becomes :

$$m = n + n_e \tag{4.49}$$

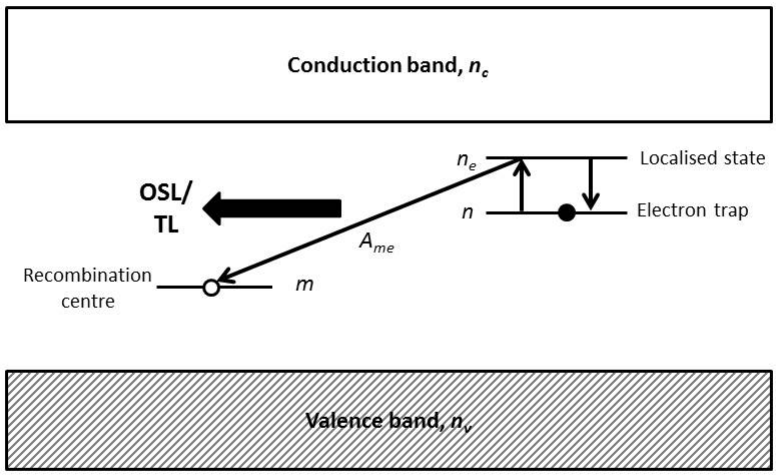

Fig. 4.12. Schematic diagram of an energy level diagram with an electron trap, a recombination centre and a localised state, showing the excitation stage of a localised transition. Redrawn from Chen and Pagonis (2011, p. 56).

The electrons travelling to localised states, below the conduction band require less energy to escape from their traps. Another difference lies in the recombination process; an electron moving to a localised state will recombine only at the closest recombination centre (nearest neighbour) and not with a random one, as occurs in delocalised transitions (Fig. 4.12).

Halperin and Braner (1960) developed the following equations governing localised transitions :

$$-\frac{dm}{dt} = n_e m A_{me}, \tag{4.50}$$

$$\frac{dn}{dt} = s n_e - s \exp\left\{-\frac{E_e}{kT}\right\}, \tag{4.51}$$

$$\frac{dn_e}{dt} = sn \exp\left\{-\frac{E_e}{kT}\right\} - n_e(mA_{me} + s), \tag{4.52}$$

where n_e is the concentration of electron in the localised state, E_e the difference of energy between the electron trap and the localised state, and A_{me} the recombination coefficient for the transition of an electron from the localised state to the recombination centre.

By assuming the population of the localised states to be negligible compared with the one of the trapping states ($m = n_e + n \approx n$), and by setting the term mA_{me} to a constant ($mA_{me} = \nu$), Eq. 4.50 can be simplified to :

$$I = -\frac{dn}{dt} = -\frac{dm}{dt} = n_e\nu. \tag{4.53}$$

Similarly to the OTOR model, the quasi-equilibrium of the localised state population ($dn_e/dt \approx 0$) is assumed.

Since the work of Halperin and Braner (1960), many authors have made use of localised models (e.g., Bull 1989; Sunta et al. 2006) or semi-localised models, some of them taking into account transition through delocalised states (Pagonis 2005; Mandowski 2005). A new model was developed by Jain et al. (2012) to account for localised electronic recombination via tunnelling between donor-acceptor pairs in inorganic crystalline phosphors. This model was developed in the hope of describing the anomalous fading undergone by feldspar minerals (see Section 4.6.2). The set of equations describing this model are, as follows :

$$\frac{dn_g}{dt} = -An_g + Bn_e, \tag{4.54}$$

$$\frac{dn_e}{dt} = An_g - Bn_e - \frac{3n_e\rho'^{1/3}}{\tau_c}\left(\ln\frac{n_0}{n}\right)^{2/3} z, \tag{4.55}$$

$$I(t) = -\frac{dm(t)}{dt} = \frac{3n_e\rho'^{1/3}}{\tau_c}\left(\ln\frac{n_0}{n}\right)^{2/3} z, \tag{4.56}$$

$$m = n + N = (n_g + n_e) + N, \text{ the charge neutrality equation} \tag{4.57}$$

Here, n_g describes the concentration of electrons in the (donor) ground states, when n accounts for the total concentration of electrons in donors, both in the ground and excited state ($n = n_g + n_e$).

τ_c (s) is the critical tunnelling lifetime, z a constant($z = d\tau_c/dt$) and ρ' is the (dimensionless) density of acceptors.

An analytical equation of this model, developed by Kitis and Pagonis (2013), gave a luminescence intensity of :

$$I(t) = -\frac{dn_g}{dt} = 3n_0\rho' F(t)^2 zpe^{-F(t)}e^{-\rho'[F(t)]^3}, \tag{4.58}$$

where z=1.8, $F(t) = \ln(1 + zpt)$ for CW-OSL, and $F(t) = \ln\left(1 + \frac{zskT^2}{\beta E}e^{-E/kT}\left(1 - \frac{2kT}{E}\right)\right)$ for TL.

4.4.5 Continuum of traps

The discussed models above assumed discrete trapping levels. Although this assumption can be true for crystalline materials, amorphous or semi-amorphous materials (with some crystalline regions) rather exhibit a density of trapping states in the band gap (Mott and Davis, 1979, p. 210). This is often the case in polymeric materials (McKeever, 1988, p. 105).

Rudlof et al. (1978) described a TL peak arising from a distribution of trapping levels with the equation :

$$I(T(t)) = c\sum_{N=1}^{M} s_N \exp(-E_N/kT(t))H_N \exp\left[-\int_{t_0}^{t} s_N \exp(-E_N/kT(t'))dt'\right], \tag{4.59}$$

where c is a constant, M the number of trapping levels in the distribution, s_N the frequency factor of each level, and E_N their activation energy. H_N describes the distribution of energies. Several forms of distribution of localised states have been used, such as uniform, Gaussian (Rudlof et al., 1978; Grenet et al., 1973), or exponential distributions (Owen and Charlesby, 1974).

4.5 Analysing TL and OSL curves : extraction of the required parameters

4.5.1 What are the important parameters?

TL and OSL curves provide information on the exposure of the sample to ionising radiation, but also on the structure of the trapping levels and recombination centres.

The study of luminescence models above emphasised how the resulting outputs of a luminescence measurement (TL glow curve or OSL decay curve) are dependent on the kinetics parameters (i.e., activation energy, order of kinetics, frequency factor), that will influence the shape of the resulting OSL or TL curves. For example, the maximum intensity of a TL peak, I_m, depends on both the dose rate (absorbed dose per unit of time) and time of irradiation, on X, the rate of production of electron-hole pairs by ionising irradiation, and on the trap density.

When conducting a kinetics analysis, the values of the activation energy, order of kinetics, lifetime, frequency factor are sought for each trapping level. The thermal/optical activation energy is of interest as being directly related to the trap depth. In dosimetry, the ability to reach deeper traps is often preferable, as they tend to be less subject to fading over time (see Section 4.6). The lifetime of a trap (i.e., how long the charges will remain in the trap) is also an important parameter in dosimetry, where hours to years may occur between irradiation and measurement. The meaning of the frequency factor lies in the number of interactions between trapped electrons and phonons (vibration of the lattice), per second, and is expected to be of the order of the Debye frequency ($10^{12} - 10^{14}$ s^{-1}). The frequency factor is calculated using the value of the activation energy, such as:

$$s = \frac{\beta E}{kT_m^2} \exp\left(\frac{E}{kT_m}\right) \times \left(1 + (b-1)\frac{2kT_m}{\beta}\right)^{-1}. \tag{4.60}$$

And from the frequency factor, the lifetime of a charge in a trap is derived such as :

$$\tau = s^{-1} \exp\left(\frac{E}{kT}\right), \tag{4.61}$$

where T is the temperature of the sample. The lifetime is essential to determine the extent of fading (see Section).

Techniques were developed to extract the kinetic parameters from TL/OSL curves, and techniques most relevant in this work are explained below.

4.5.2 Analysing TL glow curves

Initial rise method and T_{max}-T_{stop} method

The initial rise method is based on the evaluation of the slope of the initial lower temperature part of the TL peak, where the occupancy of the recombination centre and electron traps can be

approximated to be constant (Chen and McKeever, 1997).

Garlick and Gibson (1948) stated that the luminescence intensity, I in this region of the TL glow curve can be expressed as:

$$\ln(I) = C - E/kT, \tag{4.62}$$

where C is a constant. If $\ln(I)$ is plotted versus $1/T$, a flat line of slope $-E/k$ is expected, from which the activation energy can be extracted. However, as suggested by Kierstead and Levy (1991), the initial rise method does not work in the case of overlapping TL peaks, as the lower temperature side of each individual TL peak is not discernible.

To overcome this issue, Nicholas and Woods (1964) designed a procedure of "thermal cleaning", where samples are heated to a temperature T_{stop} beyond the maximum of the first TL peak following irradiation, consequently emptying the traps responsible for this peak. The sample is then cooled down and reheated to an higher temperature (T_{max}), thus recording a TL glow curve. These steps are then repeated with incrementally increasing the temperature T_{stop}, throughout the whole glow curve. Each peak is therefore gradually erased by the "preheat", providing a distinctive initial start for the next peak, from which the initial rise method can be applied and the activation energy calculated. Nonetheless, in the case of closely overlapping peaks, or in the case of a continuum of traps, this method is also not completely satisfactory. As pointed out by Haake (1957), the interference from other traps can lead to inaccurate evaluation of the activation energies.

An alternative technique using the T_{max}-T_{stop}, developed by McKeever (1980), aims to monitor the maximum peak temperature T_{max}, rather than the activation energy. Plotted against T_{stop}, the shape of the resulting curve indicate whether the glow curve results from one or several component peaks, and may even resolve the order of kinetics. For example, the case of closely overlapping peaks, the T_{max} vs T_{stop} curve will take the form of an increasing linear function. For a single peak, a straight line is predicted.

Peak shape parameters

The peak shape method is based on a dependence of the shape of the TL glow curve on the activation energy. To quantify these changes, peak shape parameters were introduced. T_m accounts for the temperature at the maximum peak intensity, T_1 is the lower temperature at half maximum, and

T_2 the higher temperature at half maximum; the parameters are indicated on a schematic TL glow curve (Fig. 4.13), where the parameters ω, τ, δ and μ_g are derived, using the following :

$$\omega = T_2 - T_1, \tag{4.63}$$

$$\tau = T_m - T_1, \tag{4.64}$$

$$\delta = T_2 - T_m, \tag{4.65}$$

$$\mu_g = \delta/\omega \tag{4.66}$$

The parameter μ_g also depends on the order of kinetics; for first order kinetics, $\mu_g = 0.42$, and for second order kinetics $\mu_g = 0.52$ (Chen and McKeever, 1997, p. 116).

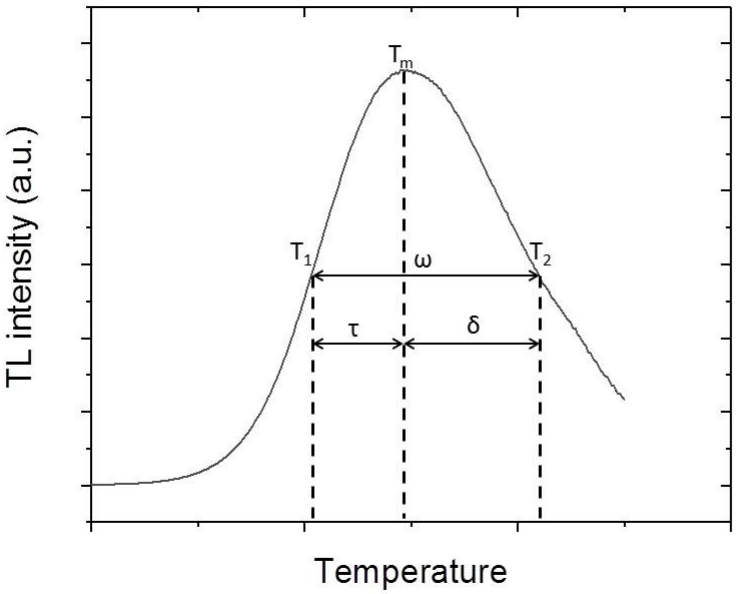

Fig. 4.13. Schematic TL peak showing the temperature at maximum intensity T_m, the low and high temperatures at half maximum T_1 and T_2, and the peak shape parameters ω, τ and δ.

For each one of the parameters (ω, τ, δ), two coefficients, c and b were defined as follows (Chen, 1969):

$$c_\omega = 2.52 + 10.2(\mu_g - 0.42); \quad b_\omega = 1, \tag{4.67}$$

$$c_\tau = 1.51 + 10.2(\mu_g - 0.42); \quad b_\tau = 1.58 + 4.2(\mu_g - 0.42), \tag{4.68}$$

$$c_\delta = 0.976 + 7.3(\mu_g - 0.42); \quad b_\delta = 0. \tag{4.69}$$

From the parameters (c_ω, c_τ and c_δ), the activation energy can be computed such as :

$$E_\alpha = c_\alpha(kT_m^2/\alpha) - b_\alpha(2kT_m), \tag{4.70}$$

where α represents ω, τ or δ. However, the accuracy of this method has been questioned as it relies only on the evaluation of three experimental points, and only assumes single TL peaks (McKeever, 1988, p. 89).

Fitting of TL glow curves

Curve fitting methods rely on theoretical models, some of which have been discussed in Section 4.4. The parameters (e.g., E, b, I_m, T_m, s,...) are firstly fixed to an arbitrary value, and the associated theoretical glow curve computed using an iterative procedure. The goodness of fit can be evaluated using the χ^2 statistic, given by Hughes and Hase (2010, p. 61):

$$\chi^2 = \left(\frac{y_i - y(x_i)}{\alpha_i}\right)^2, \tag{4.71}$$

where y_i is the experimental data point at $x = x_i$, $y(x_i)$ the theoretical value given by the model at the same point and α_i the standard error for that experimental point assuming a Gaussian distribution. The purpose of the fitting procedure is hence to minimise χ^2 by adjusting the parameters of the theoretical model. The main advantage of this method is that overlapping peaks can be separated: several single peaks are computed (usually one for each pro-eminent peak) and summed, and this sum of theoretical peaks is used in the comparison with the experimental data. An example of TL glow curve fitting is shown in Fig. 4.14. The fitted peaks, obtained by Eq. 4.44, are shown as solid lines, and their sum closely match the experimental data (open circles).

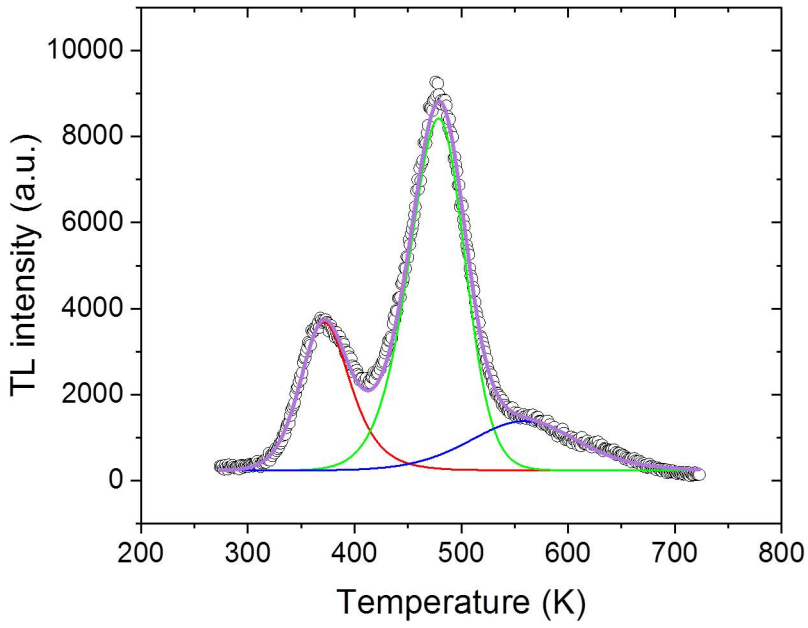

Fig. 4.14. Example of TL glow curve fitting for alumina substrate using general order kinetics equation (Eq. 4.44). The experimental data are showed as open circles, and the deconvolved peaks as solid lines. The TL glow curve was deconvolved using a Levenberg-Marquardt algorithm. β dose 1 Gy, detection window : U-340, heating rate :0.5 °.s^{-1}.

4.5.3 Analysis of OSL

The most commonly used procedures for OSL measurement is the exposure of the sample to constant intensity stimulation (CW-OSL), with the objective of emptying all traps of a certain energy and lower. Separating which traps result from the emitting light is thus complex compared with a TL deconvolution procedure.

Photo-ionisation cross section

The concept of the photo-ionisation cross section, $\sigma(E_0)$, describing the interaction of a photon with the metastable state was already introduced in Section 4.3.2. The absorption of a photon (UV-IR) of energy $h\nu$ by a defect band depends only on both the concentration of defects $n(E_0)$ and on the photo-ionisation cross section, according to (Bøtter-Jensen et al., 2003, p. 21):

$$\alpha(h\nu) = n(E_0)\sigma(h\nu, E_0) \tag{4.72}$$

For wide band-gap insulators, with deep electron traps, the photo-ionisation cross section is often approximated as (Grimmeiss and Ledebo, 1975):

$$\sigma(h\nu, E_0) \propto \frac{(h\nu - E_0)^{3/2}}{h\nu[h\nu - E_0(1 - m_0/m_e)]^2}, \tag{4.73}$$

where m_0 is the mass of the free electron and m_e the effective mass in the band. The variation of the intensity of the photo-ionisation cross section (i.e., LM-OSL) was already discussed, and others parameters, such as the energy of the incident particles ($h\nu$) can also be varied. With this in mind, another OSL method involves varying the wavelength (Chruścińska, 2015).

By varying the illumination wavelength, the energy of the photons shone onto the sample is changed, and charge stored in traps of energy less than the photon energy will be evicted whereas charge in traps of higher energy is expected to remain intact. For this type of characterisation, a narrow stimulation band is often preferable to allow a precise characterisation of the trap's depth. The presence of a peak in the spectrum of the simulation energy versus the luminescence intensity is indicative of the presence of a trap (Chruścińska, 2015).

Curve fitting

Similar to TL, the OSL signals are very rarely composed of a single component, and an OSL decay curve can be fitted with different components using the equations of Section 4.4. The procedure is similar to TL glow curve fitting, and aims to minimise the χ^2 parameter. An example of an OSL decay curve fitted using three components is shown in Fig. 4.15. It can be seen that the relative contribution of each component varies with the illumination time.

4.6 Thermal and athermal fading of luminescence

Unwanted loss of charge from their traps during storage, referred as "fading", has long been an issue in TL and OSL dosimetry and dating studies. Such as defined earlier, stimulated luminescence differs from other forms of emission of luminescence such as fluorescence or phosphorescence by being a phenomena of particularly long lifetime, with a luminescence emission being minutes to years when

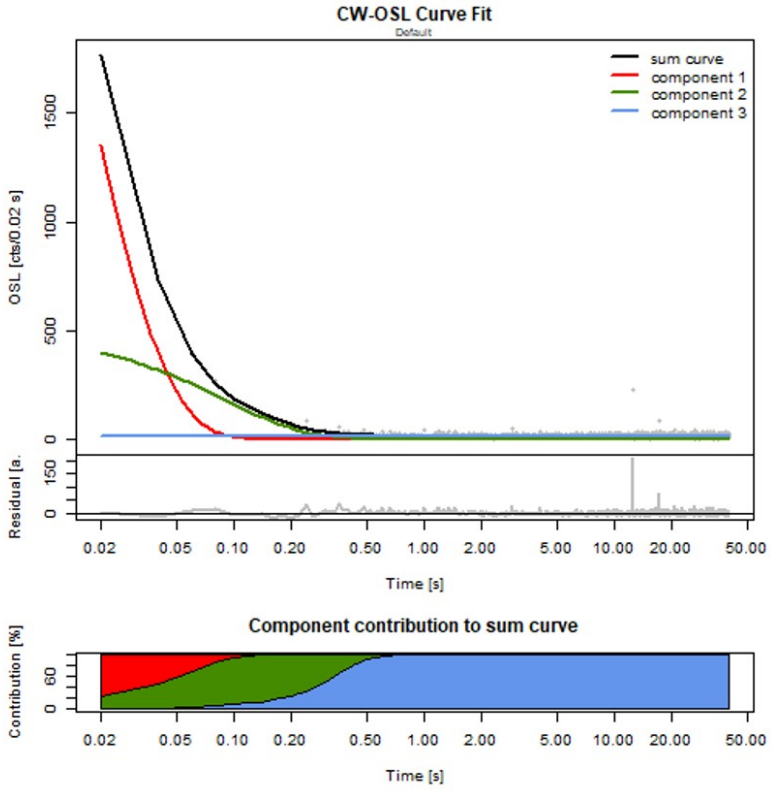

Fig. 4.15. Example of an OSL decay curve for a sample of fire retardant fabric irradiated with a β dose (10 Gy) fitted using three components. The experimental data are plotted as black lines, and the components are the red, green and blue lines. The relative component contributions as a function of time is shown beneath. β dose 10 Gy, detection window : U-340, stimulation : 470 nm.

stimulated, after the excitation of the charges. If usually either heat or light triggers the emission of photons, in some materials the signal was found to diminish over time prior to the excitation, at a rate depending on a variety of parameters (mainly nature of the sample and storage condition). A sample with a fading signal can cause a number of issues (complete loss of the signal, necessity of a fading correction increasing the propagation of errors) in retrospective and emergency dosimetry where an immediate reading of the dose is not realistically possible, thus it is necessary to have a good understanding of fading mechanisms.

Two types of fading should be distinguished : thermal fading and athermal fading, also known as anomalous fading (Chen and Pagonis, 2011, p. 82).

4.6.1 Thermal fading

The rate of loss of trapped charge in a sample held at a fixed temperature can be predicted by an analysis of the thermal fading. The thermal stability of a peak is evaluated by its lifetime, i.e., the average time spent by the charge in the trap of specified depth. In the simplest case of first order kinetics, the lifetime, τ, of a trap of energy E (eV) and of frequency factor s (s^{-1}), stored at a temperature T (K) is :

$$\tau = s^{-1} \exp(E/kT), \tag{4.74}$$

where k ($eV.K^{-1}$) is the Boltzmann constant (Chen and Pagonis, 2011, p. 82). This expression predicts that the lifetime of the trapped charge will decrease exponentially as the temperature increases. The lifetime of a charge, at room temperature (20°C, 293 K) in a trap with a typical value of frequency factor $s = 10^{12}$ s and of energy $E = 1.2$ eV is predicted to have a lifetime of ~ 14 years. The effect of thermal fading can be typically seen following storage at room temperature (~ 15 °C) in the dark. For example, the impact of storage time upon the TL glow curve of an alumina substrate is shown in Fig. 4.16 and it is clear that the 75 °C TL peak has decreased or faded significantly after just a few hours of storage in the dark.

TL peaks positioned at higher temperature are preferred for dosimetry, as they are associate with higher activation energy and thus expected to be less susceptible to thermal fading. In the case of OSL, where a mixture of traps may be read at once, a preheat of the samples can "remove" the less thermally stable part of the signal. Furetta (2010, p. 418-420) designed a procedure to determine the isothermal decay constant of dosimeters by comparing the decay in three different sets of the same type of materials stored for various periods of time, and in different conditions. A trap is considered as thermally stable (within a 5% loss of the signal) when the lifetime of a trap is 10 times greater than the storage time (Aitken, 1985, p. 50).

4.6.2 Anomalous fading

The term "anomalous fading" was introduced in the study of Wintle (1973) who tested the stability of the TL signal of volcanic minerals, although observations of this phenomena had been reported by Bull and Garlick (1950) on UV excited luminescence of diamonds stored at low temperature, and

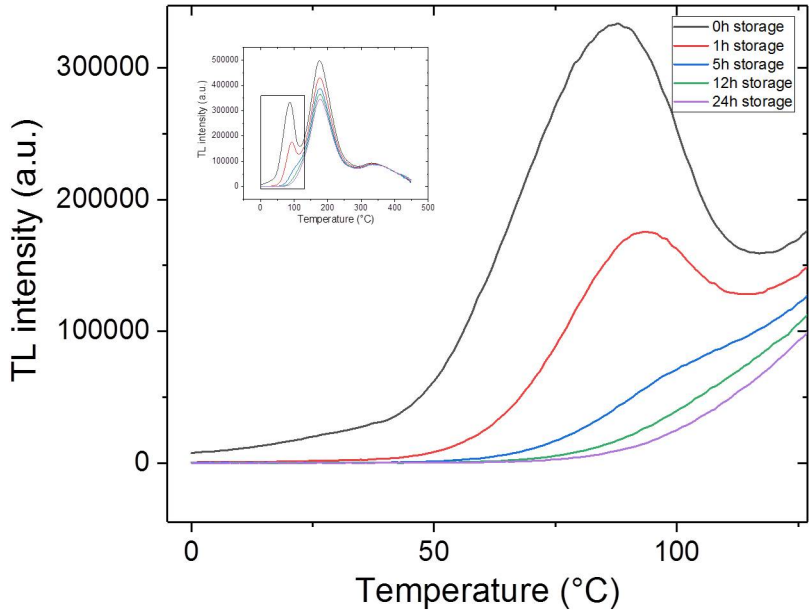

Fig. 4.16. TL fading after storage (0-24 hours) in the dark at room temperature following a 1 Gy β irradiation of alumina substrate in the low temperature region of the TL glow curve emphasizing the presence of a thermal fading mechanism. The inset shows the glow curve measured to 450 °C. Risø system, detection window : U-340.

by Hoogenstraaten (1958) on zinc sulfides samples similarly stored below room temperature. The term "anomalous" fading refers to the release of charge from traps where no significant loss of the signal is predicted on the basis of thermally activated mechanisms (Section 4.6.1). Many minerals and synthetic phosphors have been found to exhibit anomalous fading, such as feldspars (Visocekas et al. 1994, Visocekas 2000, Wintle 1977a), extraterrestrial minerals (Hasan et al. 1986; Garlick and Robinson 1972), $ZnSiO_4$ (Avouris and Morgan, 1981), alkali halides (Delbecq et al., 1976), alumina substrates (Inrig et al., 2010b), and also polymers (Charlesby, 1981).

Anomalous fading is often characterised for both OSL and TL by a rapid decrease of the signal for shorter storage times, followed by a decreased decay rate over longer period of storage (McKeever 1988, p. 145; Furetta 2010, p. 19). Fig. 4.17 shows the fading of the TL signal of alumina substrate resistors in the TL region 300-450 °C, where no thermal fading is expected and where the shape of the fading curve is characteristic of anomalous fading.

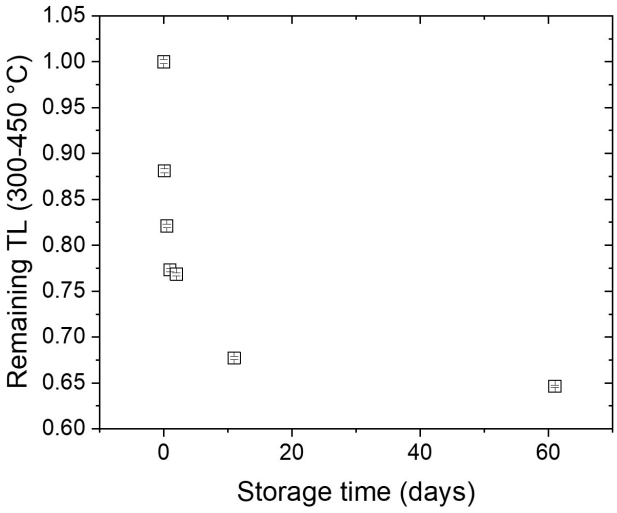

Fig. 4.17. TL remaining signal of alumina substrate resistors after β irradiation (5 Gy) and storage in the dark at ambient temperature [0.5-61] days. The TL signal was taken as the integral in the region 300-450 °C and normalised to the signal measured shortly ($\leq$ 5 min) after β irradiation. Detection : U-340.

Several explanations for anomalous fading were proposed, such as hopping of the charge (Poolton et al., 2002) when the greater density of defects creates localised states (Mott, 1969), ionic processes in alkali feldspars (Jaek et al., 2007), or hole migration (Wintle, 1977a). However, localised transition of the trapped charges, allowing recombination through transitions via an excited state common to the trap and recombination centre (Templer, 1986) and quantum mechanical tunnelling mechanism of the stored charge, from traps to recombination centres or non-radiative centres as first suggested by Hoogenstraaten (1958) for ZnS have been regarded as the most likely mechanisms.

Kinetics models accounting for anomalous fading

Tunnelling model The tunnelling model is based on the assumption that the trapped charge can cross the potential barriers separating them from the recombination centre or a non-radiative centre (Fig. 4.19 a). The tunnelling rate of an electron of frequency factor s in a trap of energy E tunnelling through a distance r is given by the relation (McKeever, 1988, p. 146):

$$K = s \exp(-\phi r), \tag{4.75}$$

where s is the frequency factor, r the distance, and ϕ is given by the equation :

$$\phi = 2(2m_e E)^{\frac{1}{2}}/\hbar, \tag{4.76}$$

with m_e the mass of the electron and $\hbar$ the reduced Planck constant. As shown in Fig. 4.18, the tunnelling rate of an electron at a depth E_0 encountering a potential well of depth E_1 decreases when the recombination distance r increases.

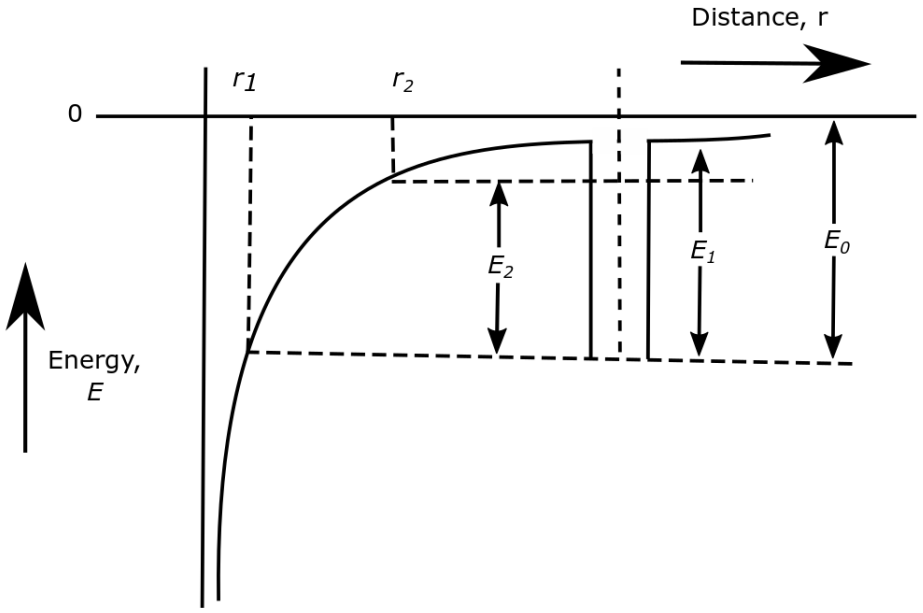

Fig. 4.18. Schematic representation of the potential barrier such as used in the description of the tunnelling model. The electron at a depth E_0 is able to reach a recombination centre situated at a distance r will have to cross the potential well of depth E_1, from which charge can escape by tunnelling. If a state exists at an energy E_2, thermally assisted tunnelling can occur. In this case, the barrier width is reduced and the probability of tunnelling increased. Redrawn from Chen and McKeever (1997, p. 62)

If first order kinetics is assumed, the luminescence intensity is proportional to the tunnelling

rate, such as :

$$I = -\frac{dn}{dt} = Kn = Kn_0 \exp(-Kt) \tag{4.77}$$

By integrating this expression, and by combining Eq. 4.75 with Eq. 4.77, the intensity at function of time for a decreasing rate of tunnelling charges is obtained :

$$I \simeq -n_0\phi/t \tag{4.78}$$

From a theoretical point of view, if tunnelling is assumed to be the cause of anomalous fading, the intensity of the signal is expected to decrease asymptotically with storage time. A $1/t$ dependence also accounts well for a first rapid decay followed by a second slower component (Fig. 4.17), as experimentally observed in the case of labradorite (Visocekas, 1985).

Another aspect of Eq. 4.78 is its thermal independence, indicating that a sample stored either, say, at room temperature or at a liquid nitrogen temperature (77 K) exhibit the same rate of anomalous fading. Some experimental observations, however, contradict that assumption (Guerin and Visocekas, 2015), implying that anomalous fading might not be caused solely by the crossing of a potential barrier by the trapped charge. Adding a thermal dependence leads to "thermally-assisted tunnelling" (Visocekas et al., 1976), where the charge is thermally excited before tunnelling to a recombination centre. In this case, the recombination probability is given by :

$$P(r) = P_0 \frac{\exp(-\alpha_1 r) + \exp(-\alpha_2 r)}{1 + \exp\left(-\frac{E_2}{kT}\right)}, \tag{4.79}$$

with $\alpha_1 = \frac{2\sqrt{2mE_1}}{\hbar}$, $\alpha_2 = \frac{2\sqrt{2m(E_1-E_2)}}{\hbar}$, E_1 the potential energy of an electron in the ground state and E_2 the thermal energy required to bring an electron from the ground state to an excited state.

The localised transition model Another widely considered model attempting to explain anomalous fading yields in the transition of the charges through localised states before reaching a recombination centre (Templer, 1986) - thus avoiding any transfer through the conduction band (Fig. 4.19 b). First presented by Halperin and Braner (1960) (see Section 4.4.4), this model was based on the assumption of a fixed tunnelling distance between the trap and the recombination centre, and therefore only predicts first order kinetics. However, more recent work by Jain et al. (2012)

managed to predict a power law decay of luminescence in some materials by assuming a random distribution of traps and recombination centres.

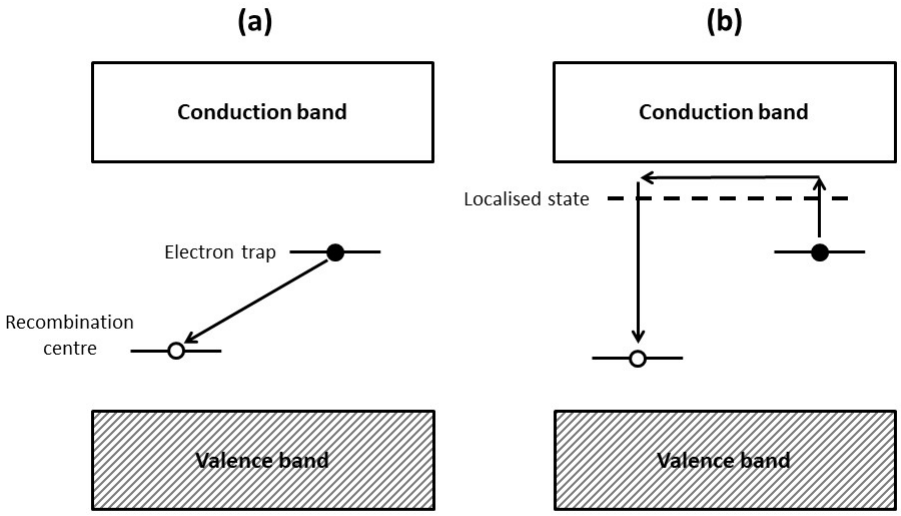

Fig. 4.19. Luminescence models accounting for anomalous fading, where (∘) are the holes and (•) the electrons. a) Tunnelling of a trapped charge from the trap to the recombination centre (–), b) transition of a charge through a localised state (- -) before reaching the recombination centre. Redrawn from Templer (1986)

Circumvention of anomalous fading?

Significant reductions of anomalous fading were observed by Bailiff (1976) by using phototransferred thermoluminescence, which will be further discussed further in subsection 4.7.2. The use of this technique on fluorapatite and zircon enabled the access to deeper traps, subsequently circumventing anomalous fading. Visocekas and Zink (1999) also found that using the 710 nm red emission of alkali feldspars accesses a stable component, when the blue emission would have nearly completely faded. It was also reported by Polymeris et al. (2006) that the anomalous fading of the OSL and IRSL signals of apatite was stronger than its TL signal.

If a sample's stability is not improved using the methods described above, the signal can be

corrected for loss by applying a fading correction to the signal. Wallinga et al. (2007), Lamothe and Auclair (1999) and Lamothe et al. (2003) presented a method to extrapolate to the OSL signal without loss for young feldspars, and using iterative procedure by defining a g factor that quantifies the loss of the luminescence signal per decade, where :

$$g = 100\kappa \ln(10), \tag{4.80}$$

and where the unit of g is of %/decade, and is κ the fractional decrease of the luminescence intensity between an arbitrary time t_c and $10t_c$.

For use in short-term dosimetry, fading corrections are necessary when employing alumina substrates (Inrig et al., 2010a) and are widely applied, as the shorter time scale between the administering of a dose and the measurement (hours to days) compared to dating applications gives an opportunity to artificially reproduce the storage in laboratory under controlled conditions and to apply a sample specific fading correction.

4.7 Additional phenomena associated with TL and OSL

4.7.1 Thermal quenching

Thermal quenching, already briefly mentioned above, is associated with non-radiative transitions (Section 4.2.2), and refers to the reduction in luminescence intensity with increasing measurement temperature (Gorbics et al. 1969, Wintle 1975b, Yukihara and McKeever 2011, p. 40, Chen and Kirsh 2013, p. 39). Wintle (1975c) reported a thermal quenching of luminescence when observing the 325 °C peak of quartz, and noted erroneous values of activation energy calculated with the initial rise method, due to a loss of luminescence at high temperatures. Thermal quenching was later observed in more materials such as Al_2O_3 (Akselrod et al., 1998), LiF (Taylor and Lilley, 1978), CaF (Gorbics et al., 1969), or BeO (Bulur and Göksu, 1998).

Two of the advanced explanations are either a decrease in the luminescence quantum efficiency, or a reduction in the concentration of recombination centres at elevated temperatures (Schön-Klassens and Mott-Seitz models respectively, see discussion below).

The efficiency is related to the probability of radiative transition p_r and non-radiative transitions p_{nr}, such as (Curie, 1963, p. 6):

$$\eta = \frac{p_r}{p_r + p_{nr}} \tag{4.81}$$

Eq. 4.11 defined the quantum efficiency as being the ratio of the number of emitted quanta to the number of absorbed quanta. The luminescence quantum efficiency can also be written as (Blasse and Grabmaier, 2012; Yukihara and McKeever, 2011):

$$\eta(T) = \frac{1}{1 + Ce^{-\frac{E}{kT}}}, \tag{4.82}$$

where C is a constant. When T increases in Eq. 4.82, and kT approaches the value of E, the efficiency starts decreasing with increasing temperatures.

The Mott-Seitz model is based on the concept of non-radiative transitions (Section 4.2.2), and was developed to explain the luminescence processes in alkali halides (Seitz, 1939). Whilst in the excited state, the system can absorb thermal energy, and if the lattice relaxation is sufficiently great, the minimum of the excited parabola (trapped charge) will be displaced from the ground state (recombination centre) parabola (Dexter et al., 1955). Secondly, upon thermal energy brought to the system, the charges will be excited to an upper level of the excited state, outside of the parabola of the ground state/recombination centre. The probability of non-radiative transition is therefore related to $\Delta R = R_0 - R_0'$, the displacement offset between the two parabolas. Fig. 4.20 shows a schematic representation of the model used in the Mott-Seitz kinetics, where W represents the phonon energy absorbed by the system, bringing charges to upper levels of the excited state.

Later on, Schön and Klasens proposed another explanation for thermal quenching, and stated that a reduction in the concentration of recombination centre at elevated temperatures could cause thermal quenching. In this model the trapped holes, considered thermally unstable, can be excited to the valence band (Bøtter-Jensen et al., 2003, p. 45). The electrons have therefore less holes to recombine with, yielding a quenching of luminescence. The system of equation describing the Schon Klasens kinetics is more complex, as the equation $I = -dm/dt$ is no longer valid (Chen and McKeever, 1997, p. 50).

4.7.2 Phototransferred thermoluminescence

Phototransferred thermoluminescence (PTTL) appeared before OSL measurements, and was one of the first techniques employing light to transfer charges between traps in phosphors. Typically, using

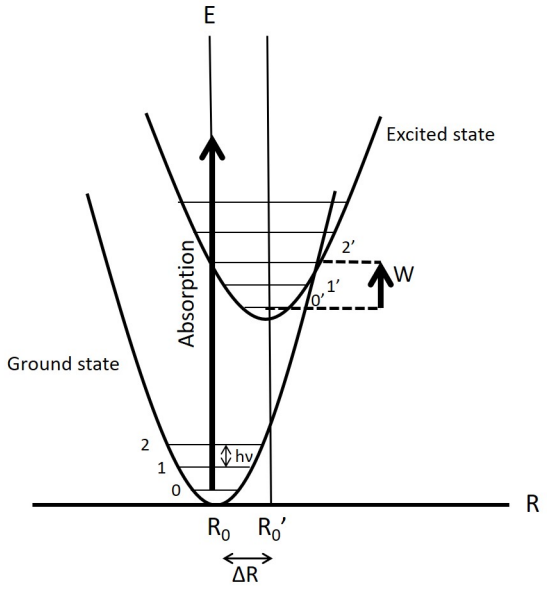

Fig. 4.20. Schematic representation of the model used to describe the Mott-Seitz kinetics. W represents the phonon energy absorbed by the system, leading to non-radiative transitions.

a PTTL procedure, the sample is : 1) given a radiation dose, 2) preheated to a temperature T_{stop} to empty the shallower traps, 3) exposed to a light source and 4) the TL (PTTL) signal measured. More energetic short wavelengths (blue or UV) are preferred for the illumination as they are more efficient in transferring charge.

PTTL is a well known means to access deep traps, by moving a proportion of charges to previously thermally cleaned shallower traps, typically by employing short illumination wavelength (UV or blue light). This prevents issues related to the readout of traps in high temperature region of the glow curve (thermal quenching and black body radiation mainly). The intensity of the PTTL signal is usually observed to be related to the length and intensity of the illumination (Alexander and McKeever, 1998), and the wavelength is also critical. However, in some materials and for some wavelength, an optically-excited TL process, often referred in the literature as photo-stimulated thermoluminescence (PSTL; Mehta and Sengupta 1977, 1978) signal may be observed. A PSTL signal is characterised by the TL emission following exposure of unirradiated materials to short wavelength (UV) light (Osvay et al., 1990). This effect is not related to dose, and thus undesirable for dosimetry.

A PTTL emission has been reported in many materials, including Al_2O_3 (Bulur and Göksu,

1999) or calcite (Lima et al., 1990), proving the presence of deeper traps. PTTL was found to be successful in reducing the fading of some materials by enabling the reading of deep traps (Bailiff, 1976). In dosimetry, this procedure is also used for dose re-assessment (McKinlay et al., 1980). The TL glow curve can be recorded in the preheat stage, providing a first dose assessment, after which the sample can be exposed to a light source, and the PTTL used for a second dose assessment.

4.8 Summary

The purpose of this chapter was to explain how the exposure of a solid to ionising radiation causes charges to be captured in localised trapping levels located in the band gap of the material. These charges may be released via thermal (TL) or optical stimulation (OSL) and recombine radiatively in recombination centres, releasing photons. TL and OSL curves carry information not only on the structure of the trapping centres of the material, but also on the quantity of ionising radiation dose administered to the sample. The next chapter will review how the photon count recorded during TL/OSL measurements can be related to dose absorbed in the material; using the photon counts recorded in laboratory during TL or OSL measurements, the amount of trapped charge, hence to the dose absorbed by the material can be deduced.

Chapter 5

Luminescence dosimetry

5.1 Introduction

Luminescence dosimetry is an accepted and widely used method for personal dosimetry that is based on the use of luminescence to determine absolute doses delivered to various materials. The mechanisms that govern the emission of luminescence under thermal or optical simulation following the exposure to ionising radiation have been detailed in Chapter 4. The present chapter will focus on the procedures using TL and OSL techniques to measure absorbed dose, and will aim to address the following issues : 1) the desired properties of a luminescence dosimeter, and 2) what experimental protocols are applied to determine absorbed dose in luminescence dosimetry? This chapter will then explore the difference in approach in conventional dosimetry and in emergency dosimetry using luminescence techniques.

5.2 Conventional luminescence dosimetry

5.2.1 Properties of luminescence dosimeters

This section identifies the ideal properties sought in a dosimeter material.

Dose response

The term OSL or TL "sensitivity" is commonly used to describe the luminescence response to dose in terms of the intensity of the signal per unit of dose. However, the sensitivity is relative, as the

strength of an TL/OSL signal depends on the readout parameters, the instrumentation, and the procedure employed. The sensitivity of a dosimeter required for a particular application depends on the dose range : in personal dosimetry, this is from mGy to a few Gy, whereas in nuclear reactors or food sterilisation units dose levels of up to 10^6 Gy may need to be detected. The range for emergency dosimetry is close to that for personal dosimetry (ca 0.1 Gy - 10 Gy).

The linearity function, $f(D)$, of a luminescence dosimeter is the function that describes the dose dependency of the signal. McKeever et al. (1995, p. 31) described this function as :

$$f(D) = \frac{F(D)/D}{F(D_1)/D_1}, \tag{5.1}$$

where D is the absorbed dose, $F(D)$ the dose response at this dose, and D_1 a low dose at which the dose response is linear $F(D_1)$. These indices are indicated on a dose response curve on Fig. 5.1. This function uses normalisation to better visualise the shape of the dose response curve. However, routinely, the function $F(D)$ is often also called "dose response". If $f(D) = 1$ over a large range of doses, the dose response is said to be linear.

For ease of calibration, and a better accuracy of the results, a linear response to absorbed dose is preferred, although deviations from linearity occur in all materials, and the onset of the deviation will be material-dependent. Firstly, in the case of OSL and TL, the trapping centres may saturate at high doses ($f(D) < 1$), which would cause the signal to reach a plateau (Yukihara and McKeever, 2011, p. 126). The dose response curve then follows a non linear function, often described as :

$$f(D) = a(1 - \exp(-bD)), \tag{5.2}$$

where $f(D)$ is the signal as a function of dose, D is the absorbed dose, and a and b constant parameters. In this case, measurement of high doses is rendered imprecise by the asymptotic limit. The other observed case of deviation from linearity is known as supralinear behaviour, where $f(D) > 1$. A supralinear behaviour is shown as the red dotted line on Fig. 5.1. In this case, the dose response is characterised by a linear behaviour at low doses, but the response has values higher than the linearity at higher doses (Chen and McKeever, 1997, p. 152). The explanation often advanced to account for this behaviour is the competition between the filling of traps and recombination centres, i.e. if additional traps (competitors) play a role at high radiation doses (Chen and Fogel, 1993).

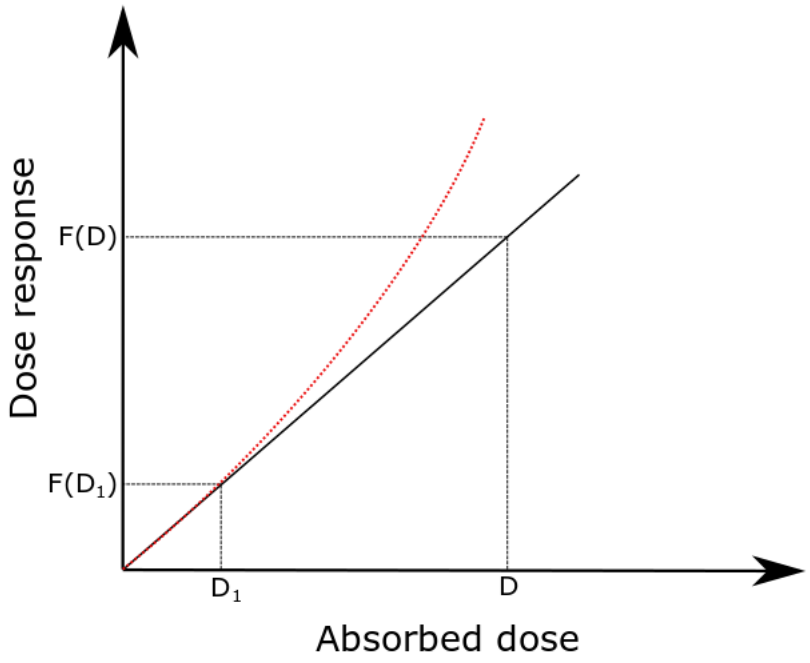

Fig. 5.1. Dose response curve, on which the level of dose D_1 and D, and the dose response, respectively $F(D_1)$ and $F(D)$ used to calculate the dose response are indicated. The black continuous line indicates a linear dose response, and the red dotted line a supralinear deviation from linearity.

Detection limit

The detection limit is related both to the sensitivity of the material, and also to the background. A basic expression used in luminescence dosimetry for the detection limit is the dose response corresponding to the background plus three times the standard deviation of the background, often related to the dark counts of the PMT (Yukihara and McKeever, 2011, p. 129), such as :

$$f(D_L) = \sigma_B + 3 \times \sigma_B, \tag{5.3}$$

where $f(D)$ is the dose response function, D_L the detection limit, and σ_B the standard deviation of the background. As explained in Chapter 3, the detection limit (the minimum dose for which the signal is strong enough to enable dose determination) is different from the decision limit (the minimum dose for which it can be said that the dosimeter has received a radiation dose).

Precision and accuracy

The precision of a dosimeter is determined through experimental measurement, and is related to the amount of fluctuation between measurements. A perfect dosimeter would show little fluctuation, thus giving good reproducibility over repeated cycle of dose and measurement and good precision in dose estimation. Fluctuations can occur due to random errors related to instrumentation, variation in the background, or ambient conditions (Attix, 2008, p. 278). The precision of a measurement is determined by the standard deviation (Attix, 2008, p. 7):

$$\sigma \cong \left[\frac{1}{n-1} \sum_{i=1}^{n} (N_i - \overline{N})^2 \right]^{1/2}, \tag{5.4}$$

where n is the number of measurements, N_i the value of the i^{th} measurement, and $\overline{N}$ the average value of all the measurements.

The accuracy of a dosimeter measurement is determined by the closeness between the given dose and the dose calculated from the dosimeter readout. Poor accuracy can arise from many factors, such as systematic experimental errors, or low sensitivity of the dosimeter.

A good dosimeter should be both precise and accurate, i.e., capable of good reproducibility and giving dose estimates close to the accurate value.

Stability

The latent luminescence signal of some materials was observed to decrease with time, which is known as fading. The mechanisms explaining the occurrence of thermal and anomalous fading of the luminescence signal for some samples were described in Chapter 4. The lack of stability of the signal (i.e., fading) causes an under-evaluation of the dose if the fading is not taken into account. Furthermore, the fading of the signal may cause the signal to disappear after a certain time interval, rendering a dose evaluation impossible. If a sample is found to exhibit fading, a correction factor may be applied. Alternatively, applying a phototransferred thermoluminescence procedure may, in some cases access deeper traps with a reduced rate of fading (Chapter 11). If there is time dependent fading, it should be as reproducible as possible from sample to sample, to enable the use of "universal" fading corrections. Furthermore, in addition to thermal fading, the dosimeters employed in conventional dosimetry (e.g., lithium fluoride) are not subject to sensitivity changes caused by variations (in a reasonable range, to which the dosimeters may be exposed to during their

routine operation) in temperature, atmospheric oxygen level, humidity, or light exposure (Attix, 2008, p. 282).

Conventional dosimeters are designed to have a stable signal over the time that it is designed to be used (often no more than a few months). This is the case for materials used in personal dosimetry, such as lithium fluoride, aluminium oxide (McKeever et al., 1995).

Photon energy response

High energy photons sources are the main particles of interest in this study, as they are the particles most likely to be found in radiological emergencies, due to their large prevalence. This section will therefore focus on the photon energy response. The energy dependence of a luminescence dosimeter describes the relationship between the luminescence response (TL or OSL output) and the energy (quantum or kinetic) of the incident radiation for a given dose (Attix, 2008, p. 283). Although several definitions of the energy response exist (Attix, 2008, p. 285), the one of interest here is defined as the dosimeter reading per unit of dose absorbed by a material in a given volume, itself divided by the radiation energy. The relative photon energy response is defined as (McKeever et al., 1995, p. 36):

$$S_E(E) = \frac{(\mu_{en}/\rho)_m}{(\mu_{en}/\rho)_{ref}}, \tag{5.5}$$

where $(\mu_{en}/\rho)_m$ denotes the mass-energy coefficient for the material measured and $(\mu_{en}/\rho)_{ref}$ the mass-energy coefficient for a reference material, sometimes taken as air (Attix, 2008, p. 285). In practice, the energy response is determined by measuring the response of a dosimeter to the same dose of different energies of ionising radiation.

A dosimeter with a flat energy response in the range of energy of interest avoids energy response corrections, and this can be obtained for materials with a low effective atomic number, Z_{eff}. Z_{eff} can be defined as a rough estimate as (Yukihara and McKeever, 2011, p. 125):

$$Z_{eff} = \left(\sum_i a_i Z_i^m \right)^{1/m}, \tag{5.6}$$

where Z_i is the atomic number of the element i of the material, m a constant usually taken as 3.5 (Attix, 2008, p. 308), as this approximation of m gives the best fit energy absorption coefficient for

a mixture of high and low Z materials (Cunningham and Johns, 1983, p. 243). a_i is the fractional electron content, equal to :

$$a_i = \frac{f_i(Z_i/A_i)}{\sum_j f_j Z_j/A_j}, \tag{5.7}$$

where f_i is the weight fraction of element i, and A_i its atomic mass. However, the true value of Z_{eff} is dependent on several factors, such as the energy range of interest, and hence on the dominant modes (e.g. photoelectric, Compton) of interaction.

Equation 5.5 describes the absorbed dose energy response. In addition, for a luminescence dosimeter, there is an additional component of the energy response describing the intrinsic processes of conversion of deposited energy into a luminescence signal as a function of the type of incident radiation (Yukihara and McKeever, 2011, p. 126). The intrinsic energy response is caused by the difference in response of the defects giving rise to the luminescence signal (e.g., LiF:Mg,Ti and LiF:Mg,Cu,P) and is thus dependent on the type and concentration of the electron traps and holes of the dosimeter.

In personal dosimetry, the dose of interest is the dose to tissue and hence, materials with a tissue equivalent energy response are preferred, such as lithium fluoride, which has a Z_{eff} of 8.6 (Suntharalingam and Cameron, 1969; Spurnỳ, 1980).

In general terms, the properties of a dosimeter sought for personal dosimetry are :

1. A linear dose response within the dose range required for the application (from a few mGy to 10 Gy);
2. High sensitivity and low detection limit;
3. Precise and accurate within 5% of the actual value above 1.1 mGy (British Standard Institution, 2016);
4. No loss of the signal over time and, if not, reproducible fading rate from one sample to another;
5. No loss of the signal over a reasonable range of environmental conditions (temperature, humidity);
6. Flat energy response over the energy range required;

7. For personal dosimetry, tissue equivalence;

8. Cheap and easy to use.

In occupational or personal dosimetry, dosimeters are designed to fulfil these conditions.

5.2.2 Dose assessment in conventional luminescence dosimetry

The absorbed dose recorded by a dosimeter is calculated by comparing the signal following exposure to an unknown dose to the response of the dosimeter to a known administered dose under the same readout conditions. The administration of a known dose and the recording of the subsequent dosimeter response is referred as the "calibration" measurement. For personal dosimetry, dosimeters are manufactured to be identical within controlled limits, to enable calibration that is not sample specific. The first step in evaluating a dose is to estimate the luminescence signal resulting from an unknown dose contained in the dosimeter. The signal is corrected for the instrumental background, such as :

$$S = S_{raw} - S_{BG}, \tag{5.8}$$

where S_{raw} is the raw signal observed, and S_{BG} the background (Yukihara and McKeever, 2011, p 113). Fig. 5.2 shows an example of a TL glow curve with its background, which will be subtracted when processing the signal. This signal, S, may be composed of several components each corresponding to a different trap that can be separated and evaluated independently. This is often the case for example for TL glow curves for which the dose response can be calculate as the integral of a specific temperature region of the TL glow curve, and individual peak may be studied separately. Fig. 5.2 shows a TL glow curve with at least two peaks. For OSL, the signal can be taken, for example, as the integral over the first second of illumination, or the integral of the total decay curve.

Each component of the signal is labelled as S_1, S_2,..., S_g, where g is an integer. Fig. 5.3 shows how the dose G can be evaluated from the components of the signal. This diagram applies to a situation where the response of the dosimeter is well characterised before use, and the response to a certain known dose is therefore already known. In this case, the dose calculation algorithms are quite straightforward and provide directly an indicated value of dose, G.

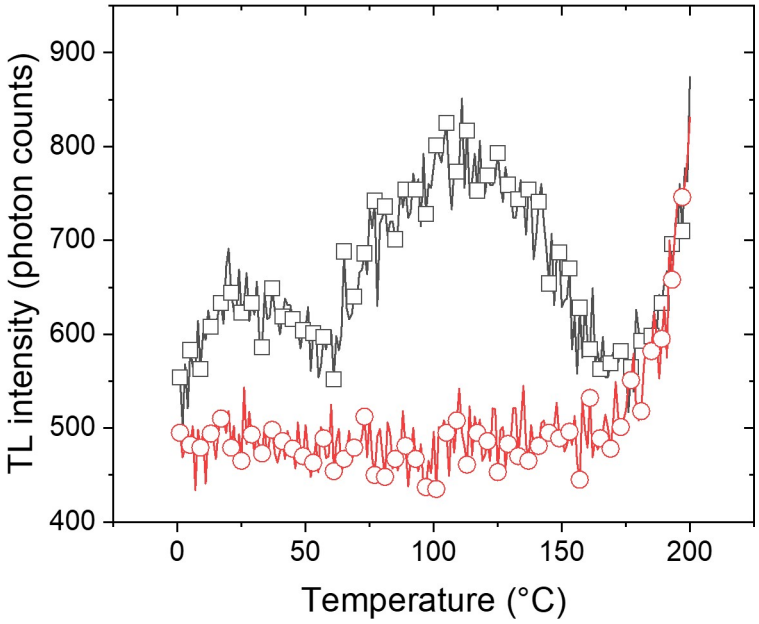

Fig. 5.2. Example of a TL glow curve of calcium carbonate fillers following β irradiation 1 Gy (black squares) and its background (red circles). Risø system, detection window: OC 12, PMT : Hamamatsu R2949, heating rate : 0.5 °C.s^{-1}.

5.3 Luminescence dosimetry for radiological emergencies

5.3.1 Properties of emergency dosimeters

This section will build on the properties of the conventional dosimeters, and assess what can be achieved in emergency dosimetry. Although the search for new surrogate dosimeters intends to meet the requirements of an ideal dosimetric system, finding a commonplace material that would encompass all of the ideal qualities does appear to be challenging.

The dose response range required is quite similar in emergency and conventional dosimetry, i.e., 0.1-10 Gy. Finding samples or procedures with the lowest possible detection limit is one of the challenges of emergency dosimetry, although the dose range required is more limited than in personal dosimetry. In emergency dosimetry, the lowest dose that has to be detected for short term assessment is often set at 0.5 Gy, thus the range of dose of interest is 0.1 Gy (lower limit) to 10 Gy (upper limit). Although for emergency dosimetry, the samples are not expected to reach saturation

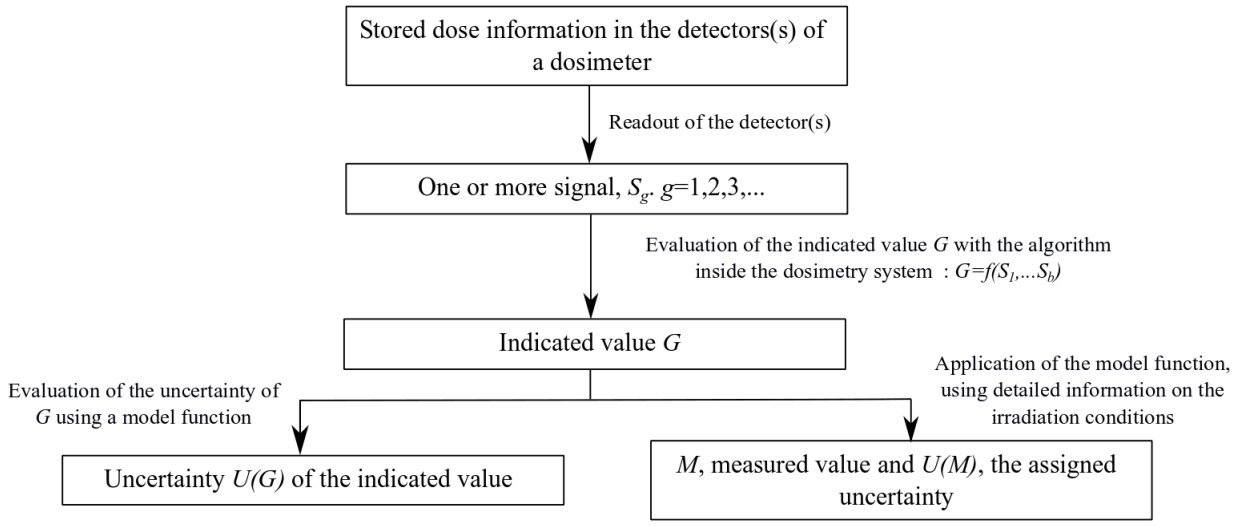

Fig. 5.3. Protocol for dose evaluation in personal dosimetry. S_g is the component number g of the signal, G is the dose value provided by the dosimetry system using a dose calculation algorithm, and M the measured value of dose, calculated using information on the irradiation conditions (e.g., geometry, type of source). Redrawn from International Electrotechnical Commission (2016).

in the range of doses of interest ($\leq$ 10 Gy), supralinearity is a potential issue.

Apart from grains of quartz used in retrospective dosimetry and salt, most of the materials investigated so far for luminescence emergency dosimetry exhibited fading (e.g., alumina substrate resistors, gorilla glass from mobile phones, see Chapter 3). Where the fading cannot be avoided, the loss of the signal should be minimised, and if possible, be reproducible. Universal fading corrections are currently employed for surface mount alumina substrate resistors, although their use is subject to discussion, and individual fading corrections are sometimes preferred (Inrig et al., 2010a).

Automated readers such as the Risø reader are commonly used for dose assessment in luminescence dating and luminescence short term dosimetry. The calibration dose is usually delivered by the dose reader's built-in ^{90}Sr/^{90}Y beta source. If the energy response is not flat, this may cause an over-response (or under-response) of the sample and an over-evaluation (or under-evaluation) of the accidental dose if the accidental dose was administered with another type of source (e.g., gamma sources ^{60}Co or ^{137}Cs). Besides, differences could also arise from the difference between irradiation

using electron versus photon sources. This requires the application of a correction for the energy response function. Furthermore, some scenarios may require correction for the irradiation geometry. This would depend on the location of the dosimeter relative to the individual and the source. If shielding had occurred (for example if the dosimeter was placed in front of the person, but the source was located on the back of the individual, the dosimeter would have therefore been shielded by the person's body) and the dose read by the dosimeter would give an under-evaluation of the critical organ doses. This issue was addressed by Eakins and Kouroukla (2015), who used particle transport codes to relate the position of the dosimeter to the organ doses for different exposure scenarios. This last case situation is slightly more complex, as it requires running simulations case by case. However, in many cases the energy and direction of the source, and location of the dosimeter, may not actually be known.

Furthermore, to the list of desired properties for conventional dosimeters (Section 5.2.1), some requirements specific for emergency dosimeters should be added :

1. Be ubiquitous amongst members of the public
2. Be easy to sample and process
3. If the process is destructive, be of small value (if not, members of the public will not be likely to be willing to give it up)
4. Fast processing and measurement time of the samples (less than a few hours per sample)
5. A sampling procedure can be developed that does not require high level of training

5.3.2 Dose assessment in emergency dosimetry

Protocol for dose evaluation in emergency luminescence dosimetry

On the contrary to conventional dosimetry, the samples used for emergency dosimetry exhibit variability (differences in shape, weight, amount of sample available), meaning that the calibration factor is unknown prior to the measurements, and that a sample specific calibration is required (Moscovitch, 1993). If the sample exhibits a linear response to dose passing through origin, a single calibration point may be used, and the unknown dose, or accident dose, D_{acc} is such as :

$$D_{acc} = D_{cal}\frac{S_i}{C_i}, \tag{5.9}$$

where S_i is the i^{th} component of the signal for the unknown dose, and C_i is the i^{th} component of the signal recorded following the administered calibration dose, D_{cal}. Such a case is illustrated in Fig. 5.4.

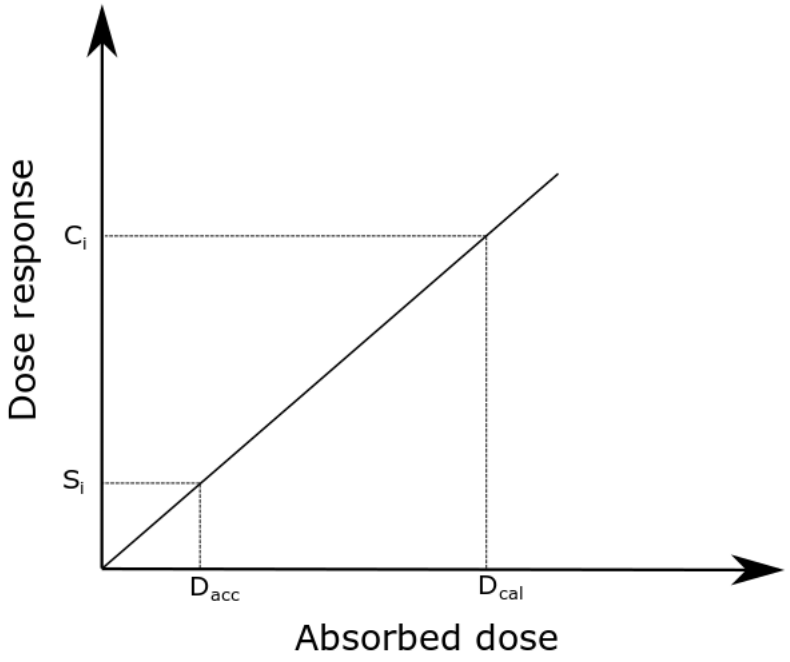

Fig. 5.4. Graphical determination of the accident dose D_{acc} using the component S_i of the accident signal, for a sample whose dose response curve is linear and passing through the origin. An unique calibration point for a dose D_{cal} calculated for the component C_i.

A more complex procedure for dose evaluations exists in luminescence dating, and includes administering multiple calibration doses to the samples, thus recording a sample-specific dose response curve (Aitken, 1998, p. 93-105). This is necessary when the sample dose response is not linear and also where dose response characteristics differ between samples. Some of these methods, such as the additive method, require a group of samples. Using the additive method, the sample to measure is divided in several groups of aliquots. One group is reserved for the measurement of the

natural signal (or accidental signal in emergency dosimetry), and the other groups given various doses. Each aliquots of a group is given the same dose, in addition to the natural dose, and the calculated dose for the group is calculated as the average of the dose of the aliquots of the group. The dose response curve is thus calculated as the average of each group's administered dose. The natural/accidental dose is found by extrapolating the dose response curve, as the laboratory dose combines to the natural/accidental dose. If the samples are bleached from their natural signal before the administration of the laboratory dose, no extrapolation is required. However, this technique requires multiple aliquots, which can be quite impracticable where only a small amount of sample is available. For example, when using alumina substrate surface mount resistors for emergency dosimetry, only enough resistors are usually found in a mobile phone to make a maximum of three aliquots. This process is also quite time consuming.

Single aliquot approaches use only one aliquot, and perform measurements of the accidental signal and calibration on the same aliquot. The Single Aliquot Regenerative protocol (SAR protocol), involves measuring the accidental signal, before administrating a series of known doses to a single aliquot, recording the luminescence signal, and also includes a correction for sensitization effects by repeating a test dose and measurement at different stage of the protocol (Murray and Wintle, 2000; Murray and Roberts, 1998). This method is based on the assumption that the sample is zeroed (i.e. the signal is cleaned from residual charges) after each measurement, or "regenerated" (e.g., by thermally bleaching the traps).

In emergency dosimetry, the precision of the results yielded by the protocol must be weighted against how lengthy the protocol is. If, like it might be the case in some scenarios, a lab is required to process hundreds of samples within weeks, applying a SAR protocol may take too much instrumentation time per sample/individual. In this case, a shorter protocol should be employed (i.e., administration of one calibration dose only). Although significantly reducing the measurement time, this method requires a thorough understanding of the behaviour of the samples, notably in terms of dose response. Furthermore, some protocols may also include the measurement of a sample specific fading correction, if the sample exhibits fading. Again, the same issue arises of accuracy of the results vs measurement time. Thus, the preferred protocol for dose assessment in emergency dosimetry may entirely depends on the scenario, and what doses assessments are needed for. In a large scale scenario where the doses are required for triage of the population, a shorter protocol may be preferred, as only a Yes/No answer is needed to the question of whether the members of

the public should be sent home (i.e., above or below 2 Gy).

Dose calculation algorithms

Fig. 5.5 shows an example of the TL response of calcium carbonate fillers to doses of [0.1-10] Gy. The TL response to dose in this range is linear, thus a linear function passing through the origin can be fitted to the experimental data points. This case represents one of the simplest cases, where the dose response follows a relation such as :

$$L = f(D) = a \times D, \tag{5.10}$$

where L is the luminescence signal, D the administered dose, and a a coefficient. The accident dose, D_{acc} is therefore obtained dividing the accidental signal, L_{acc} by the coefficient a, such as:

$$D_{acc} = \frac{L_{acc}}{a}. \tag{5.11}$$

Where the dose response is more complex, a similar approach is used, solving the equation $L_{acc} = f(D)$ for another dose response function $f(D)$. This can also be determined using random simulations by Monte Carlo methods, such as discussed in Chapter 3.

Dose calculation algorithms may include correction factors, such as fading corrections, background subtraction, shape of the dose response curve (i.e., non-linearity), or factors accounting for the stability of the reader (Yukihara and McKeever, 2011, p 114). These factors are determined in advance of the dose calculation. The final dose value G accounts for all these corrections, such as :

$$G = \left(G_{raw} - \sum_j G_j \right) \prod_i k_i, \tag{5.12}$$

where G_{raw} is the uncorrected dose value indicated by the system and G_j are the indicated values of influencing factors, such as instrumental background, electrical disturbances that needs to be subtracted from the raw signal. k_i are the correction factors that are applied. Chapter 3 showed how the uncertainties are assessed in dosimetry, and how the correction factors propagate uncertainties using GUM, Monte Carlo or Bayesian techniques.

The last step of the protocol for dose evaluation in personal dosimetry (Fig 5.3) is determining the measured value M and this is reached by applying a model function correcting for the irradiation

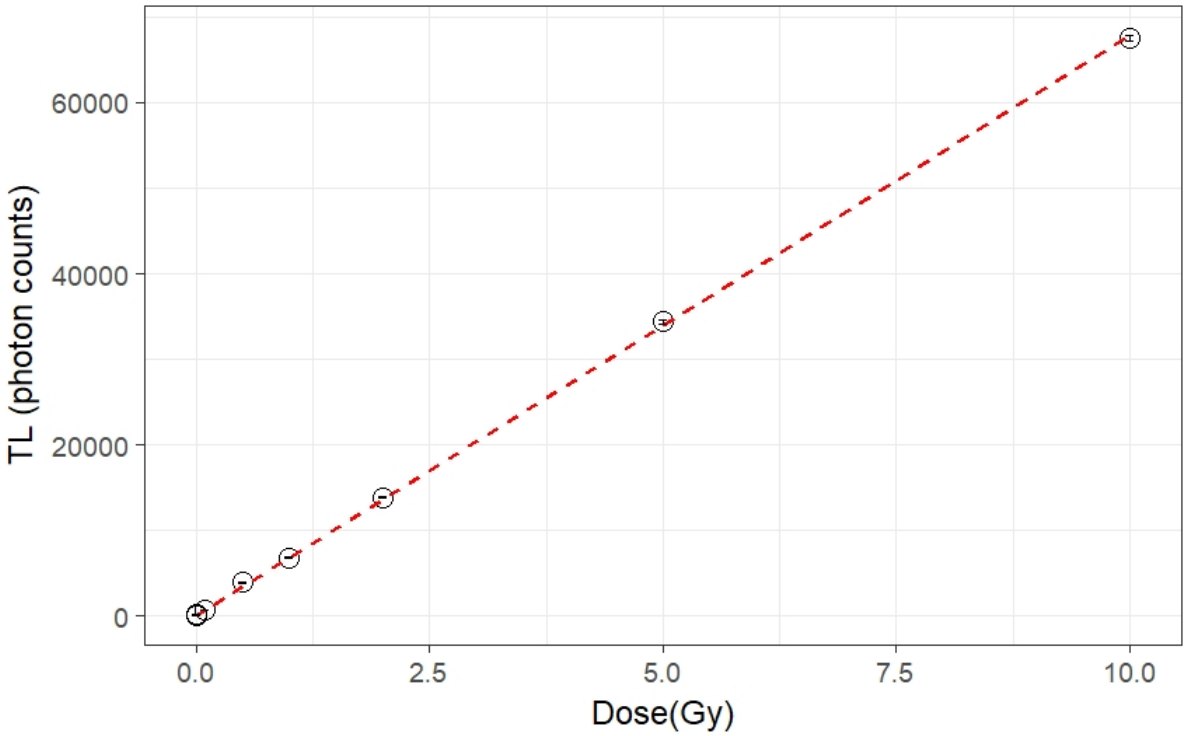

Fig. 5.5. Thermoluminescence dose response curve of calcium carbonate fillers. The thermoluminescence signal (open circles) was computed as the integral of the TL glow curve in the region 105-135 °C. The background was subtracted from experimental data, and the error bars associated with photon counting statistics are ≤ 1 % of the TL signal. The dotted red line represents a linear function fitted to the experimental data points. The glow curve associated to this signal is shown in Fig. 5.2.

conditions. This step is case specific, and requires a knowledge of the irradiation conditions, such as the type of source or the geometry of the irradiation, which is often done by using Monte Carlo simulations. Fig. 5.6 summarises the steps required for dose evaluation using surrogate dosimeters.

5.4 Summary

This chapter briefly outlined the characteristics of luminescence dosimeters used in personal dosimetry, and how the absorbed dose value can be extracted from TL/OSL measurements. Several protocols exist for dose determination using luminescence techniques, but the preferred protocols for emergency dosimetry using TL or OSL should take into consideration the requirement of the

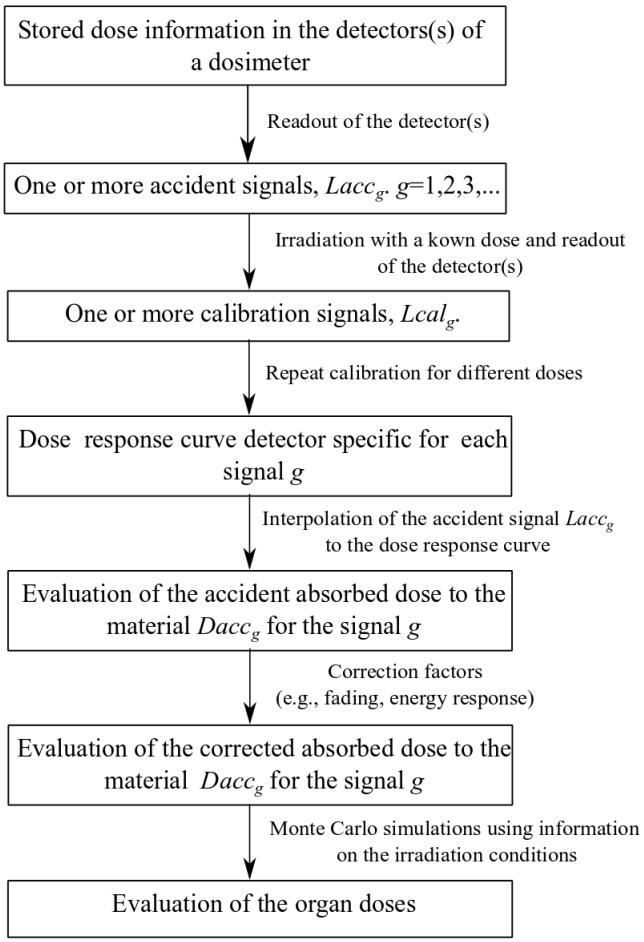

Fig. 5.6. Protocol for dose evaluation in emergency dosimetry. S_g is the component number g of the signal.

scenario to which these techniques are applied, weighing measurement time against the required accuracy of the results. It will be assessed later in the experimental chapters of this thesis how the new candidate materials investigated as surrogate dosimeters meet the requirements of the desired properties of dosimeters, especially in terms of dose response.

Chapter 6

Instrumentation

6.1 Introduction

This chapter reviews the instrumentation used to characterise the physical luminescence properties of the samples tested. A physical examination of the samples was also carried out using an X-ray diffractometer (XRD) and scanning electron microscope (SEM) equipped with a cathodoluminescence (CL) attachment.

6.2 The Risø luminescence reader

The Risø reader (DTU Nutech, model 12) enables semi - automated TL and OSL measurements. The reader includes a photon counting detection system, an optical stimulation unit, a heater plate and a $^{90}Sr/^{90}Y$ β irradiation source (Risø, 2010). Fig. 6.1 shows pictures of the reader (model 12) with the different parts indicated. For TL/OSL measurements, the samples are deposited on measurement stainless steel or discs and placed on a carousel for measurements (Fig. 6.1b). The carousel used can carry 24 cups and rotates to expose each sample to the β source or stimulation / detection unit. The chamber can be evacuated using a vacuum pump or maintained in a nitrogen atmosphere.

The photon detection system comprises a photomultuplier tube (PMT) converting photons to an electrical signal using photoelectric effect. Unless specified otherwise, an EMI 9635 PMT was used. The EMI was designed for photon detection mainly in the UV, when detection in the red was required, a red sensitive Hamamatsu R2949 PMT was used. A fused silica window was fitted

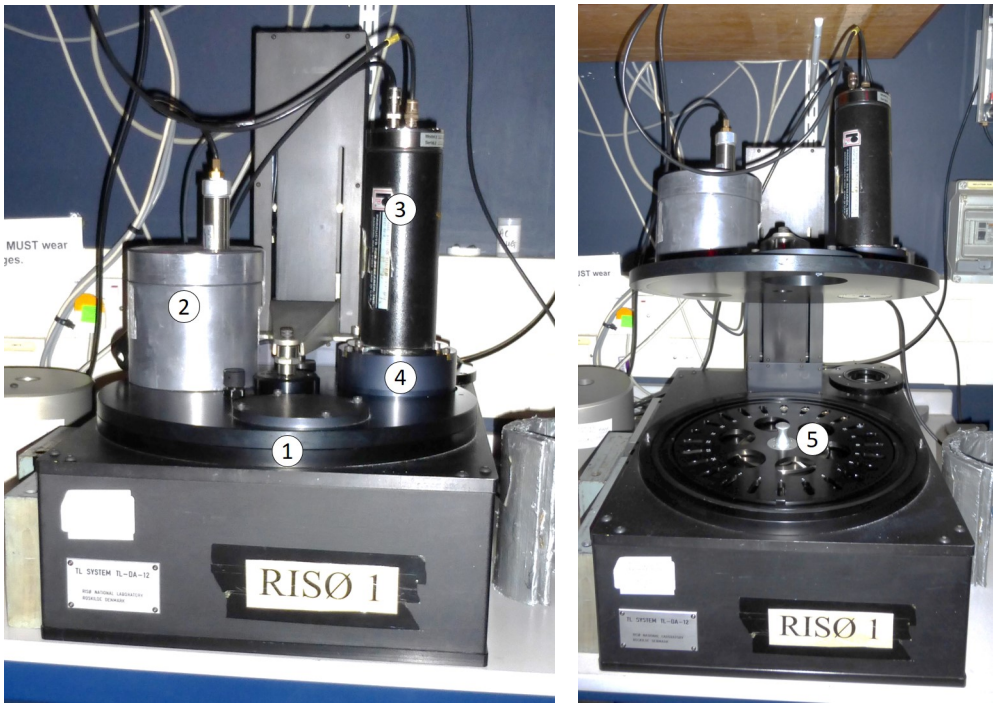

(a) **(b)**

Fig. 6.1. Picture of the Risø reader model 12 (DTU Nutech).① Lid (closed), ② lead shielding containing the β ^{90}Sr/^{90}Y source, ③ photomultiplier tube (EMI 9235 on the picture), ④ optical flange containing a filter basket and blue (470 nm) and IR (850 nm) LEDs, ⑤ carousel on which the measurements stainless steel cups are placed.

between the sample and the PMT to prevent deposition of vapour or residual impurities on the PMT window and to cut emission in the far-red. Fused silica has a broad transmission window without attenuation, from the UV ($\geq$ 200 nm) to infra-red ($\leq$ 1200 nm). In addition to the fused silica window, optical filters were inserted when a specific detection window was required. The most commonly used filters are the Schott U-340 (UV filter) and the Schott BG-39 (broad band filter). The transmission of the U-340 and the BG-39 is shown in Fig. 6.3. Additionally, a series of sharp-cut Russian optical filters type YΦC2 were used, with various transmission windows (Chapter 10). The transmission graphs for these filters is given in the chapter related to their use (Chapter 10). Typically, the U-340 was used when using the blue (470 nm) stimulated emission and the BG-39 when stimulating with infra-red (850 nm) light. For TL measurements, only the fused silica window was used.

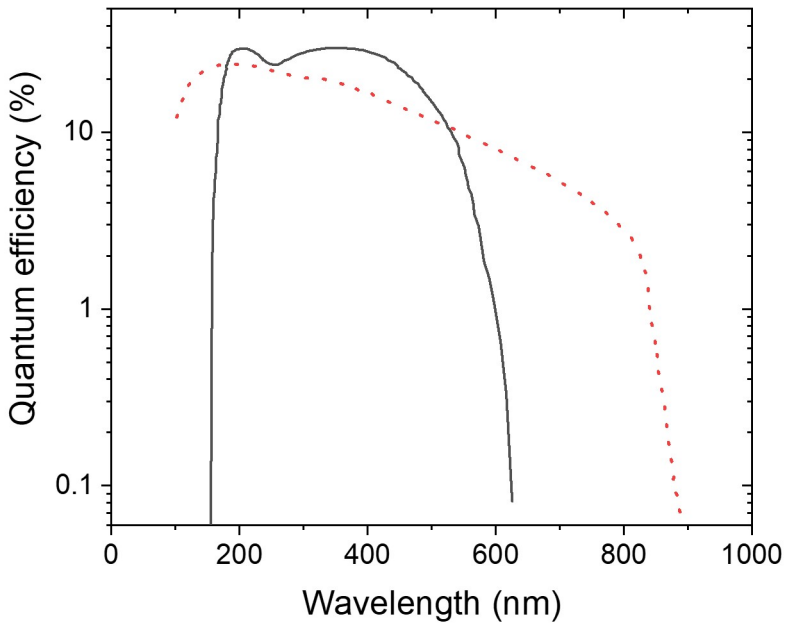

Fig. 6.2. Quantum efficiency of the Hamamatsu R2949 (broken line) and EMI 9235A (black continuous line) PMTs. Obtained from teh manufacturers datasheets.

The blue LEDs (470 nm) delivered a power at the sample position of 13 mW.cm^{-2} and the infrared LEDs of 83 mW.cm^{-2} (2018). The heating element is a nichrome heater plate located directly under the detection unit. It can either be used to perform thermoluminescence (TL) measurement by increasing the temperature of the sample while recording the luminescence, or to preheat the sample before TL/OSL measurements.

The ^{90}Sr/^{90}Y β source is mounted on a rotated stainless steel wheel. The half-life of ^{90}Sr is 28.8 years, and the source activity was 1.48 GBq in November 1990. Although the sources of interest in emergency dosimetry are photon γ sources and the β source fitted in the reader delivers electrons, photon sources ultimately deposit dose in a mass by liberating electrons (see Chapter 3) and the doses deposited by γ or β sources follow equivalent mechanisms. The source is surrounded by brass to provide shielding and an aluminium spacer to provide a safe distance between the irradiator and the user. The source rotates to its "exposed" position to irradiate the samples using a compressed

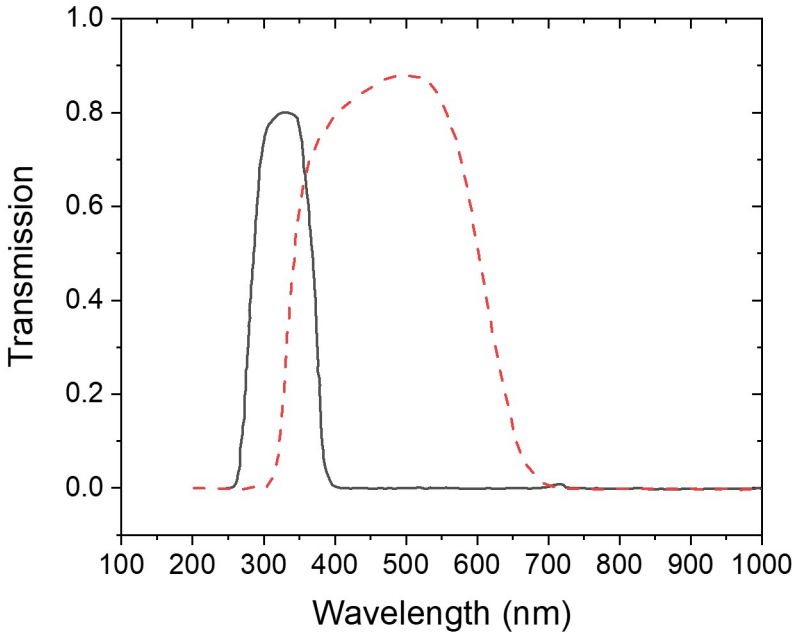

Fig. 6.3. Transmission characteristic of filters U-340 (black continuous line) and BG-39 (red dashed line).

air mechanism. A beryllium window is placed between the irradiator and the chamber allows the chamber to be evacuated. The distance between the source and the sample was 7.5 mm during irradiation. The dose rate delivered by the source depends on whether the sample is mounted on stainless steel discs or cups. As quartz is often used, the dose rate to quartz deposited on a stainless steel disc is (1.08 ± 0.02) Gy.min^{-1} (2017), determined using various types of "calibration" quartz irradiated at DTU Nutech and Public Health England, and the dose rate to quartz deposited on a stainless steep cup is (0.79 ± 0.02) Gy.min^{-1}. This difference is due to greater distance from the source to the sample when using stainless steel cups compared with discs (evaluated to be 1 mm further when using stainless steel cups).

6.3 Scanning Electron Microscope (SEM) and cathodoluminescence (CL)

The micro-structure of the sample was characterised using a Hitachi SU-70 field electron gun (FEG) scanning electron microscope (SEM) at the GJ Russell Microscopy Facility at Durham University. The SEM was also equipped with a cathodoluminescence (CL) attachment that enabled measurement of the luminescence emission spectrum under electron bombardment. The SEM produced focused electron beams with accelerating voltages in the range 0.5-30 kV with a probe current $\geq$150 nA using a Schottky field emission electron gun. Various detectors were available for imaging, including a secondary electron detector and a backscatter detector that can be used in combination. The CL was detected using a Gatan Mono-CL cathodoluminescence unit that included : 1) a parabolic mirror with a 1 mm aperture, 2) a Czerny-Turner monochromator, 3) a standard PMT (spectral range: 185-850 nm), 4) a Pixis CCD camera for parallel CL, 5) a beam control and image processing Digiscan system, and 6) a filter housing with circular 1 inch diameter colour filters. The CL spectra were corrected for instrument response. Elemental analysis was carried out by an Oxford Instruments EDX system (X-MaxN 50 Silicon Drift Detector).

Additional measurements were conducted in an environmental SEM (FEI ESEM XL30, CIEMAT) equipped with a Energy Dispersive Spectrometry probe (EDS) and a Gatan MonoCL3 probe using a PA-3 PMT. For these measurements, a low vacuum mode was used and the beam voltage was set at 20 kV.

6.4 X-ray diffraction

X-ray diffraction patterns were obtained using a Bruker AXS D8 Advance equipped with a Lynxeye Soller PSD Detector. The source of X-ray was a copper tube producing a mixture of Cu-$K_{\alpha 1}$ and Cu-$K_{\alpha 2}$ at a wavelength of 1.5406 Å. The XRD diffractometer was operating in BraggBrentano mode with a Ni filter, variable slits (set at 6mm) and sample changer.

Chapter 7

Materials survey

7.1 Introduction

In order to identify new materials to act as surrogate dosimeter during radiological emergencies, a screening of materials likely to exhibit a response to ionising radiation and to be found in the possession of members of the public was carried out. This survey aimed to identify materials that exhibit an OSL/TL signal in response to dose, focusing on fabric samples, as they would present the advantage of being near the body of the individual. Other commonplace materials such as paper, banknotes, shoes or plastic items were also investigated.

7.2 Methodology

The samples were cut to fit to stainless steel measurement cups (11.5 mm of diameter). All OSL, IRSL and TL measurements were performed with a standard configuration Risø model 12 reader (DTU Nutech, Denmark) with a $^{90}Sr/^{90}Y$ β source irradiator delivering an estimated dose rate to grains of quartz placed on stainless steel discs of (1.08 $\pm$ 0.02) Gy.min^{-1} (2017). The dose rate to fabric samples placed in a stainless steel cup was estimated to be of (0.86 $\pm$ 0.02) Gy.min^{-1} (2018, see Chapter 12 for details of the calibration). Some commonplace materials (e.g., clothings, shoes, coins, plastic cards,...) were already tested by Sholom and McKeever (2014), but only for their OSL response. The protocol used here included testing samples for their IRSL and TL response as well. A UV (250-350 nm; Schott U-340 filter) detection window was inserted when measuring blue stimulated OSL (470 nm), a broad-band detection window (350-700 nm; Schott BG39 filter)

when measuring IRSL (850 nm) and a silica window when recording TL. None of the samples were preheated following administration of dose and IRSL/OSL measurements were performed with the sample maintained at a temperature of 50 °C. TL measurements were performed using a heating rate of 0.5 °C.s^{-1} to a maximum temperature depending on the sample type. For fabric samples, the T_{max} was set to 230 °C, but for glass beads, for example the maximum temperature was set at 400 °C.

The testing procedure was as follow :

- Step 1 : Measurement of the native TL/OSL/IRSL
- Step 2 : Repeat step 1 (background)
- Step 3: β dose (10 Gy)
- Step 4: Measurement of the TL/OSL/IRSL
- Step 5 : Repeat step 4 (background)

Where the samples showed a response to β dose, a complete dose response test was carried out, by administering β doses in the range 0.1-10 Gy and recording the subsequent TL/OSL/IRSL response. The OSL/IRSL response of the samples under different atmospheric conditions (nitrogen, vacuum) was also measured to test for the sensitivity to oxygen. The samples that exhibited the strongest response to β dose are further examined in the following chapters. The dose response measurements were repeated on several samples of each material, to test for uniformity of response.

7.3 List of materials tested

The materials tested are listed in Table 7.1-7.4. Particular attention was paid to testing cotton samples, as they are amongst the most common type of fabrics used in clothing (Table 7.3). A number samples of fabric taken from different types of manufactured bags were also tested (Table 7.4). Swatches of fabrics 3, 29 and 179 and of bags "LED", 16, 19 and 21 are provided in Appendix A.

Table 7.1: List of the materials tested

Material	**Comment**
Paper	White cartridge matt coated paper
Paper	Black dyed uncoated paper
Paper	Blue cartridge glossy coated paper
Paper	White photocopier uncoated paper
Elastic hair band	Rubber band elastic
Card	Business card, glossy coated paper
Dye salt (NaCl)	DYLON dye salt
Pencil	Plastic encasing of the pencil tested, 4 pencils tested (different colours and different parts of the pencils tested)
Banknote	Polymer banknote, Australia
Banknote	Polymer banknote (new) 5 GBP (UK)
Nail polish	Three colours tested (pink, orange, concrete blue)
Optical fibre	
Electrical conduit	Thermoplastic encasing
Plastic/rubber shoe sole	Three samples tested (white, black and brown)
Plastic belt	
Glass beads	12 samples of different colours tested
Adhesive tape	Black and brown tape tested
Plastic card	Thermoset plastic loyalty card, metro card, and 2 bank cards tested
Hard polysterene	CD case, drinking plastic cup
Expanded polystyrene	Packaging polystyrene, 2 samples tested
Cycling helmet	Polystyrene, 6 samples tested
Contact lens	
Washing powder	
Polycarbonate lens	
Plastic phone case	4 samples tested
Polypropylene	3 samples tested (transparent, white, black)

Table 7.2: List of fabric samples tested

1	Dark blue	Cotton	Plain weave
2	Grey	95% viscose, 5% elastane	
3	Blue	65% polyester, 35% cotton	
4	Yellow	100% linen	
5		95% polyester, 5% elastane	
6		42% viscose, 32% cotton, 21% polyamide	
7	Yellow	100% polyester	
8	Blue	100 % polyester	
9	Beige	80% polyester, 20% viscose	
10		1% acrylic, 31% polyester, 28% cotton	
11	Grey	100% polyester	Fleece
12	Duck egg	100% polyester	
13	Blue	80% cotton, 20% polyester	Fleece
14	Dark grey	100% polyester	
15	White	100% polyester	Linen
16	White	100% polyester	Jersey
17	Black	85% viscose, 15% wool	
18	Brown	65% polyester, 30% viscose, 5% elasthane	
19	Green	100% polyester	Home dyed
20	Blue	100% polyester	Home dyed
21	Red	100% polyester	Home dyed
22	Blue	100% polyester	Multilayer (3)
23	Black	100% cotton	Waxed cotton
24	Brown	100% wool	
25	Blue	Cotton polyamide	
26	Blue/black	Polyester with waterproof laminate	

Fabric reference	**Colour**	**Composition**	**Weave plan/Other technical information**
27	Green	100% polyester	Fleece
28	Duck egg	85% polyester, 15% viscose	Fire resistant upholstery fabric
29	Lynton Blue print	60% polyester, 38% acrylic, 2% nylon	Fire resistant upholstery fabric
30	Pale teal	88% polyester, 11% viscose, 1% spandex	
31	White	100% linen	Natural linen
32	Opal	85% polyester, 15% cotton	
33	Eau de Nil	95% polyester, 5 % linen	
34	Shale cheltenham	51% Polyester 34% Polyolefin 15% Cotton	
35	Mineral	100% Polyester	
36	Clementine	100% wool	
37	Grey beige	100% Polyester	
38	Blake midnight	87% Polyester, 13% cotton, 1% polyamide	Fire resistant upholstery fabric
39	Black slate	87% Polyester, 13% cotton, 1% polyamide	||
40	Lynton dove grey	60% Polyester, 38 % acrylic, 2% nylon	||
41	Matilda steel	47% cotton, 45% Polyester, 8% viscose	||
42	Matilda teal	47% cotton, 45% Polyester, 8% viscose	||
43	Lynton mineral	60% Polyester, 38 % acrylic, 2% nylon	||
44	Lynton mint	60% Polyester, 38 % acrylic, 2% nylon	||
45	Lynton smoke	60% Polyester, 38 % acrylic, 2% nylon	||

Fabric reference	**Colour**	**Composition**	**Weave plan/Other technical information**
46	Lynton steel	60% Polyester, 38 % acrylic, 2% nylon	‖
47	Bunny tail	56% Polyester, 44% Cotton	‖
48	Bluebird feather	56% Polyester, 44% Cotton	‖
49	French macaron	72% Polyester, 28% Cotton	‖
50	Atlantic denim	72% Polyester, 28% Cotton	‖
51	Crimson sunset	72% Polyester, 28% Cotton	‖
52	Kaleidoscope ink cap mushroom	88% Polyester, 7% Rayon, % Polyacrylic	‖
53	Kaleidoscope Winter feather	88% Polyester, 7% Rayon, % Polyacrylic	‖
54	Kaleidoscope fire coral	88% Polyester, 7% Rayon, % Polyacrylic	‖
55	Burley bright fire	38% polyester, 31% cotton, 21% viscose, 10% linen	‖
56	Rudking pimento	42 % cotton, 36% acrylic, 11% viscose, 6% polyester, 5% polyamide	‖
57	Telma pacific	45% polyester, 20% acrylic, 17% viscose, 10% coton, 8% viscose	
58	Stanton putty	54.1% acrylic, 45.9% polyester	
59	Evora steel	58% polyester, 38% acrylic, 4% viscose	

Fabric reference	**Colour**	**Composition**	**Weave plan/Other technical information**
60	Brambley mocha	60% acrylic, 25% polyester, 15% cotton	
61	White	Cotton	Felting
62	White	Cotton	Plain weave
63	White	Cotton	Twill weave
64	White	Cotton	Sateen weave
65	White	Cotton	Classic interlock Jersey
66	White	Cotton	Single jersey mercerised
67	White	Cotton	Interlock jersey
68	White	Cotton	Jersey sweatshirt fabric
69	Grey	Polyester/Cotton	Rib fabric
70	White	Nylon with elastane (Lycra)	
71	White	Cotton poplin with elastane (Lycra)	
72	White	Cotton with elastane (Lycra)	
73	White	Silk satin with elastane (Lycra)	
74	White	Silk jersey with elastane (Lycra)	
75	White	Silk seersucker with elastane (Lycra)	
76	White	Cotton	Gauze
77	White	Cotton	lawn
78	White	Cotton	Duck lightweight
79	Natural	Cotton	Canvas, 12 oz
80	Natural	Cotton	Domette
81	Natural	Cotton	Brushed
82	White	Silk	Organza
83	Grey	Silk	Chiffon

Fabric reference	**Colour**	**Composition**	**Weave plan/Other technical information**
84	White	Silk	Crpe de Chine
85	Natural	Cotton	Sateen
86	White	Cotton	Poplin
87	White	Nylon	Organza
88	White	Polyester	Chiffon
89	White	Polyester	Crpe de Chine
90	White	Polyester	Sateen
91	White	Polyester/Cotton	Poplin
92	White	Silk	Satin
93	White	Viscose	Satin
94	White	Acetate	Satin
95	White	Polyester	(Crpe back) Satin
96	Natural	Wool	Gauze
97	Natural	Wool	Delaine
98	Natural	Botany wool	Serge
99	Natural	Wool	Voltaire
100	Natural	Wool	Crpe
101	Black	Wool	barathea
102	Natural / Brown pattern	Wool	Worsted Herringbone
103	Grey	Worsted	Suiting weight
104	Tweed	Wool	Tweed
105	Natural	Wool	Basket weave
106	Black	Wool	Melton
107	White	Wool	Air light
108	White	Silk	Chiffon
109	White	Silk	Mousseline
110	White	Silk	Muslin
111	White	Silk	Organze
112	White	Silk	Georgette

Fabric reference	**Colour**	**Composition**	**Weave plan/Other technical information**
113	White with metallic stripes	Silk	Organza
114	White	Silk	Habotai
115	White	Silk	Habotai, sand-washed
116	White	Silk	Charmeuse, sand-washed
117	White	Silk	Charmeuse
118	White	Silk	Crepon
119	White	Silk	Crpe de Chine
120	White	Silk	Twill
121	White	Silk	Shantung
122	White	Polyester	Wadding
123	White	Silk/Viscose	Velvet
124	White	Silk	Noil plain weave
125	White	Silk	Noil jersey
126	White	Silk	Dupion
127	Natural	Silk	
128	White	Silk	Noil canvas
129	White	Linen	Lightweight
130	Natural	Linen / Silk	
131	Grey	Linen	Holland
132	Natural	Linen	
133	White	Linen	Heavy
134	White	Rayon (spun)	
135	White	Cotton	Mousseline
136	White	Cotton	Organdie
137	White	Cotton	Broderie anglaise
138	White	Cotton	Voile
139	Natural	Cotton	Cheesecloth
140	White	Cotton	Batiste
141	White	Cotton	Poplin
142	White	Cotton	Chintz

Fabric reference	**Colour**	**Composition**	**Weave plan/Other technical information**
143	White	Cotton	Sateen
144	White	Cotton	Satin
145	White	Cotton	Twill
146	White	Cotton	Drill
147	White	Cotton	Duck
148	Natural	Cotton	Denim
149	White	Cotton	Bark weave
150	White	Cotton	Moleskin
151	White	Cotton	Jacquard
152	White	Cotton	Velvet
153	Brown	Cotton	Corduroy
154	White	Cotton	piqu
155	Black	Cotton	Marlib knit
156	Natural	Hemp	Fleece
157	Natural	Bamboo/silk	
158	Natural	Hemp and bamboo	Jersey
159	Natural	Bamboo	Jersey
160	Natural	Ramie	
161	Natural	Jute	
162	Natural	Hemp	Muslin
163	Natural	Hemp	Canvas
164	White	Nylon	Netting
165	White	Polyester	Chiffon
166	White	Polyester	Taffetas
167	White	Polyester	Airtex
168	Black	Polyester	Microfibre
169	White	PVC coated poly-cotton	
170	White	PU coated polyester twill	
171	White	Polyester	Polar fleece
172	Black/White dog-tooth	65% Polyester, 35% viscose	Twill weaving

Fabric reference	**Colour**	**Composition**	**Weave plan/Other technical information**
173	Silver	Nylon/aluminium film	Lam
174	White	Polyester/metalic hair	LUREX yarns
175	Black/gold	Rayon/Nylon	Brocade
176	Brown	Polyester	Suedette
177	Black	Poly-viscose	Piece-dyed and yarn-dyed
178	Black piece blue yarns	Poly-viscose	Piece-dyed
179	White	Nylon	Kordura
180	White	Viscose/cotton	Grosgrain
181	White	65% Nylon, 35% Viscose, 5% Elastane	Two way stretch double jersey
182	Black	Polyester/elastane	Jersey
183	White	Viscose	Jersey
184	White	Polyester/Cotton	Plain weave 4.2 oz
185	White	Polyester/Cotton	Plain weave 3.9 oz
186	Navy	Nylon	Cordura
187	Coyote	Nylon	Cordura
188	Grey	Nylon	Cordura
189	Orange	Nylon	Cordura
190	Brown	Nylon	Cordura
191	White	Nylon	Cordura
192	Burgundy	Nylon	Cordura
193	Yellow	Nylon	Cordura
194	Purple	Nylon	Cordura
195	Red	Nylon	Cordura
196	Black	Nylon	Cordura
197	Olive	Nylon	Cordura
198	Forest	Nylon	Cordura
199	Blue	Nylon	Cordura
200	Navy	Nylon	Cordura
201	Grey	Nylon	Kordura

Fabric reference	**Colour**	**Composition**	**Weave plan/Other technical information**
202	Olive	Nylon	Kordura
203	Navy	Nylon	Kordura
204	Black	Nylon	Kordura
205	Emerald	Nylon	Kordura
206	Red	Nylon	Kordura
207	Purple	Nylon	Kordura
208	White	Nylon	Kordura
209	Yellow	Nylon	Kordura
210	Royal	Nylon	Kordura
211	Orange	Nylon	Kordura
212	Wine	Nylon	Kordura
213	Pink	Nylon	Kordura
214	Taupe	Nylon	Kordura
215	Bowen	Nylon	Kordura

Table 7.3: List of cotton samples tested

1	White	Twill
2	Natural	Percale, 300 threads count
3	White	Percale, 300 threads count
4	Natural	Hessian
5	Natural	Seeded
6	White	Cotton and Lycra
7	Natural	Batiste
8	White	Batiste
9	Natural	Silk Noile
10	Natural	Muslin
11	Natural	Voile
12	White	Flannel brushed
13	Natural	Flannel brushed
14	Black	Poplin
15	Natural	Poplin
16	White	Poplin
17	Natural	Basic Calico
18	Natural	Canvas
19	White	Poplin
20	Natural	Cambridge
21	White	Batiste
22	Natural	Batiste
23	Black	Batiste
24	Natural	Bamboo silk stripes
25	Black	Bamboo silk stripes
26	Black	Bamboo drape
27	White	Bamboo drape
28	Natural	Bamboo drape
29	White	Pin-stripe Lappet
30	White	Double-stripe Lappet
31	White	Cross stitch Lappet

Cotton reference	**Colour**	**Type/technical infomation**
32	Natural	Small square bamboo/cotton muslin
33	Natural	Large square bamboo/cotton muslin
34	Black	Bamboo silk
35	Natural	Bamboo silk
36	White	Bamboo silk
37	White	Embroidered stripe
38	White	Embroidered circles
39	Natural	Embroidered circles
40	White	Batiste
41	Natural	Batiste
42	Black	Powerloom medium weight
43	Natural	Powerloom medium weight
44	White	Powerloom medium weight
45	Natural Unfinished canvas	Handloom canvas
46	Black Chunky	Handloom canvas
47	Black medium	Handloom canvas
48	Natural Chunky	Handloom canvas
49	White	Linen
50	Natural	Plump
51	Natural	Pleasant
52	Natural	Loomstate tight
53	Natural	Loomstate loose
54	Naturals, grey prints	Linen
55	Naturals, white prints	Linen
56	Smokey trout	Denim
57	Natural	Denim
58	Old white	Denim
59	White	Denim
60	White with colour stripes	Voile

Cotton reference	**Colour**	**Type/technical infomation**
61	Natural	Cambridge
62	White	Cambridge
63	Grey	Cotton and Lycra
64	White	Cotton and Lycra
65	Gridlock	Suiting wool
66	Fairfield chocolate	Suiting wool
67	Bradford Bistre	Suiting wool
68	Liberty Blue	Suiting wool
69	Chroma	Suiting wool
70	Azure	Suiting wool
71	Red	Denim
72	Incardine	Denim
73	Brinjal	Denim
74	Brassica	Denim
75	Black	Denim
76	St Miles Blue	Denim
77	Smokey trout	Denim
78	Garden Room Green	Denim
79	Natural	Denim
80	Old white	Denim
81	White	Denim
82	Chalk green	Denim
83	Brinjal	Denim brushed
84	Red	Denim brushed
85	Key blue	Denim brushed
86	Black	Denim brushed
87	Soft blue	Denim
88	Natural	Denim
89	Dark blue	Denim with Lycra
90	Purple	Corduroy
91	Interesting green	Crossweave

Cotton reference	**Colour**	**Type/technical infomation**
92	Chirpy green	Crossweave
93	Grey Marl	Crossweave
94	Stone	Crossweave
95	Multi Marl	Crossweave
96	Raised stripe Black	Crossweave
97	Light blue	Crossweave
98	Dark blue	Crossweave
99	Night red	Crossweave
100	Rich red	Crossweave
101	Aqua	Crossweave
102	Fire orange	Crossweave
103	Dark brown	Crossweave
104	Richer Blue soft	Crossweave
105	Richer Red soft	Crossweave
106	Natural	Cambridge
107	Brick	Cambridge
108	New Yellow	Cambridge
109	Red	Cambridge
110	Teal	Cambridge
111	Khaki	Cambridge
112	Green	Cambridge
113	Blue	Linen
114	Coral	Linen
115	Purple	Linen
116	Black	Linen
117	Red	Linen

Table 7.4: List of bags tested

Sample	**Colour**	**Fabric description**
"LED conference" bag	Black	Woven fibres coated with thermoplastic
"RPW conference" bag	Black	Woven fibres coated with thermoplastic
Bag 3	Dark blue	Woven fibres coated with thermoplastic
Bag 4	Blue	Woven fibres coated with thermoplastic
Bag 5	Black	Woven fibres coated with thermoplastic
Bag 6	Black	Woven fibres coated with thermoplastic
Bag 7	Blue	Woven fibres coated with thermoplastic
Bag 8	Black	Woven fibres coated with thermoplastic
Bag 9	Black	Woven fibres coated with thermoplastic
Bag 10	Black	Woven fibres coated with thermoplastic
Bag 11	Grey/brown	Woven fibres coated with thermoplastic
Bag 12	Grey	Woven fibres coated with thermoplastic
Bag 13	Blue	Woven fibres coated with thermoplastic
Bag 14	Black	Woven fibres coated with thermoplastic
Bag 15	Blue	Woven fibres coated with thermoplastic
Bag 16	Red	Faux leather thermoplastic
Bag 17	Green	Faux leather thermoplastic
Bag 18	Brown	Woven fibres, faux leather thermoplastic
Bag 19	White	Faux leather thermoplastic
Bag 20	Glossy pink	Thermoplastic
Bag 21	Black	Woven fibres coated with thermoplastic

7.4 Results

A sample was judged to have suitable dose response characteristics for further investigation when no significant native signal was observed, the detection limit (calculated as the dose for which the signal was equal to the background plus three times the standard deviation of the background, see Chapter 3) was below 0.5 Gy, and the response was uniform for different samples of the same material.

7.4.1 Miscellaneous materials

Paper

Paper, and especially coated paper (glossy paper, matt paper), showed a TL response to β dose (Fig. 7.1), similar to that of calcium carbonate (see Chapter 10). However, a strong native TL signal compared with the β induced signal was also observed above 100 °C, which would make paper unsuitable for emergency dosimetry using TL. Photocopier paper (uncoated) was not found to exhibit a response to dose.

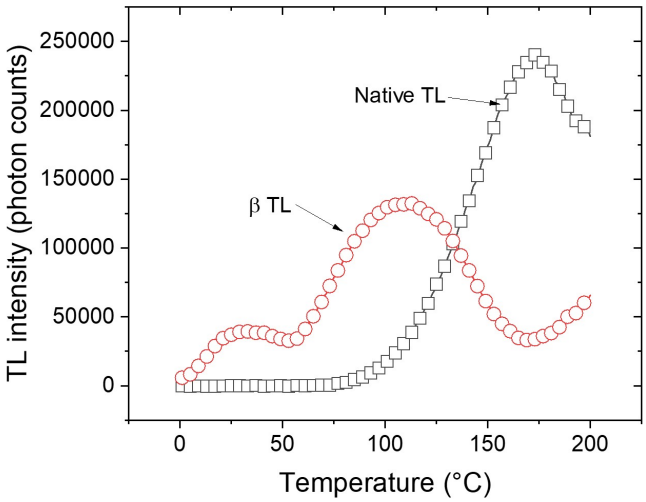

Fig. 7.1. Native (black squares) and 10 Gy β induced TL response (red circles) of glossy paper. Detection window : silica window; heating rate : 0.5 °C.s^{-1}.

Further test of the OSL and IRSL response of coated paper indicated the presence of a complex luminescence process. The OSL response of white paper was dominated by an increasing signal

with illumination time, presumed to be associated with a photo-luminescence process. No OSL dependence on dose below 10 Gy was observed. The IRSL response of white coated paper was also complex, where the IRSL signal increased with illumination time (Fig. 7.2). Following β irradiation, a peak at $\sim$ 20 s of illumination was observed, the intensity of which increased with dose. Due to the slow nature of the process, the IRSL detected include a photo-luminescence emission and an isothermal luminescence, induced by holding the samples at 50 °C during the measurement.

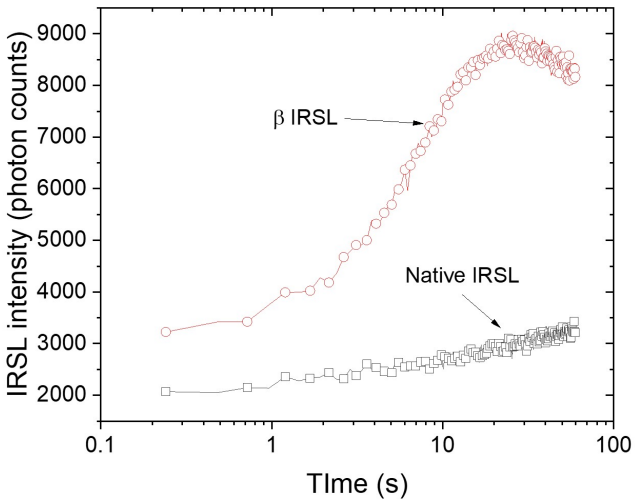

Fig. 7.2. Native IRSL (open black squares) and 10 Gy β induced IRSL response (open red circles) of glossy paper. Detection window : BG-39; sample temperature : 50 °C.

Glass beads

Glass beads exhibited a TL response to β dose, varying according to colour (Fig. 7.3a and 7.3b. A native signal with a TL peak centred at 200 °C was observed, whose strength was also variable. A weak OSL response was observed with some glass beads, but with a detection limit of $\sim$ 5 Gy. A response to dose was observed under infra-red stimulation, but the shape of the signal indicated that it was likely an isothermal decay process, induced by holding the samples at 50 °C during measurement.

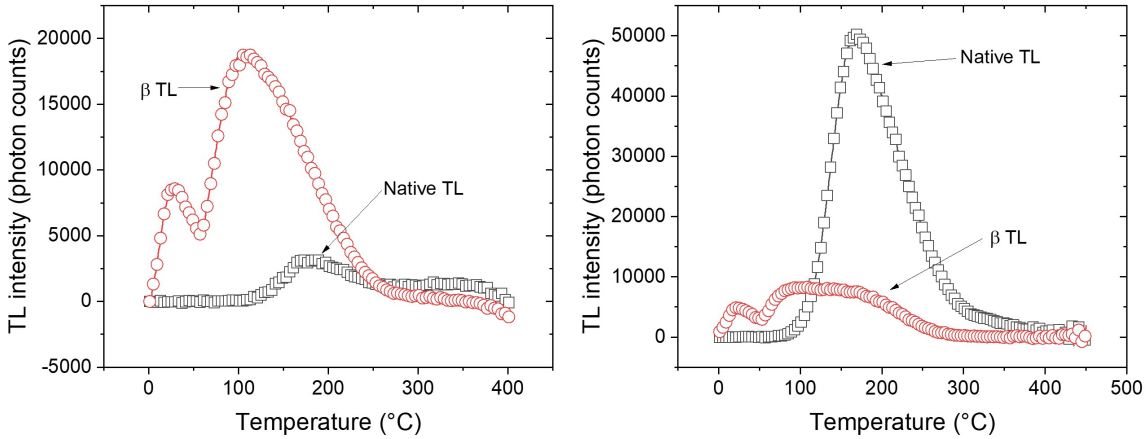

Fig. 7.3. Native (black circles) and 10 Gy β induced TL (red circles) of a) glass bead 4 (pink bead) and b) glass bead 8 (white bead). Detection window : silica window; heating rate : 0.5 °C.s^{-1}.

Shoe soles

The samples of shoe sole (thermoplastic/rubber) tested exhibited a TL response to β dose (Fig. 7.4a). The β induced TL glow curve similar in shape to calcium carbonate (see Chapter 10). A strong native signal was however present above 100 °C. An OSL response to β dose was also observed but the native OSL signal was also strong (Fig. 7.4b). No IRSL response to β dose was observed for the samples tested.

Polystyrene

An OSL response to β dose was observed for samples of polystyrene (packaging polystyrene and polystyrene exctracted from cycling helmet). However, the response was found to be very variable even from sample from the same cycling helmet or packaging polystyrene. The OSL emission might be thus associated to the presence of impurities in the samples. In most cases, the detection limit was of 5 Gy. Other types of polystyrene items (cup, CD case), did not yield a measurable response to dose.

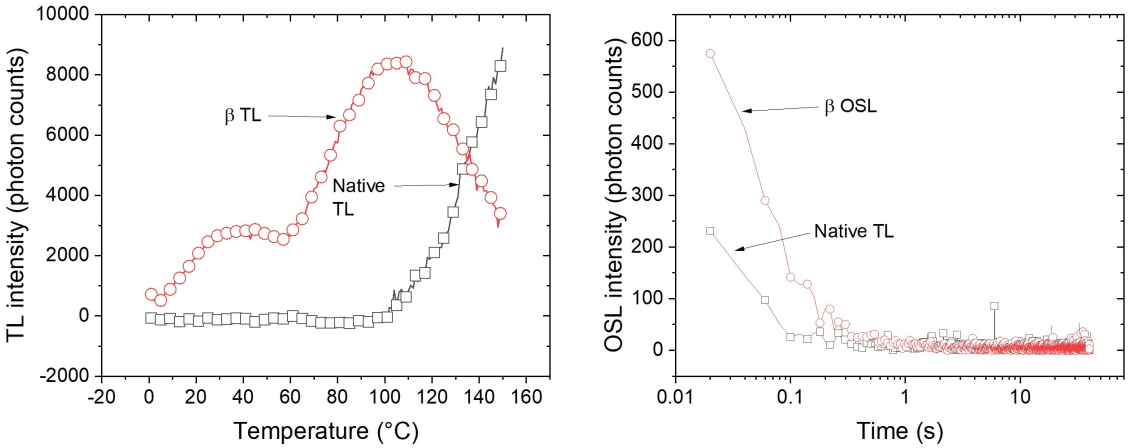

(a) **(b)**

Fig. 7.4. a) Native (black circles) and 10 Gy β induced TL (red circles) of shoe sole 2. Detection window : silica window; heating rate : 0.5 °C.s^{-1}. b) Native (black circles) and 10 Gy β induced OSL (red circles) of shoe sole 2. Detection window : U340; sample temperature : 50 °C.

Other samples

Dyeing salt (NaCl) is used in the dyeing process of fabrics to drive the dye onto the fibre. Its OSL/TL response was similar to the response of household salt, that has been documented elsewhere (Christiansson et al., 2014). Moreover, fabrics were thoroughly rinsed after washing, so it is unlikely that residual salt would remain after the dyeing process. In a similar manner, washing powder showed an OSL response following β irradiation, but for a measurement cup filled with washing powder. Such a concentration of washing powder is unlikely to be found on clothes.

The other samples listed in Table 7.1 did not exhibit a detectable response to OSL, IRSL or TL.

7.4.2 Fabrics and bags

The OSL response of some of the fabric tested (e.g. fabrics 62, 73, 87-91, 111, Tables 7.2 and 7.3) was characterised by a increasing photon count with illumination time and independent of dose (Fig. 7.5b) which was interpreted as a photo-luminescence mechanism. The samples that exhibited this form of response were generally white and had been bleached by the manufacturer. Due to the high number of counts related to the photo-luminescence process, a β induced decay curve could not be observed for these samples. OSL decay curves were however observed for some fabric samples (e.g., fabric 75, 130, 139, Fig. 7.5a), but in the majority of cases, the OSL dose response was weak (detection limit above 5 Gy), and not reproducible between samples of the same fabric.

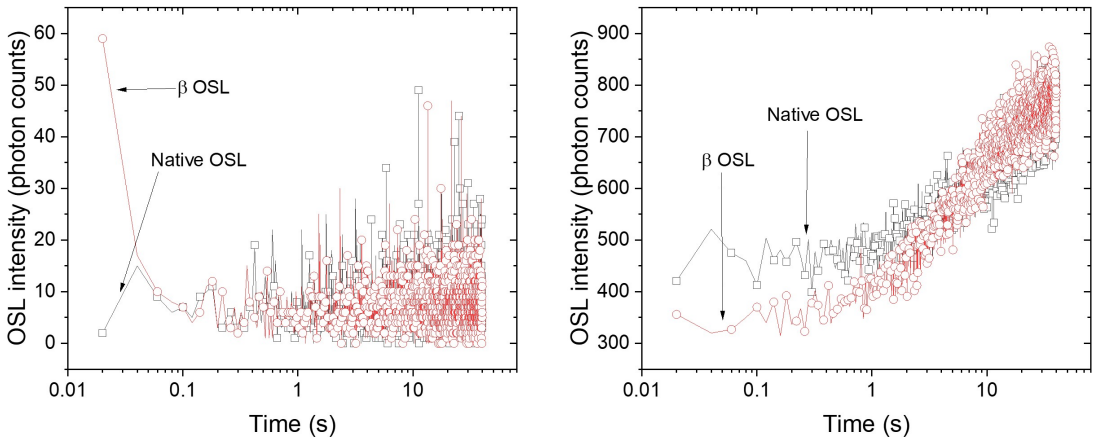

Fig. 7.5. a) Native (black circles) and 10 Gy β induced OSL response (red circles) of F# 75 (white silk seersucker with elastane). b) Native (black circles) and 10 Gy β induced OSL (red circles) of F# 90 (white sateen polyester). Detection window : U 340; sample temperature : 50 °C.

The samples showed similar behaviour under infra-red stimulation. A weak response to dose was observed on some samples when the measurements were conducted in air. However, this was significantly stronger when the measurements were performed in vacuum (Fig. 7.6).

Generally, a weak TL response to β dose was observed for fabric samples tested, although the native signal was dominant (Fig. 7.7).

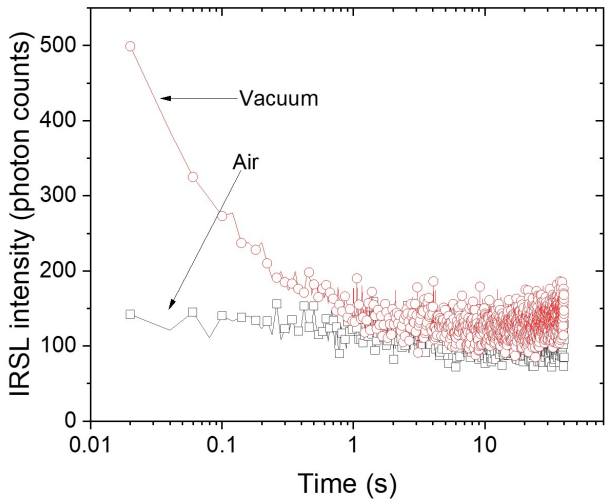

Fig. 7.6. 10 Gy β induced IRSL measured in air (open black squares) and vacuum (red circles) of F# 13 (blue fleece, 80 % cotton, 20 % polyester). Detection window : BG-39; sample temperature : 50 °C.

However, three exceptions were found :

- Fabric 3 (blue polyester), that exhibited a strong IRSL decay curve in response to β dose, when the irradiation and measurement were carried out in air (Chapter 8). No native signal was observed.

- "Lynton" fabrics (fabrics 29, 40, 43, 44, 45 and 46) that all exhibited an OSL response to dose, similar between samples of the series and no native signal present(Chapter 9).

- The fabrics of bags (handbags, backpacks and conference bags) tested; the fibres of the bags are often coated with a thermoplastic to make them waterproof, or they are sometimes directly made of a plastic fabric (e.g., faux leather). This coating was found to have a relatively strong TL response to β dose (Chapter 10 and 12).

7.5 Discussion

This chapter provided a list of all the materials that have been tested for their luminescence response to ionising radiation. Most of these materials did not exhibit a suitable response for use

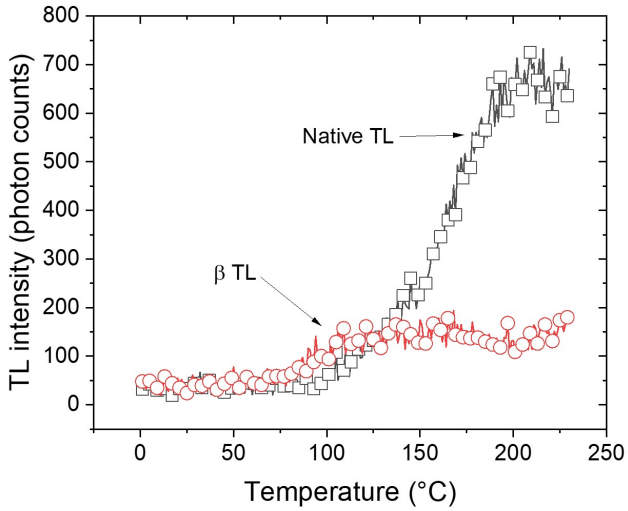

Fig. 7.7. Native TL (open black squares) and 10 Gy β induced TL (open red circles) of F# 14 (dark grey polyester). Detection window : silica window; heating rate : 0.5 °C.s^{-1}.

in emergency dosimetry, and for these further testing was not performed. Although glass beads showed an interesting TL response to dose, they are rarely used nowadays in jewellery and thus less likely to be worn by members of the public. The IRSL response of fabrics in vacuum was also of significant interest, but this result is not applicable to an radiological emergency scenario. Compared with the results obtained by Sholom and McKeever (2014), these tests confirmed the potential of fabrics for emergency dosimetry, although OSL was not always found to be the method yielding the best signal. Thus, the materials that showed the most promising response were fabric 3 (IRSL response, Chapter 8), the Lynton series of fire retardant upholstery fabric (OSL response, Chapter 9) and the thermoplastic composing the coating or fabric of bags containing calcium carbonate fillers (TL response, Chapters 10 and 12). Additional testing was carried out on these promising materials, including fading tests, attempts to identify the centres of luminescence, and assess their applicability for emergency dosimetry.

Chapter 8

Case study 1: the IRSL response of a blue polyester fabric (F# 3)

8.1 Introduction

Amongst the set of fabrics tested (Chapter 7), a blue polyester mix fabric (F# 3) from a discarded shirt presented a bright response under infra-red (IR) stimulation, following the administration of a β dose. This chapter focuses on the IRSL and TL characteristic of this fabric (dose response and fading), and the effect of exposure to air on the luminescence emission is also examined.

Polyester fibres, also known as polyethylene terephthalate (PET) are the most widely used fibres in the world (Mark et al., 1987) due to their high performance and low cost. Thus, finding a type of polyester fabric responding to ionising radiation was of interest for the development of dosimetry techniques.

8.2 Samples and protocol

The sample investigated in this chapter was a blue polyester fabric from a discarded shirt, referred to in this chapter as F# 3. A label on the fabric indicated that it was composed of 65% polyester and 35% cotton. A swatch of the fabric is provided in Appendix A. No other information regarding the manufacturing process was available. Fig. 8.1 shows a macroscopic picture of F# 3. For measurements, the samples were cut into squares fitting into stainless steel cups ($\sim 5\times5$ mm^2) used

for measurements in the Risø reader.

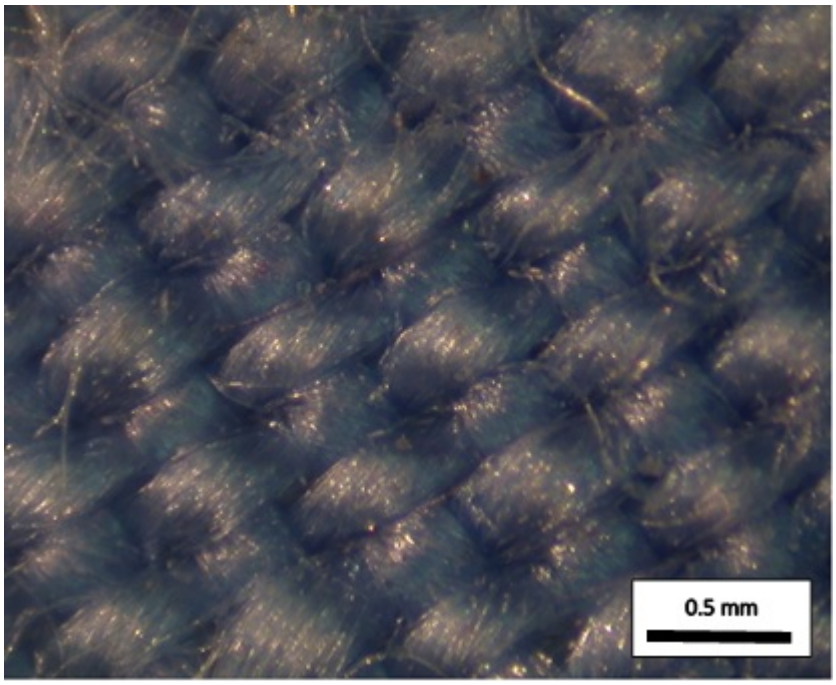

Fig. 8.1. Macroscopic picture of polyester-mix fabric F# 3

All OSL, IRSL and TL measurements were performed with a standard configuration of the Risø reader (see chapter 6 for details of the instrumentation). Since the primary calibration of the β source dose rate was performed to quartz grains, radiation transport simulations were performed to obtain a conversion factor from quartz to polymer, and the estimated dose rate to fabric samples was calculated to be (0.44 ± 0.02) Gy min^{-1} (2016). A UV (250-350 nm; Schott U-340 filter) detection window was inserted when measuring blue stimulated OSL (470 nm) and a broad-band detection window (350-700 nm; Schott BG39 filter) when measuring IRSL (850 nm). Unless stated otherwise, none of the samples were preheated and IRSL/OSL measurements were performed with the sample maintained at a temperature of 50 °C. TL measurements were performed using a heating rate of 0.5 °C.s^{-1} to a maximum temperature of 230 °C, which lies below the theoretical ignition temperature of most fabrics, and with a fused silica window inserted in the detection system. The tests (dose response, fading) were repeated on several samples obtained from various locations on the overall shirt (front, back, pockets) to test for uniformity in response. A Hitachi SU-70 scanning electron microscope (SEM) with a beam energy of 10 kV and a current of 10 mA was used to analyse the morphology of the fabric samples and spatially- and spectrally-resolved cathodoluminescence (CL)

spectra were measured using a MonoCL3 spectrometer (Gatan Ltd, Oxford) incorporating a Hamamatsu R374 PMT detector operated in single photon counting mode. The spectra recorded were corrected for instrument response within the SEM analytical software. Additional measurements were conducted in an environmental SEM (FEI ESEM XL30, CIEMAT) equipped with a Energy Dispersive Spectrometry probe (EDS) and a Gatan MonoCL3 probe using a PA-3 PMT. For these measurements, a low vacuum mode was used and the beam voltage was set at 20 kV. Details of the instrumentation are given in Section 6.3.

The X-ray diffraction pattern was obtained using a Bruker AXS D8 Advance equipped with a Lynxeye Soller PSD Detector. The source of X-ray was a copper tube producing a mixture of Cu-$K_{\alpha 1}$ and Cu-$K_{\alpha 2}$ at a wavelength of 1.5406 Å.

8.3 Material characterisation

8.3.1 Scanning electron microscope

Fig. 8.2a shows an image of F# 3 taken in an environmental scanning electron microscope (ESEM) that illustrates the structure of the fabric, composed of fibres woven in threads, themselves weaved in a plain weave pattern. Some impurities can also be observed in Fig. 8.2a, which may be grains of dust. A procedure consisting of encapsulating a piece of F# 3 in resin and polishing the surface with diamond powder enabled the observation of the cross section of this fabric (Fig. 8.2b). Using this procedure, the width of the fibres was evaluated to be of 30-40 μm of diameter. Fig. 8.2b also shows the different shape of the fibres; whilst some appear to be round in cross section, others are deformed into oval shape.

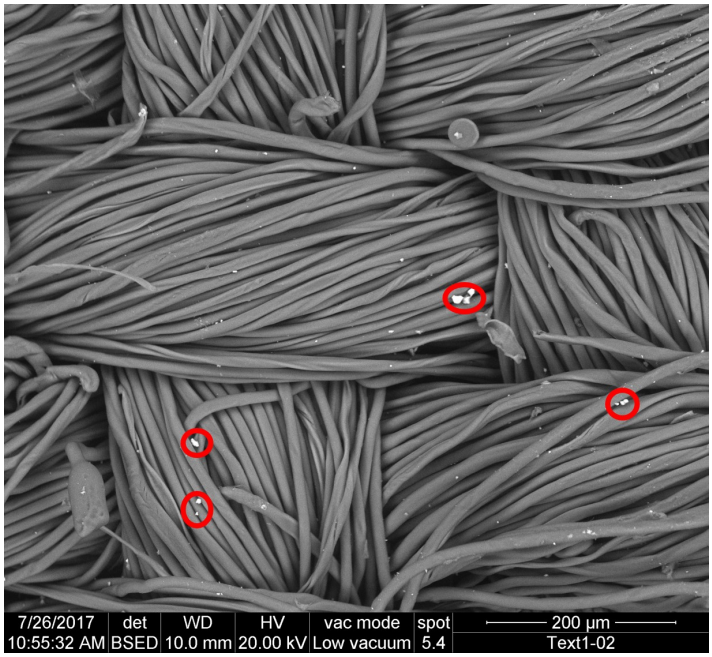

(a)

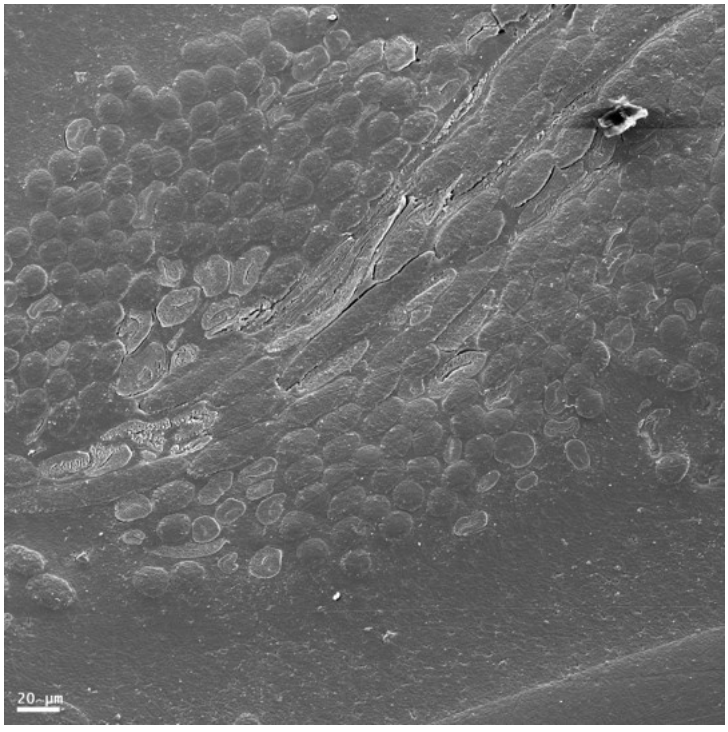

(b)

Fig. 8.2. a) Environmental SEM image of F# 3. Impurities are circled in red. Beam voltage : 20 kV; vacuum condition : low vacuum. b) SEM image of the cross section of F# 3 encapsulated in resin where the round cross-section of the fibres can be observed. Beam voltage : 10 kV.

8.3.2 Cathodoluminescence imaging and spectroscopy

The cathodoluminescence (CL) imaging of the cross section of F# 3 encapsulated in resin revealed that while some fibres were very bright, others were dim in comparison (Fig. 8.3). The majority of the fibres appeared to be bright, and the fibres emitting luminescence were the ones corresponding to the non-deformed fibres (Fig. 8.3). The CL spectrum of F# 3 revealed a complex spectrum with two main peaks closely overlapping at 450 nm (Fig. 8.4a) and with weak emission bands in the blue and UV regions. The CL spectrum on an energy scale was deconvolved using 9 Gaussian functions (Fig. 8.4b) indicating the presence of emission bands, at 1.44, 1.61, 1.77, 2.30, 2.69, 2.81, 2.93, 3.17 and 3.83 eV, several of which would potentially contribute to the TL/IRSL emission of the sample.

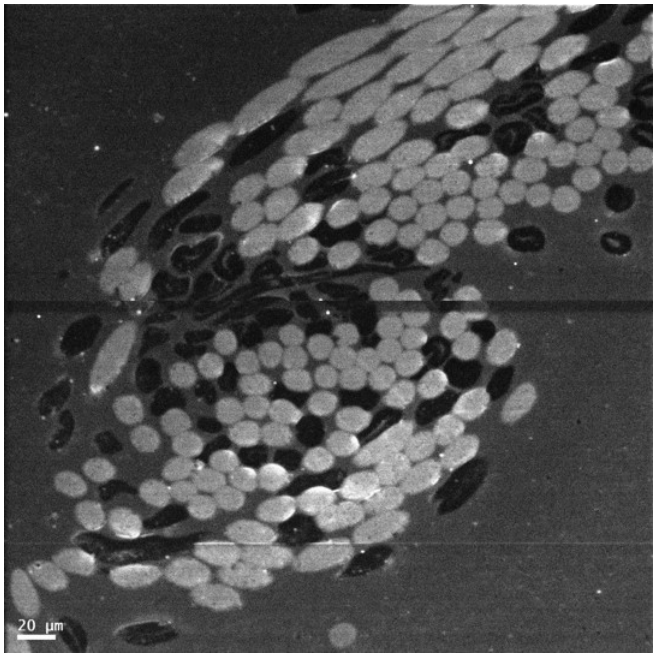

Fig. 8.3. CL image of the cross section of F# 3 encapsulated in resin. Beam voltage : 10 kV.

8.3.3 Elemental characterisation : X-ray fluorescence and X-ray diffraction measurements

Spatially resolved X-ray fluorescence (XRF) measurements were carried out in an environmental SEM. The XRF spectrum was measured at different locations of the fabric. Fig. 8.5 shows two locations at which the spectra were measured, one on a fibre (position 1) and the other on one of the impurity found on the fibre (position 2). Whilst the XRF spectrum of the fibres seemed

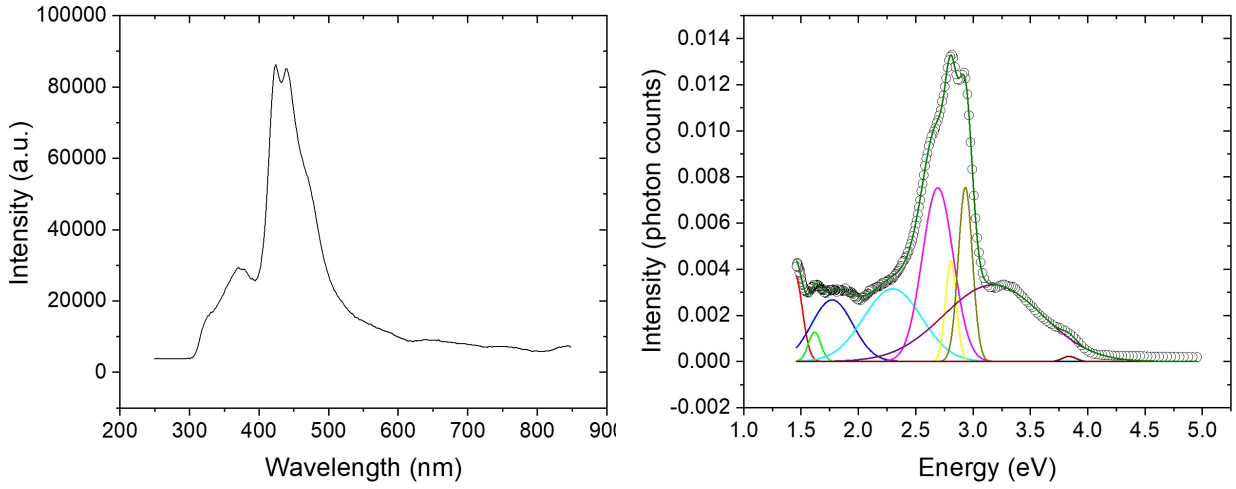

Fig. 8.4. CL spectrum of F# 3, a) wavelength scale and b) energy scale. In Fig. b the continuous lines represent Gaussian functions fitted to the experimental data points (open circles) and the spectrum intensity has been corrected for the energy scale. Energy beam : 20 kV. The spectra were corrected for instrument response.

to indicate the presence of oxygen and carbon only (Fig. 8.5), as expected for polyester, calcium and magnesium were also included in the impurities. The XRD pattern of F# 3 (Fig. 8.6 upper graph, see Chapter 6 for instrumentation details) contains narrow reflection peaks, indicating a high level of crystallinity in the sample, although the broad peaks at low angle ($\leq$ 30 °) suggest a polymer component. The XRD pattern identified calcite in the sample (Fig. 8.6 lower graph), which correlates with the presence of calcium and magnesium detected using XRF.

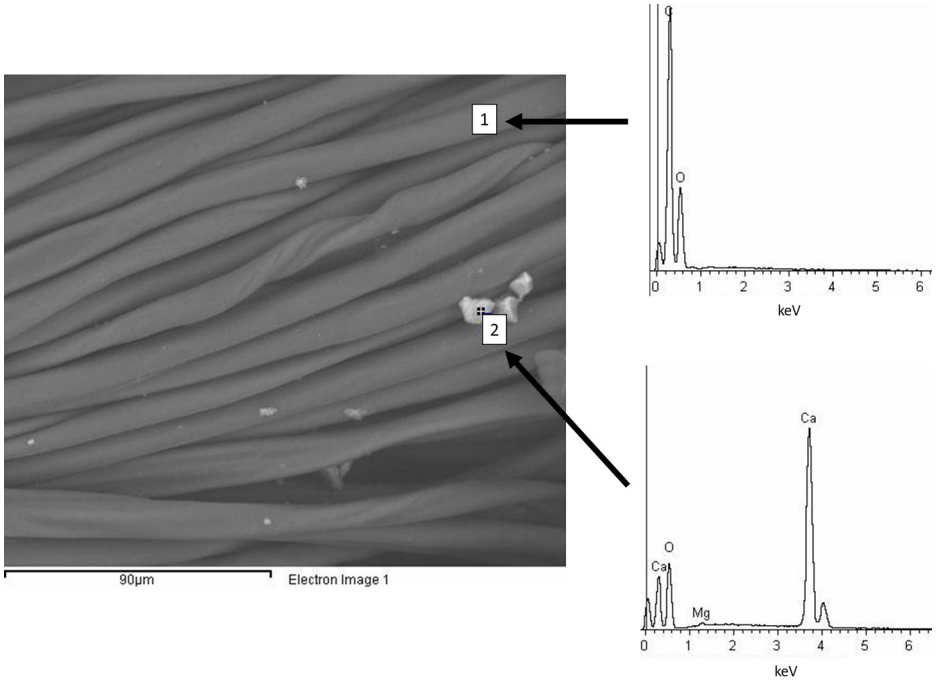

Fig. 8.5. SEM backscattered electron image of F# 3 indicating two spots at which the XRF spectrum was measured.

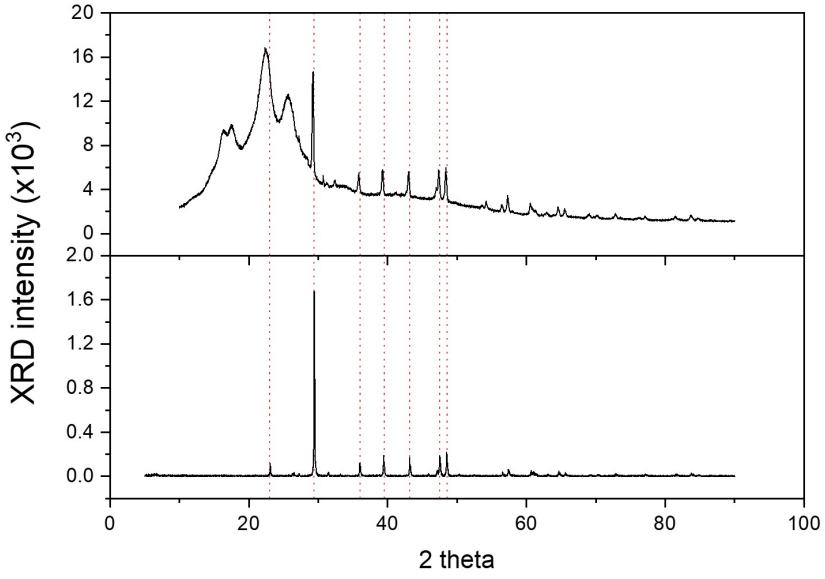

Fig. 8.6. X-ray diffraction pattern of F# 3 (top graph) and of calcite (lower graph). The dotted lines indicate the characteristic lines of calcite.

8.4 Photoluminescence

The photoluminescence (PL) behaviour of F# 3 was measured using a fluorescence spectrometer (Fluorolog) composed of a xenon lamp, an excitation monochromator, a sample compartment, an emission monochromator and a R928P photomultiplier tube to collect light. The spectrum was measured for stimulation wavelengths in the range 280-900 nm, and the resulting PL spectrum recorded. For stimulation wavelengths between 280 nm and 420 nm, an emission peak centred around 445 nm was observed (Fig. 8.7a). The intensity of that peak reached a maximum for a stimulation wavelength of 390 nm (Fig. 8.7b). Two other peaks were observed for stimulation wavelengths 430-560 nm, centred at $\sim$ 600 nm and 665 nm (Fig. 8.8a). The maximum intensity of these peaks were reached for a stimulation wavelength of 510 nm (Fig. 8.8b), and they were $\sim$100 times weaker in intensity compared with the 445 nm peak induced by light in the range 280-420 nm. No PL emission was observed for stimulation wavelength above 600 nm.

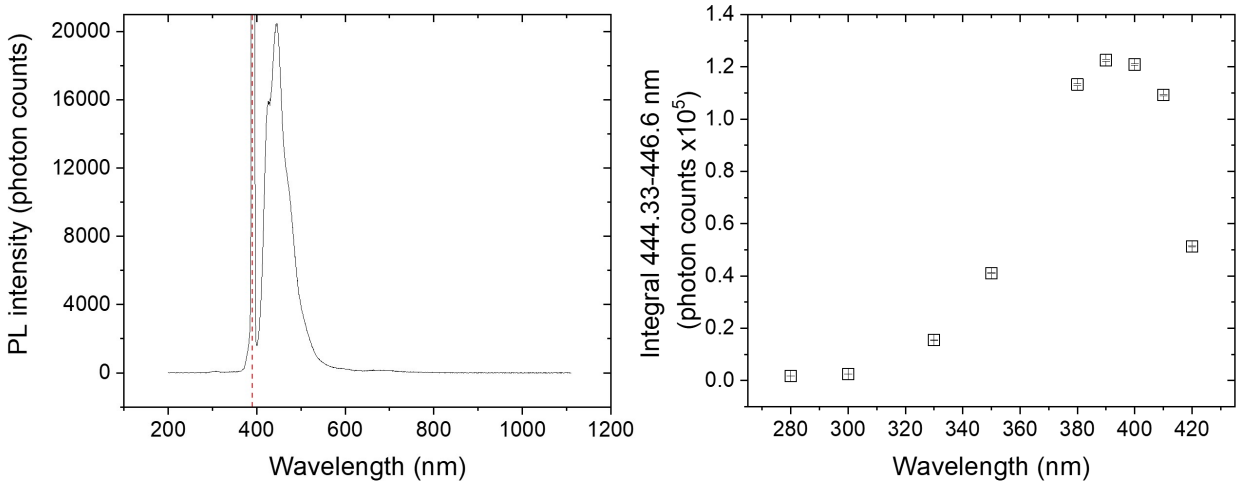

(a) **(b)**

Fig. 8.7. a) Photoluminescence spectrum of F# 3, stimulation wavelength 390 nm. The dotted vertical red line indicates the stimulation wavelength. b) Integral of the spectrum in the region 444-447 nm for stimulation wavelengths in the range 280-420 nm.

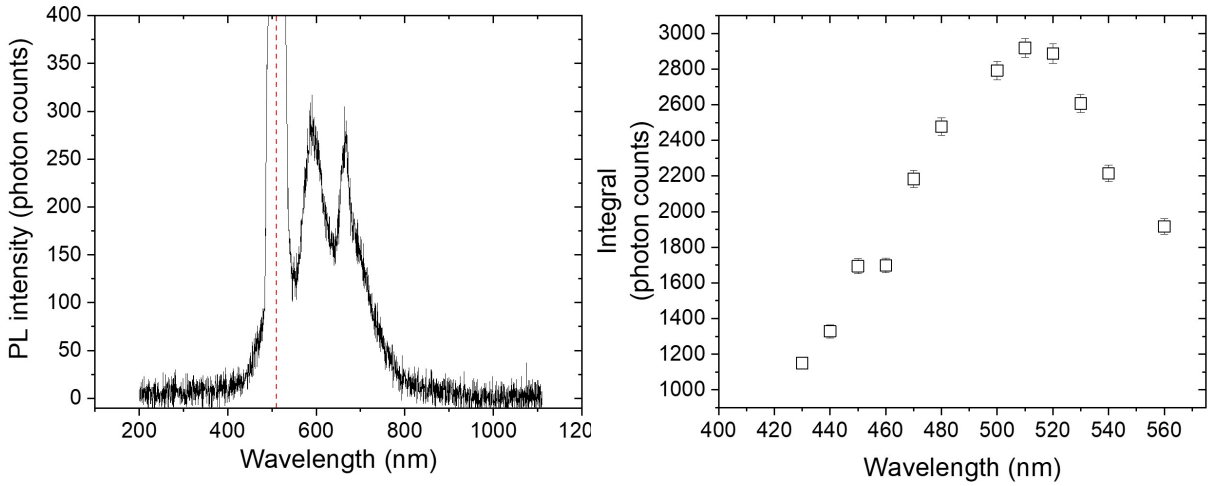

Fig. 8.8. a) Photoluminescence spectrum of F# 3, stimulation wavelength 510 nm. The dotted vertical red line indicates the excitation wavelength. b) Integral of the spectrum in the region 598-603 nm for stimulation wavelengths in the range 430-560 nm.

8.5 TL response

8.5.1 Dose response

The TL response of F# 3 was measured to T_{max}=230 °C at a heating rate of 0.5 °C.s^{-1} and the photons emitted during the TL measurements were detected through a silica window. A strong native signal taking the form of a peak centred at 180 °C was observed (Fig. 8.9a). A β induced TL was also observed, with two broad TL peaks centred at 30 and 100 °C. The β induced TL signal was reproducible. Although the TL response in the region 50-150 °C was linear with β dose in the range 0.5-5 Gy, this signal is not likely to be usable for short term dosimetry due to the strength of the native signal. The native TL peak at 180 °C was not significantly bleached by exposure to light (sun, blue or IR) and was found to have regenerated after storage for several weeks at RT in the dark. Similar results were obtained using a BG-39 detection filter.

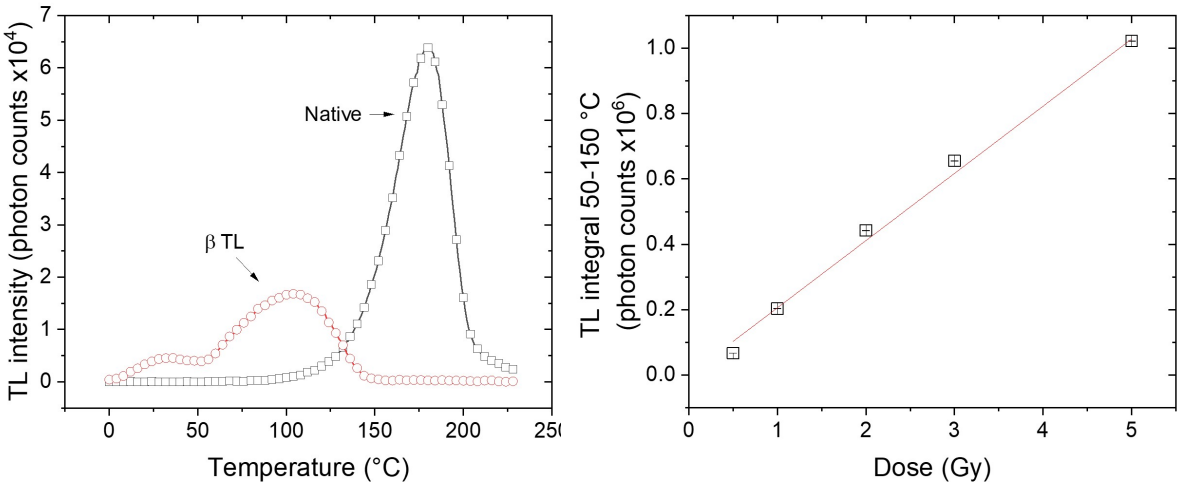

Fig. 8.9. a) Native TL of F# 3 (open black squares) and TL following β irradiation (5 Gy) of F# 3 (open red circles). The background was subtracted from the TL curves. b) Integral of the TL glow curve in the region 50-150 °C as a function of β dose (0.5-5 Gy). The red line indicates a linear function fitted to the data.

8.5.2 Fading

The fading of the TL signal of F# 3 was tested by heating the sample to 230 °C (erasing the native signal), irradiating the samples with a β dose (1 Gy) and storing them in the dark at ambient temperature until TL measurement (T_{max} = 230 °C). The β induced TL signal of F# 3 was found to quickly fade at room temperature in the dark; after a 2 hours storage, only 18% of the signal remained in the region of the glow curve 55-200 °C (Fig. 8.10). The signal appeared to decay in an exponential manner (Fig. 8.10), such as

$$y(t) = y_0 + A_1 \exp(-t/\tau_1), \tag{8.1}$$

where $y_0 = 0.15 \pm 0.02$ (dimensionless), $A_1 = 0.84 \pm 0.05$ (dimensionless) and $\tau_1 = (37 \pm 4)$ min.

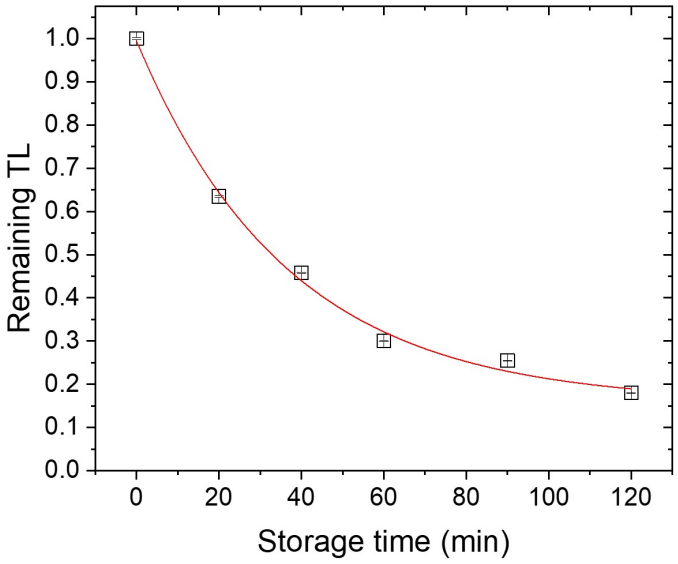

Fig. 8.10. Fading of the TL signal in the region 55-200 °C of the glow curve of F# 3 in the dark at ambient temperature following β irradiation. The red line indicates a exponential function fitted to the data.

8.6 OSL response

F# 3 exhibited a native signal under blue (470 nm) stimulation (OSL). The native OSL signal measured on an unirradiated sample showed a high native signal at the start of the illumination ($\sim$ 1400 counts per 0.02 s) that increased with illumination time (Fig. 8.11). Repeat of the measurement on a unirradiated sample exhibited a lower level of count at the start of the illumination ($\sim$ 1000 counts per 0.02 s), but quickly increased to reach the same level of counts as the native signal ($\sim$ 1800 counts /0.02 s). No difference was observed between the signal of an unirradiated sample and a β irradiated sample (Fig. 8.11). The source for this luminescence emission is more likely to be associated with a photoluminescence phenomenon (fluorescence or phosphorescence) although, as indicated in Fig. 8.8, an optical stimulation of 470 nm produces a photo-stimulated signal composed of two bans at 600 and 665 nm, outside the range of the UV filter (U-340) used for light detection during the OSL measurement.

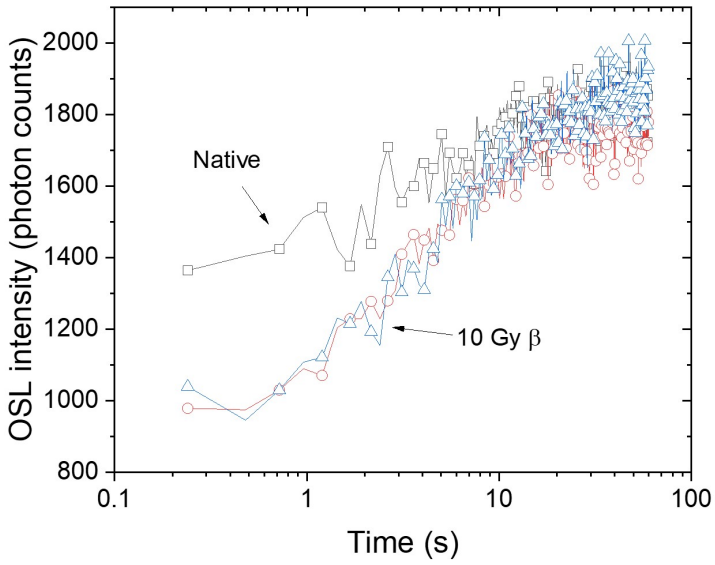

Fig. 8.11. Native OSL (stimulation 470 nm) of a sample of F# 3 (open black squares), of an unirradiated sample (open red circles) and of a β irradiated sample (10 Gy, blue open triangles). Each data point represent the integrated photon counts per 0.02 s. Detection windows : U-340.

8.7 IRSL response

8.7.1 Dose response

In contrast to the OSL measurements sample F# 3 exhibited a high sensitivity to β radiation and no native signal under infra-red stimulation (850 nm; Fig. 8.12a). The β-induced decay curve showed a fast decay that reached background level within 2-3 seconds of illumination (Fig. 8.12a). The dose response characteristic (Fig. 8.12b; corrected for fading and sensitization) is linear within the range of dose of interest for emergency dosimetry (0.75 -15 Gy). The detection limit was evaluated to be of (20±1) mGy (see Chapter 3 for details on calculations of the detection limit).

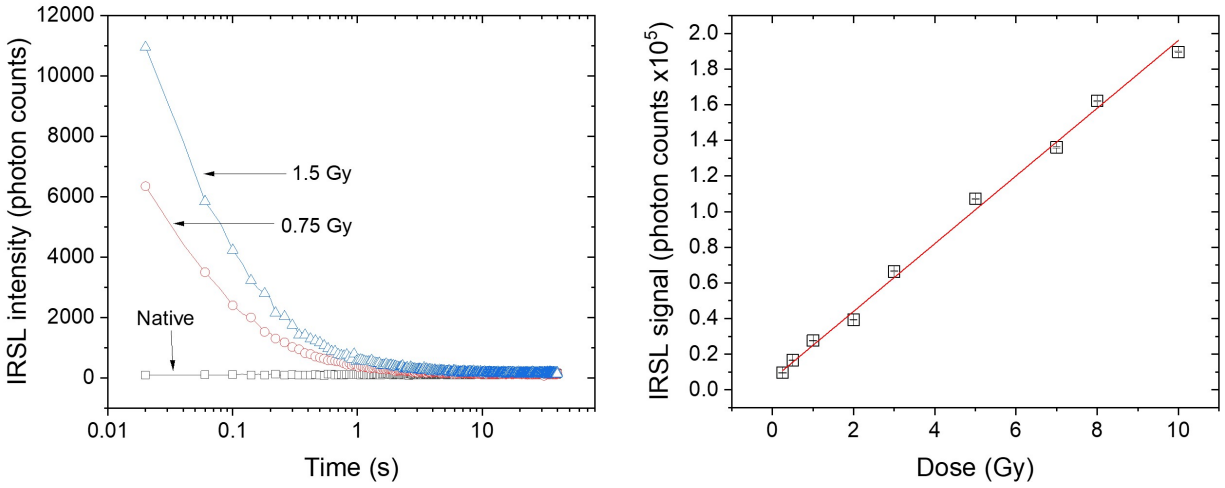

(a) **(b)**

Fig. 8.12. a) IRSL decay curves measured with a sample of blue polyester-mix fabric (F# 3) showing the initial (native) response (open black squares) and those measured following each of a sequence of β doses (0.75, open red circles; 1.5 Gy, open blue triangle). Detection window: BG-39. b) Dose response characteristic obtained with the blue polyester-mix fabric (F# 3). The IRSL intensity corresponds to photon counts recorded during the initial 5 channels (20 ms per channel) less a "late" background obtained using the average count from the final 5 signal channels recorded in the decay curve measurement, scaled to the initial time interval. The measured signals were corrected for sensitization and fading effects. The statistical uncertainty in the signal values is less than ±2%. Detection window: BG-39.

8.7.2 Sensitisation effects

Sensitisation effects were tested by repeating cycles of β irradiation (1 Gy) and IRSL measurement. To test for effects of the atmospheric conditions, the measurements were either carried out in air or in a nitrogen atmosphere. The IRSL signal of F# 3 was found to sensitise over repeated cycles of irradiation and IRSL measurements (Fig. 8.13). The signal increased linearly over repeated measurements, and the sensitisation was stronger when the measurements were carried out in nitrogen compared with air ($\sim$ 250 % increase after 4 cycles of irradiation and measurement in nitrogen versus 20 % in air). The presence of oxygen appears to have a significant effect on luminescence behaviour, and in these tests the introduction of nitrogen into the measurement chamber may suppress a quenching effect of mobile oxygen ions (Charlesby et al., 1963).

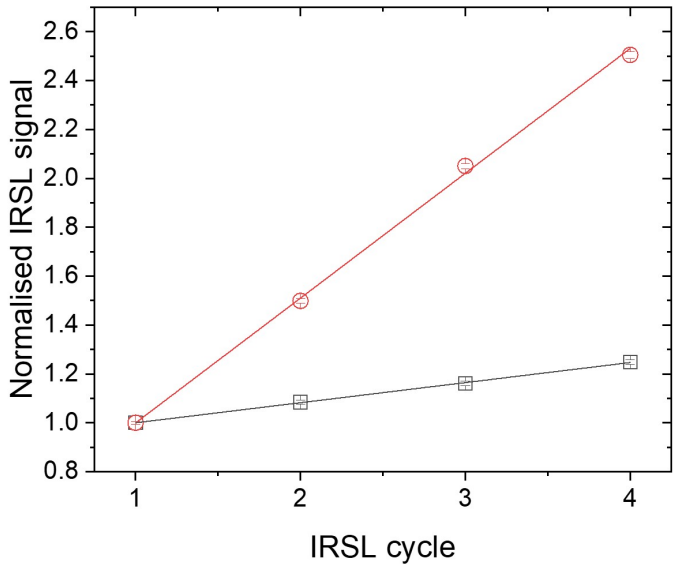

Fig. 8.13. IRSL sensitisation of F# 3 measured in atmospheric condition (black open square) and nitrogen (open red circles). The signal was normalised to the signal of the first IRSL measurement of the cycle. The lines indicate linear functions fitted to the data points.

8.7.3 Fading

Fading test procedures with four different forms of pre-treatment and measurement conditions were applied (Table 8.1). All included the administration of a dose of 6.8 Gy, storage in the dark at

ambient temperatures for periods of between 5 and 150 mins and measurement of IRSL at a sample temperature (70 °C) below the glass transition temperature of the polymer ($T_g \sim$ 80°C). The key differences in procedure were:

Procedure 1. Untreated. Storage in air and IRSL measurement in air.

Procedure 2. Pre-treated: initially preheated to 230 °C in a nitrogen atmosphere for 60s and cooled to room temperature RT. Storage in air and IRSL measurement in air.

Procedure 3. Pre-treated: "oxygen depleted" following a procedure applied by Charlesby et al. (1963), where the material was subjected a combination of radiation dose (6.8 Gy) and subsequent heating to 230 °C to deplete the population of available oxygen molecules in the fibres. Storage in air and IRSL measurement in air.

Procedure 4. Pre-treated: "oxygen depleted", as above. Storage in nitrogen atmosphere; IRSL measurement in a nitrogen atmosphere.

The fading curves obtained are shown in Fig. 8.14. The rate of fading with procedure 1, aiming to be loosely similar to an emergency scenario, is the fastest with a 98% loss of the signal within 2.5 hours; procedure 2 resulted in comparable behaviour. The application of the third and fourth procedures gave rise to a significant reduction in the fading observed. In procedure 3, where there was the opportunity for oxygen to diffuse back into the polyester filaments of the fabric, the fading was reduced, but not as effectively as in the case of procedure 4 where flushing of the measurement chamber with nitrogen was maintained throughout the storage period, giving rise to only a 20% loss in 2.5 hours. Analysis of the fading curves obtained using procedures 1 and 2 indicates that a good fit to the experimental data can be obtained with a double exponential function comprising fast (∼3.6 mins) and slow (∼28 mins) component lifetimes, and this may reflect a combination of charge (electron) transfer and slower ionic movements within the polymer structure. The timescale over which these fading measurements were performed (procedures 3 and 4) is not sufficient to fully characterise the fading behaviour at large storage times, but within the first 2.5 h, a single function, of either exponential or Bequerel decay form, could be satisfactorily fitted to this restricted dataset. Consequently these results suggest that the presence of mobile oxygen within the polymer structure has a significant influence on fading behaviour above room temperature. When exposed to daylight, the IRSL signal was optically bleached within minutes.

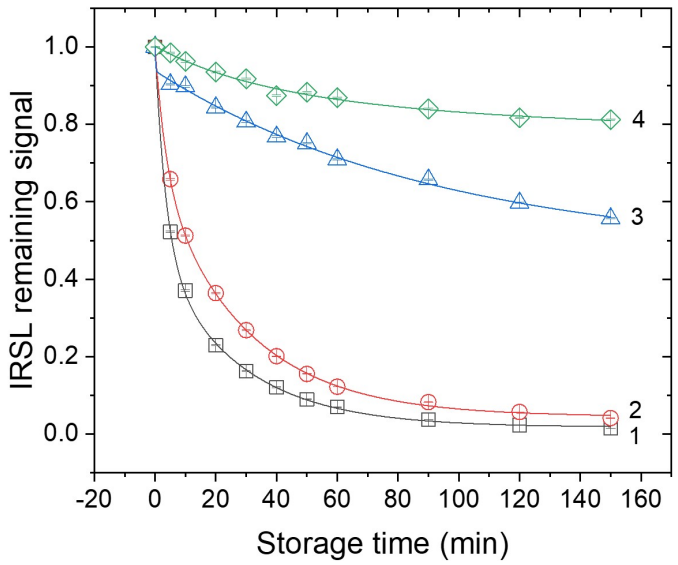

Fig. 8.14. Fading curves for the IRSL signal measured after storage periods of up to 150 mins following the administration of a β dose to samples of the blue polyester-mix fabric (F# 3), and where four procedures were applied, as discussed in the main text: Proc. 1 (open black squares); Proc. 2 (open red circles); Proc. 3 (open blue triangles); Proc. 4 (open green diamonds). Detection window: BG-39

Table 8.1: IRSL fading measurement procedures

Procedure	**Measurement sequence**
1	1. Beta dose (6.8 Gy) 2. Storage at ambient temp. (0-150 min) 3. Record IRSL (40 s, 70 °C sample measurement temp.) 4. Repeat step 3 (for residual).
2	1. Preheat (250 °C, 60s, in N_2 atmosphere) 2. Beta dose (6.8 Gy) 3. Storage at ambient temp. (0-150 min) 4. Record IRSL (40 s, 70 °C sample measurement temp.) 5. Repeat step 4 (for residual).
3	1. Record TL (to 230 °C at 0.5 °C s^{-1} in N_2 atmosphere) 2. Beta dose (6.8 Gy) 3. Record TL (to 230 °C at 0.5 °C s^{-1} in N_2 atmosphere) 4. Beta dose (6.8 Gy) 5. Storage at ambient temp. (0-150 min) 6. Record IRSL (40 s, 70 °C sample measurement temp.) 7. Repeat IRSL (for residual).
4	1. Record TL (to 230 °C at 0.5 °C s^{-1} in N_2 atmosphere) 2. Beta dose (6.8 Gy) 3. Record TL (to 230 °C at 0.5 °C s^{-1} in N_2 atmosphere) 4. Beta dose (6.8 Gy) 5. Storage at ambient temp. with continuous N_2 flow (0-150 min) 6. Record IRSL (40 s, 70 °C sample measurement temp. in N_2 atmosphere) 7. Repeat IRSL (for residual).

8.8 Kinetic parameters

8.8.1 T_{max}-T_{stop} method

An examination of the trap depths associated with the β-induced TL signal was performed by applying the T_{max}-T_{stop} method (see Section 4.5.2). The analysis of the glow curves yielded the values of thermal activation energy using the initial rise method, E, plotted against T_{stop} in Fig.8.15. The significant shift in E between 70 and 80 °C may reflect two distinct trapping levels, but it also coincides with the region of the polymer glass transition temperature (T_g) above which structural movements at a molecular level are expected to be activated in the amorphous regions of the polymer. For higher values of T_{stop}, the values of E steadily increase, but there is evidence of a plateau in the region of 100 °C, corresponding to the position of the second β-induced TL peak, with an average value of E of (0.75 ± 0.01) eV (and for the lower peak, $E = (0.68 \pm 0.01)$ eV).

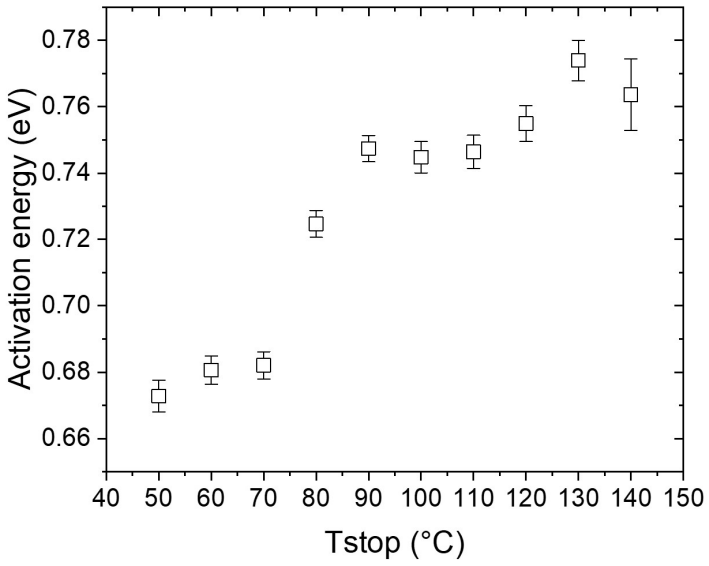

Fig. 8.15. Thermal activation energy, E, vs T_{stop}, where E was calculated by applying the initial rise method to each glow curve recorded.

8.8.2 IRSL decay curve

The form of the IRSL decay curve was analysed for five levels of absorbed dose administered (Fig. 8.16; 8 Gy measurement shown), using a deconvolution procedure that employed a Levenberg-Marquardt iteration algorithm. The best agreement was obtained using a combined function with a general kinetics term and a tunnelling term, as proposed by Jain et al. (2012), to account for localised electronic recombination via tunnelling between donor-acceptor pairs in crystalline inorganic phosphors. The values of the main function parameters calculated by the fitting procedure are given in Table 8.2; from these, the initial intensities, I_0, suggest a dominant tunnelling process and the value of b indicates second order kinetics with fast retrapping (τ_{GO}).

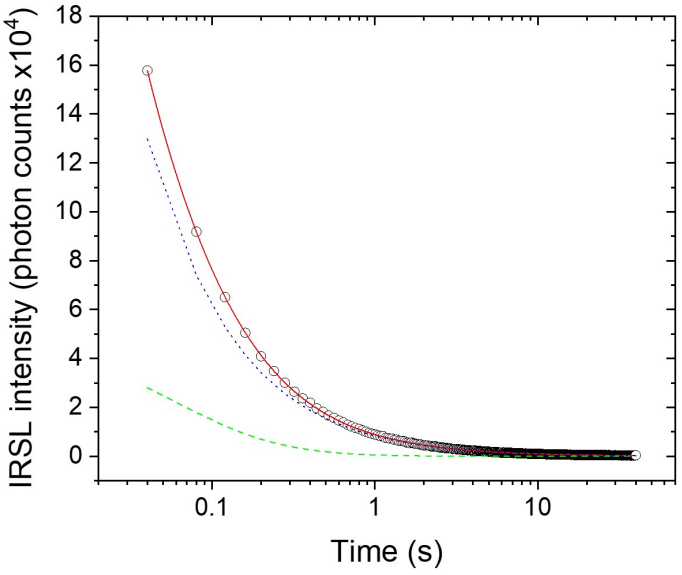

Fig. 8.16. Curve fitting to IRSL decay curve measured following the administration of a β dose of 8 Gy using a function combining (open circles) a general-order kinetics (GOK) term (green dashed line) and a tunnelling (T) term (blue dotted line), as discussed in the main text.

The combined function was fitted to the set of measured decay curves that had provided the data for the dose response characteristic (β dose ranging from 0.5 to 5 Gy), using common values for the parameters b, ρ and τ_T given in Table 8.2. The fitting yielded a value of τ_{GO} for each level of β dose administered. It can been seen in Fig. 8.17 that there is a strong, monotonic and approximately linear dependence of the parameter τ_{GO} with β dose. If we assume that the tunnelling

Table 8.2: Fitting parameters with general order kinetics and a tunnelling component for a sample of blue polyester-mix F# 3 IRSL (12 Gy). The values of τ are given in seconds.

General order kinetics component		*Tunnelling component*	
I_0	$(50 \pm 8) \times 10^3$	I_0	$(79 \pm 3) \times 10^4$
b	2.0 ± 0.2	ρ'	$(1.9 \pm 0.2) \times 10^{-4}$
τ_{GO} (s)	0.118 ± 0.004	τ_T (s)	$(1.8 \pm 0.3) \times 10^{-5}$

parameters (ρ and τ_T in Table 8.2) are more likely to remain invariant over the range of applied dose investigated, these results suggest that the conventional delocalised charge transfer process described by the general kinetics term in this particular polymer environment is very sensitive to changes in absorbed dose compared with the kGy levels applied in the studies of Charlesby and Partridge, for example (Charlesby et al., 1963).

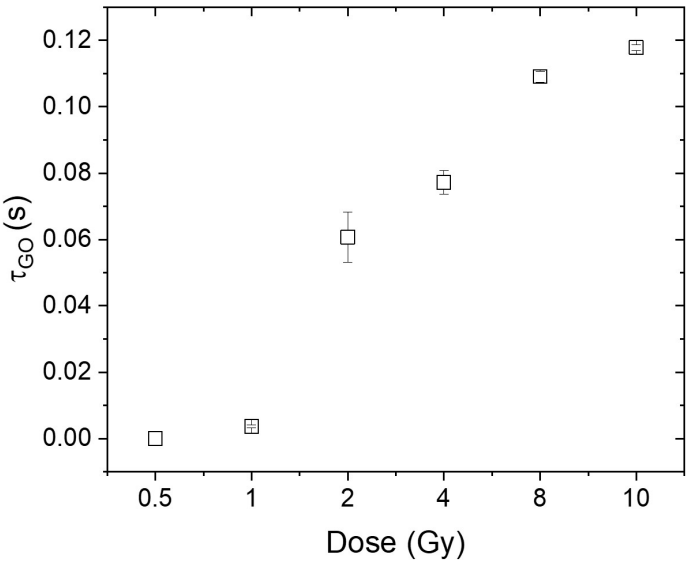

Fig. 8.17. Values of lifetime, τ_{GO}, versus β dose, where the values of τ_{GO} were obtained by deconvolution of IRSL decay curves measured with the blue polyester fabric 3 following the administration of different β doses (0.75 - 10 Gy), as discussed in the main text.

8.9 Discussion

Amongst the earlier work by Charlesby and Partridge (1965), TL emission spectra were recorded below room temperature (RT) for a range of polymers, and in the case of polyethylene they identified two broad emission bands located at ∼350 nm and ∼470 nm. Wavelength-resolved measurements of photoluminescence and recombination induced luminescence (equivalent to phosphorescence) emission from polyethylene by Tardieu et al. (2001) revealed a broad, generally featureless, emission spectrum at RT with a maximum located at ∼450 nm, but with several component bands, were better resolved within the range 390-480 nm by performing measurements at 80 K and applying spectral deconvolution techniques. They associated the phosphorescence with transitions from triplet excited states and identified a 250 nm stimulated fluorescence UV emission band (350 nm) attributed to transition from a singlet excited state. Other work by Szadkowska-Nicze and Mayer (1999) determined that the irradiation of de-oxygenated PET produces electron and positive hole pairs that react with basic polymer components, producing thermally unstable PET radical anions and cations. The recombination of the radical produces short-lived emission of luminescence with bands at 340, 370 and 400 nm. If these bands appeared to be present in the CL spectrum of F# 3, additional bands at the maximum of 425-440 nm were also present and could be related to the dye of the fabric.

In work by Qiao et al. (2016), the broad CL spectrum of polyethylene measured at RT, extending from 300 to 800 nm, was deconvolved into four bands, three of which were assigned to a different luminescence process: fluorescence (328 nm), chemiluminescence (415 nm) and recombination luminescence (505 nm), but a specific luminescence mechanism of the production of the strongest emission band located at 573 nm remained unidentified, except for its attribution to either a by-product of the fabrication process or the result of material degradation. For the blue polyester-mix (F# 3) that has been examined in this study, the emission bands associated with both recombination luminescence and chemiluminescence (associated with a chemical reaction initiated by electron bombardment) by Qiao et al. are evident in its CL spectrum, but additional bands are also present. Although we do not yet have OSL, IRSL and TL emission spectra, and also noting that the CL measurements were performed in low vacuum, it is likely that one or both of these bands contributed to the strong IRSL observed in the blue polyester-mix fabric, and these would have been efficiently transmitted by the BG39 optical filter placed in the detection system. The additional

bands observed are likely to be associated with the modification of the polymer by the dyes, amongst which the anthroquinone disperse dyes are known to exhibit strong fluorescence (Koh, 2011). With an estimated band gap of ∼8.8eV (Hoffman, 1991) for polyethylene, chromophores (e.g., additive, cross-linking by-products, oxidized groups or non-saturated bonds) can introduce potentially deep traps if they possess an electron or hole affinity (Tardieu et al., 2001).

A question yet to be resolved of this study is the origin of the IRSL emission in F# 3. Calcium carbonate or dust impurities were identified at the surface of the fabric by the means of XRD and XRF (Section 8.3) and calcium carbonate is sometimes integrated to polymelt spunbond and meltblown fibers to improve their performances (Yan et al., 2015), but this mineral is not known to exhibit IRSL emission. IRSL measurement on pure calcium carbonate (ground limestone) tested also did not show a radiation induced signal. However, calcium carbonate exhibits a bright TL signal in response to radiation dose (Medlin, 1959; Wintle, 1978; Kalita and Wary, 2016) and the TL signal of F# 3 corresponds in shape and activation energy (0.67-0.77 eV) to that of calcite (Kirsh et al., 1987). Despite these similarities between the TL response of F# 3 , discrepancies were also observed: the CL emission of calcium carbonate is characteristic with its strong peak centred around 600 nm (Down et al., 1985), and this emission band was not observed in the CL spectrum of F# 3 (Fig. 8.4). The fading rate of the TL signal of F# 3 was also notably faster than that of observed for calcium carbonate fillers (see Chapter 10). It is possible that the IRSL and TL signals observed in F# 3 are not related to each other. Furthermore, CL imaging detected uniform luminescence emission within the fibres (Fig. 8.3) that suggests that it is not related to the presence of calcium carbonate inclusions within the fibres. Also interestingly, the luminescence emission seemed to arise selectively from only certain fibres which are likely to be the polyester fibres as they were more numerous, with this mixed fibre material (65% polyester and 35 % cotton).

As discussed above, we observed strong effects when oxygen was excluded from the surrounding atmosphere during the measurement of IRSL, or by applying the oxygen depletion procedure of Charlesby and Partridge. If, as argued by Partridge (1972), mobile oxygen molecules can diffuse within the amorphous regions and do not penetrate the crystalline phases of the polymer, this suggests that the source of IRSL is either within the amorphous regions, or near the interface with crystalline regions. In supplementary thermogravimetric analysis (TGA) measurements with the blue polyester-mix fabric (F# 3), the availability of mobile oxygen was indicated in both unirradiated and irradiated sample by detecting its release from RT to beyond 200 °C, which increased

by a factor of ∼5 within this temperature interval. There is much discussion in the early literature regarding the role of oxygen (e.g., summarized in Partridge 1972) and its effects on the TL characteristics of polyethylene, from which the dual role of oxygen as an electron trap and as quencher of luminescence is most relevant to measurements above RT. Boustead (1970), studied the effects of oxygen on a TL peak measured at 140 K in different types of polyethylene, which was attributed to electron trapping on oxygen molecules (i.e., forming negative O_2 ions) following exposure to ionising radiation. However, on the basis of the calculation of the electron affinity of oxygen, the position of an "oxygen" TL peak was estimated to be in the range 370 K to 500 K, and the disparity with the results of his experimental measurements was reconciled by arguing for a reduction in the electron affinity resulting from an interaction between the polymer matrix and the oxygen molecules. Szadkowska-Nicze and Mayer (1999) also observed that the absorption characteristics of PET were very sensitive towards oxygen. The strong effect of depleting oxygen content in the fading and sensitization tests based on the measurement of IRSL adds further evidence for the involvement of oxygen in the production of IRSL above room temperature.

8.10 Summary

This chapter reported on the IRSL characteristics of a blue polyester-mix fabric (F# 3). The IRSL measured with this fabric gave a negligible native signal, a bright β-induced IRSL signal, a linear dose response in the range 0.5-10 Gy of interest and with a detection limit of $\sim$ 20 mGy. However, the fading of the IRSL signal was almost complete within several hours, and consequently the lifetime of trapped charge is insufficient for general application in short term dosimetry. A β-induced TL signal was also observed with this material, but the strength of the native signal and a fading, almost as equally fast as the IRSL signal also limited its use for dosimetry. although the IRSL signal of the blue polyester fabric was not found applicable to emergency dosimetry due to its fast fading, it could be transformed into a viable dosimeter if the fabric was kept in a oxygen free atmosphere (e.g., under vacuum). Whilst the IRSL signal was attributed to an intrinsic component of the fibre (e.g., dye), the TL signal is suggested to be associated with calcium carbonate in the sample, that could have been either added to the fibre to increase their strength.

As found in earlier studies of the TL of polyethylene, the effect of mobile oxygen within the polymer has a very strong effect on luminescence characteristics, and its removal appears to cause

a dramatic reduction in the rate of fading. Although optical fading by exposure to daylight is another issue to be anticipated when attempting to use fibres, the multi-layered construction of many garments has the potential provide shielded locations from which suitable fibres can be extracted for analysis. The next chapters of this thesis will aim to find other materials with a luminescence response to dose commonly found amongst members of the public.

Chapter 9

Case study 2: OSL response of some upholstery fabrics

When applying the screening procedure to explore the radiation sensitivity of fabrics (Chapter 7), a class of upholstery fabric was found to exhibit an OSL response to β dose. This chapter discusses an investigation of the OSL properties of this class of fabric, particularly in terms of dose response characteristics and fading of the signal.

9.1 Fire retardant fabrics

The UK Consumer Protection Act (1988) set regulations regarding the levels of fire resistance of upholstery fabrics to reduce fire risk. Polyester is inherently fire resistant (Manfredi et al., 2006), but consequent research has been carried to improve the fire resistance of fabrics. High performance polymers were developed (Bourbigot and Duquesne, 2007), offering operating temperatures ranging from 180 to 300 °C, and degradation temperatures as high as 350 °C.

According to patents (Cooke et al., 1991; Zhu and Young, 2005), the fibres forming the yarn can themselves be inflammable (Fig. 9.1a) if formed of an inorganic fire resistant core of a typical diameter of 5-6 μm (Fig. 9.1a, 11) surrounded by corespun yarn (10, 11) and a sheath of mod-acrylic intumescent fibres, which swells when exposed to a flame, and is composed of a long chain of polymer of 35-85% acrylonitrile units (C_3H_3N, boiling point 77°C, 12 on Fig.9.1b). The fire resistant core is of particular interest as it can be formed of glass, various metals, quartz, ceramics,

polyethers, polyamides, polyarylsulfones, polyketones, polyphenylene sulfides, polyaramids such as Kevlar or Nomex (Cooke et al., 1991), or stainless steel (Zhu and Young, 2005); some of these materials are potentially luminescent. On some upholstery fabrics, additional coating of the yarned fibres is added, providing further fire resistance (Fig. 9.1a). The woven fabric (20, Fig. 9.1b) is placed between a underlying flammable layer (30) such as polyurethane foam and an upholstery layer (40) preferably using an adhesive layer (45) such as a latex anti-slide adhesive.

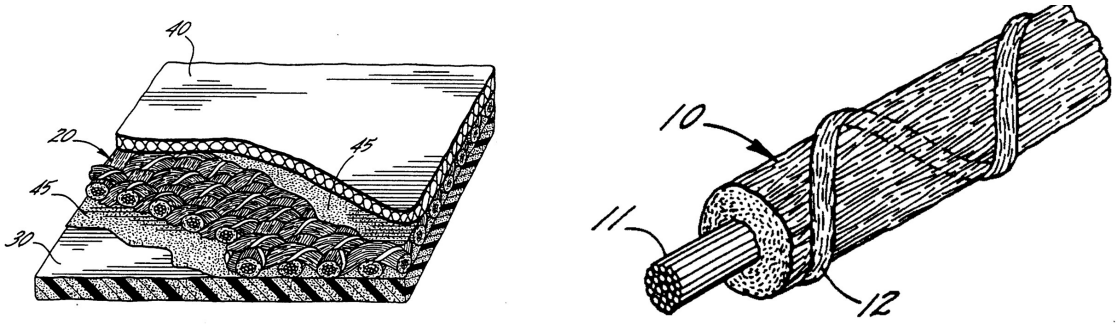

(a) **(b)**

Fig. 9.1. a) Schematic representation of a type of fire retardant fabric, and b) detail of a fire retardant fibre (Cooke et al., 1991).

Recent developments in flame retardant fabrics include coating fabrics with a nano-layer based on phosphors and silica solutions (Alongi et al. (2014); Alongi et al. (2011), Cireli et al. (2007)). However, in some cases, the layer is also designed to protect from UV radiation (Alongi et al., 2011), and would consequently attenuate any UV luminescence emission.

Moreover, mineral fillers are introduced in the coating, often to reduce the cost of production by adding a cheap material, but they are also used for their fire retardancy properties. Many types of fillers are used in the textile industry; to give some examples, aluminium trihydroxide is used as a filler in carpet backing; antimony pentoxide and antimonate of sodium are directly injected in fibres of carpet, draperies, or clothing for their flame retardancy properties; barium sulphate is widely used in all sort of coatings. Calcium carbonate is considered as the most common filler (see Chapter 10 and 12) and calcium silicate is sometimes used in polyester fibres; zeolite powder is added to some textile for absorption of odours (Wypych, 2016).

The complex structure of fire retardant fabrics provides a better chance of exhibiting a radiation induced OSL/TL signal. Furthermore, some patents (Marsh, 2003, 2000; Burnell-Jones, 2005)

proposed designs for fire retardant materials with luminescence properties, including materials that would be able to keep their luminescence properties at high temperature, which would be of interest, for example, for protective clothing of fire fighters.

The particular type of upholstery fabric examined was found to contain a "foam coating", a form of coating where a foam is sprayed onto the fabric then crushed with a roller to form the coating. Foam coatings are composed of at least two phases: a solid polymer matrix and a gas, often carbon dioxide (Sen, 2007) as a foaming agent. In addition to the solid phase, fillers such as glass, ceramic, or other polymeric materials may also be incorporated into the foam.

9.2 Material characterisation

Material and methods

A series named "Lynton" was tested in this chapter. It is available in different colours (smoke, steel, dove grey, mineral, mint or blueprint) but the composition of the fabrics was similar, with 60% polyester, 38% acrylic, and 2% nylon. The "Lynton" fabrics samples are listed in Table 9.1. An optical microscope image was also taken for each sample, to better appreciate the structure and colour of the samples; the woven fabrics were coated with a foam (Fig. 9.2). A swatch of one of the fabric (F 29) is provided in Appendix A.

For each test, the sample was cut to fit in stainless steel cups (11.5 mm of diameter). The measurements were performed in the Risø reader, and the photon detection unit comprised an EMI 9635 PMT (see chapter 6 for details of the instrumentation). A UV (250-350 nm; Schott U-340 filter) detection window was inserted when measuring blue stimulated OSL (470 nm) and a broad-band detection window (350-700 nm; Schott BG39 filter) when measuring IRSL (850 nm). Unless stated otherwise, none of the samples were preheated and IRSL/OSL measurements were performed with the sample maintained at a temperature of 50 °C or 150 °C. TL measurements were performed using a heating rate of 0.5 °C.s^{-1} to a maximum temperature of 200 °C, with a fused silica window inserted in the detection system. The tests (dose response, fading) were repeated on several samples obtained from the different swatches to test for uniformity in response.

A Hitachi SU-70 scanning electron microscope (SEM) with a beam energy of 10 kV and a current of 10 mA was used to analyse the morphology of the fabric samples and spatially- and spectrally-resolved cathodoluminescence (CL) spectra were measured using a MonoCL3 spectrometer (Gatan

Ltd, Oxford) incorporating a Hamamatsu R374 PMT detector operated in single photon counting mode. The spectra recorded were corrected for instrument response within the SEM analytical software. Details of the instrumentation are given in Section 6.3.

The X-ray diffraction pattern was obtained using a Bruker AXS D8 Advance equipped with a Lynxeye Soller PSD Detector. The source of X-ray was a copper tube producing a mixture of Cu-$K_{\alpha 1}$ and Cu-$K_{\alpha 2}$ at a wavelength of 1.5406 Å.

Table 9.1: Table listing the "Lynton" fabrics with their reference number and colour. The optical microscope photographs were taken at a magnification of ×2.

F#	Colour	Magnification × 2
29	Blueprint	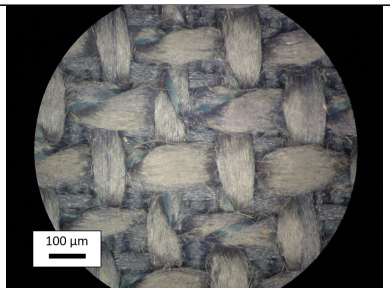
40	Dove Grey	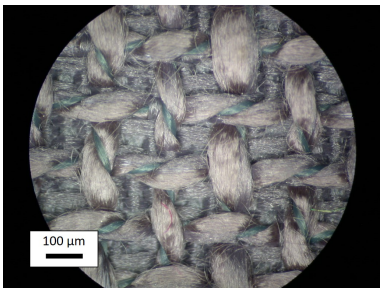
43	Mineral	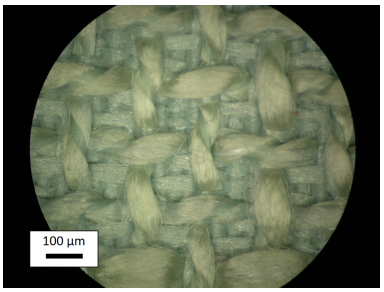

44	Mint	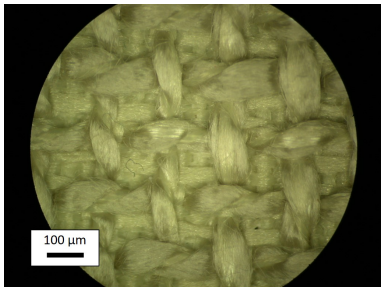
45	Smoke	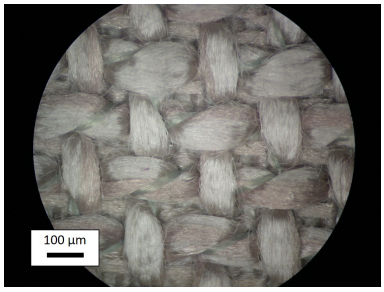
46	Steel	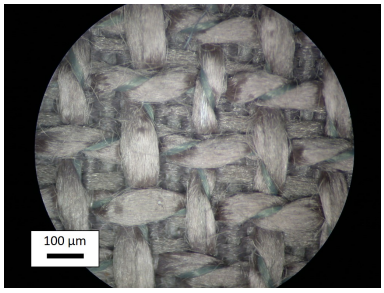

9.2.1 Elemental characterisation

A point XRF elemental identification performed on a sample of F# 43 using the Oxford Instruments EDX system (X-MaxN 50 Silicon Drift Detector) attached to the scanning electron microscope Hitachi SU-70 indicated the presence of carbon and oxygen in the fibres, with no evidence of other major elements present.

However, XRF measurements of the foam coated face indicated the presence of additional elements as shown in Fig. 9.3 for F# 29. Some small inclusions ($\leq 10\mu$m) contained oxygen, magnesium, silicon, calcium, and in some regions, iron (not shown in iug. 9.3), which are interpreted as mineral fillers. Due to the very small and fragile nature of these inclusions, extracting and isolating them from the coating was not feasible.

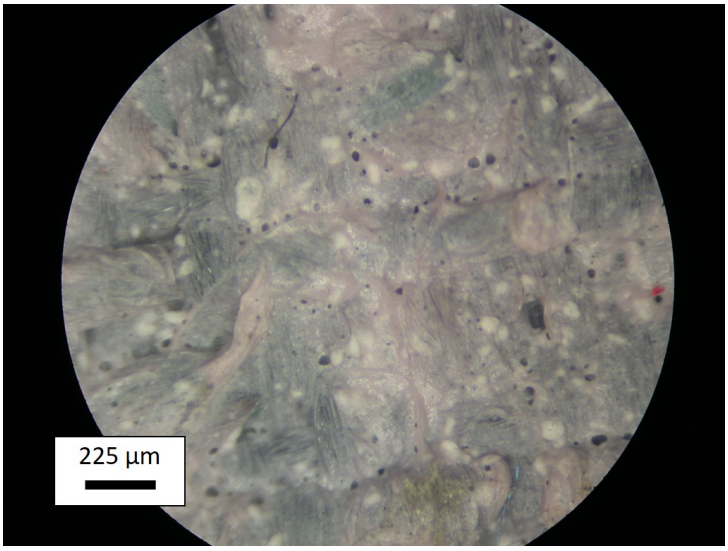

Fig. 9.2. Optical microscope image of F# 40 foam coating. Magnification ×4.5.

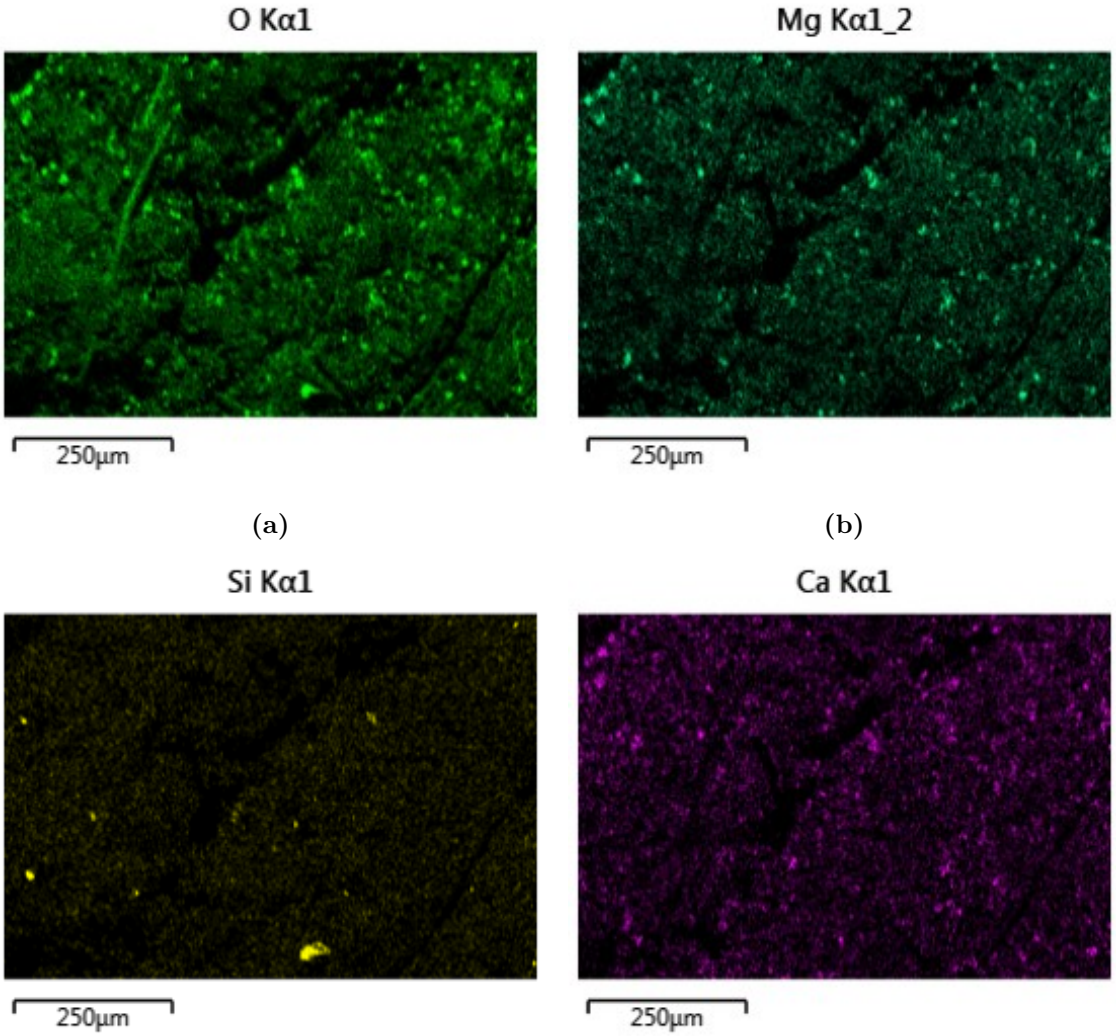

Fig. 9.3. XRF mapping using the Oxford Instruments EDX system (X-MaxN 50 Silicon Drift De-

The X-ray diffraction pattern obtained with sample F # 29 contained narrow peaks indicating the presence of crystalline phases in the sample (Fig. 9.4) that may be related to the inclusion of mineral fillers.

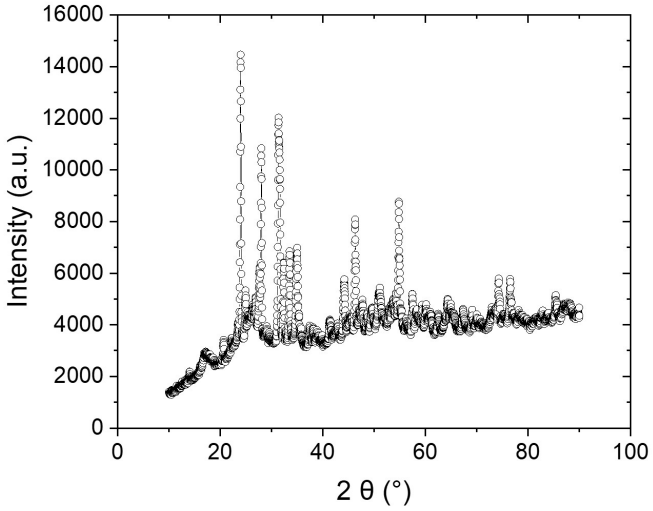

Fig. 9.4. Powder X-ray diffraction pattern of F# 29.

9.2.2 Scanning electron microscopy and cathodoluminescence

SEM and CL imaging

To allow a better understanding of the structure of the type of upholstery fabric tested here, the fabrics were encapsulated in resin to enable a polished section to be examined. The polished section was coated coated with a 10 nm layer of platinum for SEM imaging. Two SEM images are shown in Fig. 9.5a and Fig. 9.5b. In addition of the coating, many different types of fibres, of different shape and diameter were observed. The fibres of different type are ordered in layers, with a thickest layer of ca 200 μm, and the thinnest one ca 50 μm. The coating was estimated to be of ca 250 μm.

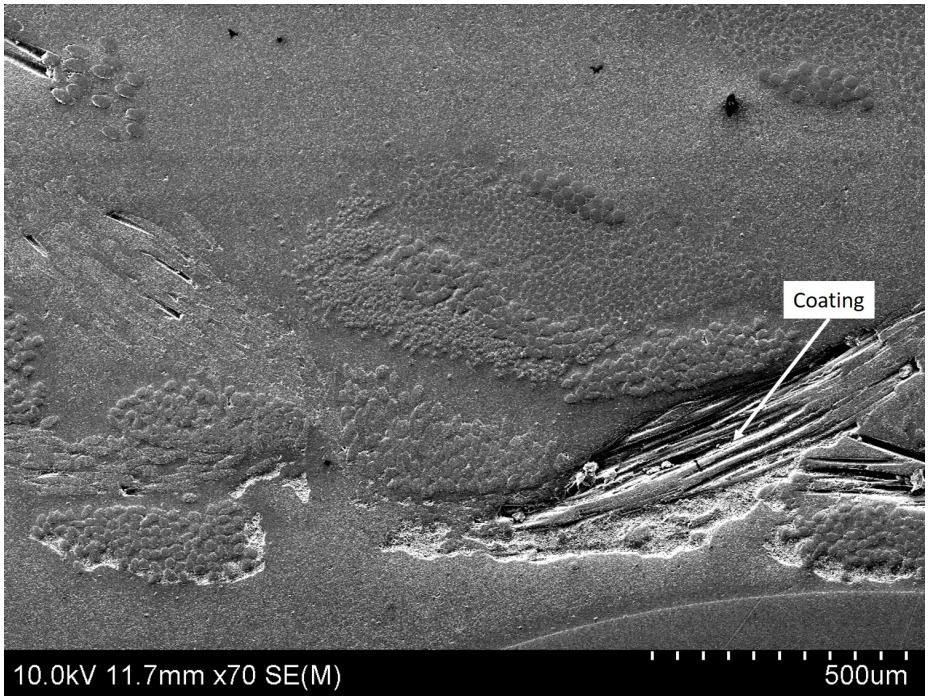

(a)

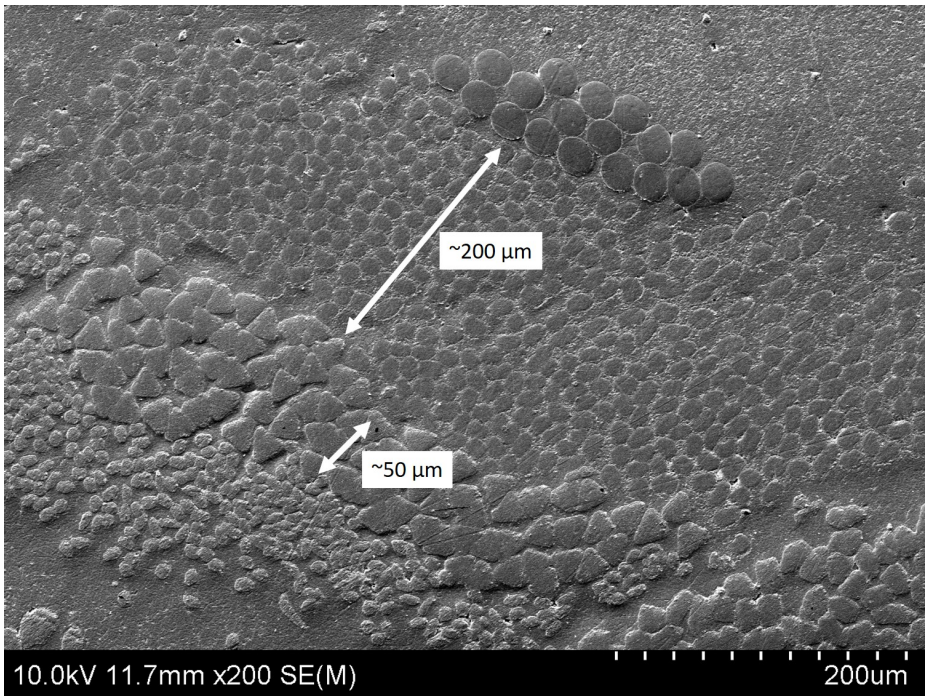

(b)

Fig. 9.5. a) and b) SEM images of sample F# 29 polished section showing end-on fibres in the fabric. Resin encapsulated fabric. Electron beam : 10 keV. The thicknesses are indicated.

CL imaging (Fig. 9.6) revealed luminescence emission amongst fibres; Fig. 9.6 shows very dim fibres (indicated in Fig. 9.6), and brighter ones. The coating also seems to exhibit a bright CL emission. Furthermore, many small bright dots seemed to be distributed in the coating. A CL image of the coating coupled with XRF measurements indicated that some of the bright dots relate to the Mg/Si/Ca inclusions (Fig. 9.7) observed in Fig. 9.3, suggesting that these are mineral fillers.

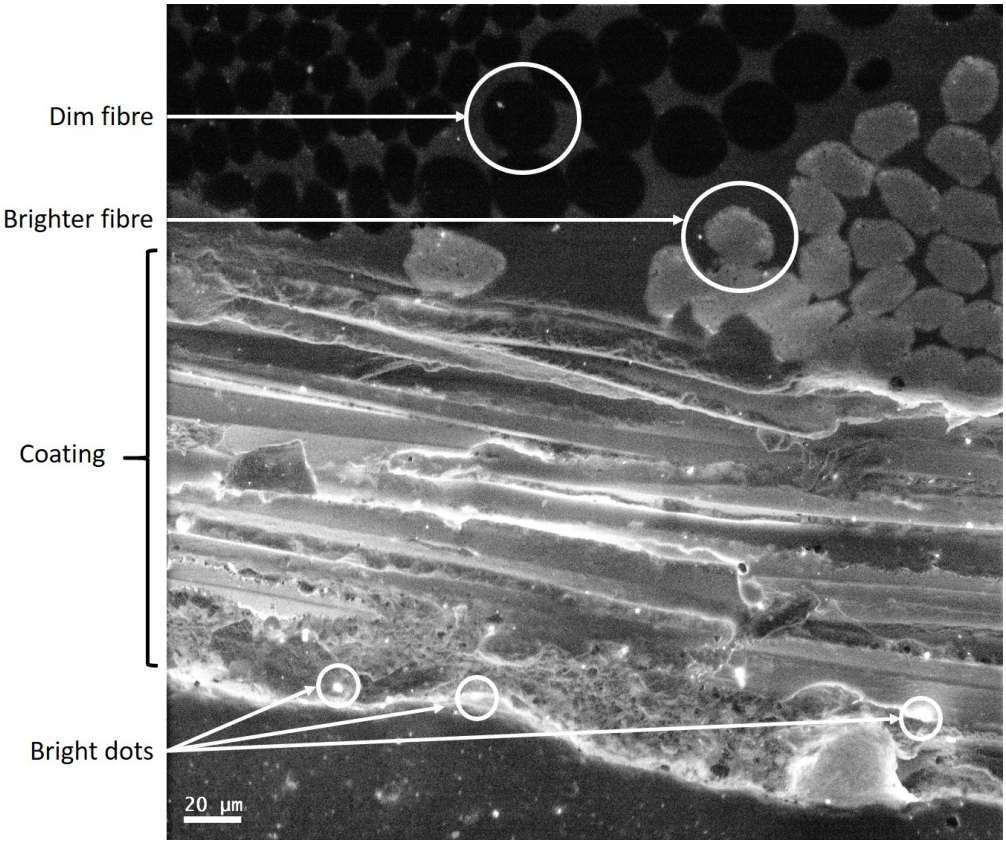

Fig. 9.6. CL image of F# 29 cross section. The fabric was encapsulated in resin, polished with diamond powder and coated with 10 nm of platinum. Electron beam : 10 keV, grating : 300 lines/nm.

Spatially averaged CL

The CL emission spectrum is shown in Fig. 9.8a. It is composed of several overlapping bands, which, if fitted with Gaussian bands indicated emissions centred at 1.71 ± 0.03, 1.95 ± 0.02 and 2.85 ± 0.01 eV. Considering that an U-340 filter was used for light detection during the OSL measurements, only the highest energy emission band (2.85 ± 0.01 eV) may account for the OSL emission (Section

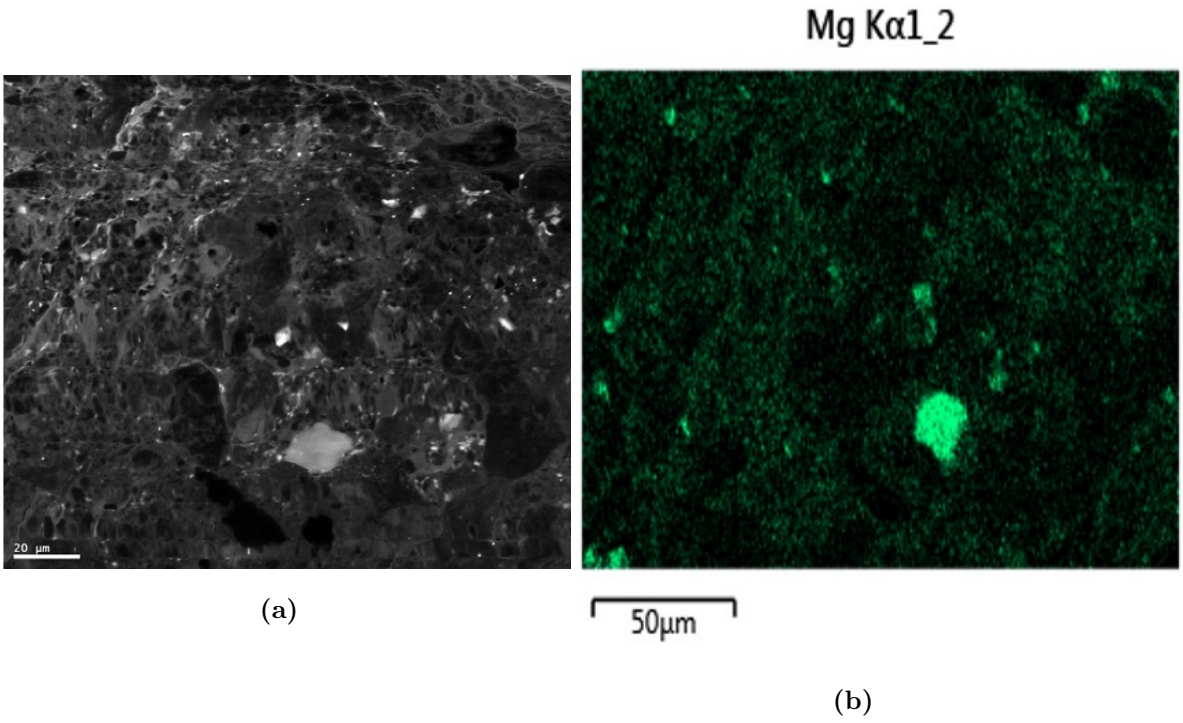

Fig. 9.7. a) CL image of F# 29 and b) XRF mapping of magnesium on the same spot. Electron beam : 10 keV.

9.5).

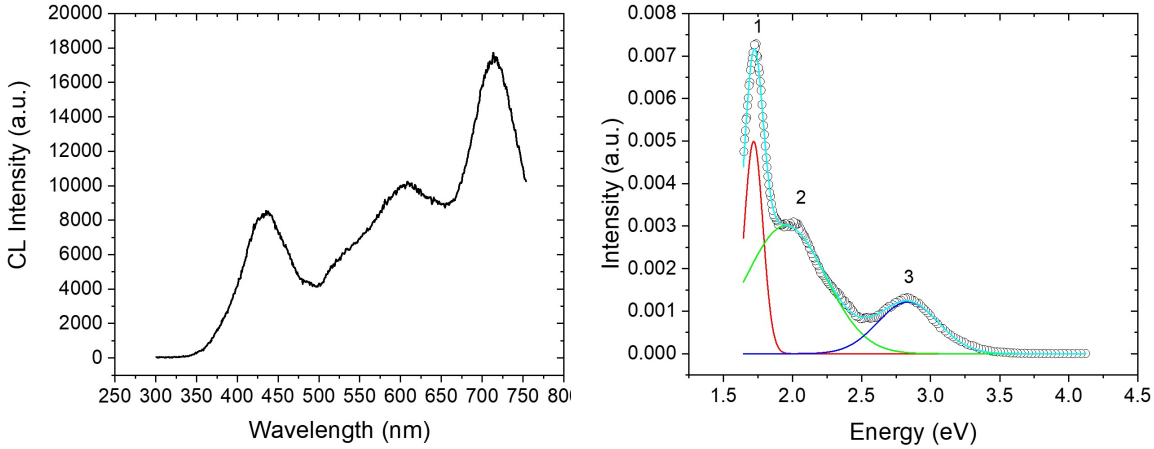

(a) **(b)**

Fig. 9.8. a) CL spectrum of F# 29, wavelength scale and b) CL spectrum of F# 29, energy scale. Three Gaussians (lines) were fitted to the experimental data (open circles) and the spectrum intensity has been corrected for the energy scale. Electron beam : 10 keV, grating : 300 lines/nm.

9.3 IRSL response

The Lynton type of fabric did not exhibit significant response to infra-red stimulation (850 nm) following β irradiation (Fig. 9.9a). However, when the measurement chamber as evacuated and the measurement cycle (irradiation and IRSL measurement) was also performed under vacuum, a dose dependent decay curve was observed, indicating that oxygen acts as a strong quencher of the luminescence. The decay curve observed under vacuum reaches a background level relatively slowly, ~10 s after the start of the stimulation (Fig. 9.9b). One or more of the CL bands if present in the IRSL spectrum could be detected with the optical detection window adopted for the IRSL measurements under vacuum.

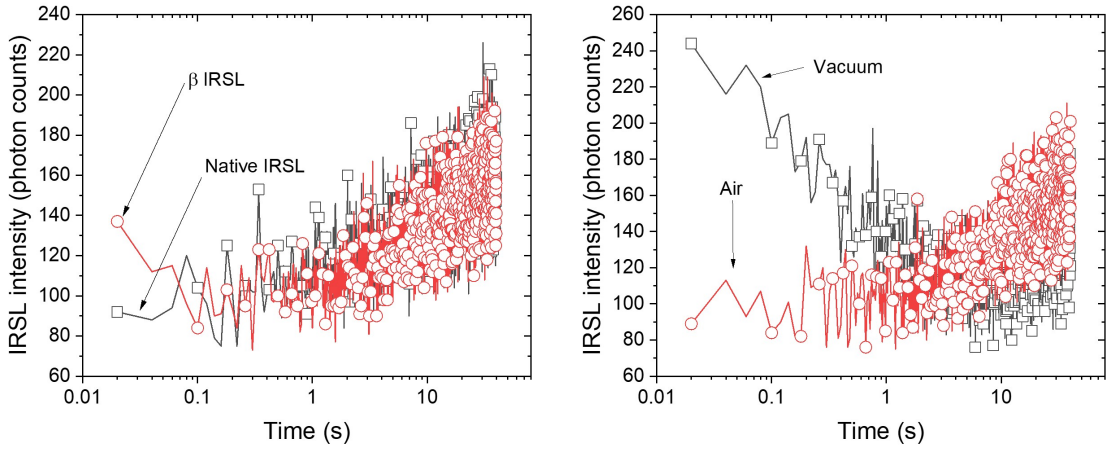

Fig. 9.9. a) Native IRSL (black squares) and IRSL measured following a 2 Gy β dose (red circles) of F# 29. b) IRSL of F# 29 following a 2 Gy β dose, irradiation and IRSL measurement conducted in vacuum (black squares), and in air (red circles). Risø reader, detection window : BG-39, sample temperature during stimulation : 50 °C.

9.4 TL response

The TL measurements showed a possible native signal, that was strong compared with the weak β TL response (Fig. 9.10a). A possible explanation for this native signal is the occurrence of a photo-stimulated luminescence process or phototransfer TL induced by the exposure to ambient light. To test this hypothesis, the TL of an unirradiated sample was measured, to erase the native TL signal. The sample was then exposed to UV for 2 mins (Mercury lamp, Hanovia Ltd, delivering a power of $\sim$ 4 mW·cm^{-2} at the sample position and its emission spectrum contained lines at 307, 364, 403, 434, 544 and 575 nm) at room temperature, and the TL glow curve recorded. This procedure yielded a TL glow curve that is interpreted to be a photo-stimulated thermoluminescence signal or phototransfer TL from deeper traps (Fig. 9.10b). The β induced TL glow curve was composed of two peaks below 200 °C, centred at ca 20 and 80 °C using a heating rate of 0.5 °C.s^{-1}, which is comparable to the shape of the TL glow curve of crystalline calcium carbonate (see Chapter 10). The shape of the TL glow curve indicated the presence of charges in deeper traps above 200 °C.

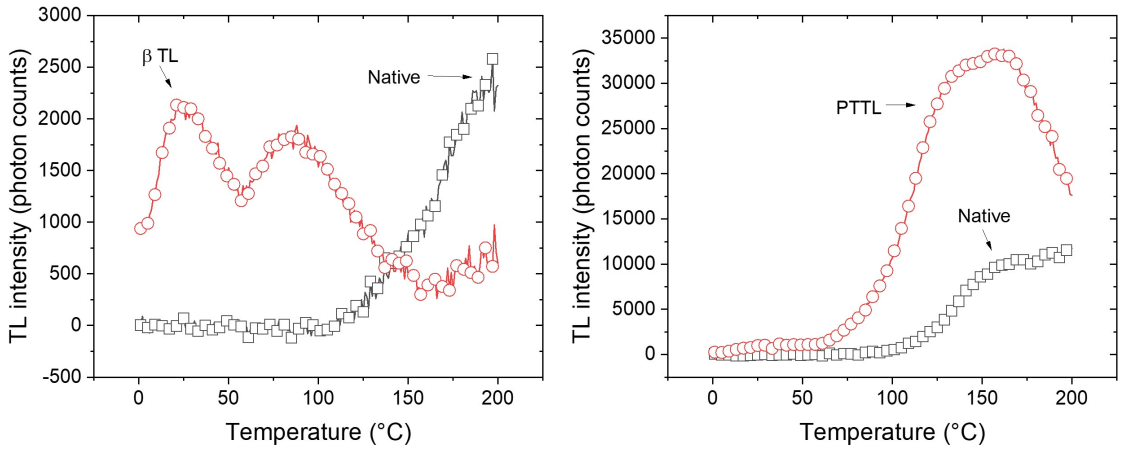

(a) **(b)**

Fig. 9.10. a) Native TL (black squares) and TL following a 10 Gy β dose (red circles) of F# 43. Risø reader, detection window : silica window, PMT : Hamamatsu R2949, heating rate : 0.5 °C.s^{-1}. b) Native TL and phototransferred TL signal of F# 29. Risø reader, detection window : silica window, heating rate : 0.5 °C.s^{-1}.

9.5 OSL response

9.5.1 Decay curve

Following β irradiation, the Lynton fabrics exhibited a decay curve under blue stimulation (470 nm) that increased with dose but had no detectable native signal (Fig. 9.11a). The decay curve contained an initial component that reached the background level within 1 second (Fig. 9.11a). The response to β radiation doses delivered under vacuum yielded a ca 25 % stronger OSL signal compared with that measured in air. Comparatively, the IRSL signal measured under vacuum was $\sim$ 6 times stronger than in air. The shape of the OSL decay curves measured under vacuum and air were similar, whereas the IRSL decay measured under vacuum was different in shape.

Some of the foam coating was removed using a scalpel and deposited on a stainless steel disc. An OSL measurement following the administration of a β dose of the extract yielded an OSL similar in shape to the fabric, indicating that the radiation sensitive material was contained in the coating.

9.5.2 Dose response

The OSL dose response curve presented in Fig. 9.11b was measured at 50 °C, and was best fitted with a quadratic function, indicating a slight supra-linearity of the signal for higher doses ($\geq$ 5 Gy). The detection limit (defined in Chapter 3) was estimated to be between (110$\pm$ 70) and (340 $\pm$ 100) mGy depending on the samples, using a quadratic fit to the data. As explained below, the samples were found to exhibit a slight sensitisation for higher doses ($\geq$ 10 Gy) using a sample temperature of 50 °C, which may account for the supra-linearity.

The intensity of the OSL signal was found to vary from one fabric of the Lynton class to another for samples of the same size; Fig. 9.12 shows the intensity of the OSL signal for a 10 Gy β dose for all colours of fabric tested. When the OSL was measured with the coating of the fabrics facing away from the detector, the strongest OSL signal was found for the white and the blue samples. If we assume that the OSL sensitive component of the fabric is not only at the surface of the fabric, but distributed throughout the coating, the weaker signal of the darker fabrics may relate to the optical attenuation of the coating and the fibres. White/blue fibres are more likely to transmit an UV emission, whilst black or grey fibres (e.g., dove grey) are more likely to attenuate it.

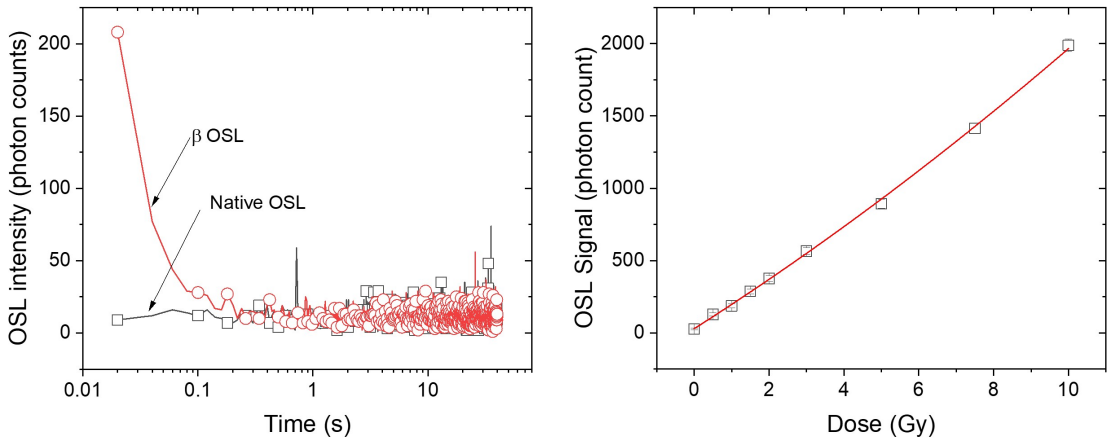

(a) **(b)**

Fig. 9.11. a) Native OSL (black squares) and OSL following a 2 Gy β dose (red circles) of F# 29. b) OSL dose response of F# 29 following absorbed β doses 0.5-10 Gy. The OSL signal was computed as the integral of the first five points of the signal minus a background subtraction. The red line indicates a parabolic function fitted to the signal. The error in count was calculated to be ≤ 10 %. Risø system, detection window : U-340, OSL temperature : 50 °C.

9.5.3 Deep traps

To access deeper traps, the OSL was measured at different sample temperatures. At elevated OSL temperature (≥ 150 °C), the background of unirradiated samples was found to increase substantially (Fig. 9.13), indicating that another luminescence process induced at higher temperatures may be present (e.g., chemiluminescence). However, once the background was subtracted from the β induced OSL, the dose response was found to be similar for different readout temperatures (room temperature to 200 °C). The sensitisation, measured by repeating cycles of irradiation and OSL measurements was found to be more important for samples measured at a readout temperature of 200 °C than for samples measured at 150 °C and lower.

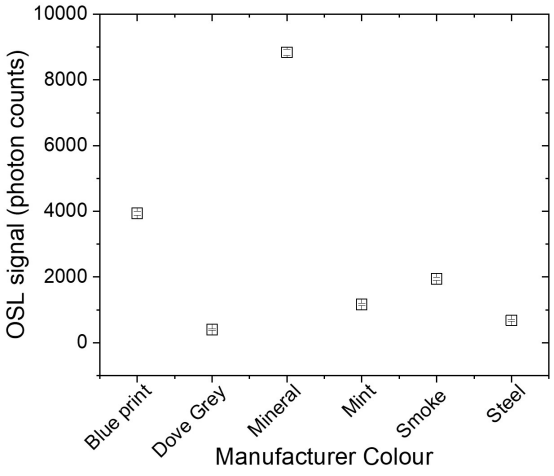

Fig. 9.12. OSL signal F# 29 (blue print), 40 (dove grey), 43 (mineral), 44 (mint), 45 (smoke) and 46 (steel) following β dose (10 Gy). Risø reader, detection window : U-340.

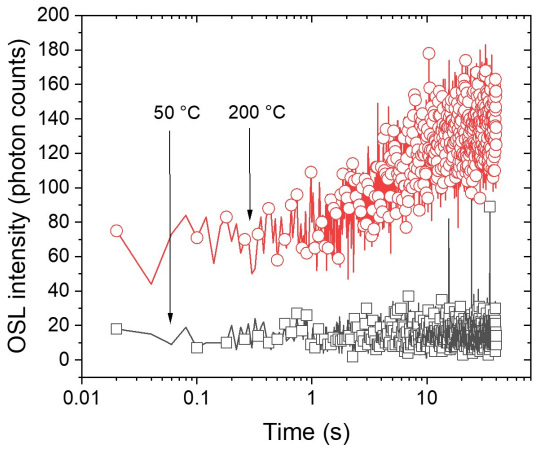

Fig. 9.13. OSL background of F# 29 at sample temperature 50 °C (black squares) and 200 °C (red circles). Risø reader, detection window : U-340.

9.5.4 Sensitisation

Fig. 9.14 shows the sensitisation for OSL sample temperature of 50 and 150 °C. The signal exhibited sensitisation over repeated cycles of irradiation/OSL measurements for both sample temperatures 50-150 °C, although increasing the sample temperature during OSL measurements also caused the rate of sensitisation to increase. The OSL signal approaches a plateau in sensitivity after 7 cycles of β dose - OSL measurements for a sample temperature of 50 °C, but continues to increase after 10 cycles for a sample held at 150 °C during the OSL measurement. The increase in intensity of the OSL signal followed a quadratic function, which can be fitted to the experimental data points, such as shown in Fig. 9.14.

The difference in rates of sensitisation with dose can be seen in Fig. 9.15; at 1 Gy no significant sensitisation was observed, whilst for doses above 5 Gy the increase of the signal over repeated cycles of measurement followed a quadratic increase. This could indicate that the sensitisation is caused by a saturation of deeper traps. For dose assessment following the administration of a blind dose, a SAR protocol or the additive method could be used to correct for sensitisation (see Chapter 5).

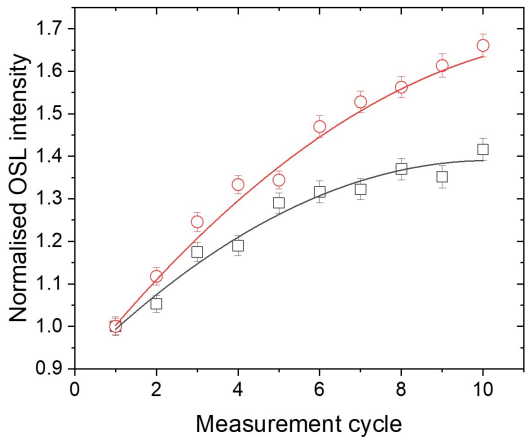

Fig. 9.14. OSL sensitisation of F# 29 for sample temperatures of 50 °C (black squares) and 150 °C (red circles). The lines indicate a quadratic function fitted to the experimental points. The sensitisation was measured by irradiating the samples with a 10 Gy β dose, measuring the OSL and repeating the cycle 10 times. Risø reader, detection window : U-340.

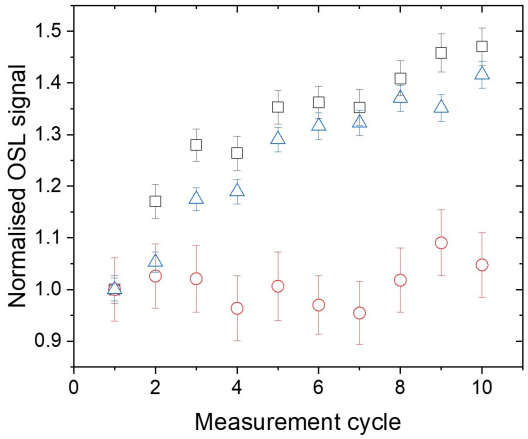

Fig. 9.15. OSL sensitisation of F# 29 for different irradiation doses. The sensitisation was measured by administering a β dose of 1 Gy (red circles), 5 Gy (black squares) and 10 Gy (blue triangles), measuring the OSL and repeating the cycle 10 times. Risø system, detection window : U-340, measurement temperature : 50 °C.

9.6 Fading

9.6.1 Storage tests in dark conditions

The extent of fading was tested by irradiating samples with a β dose of 10 Gy and storing them in the dark at ambient temperature until measurement. The fading was tested for sample readout temperatures of 50 and 150 °C; a readout temperature of 150 °C yielded significantly less fading for a storage period of less than 7 days compared with a readout temperature of 50 °C (Fig. 9.16). For longer storage periods, the fading rates with measurements temperatures 50 and 150 °C were closer. This could be explained by the presence of a component of the OSL signal that is thermally erased before the measurement of the OSL at a sample temperature of 150 °C. The fading obtained for a sample temperature of 150 °C was fitted with a single exponential function, whereas using a measurement temperature of 50 °C, the fading followed a double exponential law, such as :

$$y(t) = y_0 + A_1 \exp\left(-\frac{t}{\tau_1}\right)\left(+A_2 \exp\left(-\frac{t}{\tau_2}\right)\right). \tag{9.1}$$

The coefficients y_0, A_1, τ_1, A_2, τ_2 are listed in Table 9.2. In both cases, the presence of a constant y_0 might indicate the presence of a stable component, although longer term tests would be required to confirm this. The stable component was more important for the OSL measured at 150 °C (0.60) than for the OSL measured at 50 °C (0.48), which indicates that the OSL measured at 150 °C may be more stable.

Table 9.2: Coefficients used to fit the fading behaviour of F# 29 following Eq. 9.1.

	OSL 50 °C	OSL 150 °C
y_0	0.48 ± 0.05	0.60 ± 0.01
A_1	0.34 ± 0.04	0.37 ± 0.01
τ_1 (days)	0.07 ± 0.02	2.5 ± 0.3
A_2	0.19 ± 0.04	-
τ_2 (days)	6 ± 8	-

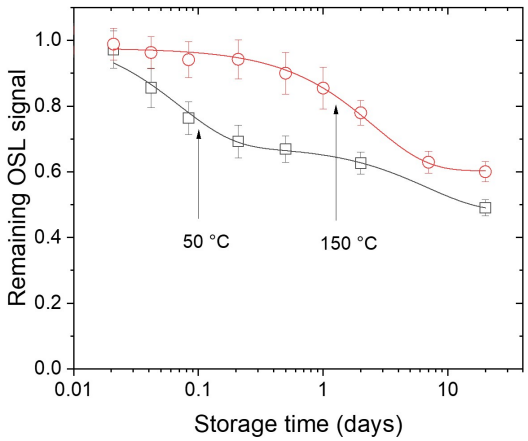

Fig. 9.16. OSL fading of F# 29 for readout temperatures of 50 °C (black squares) and 150 °C (red circles). For data obtained at sample readout temperatures of 50 °C and 150 °C, the OSL signal was corrected for sensitisation using a quadratic function. The lines indicate exponential functions fitted to the experimental data. Risø reader, detection window : U-340.

9.6.2 Optical fading

The optical fading was tested by irradiating the samples with a β dose of 10 Gy, exposing them to white light and measuring the OSL signal. These tests indicated that the signal was bleached within 1 hour of exposure to white light, although 30% of the signal remained after 0.5 h of storage in white light.

9.7 Discussion

The source of luminescence in the "Lynton" class of fire retardant fabrics is likely to be the fillers embedded in the coating, as the extracted coating yielded the OSL signal. The XRF data indicated that these fillers were minerals composed of magnesium, calcium, oxygen and silicon. Several fillers with fire retardancy properties could include these elements, such as wollastonite, sand or dolomite. The XRD spectrum did not formally correspond to these elements, it is thus possible that a mixture of mineral fillers are present in the coating. Furthermore, the TL glow curve of F# 43 (Fig. 9.10a) was similar to the one observed for dolomite or calcium carbonate, but these minerals do not yield an OSL signal.

The class of upholstery fabrics reviewed in this chapter exhibited several properties making them suitable for emergency dosimetry. Their response to dose under blue OSL was found to be sufficiently strong for emergency dosimetry, yielding a detection limit below 500 mGy. Their fading rate was much slower than the blue polyester examined in the previous chapter, rendering dose estimate days to week after the accident manageable. Finally, the homogeneity of the dose response properties amongst samples indicate that if these fabrics are to be found in the scene of a radiological emergency, it would be possible to map the absorbed dose. The type of mineral filler included in the foam coating of these fabrics, however, does not appear to be very commonly used amongst fire retardant fabrics, and more widely used fillers with a luminescence response to dose and less optical bleaching should be sought for emergency dosimetry.

Chapter 10

Case study 3: TL response of calcium carbonate fillers

10.1 Introduction

Calcium carbonate is amongst the most widespread naturally occurring minerals on earth, being 4 % of the earth crust (Wypych, 2016), and natural calcium carbonate is found in biogenic shells, limestone, or stalagmites to only name a few. The high prevalence of calcium carbonate means that it can be obtained at a very low cost; hence it soon attracted the attention of industrialists for its potential as a filler material.

Fillers are powdered minerals, usually carbonates, that are incorporated into polymers during their manufacture and these fillers fulfil several roles. The primary role being that they offer an important cost reduction; polymers made with ground calcium carbonate mineral, for example, can be about 10 times cheaper than common thermoset polymers (DeArmitt and Rothon, 2017). DeArmitt and Rothon (2017) list additional reasons for which fillers are being used, including the increase of heat resistance, stiffness, abrasion resistance, moisture resistance, biodegradability, and processability. They are also used to modify adhesion, change electrical properties, appearance, opacity, and surface gloss.

Table 10.1 lists the most common fillers used commercially, with their estimated consumption during the year 1993. Amongst the materials listed in Table 10.1, some of the mineral types have already investigated for their luminescence dosimetry properties (quartz; Göksu et al. 2006; Bailiff

Table 10.1: Most common plastic fillers and their world-predicted consumption during the year 1993, in million of kilograms (Katz and Mileski, 1987).

Plastic filler	Consumption during the year 1993 (in millions of kg)
Aluminium trihydrate	151
Antimony oxide	4
Gypsum	12
Barite	3
Calcium carbonate	**2450**
Wollastonite	107
Clay-based	147
Talc and pyrophyllite	92
Quartz and Silica	72
Carbon black	45
Microspheres	35
Synthetic silicates	5
Metal and magnetic	11
Titanium dioxide	142

1997; Ichikawa et al. 1987, and gypsum; Thompson et al. 2010), but not in the form of fillers. Although calcium carbonate is well know for its bright thermoluminescence response to dose (Fig. 10.3; Sunta 1984), its potential as a dosimeter material for emergency applications has not yet been investigated.

The high prevalence of calcium carbonate as a filler is quite striking in Table 10.1, with a consumption of some 2.5 million of tonnes per year. The market of calcium carbonate fillers seems to be in constant expansion; in 2016 Wypych (2016) reported that calcium carbonate constituted 2/3 of the fillers market with 7.5 million tonnes produced per year, most of it being destined for PVC or thermosetting polymers. Calcium carbonate fillers are manufactured from natural calcium carbonate limestone, which is crushed, washed, and through a process of coarse grinding and sieving is transformed into filler (Wypych, 2016). Fig. 10.1 shows the steps of the manufacturing process from calcium carbonate natural limestones to calcium carbonate fillers. The process is designed to be cost-efficient, and the limestones undergo relatively few transformations to become filler.

A wide range of polymer-based products incorporate calcium carbonates fillers, including plastics, construction materials, papers, paints and coatings, cosmetic and pharmaceuticals, fibres, food, and prints (Wypych, 2016), the grains selected differing according to application. Fig. 10.2 shows how limestone can be processed for different applications, beyond their use as fillers.

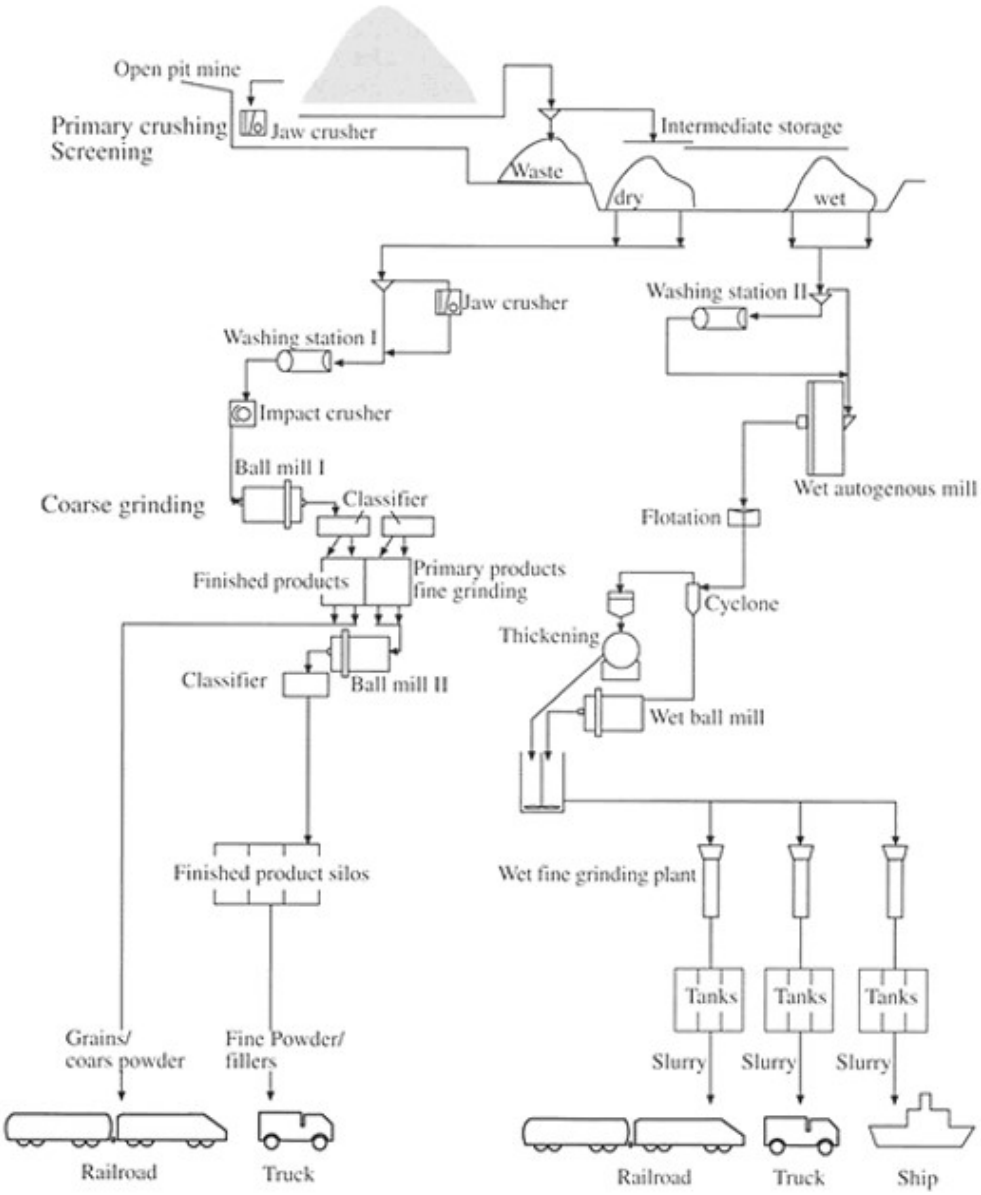

Fig. 10.1. Schematic representation of the process of transforming calcium carbonate limestone to filler material. Reprinted from http://www.calcium-carbonate.org.uk/calcium-carbonate/caco3-processing.asp.

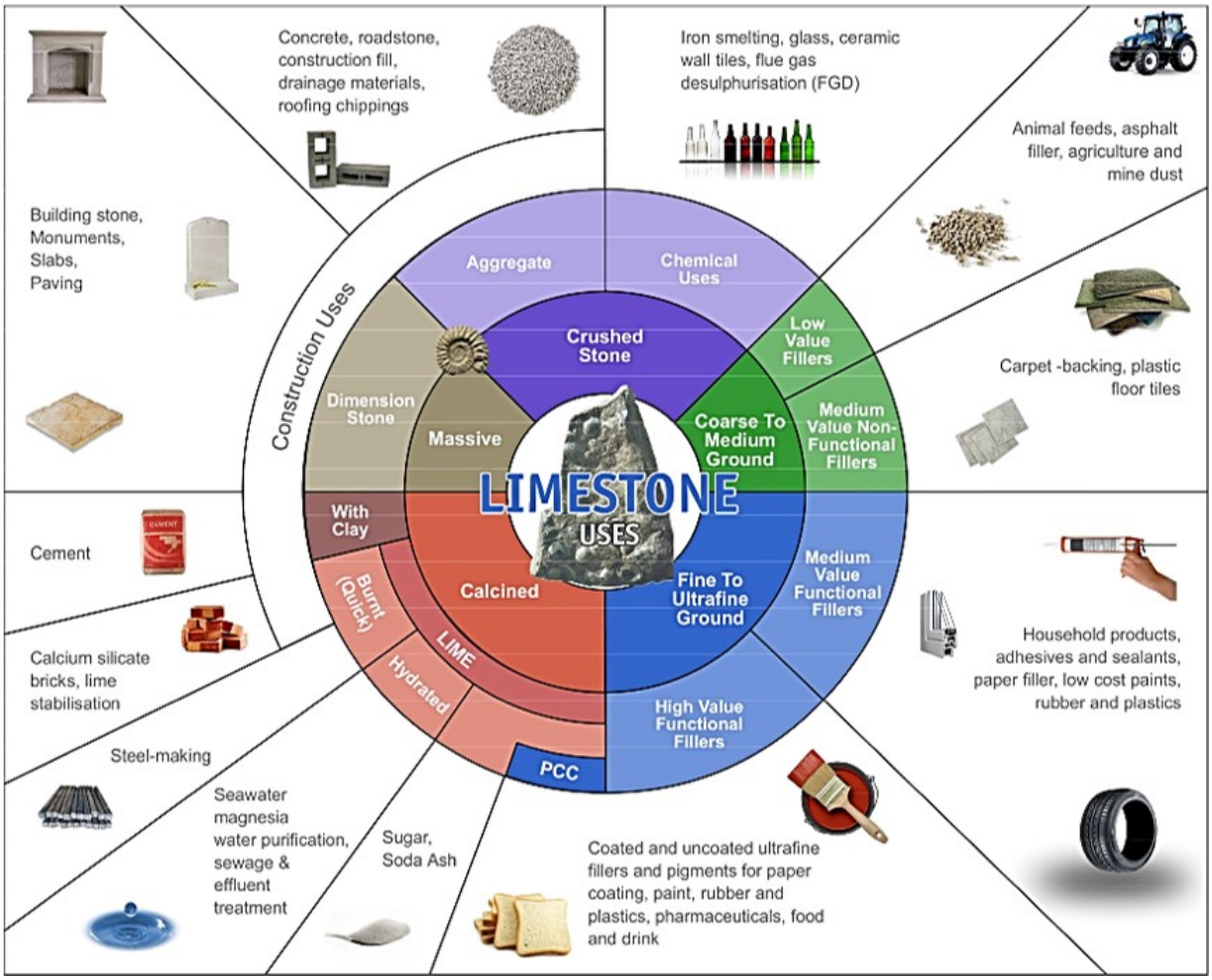

Fig. 10.2. Processing and use of calcium carbonate limestone. Reprinted from http://www.longcliffe.co.uk/pdf/ The%20Processing%20and%20Major%20Uses%20of%20Limestone.pdf.

Fig. 10.3 compares the TL signal of ground calcium carbonate limestone with that of calcium carbonate fillers extracted from a handbag polymer (use of calcium carbonate fillers, specifically in the polymer coating of the handbag), and a similar shape of TL glow curve is obtained. The TL luminescence characteristics of calcium carbonate limestone has been widely studied for over 50 years as the material produces a bright TL response to ionising radiation (McDougall, 1968), which has been applied to dating studies (Wintle, 1978; Debenham, 1983; Carmichael et al., 1994). The ubiquity of the material combined with a high radiation sensitivity makes of calcium carbonate fillers good candidates to act as a surrogate dosimeters. As naturally occurring calcium carbonate can also be found, in addition to limestone, as stalactites, stalagmites or shells, there is a significant literature on the TL properties of calcite.

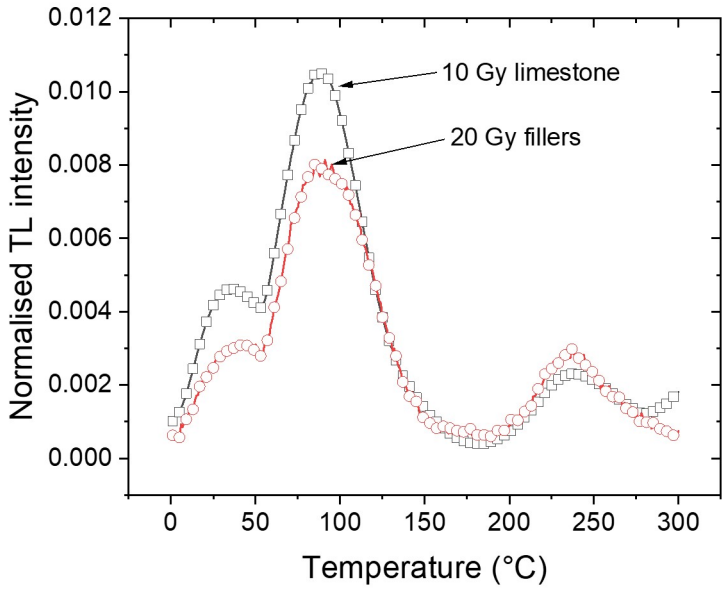

Fig. 10.3. TL glow curves of ground limestone (open black squares) and of calcium carbonate filler extracted from the coating of a handbag polymer fabric (fabric coating, open red circles), following the administration of β doses of 10 and 20 Gy respectively. Risø system, detection window : silica window, heating rate : 0.5 °C.s^{-1}. The TL intensity of each glow curve is the photon count (per 2s intervals) normalized by the total photon count.

Calcium carbonate fillers are incorporated in polymers like thermoplastics such as polyurethane during the manufacturing process. These types of plastics are very commonly found in commonplace

materials, but the work presented here focused on the coatings of bags, often made of polyurethane to improve the resistance and waterproof properties of the bags. The dose response of calcium carbonate fillers in plastics, and more specifically plastic coatings found in accessories such as handbags and backpacks were investigated as they are likely to be in the possession of members of the public in the event of a radiological emergency.

10.2 Thermoluminescence properties of calcium carbonate

10.2.1 TL glow curves

The TL glow curve of calcite was reported to be composed of five main peaks, at 82, 152, 179, 254 and 296 °C using a heating rate of ca 0.3 °C.s^{-1} (Kirsh et al., 1987), with the 82 °C peak being the most sensitive to radiation dose (Fig. 10.4). Some earlier studies (Calderon et al., 1984) have observed shifts between the position of the maximum intensity of these peaks for different types of calcites. The TL glow curve of calcium carbonate fillers does not appear to contain the 152 and 178 °C peaks, but the 82, 254 and 296 °C peaks are present (Fig. 10.3); in the following discussion, the 82 °C peak will be referred to as the "low temperature peak" and the 254 °C as the "high temperature peak". Although the 82 °C peak will be used for emergency dosimetry, the deeper traps might also contribute to the lower temperature peak through charge transfer processes, and thus also have to be examined in detail.

Calcite is well known to exhibit non-radiation-induced (also referred as "spurious") luminescence during TL measurements (Aitken, 1985; Göksu et al., 1988). Some of the spurious luminescence of calcite is attributed to a decarbonation process occurring at the surface of crushed grains during heating, and which can be suppressed by performing TL measurements in a CO_2 or N_2 atmosphere (Roque et al., 2001). Grinding the sample may also induce triboluminescence, but this can be reduced by etching the samples with an acid treatment, or by using slices of samples instead of crushed grains (Wintle, 1975a; Khanlary and Townsend, 1991). Finally, phototransfer may also induce a TL signal, and will be discussed later in Section 10.2.6. As calcium carbonate fillers originate from crushed limestone, and are exposed to natural light during the process, some form of non-radiation-induced luminescence can be expected.

As thermal annealing is generally applied in most dose evaluation procedures, the changes in both sensitivity and glow curve shape previously observed (Franklin et al., 1990; Medlin, 1968;

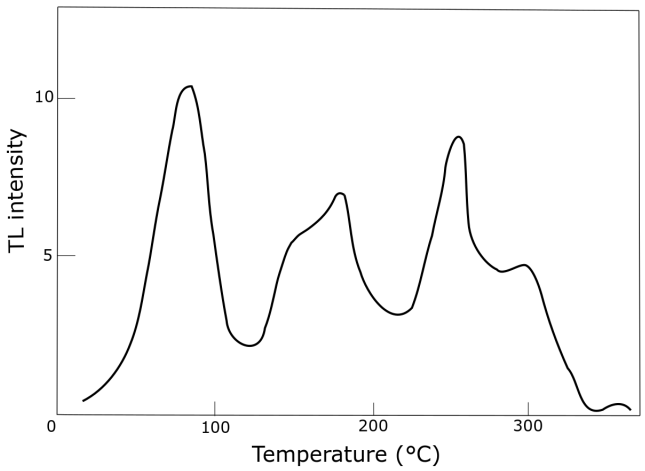

Fig. 10.4. TL glow curve of X-ray irradiated natural calcite crystals (Makhtesh Ramon, Israel). Detection window : (620 ±10) nm, heating rate : 0.33 °C.s^{-1}. The background was subtracted. Redrawn from Kirsh et al. (1987).

Pagonis and Michael, 1994; Borsi and Fornaca-Rinaldi, 1968) are relevant. These authors found that the change in sensitivity observed following annealing was related to the temperature at which the calcite had formed; for calcite formed at low temperature ($\leq$ 100 °C), the sensitivity increased while calcite formed at high temperature ($\geq$ 100 °C) displayed a sensitivity decrease upon annealing at 550 °C. The explanation advanced for this was that heating destroys traps, but also simultaneously produces additional traps because of the stress resulting from heating and cooling the crystals. Down et al. (1985) attributed the diminished sensitivity following annealing at high temperatures ($\geq$ 700 °C) to the high mobility of Mn^{2+} ion, thus destroying the ion's complex formed that acts as a recombination centre. However, annealing at temperatures up to 300 °C appeared to have no effect on the sensitivity of the lower temperature peak (De Lima et al., 2001), and for emergency dosimetry purposes, annealing at 200 °C should be sufficient to erase the trapped associated with the 82 °C peak.

10.2.2 Luminescence centres and mechanism of luminescence

Early work carried by Medlin (1959) attributed the emission of the low temperature thermoluminescence peak (82 °C) of calcium carbonate to Mn^{2+} impurities, located in substitutional sites of the lattice of calcite (Hurd et al., 1954). Introducing Mn^{2+} into a calcite sample by forming calcite crystals in a solution containing Mn ions produced a main TL peak at 77 °C, and minor peaks at 97 and 197 °C, using a heating rate of 0.2 °C.s $^{-1}$ (Medlin, 1959). The luminescence emission is attributed to a $^4G(T_{1g}) \rightarrow {}^6S$ transition of the Mn^{2+} ion (Medlin, 1964; Sommer, 1972). Mn^{2+} is a very efficient activator, and can produce bright TL for concentrations as low as 10 ppm (Visocekas et al., 1973), although Medlin (1968) found that the optimal mole fraction of Mn^{2+} in a calcite sample was of ca 0.002-0.004, after which the intensity of the 197 °C peak decreases. Although the emission is due to Mn^{2+}, the calcite host lattice acts as the electron trapping centre (Medlin, 1964). Medlin (1964, 1968) assumed that the colour centres in calcite are the Ca^+ ions, and that CO_3^- has negligible ionic contribution and low mobility compared with the Ca^+ ions. CO_3^- ions produce hole centres, whereas Ca^+ ions act as electron centres, and upon thermal stimulation (e.g., TL measurement), electrons transfer energy in a non - radiative manner to Mn^{2+} centres, exciting Mn^{2+} ions to a ^4G state. A relaxation transition brings the electrons from the ^4G state to the $^4G(T_{1g})$ state, where they decay radiatively to the ^6S level, producing the light observed during the TL measurements. Mn acts as a recombination centre in this model (referred to as "ion complex" in the previous paragraph). Medlin (1968) first proposed a band diagram for the emission of the Mn^{2+} centre in calcite (Fig. 10.5). In his model, the trapped electron recombines with the trapped hole, which then recombines in a non-radiative manner to the ^{6}S level (thermal bleaching) before being excited to the $^4G(T_{1g})$ level (excitation). Although transitions others than the $^4G(T_{1g}) \rightarrow {}^6S$ appear to be possible, the parabolas of the configuration coordinate diagram associated with the energy levels intersect each other, indicating a strong probability of non-radiative recombination, and explaining why the emission $^4G(T_{1g}) \rightarrow {}^6S$ at 600 nm is dominant. However, more recent measurements have detected additional emission bands in the blue, and prompting a revision of this model (Townsend et al. 1994) to account for the blue emission observed in some samples (see below Section 10.2.3), by showing that transitions others than the $^4G(T_{1g}) \rightarrow {}^6S$ can occur, when including higher energy levels.

In addition to Mn^{2+} ions, Pb, Tl, and Ce were also observed to act as co-activators (Medlin,

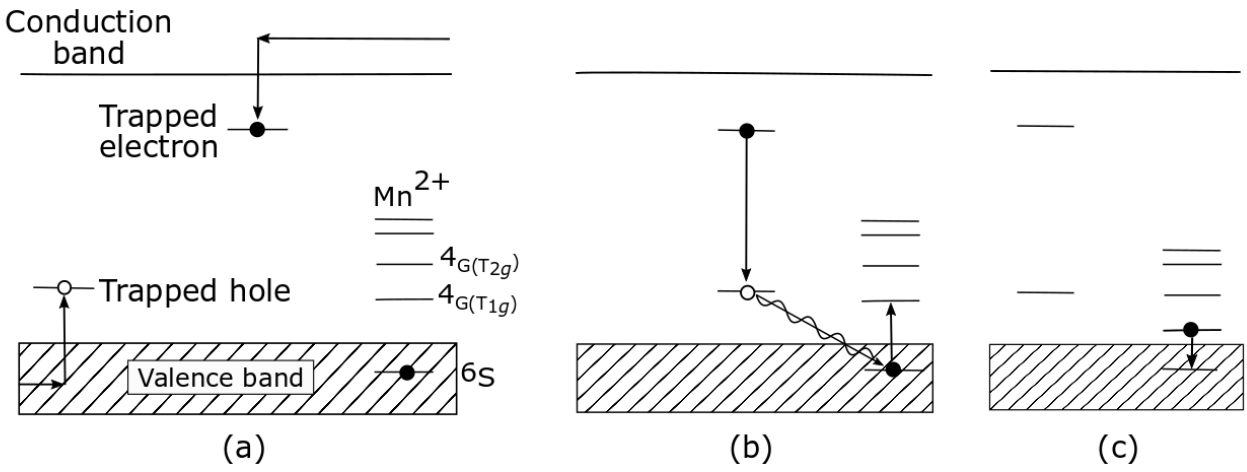

Fig. 10.5. Model for thermoluminescence emission in calcite. a) colour centre formation, b) thermal bleaching of the colour centres and excitation of a Mn^{2+} centre, and c) luminescence emission from the Mn^{2+} centre. Redrawn from Medlin (1968).

1959; Schulman et al., 1947); these ions may capture charge during irradiation and transfer it to the Mn^{2+} ions via a non - radiative cascading process. Schulman et al. (1947) compared the cathode-ray excited emission of calcite samples enriched with the above mentioned activators, and found the TL emission to be the strongest for a sample containing both Pb and Mn, whereas a sample containing only Mn impurities exhibited weak luminescence. However, natural calcite rarely contains Pb (Medlin, 1963), but commonly occurring ions such as Fe^{3+}, Fe^{2+}, Co^{2+} or Ni^{2+} were observed to act as quenchers of luminescence (Medlin, 1963).

10.2.3 Thermoluminescence emission spectroscopy

The TL emission spectrum of calcite is a characteristic orange-red emission, with a main broad peak centred between ca 600 to 700 nm (Fig. 10.6). If the lower temperature peak of the TL glow curve was associated with a broad emission peak centred at 630 nm, the spectra of the higher temperature peaks of the TL glow curve have finer structure, with bands of less than 30 nm wide centred at 560, 600, 640, 705 and 750 nm (Townsend et al., 1994; Down et al., 1985). Fig. 10.6 shows a TL emission spectrum for a calcite grain, where the occurrence of several emission bands for the higher

temperature peak can be seen. The emission of the lower temperature peak seems, however, to be a broad peak. Besides the 630 nm orange emission, Visocekas et al. (1973) observed a narrow emission peak at 373 nm in artificially grown calcite.

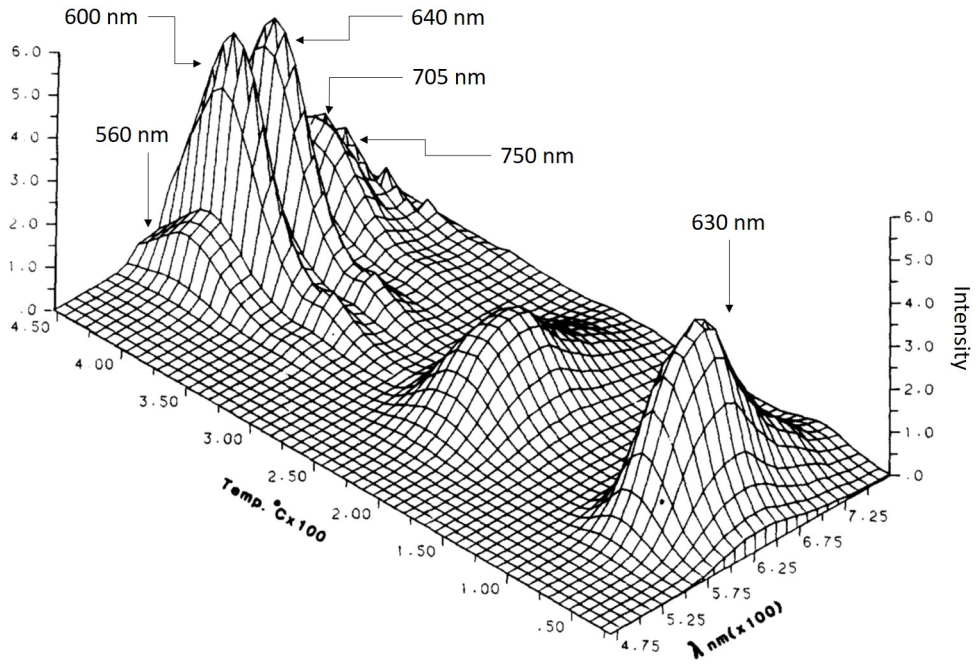

Fig. 10.6. Thermoluminescence emission spectrum of a calcite crystal following X-ray irradiation. Reprinted from Down et al. (1985). The spectrum was corrected for instrument response. Heating rate : 40 °C.min^{-1}.

The emission spectrum was found to be unchanged whether Pb, Tl, or Ce activators were added to the calcite samples (Schulman et al., 1947). However, if a luminescence quencher was added to the sample (e.g., Fe^{2+}), a second minor emission peak was observed in the blue - UV region, with a peak centred around 400 nm (Medlin, 1963). Similarly, the addition of a co-activator also provoked a significant change in the emission spectrum, with an additional strong peak at 450 nm, and a shift of the orange-red emission peak to ca 600 nm.

Sommer (1972) studied the cathodoluminescence (CL) emission spectrum of several carbonates, and revealed that, for Mg-rich calcite, the emission peak varies with the concentration of magnesium; as the concentration in magnesium increases, and the Ca^{2+} ions are replaced by Mg^{2+} ions, the maximum of the emission peak is shifted to higher wavelengths. When there is no magnesium present in the $CaCO_3$ sample, the peak maximum is around 590 nm, whilst a $MgCO_3$ sample has

an maximum of emission at 670 nm. This behaviour is predicted by crystal field theory (Sommer, 1972); as the proportion of Mg^{2+} ions increases, the metal-oxygen bond length decreases, and the crystalline electric field increases. Consequently, the energy levels of the excited states Mn^{2+} decrease, and the emission occurs at longer wavelengths.

Finally, Calderon et al. (1996) studied the emission spectrum of 28 carbonates samples, and found that a correlation could be drawn between the Mn concentration and the emission bands. For samples containing a large concentration of Mn, the emission took the form of a broad peak, whilst for samples with a low concentration of Mn, the emission was resolved into narrower bands.

10.2.4 Dose response

The peak of the TL glow curve potentially most suitable for emergency dosimetry is the lower temperature peak (82 °C), as this temperature range would enable the direct measurement of fillers embedded in the plastic (without prior removal of the fillers), and avoid issue of a native signal related to the higher temperature region. However, little is said in the literature about the dose response characteristics of the lower temperature peak. Although Chithambo et al. (2014) studied the dose response of this peak and found a sub-linear dose dependence in the range of dose 200 - 1400 Gy; and De Lima et al. (2001) found a saturation dose value for the lower temperature peak of ca 10^4 Gy, the low dose behaviour of this peak does not appear to have been well characterised in the low dose region so far. The higher temperature peak was studied for dosimetry purposes, and was found to exhibit a linear dose response in the range 0.10 mGy-5.40 Gy (Kalita and Wary, 2016).

The energy response to photons of the high temperature peak was studied by Engin and Güven (2000) and they found a peak in the energy response for photons below 200 keV. The response peaked at a photon energy of 140 keV, where the sensitivity was approximatively 8 times higher than that obtained for energies above 200 keV.

Although no TL emission has been reported following neutron exposure, Silletti et al. (2012) reported a change in some features of the cathodoluminescence spectra upon neutron irradiation, producing a shoulder in the CL spectrum at 515 nm, in addition to the main 600 nm peak. The growth of the feature at 515 nm increased linearly with neutron dose, for a neutron flux in the range (2.46×10^{12}-2.46×10^{13}) neutrons/cm^2, which prompted the authors to propose calcite as a passive

dosimeter for forensic detection of nuclear material emitting neutrons.

10.2.5 Fading

The 82 °C peak, has been examined to be unstable with storage time (Singh and Ingotombi, 1995), and kinetic studies have attributed a lifetime of a few hours at ambient temperature (see Section 10.2.7 below). Visocekas (1979) identified a mechanism of athermal loss of charges associated with TL peaks by measuring the TL of calcite samples following storage in liquid nitrogen and noticed a subsequent loss of the signal below 130 °C, which he attributed to the presence of tunnelling of charge. Section 10.2.7 contains a discussion of a tunnelling model for calcite.

Most of the literature focused on the stability of the 296 °C peak, which showed negligible fading (Kalita and Wary, 2016). Furthermore, a calculated lifetime of $\sim 10^6$ years at room temperature deemed this peak suitable for dating applications (Debenham, 1983; Wintle, 1977b).

10.2.6 Optical effects

Pure calcite has a fundamental lattice adsorption for wavelengths shorter than 225 nm (Schulman et al., 1947). Medlin (1964) noted that the ${}^4G(T_{1g}) \rightarrow {}^6S$ transition of Mn is a forbidden transition, and consequently cannot be directly directly optically excited, and for $CaCO_3$:Mn samples (containing no co-activators, such as Pb, Tl or Ce), a lack of fluorescence response under ultra-violet light was observed by Schulman et al. (1947). However, ultra-violet light may be absorbed by a co-activator centre (Pb, Tl, Ce), in the case of Pb, absorption of UV can stimulate the transition ${}^1P_1 \rightarrow {}^1S_0$ or ${}^3P_1 \rightarrow {}^1S_0$ (Medlin, 1963), from which energy is transferred directly to the activator, giving rise to "sensitised" luminescence emission (Dexter, 1953), a process in which an activator emits light because of the absorption of light in a different centre (sensitizer), and subsequent non radiative transfer from the sensitizer to the activator.

In the absence of sensitizers, Medlin (1964) noted that the Mn^{2+} colour centres associated with the TL emission were stable under UV exposure below the sublimation temperature of dry-ice (ca - 80 °C).

Ugumori and Ikeya (1980) used short wavelength stimulation (337 nm) to produce OSL decay curves, and found a linear relation between the OSL signal and the distance from the surface of a natural limestone, indicating that bleaching of the OSL signal by natural light had occurred in

natural calcite samples. Galloway (2002) used a slightly longer wavelength (370 nm), but found an OSL signal decreasing with increasing absorbed dose.

The optical bleaching of the TL signal has been investigated by several authors, for its potential to date the surface exposure of limestone to light. De Lima et al. (2001) studied the decrease of individual TL peaks of calcite following UV exposure (400 W mercury lamp), and found that the intensity of the low temperature peak decreased by about 50% within 30 min of exposure to light, for a previously irradiated sample. The portion of loss attributed to thermal fading in this study is, however, not clear. Other studies focused on the higher temperature peaks, and made similar conclusions regarding the decrease of the TL signal following exposure to sunlight (Liritzis et al., 1996; Bruce et al., 1999; Kim and Hong, 2014). Liritzis et al. (1996) found a loss of signal of the 280 °C peak of 80-90 % after 130 h of solar bleaching.

Finally, Ugumori and Ikeya (1980) found that exposing a previously irradiated sample to a 337 nm illumination reproduced the 80 °C peak, via a phototransfer of charge to the traps responsible for this peak. They attributed a lifetime of 10 hours to this phototransferred TL (PTTL) peak. Phototransfer measurements made by Bruce et al. (1999) using a solar simulator emphasised a competition between phototransfer and bleaching in the region 108-202 °C of the PTTL glow curve. The signal, taken as the TL integral in this region increases for illumination times 0-4 min, and was found to decrease for longer times.

10.2.7 Kinetic parameters

Medlin (1961) first assumed that the decay of phosphorescence observed in calcite resulted from a Gaussian distribution of trapping levels assuming that re-trapping between levels was negligible. Kirsh et al. (1987) set up an alternative model with a distribution of frequency factors, rather than energies, and reported a good correlation between their model and experimental results. Furthermore, Medlin (1961, 1964) argued on the basis of thermally stimulated conductivity measurements that a tunnelling process between holes and trapping centres was involved for the main TL peak at 80 °C. This was supported by the isothermal decay results obtained by Visocekas et al. (1976), where it was shown the isothermal decay at low temperature was independent of the temperature of the measurement, and followed a t^{-1} law (where t is the storage time) which is characteristic of tunnelling. De Lima et al. (2001) also found a t^{-1} decay law of the the TL signal under UV

Table 10.2: Value of activation energy and frequency factor found in the literature, with associated calculated lifetimes at 20 °C and -15 °C.

Reference	Activation energy (eV)	Frequency factor (s^{-1})	Lifetime at 20 °C (h)	Lifetime at -15 °C (h)
Medlin (1961)	0.625	1.4×10^{7}	1.1	32
Visocekas et al. (1976)	0.62	2×10^{7}	0.64	17
Kirsh et al. (1987)	0.73	5×10^{8}	2	100
Pagonis and Michael (1994)	0.72	7×10^{8}	0.96	46
Singh and Ingotombi (1995)	0.85	2.73×10^{10}	4.2	408
Pagonis et al. (1996)	0.78	$(1\text{-}7)\times10^{10}$	0.1-0.72	6-47
Chithambo et al. (2014)	0.90	4.9×10^{11}	1.71	215
Kim and Hong (2014)	0.75	1.1×10^{9}	2	112
Kalita and Wary (2016)	0.60	$(1.17 - 2.47)\times10^{9}$	0.23 - 0.49	6 - 12

exposure, which he similarly attributed to tunnelling, and proposed a thermally assisted tunnelling mechanism from the carbonates groups to the Mn ions in calcite. However, the higher temperature peaks ($\geq$ 100 °C) seem to originate from delocalised transitions, and follow a kinetic of order higher than 1, whilst the 80 °C peak was found to be of first order (Kirsh et al., 1987; Pagonis et al., 1996).

Values of activation energy found in the literature are listed in Table 10.2, and they appear to be relatively consistent with each others with values between 0.60-0.90 eV for the ca 100 °C peak. These relatively low activation energies at relatively high temperature are explained by a tunnelling process (Visocekas et al., 1976). Activation energies of 0.92, 1.01, 1.52 and 1.72 eV were calculated by Kirsh et al. (1987) for the additional peaks (at 152, 179, 254 and 296 °C respectively). If activation energy estimates appear to be relatively consistent, the value of the frequency factor, s, for the 100 °C peak varies between authors. Anomalously low values of 10^{7}-10^{8} s^{-1} have been reported by Medlin (1961); Visocekas et al. (1976); Kirsh et al. (1987); Pagonis and Michael (1994) while author authors reported higher values above 10^{10} s^{-1} (Singh and Ingotombi, 1995; Pagonis et al., 1996; Chithambo et al., 2014). The lifetime at 20 °C and -15 °C were calculated for each values of activation energy and frequency factors, and they indicated lifetimes of a few hours at ambient temperature and 10-400 hours at -15 °C. However, with the possibility of a distribution of traps, the peak shown in Fig. 10.3 may be associated with traps having longer lifetimes, which is a crucial issue for emergency dosimetry.

Kalita and Wary (2014) proposed a band gap model for the TL of calcite (Fig. 10.7), and although this model does not account for a distribution of trapping levels associated with the low temperature peak, the transfer of charge by UV illumination and tunnelling are illustrated in this model.

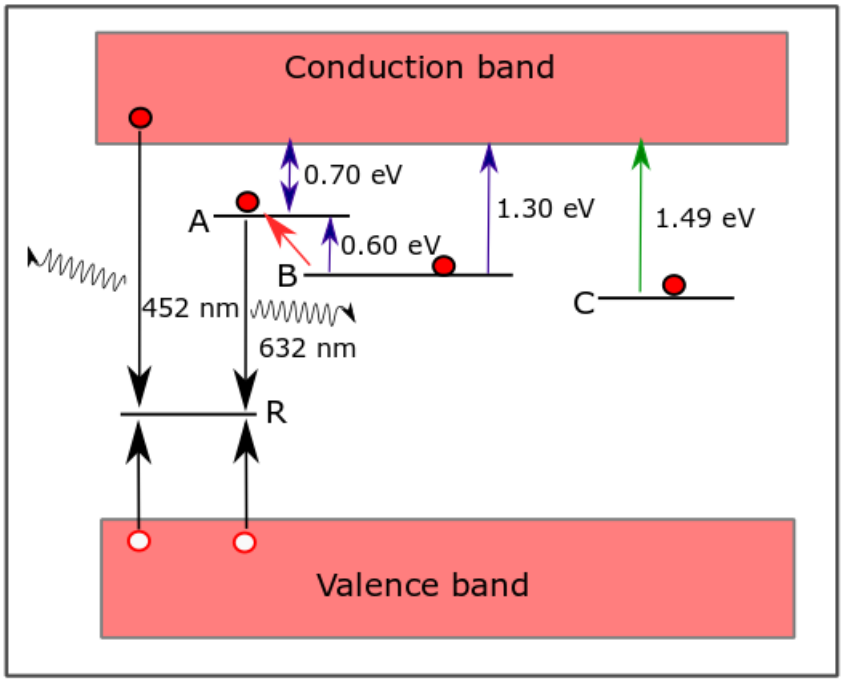

Fig. 10.7. Band gap diagram of calcite showing trapping levels (A, B and C) and a recombination centre (R). The open circles indicate holes and the red filled circles electrons. The black arrows show transitions at the recombination centre; the green arrow represents the charges transferred to the conduction band by UV stimulation; the blue arrows indicates the transfer of charges by thermal stimulation (TL); the red arrow accounts for tunnelling. Redrawn from Kalita and Wary (2014).

As the 82 °C temperature peak results from a continuum of trapping levels, the usual method to determine the kinetics parameters have to be applied cautiously. Pagonis and Michael (1994) used various techniques to calculate the kinetic parameters associated with the low temperature peak, and found some of them to be inconsistent for a peak resulting from a distribution of trapping levels. Whereas the T_{max}-T_{stop} procedure combined with the initial rise method is a good indicator of the presence of a distribution of E values, it does not always provide reliable information on the

trap depth. The whole glow peak method, using the total integral of a peak, is not applicable for overlapping peaks; and for several overlapping peaks, the isothermal decay curves would be the sum of the linear plots which are nearly impossible to analyse (McKeever, 1988, p. 103). However, a curve fitting procedure is potentially suitable, if a narrow distribution of energies can be assumed.

Thermal annealing was found to have an effect on the TL kinetic parameters of calcite (Pagonis et al., 1996; Medlin, 1961). The decay of phosphorescence yielded a significantly longer lifetime, the width of the Gaussian distribution of energies of the first peak narrowed down following annealing above 500 °C, explaining why the TL peaks change both in shape and sensitivity.

Whilst the kinetics of the 82 °C peak have been thoroughly examined, there seems to be a lack of information regarding the dose response and fading characteristics of this peak. This chapter will therefore aim to both compare the thermoluminescence characteristics of calcium carbonate used as fillers in coatings with results reported in the literature, and where needed to complete the existing literature. The issues that will be addressed in this chapter are : 1) how do the thermoluminescence properties of calcium carbonate fillers found in the coating of bags compare to the properties of the TL calcite described in the literature? 2) Are these properties suitable for emergency dosimetry applications, especially in terms of fading and dose response? And finally, 3) what are the optimal protocols and instrumentation for dose determination using calcium carbonate fillers?

10.3 Samples and protocol

10.3.1 Samples

The samples used in this chapter comprised a set of nylon fabrics coated with polyurethane (PU), and of a set of handbags and backpacks. The bags were obtained second hand, and were different in their fabric composition, colour and structure. In some cases, the fabric of the bag was made of woven fibres coated with polyurethane that contained calcium carbonate, and in others the fabric composing the bag was made of a thermoplastic fabric containing the fillers, in the case of a faux-leather polyurethane sheet. Tables 10.3 and 10.4 list the samples with their colour. Calcium carbonate fillers were identified using their characteristic TL response and powder X-ray diffraction (XRD) measurements. Fig. 10.8 shows an example of a red faux leather bag (bag 16), in which calcium carbonate fillers were identified within the red plastic outer layer, and an internal layer of padding was also found to contain a similar filler. Fig. 10.9 shows a backpack (bag 11) where calcium carbonate fillers were found in the coating of the fibres (Fig. 10.9). Swatches of fabric 179, "LED" conference bag, bag 21 (woven fibres coated with thermoplastic) and bags 16 and 19 (thermoplastic faux leather) are provided in Appendix A.

Fig. 10.8. Image of bag 16. This bag was composed of a red faux-leather fabric in which calcium carbonate fillers were identified.

Fig. 10.9. Image of bag 11 (upper image) with the coated outer side containing calcium carbonate fillers indicated (lower image).

Table 10.3: List of the nylon fabric samples coated with polyurethane and their colours. The calcium carbonate fillers were identified in the polyurethane coating.

Sample	Colour
F# 179	White
F# 201	Light grey
F# 202	Dark olive
F# 203	Dark navy
F# 204	Black
F# 205	Emerald
F# 206	Red
F# 207	Purple
F# 208	White
F# 209	Yellow
F# 210	Royal
F# 211	Orange
F# 212	Wine
F# 213	Pink
F# 214	Taupe
F# 215	Bowen

Table 10.4: List of bag samples and their colours

Sample	Colour	Fabric description
"LED conference" bag	Black	Woven fibres coated
"RPW conference" bag	Black	Woven fibres coated
Bag 3	Dark blue	Woven fibres coated
Bag 4	Blue	Woven fibres coated
Bag 5	Black	Woven fibres coated
Bag 6	Black	Woven fibres coated
Bag 7	Blue	Woven fibres coated
Bag 8	Black	Woven fibres coated
Bag 9	Black	Woven fibres coated
Bag 10	Black	Woven fibres coated
Bag 11	Grey/brown	Woven fibres coated
Bag 12	Grey	Woven fibres coated
Bag 13	Blue	Woven fibres coated
Bag 14	Black	Woven fibres coated
Bag 15	Blue	Woven fibres coated
Bag 16	Red	Faux leather plastic
Bag 17	Green	Faux leather plastic
Bag 18	Brown	Woven fibres, faux leather plastic
Bag 19	White	Faux leather plastic
Bag 20	Glossy pink	Thermoplastic
Bag 21	Black	Woven fibres coated

10.3.2 Experimental techniques

For TL and OSL measurements, the samples were cut (ca 5×5 mm) to fit in stainless steel cups, and placed with the coating facing upward. TL glow curves were measured at a heating rate of 0.5 °C.s^{-1} to a T_{max} of 200 °C. Calcium carbonate fillers were also extracted from the coating and deposited on stainless steel discs, either manually or using a vacuum pump, and for these measurements a T_{max} of 350 °C was used. A T_{max} of 200 °C was necessary when measuring the TL of coatings to minimise the thermal degradation of the plastic. Unless specified otherwise, times between exposure and read-out were less than 5 minutes. All TL and OSL measurements were conducted in a Risø model 12 reader (see Chapter 6 for details of the instrumentation) that incorporated a ^{90}Sr/^{90}Y β source. The dose rate delivered by the source in the reader was determined by placing a few grains of quartz on top of samples of fabrics cut from bags, and measuring the OSL of the quartz using a U-340 UV filter in the detection unit. A U-340 filter enables detection of the signal from the quartz, but not from the calcium carbonate fillers. The dose rate delivered was determined to be of (0.86±0.02) Gy.min^{-1}. Further details on the dose rate delivered to grains of calcium carbonate in a polyurethane (PU) matrix will be given in Chapter 12. The PMT primarily used for the detection was an EMI 9635. Another PMT, the Hamamatsu R2949 was also employed in this chapter, for its enhanced sensitivity in the red. The detection window either comprised the fused silica window, or an OC 12 filter (550-3000 nm band pass). The measurements of fading and dose response were repeated on several samples of the same bag or fabric to test for the uniformity of the response. Each sample of the set (Tables 10.3 and 10.4) was tested for its TL response and fading characteristics.

The OSL measurements were conducted using the EMI 9635 PMT, and the samples held at a temperature of 50 °C during measurements. When the blue stimulation (470 nm) LEDs were employed, the signal was detected through a UV filter (U-340), and when IR stimulation (850 nm) was used, a broad band filter (BG-39) was employed.

The scanning electron microscope (SEM) and cathodoluminescence (CL) measurements were conducted using a Hitachi SU-70 field electron gun (FEG) scanning electron microscope, coupled to a Gatan Mono-CL cathodoluminescence and a Pixis CCD for cathodoluminescence spectroscopy and imaging. The samples were cut into square and deposited on carbon patches for the SEM and CL analysis. Additional measurements were conducted on calcium carbonate fillers extracted from the

fabrics using a vacuum pump, and deposited on carbon patches. The SEM and CL measurements were conducted at a beam voltage of 10 kV (44 mA). The CL spectroscopy measurements were collected using a single photon counting mode and a monochromator 1200 lines/mm diffraction grating with entrance and exit slits set to 5 mm (30 nm FWHM).

Mapping and point X-ray fluorescence (XRF) measurements (Oxford Instruments EDX system, X-MaxN 50 Silicon Drift Detector) were conducted on calcium carbonate fillers extracted from the fabrics. The X-ray diffraction pattern was obtained using a Bruker AXS D8 Advance equipped with a Lynxeye Soller PSD Detector. The source of X-ray was a copper tube producing a mixture of Cu-$K_{\alpha 1}$ and Cu-$K_{\alpha 2}$ at a wavelength of 1.5406 Å. XRD measurements were carried out on cut samples of fabrics.

10.4 Material characterisation

An optical microscope observation of the coating of the fabrics forming the bags revealed the presence of numerous crystal - like inclusions, likely to be calcium carbonate fillers. They appear as white dots in Fig. 10.10, and they were visible at the surface of the coating, but were more readily identified once the surface of the coating had been scraped using a scalpel blade. They were loosely bonded to the PU matrix and easily removable.

10.4.1 Scanning electron microscope imaging

SEM images produced further details of the fillers embedded in the polyurethane coating or the plastic fabric of the bags (Fig. 10.11a). To better observe the shape and size of the fillers found in the coatings, the grains were extracted from the PU matrix using vacuum tweezers and deposited onto a carbon patch, suitable for SEM analysis (Fig. 10.11b). The size of the fillers was found to vary from tens of microns to a few microns, and the shape of the grains was also observed to be very variable with sharp edges, characteristic of poorly sorted recently crushed material.

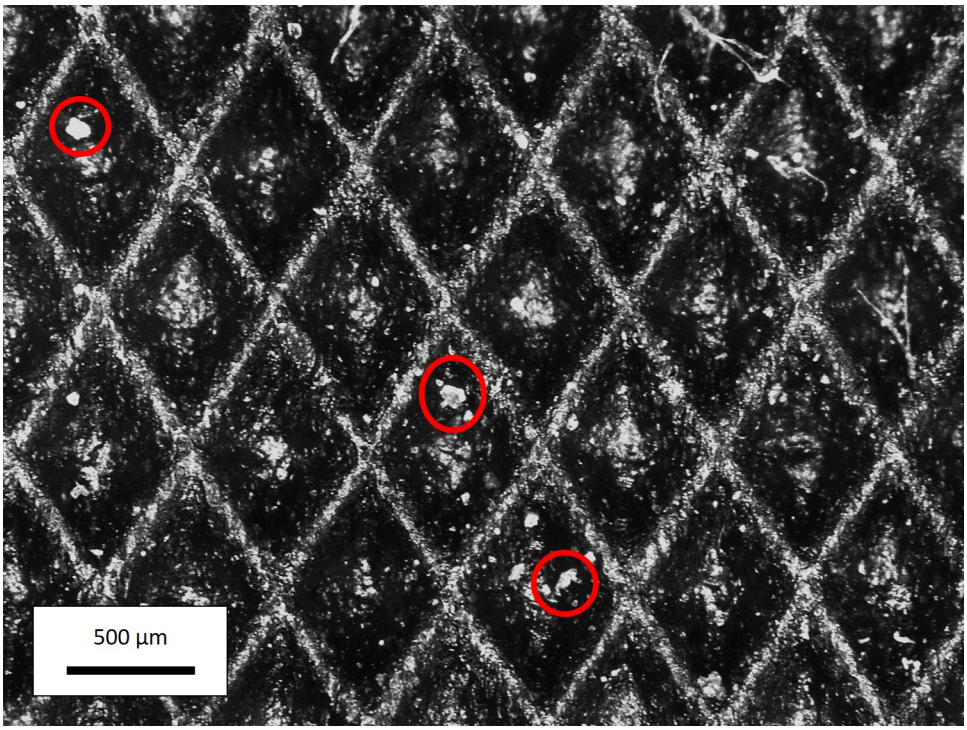

Fig. 10.10. Optical microscope image of the PU coating of the "LED conference bag", showing the calcium carbonate fillers included in the PU coating (circled in red). Magnification × 6.

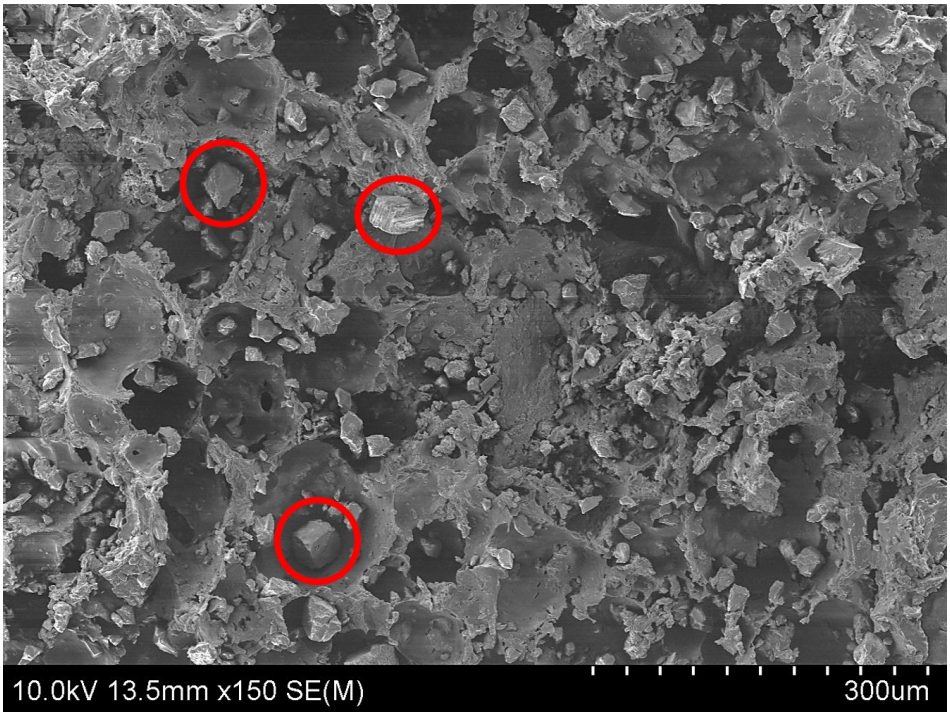

(a)

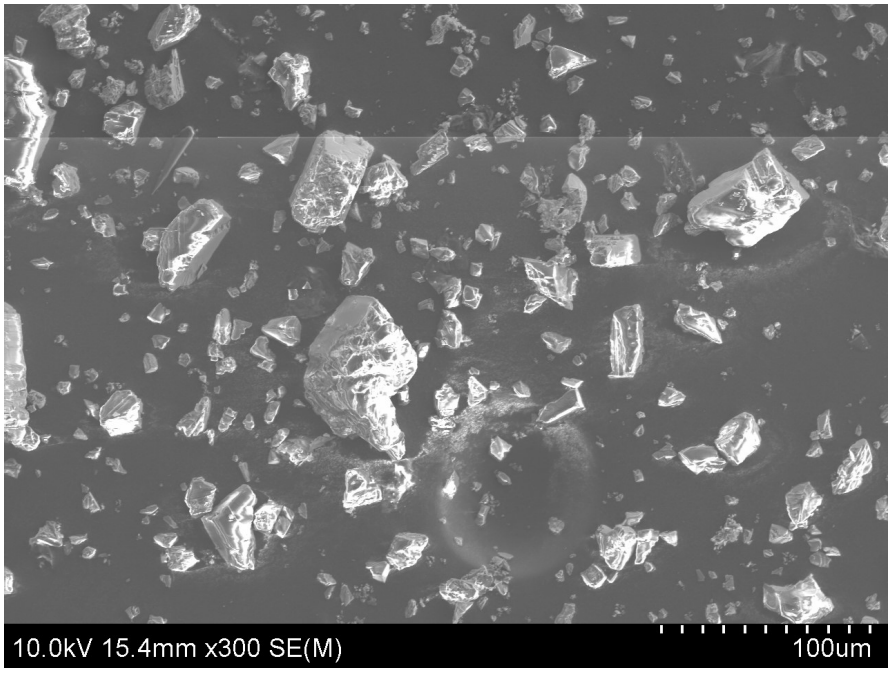

(b)

Fig. 10.11. a) SEM image (secondary electrons) of the fabric of bag 19, sample coated with 10 nm of platinum. The red circles identify some calcium carbonate fillers. b) Image of inclusions extracted from the PU matrix of F# 204 (uncoated samples). Electron beam 10 kV in both cases.

10.4.2 Elemental analysis

X-ray fluorescence

Point X-ray fluorescence (XRF) spectrum obtained with grains extracted from the PU coating are consistent with a carbonate composition (Fig. 10.12) and spatially resolved measurements indicated a homogeneous composition across the samples tested. The presence of magnesium was found in some samples (Fig. 10.12b) suggesting that the source of some fillers was a magnesium limestone.

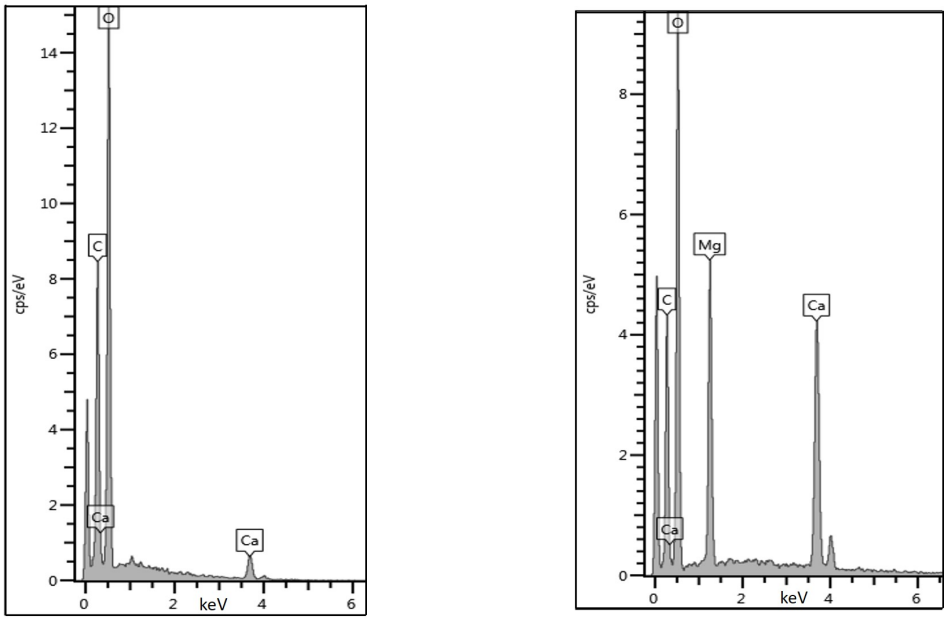

(a) **(b)**

Fig. 10.12. XRF spectrum of fillers grains extracted from the PU coating of a) bag 16 and b) bag 21 fabrics.

X-ray diffraction

Fig. 10.13d shows the X-ray diffraction pattern of F# 179 (white nylon fabric coated with PU). The many narrow peaks in the diffraction spectrum indicate the high crystallinity and the pattern corresponds to that of calcite (Fig. 10.13 a). Additional lines of unidentified minerals were also present that could correspond to minerals found in quarries (dolomite, sand or chert; Folk 1962). Other samples (e.g., bag 16, Fig. 10.13b) were dominated by calcite. The broad peaks observed in some samples at low angles (Fig. 10.13c) are likely to correspond to the plastic (polyurethane

or others) in which the calcium carbonate fillers are embedded . Although some variations were observed in the XRD pattern of the samples tested, the peaks corresponding to calcite were found in all the samples producing TL.

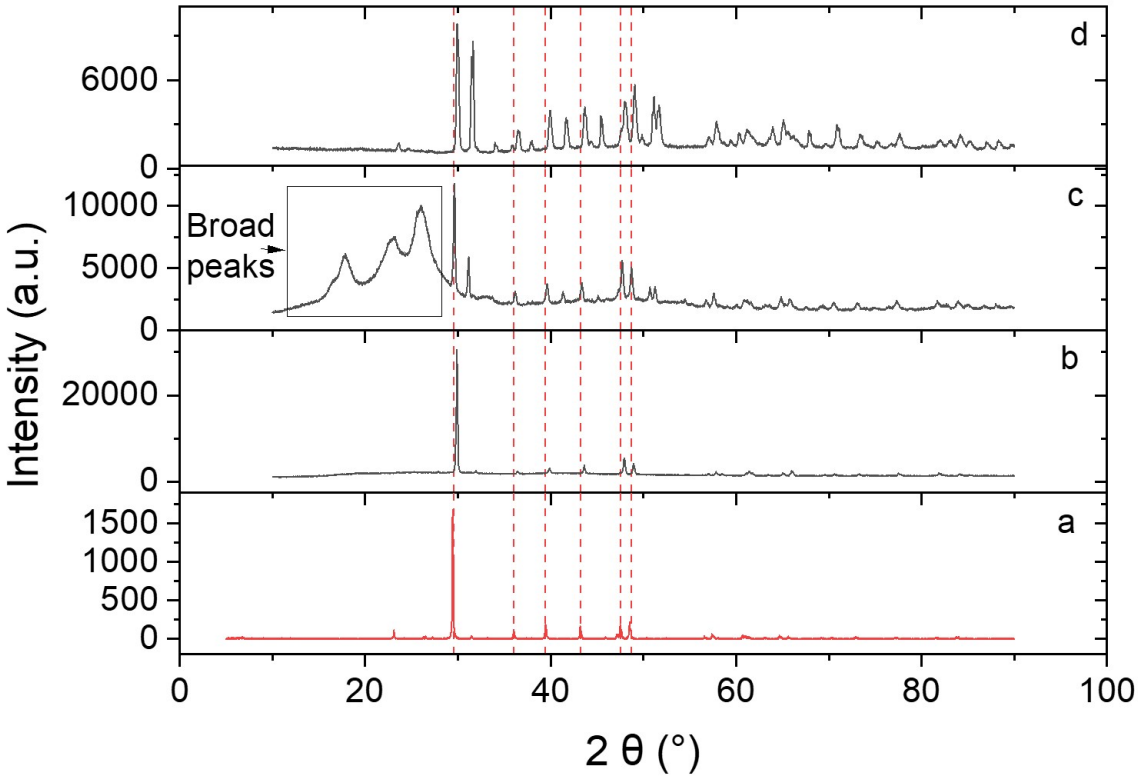

Fig. 10.13. XRD pattern a) calcite, b) bag 16, c) bag 21 and d) F# 179. The broad peaks likely to correspond to the polymer are indicated by a square in (c). The broken lines indicate position of the characteristic peaks of calcite.

The XRF and XRD spectra confirmed the nature of the inclusions found, most likely to be ground limestone.

10.4.3 Cathodoluminescence

Cathodoluminescence imaging

Cathodoluminescence (CL) imaging, performed on the PU coating of a bag (the "LED conference" bag) revealed that the fillers exhibited strong CL (Fig. 10.14), whereas the PU matrix, in comparison, was relatively dim. To obtain a better image, the surface of the coating was lightly scraped with a scalpel blade and the sample coated with 10 nm of platinum to avoid charging.

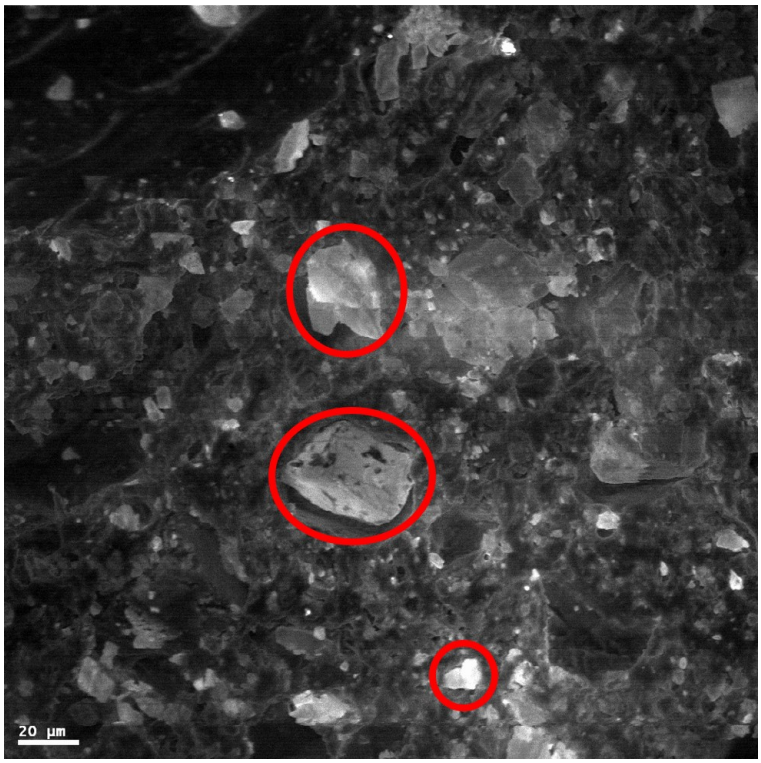

Fig. 10.14. CL image of the "LED conference bag", sample coated with 10 nm of platinum, electron beam 10 kV. The red circles indicate some calcium carbonate fillers.

Cathodoluminescence spectroscopy

The CL spectrum of the fillers was very broad, extending over the range of the spectrometer with several emission bands above 500 nm (Fig. 10.15) and a dominant peak around 630 nm, characteristic of the orange-red emission of calcite (Down et al., 1985). A second peak in the blue (400 nm) was also indicated. The spectrum, when deconvoluted using Gaussian functions, contains

peaks with energies of 1.85 eV, 1.92 eV and 2.95 eV (Fig. 10.15b). This is consistent with TL emission spectra of calcium carbonate reported, with a main emission in the red centred around 620 nm (2 eV; Sunta 1984). Based on the data obtained by Sommer (1972), a peak maximum ~ 650 nm for the "LED conference bag" corresponds to an high Mg content sample (ca 60-70 % mole content).

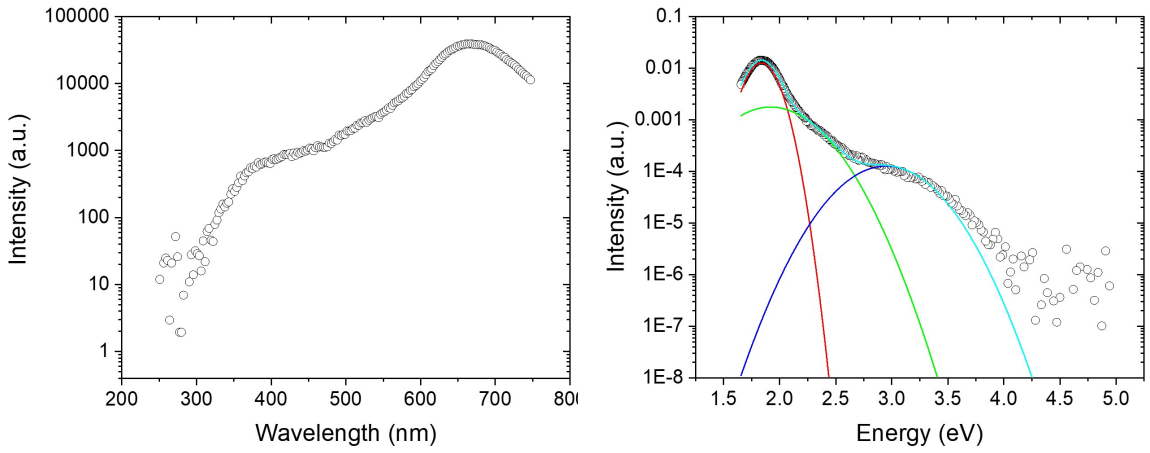

(a) **(b)**

Fig. 10.15. a) "LED conference bag" CL spectrum, wavelength scale and b) energy scale showing Gaussian functions fitted to the spectrum, centred at 1.85, 1.92 and 2.95 eV. The spectrum was corrected for instrument response and the spectrum intensity has been corrected for the energy scale.

10.5 OSL and IRSL response

The OSL (blue stimulation, 470 nm) signal of an unirradiated sample of F# 179 (white nylon fabric coated with PU) was significantly above background (ca 200 photon counts per 0.02 s, see Fig. 10.16a) that increased with the illumination time (to ca 500 photons counts per 0.02 s). Repeated measurements showed the same level of response, indicating that this sample is subject to a photo - stimulated process. Following a 10 Gy β dose, the signal read straight after the irradiation ($\leq$ 5 min) with a sample temperature of 50 °C decreased slightly. However, the photo-stimulated luminescence was only observed in white samples, indicating that it may be associated with a dye or bleaching process of the plastic, and not associated with the calcium carbonate filler. Although no significant response to β radiation was observed under OSL, the UV emission detected is consistent with the weak UV emission band in the UV region in the CL spectrum (Fig 10.15a).

The IRSL response of F# 179 (white nylon fabric coated with PU) exhibited a signal that was dependent to dose (Fig. 10.16b), although the form of the signal did not follow a conventional decay curve, remaining constant to one second of stimulation and slowly decreasing thereafter. The likely explanation for the form of this signal is a thermally assisted release of charge from shallow traps, induced by holding the sample at a temperature of 50 °C. The temperature of 50 °C was initially chosen to block the shallowest traps during the IRSL measurement. For higher samples temperature during the IRSL measurements, the intensity of the signal increased but the shape of the signal remained similar to samples temperatures of 150 °C.

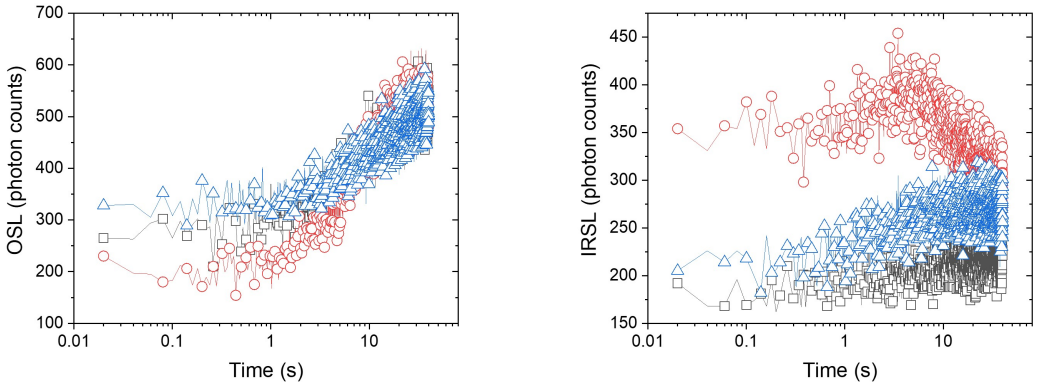

(a) **(b)**

Fig. 10.16. a) OSL response of F# 179, and b) IRSL response of F# 179. Open squares : native signal; open circles : signal following 10 Gy β dose; open triangle : subsequent residual signal. Risø system, detection filters : U-340 (OSL) and BG-39 (IRSL), sample temperature : 50 °C.

10.6 TL response

10.6.1 Detection window

The CL measurements indicated a strong luminescence emission around 630 nm (Fig. 10.15a). To optimise the measurement of the TL emission of the 82 °C peak, the TL was measured using different detection windows, by inserting various sharp cut filters (HC11, HC15, OC12, KC11, KC15 and KC19) in the detection system. Fig. 10.17a and 10.17b shows the transmission of the filters used.

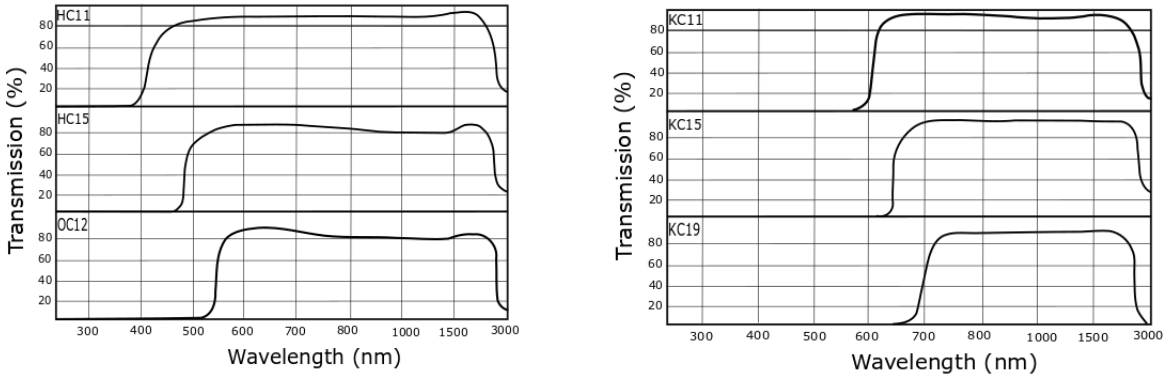

(a) **(b)**

Fig. 10.17. Transmission of the sharp-cut optical filters used. a) HC11, HC15 and OC12, b) KC11, KC15 and KC19.

The TL signals were recorded with a sample of bag 16 (red faux leather handbag) following β irradiation 1 Gy using the different filters (Fig. 10.17a and 10.17b). The TL signal (integral 140-160 °C) for each filter was normalised to the signal obtained using the fused silica window only ($\geq$ 175 nm) and plotted in Fig. 10.18 against the wavelength of the sharp-cut (lower range). As can be seen on Fig. 10.18, the TL signal was only significantly reduced when filters transmitting wavelengths longer than ca 600 nm were used. This indicates that the blue emission is minor in this sample, and that the emission around 600 nm is predominant for the 100 °C TL peak. Furthermore, the TL signal measured using the filter KC 19 ($\geq$ 700 nm) is still of ca 16% of the signal measured using filter HC 11 ($\geq$ 400 nm), indicating the presence of emission above 700 nm. These results are consistent with the broad emission bands observed by Medlin (1959).

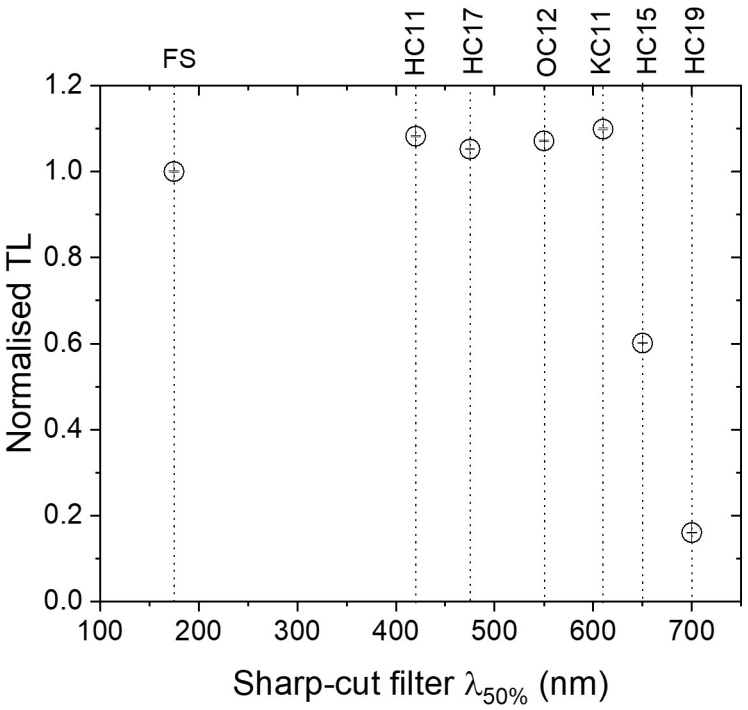

Fig. 10.18. TL integral in the region 140-160 °C of bag 16 following β irradiation (1 Gy) using different sharp-cut filters. The x axis indicates the wavelength above which the transmission of the filter is at 50% ($\lambda_{50\%}$). The TL signals have been normalised to the intensity of the signal detected through a silica window (detection above 175 nm). PMT : Hamamatsu R2949. Filters : HC11 ($\geq$ 400 nm), HC17 ($\geq$ 500 nm), OC12 ($\geq$ 550 nm), KC11 ($\geq$ 600 nm), KC 15 ($\geq$ 650 nm) and KC 19 ($\geq$ 700 nm).

10.6.2 TL glow curve

All the samples tested (Tables 10.3 and 10.4), except bags 3 and 8, were found to produce a TL signal following the administration of a radiation dose. The fibres composing the fabric (woven fibres) of bag 8 were uncoated and bag 3 was coated with a thermoplastic that did not contain calcium carbonate fillers. Bag 8 presented an interesting case, where calcite was detected in the sample by the means of XRD, but no TL signal was detected. However, additional EPR measurements did not detect the presence of the Mn^{2+} radical, indicating that the type of calcite included in the sample did not contain manganese, thus preventing the emission of light (see Section 10.2.2).

Following exposure to ionising radiation, the remaining samples exhibited a TL glow curve of similar shape when using a heating rate of 0.5 °C.s^{-1}, with two relatively broad peaks located below 200 °C, centred at ca 25 and 100 °C (Fig. 10.19a), except for some samples where the peak positions were shifted (Fig. 10.19b). A native signal was also observed in some unirradiated samples, as shown in Fig. 10.19a. The native glow curve is different in shape to the β induced TL glow curve with the TL signal increasing steadily with temperature above 125 °C. The possible origin of this native signal is discussed further below. In some samples, a high background signal was observed at temperatures above 100 °C (Fig. 10.20). This background signal was independent of dose and was also observed with unirradiated samples. It was found to be reproducible, indicating that it was not associated with residual trapped charges, but was possibly induced by a chemiluminescence process, or other form of luminescence occurring at high temperatures.

The brightness of the TL signal was found to vary from one sample to another, which is reflected in the variability of the values of the estimated detection limit of the samples (see Section 10.6.5).

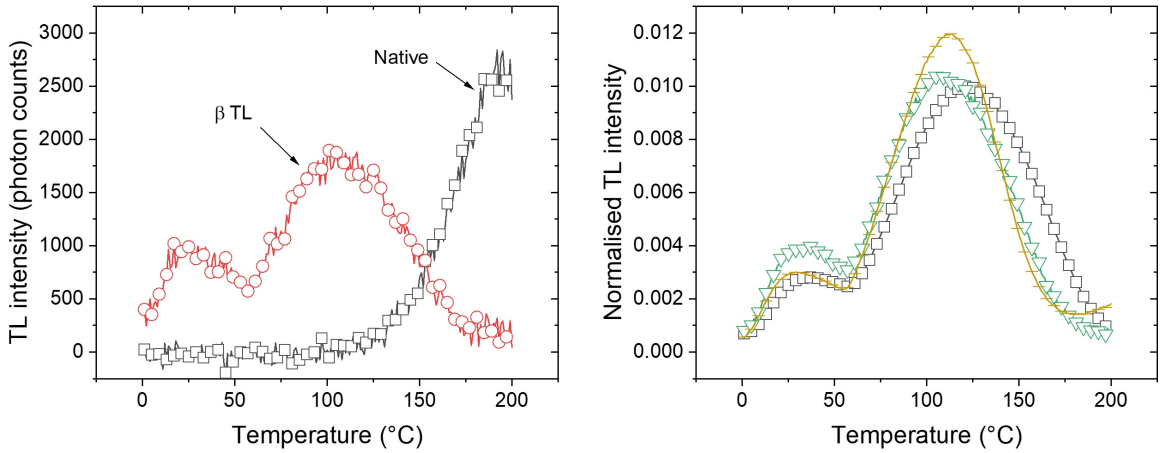

(a) **(b)**

Fig. 10.19. a) Native TL and TL following a 1 Gy β dose administered to a sample of bag 5. b) TL following a 10 Gy β dose to samples taken from bags 19 (open black squares), 4 (open inverted green triangles) and F# 179 (golden horizontal bars). The glow curves were normalised by the total number of photon counts. Detection window : fused silica window, heating rate : 0.5 °C.s^{-1}, no preheat.

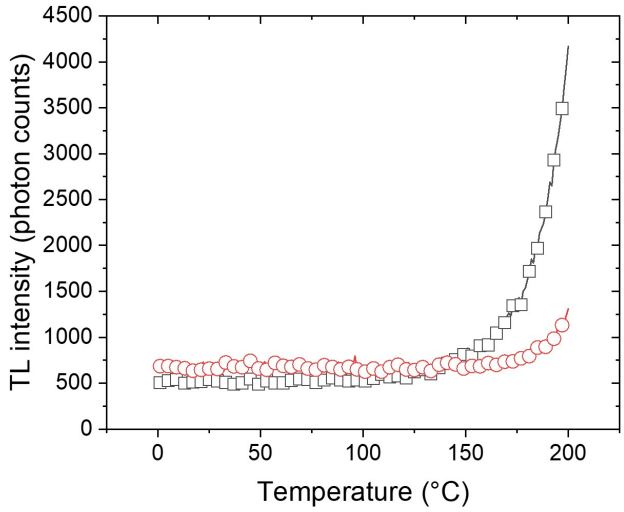

Fig. 10.20. Background TL signal of the faux leather the coated woven fibres bag 16 (black squares) and bag 4 (red circles). PMT: Hamamatsu R2949, detection window : OC 12, heating rate : 0.5 °C.s^{-1}.

The glow curve observed from the extracted fillers grains showed a shape similar to the TL of the bags and fabrics, although the 80 °C peak appeared to be narrower (Fig. 10.21), and likely to be due to reduced thermal lag. Extraction of the filler grains from the fabric coating also enabled TL measurements to be carried out to a higher temperature. Fig. 10.22 shows the native signal and the TL signal induced by a dose of 10 Gy to filler grains extracted from the coating of the LED conference bag. A strong native signal with a main peak around 300 °C, and possibly a minor overlapping peak around 250 °C was observed with the extracted filler grains, and in comparison, the β induced signal was very weak. Measurements conducted in a nitrogen atmosphere did not reduce this native signal. Due to the stability of the TL signal in the region $\sim$ 300 °C (see Section 10.2.5), a likely explanation for the origin of this signal is a residual geological signal.

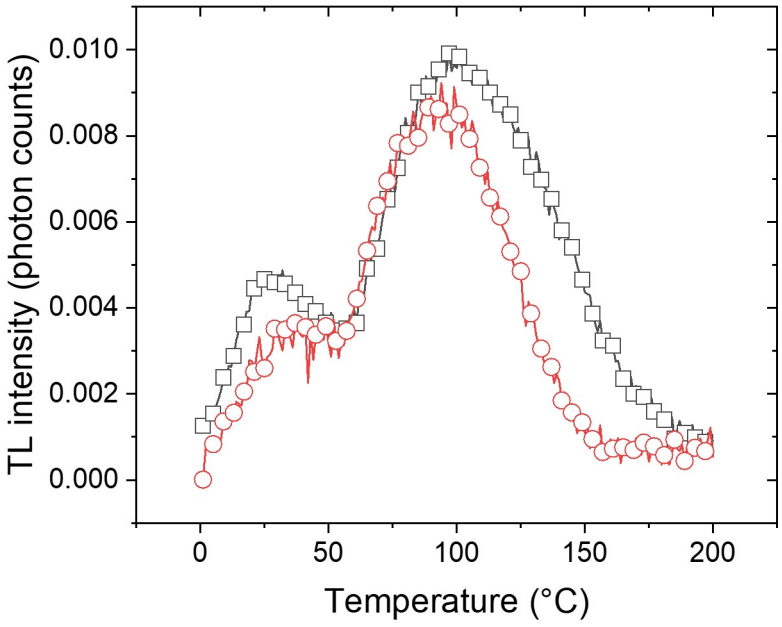

Fig. 10.21. TL of the PU coating of a sample from the "LED conference" bag (black squares) and of filler grains extracted from the coating (red circles) following a 10 Gy β dose. The TL glow curves were normalised by the total number of photon counts. Detection window : fused silica window, heating rate : 0.5 °C.s^{-1}.

The β-induced TL signal of the filler grains measured to 300 °C showed an additional TL peak centred at $\sim$ 250 °C, possibly associated to the native signal (Fig. 10.23). However, this peak

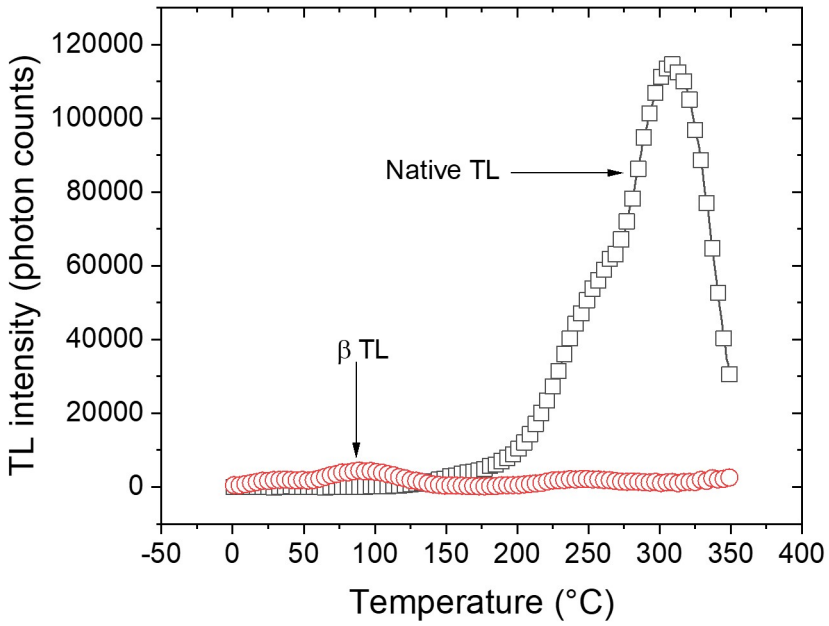

Fig. 10.22. Native TL (black squares) and TL following a β irradiation (10 Gy, red circles) of filler grains extracted from the PU coating of the LED conference bag. Detection window : fused silica window, heating rate : 0.5 °C.s^{-1}.

cannot be used for emergency dosimetry due to the strength of the native signal, and might have a potential influence on the lower temperature peaks used for short term dosimetry.

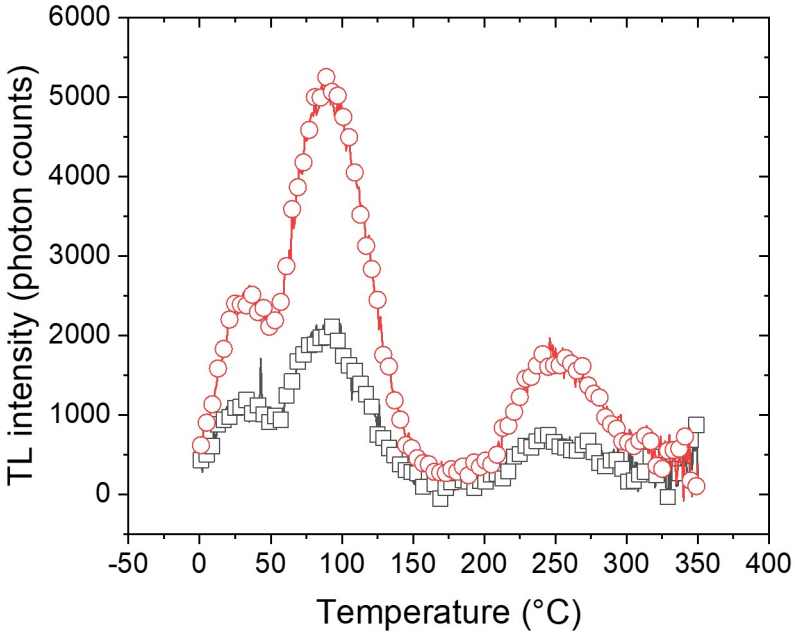

Fig. 10.23. TL following β irradiation (2 Gy, black squares; and 5 Gy, red circles) of filler grains extracted from the PU coating of the LED conference bag. Detection window : fused silica window, heating rate : 0.5 °C.s^{-1}.

10.6.3 Blue vs red sensitive PMT

A similar orange-red emission to that of calcite is expected for calcium carbonate fillers and was confirmed by CL measurements (see Section 10.4.3); therefore the detection system used for TL measurements must be able to detect wavelengths of above 600 nm. TL measurements were performed both with an EMI 9235QA and a Hamamatsu R2949 detectors. The red sensitivity of the R2949 tube made it more suitable for the detection of red emission from calcium carbonates, as discussed in Section 10.2. Fig. 10.24 compares the quantum efficiency of these two photomultipliers.

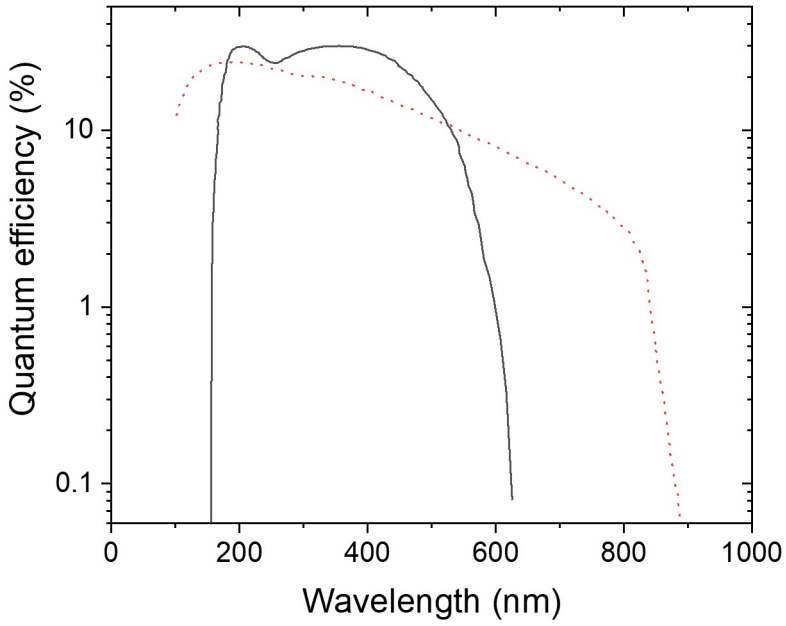

Fig. 10.24. Quantum efficiency of the Hamamtsu R2949 (red dots) and EMI 9235A (black continuous line) PMTs. Data extracted from the manufacturers' manual.

Measurement of the TL signal performed with the same sample with the EMI 9235 PMT and the Hamamatsu R2949 confirmed that the signal recorded was stronger with the Hamamatsu R2949. Optimally, the signal was 50% stronger with a filter OC12 ($\geq$ 550 nm) and a Hamamatsu R2949 compared to the EMI 9235 (Fig. 10.25).

Further comparative measurements made with the EMI 9235 and the Hamamatsu R2949 indicated that using the red sensitive R2949 tube reduced the intensity of the native signal compared

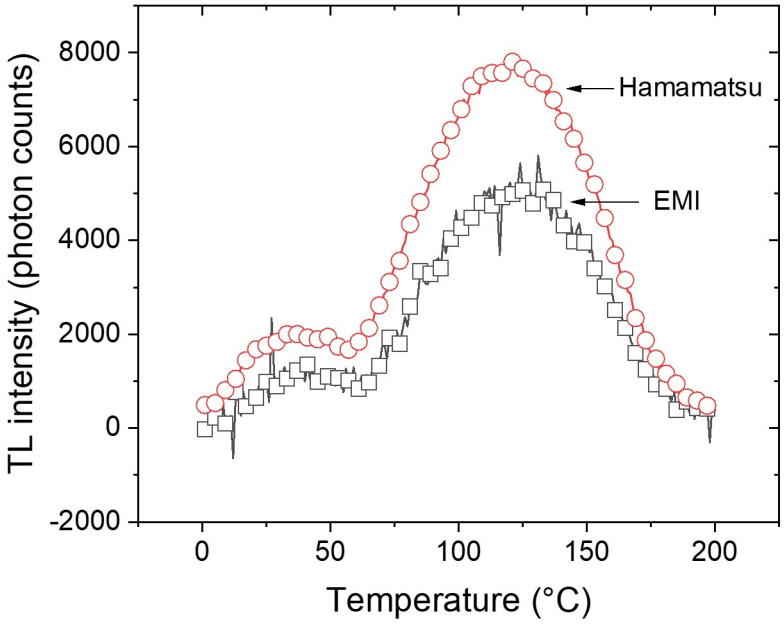

Fig. 10.25. TL glow curves measured with samples taken from bag 7 following β irradiation (10 Gy). Detection window : OC 12; PMT : EMI 9235 (open black squares) and Hamamatsu R2949 (open red circles).

relative to the β induced signal. Figs. 10.26a and 10.26b compare the native signal and the 1 Gy β induced signal for samples cut from bag 7 (dark woven fibres coated with a thermoplastic), and although the measurements were conducted on different samples (taken from the same location of the bag) there is a significant reduction in the intensity of the native signal when the red sensitive PMT is used. This may result from a native signal with a predominantly blue or green emission, contrasting the red emission of the β induced signal. Additional measurements made using an OC 12 filter ($\geq$ 550 nm) to suppress the blue and green emission also yielded a reduction of the native signal relative to the β induced signal. For example, Fig. 10.26c compares the native and 1 Gy β induced TL glow curves of a sample of bag 7, measured using an OC 12 filter and the Hamamatsu R2949 PMT, where the native signal is close to background levels. The dose equivalence of the native signal in the region 140-160 °C (calculated by constructing the dose response curve using the integral in the region 140-160 °C of the β induced signal, and comparing it to the signal of the native in the same region) for four different configurations of PMTs and detection windows is

listed in Table 10.5, and as can be seen, although the dose equivalence of the native signal is 2.6 Gy using an EMI 9235 and fused silica window, the value decreases to 0.05 Gy using the Hamamatsu R2949 and OC 12 filter. Hence this last configuration should be favoured when making dose assessment using calcium carbonate fillers, to minimise the effect of the presence of the native signal, on determination of a dose arising from a contemporary radiological accident.

Table 10.5: Dose equivalence of the native signal of bag 7 (black woven fibres coated with a thermoplastic) in the region 140-160 °C using the PMTs EMI 9235QA or Hamamatsu R2949. The signal was detected either through the fused silica window or a filter OC 12 ($\geq$ 550 nm).

Detection/filter	Dose equivalence (140-160 °C) of the TL native signal (mGy)
EMI 9235 / fused silica window	2661 ± 36
EMI 9235 / OC 12	403 ± 10
Hamamatsu R2949 / fused silica window	145 ±4
Hamamatsu R2949 / OC 12	54 ± 3

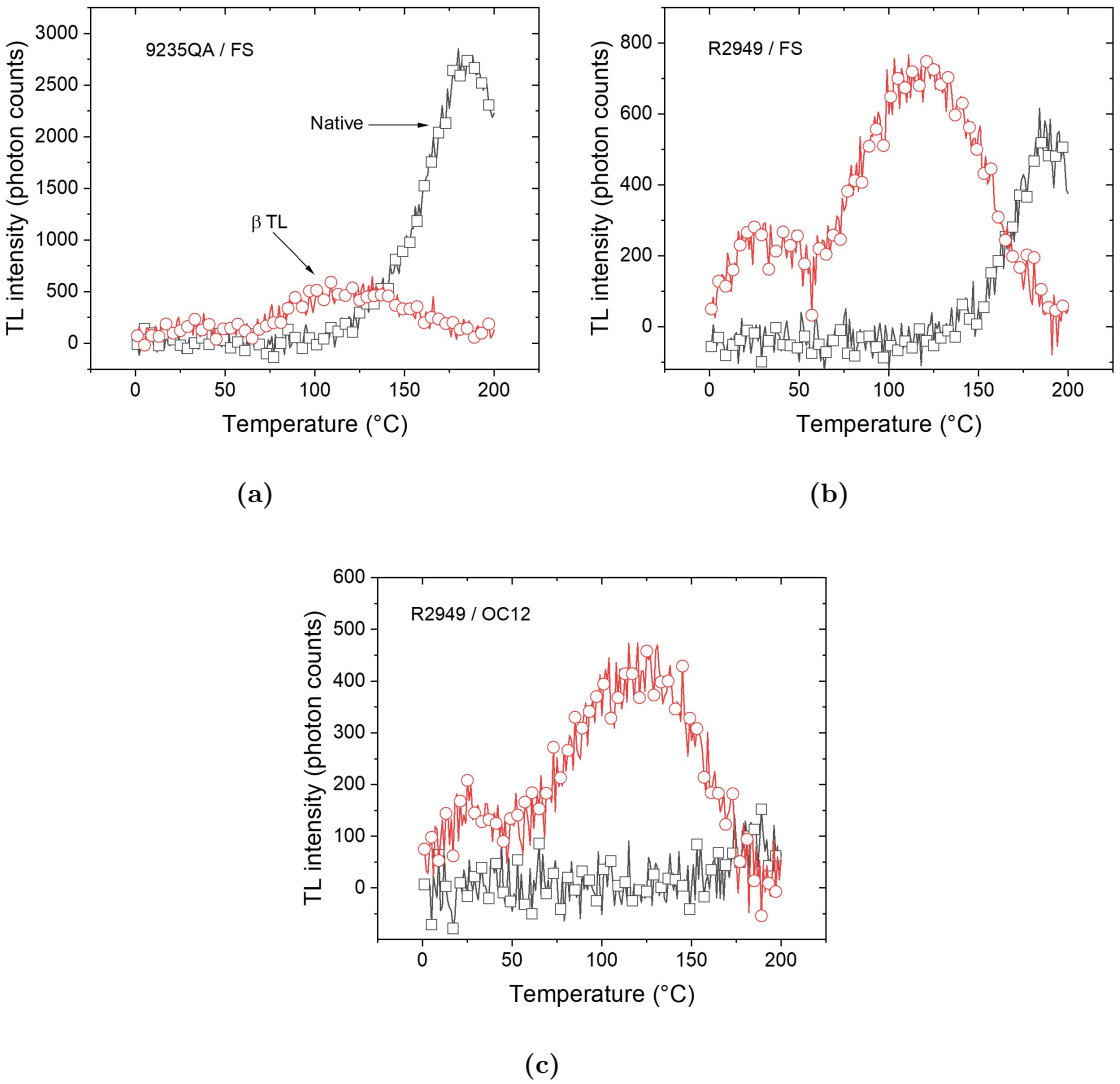

Fig. 10.26. Native (black circles) and 1 Gy β induced TL (red circles) of bag 7. The TL glow curves were detected using a) an EMI 9235QA PMT, detection window : fused silica (FS) window; b) a Hamamatsu R2949 PMT, detection window : fused silica window; c) a Hamamatsu R2949 PMT, detection window : OC 12 filter.

10.6.4 Dose response

The TL response of calcium carbonate fillers to β doses was measured by administering radiation doses to samples cut from the fabrics and bags doses in the range of interest for emergency dosimetry (0.1-10 Gy) and recording the TL response as the integral in different regions of the 100 °C peak (105-135 °C, 140-160 °C, 160-175 °C). Fig. 10.27 shows the TL response of bag 21 (black backpack, woven fibres coated with thermoplastic) in these regions as a function of dose. The three integration regions followed a linear increase in intensity with increasing β dose, in the range of doses of interest. The dose response curves were fitted with a linear function forced through the origin, such as :

$$f(D) = a \times D, \tag{10.1}$$

where D is the administered dose and a the slope of the dose response. All the fabric and bag samples tested exhibited a similar response to β doses, apart from bags 3 and 8, that did not show a response to dose.

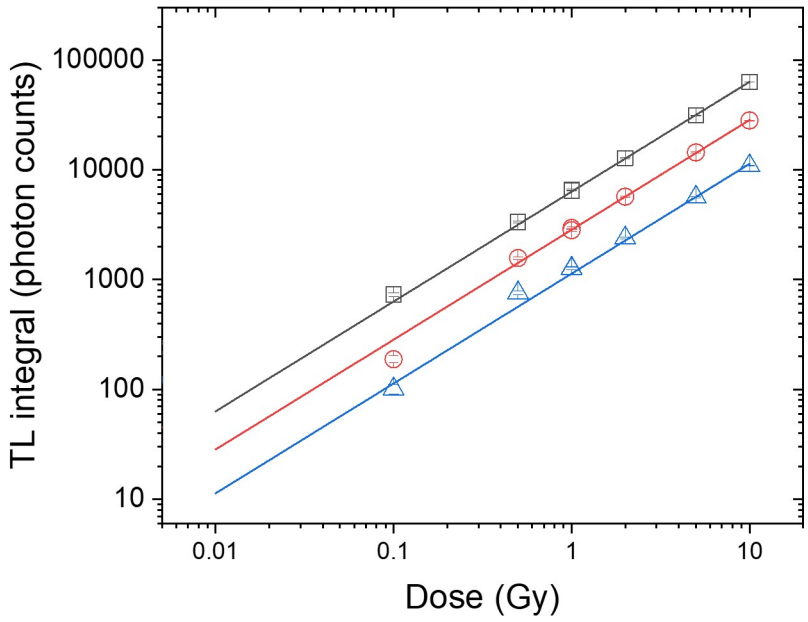

Fig. 10.27. TL dose response characteristics (β doses; 0.1-10 Gy) for a sample of bag 21 (black backpack, woven fibres coated with thermoplastics), for three integration regions : 105-135 °C (open black squares), 140-160 °C (open red circles) and 160-175 °C (open blue triangles). A linear function was fitted to the data sets as indicated by the solid lines.

A plateau test, consisting of verifying whether the dose estimates formed a plateau as a function of the region of integration, was applied, to examine the dose response characteristics for each data point of the glow curve, is shown in Fig. 10.28 for bag 16 (red faux leather thermoplastic). The "accident dose" was of 1 Gy in this case, and this value was recovered to within 5% when adopting a dose recovery procedure that used single data channels in the region of 50-175 °CC. Below 30 °C, the value uncertainty in the value of D_{acc} is likely to be due to the fading of the 30 °C peak at room temperature.

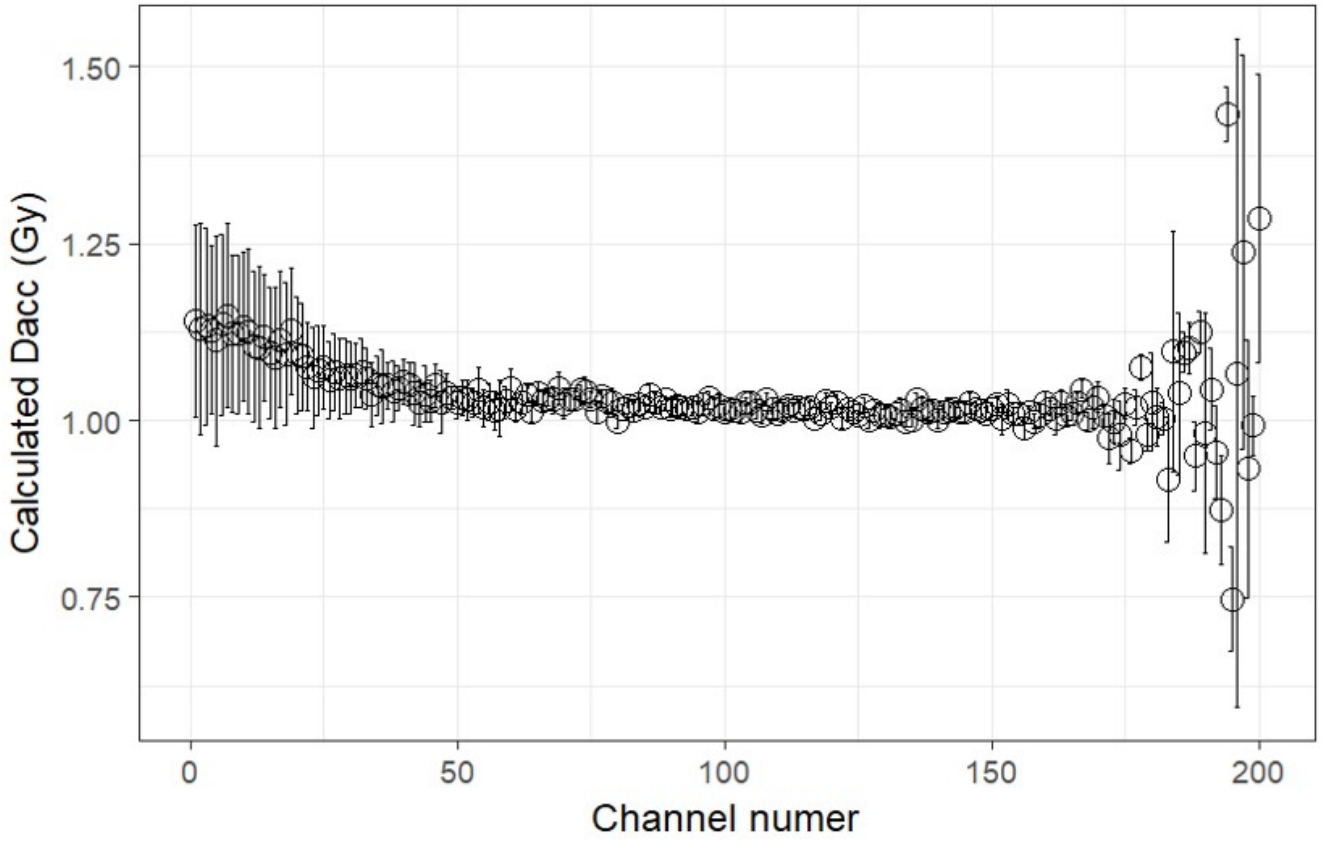

Fig. 10.28. Plateau test performed with a sample cut from bag 16 (red faux leather thermoplastic) where 1 channel = 1 °C. The value of D_{acc} (=1 Gy) was calculated as I_T/m, where I_T is the signal recorded in the interval T (2 channels) divided by the gradient m of the dose response curve. D_{acc} was calculated from the dose response data using an integration channel of 1 °C.

10.6.5 Detection limit

The detection limit was calculated as the dose for which the signal was equal to the background plus three times its standard deviation, as explained in Chapter 3. The detection limit was found to vary from sample to sample, depending on sample brightness. However, for all samples, the detection limit was considered to be sufficiently low for emergency dosimetry purposes (below 0.5 Gy) as shown in Table 10.6. For the brightest samples (e.g., bag 16, bag 19), the detection limit was found to be a few mGy in the region 140-160 °C of the glow curve. The dimmest samples (bag 10) had a detection limit below 400 mGy.

Table 10.6: Detection limit in the TL region 140-160 °C for samples of ca 5×5 mm^2. The detection limit was calculated as the dose for which the signal is equal to the background plus three times its standard deviation. The values of this table were obtained using a Hamamatsu R2949 PMT and an OC 12 filter.

Sample	Detection limit (mGy)
"RPW conference" bag	7 ± 1
"LED conference" bag	62 ± 6
Bag 4	35 ± 2
Bag 5	69 ± 7
Bag 6	1.1 ± 0.3
Bag 7	26 ± 2
Bag 9	97 ± 6
Bag 10	368 ± 22
Bag 11	26 ± 3
Bag 12	22.1 ± 0.3
Bag 13	3.5 ± 0.1
Bag 14	46 ± 11
Bag 16	2.44 ± 0.08
Bag 17	45 ± 4
Bag 18	60 ± 3
Bag 19	1.21 ± 0.07
Bag 20	245 ± 67
Bag 21	1.9 ± 0.7

10.6.6 Sensitivity changes

Repeated cycles of β irradiation (10 Gy) and TL measurement were found to give rise to a reduction of the TL signal (Fig. 10.29, bag 21) though the shape of the glow curve remained unchanged. However, further investigation indicated that this was the result of the condensation on the first detection window of vapour released from the sample during heating, causing optical opacity. This effect required regular cleaning of the window. The use of a nitrogen purge during measurements, and cleaning of the samples with distilled water, acetone, industrial methylated spirit, white spirit or dichloromethane before measurement were unsuccessful in removing this effect. Frequent cleaning of the window was necessary during measurement protocols to minimise this effect.

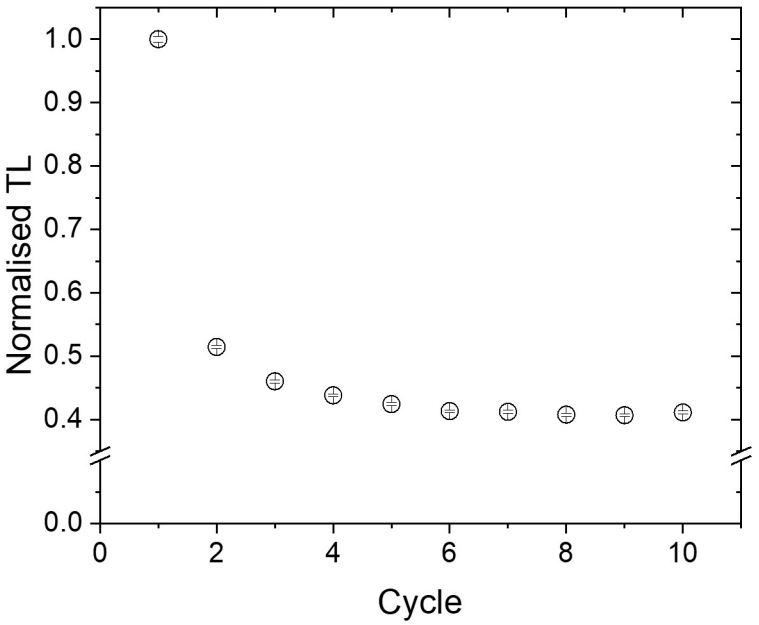

Fig. 10.29. Response of the TL signal measured with a sample of Bag 21 (black backpack, woven fibres coated with thermoplastic) with repeated cycles of β irradiation and TL measurement. The signal corresponds to the integral of the TL glow curve in the region 140-160 °C and was normalised by the first signal of the cycle. Detection window : OC 12, PMT: Hamamatsu R2949, heating rate : 0.5 °C.s^{-1}.

Mass spectrometry measurement coupled with thermal gravimetric analysis for samples of bags

16 and 21 detected the emission of nitrogen, oxygen, water, silicon, sulfur and calcium for a sample heated to 200 °C at a heating rate of 0.5 °C.s^{-1}. Fig. 10.30 shows the spectrum obtained for bag 21, but bag 16 had a similar spectrum. Furthermore, the thermal gravimetric analysis determined that a loss of 4% in mass for bag 21 after heating the sample to 200 °C (3% for bag 16).

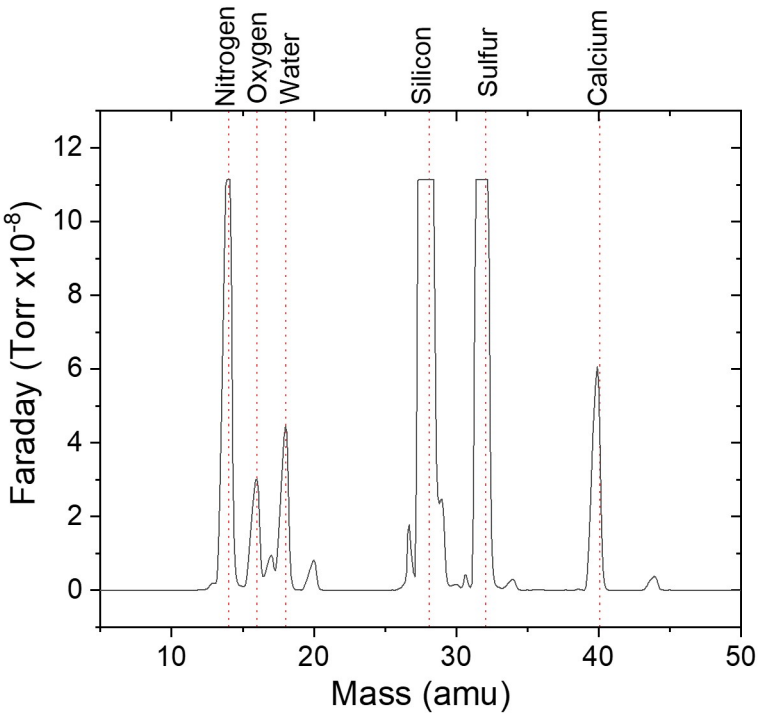

Fig. 10.30. Mass spectrometry spectrum for a sample of bag 21 (black backpack, woven fibres coated with thermoplastic) for a sample heated to 200 °C. Heating rate : 0.5 °C.s^{-1}, spectrometer : HAL IV RC RGA.

10.6.7 Discussion

The position of the second TL peak was higher than obtained for calcite (Kirsh et al., 1987), and this maybe explained by a thermal lag caused by the thickness of the fabric in which the calcium carbonate filler was distributed. A thermal lag may also account for the variability observed in the peak position between samples. Furthermore, the potential causes for the variation in intensity of the TL signal may be related to 1) the colour of the sample, 2) the thickness of the coating, 3) the density of fillers in the coatings and 4) calcium carbonate fillers of different origins. The TL signal was found to be strongest for white and red samples, which correlates with the red emission

spectrum (Fig. 10.15). The correlation between the thickness of the sample and the concentration of the fillers and the strength of the TL can be explained by the amount of calcium carbonate present in the sample; thicker coatings would have a higher quantities of calcium carbonate filer. However, if a self calibration step is included in the procedure, these variations should not matter for dose assessment.

The position of the extracted filler grains native signal corresponds to the higher temperature peaks 250-300 °C observed in calcite (Kirsh et al., 1987) and is attributed to the natural geological dose as this peak was not observed to fade significantly over time (Kalita and Wary, 2016), and as in the manufacturing process of the fillers (Fig. 10.1) the crushing and sieving operations are unlikely to thermally erase the TL signal above 200 °C. In addition, the blue/green emission of the native signal correlates with the spectroscopic measurement of the TL emission of the higher temperature peak, that indicated emission bands at 560 nm (Townsend et al., 1994; Down et al., 1985).

10.7 Phototransfer effects

10.7.1 Observations

Measurements performed exposing unirradiated samples to a blue light source (470 nm) and measuring the TL produced a strong native signal (Fig. 10.31 a) decreasing with repeated cycles of measurements, and with a shape different from the β induced TL (Fig. 10.31 b). The narrower shape of the main peak might be explained by the bleaching of the shallower traps during the blue illumination. A secondary minor peak located around 180 °C also indicates the presence of an additional trap in this region. The PTTL glow curve measured following the administration of a β dose (10 Gy) on the same sample is similar in shape, and slightly stronger in intensity compared with the native signal. The PTTL was measured by irradiating samples with a β dose, preheating to T_{max} 200 °C (and concurrent TL measurement) and exposing the samples to a light source (470 nm : 13 mW.cm^{-2}, 850 nm : 83 mW.cm^{-2} and white light : $\sim$ 50 μW.cm^2) between a few minutes to hours prior to the PTTL measurements (T_{max} 200 °C).

Although PTTL measurement are not likely to be used for dose assessment in emergency dosimetry due to the strength of the "zero dose" signal, PTTL procedures are of interest to test the sample susceptibility to light exposure before and after irradiation. The PTTL was therefore also tested by exposing the sample to white light before TL measurement. A prolonged exposure to white light (laboratory light, 11.5 hours) produced a native signal from manufactured unirradiated samples (Fig. 10.32). The PTTL signal produced by exposing the sample for 11.5 hours to white light was however relatively weak compared to the signal produced under blue (470 nm) illumination, but the shape of the signal was similar.

10.7.2 Discussion

The native TL signal might originate from the transfer of charges from the deeper traps above 200 °C. Fig. 10.22 emphasised the presence of a very strong native TL signal above 200 °C, from which charges may be transferred to shallower traps using a PTTL procedure.

Furthermore, the PTTL signal was found to fade as expected when the samples were stored in the dark. Fig. 10.33 shows the PTTL measured shortly after exposure to white light for one hour, and compares it with the PTTL measured 72 hours (storage in the dark) after the end of the 1 h white light illumination. The latter signal approximatively matches in shape the native signal

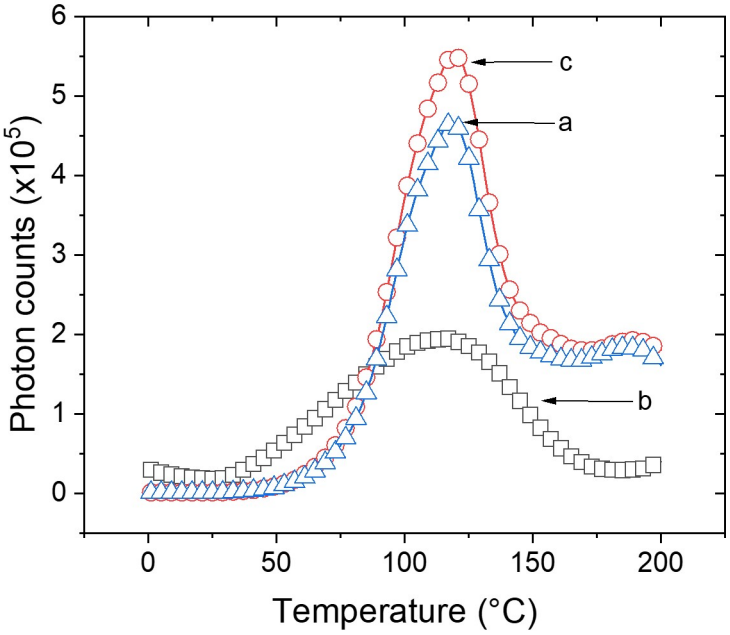

Fig. 10.31. a) Native PTTL measured with a sample of F# 179 (open blue triangles), b) TL following β irradiation (10 Gy, open black squares) and c) PTTL following β irradiation (10 Gy), TL measurement, 2 min blue illumination (470 nm) at 50 °C and subsequent PTTL measurement (open red circles). Detection window : fused silica window, heating rate : 0.5 °C.s^{-1}.

observed on the same sample.

The dose equivalence of the native signal was measured in different locations of bag 11 (brown backpack, woven fibres coated with thermoplastic), some of them being directly exposed to daylight, others being shielded from light (e.g., pockets). The dose equivalence of the native signal in the region 140-160 °C was found to be (470 ± 13) mGy for a sample taken in a location shielded from light, whereas it was (2650 ± 40) mGy for a sample taken from the front of the bag, that had been exposed to daylight. Bag 21, bought new, exhibited a very weak native TL signal (less than a few mGy).

Part of the β PTTL signal could be caused by remaining charges from the native signal - not exhausted by the first measurement of the native PTTL signal. This hypothesis was confirmed by measuring successively twice the native PTTL on the same sample (TL, blue illumination, PTTL measurement on a fresh unirradiated sample). The measurement procedure yielded a similar signal

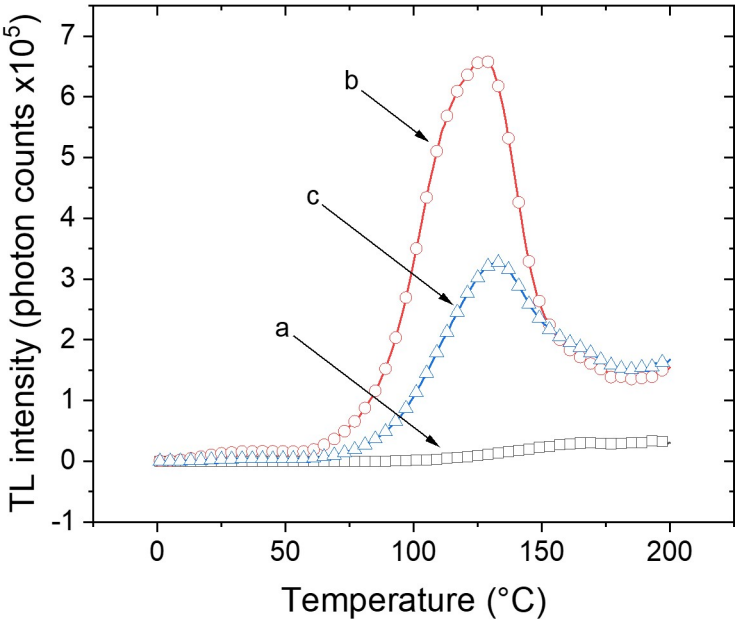

Fig. 10.32. a) Native TL (open black squares) measured with a sample of F# 179 (white woven nylon PU coated fabric), b) native PTTL using 2 min blue light illumination (470 nm; open red circles) and c) 11.5 h exposure to white light (open blue triangles). Detection window : fused silica window, heating rate : 0.5 °C.s^{-1}.

for the first and the second readout, indicating that the native PTTL reservoir of charge was not exhausted by the first measurement. Another explanation for the native signal could also be that it originates from a photo-stimulated TL (PSTL) process not depending on dose.

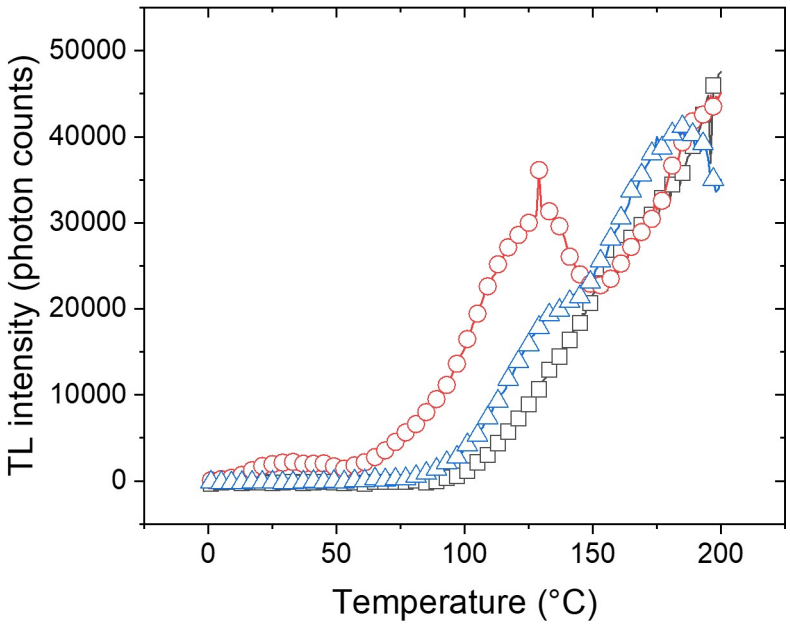

Fig. 10.33. Native TL measured with a sample of F# 179 (black squares), PTTL following 1 h white light illumination measured shortly after the end of the illumination (red circles) and PTTL measured following white light illumination 1 h and storage in the dark 72 h. Detection window : fused silica window, heating rate : 0.5 °C.s^{-1}.

10.8 Fading

10.8.1 Ambient temperature fading

The fading behaviour of the TL was tested by irradiating the samples with a β dose (10 Gy), storing them in the dark at ambient temperature, and measuring the TL following storage. Fig. 10.34 shows the TL glow curves of bag 16 (red faux leather) measured immediately after the β irradiation, and after storage periods of 0.5 and 24 h. In addition to the decrease in intensity of the TL, the peak maximum shifts to higher temperature with increasing storage time, reflecting a continuum of trapping levels. The fading rate is therefore critically dependent on the region of integration, and for more precise results, narrow integration intervals (2 °C) were preferred.

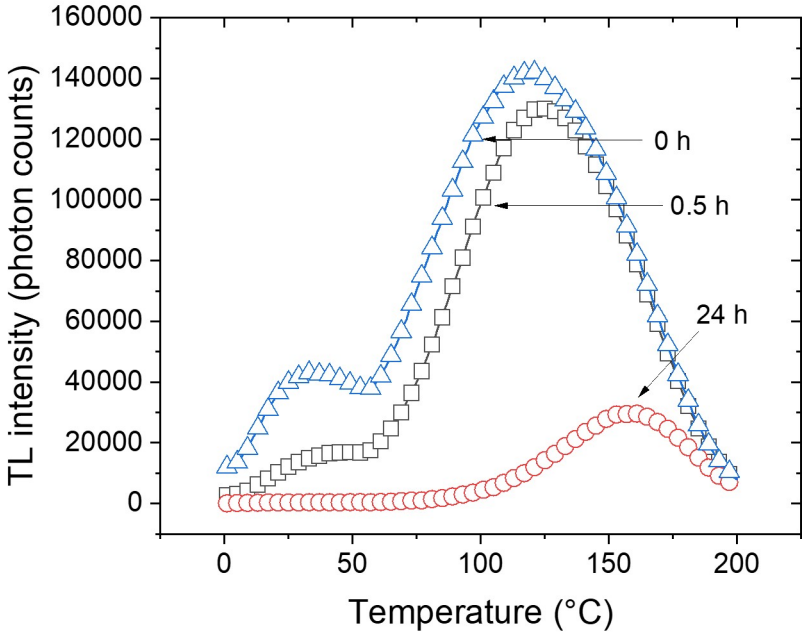

Fig. 10.34. TL glow curves measured with a sample of bag 19 (white faux leather) following β irradiation (10 Gy) and storage in the dark at room temperature 0 h (open blue triangles), 0.5 h (open black squares) and 24 h (open red circles). PMT : Hamamatsu R2949, detection window : OC 12, heating rate: 0.5 °C.s^{-1}.

Fig. 10.35 shows the remaining TL signal of F# 179 (white woven fibres of nylon coated with PU) in the regions 140-142 °C and 158-160 °C after storage in the dark at ambient temperature

for storage periods 0.5 - 744 h. The interval of the TL glow curve that was found most suited for emergency dosimetry was between 140-160 °C as it combined a greater stability of the signal, a lower native signal and intensity sufficiently high in this region. The intervals 140-142 °C and 158-160 °C were thus chosen on Fig. 10.35 as the extremity of the TL glow curve temperature interval. The fading behaviour appears to be complex for this sample (F# 179), as 1) for periods of storage up to ca 5 h, the fading rate in the 140-142 °C integral region is slightly less than in the integral region 158-160 °C, and 2) for storage periods longer than 5 h, the fading rate for the integration region 158-160 °C is lower.

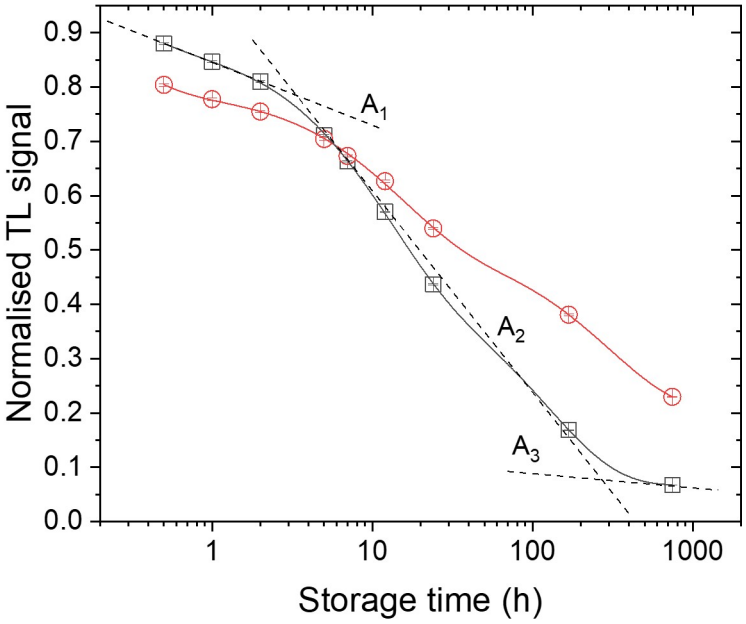

Fig. 10.35. TL signal remaining following β irradiation and storage in the dark at room temperature 0.5-744 h of F# 179 (white nylon woven fibres coated with PU). The remaining signal was calculated as the integral in the region 140-142 °C (open black squares) and 158-160 °C (open red circles) and normalised to the signal measured immediately after the irradiation ($\leq$ 5 min). The solid lines indicate function 10.2 fitted to the experimental data. The broken lines, and A_1, A_2 and A_3 are the components of the fading in the 140-142 °C region. Detection window : fused silica window, heating rate : 0.5 °C.s^{-1}.

However, the fading in both cases was fitted with a combination of exponential functions, such

as :

$$y(t) = y_0 + A_1 \exp\left(-\frac{t}{\tau_1}\right) + A_2 \exp\left(-\frac{t}{\tau_2}\right) + A_3 \exp\left(-\frac{t}{\tau_3}\right). \quad (10.2)$$

The coefficients y_0, A_1, t_1, A_2, t_2, A_3, t_3 are listed in Table 10.7 for the integration regions 140-142 and 158-160 °C. The coefficients indicate the presence of a stable component for the region 158-160 °C ($y_0 = 0.20 \pm 0.01$) for storage times up to 744 h, whilst for the region 140-142 °C, the value of the stable component appears to tend toward zero. Furthermore, if the first two components (component 1 and component 2) seem to have a similar lifetime (τ_1 and τ_2 respectively) for both integration regions, component 3 has a significantly longer lifetime for an integration region 158-160 °C ($\tau_3 = 301 \pm 62$ h) compared with the region 140-142 °C ($\tau_3 = 126 \pm 6$ h).

Table 10.7: Fading coefficient of F# 179 calculated by fitting function Eq. 10.2 to the experimental data, calculating the remaining TL signal as the ratio of the signal in the regions 140-142 °C and 158-160 °C, for storage periods 0.5-744 h, to the signal measured immediately after β irradiation.

	Integral 140-142 °C	**Integral 158-160 °C**
y_0	0.066 ± 0.003	0.20 ± 0.01
A_1	0.116 ± 0.005	0.206 ± 0.007
τ_1 (h)	0.25 ± 0.04	0.21 ± 0.03
A_2	0.43 ± 0.01	0.28 ± 0.02
τ_2 (h)	11.3 ± 0.6	14 ± 2
A_3	0.38 ± 0.01	0.31 ± 0.01
τ_3 (h)	126 ± 6	301 ± 62

However, variability in the fading rates was observed between samples (Fig. 10.36) as indicated by the TL fading rate (integral in the region 158-160 °C) of bags 11 (brown backpack woven fibres coated with a thermoplastic), 19 (white faux leather fabric) and 21 (black woven fibres coated with a thermoplastic) and F# 179 (white woven nylon fibres coated with PU). The TL faded by 34 % and 70% after 24 h of storage in the dark for bags 19 and 21 respectively. This suggests that the use of common fading correction would be inappropriate, although all the samples tested appeared

to follow an exponential decay.

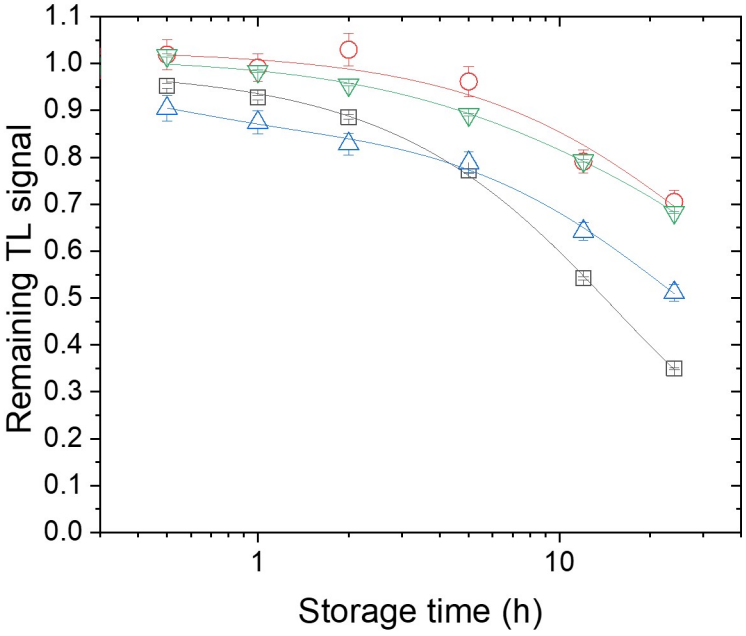

Fig. 10.36. TL signal remaining following irradiation and storage in the dark at room temperature 0.5-24 h of bag 19 (white faux leather, open black squares), bag 21 (black backpack, woven fibres coated with a thermoplastic, open red circles), bag 11 (brown backpack, woven fibres coated with a thermoplastic, open blue triangles) and F# 179 (white woven nylon fibres coated with PU, open inverted green triangles). The remaining signal was computed as the integral in the region 158-160 °C and normalised to the signal measured immediately after the irradiation (0 h). Risø system, detection window : OC 12, PMT : Hamamatsu R2949, heating rate : 0.5 °C.s^{-1}.

The higher temperature peak (ca 250 °C), observed in the filler extracted from bags or fabrics exhibited negligible fading compared to the lower temperature peaks (Fig. 10.37), consistent with expectation (Kalita and Wary, 2016). However, due to the strength of the native signal in this region, this peak cannot be used for emergency dosimetry.

10.8.2 Low temperature storage

An efficient way to reduce the fading rate is to store the sample at a lower temperature, and tests were conducted by storing the samples at -15 °C in a freezer. The fading was measured with

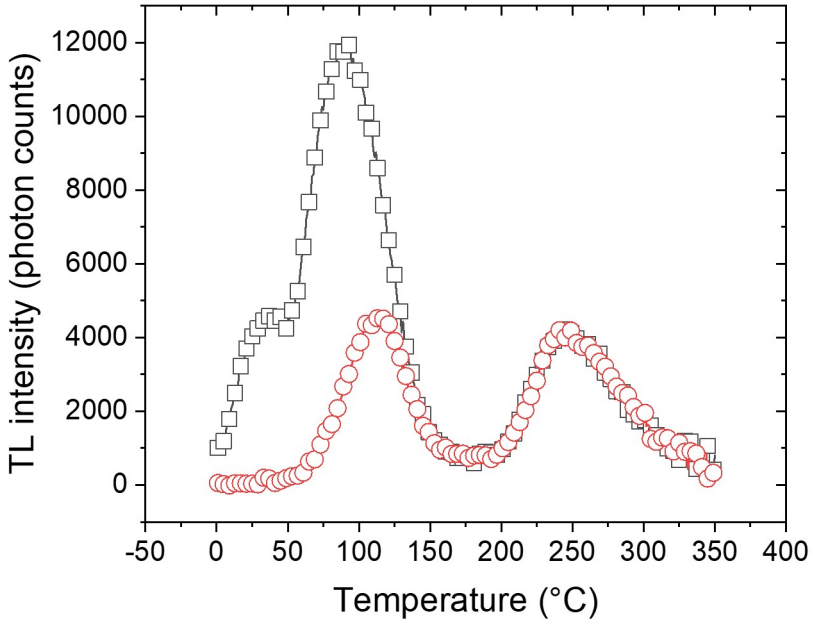

Fig. 10.37. TL glow curves of calcium carbonate filler grains extracted from a sample taken from the "LED conference" bag, measured immediately after β irradiation (10 Gy, open black squares) and after 5 h storage in the dark at ambient temperature following β irradiation (10 Gy, open red circles). Detection window : fused silica window, heating rate : 0.5 °C.s^{-1}.

multiple samples, but reproducibility was tested with samples of the same bag or fabric. Fig. 10.38 shows the fading of the TL signal in integration regions 140-142 °C and 158-160 °C of F# 179, after irradiation and storage in the dark at -15 °C for periods of storage 0.125-183 days. Compared with the fading at room temperature, for which only ca 6% of the signal in the region 140-142 °C remained after 30 days of storage, the loss in TL signal for the sample stored at -15 °C is significantly less. After 30 days of storage at -15 °C, the region 140-142 °C retained 75 % of initial signal and in the region 158-160 °C, 89 % remained, and after two days of storage, no significant fading was detected. The significant reduction in fading for samples stored at -15 °C indicates that the dominant mechanism of fading is a thermal loss of the charges. Measurements conducted on other samples indicate negligible fading for the integration region 158-160 °C when tested for up to two days of storage at -15 °C. However, for longer storage periods where the fading was not negligible, the fading rate was also found to be sample dependent, where the samples that exhibited

the highest rate of fading at ambient temperature were also found to have the fastest fading rate at -15 °C (e.g., 43 % of remaining signal for F 179 vs 13 % of remaining signal for bag 16 after 183 days of storage at -15 °C).

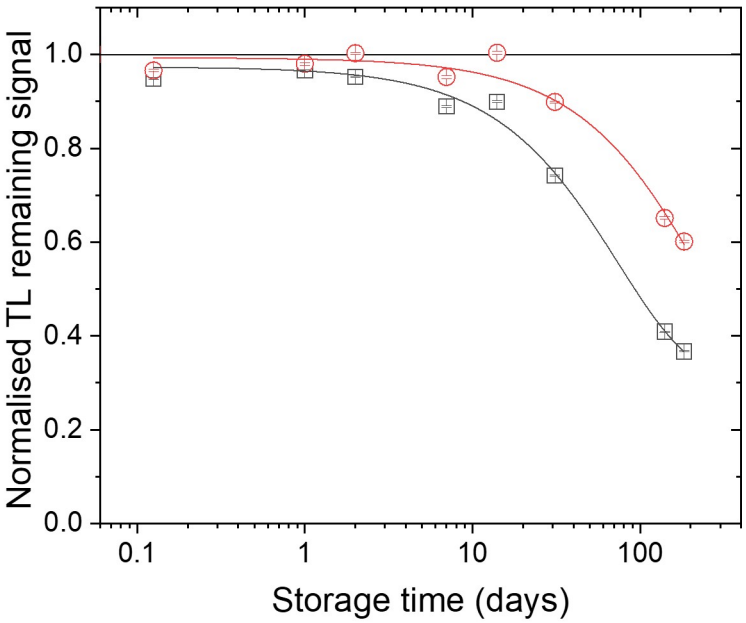

Fig. 10.38. TL signal remaining following β irradiation 10 Gy and storage in the dark at -15 °C for storage periods 0.125-183 days of F# 179 (white woven nylon fibres coated with PU). The remaining signal was calculated as the integral in the region 140-142 °C (open black squares) and 158-160 °C (open red circles) and normalised to the TL signal measured immediately after the irradiation ($\leq$ 5 min). The horizontal line indicates the absence of fading (y=1) and the curves exponential functions fitted to the experimental data. Detection window : fused silica window, heating rate : 0.5 °C.s^{-1}.

10.8.3 Storage at 35 °C

The dependence of the fading rate on the storage temperature and the dominant thermal nature of the fading was confirmed by comparing the fading for samples stored at room temperature (20 °C) with samples stored at 35 °C. The fading rate in the latter case showed a loss of the signal significantly quicker for storage 0.5-24 h long (Fig. 10.39). Interestingly, the fading rate showed less variability between samples of different bags for samples stored at 35 °C compared with samples

stored at ambient temperature.

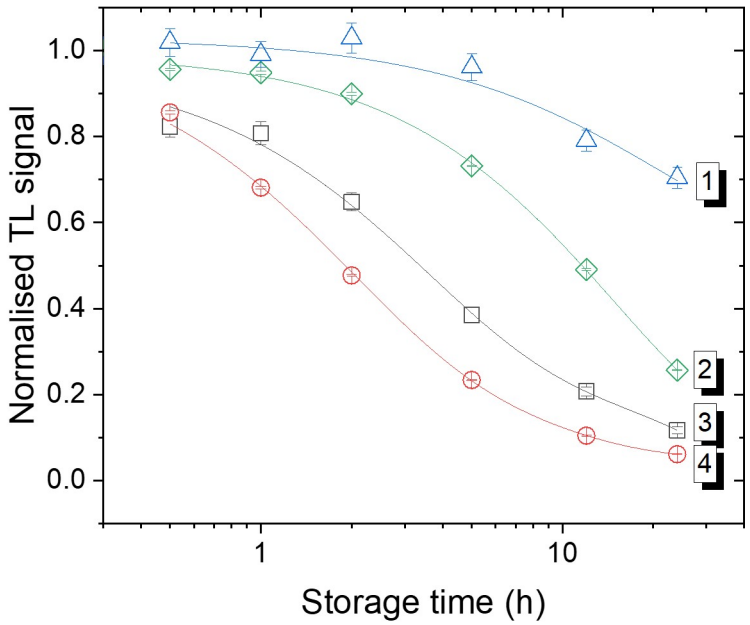

Fig. 10.39. TL signal remaining following β irradiation 1 Gy and storage in the dark for storage periods 0.5-24 h. 1) Storage at room temperature, bag 21 (black fibres coated with thermoplastic backpack); 2) Storage at room temperature, bag 16 (red faux leather handbag); 3) Storage at 35 °C, bag 16; 4) Storage at 35 °C, bag 21. The remaining signal was calculated as the integral in the region 158-160 °C (open red circles) and normalised to the TL signal measured immediately after the irradiation ($\leq$ 5 min). The lines indicate exponential functions fitted to the experimental data. PMT : Hamamatsu R2949, detection window : OC 12, heating rate : 0.5 °C.s^{-1}.

10.8.4 Optical effects

As discussed above exposure to white light may cause the transfer of charges from traps associated with the higher temperature TL peaks ($\geq$ 200 °C) to traps associated with TL peaks below 200 °C, and prolonged exposure to white light produced a peak at $\sim$ 120 °C with an unirradiated sample. Although samples can be obtained in parts of bags protected from light (e.g., pockets, or in seams), testing the influence of the exposure to white light on the radiation induced signal is also important, as bags are likely to be exposed to white light. Samples were here irradiated with a β dose (10 Gy)

and exposed to white light for 1-5 hours, and the TL signal recorded. Fig. 10.40 shows the TL signal of bag 11 after irradiation and a) a 1 h storage under white light and b) in the dark, both at ambient temperature. As can be seen, the TL glow curves are similar, indicating the absence of optical bleaching.

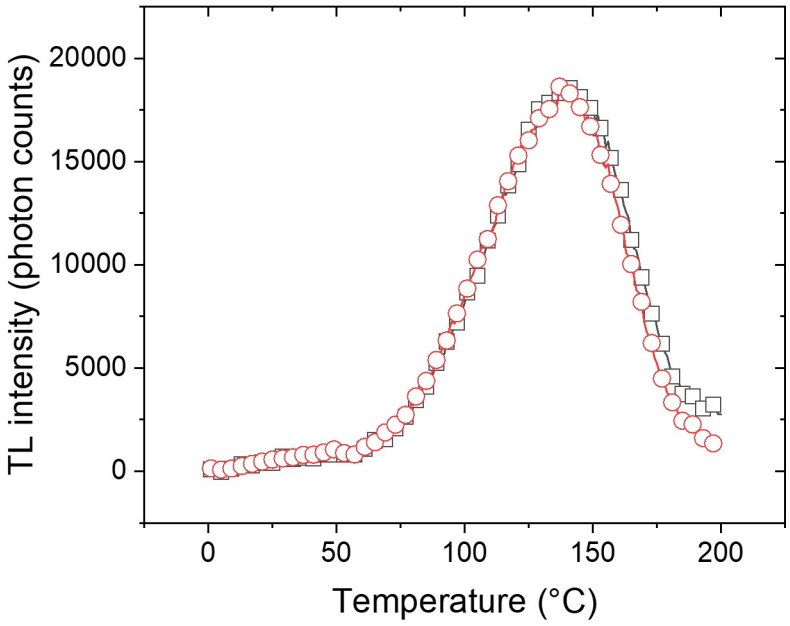

Fig. 10.40. TL glow curves fro a sample taken from bag 11 (brown backpack, woven fibres coated with a thermoplastic) after β irradiation (10 Gy) and after 1 h storage under white light (open black squares) and in the dark (open red circles) at ambient temperature. Detection window : fused silica window, heating rate : 0.5 °C.s^{-1}.

10.8.5 Discussion

Based on the fading measurements, the part of the glow curve usable for short term dosimetry is between ca 140-170 °C. Below this interval, the fading is likely to be too fast to enable dose assessment within the time range required for emergency dosimetry. Fig. 10.41 shows the remaining signal after 24 h of storage at ambient temperature of a sample of F# 179 (white woven nylon fibres coated with PU) for 2 °C integration intervals in the range 50-200 °C. In the region of the glow curve below 140 °C, there is less than 50 % of remaining signal after 24 h, and this value decreases with

lower temperature of the TL glow curve. Integration intervals above 140 °C will be thus preferred for short term dosimetry to minimise the loss of the signal at ambient temperature.

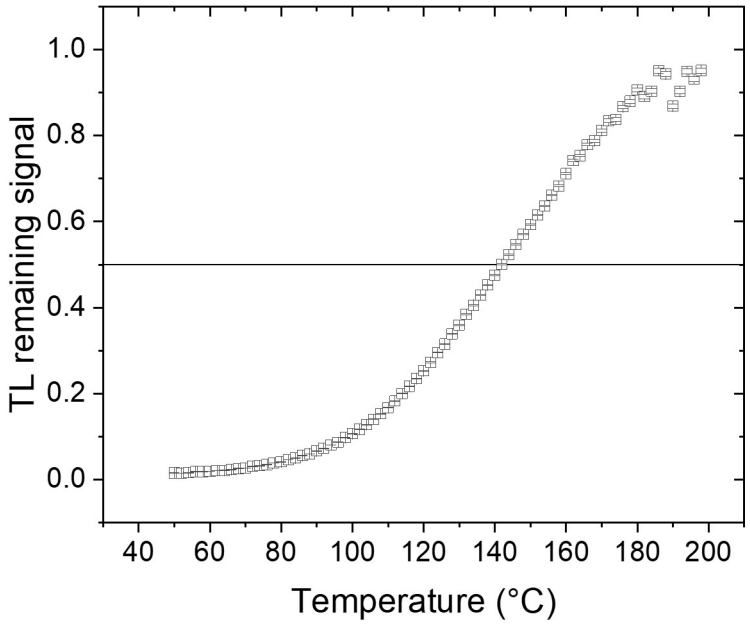

Fig. 10.41. TL signal remaining following β irradiation 10 Gy and storage in the dark at ambient temperature for 24 h of F# 179 (white woven nylon fibres coated with PU) as a function of the temperature at which the integration was made. The remaining signal was calculated as the integral in 2 °C intervals in the region 50-200 °C and normalised to the TL signal measured immediately after the irradiation ($\leq$ 5 min). The horizontal line indicate 50% of remaining signal. Detection window : fused silica window, heating rate : 0.5 °C.s^{-1}.

Several explanations could be advanced for the difference in fading rate of the samples. The first one being the difference in thermal lag of the sample, leading to a shift in the peak position, and meaning that a certain region of the glow curve would not be associated to the same traps in all samples. The other possible explanation is that calcium carbonate fillers of different origins do not have the same fading rate. The XRF data already indicated that some samples are rich in magnesium, whilst in others the presence of magnesium was not detected. Furthermore, the XRD measurement indicated the presence of additional minerals beside calcite, such as dolomite that could also contribute to the luminescence signal in some samples. For example, F# 179 and bag

21 both contained dolomites and had the slowest fading rates amongst the sample measured. The fading measurements also suggested that the main mechanism of fading was thermal, although the existing literature emphasised the presence of tunnelling for the traps from which this peak originate (Medlin, 1964). The next section will explore further the kinetics, and emphasise the presence of tunnelling or hopping of the charges from their traps. The kinetic studies listed in Tables 10.2 predicted lifetimes of the order of a few hours at room temperature to a few hundreds of hours at -15 °C. The data collected in this section indicated much longer lifetime that suggested that the region 140-160 °C used in this fading study is associated to traps with a greater stability. The fading of the glow curve in the region 105-135 °C showed however a rate of fading in closer agreement with the predicted lifetimes, with, for example a 50% loss of the signal in 5 hours for F 179.

Although the fading of the 100 °C peak has not been studied extensively in the literature, more studies exist about the fading behaviour of the 250 °C peak, and they proved negligible fading for this peak. This is consistent with the behaviour of the 250 °C TL peak of calcium carbonate fillers. However, the stability of this peak means that the charges induced by the natural radioactivity accumulate in the traps responsible for this peak, giving rise to a native signal.

10.9 Trap depth

10.9.1 T_{max}-T_{stop}

The T_{max}-T_{stop} method was applied by administering a β dose (10 Gy) to a sample of F# 179 (white woven nylon fibres coated with PU), preheating (cut-heat) to temperatures 50-170 °C and recording the subsequent TL glow curve. The procedure was then repeated increasing the preheat temperature by 10 °C for T_{stop} in the range 20-180 °C. The set of TL glow curves obtained following this procedure is shown in Fig. 10.42. The intensity of the 100 °C peak decreases for preheat temperatures above 80 °C, and the peak maximum shifts to higher temperatures with increasing preheat temperatures. If this might indicate the presence of a non first-order kinetic process, this hypothesis was discarded here as the peak position was found to be constant for various level of doses, within the uncertainties associated to the thermal lag (Fig. 10.43). Thus, it was more likely that the shift in peak position with increasing preheat temperature was an indicator that the 100 °C TL peak originates from a continuum of traps and multiple competition processes (Coleman and Yukihara, 2018), as discussed earlier.

Following Mckeever's method (McKeever, 1988, p. 80) to identify overlapping peaks in a TL glow curve, the position of the peak maximum was recorded as a function of the preheat temperature in the range 20-180 °C (Fig. 10.44a). The graph obtained shows that the position of the main TL peak (ca 100 °C) is stable for preheat temperatures in the range 20-100 °C, when the preheat temperature applied is below the peak maximum. For preheat temperature above 100 °C, the peak position steadily increases, as expected for a continuum of trapping levels. Although it had been acknowledged that the initial rise method does not always give reliable results for a continuum of trapping levels, this method was applied to the T_{max}-T_{stop} set of glow curves, and the values of activation energies for the TL glow curve calculated using different preheat temperatures (Fig. 10.44b). The value of activation energy also steadily increases between 0.42 eV and ca 0.65 eV for preheats from 20 to 130 °C. A value of 0.65 eV is consistent with the values previously found in the literature (Kim and Hong, 2014; Pagonis et al., 1996; Medlin, 1964; Pagonis and Michael, 1994). If these values are correct, the region of the glow curve between 140-160 °C should be privileged when performing dose assessment, as the values of activation energy where similar ad highest in this region (10.44b).

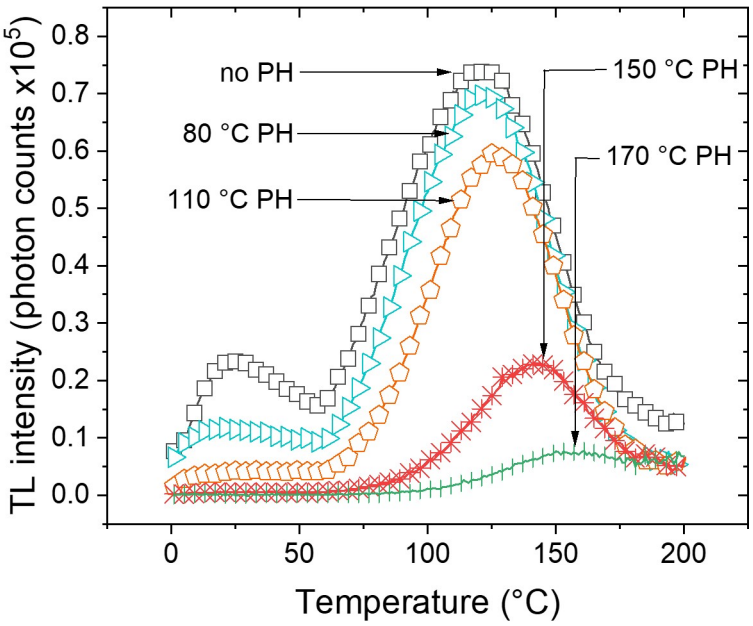

Fig. 10.42. Glow curves obtained by applying the T_{max}-T_{stop} method to a sample of F# 179 (white woven nylon fibres coated with PU), where the following treatments were applied : no preheat (open black squares); 80 °C (open blue triangles); 110 °C (open orange polygons); 150 °C (red stars) and 170 °C (green lines). Preheat : cut-heat, detection window : fused silica window, heating rate : 0.5 $^{\circ}C.s^{-1}$.

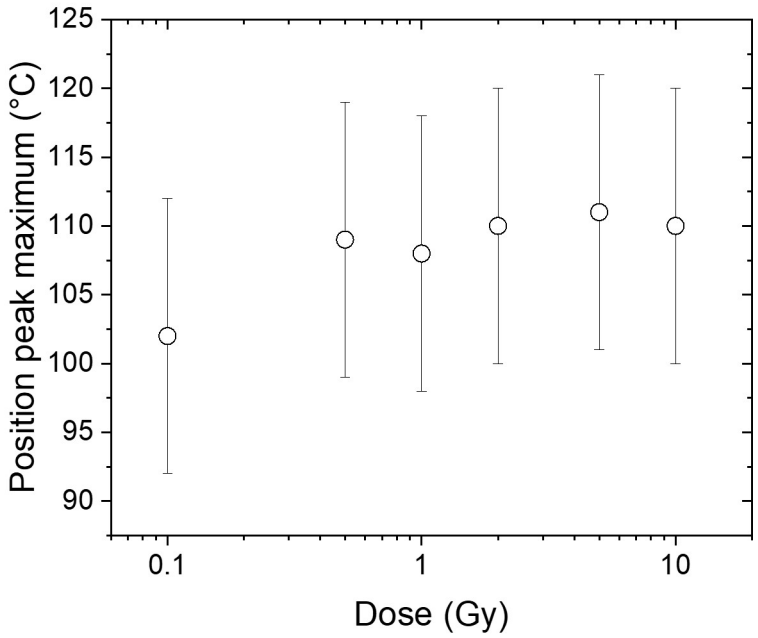

Fig. 10.43. Maximum TL peak position measured following the administration of various level of β doses (0.1-10 Gy) with samples taken from bag 16 (red faux leather). The uncertainties indicated are associated with the effect of the thermal lag (see Chapter 12). No preheat, PMT : Hamamatsu R2949, detection window : OC12, heating rate : 0.5 °C.s^{-1}.

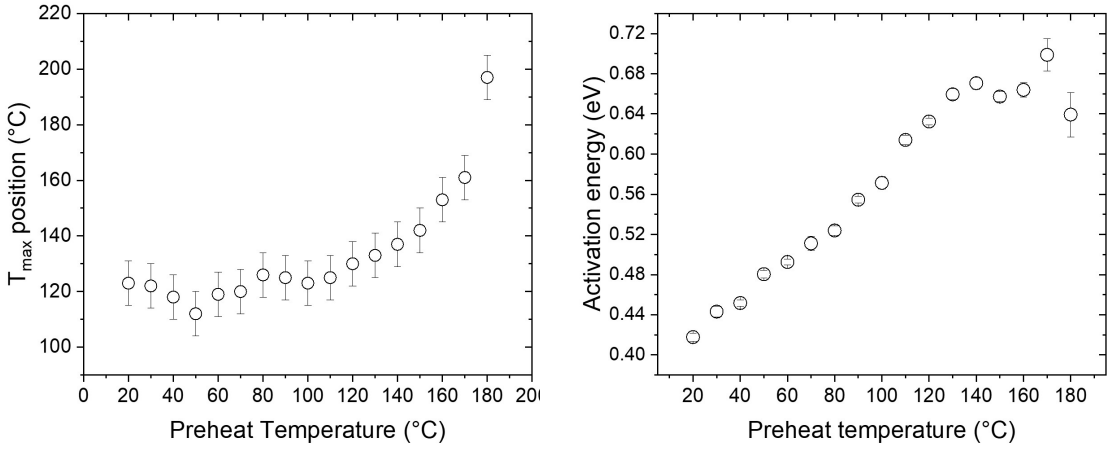

(a) **(b)**

Fig. 10.44. a) Position of the main TL peak (ca 100 °C) of the TL glow curve of a sample of F# 179 (white woven nylon fibres coated with PU) following β irradiation (1 Gy) and preheat in the range 20-180 °C. b) Activation energies calculated applying the initial rise method to a sample of F# 179 following β (1 Gy) irradiation and preheat in the range 20-180 °C.

10.9.2 Irradiation at various temperatures

Van den Eeckhout et al. (2013) developed a method to probe trap depth distribution and resolve the shape of the distribution by combining TL measurements for various irradiation temperatures with the initial rise method to estimate the trap depth for each irradiation temperatures tested. The method differs from the T_{max}-T_{stop} method by the assumption that when the sample is irradiated at high temperature, the shallowest traps are immediately bleached, whereas using the T_{max}-T_{stop} method, the traps are allowed to be filled then depleted by the preheat. A set of TL glow curves obtained using different irradiation temperatures is shown in Fig. 10.45. If compared with the glow curves obtained using the T_{max}-T_{stop} method (Fig. 10.42), some differences can be observed. Firstly, changes in the intensity and shape of the 100 °C TL peak are observed for relatively low irradiation temperatures; between irradiations at 20°C and 30 °C, the intensity of the whole TL glow curve decreases, although the shape of the peak remains similar. A preheat of 80 °C was necessary to observe changes in the T_{max}-T_{stop} procedure. Furthermore, the TL signal was bleached for irradiation temperatures above 125 °C, whereas a preheat of 180 °C was necessary to suppress the signal in the T_{max}-T_{stop} procedure. These observations might be related to a transfer a charges and interactions between traps that might be blocked by the quick bleaching of the shallow traps for samples irradiated at high temperatures. However, for irradiations carried out 50-60 °C, the 30 °C peak was not bleached, indicating that there is a charge transfer process from deeper traps to the traps giving rise to this peak.

An initial rise analysis was conducted on the set of glow curves obtained with a sample of bag 16 irradiated at various temperatures. However, for irradiation temperatures below 60 °C, the values of activation energy obtained using the initial rise method have to be taken very cautiously, as the 30 °C peak overlapped with the 100 °C, hiding the initial part of this peak. The graph of the activation energy as a function of the irradiation temperature (Fig. 10.46a) showed a progressive increase in the activation energy, although steps were identified at ca 0.32, 0.48 and 0.54 eV. This set of data also contrast with that obtained using the T_{max}-T_{stop} method, where a steady increase in activation energy was observed. The area of the 100 °C peak was however found to decrease linearly with increasing irradiation temperature (Fig. 10.46b).

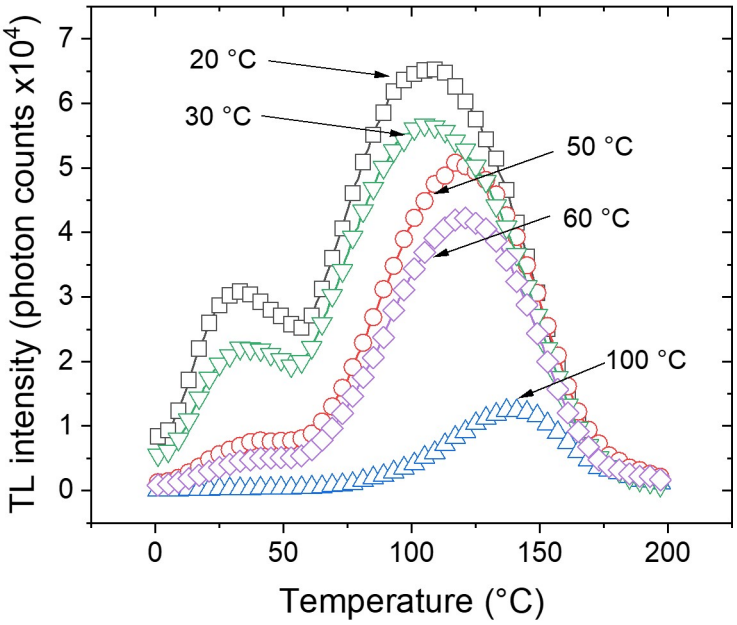

Fig. 10.45. TL glow curves of a sample taken from bag 16 (red faux leather fabric) irradiated with a β dose (0.8 Gy) at various sample temperatures in the range 20-100 °C. No preheat, PMT : Hamamatsu R2949, detection window : OC12, heating rate : 0.5 °C.s^{-1}.

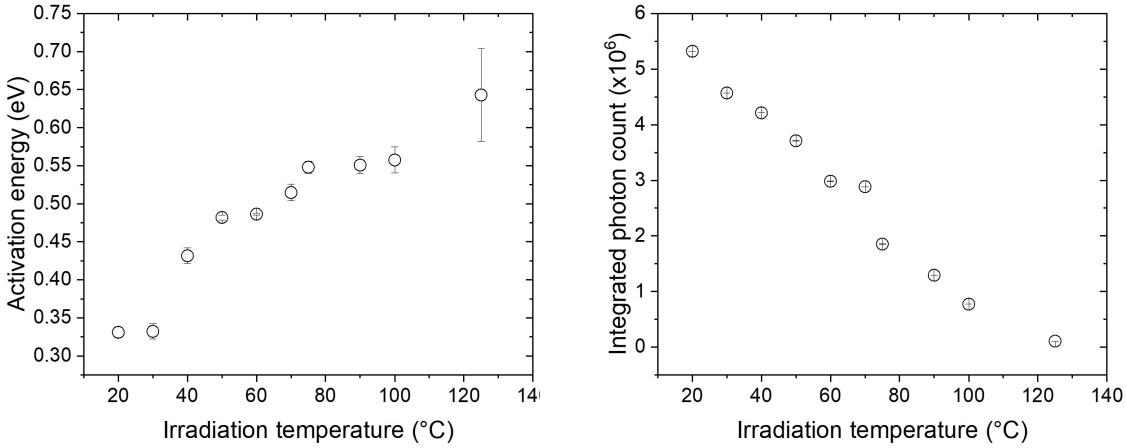

(a) **(b)**

Fig. 10.46. a) Activation energy calculated using the initial rise method as a function of the sample temperature during irradiation for samples taken from bag 16 (red faux leather) and b) integral of the TL peak in the region 50-200 °C as a function of the irradiation temperature.

10.9.3 Isothermal decay

As the procedure or outcome for materials with a continuum of trapping levels suggested by Pagonis and Michael (1994), isothermal decay measurements did not yield a simple exponential decay curve from which kinetic parameters could be extracted. The isothermal decay was measured by irradiating the samples with a β dose (10 Gy) and maintaining them at an elevated temperature in the range 30-180 °C while recording the photon counts. Two different regimes of isothermal decay could be differentiated. For temperature 30-90 °C, the signal slowly increased with time to reach a peak maximum (reached after 30-5 s of thermal excitation), then decreased (Fig. 10.47a). This indicates a complex process, unlikely to originate from a single trap, possibly from at least two spatially closely related traps interacting with each other. The peak position shifting to shorter stimulation time with increasing temperature might indicate that the charge transfer equilibrium is reached quicker.

For the isothermal TL measurements above 90 °C (Fig. 10.47b), the increase was much weaker, and the signal decayed, but only after the first second of the measurement. It did not follow a simple exponential form although it could be approximated using several exponentials, indicating that the process was also complex. Above 150 °C, no increase of the signal was observed. None of the isothermal decay curves could be fitted using an expression such as :

$$I(t) = I_0 \left(\frac{b}{b+t} \right)^m , \tag{10.3}$$

where I_0, b and m are constant, as used by Medlin (1961) to describe the phosphorescence decay of calcite.

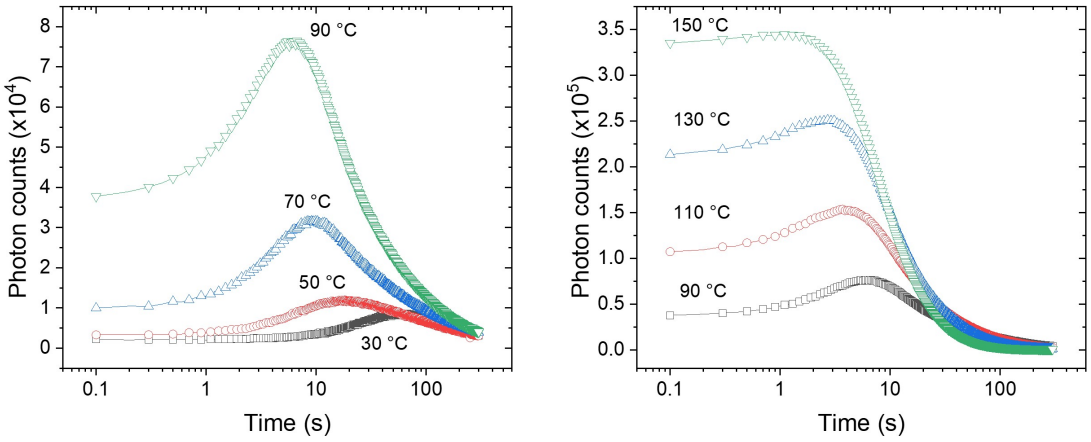

(a) **(b)**

Fig. 10.47. Isothermal TL decay curves for samples of F# 179, measured in the range 30-90 °C (a) and 90-150 °C (b). Detection window : fused silica window.

10.10 Calcium carbonate fillers as dosimeters

Calcium carbonate fillers present several properties that makes them potentially suitable as dosimeters. Firstly, the high sensitivity of their TL response to radiation dose, yields a detection limit from a few mGy to a few hundreds of mGy, well below the 2 Gy required for emergency dosimetry. Furthermore, the linearity of the dose response in the range of doses of interest for emergency dosimetry (ca 0.1-10 Gy) potentially indicates that only one calibration dose could be used, if time is critical, as a linear function forced through the origin was successfully fitted to the dose response experimental data. This type of function also reduces the uncertainties in dose assessment, as only one coefficient (the slope) needs to be determined. Finally, calcium carbonate fillers are good potential dosimeters as they are widely used in thermoplastics, which are found in items such as bags and are therefore likely to located near members of the public in the event of a radiological emergency. If procedure A below is applied using one calibration dose, the measurement time for one sample should be of ca 15 min using a heating rate of 0.5 °C.s^{-1}, depending on the dose rate of the source. Additionally, the preparation of the samples is minimal and requires no more than a few minutes, even for an untrained operator, as the samples are simply cut from the bag and placed into stainless steel cups for measurement. The processing time is thus fast enough to enable laboratories to process quickly a large number of samples in the case of an emergency.

A proposed protocol for dose determination using the TL signal of calcium carbonate fillers is as follow (procedure A):

- Step 1: TL measurement of the "accident" (initial) signal, $T_{max} = 200$ °C
- Step 2: Repeat step 1 (TL background)
- Step 3: Calibration, known β dose
- Step 4: Measurement of the TL response, $T_{max} = 200$ °C
- Step 5: Repeat step 4 (TL background)
- Step 6: Repeat steps 3-5 for another known dose, if necessary

A low heating rate should be preferred when performing TL, as it minimises the thermal lag induced by the thickness of the fabric. By following Procedure A, the "accident dose" is evaluated

by 1) integrating the TL within a selected interval, 2) calculating the gradient of the dose response curve for this interval, and 3) dividing the accident signal for the same interval by the slope of the dose response curve. A fading correction is required. The value of the accidental dose is thus given by the relation :

$$D_{acc} = \frac{L_{acc}}{a} \times f, \tag{10.4}$$

where D_{acc} is the accident dose, L_{acc} the accident signal, a the gradient, and f the fading correction. L_{acc}, a and f are interval specific.

The interval 140-160 °C was preferred for its strong intensity ($\leq$ 160 °C) that provided a plateau for dose assessment procedures, its greater stability (more than 50 % of remaining signal above 140 °C for F 179) and a relatively low native signal. As was explained above, due to the presence of a continuum of traps, narrow intervals of integration are preferred (e.g. intervals of 2 °C). If the fading corrections and the calculations are correct, the values of dose obtained for each integration interval should be similar. This is tested by a plateau test, where the dose values for each 2 °C interval are plotted. The plateau test for a blind dose of bag 19 is shown in Fig. 10.48. In this figure, a plateau is present, indicating that the dose evaluation might be accurate, within 10%.

The main issues identified here for the use of calcium carbonate fillers are 1) the relatively fast fading rate at ambient temperature, 2) the absence of an universal fading correction, and 3) the presence of a native signal. The first of this issue could be circumvented by placing the samples in freezers as soon as possible on the site of the event before processing by the laboratories, thus the samples would be held at ambient temperature only for a few hours. Once placed into a freezer, the samples could be measured up to months following the accident. The absence of an universal fading curve is, however, problematic and if individual fading correction are required would slow down the processing of the results. However, if the fading of the samples once placed at low temperature is negligible or identical, the individual fading correction would only have to be measured for the time the sample was held at room temperature (supposedly less than a day). Finally, the native signal is circumvented by either using a red sensitive PMT partially cutting the blue or green emission, or by sampling in parts of the bags protected from light (e.g., inside of pockets) and, consequently, it could be neglected.

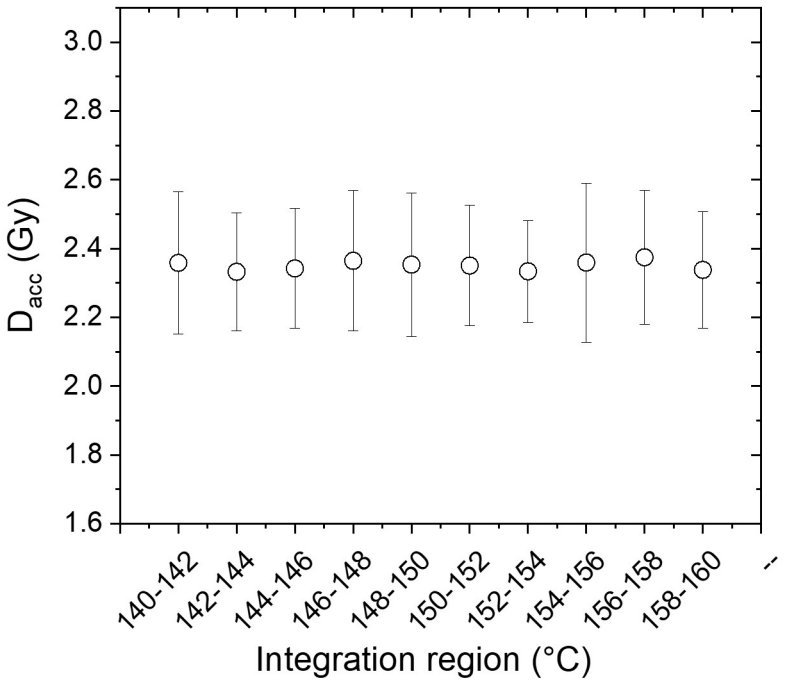

Fig. 10.48. Plateau test for samples taken from bag 19. The blind dose was reconstructed for each 2 °C intervals in the range 140-160 °C by applying fading corrections specific to each intervals.

10.11 Summary

The strength of the TL response of calcium carbonate fillers coupled with the apparent ubiquity of the material in thermoplastics and others polymer-based materials makes of calcium carbonate fillers a strong candidate for a surrogate dosimeter in radiological emergencies.

The TL measurements obtained with calcium carbonate fillers are generally consistent with those of calcite. The CL spectroscopy and TL measurements conducting using different filters indicated luminescence emission centred in the red (ca 600-620 nm), and the shape of the glow curve of calcium carbonate fillers extracted from the fabrics is similar to those reported in the literature with a TL peak with maximum between 80-100 °C following β irradiation. This peak is associated with a continuum of traps of low activation energy (ca between $\sim$ 0.4 eV and $\sim$ 0.62 eV). However, the fading rate observed with filler grains (ca 50% loss in 24 h in the region (140-142) °C) is slower than that calculated for the 80°C peak (of the order of a few hours at room temperature, Kirsh et al. 1987), but this is critically dependent on the integration integral selected. Storing samples at

low temperature in freezers could provide means for longer term dosimetry (up to months after the accident).

The effect of the presence native signal, which could be a potential disadvantage for short-term dosimetry by leading to an over-estimation of the "accident" dose was found to be circumvented by detecting the TL emission above 500 nm, indicating that the components of the native signal are emitting at lower wavelengths (blue/green emission), and are associated with the higher temperature peaks, arising from traps filled by natural radioactivity.

However, further work is needed to address some issues raised in this Chapter. By employing various combination of optical filter, it was assumed that the emission of the native TL signal of calcium carbonate fillers caused by the geological signal was predominantly in the blue / green whereas the β induced emission was predominantly in the red. This assumption could be verified by measuring the TL emission spectrum using a spectrometer to fully characterise the emission spectrum of the native and the β induced TL signal. Obtaining a spatial resolution of the TL emission of fabrics containing calcium carbonate fillers in the samples might also be useful in order to determine which exact part of the sample emits the most signal, or if the luminescence emission is completely uniform (e.g., whether all the fillers are equally bright, or if only the TL emission of the fillers at the surface is detectable). Further work is also needed to address the variability in fading rate observed between samples. It had been emphasised in that many other materials than the fabric of bags contain calcium carbonate fillers (Fig. 10.2), cement, paints, paper or food supplements). Some of these materials have been tested in during the material survey (Chapter 7) such as paper and shoe sole, and indeed yielded a TL signal similar to that of the calcium carbonate fillers observed in bags. Further testing is necessary to fully assess the potential of these materials, but it indicates that the study presented here could have a much broader range of application for emergency dosimetry. Although calcium carbonates are the most commonly employed fillers in the industry (Introduction of this chapter), other fillers employed (e.g., wollastonite) could also be investigated.

The tests conducted in this Chapter indicate that calcium carbonate fillers may be suitable for dosimetry with appropriate measurement procedures. To test this potential, an experiment replicating a radiological emergency by administering a "blind dose" was performed using a phantom and bags and is described in Chapter 12.

Chapter 11

Dosimetry in the long term : application of phototransferred TL (PTTL) properties of alumina substrates

11.1 Introduction

This chapter will focus on a relatively well-characterised material for short term dosimetry, that is the alumina substrate resistors such as found in electronic devices (e.g., mobile phones). They have been so far the favoured material for short term dosimetry using luminescence techniques, as was mentioned in Chapter 3 (Inrig et al., 2008b; Ekendahl and Judas, 2011; Bassinet et al., 2014; Kouroukla, 2015), for their common availability in mobile devices used by members of the public combined with their favourable OSL and TL properties. As a polycrystalline form of aluminium oxide, the alumina substrates exhibit bright OSL and TL signals in response to exposure to ionising radiation (Inrig et al., 2008b). The dose response was found to be linear (Bassinet et al., 2010) in the range of dose of interest for short term dosimetry (0.1-10 Gy), with a detection limit below 100 mGy for OSL and TL measurements (Mesterházy et al., 2012). Dose reconstruction of irradiated mobile phones using alumina substrate resistors extracted from the main circuit boards of mobile phones demonstrated the potential of this technique on irradiated mobile phones (Bassinet et al.,

2010; Ekendahl and Judas, 2011; Mrozik et al., 2014a).

However, although the components of the OSL/TL signal associated with charges in shallow traps that are subject to thermal fading can be removed by employing preheat treatments (Woda et al., 2010; Kouroukla, 2015), the signal of alumina substrate was found to exhibit anomalous fading. The rate of fading was not negligible, for the time scale considered for emergency dosimetry (hours to weeks). Following a preheat at 120 °C (10 s) and an OSL measurement with a sample temperature of 100 °C, 50% of the signal remained after 23 h in the dark, at ambient temperature (Kouroukla, 2015, p. 250). Besides a loss of the signal, that could lead to a higher detection limit and a complete loss of the signal months after the irradiation, the fading correction was thus necessary to proceed to dose assessment with an accompanying increase in uncertainty. Furthermore, the fading factor was found to depend on dose (Sholom and McKeever, 2017), and discrepancies exist between the fading correction reported in the literature, perhaps due to differences between resistors (Inrig et al., 2010a; Ekendahl and Judas, 2011; Kouroukla, 2015; Geber-Bergstrand et al., 2018). Hence reducing the rate of fading is of potential interest to strengthen the use of luminescence dosimetry with alumina substrate components.

The measurement of phototransferred thermoluminescence (PTTL) is a well-established procedure used as a means to access charges in deep traps in luminescent minerals and phosphors (Bailiff et al., 1977). This is achieved by moving a proportion of charge stored in deep traps to previously thermally cleaned shallower traps, typically by using short wavelength optical stimulation. Prompt measurement of the resultant PTTL glow curve enables an indirect measurement of the population of charge in the deep traps. PTTL procedures have been developed for variety of materials, including lithium fluoride (Kharita et al. 1994; Charles 1983), quartz (Bailiff et al., 1977) and aluminium oxide (Akselrod and Gorelova 1993; Colyott et al. 1996; Bulur and Göksu 1999; Polymeris and Kitis 2012; Nyirenda et al. 2016; Chithambo et al. 2017). The primary advantage of using this procedure is to avoid the effects of interfering black-body radiation and thermal quenching where the thermoluminescence (TL) peaks associated with the deep traps are measured directly (i.e., $\geq$ 500 °C). Also, the PTTL may potentially provide a means of circumventing the effects of anomalous fading (Bailiff 1976; McKeever et al. 2017). Thus, this chapter will aim to investigate the PTTL emission of alumina substrate resistors, and to assess whether this can be used to reduce the rate of fading.

11.2 Materials and protocol

All OSL and TL measurements were performed with a Risø model 12 reader (DTU Nutech, Denmark, see Chapter 6 for details of the instrumentation) that incorporates a Sr^{90}/Y^{90} β source irradiator delivering an estimated dose rate to alumina substrates of 0.74 Gy·min^{-1} (see Chapter 12 for details of the calibration procedure). A UV (250-350 nm; Schott U-340 filter) and broad band (360 - 580 nm; Schott BG-39 filter) detection windows were used when measuring blue (470 nm) stimulated OSL and TL. Two illumination sources were employed to transfer charge from deep traps for the PTTL measurements, comprising either the 470 nm LEDs in the Risø reader, delivering a power of 14 mW.cm^{-2} at the sample position, or UV radiation from an unfiltered medium - pressure mercury lamp. The mercury lamp (Hanovia Ltd) delivered a power of $\sim$ 4 mW·cm^{-2} at the sample position and its emission spectrum contained lines at 307, 364, 403, 434, 544 and 575 nm. The abbreviated terms PTTL[UV] and PTTL[470 nm] are used to distinguish the type of illumination source used to obtain the PTTL. For each set of measurements, five alumina substrate surface-mount resistors of type 1206 (RS pro, $\sim$ 5.2 mm^2), were placed in a stainless steel cup with the alumina substrate layer facing up, and each test was repeated at least twice to test for reproducibility. The TL peak temperatures were calculated by applying a curve fitting procedure to the measured glow curve data (using Origin 2017 software) and hence the values obtained reflect the precision of the fitting procedure only. Independent thermocouple measurements of the heater plate temperature indicated that the temperatures displayed by the Viewer software (DTU Nutech) are within 6 °C of the measured value and that, when taking into account thermal lag introduced by the samples and the stainless steel pans, the overall uncertainty in the average resistor temperature is likely to be the order of ± 8 °C. The PTTL (470 nm) measurement procedure (A) followed is summarised in Table 11.1.

Table 11.1: PTTL measurement procedures A and B

Step	Measurement
1	TL to T_{stop} 450 °C (procedure A) or 500 °C (procedure B); 5 °C.s^{-1}
2	Repeat step 1 (background); subtraction of the background from the TL glow curve (step 1)
3	Phototransfer illumination, 470 nm LEDs, 120 s at sample temp. of 150 °C; concurrent measurement of OSL
4	PTTL to T_{stop} (500 °C); 0.5 °C.s^{-1}
5	Repeat step 4 (background); subtraction of the background from the PTTL glow curve (step 4)
6	Anneal to 700 °C in a furnace, in air, 20 min

11.3 PTTL characteristics

11.3.1 Detection window

Measurements performed using the BG-39 detection filter yielded a PTTL[470 nm] signal about three times stronger (Fig. 11.1) than with a U-340 filter, indicating that the PTTL emission spectrum is not confined to the UV region. This is consistent with radioluminescence (RL) spectra measured with alumina substrates by Kouroukla (2015, p. 132) and Lee et al. (2017) which indicated complex emission that included UV, blue and red bands. It was also observed that the intensity of the shorter wavelength emissions was thermally quenched, giving rise to predominantly red emission at higher temperatures (Kouroukla, 2015, p. 132). However, recording the red TL emission above 400 °C using the BG-39 filter gave rise to a strong thermal background signal, making the detection of weak signals associated with low dose difficult to resolve above the thermal background signal.

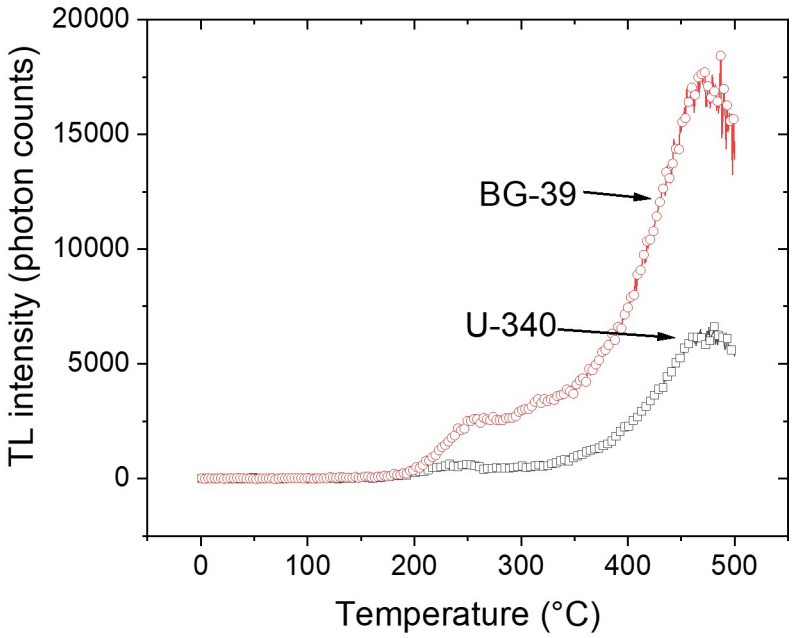

Fig. 11.1. PTTL[470 nm] glow curves measured with alumina substrate chips following β irradiation (10 Gy). Detection window: U-340 (black open squares) and BG-39 (red open circles); heating rate 0.5 °C·s^{-1}. The thermal background signal was subtracted.

11.3.2 Variation of PTTL with 470 nm illumination parameters

The PTTL (470 nm) glow curve was recorded following a 2 min 470 nm exposure (concurrently measuring the OSL) at a sample temperature selected in the range 50-400 °C (Fig. 11.2). The shape of the PTTL glow curve changes with the sample temperature during illumination and, as the temperature increases, a more efficient transfer of charge to shallower traps gives rise to relatively stronger lower temperature PTTL peaks. Above 200 °C the transfer process competes with thermal bleaching of the PTTL traps during illumination, leading to a progressive decrease of the PTTL signal. A similar measurement procedure was applied by varying the illumination time (30-300 s) for a fixed sample temperature. A plot of the integral of the PTTL glow curve (150-500 °C) vs both sample temperature and duration of illumination, shown in the form of a contour plot in Fig. 11.3, indicates that the maximum PTTL intensity was obtained for an illumination of 2 mins with a sample temperature of 150 °C, and these measurement conditions were adopted using procedure A (Table 1).

11.3.3 Dose response

The PTTL (470 nm) glow curve contains several overlapping peaks (Fig. 11.4a), positioned at 190, 240, 335 and 465 °C. The presence of a native signal was tested by measuring a fresh set of unirradiated resistors, but found to be negligible using 470 nm illumination (Fig. 11.4a). Fig. 11.4b shows the growth of the PTTL peaks (integrated TL, 150 -500 °C) with absorbed β dose, measured with the same aliquot, which exhibits a supralinear dose dependence (Fig. 11.4b) that was also observed for each peak analysed individually. Two preheat temperatures were tested : 450 °C (procedure A) and 500 °C (procedure B), using a heating rate of 0.5 °C.s^{-1}. An additional TL background measured after step 2 in procedure B indicated that some residual TL remained after this step above 300 °C (Procedure A) or 350 °C (Procedure B). The integration region of the PTTL glow curve was between 150-300 °C to avoid this residual TL. The glow curves measured using procedures A and B contained similar peaks but the signal was weaker using procedure B, although the dose response appeared to be more linear. Interestingly, similar analysis performed using an integration range of 300-500 °C produced similar outcomes.

The reproducibility of the PTTL signal, tested by repeating procedure A five times for a given dose, exhibited similar values of integrated photon counts (within 10 %). Using procedure A, and

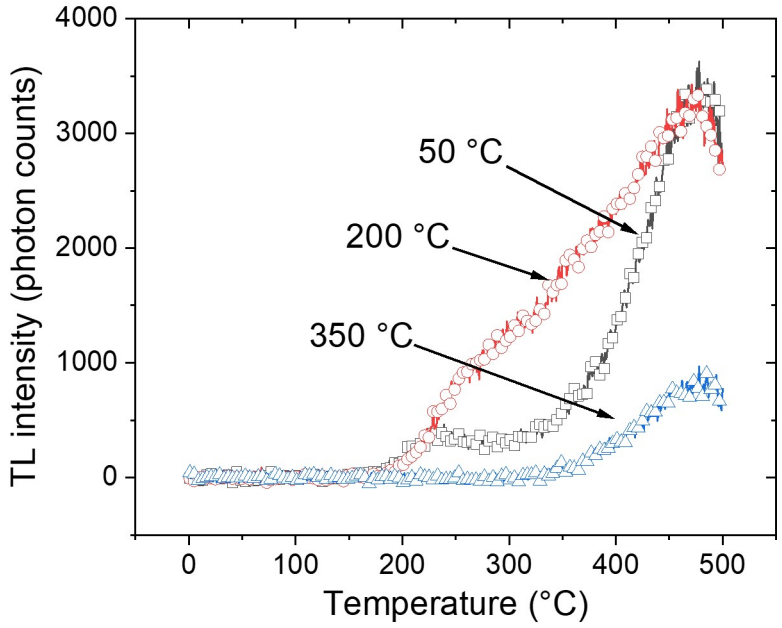

Fig. 11.2. Phototransferred TL glow curves of alumina substrate measured following a β irradiation (10 Gy), a 2 mins 470 nm illumination at a sample temperature selected in the range 50-350 °C, three examples of which (50, 200 and 350 °C) are shown. Detection filter: U-340; heating rate 0.5 $^{\circ}C.s^{-1}$.

a quadratic function fitted to the dose response data, the detection limit (calculated as the dose for which the PTTL signal is equal to the background signal plus three times its standard deviation) was estimated to be $\sim$ 100 mGy. The final annealing step (6) was applied to minimise sensitization effects by thermally cleaning the deep electron traps. If this step is omitted, a non-linear increase in sensitivity is observed over repeated cycles of measurements. During 470 nm illumination at elevated sample temperatures (Step 3), the OSL signal was also recorded (Fig. 11.5a) and its slow evolution and subsequent decay reflect a thermally-assisted process (TA-OSL), similar to that observed with Al_2O_3:C (Polymeris et al., 2010), together a supralinear dependence with dose (Fig. 11.5b).

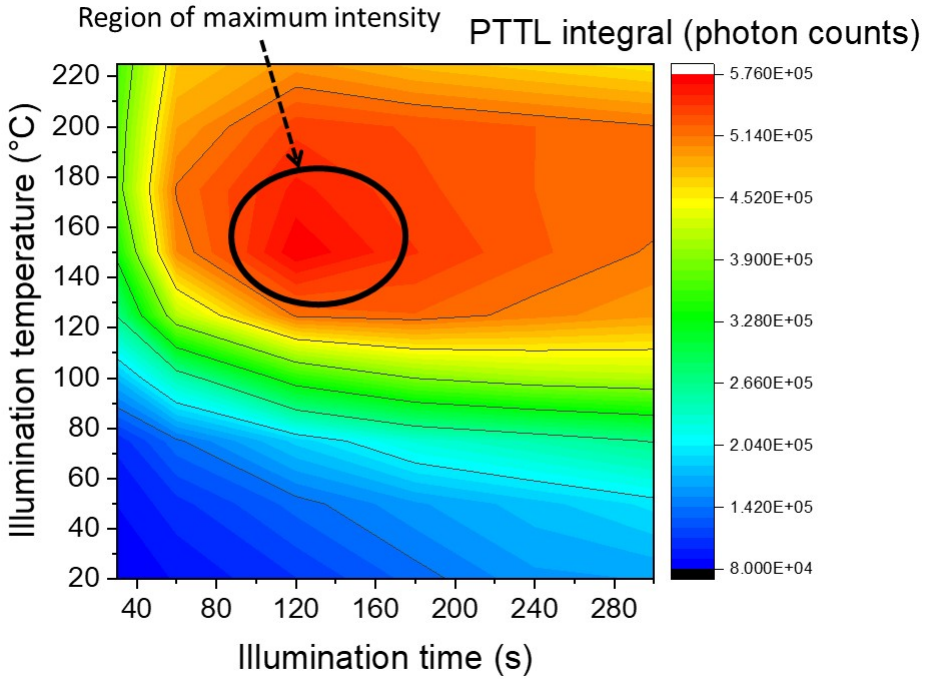

Fig. 11.3. PTTL intensity vs the illumination parameters (duration and temperature). The PTTL intensity corresponds to the integral of the signal recorded between 150 and 500 °C.

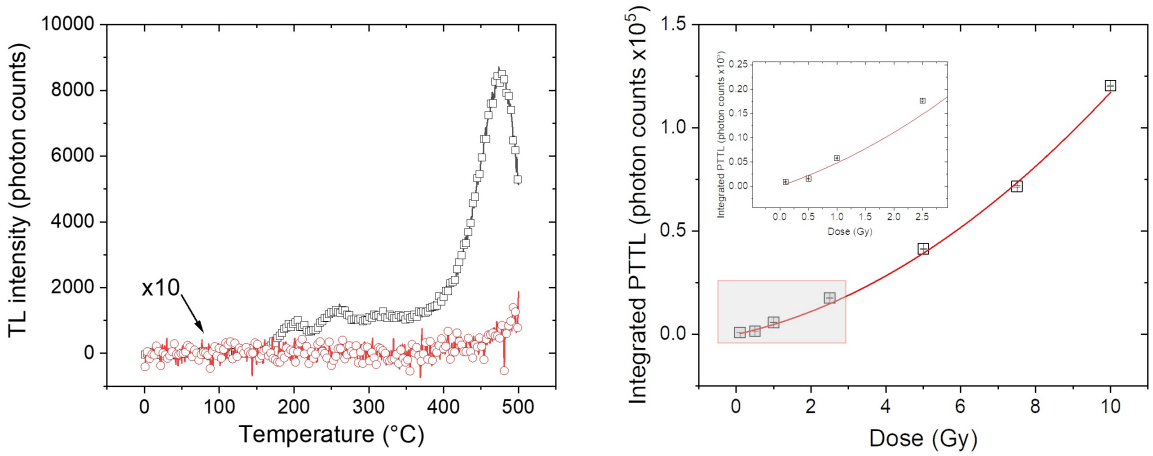

Fig. 11.4. a) Native (open circle) and β-induced (10 Gy; black squares) PTTL glow curves measured with five alumina substrate chips, measured following the PTTL procedure (Table 11.1). b) Integral of the PTTL signal (150-300 °C) vs administered β dose, where the solid line represents a quadratic function fitted to the experimental data. Type A error in counts $\leq$ 1 %. Detection window: U-340; heating rate 0.5 °C.s^{-1}.

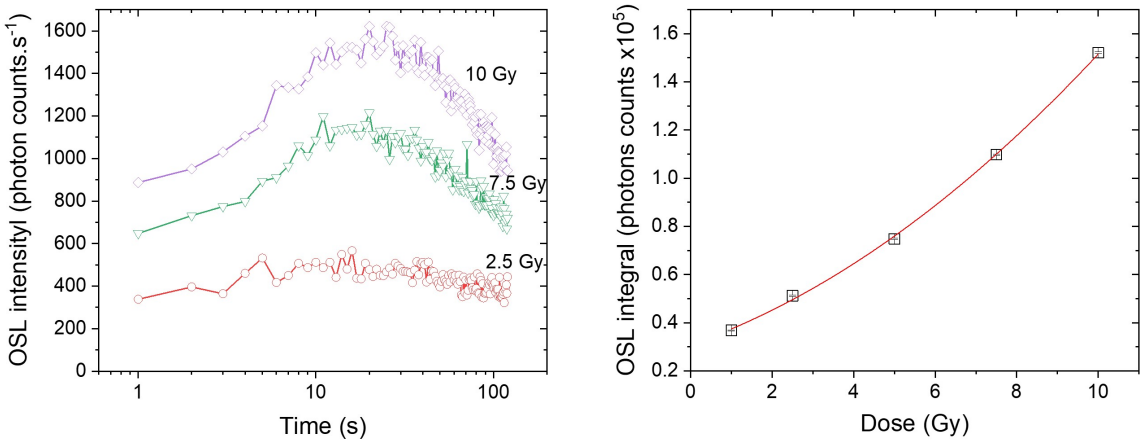

(a) **(b)**

Fig. 11.5. a) 470 nm stimulated OSL recorded following β irradiation and 450 °C preheat (Step 3 , Table 11.1). Detection window : U-340. b) Integral of the OSL signal vs administered β dose, where the solid line represents a quadratic curve fitted to the experimental data. Type A error in counts $\leq$ 1 %. Detection window: U-340; sample temperature : 150 °C.

11.4 UV illumination

As the supralinear dose response of the PTTL[470 nm] is a potential disadvantage for absorbed dose determinations below ca 0.5 Gy, optimisation of the PTTL response was explored using shorter wavelength illumination. In contrast to the PTTL[470 nm] results, fresh unirradiated samples, when illuminated (2 mins) with UV produced a "native" glow curve containing two peaks (Fig. 11.6a). The native signal measured after UV illumination is interpreted as a non-radiation-induced UV-stimulated signal, which is observed, for example, with Al_2O_3:Si,Ti, and applied in UV dosimetry (referred to as photo-stimulated TL, PSTL; Mehta and Sengupta 1977, 1978). A PSTL contribution, if present, needs to be accounted for when applying PTTL to perform dosimetry measurements with a UV light source. The PTTL (UV) glow curve recorded following a β dose of 10 Gy and a 2 min illumination at RT, contains three main peaks (Fig. 11.6a) at ca 190, 315 and 460 °C, and the PTTL (470 nm) glow curve is shown for comparison. Under the particular illumination conditions used in these experiments, UV transfers significantly more charge into the PTTL traps compared with 470 nm illumination (the integrated PTTL is $\sim$ 4 times greater for a 10 Gy β dose). By annealing the samples at 900 °C for 30 mins and repeating the PTTL measurement procedure, the glow curve measured was similar in shape and intensity to the "native" PSTL signal. The latter indicates that this annealing procedure effectively thermally cleaned the deep traps associated with the PTTL signal. The dose response curve obtained with UV illumination is linear (Fig. 11.6b), and the estimated detection limit of 200 mGy is higher than that obtained with 470 nm illumination.

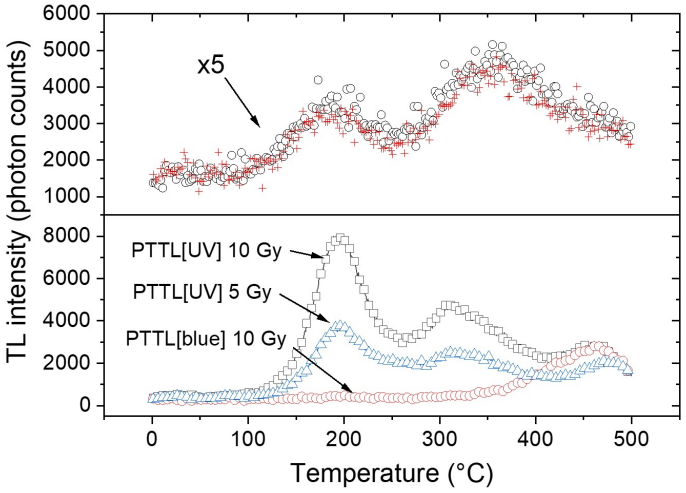

(a)

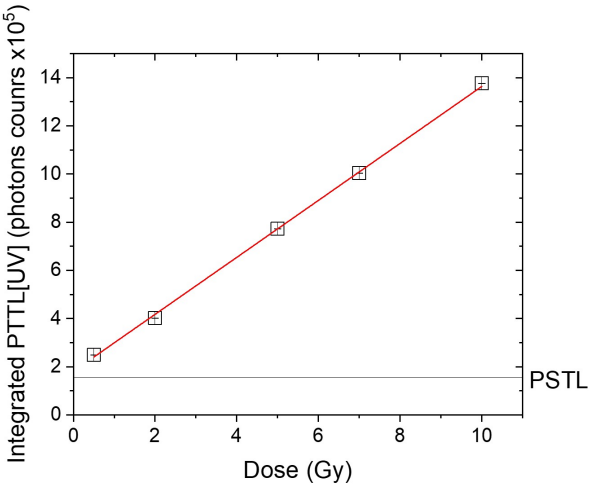

(b)

Fig. 11.6. a) Upper : "native" PSTL (black circles) and PSTL measured after a cycle of PTTL[UV] measurements and annealing at 900 °C (red crosses) of alumina substrate chips following UV illumination for 2 minutes at room temperature. Lower : PTTL[UV] following β irradiation 10 Gy and 5 Gy (open black squares and open blue triangles respectively), and PTTL[470 nm], 10 Gy β dose (open red cirles). All illuminations were carried out at room temperature and the samples were exposed to the light source for 2 minutes. b) Integral of the PTTL (UV) signal (100-500 °C) vs administered β dose (0.5-10 Gy). The solid line represents a linear curve fitted to the experimental data; the horizontal line indicate the PSTL signal. Type A error in counts ≤ 1 %. Detection filter : U-340, heating rate : 0.5 °C.s^{-1}, Risø reader.

11.5 Fading

Fading tests were performed by administering a β dose of 7.4 Gy to samples, storage in the dark at ambient temperature for periods ranging from 6 h to 224 days and measuring the PTTL (470 nm) following procedures A and B and using a integration interval of 150-300 °C. The resistors used in the fading experiments were obtained from the same manufacturer (RS Pro, UK), but they were obtained from two reels, referred to as batches 1 and 2. Measurements using four sets of 5 resistors from Batch 1 were initially conducted with single aliquots for storage periods of 0.125, 2 and ca 100 days, and the tests were repeated using aliquots that contained resistors from both batches (1 and 2), for storage periods up to 2 days and for various storage periods between 2 and 244 days. The results obtained from the fading tests shown in Fig. 11.7 include: a) the integrated PTTL (150-300 °C) recorded using procedures A (open diamonds) and B (open triangles) b) the integrated TL recorded in two temperature regions (filled circles, 150-200 °C and filled squares, 200-300 °C).

It can be seen that using the Batch 1 resistors, the extent of long-term fading over 100 days is less than ca 15%, using either of procedures A and B. Analysing the results using an integration range of 300-500 °C in the PTTL glow curve produced a similar outcome, and suggests that the inclusion of remnant TL in the higher temperature region of the PTTL glow curve does not appear to significantly affect the rate of fading. Although the repeated tests performed with resistors from the combined batches show similar behaviour for storage periods up to 2 days, a greater degree of fading for longer periods of storage is evident in these subsequent tests. Assuming that the measurement procedures were applied correctly, these results provide an alert to the possible variability of fading characteristics between batches of resistors, and this requires more detailed investigation. Nevertheless, the loss observed in these tests at ca 200 days remains some 30% less for PTTL than that obtained with conventional TL, as measured with resistors from the same batches (Fig. 11.7, filled circles and filled squares), and also obtained in previous studies (Ademola and Woda 2017; Kouroukla 2015).

The fading behaviour of the TA-OSL signal was also found to be similar to that of the PTTL. In her study of the long-term fading of OSL of alumina substrate, Geber-Bergstrand et al. (2018) also found the existence of a long-lived OSL component of the decay curve, where the average period after which the signal halved was (790 $\pm$ 210) days; she estimated that a 0.5 Gy dose could be measured after a period of 2 years, after applying a fading correction.

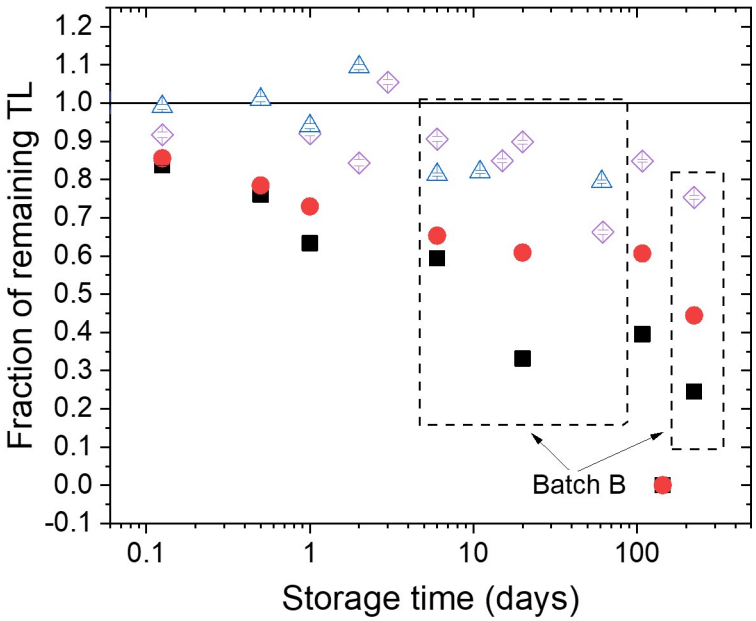

Fig. 11.7. Remaining PTTL signal (integral, 150-300 °C; purple diamonds: procedure A; blue triangles: procedure B) following storage (0.125- 224 d) in the dark at ambient temperature, compared with the TL signal remaining (integral, 150-200 °C, black squares; integral 200-300 °C, red circles). The horizontal line indicates the absence of fading (y = 1). The box (broken line) groups the results obtained with resistors drawn from combined batches 1 and 2.

11.6 Kinetics

A pulse-annealing stage was added to procedure A to examine the thermal stability of the traps that provide a reservoir of charge for the PTTL signal. The samples were heated to a temperature selected in the range 450 to 600 °C before the 470 nm illumination in Step 3 and subsequent recording of the PTTL to 500 °C. During the pulse-annealing sequence, the 480 °C PTTL peak exhibited the strongest reduction (Fig. 11.8a and 11.8b) in intensity following a preheat to 600 °C, indicating that charges in deep traps accessed by 470 nm illumination are thermally emptied by annealing in the region 450-600 °C. Similar results were obtained testing a second set of chips. Attempts to determine the thermal activation energies of the traps acting as the reservoir of charge were unsuccessful. An assessment of the Arrhenius plots obtained with data produced from a pulse annealing PTTL (470 nm) measurement procedure indicated that the nature of these traps is complex, likely to comprise a distribution of traps associated with TL peaks between 500 and 600 °C.

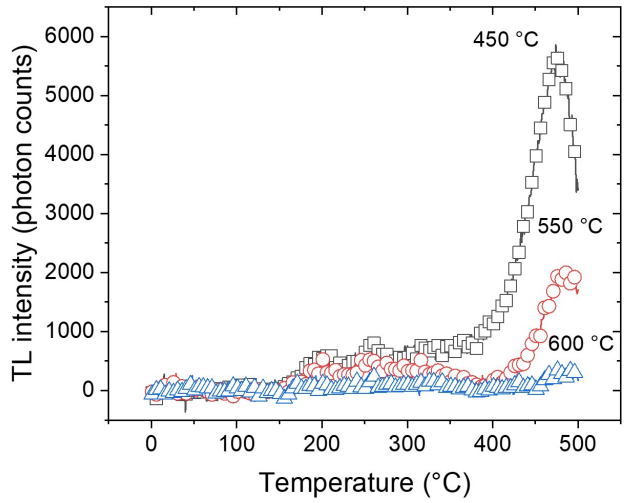

(a)

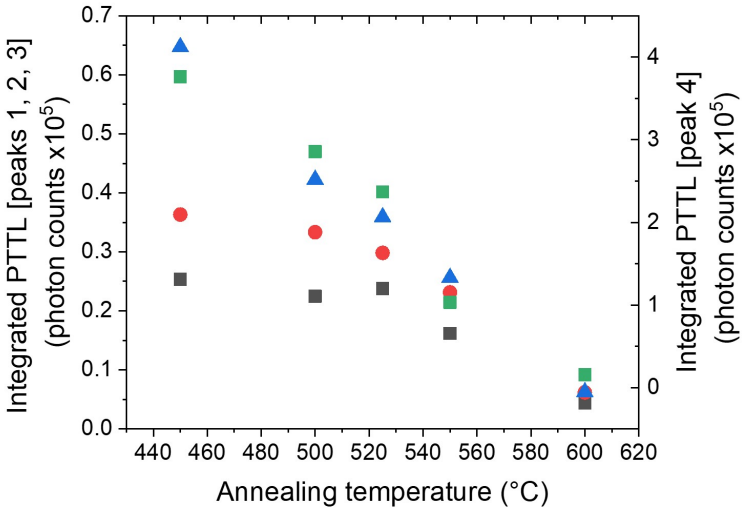

(b)

Fig. 11.8. a) PTTL [470 nm] glow curves of alumina substrate measured following β irradiation (10 Gy) and annealing at the indicated temperatures in the range 450-600 °C . b) PTTL vs annealing temperature: Peak 1 (integrated TL 150-223 °C, black filled squares), Peak 2 (223-284 °C, filled circles), Peak 3 (283-377 °C, blue filled triangles), and peak 4 (377-500 °C, green inverted filled triangles). Detection window: U-340. Heating rate: 0.5 °C·s^{-1}.

11.7 Discussion

The results of the pulse annealing and phototransfer experiments confirm the presence of deep traps that provide a reservoir of charge probed by the PTTL measurement procedure. If we examine for parallels between the PTTL behaviour of alumina substrates and crystalline Al_2O_3, amongst the earlier work on the latter, Akselrod and Gorelova (1993) proposed three types of traps that, in addition to type I traps producing the main dosimetry TL peak at 190 °C, included deep type II and type III traps associated with TL peaks at 550 °C and ca 900 °C respectively. Colyott et al. (1997) studied three PTTL peaks located at -8, 37 and 177 °C measured following preheat treatments ranging from RT to 900 °C, and they found the PTTL to be most efficiently produced when induced by 300 nm illumination. Later work has linked the PTTL with one or more traps associated with TL peaks above 500 °C (Bulur and Göksu, 1999) and above 600 °C (Chithambo et al., 2017). Although the nature of the traps providing the reservoir of charge for PTTL in Al_2O_3 has not been identified, these studies point to the type II and III traps proposed by Akselrod and Gorelova as providing the most likely reservoirs of charge. The results obtained with our alumina substrate samples using 470 nm illumination indicate that the reservoir of charge may originate mainly from traps of similar depth to the type II traps, and under UV illumination ($\geq$ 300 nm) they are likely to be associated with both type II and type III traps, given that annealing at ca 900 °C was required to erase the PTTL (UV) signal. As found with alumina substrate, sensitization effects were reported in monocrystalline Al_2O_3 by Yukihara et al. (2003), and explained by the presence of deeper traps.

In addition to characterisation of the deep traps, the nature of the traps into which the charge is transferred associated with the PTTL is also of interest. Again, seeking parallels with crystalline aluminium oxide, Chithambo et al. (2017) found that the peaks in the PTTL and TL glow curves were similar, suggesting that similar traps participate in both modes of measurement. We have made broadly similar observations with the alumina substrate tested, although the distribution of charge in the traps participating in the PTTL and TL processes differ (Fig. 11.9), with the lower temperature peak more prominent in the glow curve. In the higher temperature region, the 314 and 480 °C TL peaks are reproduced in the PTTL[470 nm] and PTTL[UV] glow curves and the 260 °C TL peak is also present in the PTTL[470 nm] glow curve. However, the 197 °C peak observed in the PSTL and the PTTL[470 nm; UV] glow curves differs in position relative to the main TL peak

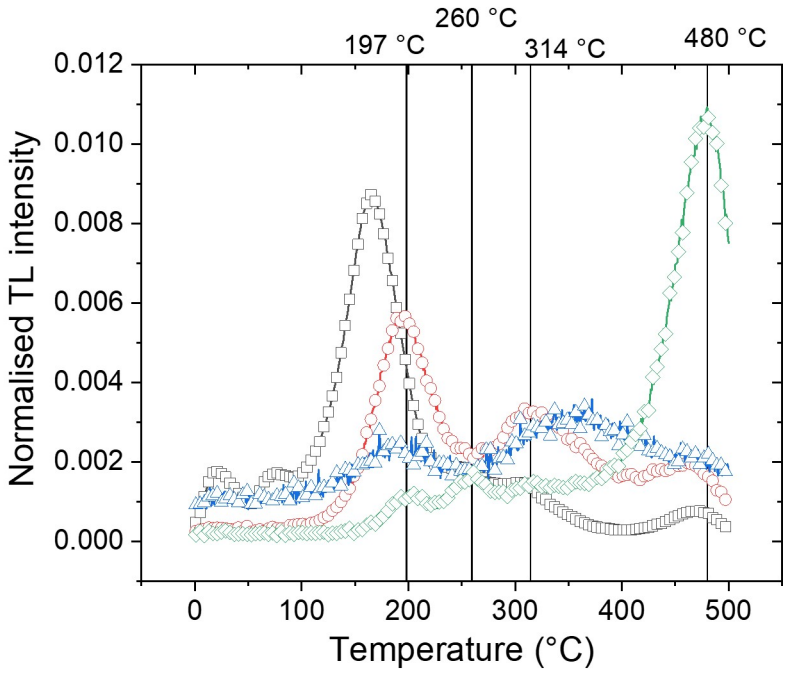

Fig. 11.9. Alumina substrate glow curves of 1) TL, β dose 10 Gy (open black squares), 2) PTTL induced by a 2 min UV illumination at room temperature, β dose 10 Gy (open red circles), 3) photo-stimulated signal induced by a 2 min UV exposure at room temperature (no dose, open blue triangles), and 4) PTTL induced by blue illumination 2 min at 150 °C, β dose 10 Gy (open green diamonds). Some of the peak positions (197, 260, 314, and 480 °C) are indicated by a vertical line. The glow curves were normalised to the total integral of the signal. Risø system, U-340, detection window : U-340, heating rate : 0.5 °C·s^{-1}.

(165 °C).

11.8 Blind test

11.8.1 Conventional OSL procedure

Three additional 1206 surface mount alumina substrate resistors were glued to the circuit board of a mobile phone irradiated with a blind dose (reference dose: 4.1 Gy, ^{60}Co source, irradiation carried out by Celine Bassinet, at the IRSN, France in the scope of a EURADOS working group 10 inter-laboratories comparison). A LiF TLD was placed inside the phone and indicated an absorbed dose

of 3.9 ± 0.2 Gy. Following irradiation, the sample was stored at ambient temperature and measured 12 days after the irradiation. The absorbed dose to the resistors extracted from the circuit board was determined using an OSL procedure following the conventional "full mode" protocol (Bassinet et al., 2014), as follows :

1. Preheat to 120 °C, 2 °C.s^{-1}, 10 s
2. Measure OSL (470 nm) at sample temperature 100 °C, 30 s (accident signal)
3. Administering calibration dose (β, 5 Gy)
4. Preheat to 120 °C, 2 °C.s^{-1}, 10 s
5. Measure OSL (470 nm) at sample 100 °C, 30 s (accident signal)

The equivalent dose, D_e, administered was calculated by dividing the "blind" OSL signal (step 2) by the OSL response to the 5 Gy dose (step 5). The OSL signal was corrected for fading using a sample-specific fading correction, determined by irradiating the sample with a known dose, storing it for 12 days, measuring the OSL signal and comparing it with the signal measured less than 5 min following irradiation. After 12 days of storage in the dark at ambient temperature, and for this sample, the percentage of remaining signal was estimated of (38.2 ±0.3) %. A value of (4.03 ± 0.04) Gy was obtained for D_e using the OSL signal from the resistors extracted from the circuit board.

11.8.2 TL and PTTL protocols

The TL and PTTL of the additional resistors glued to the circuit board were measured following the procedure A described in Table 11.1. Three levels of dose were used (3, 4 and 5 Gy) to construct the TL and PTTL dose response curve. The equivalent dose was determined using the TL integral in the region 200-300 °C of the glow curve and fitting a linear function to the TL dose response curve, and applying the fading correction determined in Section 11.5 for a similar type of resistor (resistors 1206, RS pro, see Fig. 11.7, 60 ±0.06 % of remaining signal in the region 200-300 °C after 12 days of storage in the dark at ambient temperature); yielding a dose of 3.82 ± 0.09 Gy.

The blind dose was determined using PTTL procedure A (Table 11.1); a quadratic function fitted to the PTTL dose response curve and a fading correction was also applied, such a determined

in Section 11.5 for a similar type of resistor (resistors 1206, RS pro, see Fig. 11.7). For a 12 days storage in the dark at room temperature, the percentage of PTTL remaining signal was determined of 87 ±0.2 %. The dose determined using PTTL was of 3.79±0.2 Gy.

Table 11.2 summarises the equivalent dose determinations obtained using the three methods (OSL, TL and PTTL); they agree with the applied "blind" reference dose of 4.1 Gy within 10%.

Table 11.2: Estimation of applied dose obtained using OSL, TL and PTTL measurement procedures applied to resistors following a blind irradiation (IRSN). The correction factor, f indicated here is defined as $D_e(corrected) = D_e(uncorrected) \times f$. The error indicated in the fading correction were propagated to the values of blind dose.

Method	Value of blind dose (Gy)	Fading correction applied, f
OSL (full mode)	4.03 ± 0.04	2.6±0.2
TL (integral 200-300 °C)	3.82 ±0.09	1.7 ± 0.1
PTTL	3.79 ± 0.2	1.14±0.02
LiF TLD inside phone	3.9 ± 0.2	
Reference dose	4.1	

11.9 Summary

The results obtained indicate that a PTTL measurement procedures can be applied to polycrystalline Al_2O_3 substrates for dose determination using blue and shorter wavelength illumination. For the substrates tested, and using blue illumination, the dose response was found to be supralinear, with a detection limit of ca 100 mGy for a resistor surface area of 22.5 mm^2. By employing UV illumination ($\geq$ 300 nm) the dose response obtained was linear, although with a higher detection limit of ca 200 mGy, partly arising from the presence of a photo-stimulated thermoluminescence (PSTL) signal. The trapped charge transferred in the PTTL procedure originates from deep traps and although their depths could not be determined using blue illumination, we conclude that 1) the trapped charge associated with the PTTL signal originates from a range of deep traps that are thermally erased in the region 450-600 °C and 2) UV illumination enables access to charge in deeper traps that are thermally erased by heating to 900 °C. Significantly, we found that in laboratory

fading tests in the dark at room temperature the measured loss of PTTL was less than 30 % for storage periods of up to 224 days. This is to be compared with a typical loss of 47 % in 50 days using conventional TL (Ademola and Woda 2017; Kouroukla 2015). A blind test was successful in reconstructing the administered dose after a storage of 12 days using PTTL on alumina substrate resistors attached to the circuit board of a mobile phone, and indicating that the correction factor applied to account for fading was lower using PTTL compared with OSL and TL. The PTTL procedure has sufficient sensitivity for dosimetry measurements following radiological emergencies, although further optimisation of the procedure would be required to address the issue of the trend of the decreasing size of surface mount resistors. Although the physical mechanisms associated with the deep traps in the alumina substrate probed by the PTTL measurements require further clarification, the possibility of reducing the extent of the significant fading observed in conventional TL or OSL measurements introduces a potentially valuable tool in the use of this material for short and long term retrospective dosimetry.

Chapter 12

Dosimetry using calcium carbonate fillers

12.1 Introduction

Chapter 10 demonstrated the great potential of calcium carbonate fillers such as found in the coating of bags, to act as surrogate dosimeters. However, the tests described in Chapter 10 were carried out under very controlled conditions, and do not reflect an actual emergency situation. Their applicability in radiological emergency scenarios have not yet been tested. This chapter describes the testing of this technique with a blind test simulating a radiological "accident". The setup for the blind test comprised bags with calcium carbonate fillers, a mobile phone and a tube test of blood positioned on a anthropomorphic phantom, irradiated using a ^{60}Co source. This blind test aimed to answer the questions of 1) whether bags containing calcium carbonate fillers could be used for dose reconstruction? 2) How can the protocol be optimised? 3) How does the TL of calcium carbonate fillers perform compared with other methods of short term dosimetry (i.e., OSL of surface mount alumina substrate resistors, TL of glass display, dicentric chromosome assay)? 4) What are the advantages and disadvantages of each technique? MCNP simulations have also been carried out in order to characterise the absorbed dose in calcium carbonate fillers embedded in polyurethane, as a function of source energy, position, and depth of the fillers. The issue of dose conversion coefficient from absorbed dose to fillers to organ dose will also be addressed.

12.2 Radiation transport simulation

The Monte Carlo N-Particle Transport version 6 (MCNP6) code developed by Los Alamos National Laboratory was used to simulate the transport and interactions of particles using repeated random processes. The behaviour of each particle is simulated and recorded in specific volumes (cells). The main particle of interest was photon, but electrons were also used as they are the particles used in the Risø reader source. MCNP can calculate a surface current or fluence (F1 and F2 tallies respectively), a cell fluence (F4 tally), the energy deposition in a cell (F6 tally) or the pulse height in a cell times the energy deposited (*F8). To calculate the absorbed dose in a volume, the F6 tally was used when charge particle equilibrium was assumed and the *F8 tally otherwise. The F6 tally indeed produces electrons into photons that are locally deposited into matter (photons only mode, operating under the kerma approximation), whereas the *F8 tally takes into account all the interactions between particles and matter (i.e., photoelectric effect, Compton scattering, pair production), except elastic scattering (i.e., photons interact with matter, they change direction but their energy is not reduced).

MCNP6 was used here to 1) simulate the absorbed dose in various materials in the Risø reader configuration, for calibration purpose, 2) to simulate the absorbed dose effect at a scale that could not be tested experimentally (e.g. looking at the behaviour of single grains of calcite in a PU matrix), 3) to study the behaviour of the dosimeters investigated in a radiological emergency scenario and 4) to convert the dose absorbed in the dosimeter to the organ doses.

12.2.1 Dose deposited in calcium carbonate fillers using the Risø reader β source

A radiation transport model was set up using MCNP 6 (Goorley et al., 2012) for the β source in the Risø reader in order to estimate the dose absorbed in calcium carbonate fillers compared with quartz grains. Calcium carbonate fillers were modelled as spheres of 100 μm of diameter ($CaCO_3$, density : 2.71 g.cm^{-3}) separated each by a distance of 100 μm and distributed in a matrix of polyurethane (PU, $C_{0.33}O_{0.62}H_{0.04}$, density : 1.10 g.cm^{-3}) using a repeated structure (Fig. 12.1). The matrix containing the calcium carbonate fillers was placed in air on a stainless steel disc positioned 6.5 mm away from the $^{90}Sr/^{90}Y$ source, modelled as a plan parallel source. The primary β particle energy spectrum was obtained from the MIRD database. For calibration purposes, the dose absorbed in the fillers was compared with the dose in quartz grains (100 μm of diameter, SiO_2, density : 2.6

g.cm^{-3}) placed on the stainless steel disc, since the β source was primarily calibrated to quartz. Different thicknesses of fabric were considered (400 μm, 1000 μm and 1200 μm) which corresponded to the measured thickness of bags 21, 19 and 16 respectively (see Chapter 10 for list of the samples). These bags were later used in the blind test (Section 12.3). The absorbed dose was calculated for grains positioned at the surface of the fabric and at different thicknesses in the PU (centred at 100-1100 μm from the surface depending on the thickness).

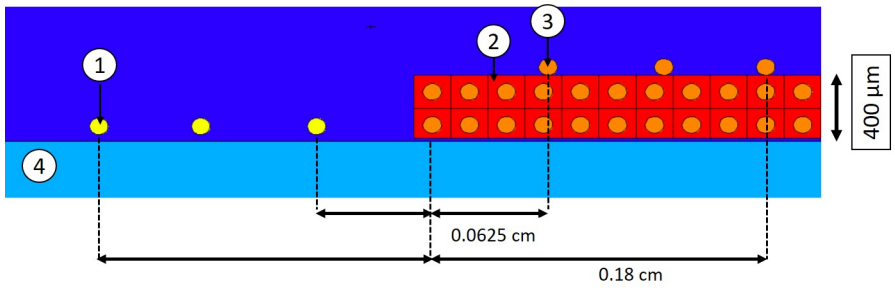

(a)

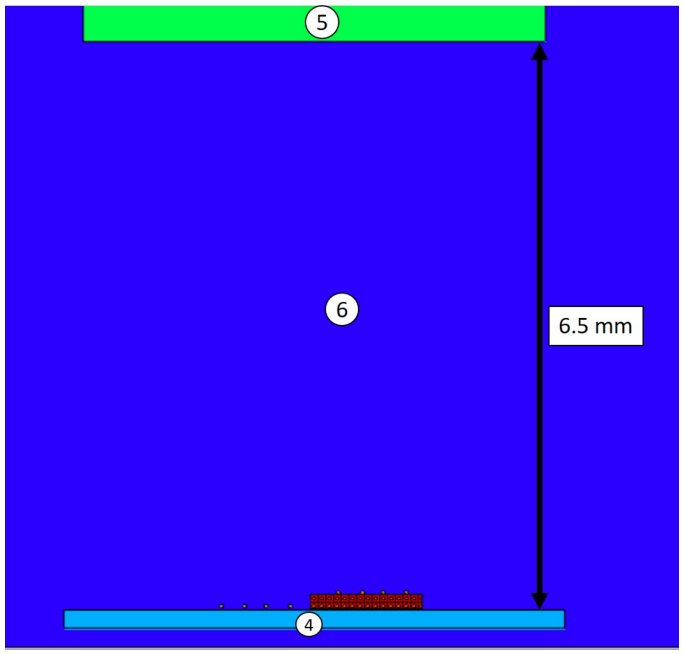

(b)

Fig. 12.1. MCNP model used to calculated the dose absorbed in calcium carbonate fillers distributed in a PU matrix in the β source. The dose absorbed in calcium carbonate fillers was compared to that of quartz grains. The PU matrix containing the calcium carbonate fillers, and the grains of quartz were placed on a stainless steel disc, positioned 6.5 mm from the β source. ① Quartz grain, ② PU matrix, ③ calcium carbonate filler, ④ stainless steel disc, ⑤ $^{90}Sr/^{90}Y$ source (plan parallel), ⑥ air. Thickness of the fabric : 400 μm.

The absorbed dose in the calcium carbonate fillers was normalised to the absorbed dose to quartz grains positioned at the same radial position (i.e. modelled at x=0.0625-0.24 cm from the centre of the disc, Fig. 12.1a). Fig. 12.2 shows the absorbed dose in calcium carbonate filler grains at position 0.0625 and 0.18 cm from the centre at various depths in the PU (Fig. 12.1a), normalised to the absorbed dose in quartz grains at a similar distance from the centre position on the stainless steel disc. The dose given to the grains of calcium carbonate (100 μm of diameter) positioned on the surface of the fabric (depth : 0 μm) was lower than the value of dose to quartz deposited on a stainless steel disc by ∼10-15 % (depending upon the position of the $CaCO_3$ grain), even though the calcium carbonate was closer to the source. This may due to 1) the lack of build up, that is the absence of charge particle equilibrium in thin detectors closer to the source, or 2) the reduction in backscatter from the stainless steel disc for a grain placed at the surface of the sample of fabric. The value of absorbed dose increases as the grains are further from the surface in the PU. A plateau is reached at a depth of ∼500 μm, probably when the charge particle equilibrium is reached in the medium. When the plateau is reached, the value in absorbed dose in calcium carbonate fillers in PU was about 10-20 % higher compared with grains of quartz on a stainless steel disc. Grains located in the centre of the fabric (0.18 cm from the centre, Fig. 12.2) also registered a higher dose compared with grains at the edge (0.0625cm from the centre, Fig. 12.2).

Fig. 12.3 shows the profile of absorbed dose to calcium carbonate filler grains in PU fabric at different depths (400-1200 μm in the fabric) placed on a stainless steel disc. Interestingly, the value of absorbed dose for grains at the surface of the fabric is the same for all thickness (∼ 10% lower compared with the absorbed dose to grains of quartz on the surface of the disc). The thinnest fabric (400 μm) showed a steeper increase in dose, where the difference between a grain on the surface of the fabric and a grain at a depth of 300μm (near the stainless steel disc) was of about 30%. The difference in the absorbed dose to a grain on the surface and a grain at a depth where the plateau was reached was between 25-30 %.

A calibration experimental procedure was adopted using a few grains of quartz (three samples, each given doses of 1 and 3 Gy when irradiated with a γ source) placed upon samples of fabrics cut from bags 21 (fig. 12.4), 19 and 16, with OSL used to assess the dose. The samples of bags were of different thickness (bag 21 : (400 ± 100) μm; bag 19 : (1050 ± 100) μm; bag 16 : (1200 ± 100) μm) and thus the surface was at a different distance from the source and the stainless steel

cup. The distance between the bottom of the stainless steel cup and the source was of 7.5 mm. The OSL signal was measured using a UV filter (U340), to select the emission from the quartz only. The measurements were repeated three times for each bag, and yielded similar values for the three bags. The dose rate of the β source for quartz (100-250 μm of diameter) on samples of bags placed in cups was thus estimated to be of (0.86 $\pm$ 0.01) Gy.min^{-1}, which compares to the dose rate to quartz grains on stainless steel cups, of (0.79 $\pm$ 0.02) Gy.min^{-1}.

This measurement also enabled an estimation of the thermal lag in TL measurements. The TL of the quartz was measured at a heating rate of 0.5 °C.s^{-1} and detected through the U-340 filter, and the position of the ~100 °C peak compared with that measured with quartz grains deposited directly in a stainless steel cup. The difference in position of the TL peak yielded an estimate of thermal lag of ~5 °C for a fabric of thickness 300 μm and ~10 °C for fabrics 1000-1200 μm thick.

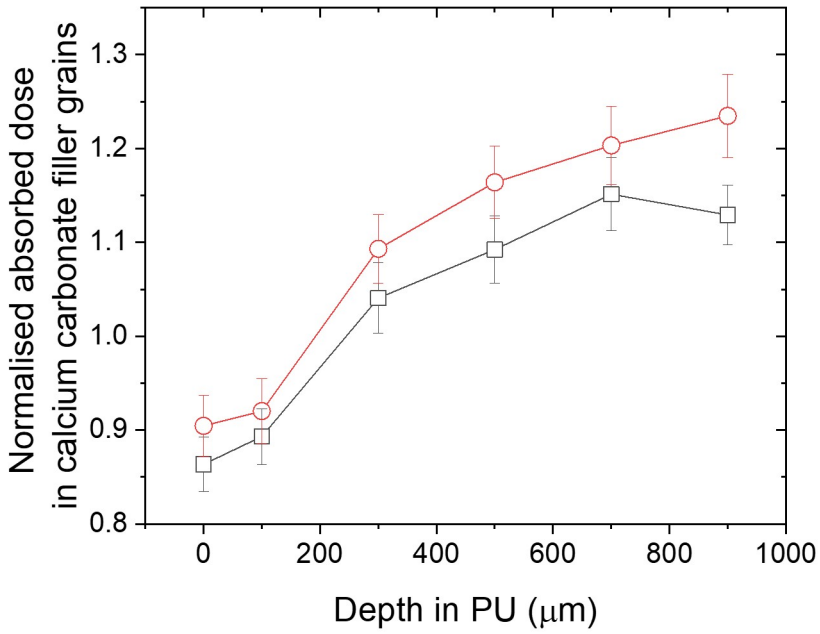

Fig. 12.2. Calculated absorbed dose to calcium carbonate filler grains (100 μm or diameter) in a PU matrix positioned at 0.0625 (open black squares) and 0.18 cm (open red circles) from the centre as a function of the depth from the surface of the PU matrix (1000 μm thick in total). The values of absorbed dose to calcium carbonate filler grains were normalised to the absorbed dose in quartz grains at the same distance from the centre positioned on the stainless steel disc. The points at a depth of 0 μm indicate grains deposited on the surface of the fabric. The fabric samples were placed on a stainless steel disc and exposed to the β source in the Risø reader (distance source-disc :6.5 mm). The doses were calculated using a radiation transport code (MCNP6).

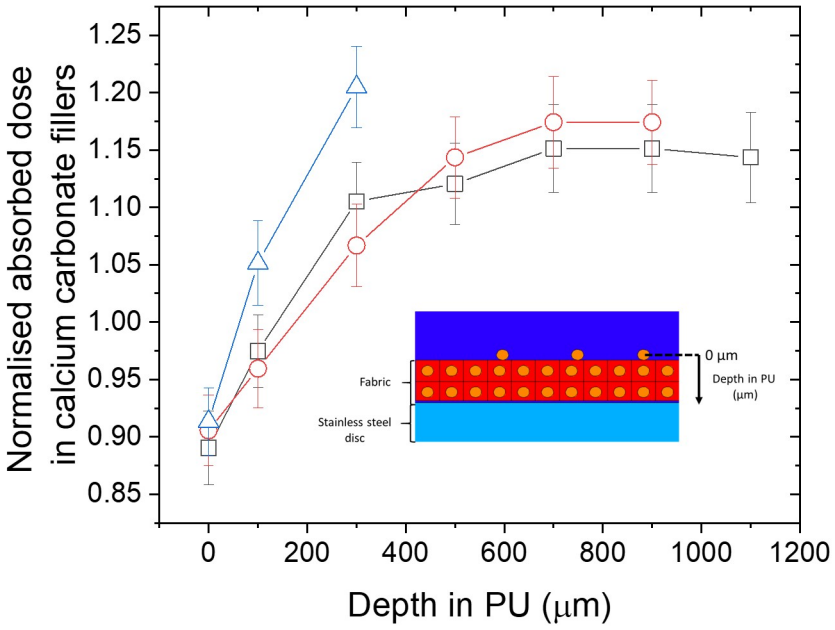

Fig. 12.3. Calculated absorbed dose to calcium carbonate filler grains (100 μm of diameter) in a PU matrix positioned at 0.125 cm from the centre of the disc as a function of the distance from the surface of the PU matrix for different thickness of PU fabric (open black squares : 1200 μm; open red circles : 1000 μm; open blue triangles : 400 μm). The values of absorbed dose in calcium carbonate filler grains were normalised to the absorbed dose in quartz grains (100 μm of diameter) at a similar distance from the centre of the stainless steel disc. The points at a depth of 0 μm indicate grains deposited on the surface of the fabric. The fabric samples were placed on a stainless steel disc and exposed to the β source in the Risø reader (distance source-disc :6.5 mm). The doses were calculated using a radiation transport code (MCNP6). The inset graph shows partially the geometry for a fabric 400 μm thick.

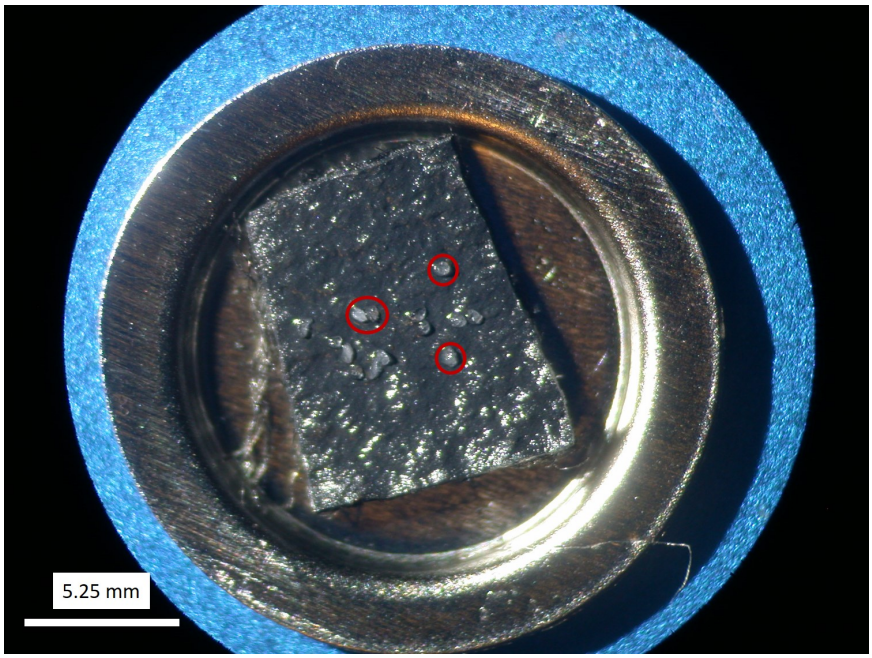

Fig. 12.4. Image of a sample of bag 21 in a stainless steel cup, with grains of quartz placed on the surface of the fabric for β calibration purposes. Some of the grains of quartz are circled in red.

12.2.2 Energy response

The energy response in terms of absorbed dose per source fluence of calcium carbonate filler grains to photon sources of energy 0.01-2 MeV was calculated using an MCNP model of grains of calcium carbonate embedded in PU (similar to Fig. 12.1). The volume of PU containing calcium carbonate filler grains of 100 μm diameter was placed free in air, and at a sufficient distance (3 m for source of energy $\leq$ 1 MeV; 9 m for 2 MeV source) from the source to allow sufficient build-up. The source of photons in this model was specified as a mono-energetic (0.01-2 MeV) plane parallel source. The absorbed dose was calculated for grains at difference depths in the PU (50-850 μm) to observe attenuation effects. The results of the simulations indicated that the energy response of calcium carbonate filler grains was dependent on the depth of the calcium carbonate fillers in the fabric. At low energies ($\leq$ 0.02 MeV), the absorption that occurs within a thickness of PU of 800 μm leads to a significant reduction in the absorbed dose to calcium carbonate filler grains with increasing depth (Fig. 12.5a). For 0.01 MeV photons, the absorbed dose decreases by a factor of $\sim$5.6 between a depth of 50 μm and 850 μm from the surface, whereas for energy above 1 MeV, the absorbed dose increases with the depth, reflecting the build up effect (Fig. 12.5b). For a photon energy of 1 MeV, the build up region is reached at a depth of 650 μm, for a source place 3 m away from the sample.

Fig. 12.6a shows the calculated energy response of calcium carbonate filler grains at a depth of 50 and 850 μm in PU. As described above, the behaviour varies depending on the depth of the filler grains. This has to be compared with previous work on the TL energy response of calcite measured by Engin and Güven (2000) that indicated a peak in the energy response at 140 keV, and a flat energy response between 200 keV and 1.25 MeV. Fig. 12.6a can be compared with the X-ray mass attenuation coefficient for calcium (Fig. 12.6b) that indicates a rising edge for energies below 0.1 MeV. The sudden drop in energy response for the fillers in Fig. 12.6a could be attributed by the strong attenuation induced by the PU at low energies.

These simulations indicate that in order to approach the air kerma dose at the location:

1. If the sample is irradiated with a low energy source ($\leq$ 0.05 MeV), sampling should be performed as close as possible to the surface.

2. If the sample is irradiated with a high energy source $\geq$ 100 keV), measurements should be performed using, as much as is practicably possible, a sample taken as far as possible from the

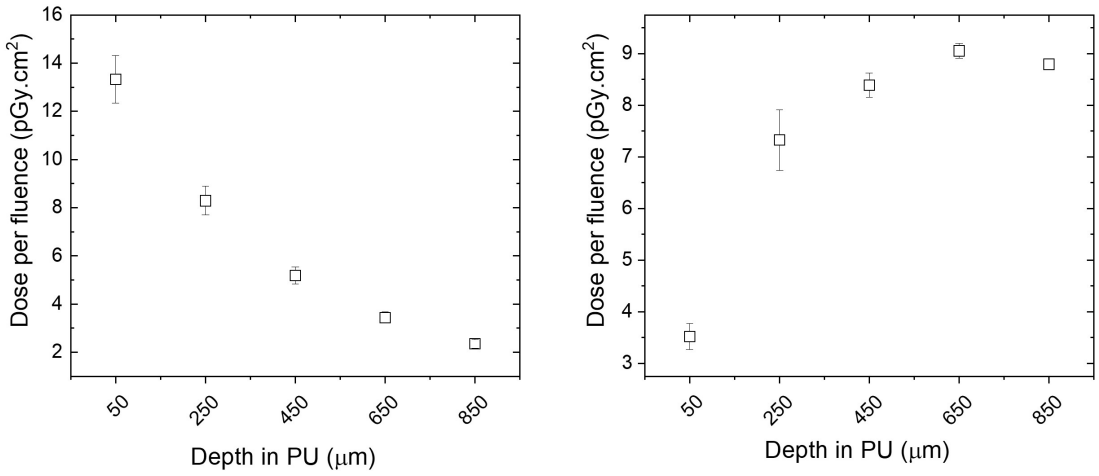

(a) **(b)**

Fig. 12.5. Calculated absorbed dose in calcium carbonate filler grains embedded in a PU matrix as a function of depth of the filler grain in the PU (50-850 μm). The fluence was calculated for the source area. The source was specified as a plane parallel field of 0.01 MeV (a, left hand side graph) and 1 MeV (b, right hand side graph), positioned at 3 m from the sample. The sample was placed free in air in the model geometry.

surface to allow sufficient built-up. This could be done by scraping the surface of the fabric with a scalpel blade.

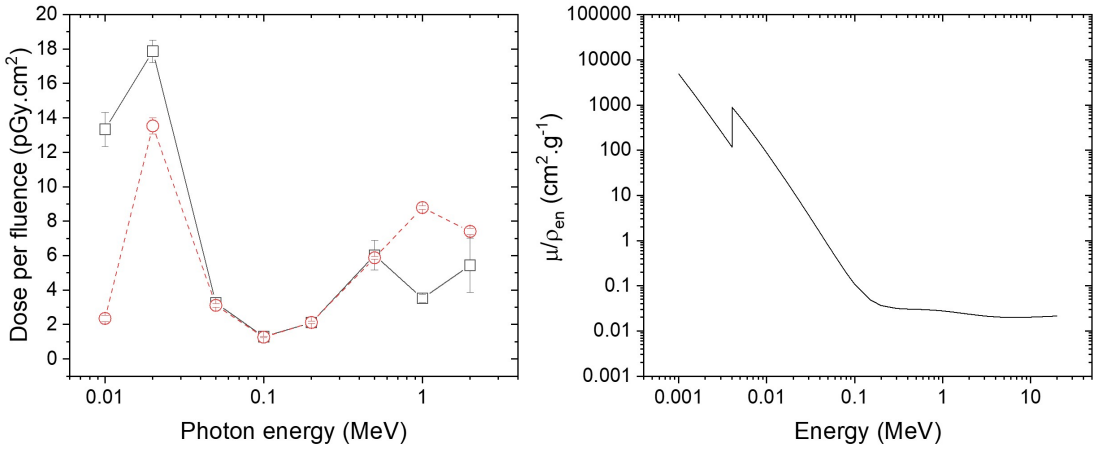

(a) **(b)**

Fig. 12.6. a) Energy response of calcium carbonate fillers, modelled using MCNP6 as spheres of calcite of 100 μm of diameter embedded in a PU matrix. The black continuous line and open squares represent the calculated energy response of a grain of calcium carbonate 50 μm from the surface; the red broken line and the open circle a grain located 850 μm from the surface; to be compared with b) X-Ray mass attenuation coefficient of calcium. Taken from the National institute of standards and technology database (https://www.nist.gov/)

12.2.3 Dose deposited in carbonate minerals at various locations on a phantom

In realistic scenarios, it is unlikely that the calcium carbonate fillers will be placed free in air facing a plane parallel source. If the calcium carbonate filler grains are embedded in the coating of bags, they are more likely to be located near the body, either on its back or side. The consequences of this could be twofold : 1) the calcium carbonate filler grains might be partially shielded by the body, and 2) the backscattered radiation from the body should be taken into account. Furthermore, by sampling different parts of the bag, partial mapping of the dose at the surface of the bags may be possible. To investigate these issues, an MCNP model was constructed comprising four cubes ($1\times1\times1$ cm^3) of calcite distributed at different locations where a bag might be placed on an individual on a voxel phantom corresponding to the ICRP reference male (ICRP, 2009), i.e., at :

1. The right hand side of the phantom (centred at $x = -17.2$ cm, $y = 0$ cm, and $z = 27.5$ cm from the central axis, see Fig. 12.7a)
2. The left hand side of the phantom (centred at $x = 15.8$ cm, $y = 0$ cm, and $z = 27.5$ cm from the central axis, see Fig. 12.7a)
3. The lower back of the phantom (centred at $x = 0$ cm, $y = 11.5$ cm, and $z = 26.5$ cm from the central axis, see Fig. 12.7b)
4. The upper back of the phantom (centred at $x = 0$ cm, $y = 11.5$ cm, and $z = 55.5$ cm from the central axis, see Fig. 12.7b)

Cubes of calcite were used in this model rather than the model of fabric containing calcium carbonate fillers used in Section 12.2.2 to save computational time and achieve reasonable precision. Although this model does not reflect precisely the dosimetry of calcium carbonate fillers, it evaluates whether there is sufficient variation in the doses deposited in crystalline calcium carbonate to attempt mapping of body doses, if sufficient material is present around the body. All of the cubes were placed less than 1 cm away from the phantom. Six exposure geometries were considered :

1. AP : anterior-posterior; plane parallel source in front of the phantom
2. PA : posterior-anterior; plane parallel source in the back of the phantom
3. LLAT : left-lateral; plane parallel source on the left hand side of the phantom

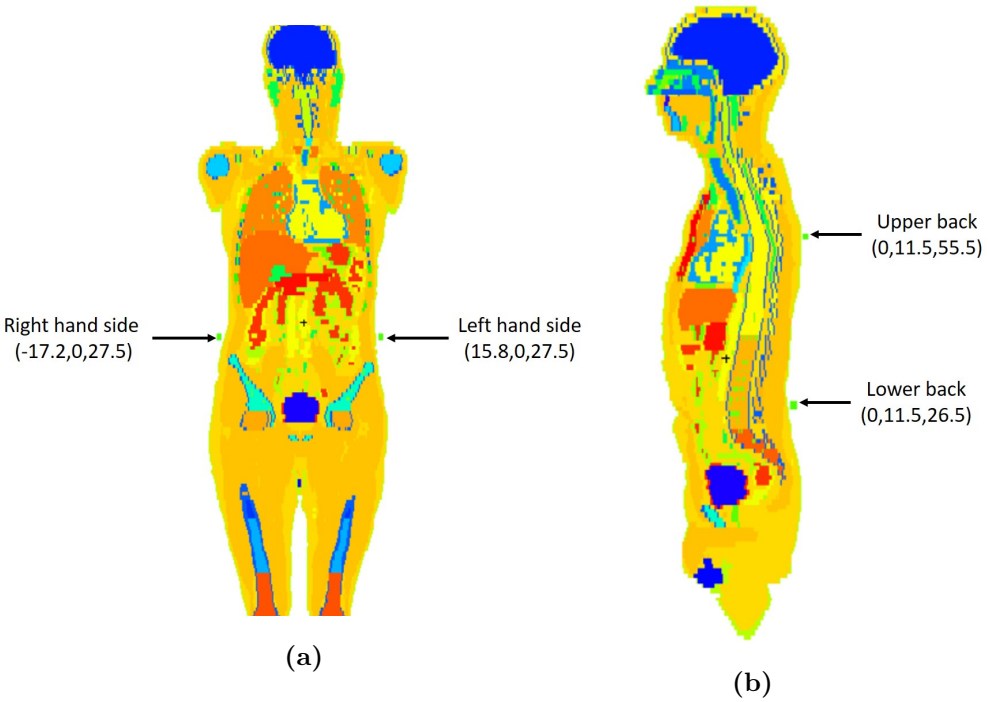

Fig. 12.7. Representation of the voxellised phantom, with the positions of the calcium carbonate cubes indicated.

4. RLAT : right-lateral; plane parallel source on the right hand side of the phantom
5. ISO : isotropic; sphere source surrounding the phantom
6. FLOOR : plan parallel source below the phantom

Three types of sources were also considered : ^{60}Co (E=1.1732 and 1.3325 MeV), ^{137}Cs (E=0.6617 MeV) and 100 keV mono-energetic photons. These sources correspond to the most commonly found isotopes, thought the most likely to occur in a radiological emergency.

Tables 12.1, 12.2 and 12.3 show the value of absorbed dose per fluence for cubes of calcite at different positions for each of the source geometry (AP, PA, LLAT, RLAT, ISO and FLOOR) and energy (^{60}Co (E=1.1732 and 1.3325 MeV), ^{137}Cs (E=0.6617 MeV) and 100 keV mono-energetic photons) stated above. The fluence was calculated as the source area. Although the geometry was simplified in this model, these simulations show what relative variation in dose can be expected in calcite at different positions on the body. They also indicate that determining the geometry of the irradiation may be possible where sampling at different positions is possible. For example, for a left

lateral irradiation, the dose to calcite on the right hand side of the body is 76% lower compared with dose to the left hand side of the body for a cobalt source (86% lower for a ^{137}Cs source; 97.5% lower for a 100 keV mono-energetic photon source).

Table 12.1: Calculated dose per fluence (pGy.cm^2) for calcite cubes (volume : 1 cm^3) placed at different locations of the phantom, for different source configurations. Source : ^{60}Co.

Source configuration	Right hand side	Left hand side	Lower back	Upper back
AP	5.56 ± 0.03	5.57 ±0.04	2.76 ± 0.02	2.69 ± 0.02
PA	6.04 ± 0.04	5.88 ± 0.04	5.57 ± 0.04	5.44 ± 0.04
LLAT	1.32 ± 0.01	5.52 ± 0.03	4.63 ± 0.02	5.32 ± 0.03
RLAT	5.51 ± 0.03	1.33 ± 0.01	4.48 ± 0.02	5.25 ± 0.03
ISO	16.28 ± 0.16	16.31 ± 0.16	15.88 ± 0.16	16.62 ± 0.16
FLOOR	4.02 ± 0.05	3.98 ± 0.05	3.80 ± 0.05	3.15 ± 0.05

Table 12.2: Calculated dose per fluence (pGy.cm^2) for calcite cubes (volume : 1 cm^3) placed at different locations of the phantom, for different source configurations. Source : ^{137}Cs.

Source configuration	Right hand side	Left hand side	Lower back	Upper back
AP	3.42 ± 0.02	3.45 ± 0.02	1.37 ± 0.01	1.31 ± 0.01
PA	3.74 ± 0.02	3.59 ± 0.02	3.46 ± 0.02	3.34 ± 0.02
LLAT	0.50 ± 0.005	3.39 ± 0.02	0.00 ± 0.01	3.04 ± 0.01
RLAT	3.38 ± 0.02	0.50 ± 0.005	2.43 ± 0.01	3.00 ± 0.01
ISO	9.37 ± 0.07	9.40 ± 0.08	9.10 ± 0.07	9.49 ± 0.07
FLOOR	2.26 ± 0.02	2.27 ± 0.02	2.13 ± 0.02	1.82 ± 0.02

Table 12.3: Calculated dose per fluence (pGy.cm^2) for calcite cubes (volume : 1 cm^3) placed at different locations of the phantom, for different source configurations. Source : 100 keV.

Source configuration	Right hand side		Left hand side		Lower back		Upper back	
AP	1.121	± 0.003	1.151	± 0.007	0.255	± 0.003	0.227	± 0.003
PA	1.044	± 0.006	1.004	± 0.006	1.266	± 0.007	1.168	± 0.007
LLAT	0.041	± 0.001	1.168	± 0.005	0.463	± 0.003	0.625	± 0.003
RLAT	1.149	± 0.049	0.042	± 0.001	0.407	± 0.003	0.603	± 0.003
ISO	2.63	± 0.03	2.64	± 0.03	2.45	± 0.02	2.52	± 0.03
FLOOR	0.579	± 0.007	0.607	± 0.007	0.543	± 0.007	0.458	± 0.006

12.2.4 Dose conversion factors : calcium carbonate to organ doses

The dose of interest for medical treatment is the dose to individuals and more specifically the dose to some critical organs (e.g., red bone marrow, stomach and small intestine). Tables 12.4, 12.5, 12.6 give the conversion coefficients from dose to calcite to whole body dose for calcite detectors placed at different location of the body (same positions as section above), for different irradiation geometry and source energy. The whole body dose was calculated as the average of all the organ doses. The conversion coefficients to certain organ doses are given in Appendix B.

Although this procedure requires knowledge of the exposure conditions and of the position of the dosimeter during the irradiation, in the case of bags, organ dose assessment should be more precise if sampling can be done in several locations of the bag, allowing partial mapping of the dose if it provides sufficient spatial extension.

Table 12.4: Conversion factor from dose to calcite at different position to whole-body dose for various exposure geometries. Source : ^{60}Co.

	Calcite right hand side	Calcite left hand side	Calcite lower back	Calcite upper back
AP	0.92 ± 0.01	0.92 ± 0.01	1.86 ± 0.02	1.90 ± 0.02
PA	0.77 ± 0.01	0.79 ± 0.01	0.84 ± 0.01	0.86 ± 0.01
LLAT	2.99 ± 0.03	0.72 ± 0.01	0.85 ± 0.01	0.74 ± 0.01
RLAT	0.70 ± 0.01	2.90 ± 0.03	0.87 ± 0.01	0.74 ± 0.01
ISO	0.99 ± 0.01	0.99 ± 0.01	1.02 ± 0.01	0.98 ± 0.01
FLOOR	0.81 ± 0.01	0.81 ± 0.01	0.85 ± 0.01	1.03 ± 0.02

Table 12.5: Conversion factors from dose to calcite at different position to whole-body dose for various exposure geometries. Source : ^{137}Cs.

	Calcite right hand side	Calcite left hand side	Calcite lower back	Calcite upper back
AP	0.88 ± 0.01	0.87 ± 0.01	2.19 ± 0.02	2.28 ± 0.02
PA	0.71 ± 0.01	0.74 ± 0.01	0.77 ± 0.01	0.79 ± 0.01
LLAT	4.31 ± 0.05	0.63 ± 0.01	0.84 ± 0.01	0.71 ± 0.01
RLAT	0.62 ± 0.01	4.14 ± 0.05	0.86 ± 0.01	0.70 ± 0.01
ISO	0.95 ± 0.01	0.95 ± 0.01	0.98 ± 0.01	0.94 ± 0.01
FLOOR	0.76 ± 0.01	0.75 ± 0.01	0.81 ± 0.01	0.95 ± 0.01

Table 12.6: Conversion factors from dose to calcite at different position to whole-body for various exposure geometries. Source : 100 keV mono-energetic photons.

	Calcite right hand side	Calcite left hand side	Calcite lower back	Calcite upper back
AP	0.43 ± 0.01	0.42 ± 0.01	1.89 ± 0.03	2.11 ± 0.03
PA	0.36 ± 0.01	0.37 ± 0.01	0.30 ± 0.01	0.33 ± 0.01
LLAT	6.9 ± 0.2	0.24 ± 0.01	0.60 ± 0.01	0.44 ± 0.01
RLAT	0.23 ± 0.01	6.4 ± 0.2	0.66 ± 0.01	0.44 ± 0.01
ISO	0.46 ± 0.01	0.46 ± 0.01	0.49 ± 0.01	0.48 ± 0.01
FLOOR	0.38 ± 0.01	0.36 ± 0.01	0.40 ± 0.01	0.47 ± 0.01

12.3 Blind test

12.3.1 Design

Chapter 10 described the properties of calcium carbonate fillers, and identified their potential as surrogate dosimeters. Their strong TL response following exposure to ionising radiation, the linearity of their dose response and their apparent ubiquity in bags indicate their suitability. Although the fading of the TL signal at room temperature was relatively fast, this could be slowed down by placing the samples in a freezer (-15 °C). Chapter 10 also described a protocol used for dose assessment using calcium carbonate fillers. The blind test described in this chapter aimed to answer several additional questions : 1) whether calcium carbonate fillers are suitable for dose assessment in emergency dosimetry; 2) assess where and how the protocol using the TL signal of calcium carbonate fillers could be improved; 3) to assess whether accurate estimate of dose can be obtained using calcium carbonate fillers; and 4) compare different materials and techniques of emergency dosimetry, and identify the strengths of each method. Furthermore, and as identified by McKeever and Sholom (2016), few studies directly compared results obtained using physical and biological dosimetry within the same test.

The surrogate dosimeters selected for this test were :

1. Bag 16 (Fig. 12.8a)
2. Bag 19 (Fig. 12.8b)
3. Bag 21 (Fig. 12.8c)
4. Mobile phone Nokia Lumia 520
5. One tube of human blood

Swatches of bags 16, 19 and 21 are provided in Appendix A. Conventional LiF:Mg,Cu,P TLDs were attached on the bags at various positions, or taped on the phantom at various locations (Fig. 12.8).

The samples were placed on a whole body Rando - Alderson (RA) anthropomorphic phantom (synthetic isocyanate rubber) as follows (Fig. 12.9):

1. Bag 16 : right hand side of the phantom

(a) **(b)**

(c)

Fig. 12.8. Pictures of a) bag 16, b) bag 19 and c) bag 21.

2. Bag 19 : left hand side of the phantom

3. Bag 21 : back of the phantom

4. Mobile phone: inside of bag 19

5. Blood tube : inside of bag 19

The blind test was carried out at the Medical Research Centre (MRC) facility on Harwell campus (Didcot), using a Cobalt 60 γ source (Reviss, RSL2010). The source was composed of four ^{60}Co pellets in copper tubes separated by 7.5 cm each, with a total activity of 3.216×10^{13} Bq at the date of measurement (July 19 2018). The source was located 35.5 cm from the floor below the phantom,

thus resulting in a divergent radiation field. Two positions were calibrated for air kerma, shelf ① at (0.28±0.01) Gy.min^{-1} (75.5 cm from the source) and shelf ② at (0.064± 0.004) Gy.min^{-1} (indicated in Fig. 12.9b). The exposure lasted 9 min, giving a dose of (2.52± 0.09) Gy at position ① and (0.58±0.04) Gy at position ②. The dose given was unknown at time of the measurements and analysis, thus the analysis was "blind". The phantom was placed on a Poly(methyl methacrylate) (PMMA) shelf (thickness 0.6 cm) 81 cm from the floor (45.5 cm away from the source). The distances are indicated on the schematic representation of the setup (Fig. 12.10).

Following the exposure, the bags were stored at ambient temperature in daylight for exactly 6 hours before being stored in a freezer at -15 °C until the measurements were performed. The mobile phone was kept at ambient temperature until the alumina substrate surface mounts resistors and the glass display were extracted and measured.

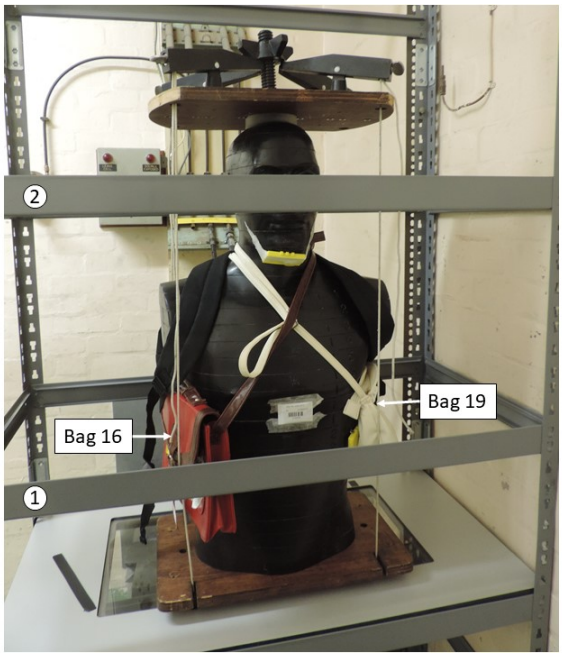

(a)

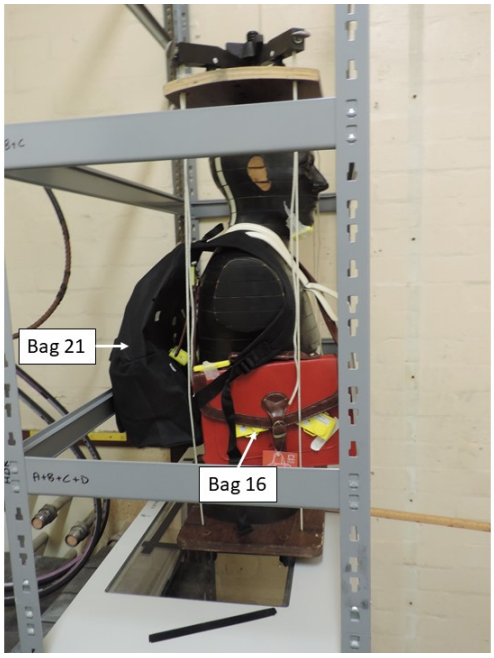

(b)

Fig. 12.9. Experimental set-up used for the blind test (MRC ^{60}Co irradiation facility); phantom front view (a) and side view (b). The bags, as indicated, were placed on the anthropomorphic phantom, and a mobile phone and a sample of human blood were placed inside bag 19. (1) indicates the position of the shelf calibrated at (0.28±0.01) Gy.min^{-1} and (2) the shelf calibrated at (0.064± 0.004) Gy.min^{-1} (air kerma doses).

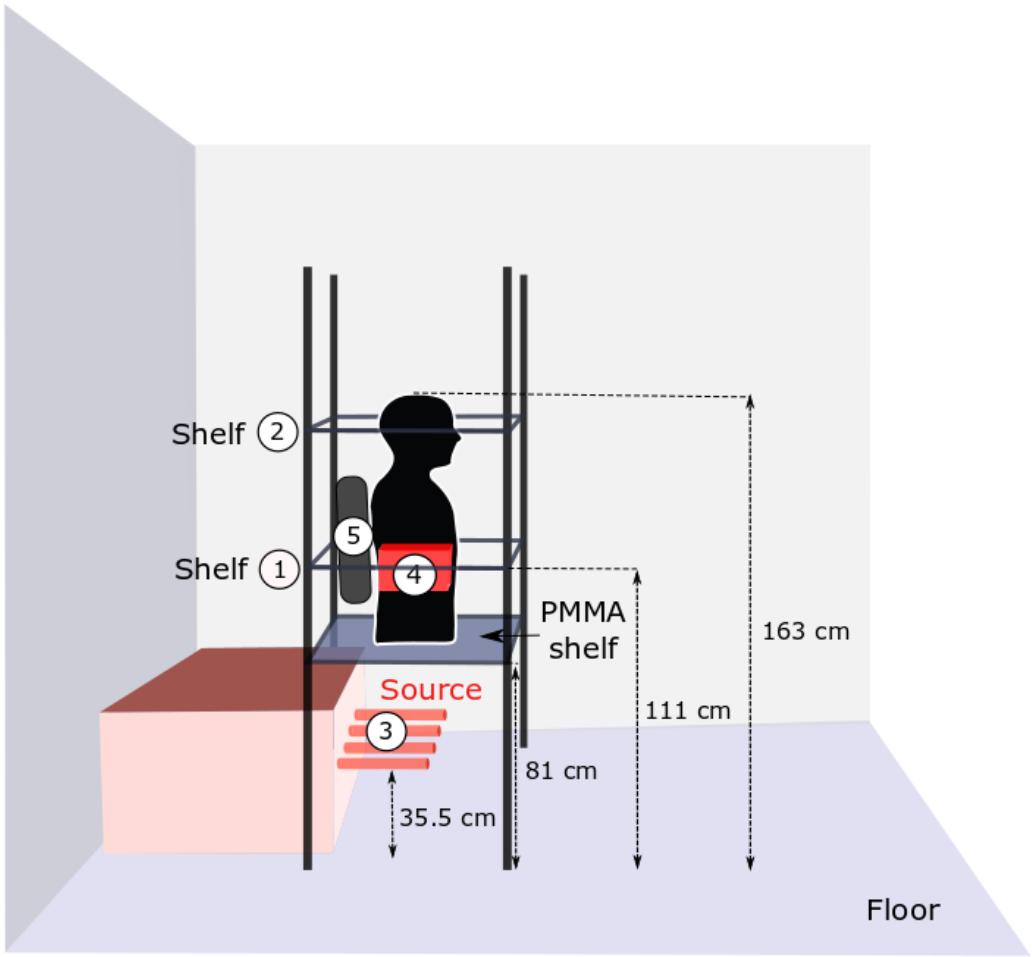

Fig. 12.10. Schematic representation of the experimental set-up for the blind test (MRC ^{60}Co irradiation facility). ① Shelf calibrated at (0.28±0.01) Gy.min^{-1}; ② shelf calibrated at (0.064± 0.004) Gy.min^{-1}; ③ brass tubes in which the sources (^{60}Co pellets) are positioned during the irradiation; ④ bag 16; ⑤ bag 21. The distances are indicative, graph not to scale.

12.3.2 Results

Conventional dosimetry : LiF:Mg,Cu,P TLDs

The PHE conventional LiF:Mg,Cu,P TL dosimeters (Gilvin et al., 2007) were used to obtain control values of absorbed dose to air. The TLDs were placed at various locations on the phantom and the bags. Some of the TLDs were placed facing the source (parallel to the source), and others were orthogonal to the source. The TLDs measurements produced values of Hp(0.07) and Hp(10); where the TLDs were placed parallel to the source a conversion coefficient was supplied to translate the Hp(10) dose preferred for high energy radiation (ICRU, 1993) to air kerma dose (ICRU 1997, Table A.24), and where the dosimeters faces were orthogonal to the source, a MCNP model (Eakins et al., 2007) was used to calculate a conversion coefficient between the absorbed dose in the LiF chip for a source placed below the dosimeter (90 °) and a source placed facing the dosimeter (0 °). However, this model was quite approximative as the exact angle of the TLDs relative to the source was not known (e.g., 85 ° or 95 °), and this could induce further variations in the estimate of doses. Table 12.7 summarises the dose values obtained for the dosimeters, in the form of of Hp(10), Hp(0.07) and air kerma, and Fig. 12.11, 12.12, 12.13 and 12.14 shows the spatial repartition of the values of dose on the samples and experimental setup. The values of dose showed a strong gradient, between 0.09 Gy at the top of the phantom and 8.67 Gy under his base (Fig. 12.11). The dose estimates were not provided with an uncertainty, but for approved conventional dosimetry, the error should be below 5%, for doses superior to 100 mGy.

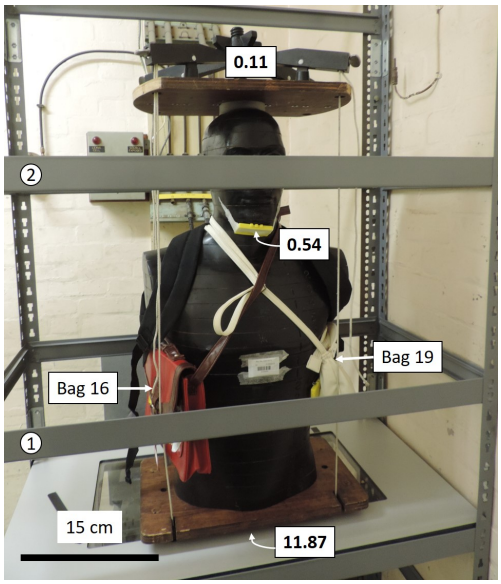

Fig. 12.11. Experimental set up used for the blind test (MRC ^{60}Co irradiation facility). Phantom front view with the values of dose provided by the TLDs shown in boxes. The values are given as air kerma doses (units: Gy). (1) indicates the position where the dose is calibrated at 2.52± 0.09 Gy and (2) the position calibrated at 0.58±0.04 Gy (air kerma doses).

Table 12.7: Values of the doses registered by the conventional LiF:Mg,Cu,P TLDs placed at various location of the phantom and bags during the blind test.

Position	Vertical distance from the source (cm)	Angle θ from the source (°)	Hp(10) (Sv)	Hp(0.07) (Sv)	Air kerma dose converted from Hp(10) (Gy)
Bag 21 sample 2 (Fig. 12.12a)	84	∼90	4.56	4.52	4.53
Bag 21 sample 1 (Fig. 12.12a)	93	∼90	1.63	1.60	1.62
Bag 21 sample 4 (Fig. 12.12a)	65	∼90	4.15	4.22	4.11
Bag 21 sample 9 (Fig. 12.12b)	75	∼90	4.35	4.85	4.31
Bag 16 sample 1 (Fig 12.13a)	75	∼90	3.61	4.26	3.58
Bag 16 sample 4 (Fig 12.13a)	75	∼90	3.37	3.29	3.34
Bag 16 sample 5 (Fig 12.13b)	75	∼90	4.14	4.67	4.10
Bag 16 sample 8 (Fig 12.13b)	75	∼90	4.46	4.37	4.42
Bag 16 top (Fig 12.13a)	87	0	2.51	2.78	2.21
Bag 19 sample 1 (Fig 12.14a)	75	∼90	3.10	3.66	3.08
Bag 19 sample 4 (Fig 12.14a)	75	∼90	2.41	2.67	2.39
Bag 19 sample 7 (Fig 12.14b)	75	∼90	3.56	3.81	3.53
Under phantom (Fig. 12.11)	45	0	9.87	13.77	8.67
Top of phantom (Fig. 12.11)	127	0	0.10	0.13	0.09
Under chin of phantom (Fig. 12.11)	100	0	0.30	0.63	0.27

(a) **(b)**

Fig. 12.12. Picture of bag 21 with dose estimates indicated (in Gy), measured using conventional LiF TLDs. The values are given as air kerma dose (units: Gy). The broken line indicates the position for which the air kerma dose was of 2.52± 0.09 Gy. a) Back of the bag; b) front of the bag.

(a) **(b)**

Fig. 12.13. Picture of bag 16 with dose estimates at positions indicated (in Gy), measured using conventional LiF TLDs. The values are given as air kerma dose (units: Gy). The broken line indicates the position for which the air kerma dose was of 2.52± 0.09 Gy. a) Back of the bag (side against phantom during blind test); b) front of the bag.

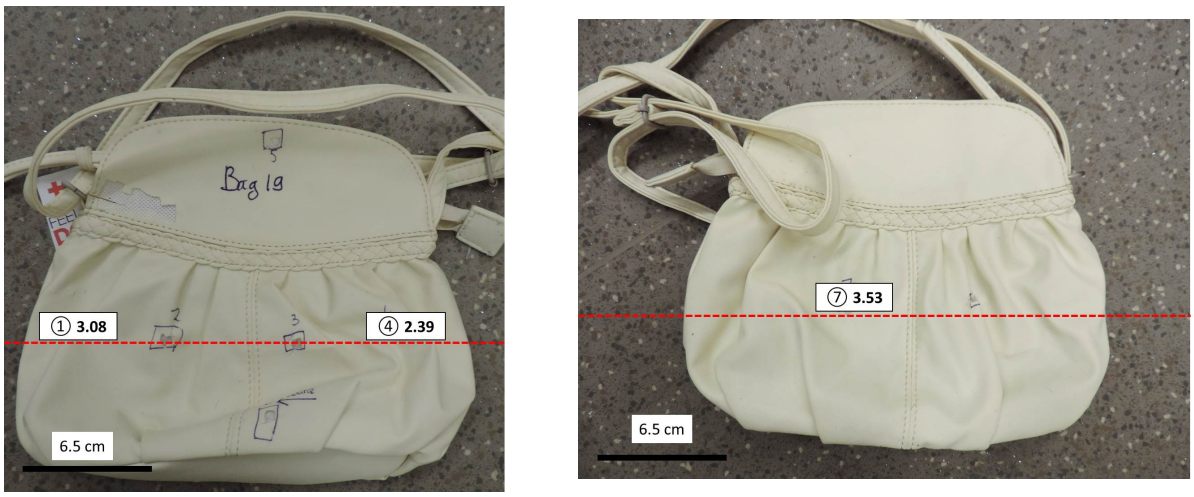

(a) **(b)**

Fig. 12.14. Picture of bag 19 with dose estimates at positions indicated (in Gy), measured using conventional LiF TLDs. The values are given as air kerma dose (units: Gy). The broken line indicates the position for which the air kerma dose was of 2.52± 0.09 Gy. a) Back of the bag (side against phantom during blind test); b) front of the bag.

Dose evaluation using bags fabric

Fig. 12.15 shows the positions of bags 16, 19 and 21 on the phantom. A number of samples were cut from different locations of the bags (12 samples from bag 21, 8 samples from bag 16 and 8 samples from bag 19).

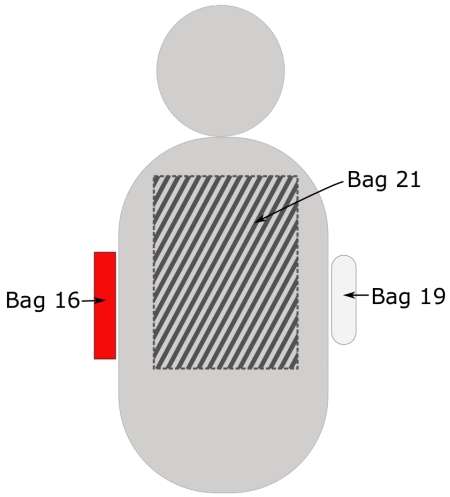

Fig. 12.15. Schematic representation of the positions of bag 16, 19 and 21 on the phantom. Experimental set up used for the blind test (MRC ^{60}Co irradiation facility). Bag 21 was placed on the back of the phantom.

The samples were cut to fit in stainless steel pans (5×5 mm^2) with the coating facing up for TL measurements. The dose rate of the Risø reader β source was determined to be 0.86±0.02 Gy.min^{-1} (see Section 12.2.1). All the samples were measured using the procedure (Procedure A) :

- Step 1 : TL measurement to T_{max} = 200 °C, heating rate 0.5 °C.s^{-1}; measurement of the signal associated with the "blind" γ exposure
- Step 2 : Administered β dose (0.43 ± 0.01 Gy)
- Step 3 : TL measurement to T_{max} = 200 °C, heating rate 0.5 °C.s^{-1}; measurement of the dose response calibration signal 1, measured less than 5 minutes following dose
- Step 4 : Administered β dose (1.72 ± 0.04 Gy)

- Step 5 : TL measurement to T_{max} = 200 °C, heating rate 0.5 °C.s^{-1}; measurement of the dose response calibration signal 2, measured less than 5 minutes following dose
- Step 6 : Administered β dose (4.3 ± 0.1 Gy)
- Step 7 : TL measurement to T_{max} = 200 °C, heating rate 0.5 °C.s^{-1}; measurement of the dose response calibration signal 3, measured less than 5 minutes following dose

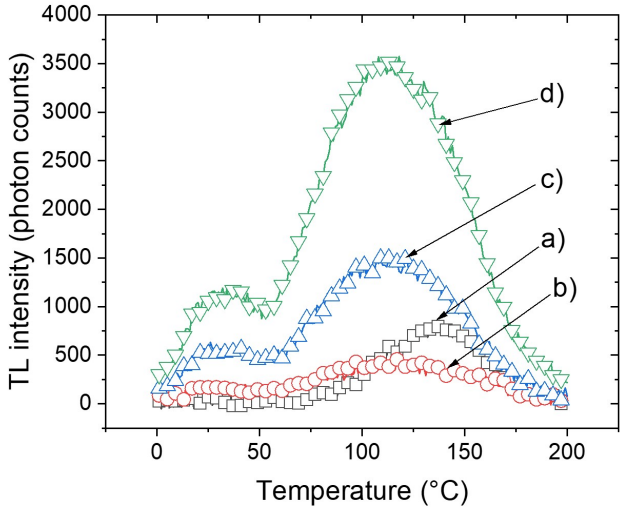

Fig. 12.16. TL signal for sample 1 bag 21 a) blind γ dose (black squares) measured 1 day after the irradiation (6 h at ambient temperature, 18 h in a freezer at -15 °C), b) calibration dose 0.43 Gy (red circles), c) 1.72 Gy (blue triangles) and d) 4.3 Gy (green triangles) measured following Procedure A. Risø system, detection window : OC12, PMT : Hamamatsu R2949, heating rate : 0.5 °C.s^{-1}.

The set of glow curves obtained for sample 1 taken from bag 21 following procedure A is shown in Fig. 12.16. The three calibration β response curves in Procedure A were used to build a dose response curve, by integrating the TL signal for intervals of 2 °C between 140 and 160 °C. The dose response curve obtained for bag 21 sample 1 (Fig. 12.17) was obtained by fitting a linear function passing through the origin to the experimental data. The blind γ dose signal was corrected for fading by applying fading correction specific to the bag for the relevant integration interval (i.e., 140-142 °C; 158-160 °C); and the corrected signal was then divided by the slope of the dose response

curve obtained for this interval, such as :

$$D = \frac{S_g}{a} \times f_g, \tag{12.1}$$

where D is the calculated dose (Gy), S_g the signal for the interval g, a the slope of the dose response for the signal g and f_g the fading correction for the interval g. Thus, for each sample 10 dose estimates (one for each integration interval between 140-160 °C) were obtained.

The errors associated with photon counts, fading correction and fitting of the dose response curve were propagated using a Monte-Carlo routine implemented in R (metRology package, https://cran.r-project.org/web/packages/metRologyl). Where the fading corrections and dose estimates were correct, a plateau between the dose estimates in the region 140-160 °C was observed (Fig. 12.18), within the uncertainties. Fig. 12.18 shows the dose to calcium carbonate fillers obtained for bag 21 sample 1, for each 2 °C intervals in the region 140-160 °C. The mean value of the 10 dose estimates in the region 140-160 °C was 1.61 Gy, with a standard deviation of 0.06 Gy, and the mean value was within the errors of each dose estimate, indicating that the fading correction was correctly applied for this sample. The estimated dose for the last interval (158-160 °C) showed a significant increase in uncertainties (1.7 ± 0.7 Gy), likely due to a lower intensity of the TL signal in this region, reaching the end of the TL peak. The final absorbed dose value was calculated as the integral in the region 140-160 °C, for which a specific fading correction was applied (see Chapter 10). For bag 21 sample 1, the absorbed dose estimate was therefore of 1.7 ± 0.1 Gy.

Additional measurements were made 5 months and 8 days (161 days) after the irradiation for bags stored in a freezer at -15 °C. The samples measured were bag 21 sample 3, bag 19 sample 3 and bag 16 sample 3. For this extended period of storage at -15 °C, fading correction accounting of the loss of the signal at -15 °C had to be applied (see Chapter 10). However, a fading correction for samples stored at -15 °C for periods of up to 5 months was only available for bag 16. For bags 19 and 16, the fading correction calculated for another bag was applied and was chosen according to the agreement of the fading rate at room temperature. For example, the fading at room temperature of bag 21 was similar to that of F 179, thus the fading correction of F 179 for 5 months of storage at -15 °C (see Chapter 10) was applied to bag 21. The fading of bags 19 and 16 was also comparable at room temperature, and the correction accounting for the loss of signal at -15 °C calculated for bag 16 (see Chapter 10) was applied to both bag. The dose estimates after 5 months of storage at

-15 °C gave results of 3.0 ±0.3 Gy for bag 21 sample 3 (versus 2.9 ± 0.2 Gy for a sample measured after 2 days at -15 °C); 2.4 ± 0.1 Gy for bag 19 sample 3 (versus 1.8 ± 0.1 Gy) and 3.4 ± 0.2 Gy for bag 16 sample 2 (versus 2.10 ± 0.07 Gy). The results of dose measured 5 months after the blind test thus appeared to be in agreement for bags 21 and 19 but overestimated the dose for bag 16.

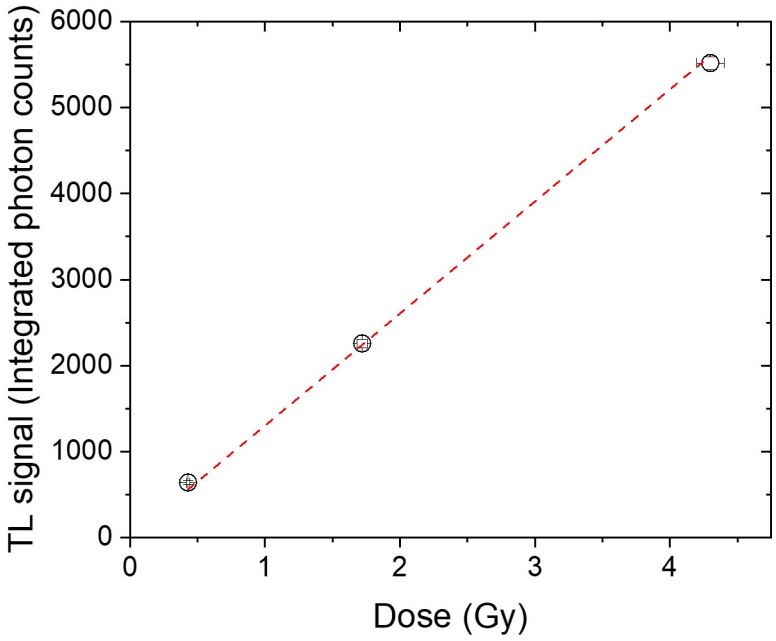

Fig. 12.17. TL dose response curve of sample 1 taken from bag 21. The dose response curve was constructed by integrating the TL signal in the region 140-142 °C following the administration of β doses of 0.43, 1.72 and 4.3 Gy. The broken red line represents a linear function passing through the origin fitted to the experimental data. The error bars shown are the Poisson errors in recorded counts.

The dose results for bag 21 are summarised in Table 12.8, the results for bag 19 in Table 12.9 and the results for bag 16 in Table 12.10.

Table 12.8: Estimated absorbed dose for samples of bag 21 (see Fig. 12.19 for locations), calculated as the integral in the region 140-160 °C, and corrected for fading. Positions 1-8 were against the back of the phantom.

Sample	Dose (Gy)	Dose measured 5 months later (Gy)	Distance from the source (cm)
1	1.7 ± 0.1		93
2	1.8 ± 0.1		84
3	2.9 ± 0.2	3.0 ± 0.3	75
4	3.4 ± 0.2		65
5	2.6 ±0.2		75
6	2.3±0.1		75
7	2.3 ± 0.1		84
8	1.7 ±0.1		84
9	3.2 ± 0.2		75
10	3.5±0.2		74
11	1.32 ± 0.07		102
12	5.0± 0.3		58

Table 12.9: Estimated absorbed dose for samples of bag 19 (see Fig. 12.20 for locations), calculated as the integral in the region 140-160 °C, and corrected for fading. Positions 1-6 were on the side placed against the side of the phantom.

Sample	Dose (Gy)	Dose measured 5 months later (Gy)	Distance from the source (cm)
1	2.04 ± 0.09		75
2	2.0 ± 0.1		75
3	1.8 ± 0.1	2.4 ± 0.1	75
4	1.65 ± 0.08		75
5	0.90 ± 0.05		87
6	3.4 ± 0.4		68
7	2.4 ± 0.1		75
8	2.40 ± 0.09		75

Table 12.10: Estimated absorbed dose for samples of bag 16 (see Fig. 12.21 for locations), calculated as the integral in the region 140-160 °C, and corrected for fading. Positions 1-4 were on the side placed against the side of the phantom.

Sample	Dose (Gy)	Dose measured 5 months later (Gy)	Distance from the source (cm)
1	2.74 ± 0.09		75
2	2.15 ± 0.07		75
3	2.11 ± 0.07	3.4 ± 0.2	75
4	1.88 ± 0.06		75
5	2.75 ± 0.09		75
6	2.51 ± 0.08		75
7	2.50 ± 0.08		75
8	3.3 ± 0.1		75

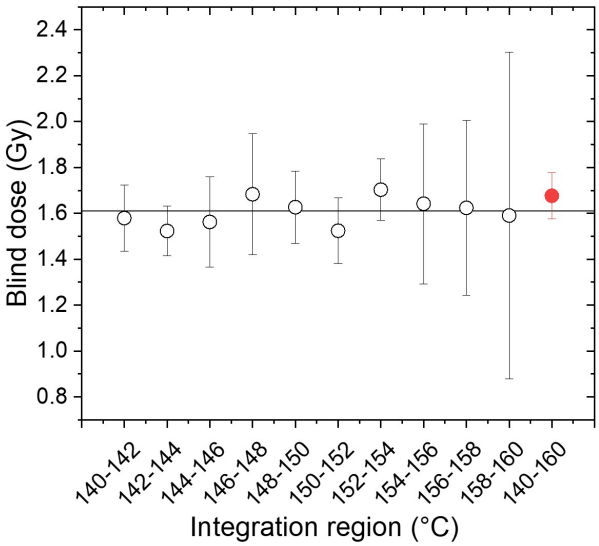

Fig. 12.18. Blind exposure dose estimates obtained using sample 1 of bag 21 obtained using Procedure A and evaluated for each 2 °C intervals in the region 140-160 °C. The dose calculated in the region 140-160 °C is also shown (red filled circle). The dose estimates were corrected for fading, with a fading correction specific for each integration interval. The straight line indicates the mean value of the 10 dose estimates (1.61 ± 0.06 Gy).

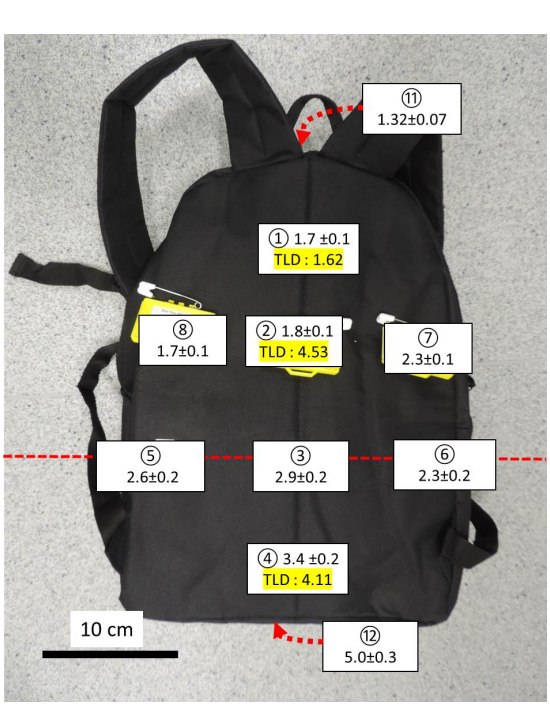

(a)

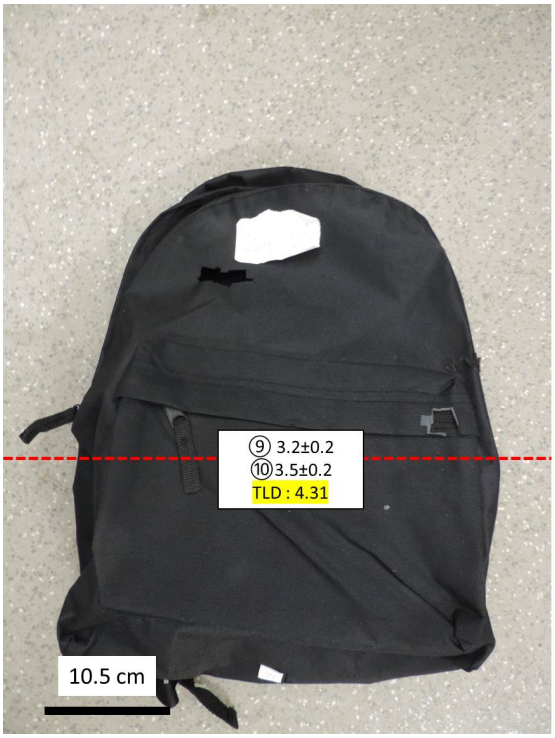

(b)

Fig. 12.19. Picture of bag 21 with dose estimates indicated (in Gy), calculated using the TL response of calcium carbonate fillers. The encircled numbers (① -⑫) indicate the positions of the samples cut from the bag. Sample ⑨ was located on the outside fabric of the pocket, and sample ⑩ inside of the pocket. The broken line indicates the position at which the air kerma dose was 2.52± 0.09 Gy. a) Back of the bag; b) front of the bag.

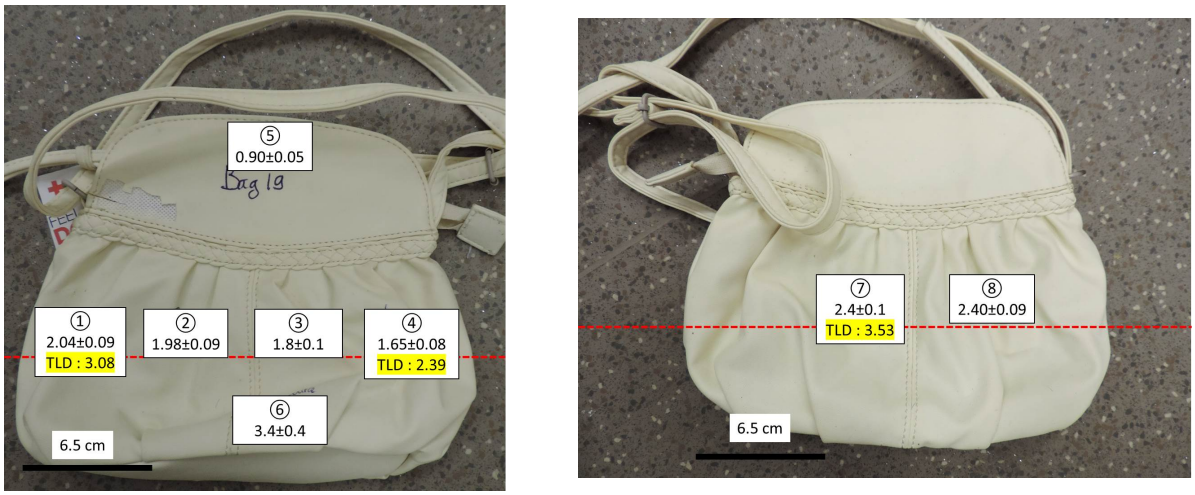

(a) **(b)**

Fig. 12.20. Picture of bag 19 with dose estimates at the positions indicated (in Gy), calculated using the TL response of calcium carbonate fillers. The encircled numbers (① -⑧) indicate the positions of the samples cut from the bag. The broken line indicates the position at which the air kerma dose was 2.52± 0.09 Gy. a) Back of the bag (side against phantom during blind test); b) front of the bag.

(a) **(b)**

Fig. 12.21. Picture of bag 16 with dose estimates at the positions indicated (in Gy), calculated using the TL response of calcium carbonate fillers. The encircled numbers (① -⑧) indicate the positions of the samples cut from the bag. The broken line indicates the position at which the air kerma dose was 2.52± 0.09 Gy. a) Back of the bag(side against phantom during blind test); b) front of the bag.

Mobile phone Gorilla glass

Samples of glass display were extracted from the mobile phone Nokia Lumia 520 following the method developed by Discher and Woda (2013) and cut in squares (5×5 mm) to fit into the stainless steel cup. The samples were washed in ethanol following extraction and etched with 40% hydrofluoric acid for 4 min to reduce the background signal by suppressing the protective layer on the glass (Discher et al., 2013). The samples were measured 6 days after the irradiation, following the procedure of Discher and Woda (2013), as followed (Procedure B) :

- Step 1 : 500 s illumination, blue LEDs (470 nm)
- Step 2 : Record TL glow curve to T_{max} = 450 °C, heating rate 2 °C.s^{-1}; measurement of the blind γ exposure signal
- Step 3 : Administer β dose (5 Gy)
- Step 4 : 500 s illumination, blue LEDs (470 nm)
- Step 5 : TL measurement to T_{max} = 450 °C, heating rate 2 °C.s^{-1}; measurement of the β response (illumination and TL measurement performed less than 5 min following βs dose)

The dose rate of the Risø reader β source to glass display placed in cups was calibrated using glass irradiated with a ^{60}Co source (1 Gy exposure dose, irradiated at IRSN), and measured following procedure B. The TL signal was calculated in the region of the glow curve 300-400 °C to minimise loss of the signal, and corrected for fading, using a fading correction specific for that interval. The Risø reader source dose rate obtained was of (0.77 ± 0.02) Gy.min^{-1} to display glass on stainless steel discs, which compares to the dose rate to quartz grains deposited in stainless steel cups ((0.79 ± 0.02) Gy.min^{-1}).

The absorbed dose in Gorilla glass in a configuration similar to that of the Risø reader for a ^{90}Sr/^{90}Y β source 6.5 mm away from the sample was modelled using MCNP6. The Gorilla glass was modelled as a rectangular parallelepiped (0.5×0.25 cm, thickness varying 0.002-0.004 cm^2) with a composition and density similar to that of described by Discher et al. (2015). In this model, the glass was mounted on a stainless steel disc and exposed to the β source . The simulations indicated that glass of thickness 200-400 μm had less than 2% difference in absorbed dose using the β source and that the dose absorbed in Gorilla glass was 14% higher compared with that of grains of quartz

of 100 μm of diameter in the same configuration (e.g., on a stainless steel disc).

10 glass samples were measured following Procedure B. An example of the glow curves measured using Procedure B Step 2 (blind γ dose signal) and Step 5 (5 Gy dose response signal) is shown in Fig. 12.22. The signal was calculated as the integral in the region 100-250 °C, in order to avoid the region where a native signal occurs and where the thermal stability of the signal is sufficient (Discher and Woda, 2013); a plateau test was performed and indicated that a plateau was present in this region, which was thus deemed as the most suitable for dose assessment. The blind dose signal in this region was divided by the calibration signal, and an universal fading correction was applied (Discher and Woda, 2013) to assess the accident dose. The dose results for each of the 10 samples are shown in Fig. 12.23; the mean value obtained was (3.6 ± 0.5) Gy.

A model of mobile phone was set up in MCNP to convert the dose to the resistors to the air kerma dose. In this model, the phone was placed orthogonal to a ^{60}Co plan parallel source. The phone was free in air and the distance between the phone and the source was of 4 m to allow sufficient build up. The absorbed dose was calculated to the glass display and was compared with the absorbed dose in a small volume of air (0.5×0.5×0.5 cm^3) placed at the position of the phone (with the phone removed from the model). The ratio of the absorbed dose to the glass display to air kerma dose was such as :

$$\frac{D_{\text{glass display}}}{D_{\text{air kerma}}} = 1.22 \pm 0.02 \tag{12.2}$$

Thus, if the dose to the glass display is converted to the air kerma doses at the phone's position, the air kerma doses estimated using the TL signal of the glass display is of 2.9 ±0.4 Gy.

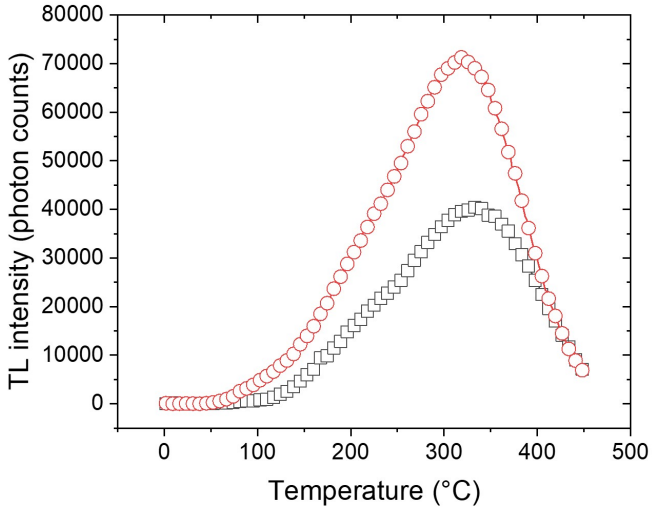

Fig. 12.22. TL blind γ dose test signal (blind test dose, black squares) measured 6 days after the γ irradiation, following Procedure B of sample 1 Gorilla glass extracted from the mobile phone Nokia Lumia 520 and the TL glow curve measured following the administration of β dose (5 Gy; red circles, Procedure B). Risø system, detection window : U-340, PMT : EMI9235, heating rate : 2 °C.s^{-1}.

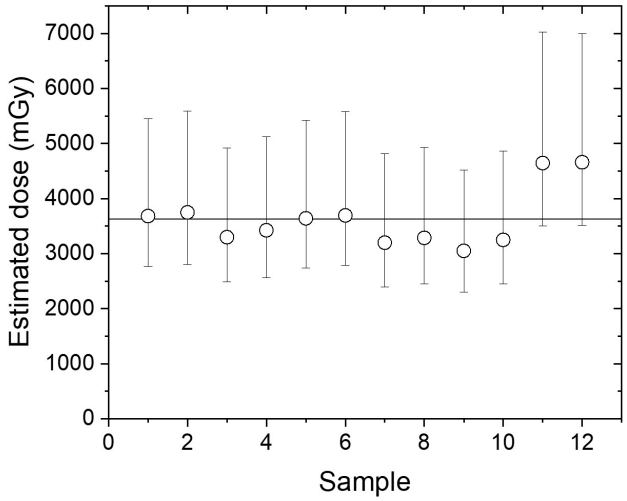

Fig. 12.23. Estimated absorbed dose for 10 samples of glass display extracted from a Nokia Lumia 520 mobile phone, obtained following the procedure described by Discher and Woda (2013). "Blind test" irradiation ^{60}Co, estimated dose at the position of the phone: 2.52± 0.09 Gy (air kerma). The straight line indicates the mean value of the results : 3.6 ± 0.5 Gy. The error bars represents the 95% confidence intervals, calculated using a Monte-Carlo procedure implemented in Excel.

Mobile phone alumina substrate resistors

The alumina substrate surface mount resistors were extracted from the mobile phone (Nokia Lumia 520), and enough resistors were collected to fill two stainless steel measurement cups, each with ca 20 resistors of small and medium sizes. The resistors were washed in ethanol before measurement to eliminate residual glue. Similarly to previous inter-comparisons (Bassinet et al., 2014), each cup was measured with a different procedure; namely the "full mode" protocol and the "fast mode" protocol. Table 12.11 summarises the steps of the measurement procedure following the "full mode" protocol (Procedure C) and the "fast mode" protocol (Procedure D). Fig. 12.25 shows the OSL decay curves obtained with Step 2, Procedure C (blind γ dose signal) and Step 5, Procedure C (dose response signal, 5 Gy).

Table 12.11: Measurements procedures C and D : "full mode" protocol and "fast mode" protocol (Bassinet et al., 2014) for alumina substrate resistors.

	Full mode protocol (Procedure C)	Fast mode protocol (Procedure D)
Step 1	Preheat to 120 °C, 2 °C.s^{-1}, 10 s	OSL (470 nm) at ambient temperature, 30 s (accident signal)
Step 2	OSL (470 nm) at 100 °C, 30 s (accident signal)	β irradiation 5 Gy
Step 3	β irradiation 5 Gy	Pause 600 s
Step 4	Preheat 120 °C, 2 °C.s^{-1}, 10 s	OSL (470 nm) at ambient temperature, 30 s (calibration signal)
Step 5	OSL (470 nm) at 100 °C, 30 s (calibration signal)	

The β source was calibrated for alumina substrate resistors using chips (310 μm thick) irradiated with a ^{60}Co source (6 Gy). The dose was evaluated using a single aliquot regenerative procedure (SAR protocol), and corrected for fading using the fading correction calculated by (Kouroukla, 2015). The calculated dose rate was (0.77 $\pm$ 0.03) Gy.min^{-1} for 310 μm thick alumina substrate resistors placed in stainless steel cups, which compares to the dose rate calculated for quartz in stainless steel cups ((0.79 $\pm$ 0.02) Gy/min).

To account for the difference in thickness of the resistors measured, the dose absorbed in the alumina susbtrate resistors was modelled using MCNP6 for resistors of thickness 310, 400 and 550 μm, employing the model for alumina substrate resistors developed by Eakins and Kouroukla (2015) to assess to what extent the difference in size of the resistors influences the values of dose rate. These thicknesses correspond to measured values of various resistors thicknesses. The resistors were irradiated on a stainless steel disc in the reader β source configuration (6.5 mm between the source and the stainless steel disc), and compared with the calculated dose delivered to grains of quartz (100 μm of diameter) in a similar configuration (i.e. grains on a stainless steel disc). The absorbed dose was either calculated in the total volume of the resistor, or in a layer 100 μm from the surface. The last configuration was prompted by the fact that during an OSL measurement, the light only penetrates through in thin layer of an opaque material. Thus, the value of dose given by OSL only reflects the dose in a superficial layer in the material, and not throughout the volume. The simulations indicated that :

1. If the total volume of alumina substrate is considered, the dose rate delivered to resistors of thickness 400 μm and 550 μm are respectively 11% and 22% lower than the 310 μm.

2. If a 100 μm thick layer below the surface of the resistor is considered (optically active layer, see Fig. 12.24), the dose in the layer is 6% lower for 400 μm thick resistors (2% for 550 μm resistors) compared with 310 μm resistors.

3. The absorbed dose in the 100μm surface layer of the resistors was 6.5% higher for a resistor of thickness 310 μm (1% for a thickness of 400 μm, 3.5 % for a thickness of 550 μm) compared with that of a grain of quartz at the same position (i.e., centre of the disc).

4. The position of the resistor on the stainless steel disc also induces small variations in the dose rate of the β source : a resistor placed at 0.24 cm from the centre results in a decrease in the absorbed dose of 6% compared to a resistor placed at the centre.

A sample specific fading correction was used to correct the dose for fading. Each cup of extracted resistors was irradiated with a β dose (5 Gy) and stored in the dark at ambient temperature for a period similar to the delay between the blind γ dose and the extraction and measurement of the resistors (6 days). Once corrected for fading, the results gave values of absorbed dose to the resistors of :

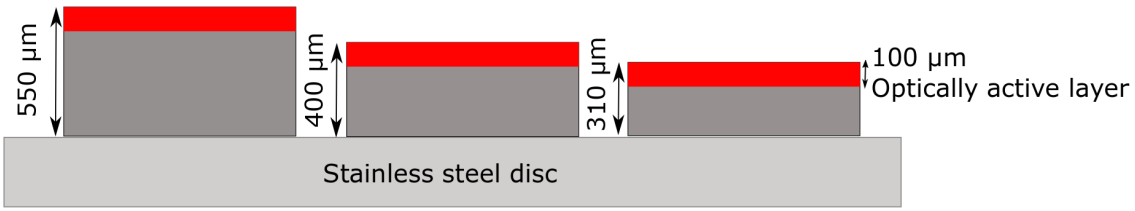

Fig. 12.24. Thickness of resistors used in the MCNP modelling (550, 400 and 310 μm). The red layer indicates a 100 μm-thick active layer beneath the surface of each resistor.

- Full mode protocol : (3.76 ± 0.04) Gy

- Fast mode protocol : (4.26 ± 0.07) Gy

However, the ≥10% difference in the 2 dose estimates might imply that the ≤2% uncertainty estimates are not very accurate.

A model of mobile phone was set up in MCNP to convert the dose to the resistors to the air kerma dose. In this model, the phone was placed orthogonal to a ^{60}Co plan parallel source. The phone was free in air and the distance between the phone and the source was of 4 m to allow sufficient build up. The absorbed dose was calculated in resistors of the circuit board and was compared with the absorbed dose in a small volume of air ($0.5\times0.5\times0.5$ cm^3) placed at the position of the phone (with the phone removed from the model). The ratio of the absorbed dose to a resistor to air kerma dose was such as :

$$\frac{D_{\text{resistor}}}{D_{\text{air kerma}}} = 1.51 \pm 0.04 \tag{12.3}$$

Thus, if the doses to the resistors are converted to the air kerma doses at the phone's position, the air kerma doses estimated using the OSL signal of the resistors contained in the mobile phone are :

- Full mode protocol : (2.49 ± 0.07) Gy

- Fast mode protocol : (2.82 ± 0.09) Gy

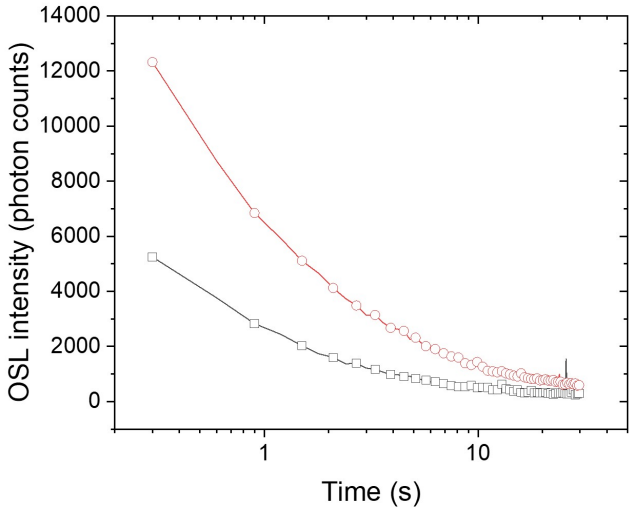

Fig. 12.25. OSL decay curves measured with resistors extracted from the mobile phone Nokia Lumia 520, following the full mode protocol (Procedure C, Table 12.11). Blind test dose : black square; calibration dose 5 Gy : red circles. Risø system, detection window : U-340.

Dicentric chromosome assay (processed and measured by Public Health England Cytogenetics group)

The blood sample was taken by venipuncture at PHE from a healthy volunteer with informed consent in accordance with local ethical approval for PHE's radiation dosimetry research programme (Berkshire REC 09/H0505/87). Following the irradiation, the blood was prepared and the dicentric chromosomes manually scored following standards methods (International Atomic Energy Agency, 2011) by the Public Health England Cytogenetics group. The results yielded 99 dicentrics in 231 cells scored, and the result extrapolated using the Public Health England calibration curve (Lloyd et al., 1986), such as :

$$Y(D) = 0.0005(\pm 0.0005) + 0.0142(\pm 0.0044)D + 0.0759(\pm 0.0027)D^2, \tag{12.4}$$

where D is the absorbed dose, and Y the number of dicentrics. The result obtained using a dose estimate software (Ainsbury and Lloyd, 2010) gave whole body dose of 2.3 ± 0.1 Gy, with an upper confidence interval of 2.471 Gy and a lower confidence interval of 2.095 Gy. Applying a conversion factor from dose to blood to air kerma dose (International Atomic Energy Agency, 2011), this dose

is equivalent to an air kerma dose of (2.09 ± 0.09) Gy.

Radiation transport simulations

The dosimetry of the γ irradiation chamber (MRC, Harwell campus) was modelled using MCNP6 following a simplified geometry shown in Fig. 12.10. The source was comprised of four ^{60}Co pellets positioned within stainless steel tubes housed in brass tubes (Fig. 12.26). The four tubes are separated by a distance of 7.5 cm from each other, and are placed 35.5 cm from the floor (45 cm from the PMMA plate on which the phantom was set). The total activity was 3.216×10^{13} Bq at the date of measurement (July 19 2018). The errors indicated in this section are just MCNP statistical uncertainties, and the true uncertainties would be much larger. A voxellised phantom (implemented in MCNP by Dr. Jansen, Public Health England) corresponding to the ICRP reference phantom (ICRP, 2009) was used to render the Rando - Alderson (RA) anthropomorphic phantom.

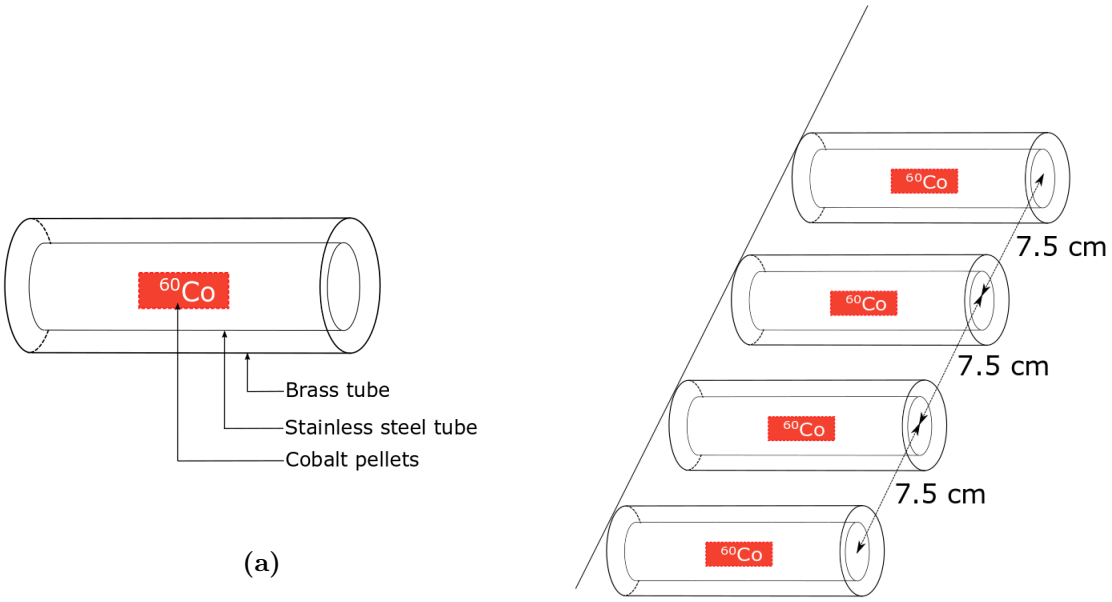

Fig. 12.26. Schematic representation of the design of the MRC γ source model (a). Four similar tubes separated by 7.5 cm containing the ^{60}Co pellets constitute the source (b).

Simulations were carried out without the voxellised phantom in the irradiation chamber to better characterise the radiation field. The position that was calibrated at (2.52± 0.09) Gy, the calculated

doses was (2.43±0.01) Gy. As the four tubes composing the source were spread over 22.5 cm in total, a radial dependence on the calculated values of dose was found (Fig. 12.27a). 30 cm from the central axis, the value of dose 75.5 cm away from the source dropped to (2.11 ± 0.01) Gy, versus (2.43 ±0.01) Gy at the central axis. The calculated values of dose varies as a function of the distance z from the source following an $1/z^2$ law (Fig. 12.27b).

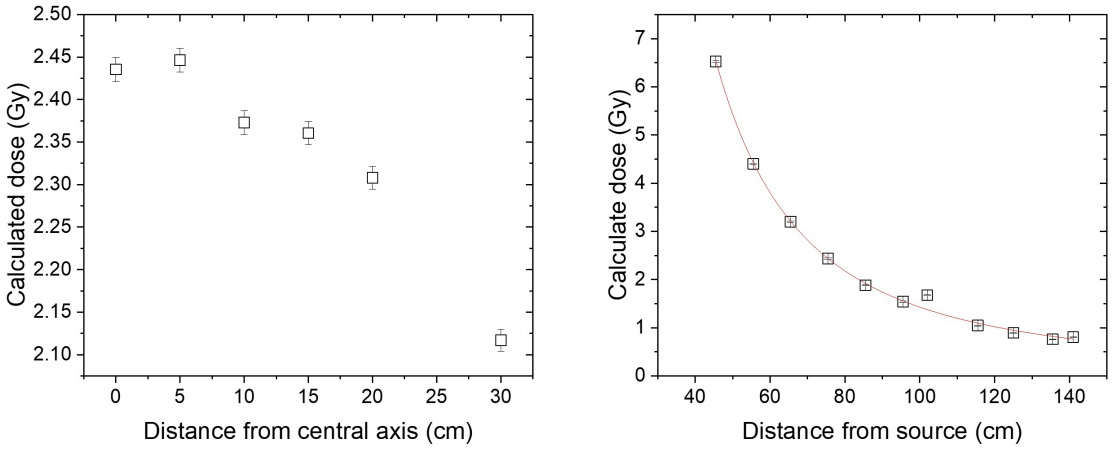

Fig. 12.27. a) Calculated air kerma doses in the γ irradiation chamber (MRC, Harwell campus) 75.5 cm away from the source for a 9 min irradiation, as a function of distance from the central axis of the source. The dose measured 75.5 cm from the source was (2.52± 0.09) Gy, along the central axis of the source ($r = 0$ cm). b) Calculated air kerma dose in the γ irradiation chamber (MRC, Harwell campus) for a 9 min irradiation a function of the distance z from the source. The curve indicates a $1/z^2$ function fitted to the calculated dose values.

Table 12.12 lists the blind test air kerma doses calculated using MCNP at different position relative to the phantom. The positions at 75.5 cm from the source were calibrated at 2.52± 0.09 Gy, without the phantom. A strong dependence on the distance between the dosimeter material and the edge of the phantom was found; the air kerma dose calculated 75.5 cm away from the source at the back of the phantom was 0.826±0.005 Gy 0.5 cm from the phantom and 2.429±0.009 Gy 10 cm away from the phantom (Fig. 12.28).

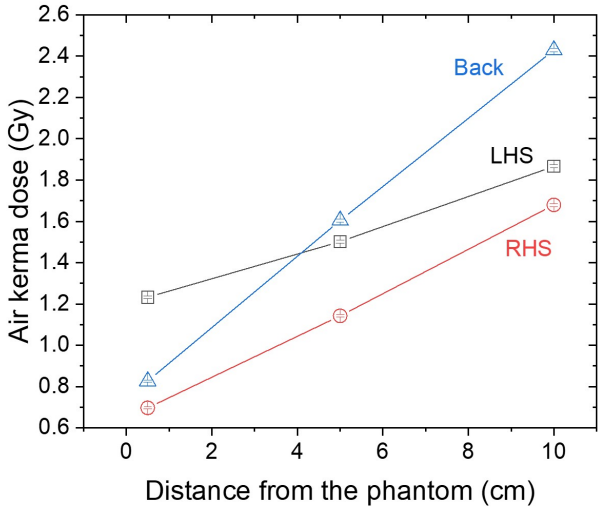

Fig. 12.28. Blind test calculated air kerma dose 75.5 cm from the source at the left hand side of the phantom (LHS, open black squares), right hand side (RHS, open red circles) and back (open blue triangles). The positions relative to the phantom are shown in Fig. 12.29. The values of air kerma dose are plotted as a function of the distance from the phantom. The measured calibrated dose was 2.52± 0.09 Gy measured using an ionisation chamber (without the phantom).

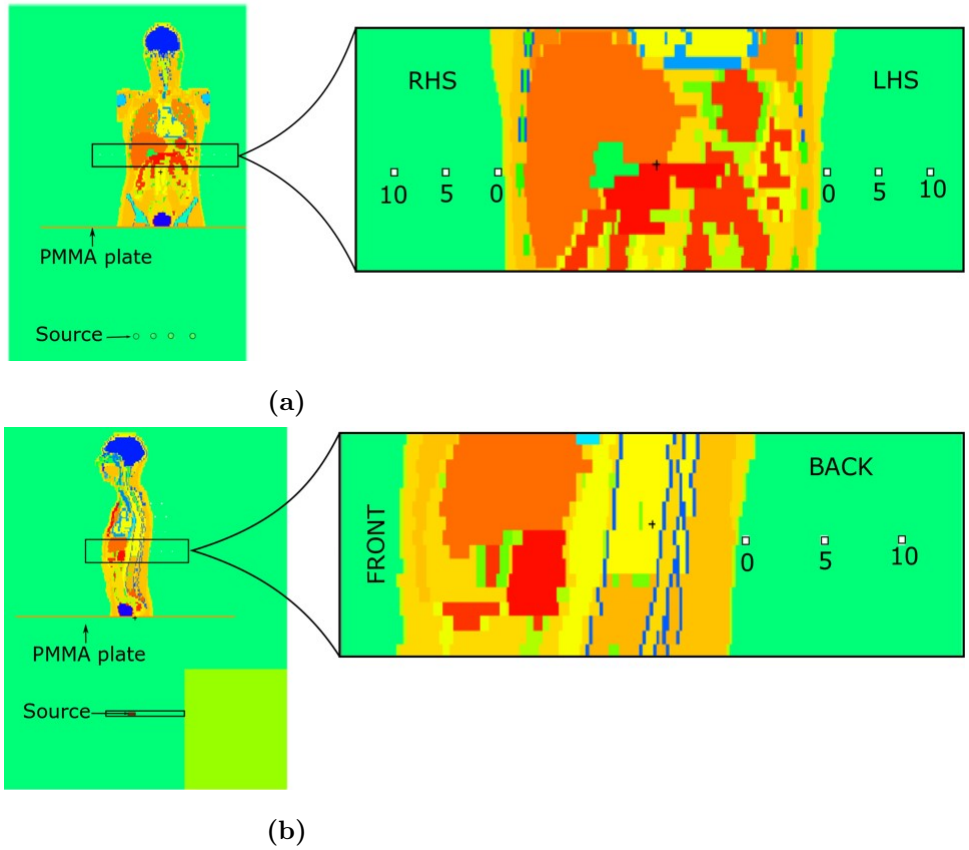

Fig. 12.29. a) Front view of the MCNP model of the anthropomorphic phantom setup in the MRC facility and b) side view. "RHS" and "LHS" indicate respectively the right hand side and the left hand side of the phantom. The white squares are the position at which the air kerma doses of Fig. 12.28 were calculated relative to the phantom (right and side, left and side and back) and 0, 5 and 10 indicate the distance, in cm, from the phantom. The position used to calculate the air kerma dose was 75.5 cm from the source.

Table 12.12: Blind test air kerma dose values calculated using MCNP, positioned at 75.5 cm from the source, as represented in Fig. 12.29.

Location relative to the phantom	Distance from the source (cm)	Air kerma dose 0.5 cm from phantom (Gy)	Air kerma dose 5 cm from phantom (Gy)	Air kerma dose 10 cm from phantom (Gy)
Left hand side	66	0.764 ± 0.005	2.20712 ± 0.0085	
Left hand side	75.5	1.232 ± 0.006	1.502 ± 0.007	1.866 ± 0.008
Left hand side	85	0.546 ± 0.004	1.067 ± 0.006	
Right hand side	75.5	0.696 ± 0.004	1.142 ± 0.006	1.679 ± 0.007
Back	57	2.817 ± 0.009	4.24 ± 0.01	
Back	75.5	0.827 ± 0.005	1.604 ± 0.007	2.429 ± 0.009
Back	85	0.639 ± 0.004	1.195 ± 0.006	
Back	98	0.121 ± 0.002	0.592 ± 0.004	
Back	92	0.341 ± 0.003	0.933 ± 0.005	
Above PMMA	46	5.872 ± 0.007		
Above phantom	127	0.0146 ± 0.0006		

The MCNP model provided the values of organ doses for the phantom. Due to the non-uniformity of the radiation field, the absorbed dose in different organs varies within the phantom (Table 12.13). Some of the critical organ doses are listed in Table 12.13, and show that while some organs were given a dose inferior to the 2 Gy threshold (e.g. stomach : 0.70 Gy), other critical organs registered a significant dose (e.g., bone marrow : 1.67 Gy; colon : 2.19 Gy). The whole body dose (calculated as the average of all the organ dose) was of 0.768 ± 0.002 Gy for this case, which is significantly lower than the value of dose of some critical organs. Thus, this test illustrates a case where the whole body dose might not be an appropriate quantity.

Table 12.13: Values of organ dose for a phantom irradiated in the MRC source configuration for a 9 min irradiation, obtained using MCNP transport code.

Tissue or organ	**Organ dose (Gy)**	**Error**
Bone marrow (red)	1.6655	0.0003
Colon	2.1880	0.0002
Lung	0.3123	0.0001
Stomach	0.7022	0.0002
Bladder	0.8591	0.0004
Breast	0.7022	0.0002
Liver	0.6505	0.0001
Oesophagus	0.2709	0.0002
Thyroid	0.1254	0.0002
Skin	0.5768	0.0001
Bone surface	0.5893	0.0001
Remainders	0.9388	0.0003
Salvary glands	0.0751	0.0001
Brain	0.0347	0.0000

12.3.3 Comparison of the results and discussion

Table 12.14 compares the dose estimates obtained using the different materials and methods of dosimetry employed in this test. Furthermore, the fabric sample containing calcium carbonate fillers, the blood sample and the mobile phone can be compared as the phone was associated with bag 19. Fig. 12.30 shows the position of these samples in bag 19, with their respective estimates of dose.

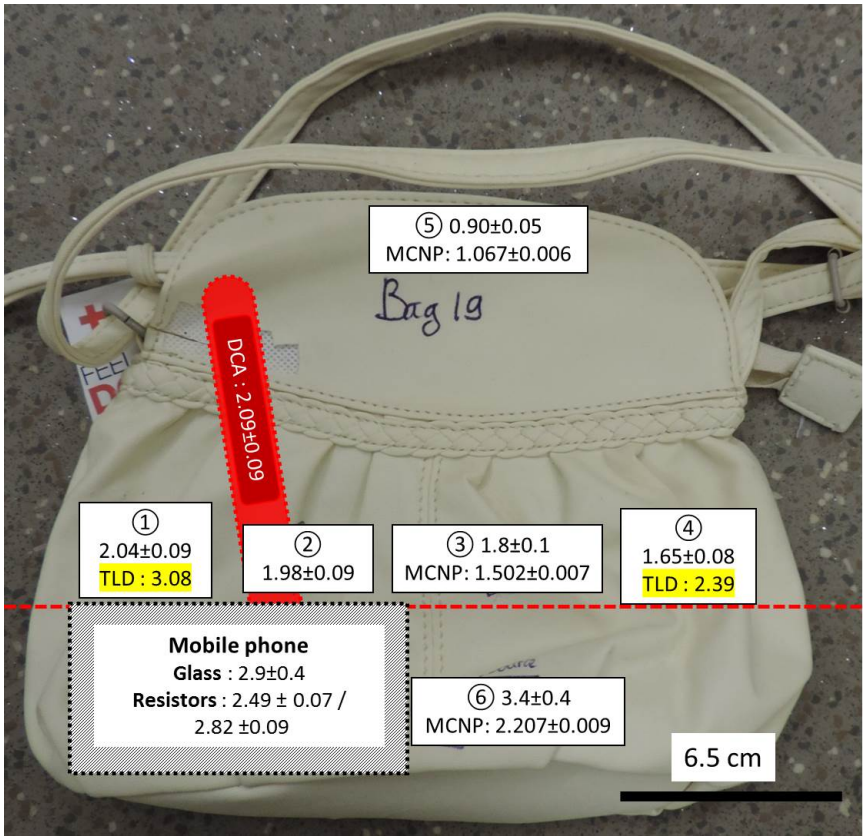

Fig. 12.30. Blind test dose estimated using different dosimetry materials, showing where the samples were positioned in the bag during the blind test. The white rectangles show the position of the fabric samples, the dose values highlighted in yellow are the TLDs dose estimates. The red rectangle (DCA) indicates the position of the blood sample tube dose obtained using a dicentric chromosome assay, the rectangle with crossed hatched perimeter indicates the position of the mobile phone within the bag and the dose estimates obtained with the glass display ("glass") and "resistors" the OSL signal of alumina substrate resistors (full mode/fast mode). The broken indicated the position calibrated at 2.52 ± 0.09 Gy. All values of dose are indicated in Gy.

Table 12.14: Comparison of the blind test dose estimates obtained using different methods of dosimetry (conventional TLD, MCNP, fabric, mobile phone and dicentric chromosome assay).

Position	LiF TLDs (converted to air kerma, Gy)	MCNP (air kerma, Gy)	TL fabrics (Gy)	DCA (converted to air kerma, Gy)	Glass display (converted to air kerma, Gy)	Alumina substrate resistors (converted to air kerma, Gy)
Bag 21 position 1	1.62	0.933 ± 0.005	1.7 ± 0.1			
Bag 21 position 2	4.52	1.195 ± 0.006	1.8 ± 0.1			
Bag 21 position 3		1.604 ± 0.007	2.9 ± 0.4			
Bag 21 position 4	4.11		3.4 ± 0.2			
Bag 21 position 9	4.31		3.2 ± 0.2			
Bag 21 position 12		4.24 ± 0.01	5.0 ± 0.3			
Bag 16 position 1	4.58		2.74 ± 0.09			
Bag 16 position 4	3.34	1.142 ± 0.006	1.88 ± 0.06			
Bag 16 position 5	4.10		2.75 ± 0.09			
Bag 16 position 8	4.42		3.3 ± 0.1			
Bag 19 position 1	3.08	1.502 ± 0.007	2.04 ± 0.09	2.04 ± 0.09	2.9 ± 0.4	Full mode : 2.49 ± 0.07 Fast mode : 2.82 ± 0.07
Bag 19 position 4	2.39		1.65 ± 0.08			
Bag 19 position 5		1.067 ± 0.006	0.90 ± 0.05			
Bag 19 position 6		2.207 ± 0.009	3.4 ± 0.4			
Bag 19 position 7	3.53		2.4 ± 0.1			

The dose estimates using fabrics were in agreement with the expected value of dose (2.52± 0.09 Gy) at the calibrated position for the back of bag 21 (Fig. 12.19a) positioned against the phantom, where the span of the three dose estimates (2.3-2.89 Gy) at this position included the calibrated value 2.52± 0.09 Gy. However, the dose estimates on the other side of the bag were slightly higher than the expected 2.52± 0.09 Gy (3.22-3.15 Gy). The dose estimates of bag 19 at the calibrated position (2.52± 0.09 Gy) gave lower values on the side of the bag that was placed against the phantom (1.65-2.04 Gy, Fig. 12.20a) compared with the other side of the bag at the same distance from the source (2.4 Gy, Fig. 12.20b). Bag 16 gave similar results, with dose estimates at the position calibrated at 2.52± 0.09 Gy in the range 1.88-2.74 Gy, with a mean value of 2.2 ±0.4 Gy (Fig. 12.21a) on the side of the bag near the phantom, and 2.50-3.32 Gy, with a mean of 2.8 ± 0.4 Gy on the other side, further from the phantom (Fig. 12.21b). These results are consistent with the attenuation induced by the phantom, as was predicted by MCNP. Bag 19, that gave the lowest dose estimates on the side positioned near the phantom was made of a soft flexible fabric, that was closely following the contour of the phantom, while bag 21 and 16 were made of a rigid fabric, thus inducing a greater distance between the fabric and the phantom. However, the dose estimates on the side of bags 16 and 19 opposed to the phantom were in close agreement with the 2.52± 0.09 Gy calibrated value of dose. The air kerma doses calculated using MCNP are consistently lower than expected, but they seem to follow a similar trend compared with the dose estimates from the bags (Fig. 12.31). This could be due to a calibration factor (e.g., source activity).

The agreement between the dose results between the TLDs and the calcium carbonate fillers was found to be variable. At some position (e.g. bag 21 sample 1, bag 21 sample 4), the doses are in good agreement (Table 12.14). For some positions, the value given by the TLDs seemed anomalous; for example the TLD positioned on bag 21 sample 2 gave a value of 4.53 Gy, higher than the value of bag 21 sample 4 (4.11 Gy) which was positioned 19 cm closer to the source. The dose estimate using calcium carbonate fillers at this position (bag 21 sample 2) seemed to get a more reasonable value of dose (1.8 ± 0.1) comprised between the dose estimates in the position above and below (1.7 ± 0.1 and 2.9 ± 0.2 Gy respectively). Generally, the calcium carbonate fillers seemed to underestimate the values of doses compared with the TLDs (Table 12.14). However, if the doses are compared with the estimated air kerma calibration at 113 cm from the source (2.52± 0.09 Gy), the calcium carbonate fillers seemed to give better estimates (2.6±0.2 Gy for bag 21; 2.45±0.3 Gy for bag 16;2.2±0.2 Gy for bag 19) compared with the TLDs (e.g., above 4 Gy for bag

21, see table 12.14). The dicentric chromosome assay provided a dose estimate (air kerma dose : 2.09 ±0.09 Gy) closer to the estimate provided by the calcium carbonate fillers of the bag (bag 19) in which the blood tube was placed (2.03±0.09, 1.65 ±0.08 and 2.4±0.1 Gy). The doses estimated using the mobile phone component (air kerma doses using glass display and resistors full and fast mode, respectively 2.9±0.4 Gy, 2.49 ±0.07 Gy and 2.82 ±0.09) placed next to the blood tube in bag 19 were in closer agreement with the calibrate dose of 2.52± 0.09 Gy at this location, but slightly higher compared with the doses to calcium carbonate. The reason for this discrepancies could be the lack of build up in thin dosimeters such as calcium carbonate fillers in PU compared with mobile phone glass display or resistors, where the structure of the phone offers more build up. However, the values of air kerma doses estimated using phone components (resistors and glass display) were comprised between the value of doses of calcium carbonate fillers samples at z positions below and above the phone on the bag (3.40 ± 0.6 Gy and 1.65 ± 0.08 Gy).

The blind test presented here showed an example where a dose assessment at a single point could lead to a wrong interpretation of the results, due to the strong gradient in dose. If the dose was assessed near the head a phantom, the estimate of dose would have been of ∼0.10 Gy (Table 12.7), which would largely underestimate the dose of certain organs (i.e., stomach, intestine, liver, see Table 12.13). On the contrary, if the dose had been estimated at the base of the phantom (on the hips), the dose would have been overestimated (∼ 12 Gy, Table 12.7). These examples illustrate a case where the patient would have been sent to the wrong triage category, if it were a radiological emergency. Although this scenario is unlikely, this test emphasised that estimating doses at several locations of the body might be preferable in cases where the radiation field is not uniform or the irradiation condition unknown. In this case, dose assessment using calcium carbonate fillers in backpacks would provide an advantage, as pieces of fabrics could be sampled at various locations of the bag. This was illustrated in the case of the blind test by the samples extracted along the spine from bag 21. Fig. 12.31 shows the blind test doses obtained at different distance from the source in bag 21. The doses appeared to follow an inverse square relation to the distance from the source.

The results of the blind test indicated the following advantages of using calcium carbonate fillers for short term assessment compared with the other emergency dosimetry methods :

1. Possibility of sampling at various locations, providing a partial mapping of the dose (especially with backpacks), indicating that the exposure geometry may, in certain cases, be

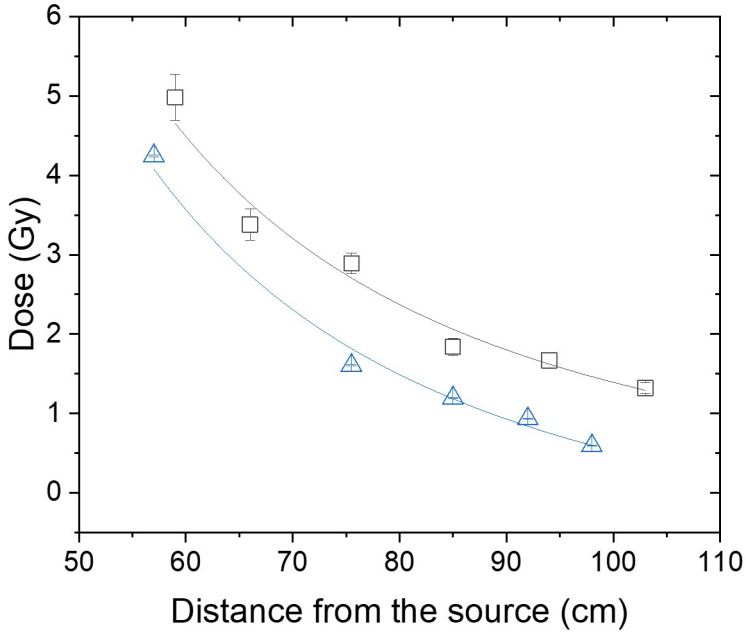

Fig. 12.31. Dose to calcium carbonate fillers in the coating of bag 21 fabric (open black squares) and air kerma doses at similar positions calculated using MCNP (open blue triangles) as a function of the distance from the source. The solid lines represent a function $y = a + \frac{b}{r^2}$ fitted to the experimental data points, where r is the distance from the γ source.

reconstructed.

2. Possibility of extracting a large number of samples (4 samples per cm^2). When resistors from mobile are used, a maximum of three aliquots providing sufficient signal can be extracted form modern mobile phones.

3. Fast processing of the samples (a few minutes) compared with the time needed to extract resistors or glass display from mobile phones.

4. Material of low value, and only a small surface of the bags could be sampled for short term dosimetry, that could be easily patched by the patients. One of the main concerns using mobile phone was the unlikeness of members of the public to give up their phone, due to their high value and interest from the security services.

However, the main disadvantages of calcium carbonate fillers for short term dosimetry are 1) the lack of built up in calcium carbonate fillers at the surface of the fabric, caused by the very small thickness of the dosimeters (≤ 100 μm) and the absence of material to act as built up in radiological emergency scenarios, 2) the faster fading of the signal compared with alumina substrate resistors and Gorilla glass and 3) the variability in fading rates between samples.

The dosimeters tested in this blind test all seemed to perform relatively well, and were able to correctly assess that the "patient" dose was above the 2 Gy threshold. Ideally, all materials and methods for emergency dosimetry would operate in tandem to give a better estimate of the radiation dose.

12.4 Summary and future work

The blind test replicating a ground source irradiation confirmed that calcium carbonate fillers contained in bags may be used for dose assessment in short term dosimetry. A comparison of the dose estimates obtained using different means of dosimetry during the blind test showed that the strength of the TL of calcium carbonate fillers compared with other methods used in short term dosimetry was to provide a spatial resolution of the doses where irradiation was not uniform. However, calcium carbonate fillers seemed to slightly underestimate the doses compared with other surrogate dosimeters (mobile phone component), possibly due to a lack of built up in the material. Simpler irradiation geometry should be carried out in future work, to test the performance of calcium carbonate fillers in more controlled conditions. This could be for example done by cutting a piece of a bag containing calcium carbonate fillers and placing it in parallel to the source, such that the surface of the fabric would be flat. In particular, this would test the hypothesis made regarding the lower dose obtained in this test supposedly due to the lack of built up in thin detectors without built up materials. Performing exposures on a ISO slab phantom, rather than on an anthropomorphic phantom, would allow for more control too, and allow TLDs to be placed more accurately. For future tests, aluminium oxide detectors should also be studied further to obtain a dose estimate to the material directly, as the body dose and skin dose was of less interest for this test. The TLDs employed in this blind test were also sensitive to the geometry of irradiation (i.e., facing the source or not) and this required additional correction factors which could be avoided if aluminium oxide chips were employed.

Chapter 13

Conclusion

13.1 Answers to the research questions

This thesis primarily aimed to answer the following research questions, defined in the Introduction (Chapter 1) :

1. Which materials are suitable for luminescence emergency dosimetry and which ones are not?
2. What are the luminescence characteristics of a new materials investigated? What is the physical origin of the luminescence emission?
3. How accurate are the dose estimates obtained using a new surrogate dosimeter materials?
4. What are the advantages / disadvantages of the new surrogate dosimeter materials?

To answer the first of these questions, a screening of commonplace materials likely to be found near members of the public was carried out. The materials tested included paper, plastic items, contact lenses, polystyrene, nail polish, glass beads, and fabrics (**Chapter 7**). The latter were selected as the most promising, and samples were examined further for their OSL and TL response to ionising radiation. Three types of fabrics were selected for their strongest response to ionising radiation : a blue polyester-mix fabric (F 3), a type of upholstery fabric and the fabric of bags containing calcium carbonate fillers.

The work described in **Chapter 8**, **9** and **10** aimed to answer to research question 2, by characterising the luminescence response of the most promising materials. The luminescence behaviour of

the polymer-mix fabric F# 3 (**Chapter 8**) was characterised by a strong IRSL response to β dose. The detection limit of this fabric was low (20 mGy), which, combined with a linear dose response and the absence of a native signal, indicated favourable characteristics for emergency dosimetry in terms of response to ionising radiation. Although the fading rate at room temperature was found to be fast ($\sim$ 1% of the signal remaining after 2.5 h storage in the dark at room temperature), applying a procedure where the samples were stored in an oxygen free atmosphere following irradiation was found to considerably reduce the rate of fading (80% of signal remaining after 2.5 h). Furthermore, the IRSL signal of F 3 was found to be enhanced when measured with nitrogen flowing into the chamber compared with measurements carried out in air, confirming earlier findings that the oxygen acts as a quencher of luminescence in polymers. This type of strong IRSL response to β dose was not observed in the other polyester fabrics tested.

A type of upholstery fire retardant fabric exhibited an OSL signal in response to β dose (**Chapter 9**). Despite a weaker luminescence response to ionising radiation dose compared with the IRSL signal of the blue polyester F# 3 (detection limit $\sim$ 100 mGy), this series of fabrics presented favourable characteristics for emergency dosimetry (detection limit below 2 Gy, linear dose response) as the fading rate was lower ($\sim$ 50 % of remaining signal after 11 days of storage in the dark at ambient temperature). The source of luminescence in these fabrics is likely to be the mineral fillers incorporated into the coating, although the exact nature of the fillers was not formally identified. Furthermore, the main disadvantage of these upholstery fabric and of F3 was that they are unlikely to be useful for triage dosimetry in general, unless in the case of an event within a domestic or office environment.

The TL response of the fabric of bags containing calcium carbonate fillers showed the most potential as a surrogate dosimeter material (**Chapter 10**). Calcium carbonate fillers are widely used in the manufacture of thermoplastics that are found in the coating or fabric of bags, and they produce a strong TL sensitivity to β dose, yielding low detection limits (from a few mGy to 400 mGy). The 100 °C peak of the TL response was deemed suitable for emergency dosimetry due to the relatively low native signal in this region. The native signal observed in some samples can also be reduced by the use of a red-sensitive PMT coupled with a sharp-cut filter cutting emission below 550 nm. Although the fading of the 100 °C peak, which was associated with a continuum

of trapping level was relatively fast at room temperature (depending on the sample between 34 % and 70% of remaining signal in the region 158-160 °C after 24 h of storage in the dark at ambient temperature), storing the samples in a freezer at -15 °C reduces the rate of fading (loss of the signal after a 24 h storage $\leq$ 5%).

A preliminary answer to the third research question was given in **Chapter 10**, where dose recovery tests were conducted. An attempt to further answer this question was made in **Chapter 12**, where a blind test dose was performed using the TL signal from fabrics of bags containing calcium carbonate fillers. Doses estimates using calcium carbonate fillers were accurately estimated to the nearest Gray in most of the cases, a level of precision that is sufficient for triage.

Research question 4, related to the strengths and weaknesses of this new technique was addressed in **Chapters 10** and **12**. The main advantages of using the TL signal calcium carbonate fillers compared with other methods of dosimetry (e.g. resistors extracted from mobile phones) are : a) its rapidity in producing a dose estimates following the receipt of the sample ($\sim$ 15 min if only one calibration point is used compared with at least an hour using mobile phone resistors) if the fading correction is known, b) the possibility of obtaining a large number of samples from a single bag, and c) the ease of the sampling protocol that requires little operator time, and can be performed by untrained operators. The fast processing time combined with rapid analysis techniques for operators means that the capacity of the network for emergency dosimetry (e.g., RENEB) could be increased. Besides, for small-scale accidents where time management is not critical, a partial mapping of the body dose could be obtained, if the fabrics containing calcium carbonate cover a sufficient surface area. Furthermore, as most bags tend to be of relatively low value and not primarily needed by members of the public or security forces in an emergency situation, they are likely to be easy to obtain for dosimetry purposes. They could be easily repaired after the sample is cut from them. They are also quite common, and likely to be carried by many individuals (like phones, but unlike e.g. F3 and upholstery fabric).

However, it is also acknowledged that this approach has some weaknesses. As the calcium carbonate used as fillers is natural and obtained from quarries, it is expected that there will be great variability in the composition of the fillers. This may mean that there will be a variety of fading

rates and hence it cannot be expected that a "universal" fading curve may be constructed. The difference in fading between samples was observed and can be important, with up to a 40 % of difference in the remaining signal in the region 158-160 °C being observed after 24 h of storage in the dark at room temperature. This variability in fading cannot be neglected or approximated at the risk of overestimating or underestimating the dose, thus placing the patient in the wrong triage category. Another issue is the fast rate of fading at room temperature, and although this could be circumvented by placing the samples in a freezer, it requires that the samples should be collected relatively quickly after the accident. This method is thus more adapted to short term dosimetry and a pre-triage quick check rather than post-triage in the longer term to obtain an exact measure of dose. The main mechanism of fading appears thermal and one of the consequences of a dominant thermal fading is that the fading rate is dependent on the temperature of storage, which could be a disadvantage if the temperature at which the samples are held (i.e., in a freezer) before being collected is unknown (with up to 40% difference between samples stored at 20 and 35 °C after 24 h of storage).

Finally, the issue of the fading of the TL signal of alumina substrate resistors was studied (**Chapter 11**) as this is a known disadvantage of using such devices as surrogate dosimeters. Applying a photo-transfer TL (PTTL) procedure partially circumvented the fading rate, for periods of storage 6 hours to 224 days in the dark at ambient temperature. Two light sources were used to induce the photo-transfer mechanism, a blue light source (470 nm) and a UV light source. Whilst the UV light source induced a stronger PTTL signal, it also produced a non dose dependent photo-simulated TL signal. The signal of the resistors found in mobile phones has several advantages compared with the calcium carbonate fillers of bags, but the main one is the longer lived luminescence signal, that can be detected after months of irradiation for samples stored at room temperature. The use of the PTTL technique reinforce the longer term use of alumina substrate surface mount resistors.

13.2 Future work

This thesis primarily aimed to define the strongest candidate materials for emergency dosimetry using luminescence techniques (TL and OSL), and beyond their basic characterisation, there is yet some work to be carried out to improve the protocols used or fully understand the luminescence

emission and dose absorption mechanisms in calcium carbonate fillers and other material investigated. More broadly, this study also raised some questions that have not been answered yet :

1. A limited range of samples have been tested here. Future work might include testing a larger set of bags or materials containing mineral fillers, or focusing on the calcium carbonate suppliers to obtain fillers from various quarries.

2. One of the main disadvantage of the calcium carbonate technique was the fading rate that was found to be relatively fast at room temperature (50% loss of the signal in 24 h in the region of the glow curve 140-142 °C) and to differ between samples, although all the samples were found to follow an exponential decay of the latent TL signal at room temperature. To address this issue, further investigation is required : 1) storing samples at two temperatures (room temperature and -15 °C), 2) collecting samples shortly after the accident (ideally within 24 h) to store them at -15 °C, and 3) the work and time required in an emergency situation to establish a sample specific fading correction is required.

3. The issue of the timescale between the receipt of the sample and the dose report to the medical team was briefly raised when it was assessed that the time to measure one sample was of ca 15 min. Depending on the number of samples to process, the time interval between the accident and the dose estimate might reach a week for mass casualty accident, and it is not known so far if that time scale is workable for emergency responders. The time necessary to obtain dose results using dicentric chromosome assay was evaluated to be of 52 h (Kulka et al., 2017), which was deemed sufficient for post hospital dose assessment.

4. For the blind test, the doses determined using different techniques have been translated to air kerma to enable a straightforward comparison of the results. There are however discussions as to which quantities should be employed for emergency dosimetry (Eakins and Ainsbury, 2018a); e.g., dose to the material, air kerma dose, Hp(10), effective dose, whole body dose, dose to specific organs,... which can be obtained applying conversion factors determined using radiation transport codes (e.g., MCNP). It has not yet been assessed how long it would take to translate the dose to the material to another quantity in an emergency scenario, where time would be critical. Furthermore, employing these conversion factors increases the uncertainty

in dose uncertainties, with the main uncertainties arising from lack of knowledge of the precise exposure conditions.

5. All the measurements in this study were performed in a laboratory. In the case of a radiological accident, it may be necessary to have on-site dose assessment, using portable instrumentation.

13.3 Impact and implementation

Table 13.1 shows the performance of calcium carbonate fillers compared with other methods of emergency dosimetry. The main gaps identified by Table 13.1 are the need for a method of emergency dosimetry with a shorter delay between sample receipt and dose estimate (for use in triage rather than dose assessment), with a high capacity (number of individuals per week) and that could detect partial body exposure. This last point could be addressed by TL measurements on fabrics containing calcium carbonate fillers, presuming that the fabric covers a sufficient surface area. If calcium carbonate fillers appear so far to be the fastest mean of emergency dosimetry listed in Table 13.1, but also the one for which samples might be the easiest to obtain, it could be proposed that they could fit in the emergency response plan as the first triage technique in case of a large scale radiological accident, before other types of assay (i.e., OSL using phones, ad dicentric chromosome assays) are employed on individuals with symptoms of the highest dose.

Table 13.1: Comparison of the performance of calcium carbonate fillers as fortuitous dosimeters to other methods of dosimetry (Kulka et al., 2017; Wojcik et al., 2017).

		Time span after exposure during which the assay can yield usable results				Exposure scenario that can be detected by each method alone						
Assay	Sample type	Days	Weeks	Months	Years	Acute	Pro-tracted	Partial body	Time from sample receipt to result (hours)	ReneB capacity (individuals/week)	Detection range (Gy)	Implication of individual sensitivity
Dicentric chromosome assay	Blood	✓	✓	✓		✓	✓	✓	52	ca 1000	0.1-5	Yes
Micronucleus test	Blood	✓	✓	✓		✓	✓	✓	75	ca 400	0.2 - 5	Yes
FISH	Blood	✓	✓	✓	✓	✓	✓		120	ca 100	0.3 - 4	Yes
γ-H2AX	Blood	✓				✓		✓	3	ca 1800	0.2-5	?
EPR using glass	Mobile phone	✓	✓	✓	✓	✓	✓		$\leq$1	ca 770	$\geq$1	No
OSL using resistors	Mobile phone	✓	✓			✓	✓		$\leq$1	ca 500	$\geq$0.1	No
TL using calcium carbonate fillers	Calcium carbonate/bags	✓	✓[1]	✓[1]		✓		✓	$\leq$0.5	336 [2]	$\geq$0.1	No

[1] For samples stored at -15 °C

[2] samples per Risø reader, assuming 1 calibration point (20 min/sample) and that a 48 positions carousel is used

Implementation Step 1 : validation of the technique

The first step of the implementation of TL dosimetry using calcium carbonate fillers would be to test the applicability of this technique to a wider range of materials and to develop a protocol to reliably assess the radiation doses received by one person for an unknown type of fabric containing calcium carbonate fillers (e.g., a fabric that has not been previously tested in laboratory under controlled conditions). In order to achieve this goal, a larger series of blind test should be carried out. This would enable to precisely assess whether the dose estimate is accurate and the validity of conversion coefficients. Using the results obtained in the blind tests, the measurement protocol proposed in Chapter 10 and used in Chapter 12 would be either validated or modified to provide a more reliable estimate of dose. Ultimately and ideally this step would lead to the validation of the technique as a means of dosimetry.

This first stage could also see the first inter-laboratory comparisons being carried out, once the protocol is consolidated. The goal of these first stage intercomparisons would be twofold : 1) to test how other laboratories perform and if a common estimate of dose can be reached and 2) to test the network for sending samples maintained at low temperature. A similar scheme was used for some blood assays (e.g. γ-H2AX) that requires samples to be kept in the cold. If this first step gives satisfactory results, the implementation of TL dosimetry using calcium carbonate fillers could be incorporated in radiological emergency response plans to asses the radiation doses of larger cohorts.

Implementation Step 2 : pre-planning before the accident

The ISO standard 21243:2008 (International Organization for Standardization (ISO), 2008) states the performance criteria that laboratories performing cytogenetic triage for assessment of mass casualties in radiological or nuclear emergencies are required to meet in order to be integrated in the response plan (Chapter 2). Although being very specific to cytogenetic assays, this document provides a baseline of the procedures and standards to be reached by other techniques, as cytogenetic assays are so far the most employed techniques for short term dosimetry in radiological emergency. However, as was briefly discussed at the beginning of this section, it was proposed that TL dosimetry using mineral fillers might play a different role in the radiological emergency response plan, as will be discussed below.

The pre-planning response as described in the ISO standard 21243:2008 includes :

1. Raising the awareness of the technique, standard and procedures to follow at all level (health care facilities, governmental agencies). Dissemination of the work is critical especially for a new technique so that the first responders are aware of the availability of the technique, how samples may be collected and be sent to the reference laboratory.

2. Defining the role of the healthcare facilities in relation to the dosimetry laboratory. As defined in the ISO standard 21243:2008, for cytogenetic assays, the role of the hospital is to firstly take the patients in charge, select the cohort that would require dosimetry and collect blood samples to send to the biodosimetry laboratory. Using TL dosimetry of calcium carbonate fillers, a wider cohort could be examined, which would not necessarily require the selection of patients. Furthermore, as no biological material needs to be sampled for the TL dosimetry of calcium carbonate, the role of the healthcare facilities could be considerably lessen (no blood sampling and consent forms) compared with biological dosimetry, which could partially compensate the scarcity of medical resources during mass casualty accidents. Furthermore, if on site dose evaluation is required, TL portable instrumentation could be developed for emergency dosimetry.

3. Defining the role and responsibilities of the laboratories. The role of the the dosimetry laboratories before the accident would be quite similar to that described in the ISO standard 21243:2008, i.e. : 1) maintaining a stockpile of consumables, ensuring that the instrumentation is in working order and calibration is up to date, 2) maintaining communication links with local / national / international healthcare facilities and agencies, 3) specifying and documenting the responsibilities, roles, and interrelations of all laboratory personnel who might be in charge of the dosimetry response, 4) assessing the laboratory maximum capacity (nominally evaluated at 336 samples per Risø reader per week, although it might depend on the source dose rate), 5) maintaining its own quality control and quality assurance programme (performance checks of the instrumentation, the sample protocol, the dose estimate and the associated uncertainties, the generation of results reports), notably by the training of new laboratory members and 6) participating in relevant inter-laboratory comparison, blind tests, training and exercises.

Implementation Step 3 : during the accident

Once samples reached the laboratory, they should be processed in order of priority, with the samples associated with the individuals likely to have the highest doses processed beforehand. Once the nature and scale of the accident is known, the laboratory may decided whether it can process samples on its own, or should call for a network of laboratories if the number of samples to be measured is above its own capacity. Such network of laboratories already exists for physical dosimetry using luminescence techniques (e.g., ReneB, EURADOS working group 10; Ainsbury et al. 2017), to which TL dosimetry of calcium carbonate fillers could be implemented. The network would work as previously described (Kulka and Wojcik, 2017), with a reference laboratory responsible for activating the network, collecting and dispatching samples, communication between laboratories and the local emergency responders and arranging cross checks of the data by at least one other laboratory. Once processed, the results should be presented in a standard report form and communicated to the medical team. Although usable during small or large scale accident, it is recognised that TL dosimetry using calcium carbonate fillers has the most potential compared with other means of emergency dosimetry for mass casualty events, in which time is critical.

Chapter 14

Appendix A : Swatches

This appendix provides swatches of some samples tested in this thesis : fabric 3 (Chapter 8), fabric 29 (Chapter 9), fabric 179 (Chapter 10), the "LED" conference bag (Chapter 10), and bags 16, 19 and 21 (Chapter 10 and 12).

Table 14.1: Swatches

Swatch	Fabric reference and description
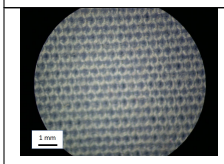	Fabric 3 "blue polyester" (Chapter 8).
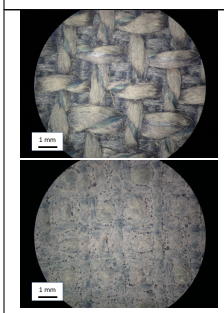	Fabric 29 "Lynton" series (Chapter 9). Upper swatch : fibres side; lower swatch : coating side.

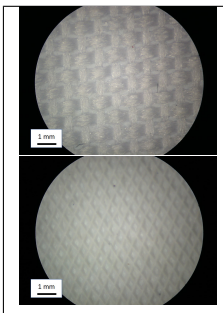	Fabric 179 “Kordura” white nylon fibres coated with polyurethane (Chapter 10). Upper swatch : fibres side; lower swatch : coating side.
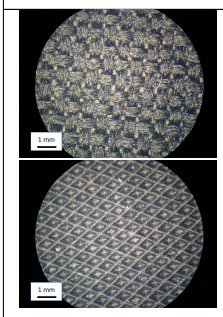	“LED” conference bag; black fibres coated with polyurethane containing calcium carbonate fillers (Chapter 10). Upper swatch : fibres side; lower swatch : coating side.
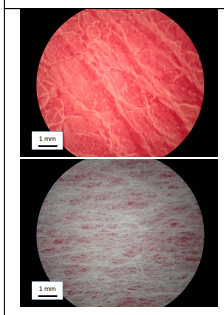	Bag 16; red faux-leather containing calcium carbonate fillers (Chapter 10 and 12). Upper swatch : front; lower swatch : back.
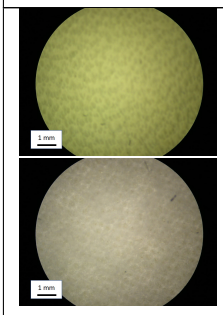	Bag 19; white faux-leather containing calcium carbonate fillers (Chapter 10 and 12). Upper swatch : front; lower swatch : back.
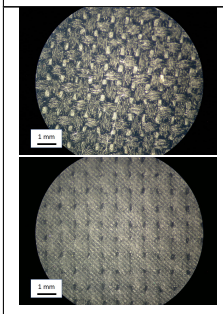	Bag 21; black fibres coated with polyurethane containing calcium carbonate fillers (Chapter 10 and 12). Upper swatch : fibres side; lower swatch : coating side.

Chapter 15

Appendix B : Dose conversion factors from calcium carbonate to organ dose

Dose conversion coefficient from a cube of calcite ($1cm^3$) located at different position of an voxellised anthropomorphic phantom to organ doses for different irradiation geometry and sources (Chapter 12). The positions of the calcite cube were such as follow :

- The right hand side of the phantom (centred at $x = -17.2$ cm, $y = 0$ cm, and $z = 27.5$ cm from the central axis)
- The left hand side of the phantom (centred at $x = 15.8$ cm, $y = 0$ cm, and $z = 27.5$ cm from the central axis)
- The lower back of the phantom (centred at $x = 0$ cm, $y = 11.5$ cm, and $z = 26.5$ cm from the central axis)
- The upper back of the phantom (centred at $x = 0$ cm, $y = 11.5$ cm, and $z = 55.5$ cm from the central axis)

And the irradiation geometry :

- AP : anterior-posterior; plane parallel source in front of the phantom
- PA : posterior-anterior; plane parallel source in the back of the phantom
- LLAT : left-lateral; plane parallel source on the left hand side of the phantom

- RLAT : right-lateral; plane parallel source on the right hand side of the phantom
- ISO : isotropic; sphere source surrounding the phantom
- FLOOR : plan parallel source below the phantom

15.1 ^{60}Co source

Table 15.1: Conversion coefficient from a calcite cube 1 cm^3 at location (right hand side, left hand side, lower back, upper back) to organ dose. Source : ^{60}Co, irradiation geometry : AP.

	Calcite right hand side	Calcite left hand side	Calcite lower back	Calcite upper back
Gonads	1.06	1.05	2.13	2.18
Bone marrow (red)	0.90	0.90	1.82	1.87
Colon	0.95	0.95	1.92	1.97
Lung	0.94	0.94	1.90	1.95
Stomach	0.95	0.94	1.91	1.96
Bladder	0.88	0.87	1.77	1.81
Breast	0.95	0.94	1.91	1.96
Liver	0.88	0.88	1.78	1.82
Oesophagus	0.91	0.91	1.83	1.88
Thyroid	1.09	1.09	2.20	2.26
Skin	0.96	0.96	1.94	1.99
Bone surface	0.86	0.86	1.74	1.78
Remainders	0.91	0.91	1.83	1.88
Salvary glands	0.96	0.96	1.93	1.98
Brain	0.79	0.78	1.58	1.62

Table 15.2: Conversion coefficient from a calcite cube 1 cm^3 at location (right hand side, left hand side, lower back, upper back) to organ dose. Source : ^{60}Co, irradiation geometry : PA.

	Calcite right hand side	Calcite left hand side	Calcite lower back	Calcite upper back
Gonads	0.74	0.76	0.80	0.82
Bone marrow (red)	0.83	0.85	0.90	0.92
Colon	0.74	0.76	0.80	0.82
Lung	0.83	0.85	0.90	0.92
Stomach	0.68	0.70	0.74	0.76
Bladder	0.71	0.73	0.77	0.79
Breast	0.68	0.70	0.74	0.76
Liver	0.74	0.76	0.80	0.82
Oesophagus	0.78	0.80	0.85	0.87
Thyroid	0.71	0.73	0.78	0.79
Skin	0.87	0.90	0.95	0.97
Bone surface	0.80	0.82	0.87	0.89
Remainders	0.85	0.87	0.92	0.94
Salvary glands	0.89	0.92	0.97	0.99
Brain	0.76	0.78	0.83	0.85

Table 15.3: Conversion coefficient from a calcite cube 1 cm^3 at location (right hand side, left hand side, lower back, upper back) to organ dose. Source : ^{60}Co, irradiation geometry : LLAT.

	Calcite right hand side	Calcite left hand side	Calcite lower back	Calcite upper back
Gonads	2.66	0.64	0.76	0.66
Bone marrow (red)	2.88	0.69	0.82	0.72
Colon	3.09	0.74	0.88	0.77
Lung	2.55	0.61	0.73	0.63
Stomach	3.71	0.89	1.06	0.92
Bladder	2.31	0.55	0.66	0.57
Breast	3.71	0.89	1.06	0.92
Liver	2.15	0.52	0.61	0.53
Oesophagus	2.71	0.65	0.77	0.67
Thyroid	2.92	0.70	0.83	0.73
Skin	3.25	0.78	0.93	0.81
Bone surface	2.73	0.65	0.78	0.68
Remainders	2.82	0.67	0.81	0.70
Salvary glands	3.80	0.91	1.08	0.94
Brain	3.72	0.89	1.06	0.92

Table 15.4: Conversion coefficient from a calcite cube 1 cm^3 at location (right hand side, left hand side, lower back, upper back) to organ dose. Source : ^{60}Co, irradiation geometry : RLAT.

	Calcite right hand side	Calcite left hand side	Calcite lower back	Calcite upper back
Gonads	0.60	2.50	0.74	0.63
Bone marrow (red)	0.69	2.86	0.85	0.73
Colon	0.69	2.83	0.84	0.72
Lung	0.60	2.49	0.74	0.63
Stomach	0.55	2.28	0.68	0.58
Bladder	0.90	3.73	1.11	0.95
Breast	0.55	2.28	0.68	0.58
Liver	0.86	3.54	1.05	0.90
Oesophagus	0.61	2.52	0.75	0.64
Thyroid	0.75	3.09	0.92	0.79
Skin	0.77	3.19	0.95	0.81
Bone surface	0.65	2.70	0.81	0.69
Remainders	0.67	2.78	0.83	0.71
Salvary glands	0.91	3.74	1.11	0.95
Brain	0.90	3.70	1.10	0.94

Table 15.5: Conversion coefficient from a calcite cube 1 cm^3 at location (right hand side, left hand side, lower back, upper back) to organ dose. Source : ^{60}Co, irradiation geometry : ISO.

	Calcite right hand side	Calcite left hand side	Calcite lower back	Calcite upper back
Gonads	1.01	1.00	1.03	0.99
Bone marrow (red)	1.02	1.02	1.05	1.00
Colon	0.92	0.92	0.95	0.91
Lung	0.98	0.98	1.01	0.96
Stomach	0.91	0.91	0.94	0.89
Bladder	0.89	0.88	0.91	0.87
Breast	0.91	0.91	0.94	0.89
Liver	0.91	0.91	0.93	0.89
Oesophagus	0.93	0.92	0.95	0.91
Thyroid	1.01	1.00	1.03	0.99
Skin	1.14	1.14	1.17	1.12
Bone surface	0.99	0.99	1.02	0.97
Remainders	1.03	1.02	1.05	1.00
Salvary glands	1.09	1.09	1.12	1.07
Brain	1.09	1.09	1.12	1.07

Table 15.6: Conversion coefficient from a calcite cube 1 cm^3 at location (right hand side, left hand side, lower back, upper back) to organ dose. Source : ^{60}Co, irradiation geometry : FLOOR.

	Calcite right hand side	Calcite left hand side	Calcite lower back	Calcite upper back
Gonads	1.35	1.37	1.43	1.72
Bone marrow (red)	1.15	1.16	1.22	1.47
Colon	0.85	0.85	0.89	1.08
Lung	0.65	0.66	0.69	0.83
Stomach	0.71	0.72	0.75	0.91
Bladder	0.71	0.72	0.75	0.90
Breast	0.71	0.72	0.75	0.91
Liver	0.70	0.71	0.74	0.89
Oesophagus	0.57	0.57	0.60	0.72
Thyroid	0.55	0.56	0.58	0.70
Skin	1.34	1.35	1.42	1.71
Bone surface	1.03	1.04	1.08	1.31
Remainders	1.11	1.12	1.17	1.42
Salvary glands	0.62	0.62	0.65	0.79
Brain	0.53	0.54	0.56	0.68

15.2 ^{137}Cs source

Table 15.7: Conversion coefficient from a calcite cube 1 cm^3 at location (right hand side, left hand side, lower back, upper back) to organ dose. Source : ^{137}Cs, irradiation geometry : AP.

	Calcite right hand side	Calcite left hand side	Calcite lower back	Calcite upper back
Gonads	1.05	1.04	2.61	2.73
Bone marrow (red)	0.85	0.85	2.13	2.23
Colon	0.92	0.91	2.30	2.40
Lung	0.90	0.89	2.25	2.35
Stomach	0.92	0.91	2.29	2.39
Bladder	0.83	0.82	2.07	2.16
Breast	0.92	0.91	2.29	2.39
Liver	0.84	0.83	2.09	2.18
Oesophagus	0.86	0.86	2.16	2.25
Thyroid	1.10	1.09	2.74	2.86
Skin	0.91	0.91	2.28	2.38
Bone surface	0.83	0.83	2.08	2.17
Remainders	0.86	0.85	2.13	2.23
Salvary glands	0.90	0.89	2.25	2.35
Brain	0.70	0.69	1.74	1.81

Table 15.8: Conversion coefficient from a calcite cube 1 cm^3 at location (right hand side, left hand side, lower back, upper back) to organ dose. Source : ^{137}Cs, irradiation geometry : PA.

	Calcite right hand side	Calcite left hand side	Calcite lower back	Calcite upper back
Gonads	0.65	0.68	0.70	0.73
Bone marrow (red)	0.77	0.81	0.84	0.87
Colon	0.67	0.69	0.72	0.75
Lung	0.78	0.81	0.84	0.87
Stomach	0.60	0.63	0.65	0.68
Bladder	0.64	0.66	0.69	0.71
Breast	0.60	0.63	0.65	0.68
Liver	0.67	0.70	0.73	0.75
Oesophagus	0.72	0.75	0.78	0.81
Thyroid	0.63	0.66	0.69	0.71
Skin	0.82	0.85	0.89	0.92
Bone surface	0.77	0.80	0.84	0.86
Remainders	0.80	0.83	0.86	0.89
Salvary glands	0.83	0.87	0.90	0.93
Brain	0.68	0.71	0.74	0.77

Table 15.9: Conversion coefficient from a calcite cube 1 cm^3 at location (right hand side, left hand side, lower back, upper back) to organ dose. Source : ^{137}Cs, irradiation geometry : LLAT.

	Calcite right hand side	Calcite left hand side	Calcite lower back	Calcite upper back
Gonads	3.51	0.52	0.69	0.57
Bone marrow (red)	4.14	0.61	0.81	0.68
Colon	4.49	0.66	0.88	0.74
Lung	3.43	0.50	0.67	0.56
Stomach	5.63	0.83	1.10	0.92
Bladder	2.93	0.43	0.57	0.48
Breast	5.63	0.83	1.10	0.92
Liver	2.72	0.40	0.53	0.45
Oesophagus	3.73	0.55	0.73	0.61
Thyroid	4.16	0.61	0.81	0.68
Skin	4.74	0.70	0.93	0.78
Bone surface	4.02	0.59	0.78	0.66
Remainders	4.01	0.59	0.78	0.66
Salvary glands	5.78	0.85	1.13	0.95
Brain	5.61	0.82	1.09	0.92

Table 15.10: Conversion coefficient from a calcite cube 1 cm^3 at location (right hand side, left hand side, lower back, upper back) to organ dose. Source : ^{137}Cs, irradiation geometry : RLAT.

	Calcite right hand side	Calcite left hand side	Calcite lower back	Calcite upper back
Gonads	0.48	3.21	0.67	0.54
Bone marrow (red)	0.61	4.10	0.85	0.69
Colon	0.60	3.99	0.83	0.67
Lung	0.50	3.35	0.70	0.56
Stomach	0.43	2.90	0.60	0.49
Bladder	0.84	5.65	1.18	0.95
Breast	0.43	2.90	0.60	0.49
Liver	0.79	5.31	1.10	0.89
Oesophagus	0.51	3.39	0.71	0.57
Thyroid	0.66	4.45	0.93	0.75
Skin	0.69	4.64	0.97	0.78
Bone surface	0.59	3.97	0.83	0.67
Remainders	0.59	3.94	0.82	0.66
Salvary glands	0.85	5.67	1.18	0.95
Brain	0.83	5.57	1.16	0.94

Table 15.11: Conversion coefficient from a calcite cube 1 cm^3 at location (right hand side, left hand side, lower back, upper back) to organ dose. Source : ^{137}Cs, irradiation geometry : ISO.

	Calcite right hand side	Calcite left hand side	Calcite lower back	Calcite upper back
Gonads	0.96	0.96	0.99	0.95
Bone marrow (red)	0.98	0.98	1.01	0.97
Colon	0.87	0.87	0.90	0.86
Lung	0.93	0.93	0.96	0.92
Stomach	0.85	0.85	0.88	0.84
Bladder	0.82	0.82	0.85	0.81
Breast	0.85	0.85	0.88	0.84
Liver	0.85	0.85	0.88	0.84
Oesophagus	0.87	0.86	0.89	0.86
Thyroid	0.96	0.96	0.99	0.95
Skin	1.13	1.12	1.16	1.11
Bone surface	0.98	0.98	1.01	0.97
Remainders	0.99	0.98	1.01	0.97
Salvary glands	1.06	1.06	1.09	1.05
Brain	1.05	1.05	1.08	1.04

Table 15.12: Conversion coefficient from a calcite cube 1 cm^3 at location (right hand side, left hand side, lower back, upper back) to organ dose. Source : ^{137}Cs, irradiation geometry : FLOOR.

	Calcite right hand side	Calcite left hand side	Calcite lower back	Calcite upper back
Gonads	1.35	1.34	1.43	1.67
Bone marrow (red)	1.11	1.11	1.18	1.39
Colon	0.79	0.79	0.84	0.99
Lung	0.59	0.59	0.63	0.73
Stomach	0.65	0.65	0.69	0.81
Bladder	0.64	0.64	0.68	0.80
Breast	0.65	0.65	0.69	0.81
Liver	0.64	0.64	0.68	0.80
Oesophagus	0.49	0.49	0.52	0.61
Thyroid	0.48	0.47	0.50	0.59
Skin	1.35	1.34	1.43	1.67
Bone surface	1.01	1.01	1.08	1.26
Remainders	1.08	1.07	1.14	1.34
Salvary glands	0.58	0.58	0.62	0.73
Brain	0.48	0.48	0.51	0.60

15.3 100 keV source

Table 15.13: Conversion coefficient from a calcite cube 1 cm^3 at location (right hand side, left hand side, lower back, upper back) to organ dose. Source : 100 keV, irradiation geometry : AP.

	Calcite right hand side	Calcite left hand side	Calcite lower back	Calcite upper back
Gonads	0.58	0.56	2.55	2.86
Bone marrow (red)	0.45	0.44	1.97	2.20
Colon	0.46	0.45	2.04	2.29
Lung	0.42	0.41	1.85	2.07
Stomach	0.48	0.46	2.09	2.35
Bladder	0.41	0.40	1.81	2.03
Breast	0.48	0.46	2.09	2.35
Liver	0.42	0.41	1.83	2.05
Oesophagus	0.40	0.39	1.74	1.95
Thyroid	0.62	0.60	2.71	3.04
Skin	0.38	0.37	1.66	1.87
Bone surface	0.91	0.89	4.01	4.49
Remainders	0.38	0.37	1.65	1.86
Salvary glands	0.35	0.34	1.55	1.74
Brain	0.25	0.24	1.08	1.21

Table 15.14: Conversion coefficient from a calcite cube 1 cm^3 at location (right hand side, left hand side, lower back, upper back) to organ dose. Source : 100 keV, irradiation geometry : PA.

	Calcite right hand side	Calcite left hand side	Calcite lower back	Calcite upper back
Gonads	0.28	0.29	0.23	0.25
Bone marrow (red)	0.47	0.49	0.39	0.42
Colon	0.32	0.33	0.26	0.28
Lung	0.40	0.41	0.33	0.35
Stomach	0.27	0.28	0.22	0.24
Bladder	0.29	0.30	0.24	0.26
Breast	0.27	0.28	0.22	0.24
Liver	0.33	0.35	0.28	0.30
Oesophagus	0.35	0.37	0.29	0.31
Thyroid	0.28	0.29	0.23	0.25
Skin	0.40	0.42	0.33	0.36
Bone surface	1.02	1.06	0.84	0.91
Remainders	0.42	0.44	0.35	0.38
Salvary glands	0.36	0.38	0.30	0.32
Brain	0.31	0.32	0.25	0.28

Table 15.15: Conversion coefficient from a calcite cube 1 cm^3 at location (right hand side, left hand side, lower back, upper back) to organ dose. Source : 100 keV, irradiation geometry : LLAT.

	Calcite right hand side	Calcite left hand side	Calcite lower back	Calcite upper back
Gonads	3.78	0.13	0.33	0.25
Bone marrow (red)	7.29	0.25	0.64	0.47
Colon	7.26	0.25	0.64	0.47
Lung	4.36	0.15	0.38	0.28
Stomach	9.73	0.34	0.85	0.63
Bladder	2.87	0.10	0.25	0.19
Breast	9.73	0.34	0.85	0.63
Liver	2.79	0.10	0.24	0.18
Oesophagus	4.84	0.17	0.42	0.31
Thyroid	6.43	0.22	0.56	0.42
Skin	6.72	0.23	0.59	0.44
Bone surface	15.12	0.53	1.32	0.98
Remainders	5.90	0.21	0.52	0.38
Salvary glands	9.51	0.33	0.83	0.62
Brain	9.15	0.32	0.80	0.59

Table 15.16: Conversion coefficient from a calcite cube 1 cm^3 at location (right hand side, left hand side, lower back, upper back) to organ dose. Source : 100 keV, irradiation geometry : RLAT.

	Calcite right hand side	Calcite left hand side	Calcite lower back	Calcite upper back
Gonads	0.11	3.07	0.32	0.56
Bone marrow (red)	0.26	7.13	0.73	1.31
Colon	0.21	5.92	0.61	1.09
Lung	0.15	4.21	0.43	0.77
Stomach	0.11	2.90	0.30	0.53
Bladder	0.35	9.72	1.00	1.78
Breast	0.11	2.90	0.30	0.53
Liver	0.33	9.13	0.94	1.68
Oesophagus	0.15	4.08	0.42	0.75
Thyroid	0.25	6.89	0.71	1.26
Skin	0.23	6.44	0.66	1.18
Bone surface	0.54	14.76	1.51	2.71
Remainders	0.21	5.70	0.58	1.05
Salvary glands	0.33	9.16	0.94	1.68
Brain	0.33	9.06	0.93	1.66

Table 15.17: Conversion coefficient from a calcite cube 1 cm^3 at location (right hand side, left hand side, lower back, upper back) to organ dose. Source : 100 keV, irradiation geometry : ISO.

	Calcite right hand side	Calcite left hand side	Calcite lower back	Calcite upper back
Gonads	0.46	0.46	0.50	0.48
Bone marrow (red)	0.53	0.53	0.57	0.56
Colon	0.41	0.40	0.44	0.42
Lung	0.41	0.41	0.44	0.43
Stomach	0.40	0.39	0.42	0.41
Bladder	0.37	0.37	0.40	0.39
Breast	0.40	0.39	0.42	0.41
Liver	0.40	0.40	0.43	0.41
Oesophagus	0.37	0.37	0.40	0.39
Thyroid	0.47	0.47	0.51	0.49
Skin	0.51	0.51	0.54	0.53
Bone surface	1.13	1.12	1.21	1.18
Remainders	0.45	0.45	0.49	0.47
Salvary glands	0.46	0.46	0.49	0.48
Brain	0.47	0.47	0.50	0.49

Table 15.18: Conversion coefficient from a calcite cube 1 cm^3 at location (right hand side, left hand side, lower back, upper back) to organ dose. Source : 100 keV, irradiation geometry : FLOOR.

	Calcite right hand side	Calcite left hand side	Calcite lower back	Calcite upper back
Gonads	0.74	0.70	0.79	0.93
Bone marrow (red)	0.62	0.59	0.66	0.78
Colon	0.38	0.37	0.41	0.48
Lung	0.24	0.23	0.26	0.31
Stomach	0.30	0.29	0.32	0.38
Bladder	0.29	0.28	0.31	0.37
Breast	0.30	0.29	0.32	0.38
Liver	0.30	0.29	0.32	0.38
Oesophagus	0.19	0.18	0.20	0.24
Thyroid	0.18	0.17	0.19	0.23
Skin	0.65	0.62	0.69	0.82
Bone surface	1.20	1.14	1.28	1.52
Remainders	0.52	0.50	0.55	0.66
Salvary glands	0.26	0.25	0.27	0.33
Brain	0.18	0.17	0.19	0.23

References

Ackerman, G. and Halverson, J. (2016). Radiological Weapons and Jihadist Terrorism, chapter 7, pages 173–192. Routledge.

Ademola, J. A. and Woda, C. (2017). Thermoluminescence of electronic components from mobile phones for determination of accident doses. Radiation Measurements, 104:13–21.

Ainsbury, E., Badie, C., Barnard, S., Manning, G., Moquet, J., Abend, M., Antunes, A. C., Barrios, L., Bassinet, C., Beinke, C., et al. (2017). Integration of new biological and physical retrospective dosimetry methods into EU emergency response plans–joint RENEB and EURADOS inter-laboratory comparisons. International Journal of Radiation Biology, 93(1):99–109.

Ainsbury, E., Bakhanova, E., Barquinero, J., Brai, M., Chumak, V., Correcher, V., Darroudi, F., Fattibene, P., Gruel, G., Guclu, I., et al. (2010). Review of retrospective dosimetry techniques for external ionising radiation exposures. Radiation Protection Dosimetry, 147(4):573–592.

Ainsbury, E. A. and Lloyd, D. C. (2010). Dose estimation software for radiation biodosimetry. Health Physics, 98(2):290–295.

Ainsbury, E. A., Samaga, D., Della Monaca, S., Marrale, M., Bassinet, C., Burbidge, C. I., Correcher, V., Discher, M., Eakins, J., Fattibene, P., Gl, n., Higueras, M., Lund, E., Maltar-Strmeki, N., McKeever, S., Rf, C. L., Sholom, S., Veronese, I., Wieser, A., Woda, C., and Trompier, F. (2018). Uncertainty on radiation doses estimated by biological and retrospective physical methods. Radiation Protection Dosimetry, 178(4):382–404.

Aitken, M. J. (1985). Thermoluminescence Dating. Academic Press, Cambridge.

Aitken, M. J. (1998). Introduction to optical dating: the dating of Quaternary sediments by the use of photon-stimulated luminescence. Clarendon Press, Oxford.

Akselrod, M., Agersnap Larsen, N., Whitley, V., and McKeever, S. (1998). Thermal quenching of F-center luminescence in Al_2O_3:C. Journal of Applied Physics, 84(6):3364–3373.

Akselrod, M. and Gorelova, E. (1993). Deep traps in highly sensitive α-Al_2O_3:C TLD crystals. Nuclear Tracks and Radiation Measurements, 21(1):143–146.

Alexander, C. and McKeever, S. (1998). Phototransferred thermoluminescence. Journal of Physics D: Applied Physics, 31(20):2908.

Alongi, J., Carosio, F., and Malucelli, G. (2014). Current emerging techniques to impart flame retardancy to fabrics : an overview. Polymer Degradation and Stability, 106:138–149.

Alongi, J., Ciobanu, M., and Malucelli, G. (2011). Novel flame retardant finishing systems for cotton fabrics based on phosphorus-containing compounds and silica derived from solgel processes. Carbohydrate Polymers, 85(3):599–608.

Attix, F. H. (1986). Introduction on Radiological Physics and Radiological Dosimetry. John Wiley & Sons, New York.

Attix, F. H. (2008). Introduction to radiological physics and radiation dosimetry. John Wiley & Sons.

Avouris, P. and Morgan, T. (1981). A tunneling model for the decay of luminescence in inorganic phosphors : the case of Zn_2SiO_4: Mn. The Journal of Chemical Physics, 74(8):4347–4355.

Ayda, C., lk R. Yce, Engin, B., and Polymeris, G. S. (2016). Dosimetric and kinetic characteristics of watch glass sample. Radiation Measurements, 85:78–87.

Baba, M. (2013). Fukushima accident: What happened? Radiation Measurements, 55(Supplement C):17–21.

Bailiff, I. (1976). Use of phototransfer for the anomalous fading of thermoluminescence. Nature, 264(5586):531–533.

Bailiff, I. (1995). The use of ceramics for retrospective dosimetry in the Chernobyl exclusion zone. Radiation Measurements, 24(4):507–511.

Bailiff, I. (1997). Retrospective dosimetry with ceramics. Radiation Measurements, 27(5-6):923–941.

Bailiff, I., Correcher, V., Delgado, A., Göksu, Y., and Hbner, S. (2002). Luminescence characteristics of dental ceramics for retrospective dosimetry: A preliminary study. Radiation Protection Dosimetry, 101(1-4):519–524.

Bailiff, I. and Mikhailik, V. (2004). The use of calcium silicate bricks for retrospective dosimetry. Radiation Measurements, 38(1):91–99.

Bailiff, I., Sholom, S., and McKeever, S. (2016). Retrospective and emergency dosimetry in response to radiological incidents and nuclear mass-casualty events: A review. Radiation Measurements, 94:83–139.

Bailiff, I., Stepanenko, V., Göksu, H., Bøtter-Jensen, L., Brodski, L., Chumak, V., Correcher, V., Delgado, A., Golikov, V., Jungner, H., et al. (2004a). Comparison of retrospective luminescence dosimetry with computational modeling in two highly contaminated settlements downwind of the Chernobyl NPP. Health Physics, 86(1):25–41.

Bailiff, I. K., Bowman, S., Mobbs, S., and Aitken, M. (1977). The phototransfer technique and its use in thermoluminescence dating. Journal of Electrostatics, 3(1-3):269–280.

Bailiff, I. K., Stepanenko, V. F., Göksu, H. Y., Bøtter-Jensen, L., Correcher, V., Delgado, A., Jungner, H., Khamidova, L. G., Kolizshenkov, T. V., Meckbach, R., et al. (2005). Retrospective luminescence dosimetry: development of approaches to application in populated areas downwind of the Chernobyl NPP. Health Physics, 89(3):233–246.

Bailiff, I. K., Stepanenko, V. F., Göksu, H. Y., Jungner, H., Balmukhanov, S. B., Balmukhanov, T. S., Khamidova, L. G., Kisilev, V. I., Kolyado, I. B., Kolizshenkov, T. V., et al. (2004b). The application of retrospective luminescence dosimetry in areas affected by fallout from the Semipalatinsk nuclear test site: an evaluation of potential. Health Physics, 87(6):625–641.

Baklanov, A., Srensen, J. H., Hoe, S. C., and Amstrup, B. (2006). Urban meteorological modelling for nuclear emergency preparedness. Journal of Environmental Radioactivity, 85(2):154–170.

Barnett, D. J., Parker, C. L., Blodgett, D. W., Wierzba, R. K., and Links, J. M. (2006). Understanding radiologic and nuclear terrorism as public health threats: preparedness and response perspectives. Journal of Nuclear Medicine, 47(10):1653–1661.

Barthe, J., Kamenopoulou, V., Cattoire, B., and Portal, G. (1989). Dose evaluation from textile fibers: a post-determination of initial ESR signal. International Journal of Radiation Applications and Instrumentation. Part A. Applied Radiation and Isotopes, 40(10):1029–1033.

Bassinet, C., Trompier, F., and Clairand, I. (2010). Radiation accident dosimetry on glass by TL and EPR spectrometry. Health Physics, 98(2):400–405.

Bassinet, C., Woda, C., Bortolin, E., Monaca, S. D., Fattibene, P., Quattrini, M., Bulanek, B., Ekendahl, D., Burbidge, C., Cauwels, V., Kouroukla, E., Geber-Bergstrand, T., Mrozik, A., Marczewska, B., Bilski, P., Sholom, S., McKeever, S., Smith, R., Veronese, I., Galli, A., Panzeri, L., and Martini, M. (2014). Retrospective radiation dosimetry using OSL of electronic components: Results of an inter-laboratory comparison. Radiation Measurements, 71:475–479.

Beerten, K. and Vanhavere, F. (2010). Photon energy dependence of three fortuitous dosemeters from personal electronic devices, measured by optically stimulated luminescence. Radiation Protection Dosimetry, 140(3):294–299.

Beerten, K., Woda, C., and Vanhavere, F. (2009). Thermoluminescence dosimetry of electronic components from personal objects. Radiation Measurements, 44(5):620–625.

Bernhardsson, C., Christiansson, M., Mattsson, S., and Rääf, C. L. (2009). Household salt as a retrospective dosemeter using optically stimulated luminescence. Radiation and Environmental Biophysics, 48(1):21–28.

Blakely, W. F., Carr, Z., Chu, M. C.-M., Dayal-Drager, R., Fujimoto, K., Hopmeir, M., Kulka, U., Lillis-Hearne, P., Livingston, G. K., Lloyd, D. C., et al. (2009). WHO 1st consultation on the development of a global biodosimetry laboratories network for radiation emergencies (BioDoseNet). Radiation Research, 171(1):127–139.

Blasse, G. and Grabmaier, B. (2012). Luminescent materials. Springer, Berlin.

Borsi, S. and Fornaca-Rinaldi, G. (1968). Relationship between crystallization temperature and some properties of thermoluminescence in natural calcites. In Thermoluminescence of Geological Materials, pages 225–231. Academic Press New York.

Bortolin, E., Boniglia, C., Monaca, S. D., Gargiulo, R., and Fattibene, P. (2011). Silicates collected from personal objects as a potential fortuitous dosimeter in radiological emergency. Radiation Measurements, 46(9):967–970.

Bos, A. J. (2011). Fundamentals of radiation dosimetry. In AIP Conference Proceedings, volume 1345, pages 5–23. AIP, American Institute of Physics, College Park.

Bostick, N. A., Subbarao, I., Burkle, F. M., Hsu, E. B., Armstrong, J. H., and James, J. J. (2008). Disaster triage systems for large-scale catastrophic events. Disaster Medicine and Public Health Preparedness, 2(S1):S35S39.

Bøtter-Jensen, L., McKeever, S. W., and Wintle, A. G. (2003). Optically stimulated luminescence dosimetry. Elsevier, Amsterdam.

Bougrov, N., Göksu, H., Haskell, E., Degteva, M., Meckbach, R., and Jacob, P. (1998). Issues in the reconstruction of environmental doses on the basis of thermoluminescence measurements in the Techa riverside. Health Physics, 75(6):574–583.

Bourbigot, S. and Duquesne, S. (2007). Fire retardant polymers: recent developments and opportunities. Journal of Materials Chemistry, 17(22):2283–2300.

Boustead, I. (1970). Molecular oxygen as an electron trap in the thermoluminescence of saturated hydrocarbons. Nature, 225(5235):846.

Brady, J. M., Aarestad, N. O., and Swartz, H. M. (1968). In vivo dosimetry by electron spin resonance spectroscopy. Health Physics, 15(1):43–47.

British Standard Institution (2016). Bs en 62387:2016 : Radiation protection instrumentation. passive integrating dosimetry systems for individual, workplace and environmental monitoring of photon and beta radiation.

Bruce, J., Galloway, R., Harper, K., and Spink, E. (1999). Bleaching and phototransfer of thermoluminescence in limestone. Radiation Measurements, 30(4):497–504.

Brzozowska, B., Ainsbury, E., Baert, A., Beaton-Green, L., Barrios, L., Barquinero, J. F., Bassinet, C., Beinke, C., Benedek, A., Beukes, P., et al. (2017). RENEB accident simulation exercise. International Journal of Radiation Biology, 93(1):75–80.

Buddemeier, B. and Dillion, M. (2010). Key response planning factors for the aftermath of a nuclear detonation. Technical report, Lawrence Livermore National Laboratory.

Bull, C. and Garlick, G. (1950). The luminescence of diamonds. Proceedings of the Physical Society. Section A, 63(11):1283.

Bull, R. K. (1989). Kinetics of the localised transition model for thermoluminescence. Journal of Physics D: Applied Physics, 22(9):1375.

Bulur, E. (1996). An alternative technique for optically stimulated luminescence (OSL) experiment. Radiation Measurements, 26(5):701–709.

Bulur, E. and Göksu, H. (1998). OSL from BeO ceramics: new observations from an old material. Radiation Measurements, 29(6):639–650.

Bulur, E. and Göksu, H. (1999). Phototransferred thermoluminescence from α-Al_2O_3: C using blue light emitting diodes. Radiation Measurements, 30(2):203–206.

Bureau International des Poids et Mesures, Commission électrotechnique internationale, International Federation of Clinical Chemistry, International Laboratory Accreditation Cooperation, International Organization for Standardization , International Union of Pure and Applied Chemistry, International Union of Pure and Applied Physics, and International Organization of Legal Metrology (1995). Guide to the Expression of Uncertainty in Measurement. International Organization for Standardization, Geneva.

Bureau International des Poids et Mesures, Commission électrotechnique internationale, International Federation of Clinical Chemistry, International Laboratory Accreditation Cooperation, International Organization for Standardization , International Union of Pure and Applied Chemistry, International Union of Pure and Applied Physics, and International Organization of Legal Metrology (2008). Evaluation of measurement data - Supplement 1 to the Guide to the expression of uncertainty in measurement Propagation of distributions using a Monte Carlo method. Joint Committee for Guides in Metrology, JCGM 101: 2008. International Organization for Standardization, Geneva.

Burnell-Jones, P. (2005). Heat curable thermosetting luminescent resins. US Patent 6,905,634.

Calderon, T., Aguilar, M., Jaque, F., and Coy-Yll, R. (1984). Thermoluminescence from natural calcites. Journal of Physics C: Solid State Physics, 17(11):2027.

Calderon, T., Townsend, P., Beneitez, P., Garcia-Guinea, J., Millan, A., Rendell, H., Tookey, A., Urbina, M., and Wood, R. (1996). Crystal field effects on the thermoluminescence of manganese in carbonate lattices. Radiation Measurements, 26(5):719–731.

Callens, F., Vanhaelewyn, G., Matthys, P., and Boesman, E. (1998). EPR of carbonate derived radicals: Applications in dosimetry, dating and detection of irradiated food. Applied Magnetic Resonance, 14(2):235–254.

Carlsson, G. A. (1979). Definition of energy imparted: a new formulation adapted to exact solutions of the absorbed dose equation under nonequilibrium conditions. Radiation Research, 77(2):209–220.

Carmichael, L., Sanderson, D., and Riain, S. N. (1994). Thermoluminescence measurement of calcite shells. Radiation Measurements, 23(2-3):455–463.

Cevc, P., Schara, M., and Ravnik, Č. (1972). Electron paramagnetic resonance study of irradiated tooth enamel. Radiation Research, 51(3):581–589.

Charles, M. (1983). An extended role for thermoluminescent phosphors in personnel environmental and accident dosimetry using sensitisation, re-estimation and fast fading. Nuclear Instruments and Methods in Physics Research, 206(1-2):239–242.

Charlesby, A. (1981). Field enhanced luminescence of irradiated organics due to electron tunnelling. Radiation Physics and Chemistry (1977), 17(6):399–411. Special Issue Electrons at Low Temperature.

Charlesby, A. et al. (1963). The effect of oxygen on the thermoluminescence of irradiated polyethylene. Proc. R. Soc. Lond. A, 271(1345):188–206.

Charlesby, A. and Partridge, R. (1965). The identification of luminescence centres in polyethylene and other polymers. Proc. R. Soc. Lond. A, 283(1394):312–328.

Chen, R. (1969). On the calculation of activation energies and frequency factors from glow curves. Journal of Applied Physics, 40(2):570–585.

Chen, R. and Fogel, G. (1993). Supralinearity in thermoluminescence revisited. Radiation Protection Dosimetry, 47(1-4):23–26.

Chen, R. and Kirsh, Y. (2013). The analysis of thermally stimulated processes. Elsevier, Amsterdam.

Chen, R. and McKeever, S. W. (1997). Theory of thermoluminescence and related phenomena. World Scientific.

Chen, R. and Pagonis, V. (2011). Thermally and optically stimulated luminescence: a simulation approach. John Wiley & Sons, New York.

Chen, W., Luan, Y., Shieh, M., Chen, S., Kung, H., Soong, K., Yeh, Y., Chou, T., Mong, S., Wu, J., et al. (2007). Effects of Cobalt-60 exposure on health of Taiwan residents suggest new approach needed in radiation protection. Dose-Response, 5(1):63–75.

Chithambo, M., Pagonis, V., and Ogundare, F. (2014). Spectral and kinetic analysis of thermoluminescence from manganiferous carbonatite. Journal of Luminescence, 145:180–187.

Chithambo, M., Seneza, C., and Kalita, J. (2017). Phototransferred thermoluminescence of α-Al_2O_3:C: Experimental results and empirical models. Radiation Measurements, 105(Supplement C):7–16.

Christiansson, M., Bernhardsson, C., Geber-Bergstrand, T., Mattsson, S., and Rääf, C. L. (2014"). Household salt for retrospective dose assessments using OSL: signal integrity and its dependence on containment, sample collection, and signal readout. Radiation and Environmental Biophysics, 53(3):559–569.

Christodoulides, C. (1990). General-order kinetics in thermoluminescence resulting from a distribution of the frequency factor. Physica Status Solidi (a), 118(1):333–342.

Chruścińska, A. (2015). Estimating the parameters of traps in quartz by the variable energy of stimulation optically stimulated luminescence (VES-OSL) method. Radiation Measurements, 81:205–211.

Chumak, V., Likhtarev, I., Shalom, S., Meckbach, R., and Krjuchkov, V. (1998). Chernobyl experience in field of retrospective dosimetry: Reconstruction of doses to the population and liquidators involved in the accident. Radiation Protection Dosimetry, 77(1-2):91–95.

Chumak, V., Sholom, S., and Pasalskaya, L. (1999). Application of high precision EPR dosimetry with teeth for reconstruction of doses to Chernobyl populations. Radiation Protection Dosimetry, 84(1-4):515–520.

Cireli, A., Onar, N., Ebeoglugil, M. F., Kayatekin, I., Kutlu, B., Culha, O., and Celik, E. (2007). Development of flame retardancy properties of new halogen-free phosphorous doped SiO_2 thin films on fabrics. Journal of Applied Polymer Science, 105(6):3748–3756.

Clairand, I., Trompier, F., Bottollier-Depois, J.-F., and Gourmelon, P. (2006). Ex vivo ESR measurements associated with Monte-Carlo calculations for accident dosimetry: application to the 2001 Georgian accident. Radiation Protection Dosimetry, 119(1-4):500–505.

Coleman, A. and Yukihara, E. (2018). On the validity and accuracy of the initial rise method investigated using realistically simulated thermoluminescence curves. Radiation Measurements, 117:70–79.

Coleman, C. N., Hrdina, C., Bader, J. L., Norwood, A., Hayhurst, R., Forsha, J., Yeskey, K., and Knebel, A. (2009). Medical response to a radiologic/nuclear event: integrated plan from the Office of the Assistant Secretary for Preparedness and Response, Department of Health and Human Services. Annals of Emergency Medicine, 53(2):213–222.

Coleman, C. N., Sullivan, J. M., Bader, J. L., Murrain-Hill, P., Koerner, J. F., Garrett, A. L., Weinstock, D. M., Case Jr, C., Hrdina, C., Adams, S. A., et al. (2015). Public health and medical preparedness for a nuclear detonation: the nuclear incident medical enterprise. Health Physics, 108(2):149.

Coleman, C. N., Weinstock, D. M., Casagrande, R., Hick, J. L., Bader, J. L., Chang, F., Nemhauser, J. B., and Knebel, A. R. (2011). Triage and treatment tools for use in a scarce resources-crisis standards of care setting after a nuclear detonation. Disaster Medicine and Public Health Preparedness, 5(S1):S111–S121.

Colyott, L., Akselrod, M., and McKeever, S. (1996). Phototransferred thermoluminescence in α-Al_2o_3: C. Radiation Protection Dosimetry, 65(1-4):263–266.

Colyott, L., Akselrod, M., and McKeever, S. (1997). An integrating Ultraviolet-B Dosemeter using

Phototransferred Thermoluminescence in α-Al_2O_3:C. Radiation Protection Dosimetry, 72(2):87–94.

Consumer Protection Act (1988). The Furniture and Furnishings (Fire Safety) Regulations.

Cooke, W. M., Hendrix, J. E., and Tolbert, T. W. (1991). Fire-resistant fabric. US Patent 4,996,099.

Cunningham, J. R. and Johns, H. E. (1983). The physics of radiology. Charles C. Thosmas, Springfield.

Curie, D. (1963). Luminescence in crystals. Methuen, London.

Currie, L. A. (1968). Limits for qualitative detection and quantitative determination. application to radiochemistry. Analytical chemistry, 40(3):586–593.

De Lima, J., Valerio, M., and Okuno, E. (2001). Thermally assisted tunneling: An alternative model for the thermoluminescence process in calcite. Physical Review B, 64(1):014105.

DeArmitt, C. and Rothon, R. (2017). Particulate fillers, selection, and use in polymer composites. Fillers for Polymer Applications, pages 3–27.

Debenham, N. (1983). Reliability of thermoluminescence dating of stalagmitic calcite. Nature, 304(5922):154.

Delbecq, C. J., Hartford, R., Schoemaker, D., and Yuster, P. H. (1976). Sn+ centers and thermal motion of associated vacancies in KCl: Sn Cl_2. Phys. Rev. B, 13:3631–3644.

DeWitt, R., Klein, D., Yukihara, E., Simon, S., and McKeever, S. (2010). Optically stimulated luminescence (OSL) of tooth enamel and its potential use in post-radiation exposure triage. Health Physics, 98(2):432.

Dexter, D. L. (1953). A theory of sensitized luminescence in solids. The Journal of Chemical Physics, 21(5):836–850.

Dexter, D. L., Klick, C. C., and Russell, G. A. (1955). Criterion for the occurrence of luminescence. Phys. Rev., 100:603–605.

DiCarlo, A. L., Maher, C., Hick, J. L., Hanfling, D., Dainiak, N., Chao, N., Bader, J. L., Coleman, C. N., and Weinstock, D. M. (2011). Radiation injury after a nuclear detonation: Medical consequences and the need for scarce resources allocation. Disaster Medicine and Public Health Preparedness, 5(S1):S32–S44.

Discher, M., Greiter, M., and Woda, C. (2014). Photon energy dependence and angular response of glass display used in mobile phones for accident dosimetry. Radiation Measurements, 71:471–474.

Discher, M., Hiller, M., and Woda, C. (2015). MCNP simulations of a glass display used in a mobile phone as an accident dosimeter. Radiation Measurements, 75:21–28.

Discher, M. and Woda, C. (2013). Thermoluminescence of glass display from mobile phones for retrospective and accident dosimetry. Radiation Measurements, 53-54:12–21.

Discher, M. and Woda, C. (2014). Thermoluminescence emission spectrometry of glass display in mobile phones and resulting evaluation of the dosimetric properties of a specific type of display glass. Radiation Measurements, 71:480–484.

Discher, M., Woda, C., and Fiedler, I. (2013). Improvement of dose determination using glass display of mobile phones for accident dosimetry. Radiation Measurements, 56:240–243.

Domenech, H. (2016). Radiation Safety: Management and Programs. Springer, Berlin.

Down, J., Flower, R., Strain, J., and Townsend, P. (1985). Thermoluminescence emission spectra of calcite and Iceland spar. Nuclear Tracks and Radiation Measurements (1982), 10(4-6):581–589.

Eakins, J., Bartlett, D., Hager, L., Molinos-Solsona, C., and Tanner, R. (2007). The MCNP-4C2 design of a two element photon/electron dosemeter that uses magnesium/copper/phosphorus doped lithium fluoride. Radiation Protection Dosimetry, 128(1):21–35.

Eakins, J. and Kouroukla, E. (2015). Luminescence-based retrospective dosimetry using Al_2O_3 from mobile phones: a simulation approach to determine the effects of position. Journal of Radiological Protection, 35(2):343.

Eakins, J. S. and Ainsbury, E. A. (2018a). Quantities for assessing high doses to the body: a short review of the current status. Journal of Radiological Protection, 38(2):731.

Eakins, J. S. and Ainsbury, E. A. (2018b). Quantities for assessing high photon doses to the body: a calculational approach. Journal of Radiological Protection, 38(2):743.

Ekendahl, D. and Judas, L. (2011). Retrospective dosimetry with alumina substrate from electronic components. Radiation Protection Dosimetry, 150(2):134–141.

Ekendahl, D. and Judas, L. (2012). Retrospective dosimetry with alumina substrate from electronic components. Radiation Protection Dosimetry, 150(2):134–141.

Ekendahl, D., Judas, L., and Sukupova, L. (2013). OSL and TL retrospective dosimetry with a fluorapatite glass-ceramic used for dental restorations. Radiation Measurements, 58:138–144.

Engin, B., Ayda, C., and Demirta, H. (2006). ESR dosimetric properties of window glass. Nuclear Instruments and Methods in Physics Research Section B: Beam Interactions with Materials and Atoms, 243(1):149–155.

Engin, B. and Güven, O. (2000). The effect of heat treatment on the thermoluminescence of naturally-occurring calcites and their use as a gamma-ray dosimeter. Radiation Measurements, 32(3):253–272.

Evans, R. D. (1955). The Atomic Nucleus, 1955. McGrawHill, New York.

Fattibene, P. and Callens, F. (2010). EPR dosimetry with tooth enamel: a review. Applied Radiation and Isotopes, 68(11):2033–2116.

Fattibene, P., Duckworth, T., and Desrosiers, M. (1996). Critical evaluation of the sugar-EPR dosimetry system. Applied Radiation and Isotopes, 47(11):1375–1379.

Fattibene, P., Trompier, F., Wieser, A., Brai, M., Ciesielski, B., De Angelis, C., Della Monaca, S., Garcia, T., Gustafsson, H., Hole, E. O., et al. (2014). EPR dosimetry intercomparison using smart phone touch screen glass. Radiation and Environmental Biophysics, 53(2):311–320.

Ferguson, C. D. (2009). Radiological Weapons and Jihadist Terrorism, chapter 7, pages 173–192. CRC Press.

Finch, S. (1987). Acute radiation syndrome. JAMA, 258(5):664–667.

Finnon, P., Lloyd, D., and Edwards, A. (1995). Fluorescence in situ hybridization detection of chromosomal aberrations in human lymphocytes: applicability to biological dosimetry. International Journal of Radiation Biology, 68(4):429–435.

Flynn, D. F. and Goans, R. E. (2006). Nuclear terrorism: triage and medical management of radiation and combined-injury casualties. Surgical Clinics, 86(3):601–636.

Folk, R. L. (1962). Spectral subdivision of limestone types.

Fox, M. (2002). Optical properties of solids. Oxford University Press, Oxford.

Franklin, A., Hornyak, W., Pagonis, V., and Kristianpoller, N. (1990). Thermoluminescence study of annealing a geological calcite. International Journal of Radiation Applications and Instrumentation. Part D. Nuclear Tracks and Radiation Measurements, 17(4):517–523.

Furetta, C. (2010). Handbook of thermoluminescence. World Scientific, Singapore.

Galloway, R. (2002). Does limestone show useful optically stimulated luminescence? Ancient TL, 20(1):1–5.

Garlick, G. and Robinson, I. (1972). The thermoluminescence of lunar samples. In The Moon, volume 47, page 324.

Garlick, G. F. J. and Gibson, A. F. (1948). The electron trap mechanism of luminescence in sulphide and silicate phosphors. Proceedings of the Physical Society, 60(6):574.

Geber-Bergstrand, T., Bernhardsson, C., Christiansson, M., Mattsson, S., and Rääf, C. L. (2018). Optically stimulated luminescence (OSL) dosimetry in irradiated alumina substrates from mobile phone resistors. Radiation and Environmental Biophysics, 57(1):69–75.

Geber-Bergstrand, T., Bernhardsson, C., Christiansson, M., Mattsson, S., and Rf, C. L. (2015). Desiccants for retrospective dosimetry using optically stimulated luminescence (OSL). Radiation Measurements, 78:17–22.

Gilvin, P., Baker, S., Daniels, T., Eakins, J., McClure, D., Bartlett, D., and Boucher, C. (2007). Type testing of a new TLD for the UK Health Protection Agency. Radiation Protection Dosimetry, 128(1):36–42.

Göksu, H., Bailiff, I., and Mikhailik, V. (2003). New approaches to retrospective dosimetry using cementitious building materials. Radiation Measurements, 37(4-5):323–327.

Göksu, H., Degteva, M., Bougrov, G., Meckbach, R., Haskell, E., Bailiff, I., Bøtter-Jensen, L., Jungner, H., and Jacob, P. (2002). First international intercomparison of luminescence techniques using samples from the Techa river valley. Health Physics, 82(1):94–101.

Göksu, H., Heide, L., Bougrov, N., Dalheimer, A., Meckbach, R., and Jacob, P. (1996). Depth-dose distribution in bricks determined by thermoluminescence and by Monte-Carlo calculation for external γ-dose reconstruction. Applied Radiation and Isotopes, 47(4):433–440.

Göksu, H., Pennycook, S., and Brown, L. (1988). Thermoluminescence and cathodoluminescence studies of calcite and MgO: surface defects and heat treatment. International Journal of Radiation Applications and Instrumentation. Part D. Nuclear Tracks and Radiation Measurements, 14(3):365–368.

Göksu, H. Y., Stepanenko, V. F., Bailiff, I. K., and Jungner, H. (2006). Intercomparison of luminescence measurements of bricks from Dolon'village: Experimental methodology and results of european study group. Journal of Radiation Research, 47(Supplement A):A29–A37.

González, A. J. (2005). Lauriston S. Taylor Lecture: Radiation protection in the aftermath of a terrorist attack involving exposure to ionizing radiation. Health physics, 89(5):418–446.

Goorley, T., James, M., Booth, T., Brown, F., Bull, J., Cox, L. J., Durkee, J., Elson, J., Fensin, M., Forster, R. A., Hendricks, J., Hughes, H. G., Johns, R., Kiedrowski, B., Martz, R., Mashnik, S., McKinney, G., Pelowitz, D., Prael, R., Sweezy, J., Waters, L., Wilcox, T., and Zukaitis, T. (2012). Initial MCNP6 release overview. Nuclear Technology, 180(3):298–315.

Gorbics, S., Nash, A., and Attix, F. (1969). Thermal quenching of luminescence in six thermoluminescent dosimetry phosphorsi: Quenching of X-ray-excited radioluminescence. The International Journal of Applied Radiation and Isotopes, 20(12):829–841.

Grenet, J., Vautier, C., Carles, D., and Chabrier, J. (1973). Space charge conduction in presence of a Gaussian distribution of localized states. Philosophical Magazine, 28(6):1265–1277.

Grimmeiss, H. G. and Ledebo, L. A. (1975). Photo-ionization of deep impurity levels in semiconductors with non-parabolic bands. Journal of Physics C: Solid State Physics, 8(16):2615.

Gualtieri, G., Colacicchi, S., Sgattoni, R., and Giannoni, M. (2001). The Chernobyl accident: EPR dosimetry on dental enamel of children. Applied Radiation and Isotopes, 55(1):71–79.

Guerin, G. and Visocekas, R. (2015). Volcanic feldspars anomalous fading: Evidence for two different mechanisms. Radiation Measurements, 81:218–223.

Guskova, A., Barabanova, A., Baranov, A., Gruszdev, G., Pyatkin, Y., Nadezhina, N., Metlyaeva, N., Selidovkin, G., Moiseev, A., Gusev, I., et al. (1988). Acute radiation effects in victims of the Chernobyl nuclear power plant accident. United Nations, UNSCEAR, 613(647):68.

Haake, C. H. (1957). Critical comment on a method for determining electron trap depths. J. Opt. Soc. Am., 47(7):649–652.

Hadid, L., Desbrée, A., Schlattl, H., Franck, D., Blanchardon, E., and Zankl, M. (2010). Application of the ICRP/ICRU reference computational phantoms to internal dosimetry: calculation of specific absorbed fractions of energy for photons and electrons. Physics in Medicine & Biology, 55(13):3631.

Halperin, A. and Braner, A. A. (1960). Evaluation of thermal activation energies from glow curves. Phys. Rev., 117:408–415.

Harper, F. T., Musolino, S. V., and Wente, W. B. (2007). Realistic radiological dispersal device hazard boundaries and ramifications for early consequence management decisions. Health Physics, 93(1):1–16.

Hasan, F. A., Keck, B. D., Hartmetz, C., and Sears, D. W. (1986). Anomalous fading of thermoluminescence in meteorites. Journal of Luminescence, 34(6):327–335.

Hashizume, T., Maruyama, T., Shiragai, A., Tanaka, E., Izawa, M., Kawamura, S., and Nag, S. (1967). Estimation of the air dose from the atomic bombs in Hiroshima and Nagasaki. Health Physics, 13(2):149–161.

Haskell, E., Bailiff, I., Kenner, G., Kaipa, P., and Wrenn, M. (1994). Thermoluminescence measurements of gamma-ray doses attributable to fallout from the Nevada test site using building bricks as natural dosimeters. Health physics, 66(4):380–391.

Haskell, E., Kaipa, P., and Wrenn, M. (1984). The use of thermoluminescence analysis for atomic bomb dosimetry. In Proceedings of the second US-Japan joint workshop for reassessment of atomic bomb radiation dosimetry in Hiroshima and Nagasaki.

Helfand, I., Forrow, L., and Tiwari, J. (2002). Nuclear terrorism. BMJ: British Medical Journal, 324(7333):356.

Hempelmann, L., LISCO, H., and HOFFMAN, J. (1952). The acute radiation syndrome: A study of nine cases and a review of the problem. Annals of Internal Medicine, 36(2):279–510.

Hick, J. L., Weinstock, D. M., Coleman, C. N., Hanfling, D., Cantrill, S., Redlener, I., Bader, J. L., Murrain-Hill, P., and Knebel, A. R. (2011). Health care system planning for and response to a nuclear detonation. Disaster Medicine and Public Health Preparedness, 5(S1):73–88.

Higashimura, T., Ichikawa, Y., and Sidei, T. (1963). Dosimetry of atomic bomb radiation in hiroshima by thermoluminescence of roof tiles. Science, 139(3561):1284–1285.

Hoffman, J. D. (1991). Transition from extended-chain to once-folded behaviour in pure n-paraffins crystallized from the melt. Polymer, 32(15):2828–2841.

Hoogenstraaten, W. (1958). Electron traps in zinc-sulphide phosphors, volume 13. Research laboratory of NV philips.

Howe, D. (2004). Planning Scenarios: Executive Summaries: Created for Use in National, Federal, State, and Local Homeland Security Preparedness Activities. Washington, DC: Homeland Security Council.

Huber, R., Streng, S., and Bauchinger, M. (1983). The suitability of the human lymphocyte micronucleus assay system for biological dosimetry. Mutation Research/Fundamental and Molecular Mechanisms of Mutagenesis, 111(2):185–193.

Hughes, I. and Hase, T. (2010). Measurements and their uncertainties: a practical guide to modern error analysis. Oxford University Press, Oxford.

Hurd, F. K., Sachs, M., and Hershberger, W. (1954). Paramagnetic resonance absorption of Mn^{++} in single crystals of $CaCO_3$. Physical Review, 93(3):373.

Hutt, G., Brodski, L., Bailiff, I., Goksu, Y., Haskell, E., Jungner, H., and Stoneham, D. (1993). Accident dosimetry using environmental materials collected from regions downwind of Chernobyl: a preliminary evaluation. Radiation Protection Dosimetry, 47(1-4):307–311.

IAEA (1998a). Dosimetric and Medical Aspects of the Radiological Accident in Goinia in 1987. International Atomic Energy Agency, Vienna. IAEA-TECDOC-1009.

IAEA (1998b). The Radiological Accident in Tammiku. International Atomic Energy Agency, Vienna.

IAEA (2002). Advisory material for the IAEA regulations for the safe transport of radioactive material. Safety Standards series - International Atomic Energy Agency.

IAEA (2002). The Radiological Accident in Samut Prakarn. International Atomic Energy Agency, Vienna.

IAEA (2004). The Radiological Accident in Cochabamba. INTERNATIONAL ATOMIC ENERGY AGENCY, Vienna.

IAEA (2008). The international nuclear and radiological event scale user's manual 2008 edition. IAEA and OECD/NEA.

IAEA (2009). The Radiological Accident in Nueva Aldea. International Atomic Energy Agency, Vienna.

IAEA (2014). The Radiological Accident in Lia, Georgia. International Atomic Energy Agency, Vienna.

IAEA (2017). Incidents of nuclear and other radioactive material out of regulatory control: 2017 fact sheet.

Ichikawa, Y., Nagatomo, T., Hoshi, M., and Kondo, S. (1987). Thermoluminescence dosimetry of gamma rays from the Hiroshima atomic bomb at distances of 1.27 to 1.46 kilometers from the hypocenter. Health Physics, 52(4):443–451.

ICRP (1991). Quantities used in radiological protection. ICRP publication 60. Annals of the ICRP, 21(1):4–11.

ICRP (1996). Conversion coefficients for use in radiological protection against external radiation. ICRP publication 74. Annals of the ICRP, 26(3):1–205.

ICRP (2003). Relative biological effectiveness (RBE), quality factor (Q), and radiation weighting factor (w_R). ICRP publication 92. Annals of the ICRP, 33(4):1–121.

ICRP (2007). The 2007 recommendations of the international commission on radiological protection. ICRP publication 103. Annals of the ICRP, 37(2):1–332.

ICRP (2009). Realistic reference phantoms: an ICRP/ICRU joint effort. a report of adult reference computational phantoms. ICRP publication 110. Annals of the ICRP, 39(2):1.

ICRP (2012). ICRP statement on tissue reactions and early and late effects of radiation in normal tissues and organs–threshold doses for tissue reactions in a radiation protection context. ICRP publication 118. Annals of the ICRP, 41(1):1–322.

ICRU (1980). Radiation quantities and units. ICRU report 33. International Commission on Radiation, Units and Measurements.

ICRU (1993). Units in radiation protection dosimetry. ICRU report 51. ICRU Report, 51.

ICRU (1997). Conversion coefficients for use in radiological protection against external radiation, report 57.

ICRU (2011). Report 85. Journal of the International Commission on Radiation Units and Measurements, 11(1):NP.

Ikeya, M. and Ishii, H. (1989). Atomic bomb and accident dosimetry with ESR: Natural rocks and human tooth in-vivo spectrometer. International Journal of Radiation Applications and Instrumentation. Part A. Applied Radiation and Isotopes, 40(10):1021–1027.

Inrig, E., Godfrey-Smith, D., and Khanna, S. (2008a). Optically stimulated luminescence of electronic components for forensic, retrospective, and accident dosimetry. Radiation Measurements, 43(2-6):726–730.

Inrig, E., Godfrey-Smith, D., and Khanna, S. (2008b). Optically stimulated luminescence of electronic components for forensic, retrospective, and accident dosimetry. Radiation Measurements, 43(2):726–730.

Inrig, E., Godfrey-Smith, D., and Larsson, C. (2010a). Fading corrections to electronic component substrates in retrospective accident dosimetry. Radiation Measurements, 45(3-6):608–610.

Inrig, E., Godfrey-Smith, D., and Larsson, C. (2010b). Fading corrections to electronic component substrates in retrospective accident dosimetry. Radiation Measurements, 45(3):608–610".

International Atomic Energy Agency (2011). Cytogenetic dosimetry: Applications in preparedness for and response to radiation emergencies. Technical report, Vienna.

International Atomic Energy Agency (2015). Preparedness and Response for a Nuclear Or Radiological Emergency: Safety Requirements. International Atomic Energy Agency, Vienna.

International Electrotechnical Commission (2016). Radiation protection instrumentationpassive integrating dosimetry systems for personal and environmental monitoring of photon and beta radiation. International Standard IEC, 62387.

International Organization for Standardization (ISO) (2008). Radiation protection performance criteria for laboratories performing cytogenetic triage for assessment of mass casualties in radiological or nuclear emergencies - general principles and application to dicentric assay. General principles and application to dicentric assay. Geneva: ISO, 21243:2008.

Ishii, H., Ikeya, M., and Okano, M. (1990). ESR dosimetry of teeth of residents close to Chernobyl reactor accident. Journal of Nuclear Science and Technology, 27(12):1153–1155.

ISO 11929 (2010). Determination of the characteristic limits (decision threshold, detection limit and limits of the confidence interval) for measurements of ionizing radiation fundamentals and application. Standard, International Organization for Standardization.

Ivannikov, A., Skvortzov, V., Stepanenko, V., Tikunov, D., Fedosov, I., Romanyukha, A., and Wieser, A. (1997). Wide scale EPR retrospective dosimetry: Results and problems. Radiation Protection Dosimetry, 71(3):175–180.

Ivannikov, A., Zhumadilov, K., Tieliewuhan, E., Jiao, L., Zharlyganova, D., Apsalikov, K. N., Berekenova, G., Zhumadilov, Z., Toyoda, S., Miyazawa, C., et al. (2006). Results of EPR dosimetry for population in the vicinity of the most contaminating radioactive fallout trace after the first nuclear test in the semipalatinsk test site. Journal of Radiation Research, 47(SupplementA):A39–A46.

J. Thomsen, K., Bøtter-Jensen, L., and S. Murray, A. (2002). Household and workplace chemicals as retrospective luminescence dosemeters. Radiation Protection Dosimetry, 101(1-4):515–518.

Jaek, I., Molodkov, A., and Vasilchenko, V. (2007). Possible reasons for anomalous fading in alkali feldspars used for luminescence dating of quaternary deposits. Estonian Journal of Earth Sciences, 56(3):167–178.

Jain, M., Guralnik, B., and Andersen, M. T. (2012). Stimulated luminescence emission from localized recombination in randomly distributed defects. Journal of Physics: Condensed Matter, 24(38):385402.

Jasper, E., Miller, M., Sweeney, B., Berg, D., Feuer, E., and Reganato, D. (2005). Preparedness of hospitals to respond to a radiological terrorism event as assessed by a full-scale exercise. Journal of Public Health Management and Practice, 11(6):S11–S16.

Kalita, J. and Wary, G. (2014). Thermoluminescence study of X-ray and UV irradiated natural calcite and analysis of its trap and recombination level. Spectrochimica Acta Part A: Molecular and Biomolecular Spectroscopy, 125:99–103.

Kalita, J. and Wary, G. (2016). X-ray dose response of calcite - a comprehensive analysis for optimal application in TL dosimetry. Nuclear Instruments and Methods in Physics Research Section B: Beam Interactions with Materials and Atoms, 383:93–102.

Kamenopoulou, V., Barthe, J., Hickman, C., and Portal, G. (1986). Accidental gamma irradiation dosimetry using clothing. Radiation Protection Dosimetry, 17(1–4):185–188.

Katz, H. S. and Mileski, J. (1987). Handbook of Fillers for Plastics. Springer Science & Business Media, Berlin.

Kazakis, N. A., Tsetine, A. T., Kitis, G., and Tsirliganis, N. C. (2016). Insect wings as retrospective/accidental/forensic dosimeters: An optically stimulated luminescence investigation. Radiation Measurements, 89:74 – 81.

Khanlary, M. and Townsend, P. (1991). TL spectra of single crystal and crushed calcite. International Journal of Radiation Applications and Instrumentation. Part D. Nuclear Tracks and Radiation Measurements, 18(1-2):29–35.

Kharita, M., Stokes, R., and Durrani, S. (1994). Phototransferred thermoluminescence (PTTL) in LiF (Mg, Cu, P) (GR-200). Radiation Measurements, 23(2):493–496.

Khvostunov, I., Ivannikov, A., Skvortsov, V., Nugis, V. Y., and Golub, E. (2014). Review of the correlation between results of cytogenetic dosimetry from blood lymphocytes and EPR dosimetry from tooth enamel for victims of radiation accidents. Radiation Protection Dosimetry, 163(4):399–408.

Kierstead, J. and Levy, P. (1991). Validity of repeated initial rise thermoluminescence kinetic parameter determinations. International Journal of Radiation Applications and Instrumentation. Part D. Nuclear Tracks and Radiation Measurements, 18(1):19 – 25.

Kim, K.-B. and Hong, D.-G. (2014). Kinetic parameters, bleaching and radiation response of thermoluminescence glow peaks separated by deconvolution on Korean calcite. Radiation Physics and Chemistry, 103:16–21.

Kirsh, Y., Townsend, P., and Shoval, S. (1987). Local transitions and charge transport in thermoluminescence of calcite. International Journal of Radiation Applications and Instrumentation. Part D. Nuclear Tracks and Radiation Measurements, 13(2-3):115–119.

Kitis, G., Gomez-Ros, J. M., and Tuyn, J. W. N. (1998). Thermoluminescence glow-curve deconvolution functions for first, second and general orders of kinetics. Journal of Physics D: Applied Physics, 31(19):2636.

Kitis, G. and Pagonis, V. (2013). Analytical solutions for stimulated luminescence emission from tunneling recombination in random distributions of defects. Journal of Luminescence, 137(Supplement C):109 – 115.

Kittel, C. and Holcomb, D. F. (1967). Introduction to Solid State Physics. Number 6. American Association of Physics Teachers, College Park.

Knebel, A. R., Coleman, C. N., Cliffer, K. D., Murrain-Hill, P., McNally, R., Oancea, V., Jacobs, J., Buddemeier, B., Hick, J. L., Weinstock, D. M., et al. (2011). Allocation of scarce resources after a nuclear detonation: setting the context. Disaster Medicine and Public Health Preparedness, 5(S1):S20–S31.

Koh, J. (2011). Dyeing with disperse dyes. In Textile Dyeing. InTech.

Kollek, D., Welsford, M., and Wanger, K. (2009). Chemical, biological, radiological and nuclear preparedness training for emergency medical services providers. Canadian Journal of Emergency Medicine, 11(4):337342.

Kortov, V. and Ustyantsev, Y. (2013). Chernobyl accident: Causes, consequences and problems of radiation measurements. Radiation Measurements, 55(Supplement C):12–16.

Kouroukla, E. (2015). Luminescence dosimetry with ceramic materials for application to radiological emergencies and other incidents. PhD thesis, Durham University.

Kouroukla, E. C., Bailiff, I. K., and Terry, I. (2014). Emergency dosimetry using ceramic components in personnal electronic devices. International Journal of Modern Physics: Conference Series, 27:1460155.

Krefft, K., Drogoszewska, B., Kaminska, J., Juniewicz, M., Wokiewicz, G., Jakacka, I., and Ciesielski, B. (2014). Application of EPR dosimetry in bone for ex vivo measurements of doses in radiotherapy patients. Radiation Protection Dosimetry, 162(1-2):38–42.

Kulka, U., Abend, M., Ainsbury, E., Badie, C., Barquinero, J. F., Barrios, L., Beinke, C., Bortolin, E., Cucu, A., De Amicis, A., et al. (2017). RENEB–Running the European Network of biological dosimetry and physical retrospective dosimetry. International Journal of Radiation Biology, 93(1):2–14.

Kulka, U., Ainsbury, L., Atkinson, M., Barquinero, J., Barrios, L., Beinke, C., Bognar, G., Cucu, A., Darroudi, F., Fattibene, P., et al. (2012). Realising the European network of biodosimetry (RENEB). Radiation Protection Dosimetry, 151(4):621–625.

Kulka, U. and Wojcik, A. (2017). Special issue: networking in biological and EPR/OSL dosimetry: the European RENEB platform for emergency preparedness and research. International Journal of Radiation Biology, 93(1).

Lamarsh, J. and Baratta, A. (2013). Introduction to Nuclear Engineering. Pearson Education Limited, New Jersey.

Lamothe, M. and Auclair, M. (1999). A solution to anomalous fading and age shortfalls in optical dating of feldspar minerals. Earth and Planetary Science Letters, 171(3):319–323.

Lamothe, M., Auclair, M., Hamzaoui, C., and Huot, S. (2003). Towards a prediction of long-term anomalous fading of feldspar IRSL. Radiation Measurements, 37(4):493–498. Proceedings of the 10th international Conference on Luminescence and Electron-Spin Resonance Dating (LED 2002).

Lanjanian, H., Ziaie, F., Modarresi, M., Nikzad, M., Shahvar, A., and Durrani, S. (2008). A technique to measure the absorbed dose in human tooth enamel using EPR method. Radiation Measurements, 43:S648–S650".

Lee, J., Kim, H., Kim, J., Pradhan, A., Kim, M., Chang, I., Lee, S., Kim, B., Park, C., and Chung, K. (2017). Thermoluminescence of chip inductors and resistors in new generation mobile phones for retrospective accident dosimetry. Radiation Measurements, 105:26–32.

Lima, J., Trzesniak, P., Yoshimura, E., and Okuno, E. (1990). Phototransferred thermoluminescence in calcite. Radiation Protection Dosimetry, 33(1-4):143–146.

Liritzis, I., Guibert, P., Foti, F., and Schvoerer, M. (1996). Solar bleaching of thermoluminescence of calcites. Nuclear Instruments and Methods in Physics Research Section B: Beam Interactions with Materials and Atoms, 117(3):260–268.

Lister, B. (1985). Contaminated Mexican steel incident. Journal of the Society for Radiological Protection, 5(3):145.

Lloyd, D., Edwards, A., and Prosser, J. (1986). Chromosome aberrations induced in human lymphocytes by in vitro acute X and gamma radiation. Radiation Protection Dosimetry, 15(2):83–88.

Mandowski, A. (2005). Semi-localized transitions model for thermoluminescence. Journal of Physics D: Applied Physics, 38(1):17.

Manfredi, L. B., Rodríguez, E. S., Wladyka-Przybylak, M., and Vázquez, A. (2006). Thermal degradation and fire resistance of unsaturated polyester, modified acrylic resins and their composites with natural fibres. Polymer Degradation and Stability, 91(2):255–261.

Manning, G., Macaeva, E., Majewski, M., Kriehuber, R., Brzska, K., Abend, M., Doucha-Senf, S., Oskamp, D., Strunz, S., Quintens, R., Port, M., and Badie, C. (2017). Comparable dose estimates of blinded whole blood samples are obtained independently of culture conditions and analytical approaches. Second RENEB gene expression study. International Journal of Radiation Biology, 93(1):87–98.

Mark, H. F., Bikales, N., Overberger, C. G., Menges, G., and Kroschwitz, J. I. (1987). Encyclopedia of Polymer Science and Engineering, Vol. 3.

Marsh, B. D. (2000). Layered reflecting and photoluminous fire resistant material. US Patent 6,159,878.

Marsh, B. D. (2003). Layered reflecting and photoluminous fire resistant material. US Patent 6,569,786.

May, C. E. and Partridge, J. A. (1964). Thermoluminescent kinetics of alpha irradiated alkali halides. The Journal of Chemical Physics, 40(5):1401–1409.

McDougall, D. J. (1968). Thermoluminescence of Geological Materials. Academic Press, Cambridge.

McKeever, S., Akselrod, M., and Markey, B. (1996). Pulsed optically stimulated luminescence dosimetry using alpha - Al_2O_3:C. Radiation Protection Dosimetry, 65(1-4):267–272.

McKeever, S., Minniti, R., and Sholom, S. (2017). Phototransferred thermoluminescence (PTTL) dosimetry using Gorilla glass from mobile phones. Radiation Measurements, 106(Supplement C):423–430.

McKeever, S. and Sholom, S. (2016). Biodosimetry versus physical dosimetry for emergency dose assessment following large-scale radiological exposures. Radiation Measurements, 92:8–18.

McKeever, S. W. (1988). Thermoluminescence of solids, volume 3. Cambridge University Press, Cambridge.

McKeever, S. W., Moscovitch, M., and Townsend, P. D. (1995). Thermoluminescence dosimetry materials: properties and uses.

McKeever, S. W. S. (1980). On the analysis of complex thermoluminescence. glow-curves: Resolution into individual peaks. Physica Status Solidi (a), 62(1):331–340.

McKinlay, A., Bartlett, D., and Smith, P. (1980). The development of photo-transferred thermoluminescence (PTTL) technique and its application to the routine re-assessment of absorbed dose in the NRPB automated personal dosimetry system. Nuclear Instruments and Methods, 175(1):57–59.

Meckbach, R., Bailiff, I., Göksu, Y., Jacob, P., and Stoneham, D. (1996). Calculation and measurement of depth dose distributions in bricks. Radiation Protection Dosimetry, 66(1-4):183–186.

Medlin, W. (1959). Thermoluminescent properties of calcite. The Journal of Chemical Physics, 30(2):451–458.

Medlin, W. (1961). Decay of phosphorescence from a distribution of trapping levels. Physical Review, 123(2):502.

Medlin, W. (1963). Emission centers in thermoluminescent calcite, dolomite, magnesite, aragonite, and anhydrite. Journal of the Optical Society of America, 53(11):1276–1285.

Medlin, W. (1964). Trapping centers in thermoluminescent calcite. Physical Review, 135(6A):A1770.

Medlin, W. (1968). The nature of traps and emission centers in thermoluminescent rock materials. Thermoluminescence of Geological Materials, pages 193–223.

Mehta, S. and Sengupta, S. (1978). Photostimulated thermoluminescence of Al_2O_3 (Si, Ti) and its application to ultraviolet radiation dosimetry. Physics in Medicine and Biology, 23(3):471.

Mehta, S. K. and Sengupta, S. (1977). Annealing characteristics and nature of traps in Al_2O_3 thermoluminescent phosphor. Physics in Medicine and Biology, 22(5):863.

Menon, S., Singh, A., Kadam, S., Koul, D., and Datta, D. (2017). OSL studies of commonly available medicines for their use as retrospective dosimeters. Radiation Measurements, 101:7–12.

Meriç, N., Şahiner, E., Bariş, A., and Polymeris, G. S. (2015). Thermoluminescence properties of irradiated commercial color pencils for accidental retrospective dosimetry. Applied Radiation and Isotopes, 99:97–104.

Mesterházy, D., Osvay, M., Kovács, A., and Kelemen, A. (2012). Accidental and retrospective dosimetry using TL method. Radiation Physics and Chemistry, 81(9):1525–1527.

Monteiro Gil, O., Vaz, P., Romm, H., De Angelis, C., Antunes, A. C., Barquinero, J.-F., Beinke, C., Bortolin, E., Burbidge, C. I., Cucu, A., et al. (2017). Capabilities of the RENEB network for research and large scale radiological and nuclear emergency situations. International journal of radiation biology, 93(1):136–141.

Moquet, J., Barnard, S., Staynova, A., Lindholm, C., Gil, O. M., Martins, V., Rler, U., Vral, A., Vandevoorde, C., Wojewdzka, M., and Rothkamm, K. (2017). The second gamma-H2AX assay inter-comparison exercise carried out in the framework of the European biodosimetry network (RENEB). International Journal of Radiation Biology, 93(1):58–64.

Moroni, M., Maeda, D., Whitnall, M. H., Bonner, W. M., and Redon, C. E. (2013). Evaluation of the gamma-H2AX assay for radiation biodosimetry in a swine model. International Journal of Molecular Sciences, 14(7):14119–14135.

Moscovitch, M. (1993). Dose algorithms for personal thermoluminescence dosimetry. Radiation Protection Dosimetry, 47(1-4):373–380.

Mott, N. and Davis, E. (1979). Electronic processes in non-crystalline solids. Clarendon, Oxford, 465.

Mott, N. F. (1969). Conduction in non-crystalline materials. Philosophical Magazine, 19(160):835–852.

Mrozik, A., Kulig, D., Marczewska, B., and Bilski, P. (2017). Dose estimation based on OSL signal from banknotes in accident dosimetry. Radiation Measurements, 101:1–6.

Mrozik, A., Marczewska, B., Bilski, P., and Gieszczyk, W. (2014a). Investigation of OSL signal of resistors from mobile phones for accidental dosimetry. Radiation Measurements, 71:466–470.

Mrozik, A., Marczewska, B., Bilski, P., and Kosowski, M. (2014b). Investigation of thermoluminescence properties of mobile phone screen displays as dosimeters for accidental dosimetry. Radiation Physics and Chemistry, 104:88–92.

Murray, A. and Roberts, R. (1998). Measurement of the equivalent dose in quartz using a regenerative-dose single-aliquot protocol. Radiation measurements, 29(5):503–515.

Murray, A. S. and Wintle, A. G. (2000). Luminescence dating of quartz using an improved single-aliquot regenerative-dose protocol. Radiation measurements, 32(1):57–73.

Nagatomo, T., Hoshi, M., and Ichikawa, Y. (1992). Comparison of the measured gamma ray dose and the DS86 estimate at 2.05 km ground distance in Hiroshima. Journal of Radiation Research, 33(3):211–217.

Nagatomo, T., Hoshi, M., and Ichikawa, Y. (1995). Thermoluminescence dosimetry of the Hiroshima atomic -bomb gamma rays between 1.59 km and 1.63 km from the hypocenter. Health Physics, 69(4):556–559.

Nakajima, T. (1982). The use of organic substances as emergency dosimeters. The International Journal of Applied Radiation and Isotopes, 33(11):1077–1084.

Nakajima, T. and Otsuki, T. (1990). Dosimetry for radiation emergencies: radiation-induced free radicals in sugar of various countries and the effect of pulverizing on the ESR signal. International Journal of Radiation Applications and Instrumentation. Part A. Applied Radiation and Isotopes, 41(4):359–365.

Nakajima, T., Otsuki, T., and Hara, H. (1993). Radiation accident dosimetry using shells. Applied Radiation and Isotopes, 44(1):91–93.

Nakamura, N., Miyazawa, C., Sawada, S., Akiyama, M., and Awa, A. (1998). A close correlation between electron spin resonance (ESR) dosimetry from tooth enamel and cytogenetic dosimetry from lymphocytes of Hiroshima atomic-bomb survivors. International Journal of Radiation Biology, 73(6):619–627.

National Research Council (2006). Facing hazards and disasters: Understanding human dimensions. National Academies Press.

Nicholas, K. and Woods, J. (1964). The evaluation of electron trapping parameters from conductivity glow curves in cadmium sulphide. British Journal of Applied Physics, 15(7):783.

Nyirenda, A., Chithambo, M., and Polymeris, G. (2016). On luminescence stimulated from deep traps using thermally-assisted time-resolved optical stimulation in α-Al_2O_3:C. Radiation Measurements, 90:109–112.

Oestreicher, U., Samaga, D., Ainsbury, E., Antunes, A. C., Baeyens, A., Barrios, L., Beinke, C., Beukes, P., Blakely, W. F., Cucu, A., et al. (2017). RENEB intercomparisons applying the conventional Dicentric Chromosome Assay (DCA). International Journal of Radiation Biology, 93(1):20–29.

Ortiz, P., Wheatley, J., Oresegun, M., and Friedrich, V. (1999). Lost and found dangers. Orphan radiation sources raise global concerns. IAEA bulletin, 41(3):18–21.

Osvay, M., Ranogajec-Komor, M., and Golder, F. (1990). Comparative PITL and PTTL investigations on TL detectors. Radiation Protection Dosimetry, 33(1-4):135–138.

Oughton, D., Albani, V., Barquinero, F., Clero, E., Crouail, P., Fattibene, P., Kesminiene, A., Laurier, D., Liutsko, L., Ohba, T., Ostroumova, E., Pirard, P., Rogel, A., Sarukhan, A., Schneider, T., Tanigawa, K., Tomkiv, E., Vale, L., and Cardis, E. (2017). Recommendations and procedures for preparedness and health surveillance of populations affected by a radiation accident. Technical report.

Owen, G. and Charlesby, A. (1974). On charge-carrier trapping in insulating solids as investigated by the space-charge-limited current (SCLC) technique: a cautionary note. Journal of Physics C: Solid State Physics, 7(22):L400.

Pagonis, V. (2005). Evaluation of activation energies in the semi-localized transition model of thermoluminescence. Journal of Physics D: Applied Physics, 38(13):2179.

Pagonis, V., Allman, E., and Wooten Jr, A. (1996). Thermoluminescence from a distribution of trapping levels in UV irradiated calcite. Radiation Measurements, 26(2):265–280.

Pagonis, V. and Michael, C. (1994). Annealing effects on the thermoluminescence of synthetic calcite powder. Radiation Measurements, 23(1):131–142.

Pantelias, G. E. and Maillie, H. D. (1984). The use of peripheral blood mononuclear cell prematurely condensed chromosomes for biological dosimetry. Radiation Research, 99(1):140–150.

Partridge, R. H. (1972). Thermoluminescence in polymers. The Radiation Chemistry of Macromolecules, 1:194–222.

Pascu, A., Vasiliniuc, S., Zeciu-Dolha, M., and Timar-Gabor, A. (2013). The potential of luminescence signals from electronic components for accident dosimetry. Radiation Measurements, 56:384–388.

Pellmar, T. and Rockwell, S. (2005). Priority list of research areas for radiological nuclear threat countermeasures. Radiation Research, 163(1):115–123.

Podgorsak, E. B. et al. (2005). Radiation Oncology Physics. International Atomic Energy Agency, Vienna.

Polymeris, G., Raptis, S., Afouxenidis, D., Tsirliganis, N., and Kitis, G. (2010). Thermally assisted OSL from deep traps in Al_2O_3:C. Radiation Measurements, 45(3):519–522.

Polymeris, G. S. and Kitis, G. (2012). Thermally assisted photo transfer OSL from deep traps in Al_2O_3:C grains exhibiting different TL peak shapes. Applied Radiation and Isotopes, 70(10):2478–2487.

Polymeris, G. S., Tsirliganis, N., Loukou, Z., and Kitis, G. (2006). A comparative study of the anomalous fading effects of TL and OSL signals of durango apatite. Physica Status Solidi (a), 203(3):578–590.

Poolton, N. R. J., Ozanyan, K. B., Wallinga, J., Murray, A. S., and Bøtter-Jensen, L. (2002). Electrons in feldspar ii: a consideration of the influence of conduction band-tail states on luminescence processes. Physics and Chemistry of Minerals, 29(3):217–225.

Public Health England (2018). Chemical, biological, radiological and nuclear incidents: clinical management and health protection. Technical report, Public Health England.

Qiao, B., Teyssedre, G., and Laurent, C. (2016). Electroluminescence and cathodoluminescence from polyethylene and polypropylene films: Spectra reconstruction from elementary components and underlying mechanisms. Journal of Applied Physics, 119(2):024103.

Randall, J. and Wilkins, M. H. F. (1945). Phosphorescence and electron traps. I. the study of trap distributions. volume 184, pages 365–389. The Royal Society.

Reisz, J. A., Bansal, N., Qian, J., Zhao, W., and Furdui, C. M. (2014). Effects of ionizing radiation on biological molecules mechanisms of damage and emerging methods of detection. Antioxidants & Redox Signaling, 21(2):260–292.

Reyes, R., Romanyukha, A., Olsen, C., Trompier, F., and Benevides, L. (2009). Electron paramagnetic resonance in irradiated fingernails: variability of dose dependence and possibilities of initial dose assessment. Radiation and environmental biophysics, 48(3):295.

Risø (2010). Guide to "the risø TL/OSL reader. Risø DTU. Denmark.

Roberts, L. (1987). Radiation accident grips Goiania. Science, 238(4830):1028–1032.

Roesch, W. C. (1987). US-Japan joint reassessment of atomic bomb radiation dosimetry in Hiroshima and Nagasaki. Radiation Effects Research Foundation, Hiroshima.

Romanyukha, A. and Regulla, D. (1996). Aspects of retrospective ESR dosimetry. Applied Radiation and Isotopes, 47(11):1293–1297".

Romanyukha, A., Regulla, D., Vasilenko, E., and Wieser, A. (1994). South Ural nuclear workers: Comparison of individual doses from retrospective EPR dosimetry and operational personal monitoring. Applied Radiation and Isotopes, 45(12):1195–1199.

Romanyukha, A., Schauer, D. A., and Malikov, Y. K. (2006). Analysis of current assessments and perspectives of ESR tooth dosimetry for radiation dose reconstruction of the population residing near the semipalatinsk nuclear test site. Journal of Radiation Research, 47(SupplementA):A55–A60.

Romanyukha, A. A., Desrosiers, M., Sleptchonok, O., Land, C., Luckyanov, N., and Gusev, B. (2002). EPR dose reconstruction of two Kazakh villages near the Semipalatinsk nuclear test site. Applied Magnetic Resonance, 22(3):347–356.

Romanyukha, A. A., Seltzer, S. M., Desrosiers, M., Ignatiev, E., Ivanov, D., Bayankin, S., Degteva, M., Eichmiller, F., Wieser, A., and Jacob, P. (2001). Correction factors in the EPR dose reconstruction for residents of the middle and lower techa riverside. Health Physics, 81(5):554–566.

Romm, H., Ainsbury, E., Barnard, S., Barrios, L., Barquinero, J., Beinke, C., Deperas, M., Gregoire, E., Koivistoinen, A., Lindholm, C., et al. (2013). Automatic scoring of dicentric chromosomes as a tool in large scale radiation accidents. Mutation Research/Genetic Toxicology and Environmental Mutagenesis, 756(1):174–183.

Roque, C., Guibert, P., Vartanian, E., Bechtel, F., and Schvoerer, M. (2001). Thermoluminescence-dating of calcite: study of heated limestone fragments from Upper Paleolithic layers at Combe Sauniere, Dordogne, France. Quaternary Science Reviews, 20(5-9):935–938.

Rossi, A., Wafcheck, C., De Jesus, E., and Pelegrini, F. (2000). Electron spin resonance dosimetry of teeth of Goiania radiation accident victims. Applied Radiation and Isotopes, 52(5):1297–1303.

Rudlof, G., Becherer, J., and Glaefeke, H. (1978). Behaviour of the fractional glow technique with first-order detrapping processes, traps distributed in energy or frequency factor. Physica Status Solidi (a), 49(2).

Sabol, J. and Sestak, B. (2017). Assessing the real threat and mitigating the impact of a terrorist use of radiological weapons. Radiation and Applications, 2(2):134–138.

Sahiner, E. (2017). TL and OSL dose response and stability properties of various commercially glass samples obtained from Turkey for dosimetric purposes in the UV emission spectral region. Applied Radiation and Isotopes, 128:68–74.

Santoro, R. T., Egbert, S. D., Barnes, J. M., Kerr, G. D., Pace III, J. V., Roberts, J. A., and Slater, C. O. (2002). Radiation transport calculations for Hiroshima and Nagasaki. Reassessment of the atomic bomb radiation dosimetry for Hiroshima and Nagasaki dosimetry system 2002 (DS02).Radiation Effects Research Foundation, Hiroshima, 1:139–201.

Sato, H., Filas, B. A., Eaton, S. S., Eaton, G. R., Romanyukha, A. A., Hayes, R., and Rossi, A. M. (2007). Electron spin relaxation of radicals in irradiated tooth enamel and synthetic hydroxyapatite. Radiation Measurements, 42(6):997–1004.

Sato, H., Hoshi, M., and Takada, J. (2006). Intercomparison of luminescence measurements of bricks from Dolon village: Experimental methodology and results from Japanese laboratory. Journal of Radiation Research, 47(Supplement A):A23–A28.

Sato, H., Takatsuji, T., Takada, J., Endo, S., Hoshi, M., Sharifov, V. F., Veselkina, I. I., Pilenko, I. V., Kalimullin, W. A., Masyakin, V. B., et al. (2002). Measuring the external exposure dose in the contaminated area near the Chernobyl nuclear power station using the thermoluminescence of quartz in bricks. Health Physics, 83(2):227–236.

Schreiber, W., Petryakov, S. V., Kmiec, M. M., Feldman, M. A., Meaney, P. M., Wood, V. A., Boyle, H. K., Flood, A. B., Williams, B. B., and Swartz, H. M. (2016). Flexible, wireless, inductively coupled surface coil resonnator for EPR tooth dosimetry. Radiation Protection Dosimetry, 172(1-3):87–95.

Schulman, J. H., Evans, L. W., Ginther, R. J., and Murata, K. (1947). The sensitized luminescence of manganese-activated calcite. Journal of Applied Physics, 18(8):732–739.

Seitz, F. (1939). An interpretation of crystal luminescence. Transactions of the Faraday Society, 35:74–85.

Sen, A. K. (2007). Coated textiles: principles and applications. CRC Press, Baton-Rouge.

Shani, G. (2000). Radiation Dosimetry Instrumentation and Methods. CRC press, Baton-Rouge.

Shelley, L. I. (2006). Trafficking in nuclear materials: Criminals and terrorists. Global Crime, 7(3-4):544–560.

Sholom, S. and Chumak, V. (2010). EPR emergency dosimetry with plastic components of personal goods. Health physics, 98(2):395–399.

Sholom, S., DeWitt, R., Simon, S., Bouville, A., and McKeever, S. (2011a). Emergency dose estimation using optically stimulated luminescence from human tooth enamel. Radiation Measurements, 46(9):778–782. EPRBioDose 2010 International Conference.

Sholom, S., DeWitt, R., Simon, S., Bouville, A., and McKeever, S. (2011b). Emergency optically stimulated luminescence dosimetry using different materials. Radiation Measurements, 46(12):1866–1869.

Sholom, S., Haskell, E., Hayes, R., Chumak, V., and Kenner, G. (1998). Influence of crushing and additive irradiation procedures on EPR dosimetry of tooth enamel. Radiation Measurements, 29(1):105–111.

Sholom, S. and McKeever, S. (2014). Emergency OSL dosimetry with commonplace materials. Radiation Measurements, 61:33–51.

Sholom, S. and McKeever, S. (2016a). Integrated circuits from mobile phones as possible emergency OSL/TL dosimeters. Radiation Protection Dosimetry, 170(1-4):398–401.

Sholom, S. and McKeever, S. (2017). Developments for emergency dosimetry using components of mobile phones. Radiation Measurements, 106:416–422.

Sholom, S. and McKeever, S. W. S. (2016b). Emergency EPR and OSL dosimetry with table vitamins and minerals. Radiation Protection Dosimetry, 172(1-3):139–144.

Silletti, D. K., Brokus, S. A., Earlywine, E. B., Borycz, J. D., Peaslee, G. F., DeYoung, P. A., Peters, N. J., Robertson, J. D., and Buscaglia, J. (2012). Radiation-induced cathodoluminescent signatures in calcite. Radiation Measurements, 47(3):195–200.

Simon, S. L., Bouville, A., and Kleinerman, R. (2010). Current use and future needs of biodosimetry in studies of long-term health risk following radiation exposure. Health Physics, 98(2):109.

Singh, S. D. and Ingotombi, S. (1995). Thermoluminescence glow curve of gamma-irradiated calcite. Journal of Physics D: Applied Physics, 28(7):1509.

Skvortsov, V., Ivannikov, A., Stepanenko, V., Tsyb, A., Khamidova, L., Kondrashov, A., and Tikunov, D. (2000). Application of EPR retrospective dosimetry for large-scale accidental situation. Applied Radiation and Isotopes, 52(5):1275–1282.

Sommer, S. E. (1972). Cathodoluminescence of carbonates, 1. characterization of cathodoluminescence from carbonate solid solutions. Chemical Geology, 9(1-4):257–273.

Sovacool, B. K. (2010). A Critical Evaluation of Nuclear Power and Renewable Electricity in Asia. Journal of Contemporary Asia, 40(3):369–400.

Spurnỳ, Z. (1980). Some new materials for TLD. Nuclear Instruments and Methods, 175(1):71–73.

Sullivan, J. M., Prasanna, P. G., Grace, M. B., Wathen, L., Wallace, R. L., Koerner, J. F., and Coleman, C. N. (2013). Assessment of biodosimetry methods for a mass-casualty radiological incident: medical response and management considerations. Health Physics, 105(6).

Sunta, C. (1984). A review of thermoluminescence of calcium fluoride, calcium sulphate and calcium carbonate. Radiation Protection Dosimetry, 8(1-2):25–44.

Sunta, C., Yoshimura, E., and Okuno, E. (1994). Supralinearity and sensitization of thermoluminescence. i. a theoretical treatment based on an interactive trap system. Journal of Physics D: Applied Physics, 27(4):852.

Sunta, C. M., Kumar, M., Kher, R. K., and Bhatt, B. C. (2006). Thermoluminescence emission from localized recombination model. Journal of Physics D: Applied Physics, 39(21):4557.

Suntharalingam, N. and Cameron, J. (1969). Thermoluminescent response of lithium fluoride to radiations with different LET. Physics in Medicine & Biology, 14(3):397.

Szadkowska-Nicze, M. and Mayer, J. (1999). Investigation of transient species in pulse-irradiated poly (ethylene terephthalate) film. Journal of Polymer Science Part A: Polymer Chemistry, 37(15):2853–2862.

Taranenko, V., Meckbach, R., Degteva, M. O., Bougrov, N. G., Göksu, Y., Vorobiova, M. I., and Jacob, P. (2003). Verification of external exposure assessment for the upper Techa riverside by luminescence measurements and Monte Carlo photon transport modeling. Radiation and Environmental Biophysics, 42(1):17–26.

Tardieu, G., Teyssedre, G., and Laurent, C. (2001). Role of additives as recombination centres in polyethylene materials as probed by luminescence techniques. Journal of Physics D: Applied Physics, 35(1):40.

Taylor, G. and Lilley, E. (1978). The analysis of thermoluminescent glow peaks in LiF (TLD-100). Journal of physics D: Applied physics, 11(4):567.

Templer, R. (1986). The localised transition model of anomalous fading. Radiation Protection Dosimetry, 17(1-4):493–497.

Thompson, J. W., Burdette, K. E., Inrig, E. L., DeWitt, R., Mistry, R., Rink, W. J., and Boreham, D. R. (2010). Optically stimulated luminescence dosimetry with gypsum wallboard (drywall). Radiation Protection Dosimetry, 141(1):1–9.

Tominaga, T., Hachiya, M., Tatsuzaki, H., and Akashi, M. (2014). The accident at the Fukushima daiichi nuclear power plant in 2011. Health Physics, 106(6):630–637.

Townsend, P., Luff, B., and Wood, R. (1994). Mn^{2+} transitions in the TL emission spectra of calcite. Radiation Measurements, 23(2-3):433–440.

Trivedi, A. and Greenstock, C. (1993). Use of sugars and hair for ESR emergency dosimetry. Applied Radiation and Isotopes, 44(1):85–90.

Trompier, F., Bassinet, C., and Clairand, I. (2010). Radiation accident dosimetry on plastics by EPR spectrometry. Health physics, 98(2):388–394.

Trompier, F., Burbidge, C., Bassinet, C., Baumann, M., Bortolin, E., De Angelis, C., Eakins, J., Della Monaca, S., Fattibene, P., Quattrini, M. C., et al. (2017). Overview of physical dosimetry methods for triage application integrated in the new european network RENEB. International journal of radiation biology, 93(1):65–74.

Trompier, F., Della Monaca, S., Fattibene, P., and Clairand, I. (2011). EPR dosimetry of glass substrate of mobile phone LCDs. Radiation Measurements, 46(9):827–831.

Trompier, F., Kornak, L., Calas, C., Romanyukha, A., LeBlanc, B., Mitchell, C., Swartz, H., and Clairand, I. (2007a). Protocol for emergency EPR dosimetry in fingernails. Radiation Measurements, 42(6):1085–1088.

Trompier, F., Sadlo, J., Michalik, J., Stachowicz, W., Mazal, A., Clairand, I., Rostkowska, J., Bulski, W., Kulakowski, A., Sluszniak, J., et al. (2007b). EPR dosimetry for actual and suspected overexposures during radiotherapy treatments in Poland. Radiation Measurements, 42(6-7):1025–1028.

Ugumori, T. and Ikeya, M. (1980). Luminescence of $CaCO_3$ under N_2 laser excitation and application to archaeological dating. Japanese Journal of Applied Physics, 19(3):459.

United States Nuclear Regulatory Commission, Washington, D. U. S. (1975). Reactor safety study. An assessment of accident risks in US commercial nuclear power plants. Executive summary. Technical report, United States Nuclear Regulatory Commission.

Valentin, J. (2005). ICRP 96: Protecting People against Radiation Exposure in the Event of a Radiological Attack. Annals of the ICRP, 35(1):1–110.

Van den Eeckhout, K., Bos, A. J., Poelman, D., and Smet, P. F. (2013). Revealing trap depth distributions in persistent phosphors. Physical Review B, 87(4):045126.

Visocekas, R. (1979). Miscellaneous aspects of artificial TL of calcite: Emission spectra, athermal detrapping and anomalous fading. Pact. Revue du Groupe Européen d'Etudes pour les Techniques Physiques, Chimiques et Mathématiques Appliquées à l'Archéologie Rixensart, (3):258–265.

Visocekas, R. (1985). Tunnelling radiative recombination in labradorite: Its association with anomalous fading of thermoluminescence. Nuclear Tracks and Radiation Measurements (1982), 10(4):521–529. Special Issue: Thermoluminescence and Electron-Spin-Resonance Dating.

Visocekas, R. (2000). Monitoring anomalous fading of TL of feldspars by using far-red emission as a gauge. Radiation Measurements, 32(5):499–504.

Visocekas, R., Ceva, T., Lapraz, D., Iacconi, P., and Lefaucheux, F. (1973). Cathode-ray-excited luminescence and thermoluminescence of a synthetic calcite monocrystal. Physica Status Solidi (a), 15(1):61–66.

Visocekas, R., Ceva, T., Marti, C., Lefaucheux, F., and Robert, M. C. (1976). Tunneling processes in afterglow of calcite. Physica Status Solidi (a), 35(1):315–327.

Visocekas, R., Spooner, N., Zink, A., and Blanc, P. (1994). Tunnel afterglow, fading and infrared emission in thermoluminescence of feldspars. Radiation Measurements, 23(2):377–385.

Visocekas, R. and Zink, A. (1999). Use of the far red TL emission band of alkali feldspars for dosimetry and dating. Quaternary Science Reviews, 18(2):271–278.

Walker, R. I., Cerveny, T. J., and Alt, L. A. (1989). Medical consequences of nuclear warfare, volume 2. Armed Forces Radiobiology Research Institute, Maryland.

Wallinga, J., Bos, A. J., Dorenbos, P., Murray, A. S., and Schokker, J. (2007). A test case for anomalous fading correction in IRSL dating. Quaternary Geochronology, 2(1):216–221.

Waselenko, J. K., MacVittie, T. J., Blakely, W. F., Pesik, N., Wiley, A. L., Dickerson, W. E., Tsu, H., Confer, D. L., Coleman, C. N., Seed, T., et al. (2004). Medical management of the acute radiation syndrome: recommendations of the Strategic National Stockpile Radiation Working Group. Annals of Internal Medicine, 140(12):1037–1051.

Wieser, A., Aragno, D., and Baiankine, S. (2000). Dose reconstruction for workers of Mayak and for the Techa riverside residents. Technical report, Helmholtz Zentrum München, GSF-Forschungszentrum für Umwelt und Gesundheit.

Wilkins, R. C., Romm, H., Kao, T.-C., Awa, A. A., Yoshida, M. A., Livingston, G. K., Jenkins, M. S., Oestreicher, U., Pellmar, T. C., and Prasanna, P. G. (2008). Interlaboratory comparison of the dicentric chromosome assay for radiation biodosimetry in mass casualty events. Radiation Research, 169(5):551–560.

Wintle, A. (1975a). Effects of sample preparation on the thermoluminescence characteristics of calcite. Modern Geology, 5:165–167.

Wintle, A. (1975b). Thermal quenching of thermoluminescence in quartz. Geophysical Journal International, 41(1):107–113.

Wintle, A. (1977a). Detailed study of a thermoluminescent mineral exhibiting anomalous fading. Journal of Luminescence, 15(4):385–393.

Wintle, A. (1977b). Thermoluminescence dating of minerals traps for the unwary. Journal of Electrostatics, 3(1-3):281–288.

Wintle, A. (1978). A thermoluminescence dating study of some quaternary calcite: potential and problems. Canadian Journal of Earth Sciences, 15(12):1977–1986.

Wintle, A. G. (1973). Anomalous fading of thermo-luminescence in mineral samples. Nature, 245(5421):143–144.

Wintle, A. G. (1975c). Thermal quenching of thermoluminescence in quartz. Geophysical Journal of the Royal Astronomical Society, 41(1):107–113.

Woda, C., Fiedler, I., and Spttl, T. (2012). On the use of osl of chip card modules with molding for retrospective and accident dosimetry. Radiation Measurements, 47(11):1068–1073.

Woda, C., Greilich, S., and Beerten, K. (2010). On the OSL curve shape and preheat treatment of electronic components from portable electronic devices. Radiation Measurements, 45(3):746–748.

Wojcik, A., Oestreicher, U., Barrios, L., Vral, A., Terzoudi, G., Ainsbury, E., Rothkamm, K., Trompier, F., and Kulka, U. (2017). The RENEB operational basis: complement of established biodosimetric assays. International Journal of Radiation Biology, 93(1):15–19.

Wu, K., Sun, C., and Shi, Y. (1995). Dosimetric properties of watch glass: A potential practical ESR dosemeter for nuclear accidents. Radiation Protection Dosimetry, 59(3):223–225.

Wypych, G. (2016). Handbook of fillers. Elsevier, Amsterdam.

X-5 Monte Carlo Team, L. A. N. L. (2003). MCNP - version 5, Vol. I: Overview and theory. LA-UR-03-1987. University of California, Los Alamos National Laboratory.

Yamanaka, C., Ikeya, M., and Hara, H. (1993). ESR cavities for in vivo dosimetry of tooth enamel. Applied Radiation and Isotopes, 44(1):IN3–80.

Yan, Y., Xu, W., and Tsai, P. P. (2015). Determination of mineral content in polymelt nonwoven fabrics. The Journal of The Textile Institute, 106(9):919–924.

Yotaro, H., Seiji, A., Masao, F., Naoto, K., and Kenji, I. (2014). The 2011 Fukushima Nuclear Power Plant Accident: How and Why It Happened. Woodhead Publishing Series in Energy. Woodhead Publishing, Cambridge, 1st edition.

Yukihara, E., Whitley, V., Polf, J., Klein, D., McKeever, S., Akselrod, A., and Akselrod, M. (2003). The effects of deep trap population on the thermoluminescence of Al_2O_3:C. Radiation Measurements, 37(6):627–638.

Yukihara, E. G. and McKeever, S. W. (2011). Optically stimulated luminescence: fundamentals and applications. John Wiley & Sons, New York.

Zdravkova, M., Vanhaelewyn, G., Callens, F., Gallez, B., and Debuyst, R. (2005). Multi-frequency electron paramagnetic resonance study of irradiated human finger phalanxes. Spectrochimica Acta Part A: Molecular and Biomolecular Spectroscopy, 61(13):3131–3138.

Zdravkova, M., Wieser, A., El-Faramawy, N., Ivanov, D., Gallez, B., and Debuyst, R. (2003). An in vitro L-band EPR study with whole human teeth in a surface coil resonator. Radiation Measurements, 37(4):347–353.

Zhu, R. and Young, R. H. (2005). Fire-retardant fabric with improved tear, cut, and abrasion resistance. US Patent 6,840,288.